Atomic Energy Control Board
P.O. Box 1046
Ottawa, Canada
K1P 5S9

Commission de contrôle de l'énergie atomique
C.P. 1046
Ottawa, Canada
K1P 5S9

INFO-0412

INTERNATIONAL PIPING INTEGRITY RESEARCH GROUP (IPIRG) PROGRAM FINAL REPORT

(AECB Project No. 2.111.1)

by

R. Schmidt, G. Wilkowski, P. Scott,
R. Olson, C. Marschall,
P. Vieth, and D. Paul

BATTELLE

Published April 1992

Canada

Research report

92-04393/

This report is a work prepared for the United States Government by Battelle. In no event shall either the United States Government or Battelle have any responsibility or liability for any consequences of any use, misuse, inability to use, or reliance upon the information contained herein, nor does either warrant or otherwise represent in any way the accuracy, adequacy, efficacy, or applicability of the contents hereof.

INTERNATIONAL PIPING INTEGRITY RESEARCH GROUP PROGRAMME — FINAL REPORT

A report prepared by R. Schmidt et al., Battelle, Columbus, Ohio, U.S.A., under an international group programme managed by the USNRC, and in which Canada (AECB and Ontario Hydro) was a participant.

ABSTRACT

This is the final report of the International Piping Integrity Research Group (IPIRG) Programme. The IPIRG Programme was an international group programme managed by the U.S. Nuclear Regulatory Commission and funded by a consortium of organizations from nine nations : Canada, France, Italy, Japan, Sweden, Switzerland, Taiwan, the United Kingdom, and the United States.

The objective of the programme was to develop data needed to verify engineering methods for assessing the integrity of nuclear power plant piping that contains circumferential defects. The primary focus was an experimental task that investigated the behaviour of circumferentially flawed piping and piping systems to high-rate loading typical of seismic events.

To accomplish these objectives a unique pipe loop test facility was designed and constructed. The pipe system was an expansion loop with over 30 m of 406-mm diameter pipe and five long radius elbows. Five experiments on flawed piping were conducted to failure in this facility with dynamic excitation.

The report: (1) provides background information on leak-before-break and flaw evaluation procedures in piping; (2) summarizes the technical results of the programme; (3) gives a relatively detailed assessment of the results from the various pipe fracture experiments and complementary analyses, and (4) summarizes the advances in the state-of-the-art of pipe fracture technology resulting from the IPIRG Program.

RÉSUMÉ

Voici le rapport final du programme du Groupe international de recherche sur l'intégrité des canalisations (International Piping Integrity Research Group — IPIRG) administré par la Nuclear Regulatory Commission des États-Unis et financé par un groupement d'organismes de neuf pays : le Canada, les États-Unis, la France, l'Italie, le Japon, le Royaume-Uni, la Suède, la Suisse et Taïwan.

Le programme avait pour but de mettre au point les données nécessaires pour vérifier les techniques utilisées par les ingénieurs pour évaluer l'intégrité des canalisations des centrales nucléaires, qui comportent des défauts circonférentiels. On a d'abord procédé à une expérience pour étudier le comportement des canalisations ayant des défauts circonférentiels et celui des systèmes de tuyauterie soumis à de forts débits comme dans le cas de séismes.

Pour atteindre ces objectifs, on a conçu et construit une installation d'essai spéciale constituée d'une boucle de dilatation de 30 m de canalisations de 406 mm de diamètre et de cinq coudes

à grand rayon. On a effectué cinq expériences jusqu'à la rupture des canalisations défectueuses en les soumettant à l' excitation dynamique.

Le rapport : (1) fournit des données de base sur les fuites avant la rupture des canalisations et sur l'évaluation des défauts; (2) résume les résultats techniques du programme; (3) évalue de façon assez détaillée les résultats des diverses expériences de fracture de canalisations et des analyses complémentaires et (4) résume les progrès accomplis par le programme IPIRG dans les techniques de pointe des fractures de canalisations.

DISCLAIMER

The Atomic Energy Control Board is not responsible for the accuracy of the statements made or opinions expressed in this publication and neither the Board nor the author assume liability with respect to any damage or loss incurred as a result of the use made of the information contained in this publication.

CONTENTS

Page

ABSTRACT iii
LIST OF FIGURES viii
LIST OF TABLES xxi
ACKNOWLEDGMENTS xxv
LIST OF DELIVERABLES xxvii
NOMENCLATURE xxxi
GLOSSARY OF TERMS xliii
EXECUTIVE SUMMARY 1

1.0 INTRODUCTION 1-1
  1.1 Historical Perspective 1-1
    1.1.1 Material Characterization Data 1-1
    1.1.2 Pipe Fracture Data 1-2
    1.1.3 Pipe Fracture Analyses 1-5
    1.1.4 Leak-Rate Estimation Analyses 1-7
    1.1.5 Other Relevant Piping Integrity Research Programs 1-7
  1.2 Why Do We Need Pipe Fracture Evaluations? 1-7
  1.3 Why Did We Need IPIRG? 1-8
  1.4 Task Structure of IPIRG Program 1-10
    1.4.1 Task 1 Leak-Before-Break Under Simulated Seismic/Dynamic Stresses 1-11
    1.4.2 Task 2 Experimental Pipe Fracture and Pipe Material Property Data Base Development 1-11
    1.4.3 Task 3 Fracture of Piping Containing High Energy Fluids 1-11
    1.4.4 Task 4 Resolution of Unresolved Issues from the USNRC Degraded Piping Program and IPIRG Research Tasks 1-11
    1.4.5 Task 5 Information Exchange Seminars and Program Administration 1-12
  1.5 IPIRG Organizational Structure and Funding 1-12
  1.6 Structure of Final Report 1-12
  1.7 References 1-13

2.0 SUMMARY OF TECHNICAL RESULTS 2-1
  2.1 Leak-Before-Break Verification Under Simulated Seismic/Dynamic Stresses - Task 1.0 2-1
    2.1.1 Stability of Cracked Pipe Under Seismic/Dynamic Displacement-Controlled Stresses - Subtask 1.2 2-3
    2.1.2 Stability of Cracked Pipe Under Inertial Stresses - Subtask 1.1 2-9
    2.1.3 Crack Stability in a Representative Piping System Under Combined Inertial and Seismic/Dynamic Displacement-Controlled Stresses - Subtask 1.3 2-15
    2.1.4 Material Characterization of Task 1.0 Materials 2-31

2.2 Experimental Pipe Fracture and Pipe Material Property Data Base Development - Task 2.0 2-37
2.2.1 Material Property Data Base - Subtask 2.1 2-37
2.2.2 Pipe Fracture Data Base - Subtask 2.2 2-38
2.3 Fracture of Piping Containing High Energy Fluids - Task 3.0 2-38
2.4 Resolution of Unresolved Issues from the USNRC Degraded Piping Program and IPIRG Tasks - Task 4.0 . 2-38
2.4.1 Leak-Rate Estimation Modeling - Subtask 4.1 2-39
2.4.2 Disposal of Contaminated Pipe - Subtask 4.2 2-41
2.4.3 Japanese 30-Inch Diameter Quasi-Static Pipe Experiments - Subtask 4.3 2-41
2.4.4 Compression Tests on Pipe Steels - Subtask 4.4 2-44
2.4.5 Detailed FEM Analysis of Stainless Steel Pipe Experiments and J-Estimation Scheme Sensitivity Studies - Subtask 4.5 2-45
2.5 Information Exchange Seminars and Program Administration - Task 5.0 2-45
2.5.1 LBB Seminars 2-45
2.5.2 IPIRG Workshops and Round-Robin Problems 2-45
2.6 References 2-57

3.0 DETAILED ASSESSMENT OF TASK 1 RESULTS 3-1
3.1 Confidence Bounds in Pipe Fracture Data 3-2
3.1.1 Material Variability 3-3
3.1.2 Measurement Uncertainty 3-4
3.1.3 Experimental Technique 3-8
3.1.4 Summary 3-9
3.2 Fracture Analysis Predictions of Maximum Stress 3-10
3.2.1 Net-Section-Collapse 3-10
3.2.2 Dimensionless Plastic-Zone Parameter 3-12
3.2.3 J-Estimation Schemes 3-14
3.3 ASME Code and R6 Calculations of Maximum Stress 3-18
3.3.1 ASME Code Calculations 3-19
3.3.2 R6 Analysis 3-28
3.4 J-R Curves from Specimens and Pipe Experiments . . . 3-37
3.4.1 Through-Wall-Cracked Pipe Experiments 3-39
3.4.2 Surface-Cracked Pipe Experiments 3-40
3.5 Examination of Rotation Data at Crack Initiation and Maximum Load 3-42
3.6 Dynamic Finite Element Analyses of Pipe System Experiments 3-43
3.6.1 Elastic Stress Analyses 3-43
3.6.2 Predictions of Dynamic Pipe System Response - Cracked and Uncracked 3-45

3.7 Predictions of Fracture Instability 3-50
  3.7.1 Experimentally Observed Instability Behavior 3-51
  3.7.2 Instability Predictions 3-52
  3.7.3 Assessment of Stability Analyses 3-53
  3.7.4 Discussion 3-53
3.8 Integration of IPIRG Results and Past Quasi-Static Pipe Fracture Program Results 3-55
  3.8.1 Discussion on Quasi-Static Versus Dynamic Loading 3-55
  3.8.2 Monotonic Versus Cyclic Loading 3-57
  3.8.3 Inertial Versus Displacement-Controlled Loading 3-58
  3.8.4 Dynamic Pipe System Experiments Versus Quasi-Static Experiments 3-60
  3.8.5 Consistency Between Material Characterization, Separate Effects Pipe Fracture Experiments, and Pipe System Experiments 3-62
3.9 References 3-64

4.0 ADVANCES OF TECHNOLOGY AND CONCLUSIONS 4-1
4.1 Basic Questions Addressed by IPIRG 4-1
  4.1.1 Are Seismic Effects on Flawed Piping Correctly Accounted for by Current Fracture Methods? 4-2
  4.1.2 Are the use of elastic stress analysis, peak seismic stress, and quasi-static fracture methods adequate in analyzing seismic response of flawed piping? 4-4
  4.1.3 How do Inertial and Displacement-Controlled Loads Affect Fracture Stability? . 4-5
  4.1.4 Is the DEGB a Plausible Result of Seismic Loading? 4-5
4.2 Summary 4-6
  4.2.1 Material Characterization 4-6
  4.2.2 Effects of Dynamic and Cyclic Loading in Inertial and Displacement Controlled Experiments 4-7
  4.2.3 Pipe System Experiments 4-8
  4.2.4 Analytical Considerations 4-9
4.3 References 4-10

LIST OF FIGURES

Page

Figure 1.1. GE/EPRI dynamic pipe test, system schematic, Ref. 1.13. 1-17

Figure 1.2. An experimental setup for induced transient bending stresses in the dynamic pipe fracture experiments in Ref. 1.14 1-18

Figure 1.3. Change in dynamic moments at crack location due to increasing through-wall circumferential crack size. (Same applied blowdown loads in each experiment, from Ref. 1.14.) 1-18

Figure 1.4. Schematic setup of JAERI vibration test, from Ref. 1.16. 1-19

Figure 1.5. Comparison between applied maximum bending moment and net-section collapse moment for JAERI experiments, from Ref. 1.16. (Using crack size prior to applied inertial loads.). 1-19

Figure 1.6. STA pipe system for dynamic flawed pipe tests, Ref. 1.17. 1-20

Figure 1.7. Comparison of STA pipe system test failure loads with modified Net-Section-Collapse analyses using flaw size prior to dynamic load, from Ref. 1.17. . . . 1-21

Figure 1.8. Task structure of the IPIRG Program. 1-22

Figure 1.9. Organizations that were members of IPIRG 1-23

Figure 1.10. Contractual structure of IPIRG 1-24

Figure 1.11. Organizational Structure of IPIRG. 1-25

Figure 2.1. Schematic of test apparatus used for reversed bending in Subtask 1.2 2-101

Figure 2.2. Schematic of pipe strongback system used in Degraded Piping Program Experiment 4131-5. 2-102

Figure 2.3. Typical instrumentation layout for Subtask 1.2 experiments. 2-103

Figure 2.4. Schematic of system control logic used for dynamic, reversed loading (shown for R = -1 loading). 2-103

Figure 2.5. Moment versus rotation showing the effect of dynamic monotonic loading for stainless steel. 2-104

Figure 2.6. Moment versus rotation showing the effect of dynamic monotonic loading for carbon steel 2-104

Figure 2.7. Moment versus rotation showing the effect of quasi-static reversed (R = 0) loading for stainless steel. 2-105

Figure 2.8. Moment versus rotation showing the effect of quasi-static reversed (R = 0) loading for carbon steel. 2-105

Figure 2.9. Measured load versus load-line displacement for quasi-static reversed (R = 0) loading (Experiment 1.2-3) showing the cyclic loadings and displacement increments 2-106

Figure 2.10. Moment versus rotation showing the effect of quasi-static fully reversed (R = -1) loading for stainless steel. 2-107

Figure 2.11. Moment versus rotation showing the effect of quasi-static fully reversed (R = -1) loading for carbon steel 2-107

Figure 2.12. Measured load versus load-line displacement for Experiment 1.2-4 2-108

Figure 2.13. Moment versus rotation showing the effect of dynamic fully reversed (R = -1) loading for stainless steel. 2-109

Figure 2.14. Moment versus rotation showing the effect of dynamic cyclic reversed loading for carbon steel . . . 2-109

Figure 2.15. Moment versus rotation for all of the stainless steel pipe fracture experiments performed for IPIRG Subtask 1.2. 2-110

Figure 2.16. Moment versus rotation for all of the carbon steel pipe fracture experiments performed for IPIRG Subtask 1.2. 2-110

Figure 2.17. Conceptual model of Subtask 1.1 experiment 2-111

Figure 2.18. Subtask 1.1 finite element model 2-111

Figure 2.19. Basic spring-slider element. 2-112

Figure 2.20. Sketch of Subtask 1.1 test frame with dimensions of specimen 2-112

Figure 2.21. Plot of envelope of peaks of the moment rotation responses for the two Subtask 1.1 through-wall-cracked pipe experiments 2-113

Figure 2.22. Plot of envelope of peaks of the moment rotation responses for three of the five Subtask 1.1 surface-cracked pipe experiments 2-113

Figure 2.23. The pipe loop test facility. 2-114

Figure 2.24. IPIRG Subtask 1.3 pipe loop geometry 2-115

Figure 2.25. Details of end caps at test specimen used to minimize energy release in the event cracked pipe section severs 2-115

Figure 2.26. Overall photograph of Subtask 1.3 pipe loop test facility 2-116

Figure 2.27. Photograph of large mass which simulates a swing check valve. 2-117

Figure 2.28. Photograph of carriage assembly at actuator. 2-118

Figure 2.29. Photograph of spherical bearing at Node 26 2-119

Figure 2.30. Photograph of hydraulic actuator with integral 7600 lpm (2000 gpm) servo-valve attached 2-120

Figure 2.31. Photograph of piston type hydraulic accumulators with nitrogen storage vessel and water circulation vessel (pressurizer) in background 2-120

Figure 2.32. Modeling of a multilinear load-displacement curve. . . 2-121

Figure 2.33. Nonlinear cracked pipe modeling. 2-122

Figure 2.34. Overall instrumentation layout for Subtask 1.3 2-123

Figure 2.35. Photograph of hydraulic jacks at Node 6 used to infer reaction force 2-124

Figure 2.36. Node 6 hanger load cell details. 2-125

Figure 2.37. Photograph of LVDT-based rotation device used on three stainless steel experiments. 2-126

Figure 2.38. Layout/geometry of rotation device used for the three stainless steel experiments. 2-127

Figure 2.39. Strain gage layout at test section 2-127

Figure 2.40. Pipe instrumentation remote from the crack 2-128

Figure 2.41. Photograph of three orthogonally mounted string potentiometers at Elbow 3 used to calculate pipe displacement data. 2-129

Figure 2.42. Typical locations for video cameras. 2-130

Figure 2.43. Data acquisition and control system for Subtask 1.3 experiments. 2-131

Figure 2.44. Calculated mode shapes using ANSYS for first four natural frequencies of the pipe loop with the actuator as a fixed node 2-132

Figure 2.45. Calculated mode shapes using ANSYS for first two natural frequencies of the pipe loop with the actuator as a free node. 2-133

Figure 2.46. Composite plot of global displacements in x, y, and z directions for Elbow 3 as a function of time from the stainless steel base metal experiment (1.3-3) 2-134

Figure 2.47. Composite plot of global displacements in x, y, and z directions for crack location as a function of time from the stainless steel base metal experiment (1.3-3) 2-134

Figure 2.48. Composite plot of global displacements in x, y, and z directions for Node 21 as a function of time from the stainless steel base metal experiment (1.3-3) 2-135

Figure 2.49. Applied force versus time from the stainless steel base metal experiment (1.3-3). 2-135

Figure 2.50. Actuator displacement versus time from the stainless steel base metal experiment (1.3-3). 2-136

Figure 2.51. Actuator load for the PWR uncracked static push pipe test, Experiment 1.3-1. 2-136

Figure 2.52. Reaction force at Node 6 versus time from the stainless steel base metal experiment (1.3-3). 2-137

Figure 2.53. Node 6 reaction force versus time from the aged cast stainless experiment (1.3-7). 2-137

Figure 2.54. Elbow strain gage locations and numbering system for room temperature uncracked-pipe experiment 2-138

Figure 2.55. Dynamic strain gage rosette data on the top of Elbow 3 from the room temperature uncracked dynamic pipe test, Experiment 1.3-1. 2-139

Figure 2.56. Dynamic strain gage rosette data on the intrados of Elbow 4 from the room temperature uncracked dynamic pipe test, Experiment 1.3-1. 2-139

Figure 2.57. Total moment (using ANSYS static value) from the PWR uncracked static push pipe test, Experiment 1.3-1. 2-140

Figure 2.58. Total moment (using ANSYS static value) from the PWR uncracked dynamic pipe test, Experiment 1.3-1. . . 2-140

Figure 2.59. Dynamic moments at the crack, south end cap, north end cap, and location 1.83 m (6 feet) north of crack from the PWR uncracked dynamic pipe test, Experiment 1.3-1. 2-141

Figure 2.60. Calculated total crack section moment versus time from the carbon steel base metal experiment, (1.3-2). 2-141

Figure 2.61. Total moment at crack section versus time from the carbon steel weld experiment (1.3-4) 2-142

Figure 2.62. Total moment at the crack location as a function of time from the stainless steel base metal experiment (1.3-3) 2-142

Figure 2.63. Total bending moment at the crack location versus time from the stainless steel weld experiment (1.3-5). 2-143

Figure 2.64. Total moment at the cracked section versus time from the aged cast stainless experiment (1.3-7). . . . 2-143

Figure 2.65. Surface crack growth versus time for stainless steel base metal experiment (1.3-3). 2-144

Figure 2.66. Total through-wall crack length (2c) versus time from the stainless steel base metal experiment (1.3-3). 2-144

Figure 2.67. Fracture surface from the carbon steel base metal experiment (1.3-2) 2-145

Figure 2.68. Sketch of fracture surface shown in Figure 2.67 highlighting the arrest/reinitiation lines 2-145

Figure 2.69. Determination of equivalent time to crack initiation for stainless steel pipe with a surface crack (Subtask 1.3). 2-146

Figure 2.70. Engineering stress-strain curves at 288 C (550 F) for a 16-inch diameter A106 Grade B carbon steel pipe (DP2-F29) tested at several different strain rates. 2-147

Figure 2.71. Effect of strain rate on tensile properties of Task 1.0 materials at 288 C (550 F). Strain rates were approximately 10^{-4} s^{-1} for quasi-static tests and 10 s^{-1} for dynamic tests 2-148

Figure 2.72. J-resistance curves for compact specimens from a 16-inch diameter A106 Grade B carbon steel pipe tested at 288 C (550 F). 2-149

Figure 2.73. J-resistance curves for compact specimens from a submerged-arc weld in a 16-inch diameter A106 Grade B carbon steel pipe tested at 288 C (550 F). . . 2-149

Figure 2.74. Effect of displacement rate on crack growth resistance of Task 1.0 materials at 288 C (550 F). Dynamic tests were 2500 to 6000 times faster than quasi-static tests. 2-150

Figure 2.75. Sketch of test specimen showing details of final through-wall-crack geometry. 2-151

Figure 2.76. Comparison of SQUIRT predicted leakage flow rate calculations with the experimental data obtained for the fatigue-generated crack in a girth weld. 2-152

Figure 2.77. Schematic of pipe in load frame using Subtask 4.3 30-inch diameter pipe experiments. 2-153

Figure 2.78. Total load versus load-line displacement data from Experiment 4.3-1 2-154

Figure 2.79. Sketch of crack-opening profile on outside surface after Experiment 4.3-1 2-155

Figure 2.80. Total load versus load-line displacement data from Experiment 4.3-2 (includes displacement from test machine compliance). 2-156

Figure 2.81. Engineering stress-strain curves at 300 C (572 F) for 30-inch diameter Japanese pipe material. 2-156

Figure 2.82. Absorbed energy in Charpy V-notch tests for 30-inch diameter Japanese pipe material. 2-157

Figure 2.83. Deformation J-resistance curves (using ASTM E1152) for 30-inch diameter Japanese pipe material tested at 300 C (572 F) 2-157

Figure 2.84. Comparison of Subtask 4.3 results with Degraded Piping Program experiments and the Dimensionless Plastic-Zone Parameter analysis. 2-158

Figure 2.85. Comparison of predicted loads at crack initiation with experimental results for IPIRG Round-Robin Problem 1. 2-159

Figure 2.86. Battelle comparison of predicted maximum loads, using power-law extrapolated J_D-R curve, with experimental results for IPIRG Round-Robin Problem 1. 2-159

Figure 2.87. Battelle comparison of predicted maximum loads, using linearly extrapolated J_M-R curve, with experimental results for IPIRG Round-Robin Problem 1. 2-160

Figure 2.88. IPIRG member participant predictions of loads at crack initiation compared with experimental loads for IPIRG Round-Robin Problem 1. 2-161

Figure 2.89. IPIRG participants predictions of loads at crack initiation compared with experimental loads for IPIRG Round-Robin Problem 1. 2-161

Figure 2.90. Comparison of NRCPIPE load predictions with experimental data for crack initiation - Round-Robin Problem 2-3. 2-162

Figure 2.91. Comparison of NRCPIPE load predictions with experimental data at maximum moment for Round-Robin Problem 2-3. 2-162

Figure 2.92. Solutions to IPIRG Round-Robin Problem 2-4 2-163

Figure 2.93. Solutions to Round-Robin Problem 3.1a. 2-164

Figure 2.94. Comparison of FEM and experimental load versus load-line-displacement curves for Experiment 1.2-1, Round-Robin Problem 3-1b. 2-165

Figure 2.95. Early finite element predictions by different participants of crack location moment for IPIRG pipe system in Round-Robin Problem 3-2a. 2-166

Figure 2.96. Prediction (using CASTEM 2000) of crack location moment in IPIRG pipe system after analysts meeting (Round-Robin Problem 4-3). 2-167

Figure 2.97. Prediction (using ABAQUS) of crack location moment after analyst meeting (Round-Robin Problem 4-3). . . . 2-167

Figure 2.98. Prediction (using ADLPIPE) of crack location moment after analyst meeting (Round-Robin Problem 4-3). . . . 2-168

Figure 2.99. Prediction (using ANSYS) of crack location moment after analyst meeting (Round-Robin Problem 4-3). . . . 2-168

Figure 2.100. Comparison of moment versus rotation due to the crack, Round-Robin Problem 5-1b. 2-169

Figure 2.101. Comparison of moment versus time predictions (Round-Robin Problem 5-1b) 2-169

Figure 3.1. Semi-analytical approach to investigating the effects of material variability on failure moments. 3-86

Figure 3.2. Effect of material property variation or maximum for a 152-mm diameter x 9.5 mm (6 inch x 0.375 inch) thick pipe using J-estimation schemes. 3-87

Figure 3.3. Effect of material property variation on initiation moment for a 152-mm diameter x 9.5 mm thick (6 inch x 0.375 inch) pipe using J-estimation schemes 3-87

Figure 3.4. Effect of material property variation on maximum moment for a 406-mm diameter x 25.4 mm thick (16 inch x 1.00 inch) pipe using J-estimation schemes. 3-88

Figure 3.5. Effect of material property variation on initiation moment for a 406-mm diameter x 25.4 mm thick (16 inch x 1.000 inch) pipe using J-estimation schemes. 3-88

Figure 3.6. Effect of material property variability on maximum moment for "near replicate" experiments. 3-89

Figure 3.7. Crack initiation from d-c EP data. 3-90

Figure 3.8. Normalized d-c EP at crack Tip A versus load-line displacement for Experiment 1.2-6 showing point of crack initiation using envelop of cyclic data and blunting line method 3-91

Figure 3.9. Normalized d-c EP at crack Tip B versus load-line displacement for Experiment 1.2-10 showing point of crack initiation. 3-91

Figure 3.10. Uncertainty in moment from independent test setups. 3-92

Figure 3.11. Comparison of experimental results with Net-Section-Collapse analysis predictions for the through-wall-cracked pipe experiments (6-inch diameter pipe) 3-93

Figure 3.12. Comparison of experimental results with Net-Section-Collapse analysis predictions for the surface-cracked pipe experiments 3-93

Figure 3.13. Schematic showing comparison of IPIRG pipe fracture data with Degraded Piping Program data using Dimensionless Plastic-Zone Parameter [$\sigma_f = (\sigma_y + \sigma_u)/2$ for all data] 3-94

Figure 3.14. Comparison of experimental results with DPZP analysis predictions for through-wall-cracked pipe experiments (6-inch pipe diameter) 3-95

Figure 3.15. Comparison of experimental results with DPZP analysis predictions for the surface-cracked pipe experiments. 3-95

Figure 3.16. Comparison of experimental results with GE/EPRI J-estimation scheme predictions for the through-wall-cracked pipe experiments. 3-96

Figure 3.17. Pipe geometry of engineering estimate modification of LBB.ENG2 method 3-96

Figure 3.18. Comparison of experimental results with LBB.ENG2 J-estimation scheme predictions for the through-wall-cracked pipe experiments. 3-97

Figure 3.19. Comparison of experimental results with SC.TNP J-estimation scheme predictions for the surface-cracked pipe experiments 3-97

Figure 3.20. Comparison of the experimental results with the ASME IWB-3640 Approach 1 predictions [using S_m(Code)] for the stainless steel surface-cracked-pipe experiments 3-98

Figure 3.21. Comparison of the experimental results with the ASME IWB-3640 Approach 1 predictions [using S_m(Actual)] for the stainless steel surface-cracked-pipe experiments 3-98

Figure 3.22. Comparison of experimental data with IWB-3640 Approach 1 predictions for stainless steel through-wall-cracked pipe experiments using Code values for S_m 3-99

Figure 3.23. Comparison of experimental data with IWB-3640 Approach 1 predictions for stainless steel through-wall-cracked pipe experiments using actual properties as a basis for S_m 3-99

Figure 3.24. Comparison of the experimental results with the ASME IWB-3650 Approach 1 predictions [using S_m(Code)] for the carbon steel surface-cracked-pipe experiments 3-100

Figure 3.25. Comparison of the experimental results with the ASME IWB-3650 Approach 1 predictions [using S_m(Actual)] for the carbon steel surface-cracked-pipe experiments 3-100

Figure 3.26. Comparison of experimental data with IWB-3650 Approach 1 predictions for carbon steel through-wall-cracked pipe experiments using Code values for S_m 3-101

Figure 3.27. Comparison of experimental data with IWB-3650 Approach 1 predictions for carbon steel through-wall-cracked pipe experiments using actual properties as a basis of S_m 3-101

Figure 3.28. Fracture ratios for the stainless steel surface-cracked pipe experiments for the ASME Approach 2 method 3-102

Figure 3.29. Fracture ratios for the stainless steel through-wall-cracked pipe experiments for the ASME Approach 2 method 3-102

Figure 3.30. Fracture ratios for the carbon steel surface-cracked pipe experiments for the ASME Approach 2 method 3-103

Figure 3.31. Fracture ratios for the carbon steel through-wall-cracked pipe experiments for the ASME Approach 2 method. 3-103

Figure 3.32. R6 Option 1 failure analysis diagram 3-104

Figure 3.33. Comparison of the experimental results with the R6 Option 1 predictions (Approach 1) for the through-wall-cracked-pipe experiments. 3-105

Figure 3.34. Comparison of the experimental results with R6 Option 1 predictions (Approach 1) for the surface-cracked-pipe experiments 3-105

Figure 3.35. Fracture ratios for the through-wall-cracked pipe experiments for the R6 Approach 2 method. 3-106

Figure 3.36. Fracture ratios for the surface-cracked pipe experiments for the R6 Approach 2 method. 3-106

Figure 3.37. J-R curves for the A106 Grade B carbon steel pipe fracture experiments using the η-factor approach along with the C(T) specimen data 3-107

Figure 3.38. J-R curves for the TP304 stainless steel pipe fracture experiments using the η-factor approach along with the C(T) specimen data. 3-107

Figure 3.39. Effect of using Experiment 1.3-3 surface-cracked pipe η-factor J_i rather than quasi-static side-grooved C(T) specimen J_i value 3-108

Figure 3.40. Comparison of predicted moment-rotation curves from SC.TNP using C(T) or pipe J-R curves with experimental results 3-108

Figure 3.41. Experimental stress/Net-Section-Collapse stress versus rotation for all Task 1 pipe experiments. 3-109

Figure 3.42. Experimental stress/Net-Section-Collapse stress versus rotation for Task 1 through-wall-cracked pipe experiments ($2c/\pi D \simeq 0.37$). 3-109

Figure 3.43. Experimental stress/Net-Section-Collapse stress versus rotation for Task 1 surface-cracked pipe experiments ($2c/\pi D \simeq 0.5$, $d/t \simeq 0.7$). 3-110

Figure 3.44. Elastic stress analysis concepts 3-110

Figure 3.45. Calculated mode shapes using ANSYS for first four natural frequencies of the pipe loop with the actuator as a fixed node 3-111

Figure 3.46. Calculated mode shapes using ANSYS for first two natural frequencies of the pipe loop with the actuator as a free node. 3-112

Figure 3.47. Comparison of experimental and predicted crack location moment for the uncracked Subtask 1.3 pipe system 3-113

Figure 3.48. Subtask 1.1 inertial test system 3-114

Figure 3.49. Comparison of experiment and analysis for moment versus time plots of Experiment 1.1-3 (SS TWC). The analysis was valid only up to maximum moment . . . 3-115

Figure 3.50. Comparisons of experiment and pretest design analysis for displacements of the inertial mass for Experiment 1.1-3 (SS TWC) 3-116

Figure 3.51. Comparison of experiment and pretest design analysis for moment versus rotation for Experiment 1.1-3 (SS TWC) 3-117

Figure 3.52. Comparison of experiment and analysis for moment versus time plots of Experiment 1.1-2 (CS TWC) 3-118

Figure 3.53. Comparison of experiment and analysis for displacements of the inertial mass for Experiment 1.1-2 (CS TWC). 3-119

Figure 3.54. Comparison of experiment and analysis for rotations at the crack plane for Experiment 1.1-2 (CS TWC) . . . 3-120

Figure 3.55. Comparison of pre-test prediction of cracked section moment to carbon steel base metal experiment (1.3-2) results. (Analysis with 66 percent deep flaw.) 3-121

Figure 3.56. Comparison of post-test prediction of cracked section moment for the carbon steel base metal experiment (1.3-2). Analysis with 75 percent deep flaw; actual flaw depth 72.7 percent deep. 3-121

Figure 3.57. Actuator force for the carbon steel base metal experiment (1.3-2), analysis with 75 percent deep flaw 3-122

Figure 3.58. Comparison of moment-rotation curves of SC.TNP analysis to the stainless steel base metal experiment (1.3-3) 3-122

Figure 3.59. Crack section moment for the stainless steel base metal experiment (1.3-3). 3-123

Figure 3.60. Displacement for the stainless steel base metal experiment (1.3-3) 3-123

Figure 3.61. The effect of through-wall crack jet thrust forces on IPIRG Subtask 1.3 system response. 3-124

Figure 3.62. Predicted through-wall critical crack length based on Net-Section-Collapse analysis for axial tension stress as a function of the ratio of the crack length to pipe circumference 3-124

Figure 3.63. Photograph of fracture from aged cast stainless experiment (Experiment 1.3-7) 3-125

Figure 3.64. Net-Section-Collapse analyses predictions, with and without considering induced bending, as a function of the ratio of the through-wall crack length to the pipe circumference 3-125

Figure 3.65. Measured load versus load-line displacement for quasi-static reversed (R = 0) loading (Experiment 1.2-3) showing the four different cyclic displacement increments used 3-126

Figure 3.66. Crack-tip-opening-angle data from Subtask 1.2 stainless steel pipe experiments 3-126

Figure 3.67. Comparison of the normalized load-carrying capacities for the inertial and displacement-controlled carbon steel through-wall-cracked pipe experiments 3-127

Figure 3.68. Effective load ratio as a function of cycle number for Experiment 1.1-2 3-127

Figure 3.69. Comparison of the normalized load-carrying capacities for the inertial and displacement-controlled carbon steel surface-cracked pipe experiments. 3-128

Figure 3.70. Comparison of the normalized load-carrying capacities for the inertial and displacement-controlled stainless steel through-wall-cracked pipe experiments 3-128

Figure 3.71. Comparison of the normalized load-carrying capacities for the inertial and displacement-controlled stainless steel surface-cracked-pipe experiments. 3-129

Figure 3.72. Comparison of the normalized maximum experimental stress for the Subtask 1.3 pipe system experiments with the normalized maximum experimental stress for the companion quasi-static pipe experiments. 3-129

LIST OF TABLES

Page

Table 2.1 Test matrix of pipe fracture experiments for Subtask 1.2 2-62

Table 2.2 Summary of results for Subtask 1.2 stainless steel pipe experiments. 2-63

Table 2.3 Summary of results for Subtask 1.2 carbon steel pipe experiments 2-65

Table 2.4 Test matrix for Subtask 1.1 2-67

Table 2.5 Summary of results from Subtask 1.1 cracked pipe experiments 2-68

Table 2.6 Test matrix for Subtask 1.3 2-69

Table 2.7 Total list of instrumentation used during the Subtask 1.3 pipe system experiments 2-70

Table 2.8 Summary of first natural frequency measurements for Experiment 1.3-1. 2-71

Table 2.9 Summary of higher mode frequencies for Experiment 1.3-1 2-72

Table 2.10 Key results from the five Subtask 1.3 cracked pipe system experiments. 2-73

Table 2.11 Crack length measurements from closure marks on fracture surface from carbon steel base metal Experiment 1.3-2. 2-74

Table 2.12 Description of Task 1.0 pipes subjected to material characterization tests. 2-75

Table 2.13 Chemical composition of Task 1.0 pipes. 2-76

Table 2.14 Actual loading rates in tests of C(T) specimens 2-77

Table 2.15 Summary table of IPIRG pipe fracture experiments. 2-78

Table 2.16 Chemical composition of 30-inch diameter Japanese pipe in weight percent. 2-80

Table 2.17 List of IPIRG Round-Robin Problems. 2-81

Table 2.18 Round-Robin Problem 2-1 crack initiation results. 2-82

Table 2.19 Round-Robin Problem 2-1 maximum moment results. 2-83

Table 2.20 Summary of results from Round-Robin Problem 2-3 2-84

Table 2.21 Natural frequency calculations for IPIRG Round-Robin Problem 2.4-2 2-85

Table 2.22 Summary of Round-Robin Problem 5-1 predictions of initiation moments. 2-86

Table 2.23 Summary of Round-Robin Problem 5-1 predictions of maximum moments 2-87

Table 2.24 Summary of methods for Round-Robin Problem 6-1. 2-88

Table 2.25 Summary of numerical results for Round-Robin Problem 6-1 2-89

Table 2.26 Comparison of methods for Round-Robin Problem 6-1 2-90

Table 2.27 Summary of methods for Round-Robin Problem 6-2. 2-91

Table 2.28 Summary of numerical results for Round-Robin Problem 6-2 2-92

Table 2.29 Comparison of methods for Round-Robin Problem 6-2 2-93

Table 2.30 Summary of methods for Round-Robin Problem 6-3. 2-94

Table 2.31 Summary of numerical results for Round-Robin Problem 6-3 2-95

Table 2.32 Comparison of methods for Round-Robin Problem 6-3 2-96

Table 2.33 Summary of methods for Round-Robin Problem 6-4. 2-97

Table 2.34 Summary of numerical results for Round-Robin Problem 6-4 2-98

Table 2.35 Comparison of methods for Round-Robin Problem 6-4 2-100

Table 3.1 Analysis matrix for TP304 material variability investigation 3-69

Table 3.2 Analysis matrix for A106B material variability investigation 3-70

Table 3.3 "Near Replicate" pipe test data used to assess the effects of material variability on confidence bounds for bending moments 3-71

Table 3.4 Measurement uncertainty limits in maximum moments 3-72

Table 3.5 Independent test setups used for evaluating confidence bounds. 3-73

Table 3.6 Comparison of experimental results from through-wall-cracked pipe experiments with predictions from various analytical methods 3-74

Table 3.7 Comparison of experimental results from surface-cracked pipe experiments with predictions from various analytical methods. 3-75

Table 3.8 ASME analyses of IPIRG Task 1 and related Degraded Piping Program experiments. 3-76

Table 3.9 R6 Option 1 analyses of IPIRG Task 1 experiments and related Degraded Piping Program experiments 3-78

Table 3.10 Comparison of J_i values from Subtask 1.3 surface cracked pipe experiments and C(T) specimen tests. 3-79

Table 3.11 Rotation and normalized moment at initiation and maximum moment. 3-80

Table 3.12 Elastic stress analysis results for Subtask 1.1 inertially loaded pipe experiments. 3-81

Table 3.13 Elastic stress analysis results for Subtask 1.3 pipe system experiments. 3-82

Table 3.14 Summary of IPIRG Subtask 1.3 pipe system natural frequency comparisons 3-83

Table 3.15 Summary of Subtask 1.3 stability predictions. 3-84

Table 3.16 Comparison of predicted crack arrest lengths$^{(a)}$ from the Energy Balance Stability criterion with experimental results. 3-85

ACKNOWLEDGMENTS

The IPIRG Program is an international group program being coordinated by the U.S. Nuclear Regulatory Commission's Materials Engineering Branch of the Office of Nuclear Regulatory Research under Contract No. NRC-04-86-106 to Battelle. Mr. M. Mayfield is the USNRC program manager. Dr. R. Schmidt is the Battelle program manager.

The members of the IPIRG Program and their representatives to the IPIRG Technical Advisory Group (TAG) are:

Canada	
- AECB(a)	Dr. Ali Omar(b) and Dr. B. Jarman
- Ontario Hydro	Mr. M. Kozluk
France	
- CEA(a)	Mr. Ph. Jamet(b)
- EDF	Mr. C. Faidy
- Framatome	Dr. S. Bhandari
Italy	
- ENEA(a)	Dr. P. Milella(b)
Japan	
- CRIEPI(a,c)	Dr. K. Kashima(b)
Republic of China	
- AIT(a)	Mr. Y. H. Cheng(b), Taiwan Power Co.
- ROC-AEC	Mr. R. Y. Wu
- INER	Dr. K. Ting
Sweden	
- SKi(a)	Dr. B. Brickstad(b), AB Statens Anläggningsprovning
Switzerland	
- HSK(a)	Mr. D. H. Njo(b)
- Kernkraftwerk Leibstadt	Dr. D. Burns

(a) Contractual organization.
(b) TAG representative.
(c) Other Japanese members include, Mitsubishi, Toshiba, Hitachi, IHI, and 13 electric utilities.

United Kingdom	
- Nuclear Electric(a)	Dr. B. J. Darlaston(b)
United States	
- U. S. NRC-RES(a)	Mr. M. Mayfield(b)
- U. S. NRC-NRR	Mr. K. Wichman(b)
- EPRI(a)	Mr. J. Gilman(b)

We would like to express our appreciation for the support and interest of the IPIRG members in this program.

Researchers and technicians at Battelle who also contributed to this work are: R. Francini, N. Frey, R. Gertler, N. Ghadiali, D. Guerrieri, D. Hayes, P. Held, G. Kramer, J. Kramer, P. Krishnaswamy, M. Landow, J. Meyer, J. Morris, M. Oliver, D. Rider, M. Rosenfeld, J. Ryan, D. Shoemaker, D. Utz, P. Vieth, M. Wilson, and J. Wood. Quality assurance review was provided by E. Fromm, B. White, and D. Lozier. Videotape service of C. Wales is recognized. The important contributions of B. Saffell, who managed the IPIRG program when this work began, are also recognized. Additional thanks go to C. Baxley, J. Anthony, R. Chaffin, T. Goodrich, and the rest of the Battelle machine shop for their diligence and efforts in all that was asked of them.

A special note of appreciation is extended to Mrs. B. Blanton, the IPIRG Program Secretary. Her professional dedication and commitment to quality and hard work has been a key factor in the success of this program.

(a) Contractual organization.
(b) TAG representative.

IPIRG LIST OF PROGRAM DELIVERABLES

Quick-Look Reports and Data Record Books(a)

Experiment No.	DRB No.	DRB Date	QL Date
1.1-1	---	---	---
1.1-2 (Revised)	1.1.7.1	8/05/91	8/12/88
1.1-3 (Revised)	1.1.7.2	6/05/91	6/14/88
1.1-4 (Revised)	1.2.7.1	6/18/91	3/28/89
1.1-5 (Revised)	1.2.7.2	6/05/91	6/29/88
1.1-6 (Revised)	1.2.7.3	6/05/91	3/31/89
1.1-7	1.2.9.1	6/28/91	---
1.1-8	1.2.7.4	6/28/91	---
1.1-9	1.2.3.18	6/28/91	---
1.2-1	1.1.4.1	9/18/87	6/18/87
1.2-2	1.1.5.1	2/08/88	12/01/87
1.2-3	1.1.5.2	4/27/88	11/05/87
1.2-4	1.1.5.3	6/14/88	4/28/88
1.2-5	1.1.5.4	10/14/88	9/09/88
1.2-6	1.1.6.1	6/23/89	4/24/89
1.2-7	1.1.1.18	2/16/89	9/22/88
1.2-8	1.1.4.2	11/18/88	10/05/88
1.2-9	1.1.6.2	6/20/91	---

Experiment No.	DRB No.	DRB Date	QL Date
1.2-10	1.1.6.3	6/18/91	---
1.2-11	1.1.4.3	6/18/91	---
1.2-12	1.1.4.4	6/18/91	---
1.3-1	1.2.8.1	2/28/90	12/29/89
1.3-2	1.2.8.2	1/31/90	11/17/89
1.3-3	1.2.8.3	8/15/90	4/13/90
1.3-4	1.2.8.4	4/06/90	1/11/90
1.3-5	1.2.8.5	8/31/90	5/10/90
1.3-7	1.2.8.7	12/10/90	8/20/90
4.3-1	1.1.1.19	3/28/89	---
4.3-2	1.2.3.14	3/28/89	---
All DP^2II DRB's			

(a) With floppy disks.

TAG Meetings

TAG Meeting No.	Dates	Place	Meeting Handout	Minutes (Date)
1	Nov. 3-4, 1986	Columbus, Ohio	Yes	Dec. 12, 1986
2	May 11-12, 1987	Tokyo, Japan	Yes	June 16, 1987
3	Nov. 2-4, 1987	Columbus, Ohio	Yes	Dec. 14, 1987
4	May 2-4, 1988	Paris, France	Yes	June 17, 1988
5	Oct. 31-Nov. 1, 1988	Columbus, Ohio	Yes	Dec. 16, 1988
6	May 8-11, 1989	Taipei, Taiwan	Yes	June 14, 1989
7	Oct. 30-Nov. 1, 1989	Columbus, Ohio	Yes	Dec. 21, 1989
8	May 15-17, 1990	Stockholm, Sweden	Yes	June 14, 1990
9	Oct. 29-31, 1990	Columbus, Ohio	Yes	Dec. 05, 1990
10	May 29-31, 1991	Columbus, Ohio	Yes	July 9, 1991

Workshop Proceedings

Workshop No.	Dates	Assoc. TAG Meeting	Proceedings Date
1	Nov. 1987 May 9-10, 1988	3rd 4th	Nov. 1987 May 1988
2	Nov. 2, 1988	5th	Dec. 1988
3	May 10, 1989	6th	June 1989
4	Nov. 1, 1989	7th	Nov. 1989
5	May 17, 1990	8th	Sept. 1990
6	Oct. 31, 1990	9th	Nov. 1990

LBB Seminars

NUREG/CR No.	Place	Meeting Date	Proceedings Data
0077	Columbus, Ohio	October 1985	June 1986
0092	Tokyo, Japan	May 1987	March 1988
0109	Taipei, Taiwan	May 1989	February 1990

Reports

Description	Date	Authors	Revised Date	Authors
Monthly (60)				
1.1 Final	Oct. 12, 1989	M. Wilson, C. Marschall, R. Olson, R. Schmidt, G. Wilkowski	July 10, 1991	P. Scott, M. Wilson, R. Olson, C. Marschall, R. Schmidt, G. Wilkowski
1.2 Final	Sept. 29, 1989	P. Vieth, G. Kramer, C. Marschall, G. Wilkowski	July 10, 1991	P. Vieth, G. Kramer, C. Marschall, R. Francini, G. Wilkowski
1.3 Final	April 4, 1991	P. Scott, R. Olson, G. Wilkowski, C. Marschall, R. Schmidt		
4.5 Final	Jan. 31, 1990	G. Wilkowski, F. Brust	---	---
Program Final	May 10, 1991 (Sec. 1&2) May 17, 1991 (Sec. 3) May 29, 1991 (Sec. 4)	R. Schmidt, G. Wilkowski, P. Scott, R. Olson, D. Paul, C. Marschall	July 10, 1991	R. Schmidt, G. Wilkowski, P. Scott, R. Olson, C. Marschall, P. Vieth, D. Paul
DP^{3}II Final Report, 7 Semiannuals, and 10 Topicals				

Topical Reports

- "IPIRG Subtask 1.1 and 1.3 Design Report", R. Olson, M. Nakagaki, P. Scott, and M. Wilson, October 5, 1987.
- "Effect of Cyclic Loads on Ductile Fracture Resistance", C. Marschall, M. Nakagaki, F. Brust, G. Kramer, and G. Wilkowski, October 15, 1987.
- "Loading Rate Effects on Strength and Fracture Toughness of Pipe Steels Used in Task 1 of the IPIRG Program", C. W. Marschall, M. P. Landow, and G. M. Wilkowski, December 22, 1989.
- "Uncertainties in Leak-Rate Estimation Methods", D. D. Paul and G. M. Wilkowski, December 29, 1989.
- "Significance of IPIRG Subtask 1.1 and 1.2 Results", G. Wilkowski, J. Ahmad, R. Olson, and R. Schmidt, April 6, 1990.
- "Evaluation and Refinement of Leak-Rate Estimation Models", D. Paul, J. Ahmad, P. Scott, L. Flanigan, and G. Wilkowski, March 1, 1991.

Technical Papers

- "Effect of Cyclic Loads on Ductile Fracture Resistance", C. W. Marschall and G. M. Wilkowski, ASTM STP PVP Vol. 166, July 1989.
- "Unusual Effect of Periodic Unloadings on Behavior of Fracture Toughness Specimens", C. W. Marschall, M. P. Landow, and P. R. Held, ASTM STP PVP Vol. 166, July 1989.
- "Effect of Dynamic Strain Aging on Fracture Resistance of Carbon Steels Operating at Light Water Reactor Temperatures", C. Marschall, M. Landow, G. Wilkowski, ASTM STP 1074, pp 339-360, 1990.
- SMiRT-11 Paper, "The International Piping Integrity Research Group (IPIRG) Program--An Overview", R. Schmidt, G. Wilkowski, and M. Mayfield, August, 1991.

Videotapes

- "IPIRG 1.3-2 Carbon Steel Base Metal", October 1, 1989.
- "IPIRG Subtasks 1.2 & 1.1 Final Composite Video", December, 1989.
- "Experiments Conducted for the International Piping Integrity Research Group at Battelle, April 20, 1990.
- "IPIRG 1.3 Facility Construction, Boundary Conditions, Instrumentation", June 14, 1990.
- "IPIRG 1.3-7 Aged Cast Stainless Steel Experiment and Slow Motion", August 2, 1990.

Miscellaneous

- MEA PIFRAC Summary Document and eight 5-1/4 inch floppy disks, May, 1988.
- MEA PIFRAC.2 Summary Document and nine 5-1/4 inch floppy disks, November 1, 1989.
- NRCPIPE Code Version 1.4D manual and two diskettes, July 31, 1989.
- SQUIRT2 Code Version 1.1 (two diskettes), October 31, 1989.
- Slides and photographs of IPIRG experimental results, various TAG meetings.

NOMENCLATURE

1. SYMBOLS

a	Amplitude parameter from Subtask 1.1 forcing function
a	Half crack length at mean radius
A	Accelerations
A	Parameter in Z-factor expression in IWB-3650
A	Maximum amplitude of sinusoidal displacement for Subtask 1.3 forcing function
a_e	Plastic-zone size connection to half crack length in GE/EPRI method
b	Subtask 1.3 forcing function parameter
b	Half of the pipe circumference (πR)
c	Half crack length
c	Distance from neutral bending axis
c	Statistically based parameter from plastic zone size screening criteria
C	Test System Compliance
C	Circumferential
D	Pipe diameter
D	Nominal pipe diameter
d	Crack depth
d	Displacement
D_o	Outside pipe diameter
E	Elastic modulus
F_{slide}	Limiting force in spring-slider element
F_t	Correction factor for temperature for moment rotation curves

F_{T1}, F_{T2}, F_{T3}	Forces used in modeling multilinear crack behavior
F_1	Elastic f-function in GE/EPRI method
G	Modulus of rigidity
GE	General Electric
h_1	Function in EPRI/GE J-estimation scheme to calculate plastic contribution of J
h_1	Function in SC.TNP and SC.TKP J-estimation schemes
I	Area moment of inertia
J	J-integral fracture parameter
J_D	J based on deformation theory
J_e	Elastic component of J
J_i	J at crack initiation
J_{Ic}	Plane strain J at crack initiation by ASTM E813
J_m	Modified form of J
J_p	Plastic component of J
k	Ramberg-Osgood parameter
K	LEFM stress intensity factor fracture parameter
K_I	Applied linear elastic stress intensity factor
K_{I_b}	Bending component of K_I
K_{Im}	Membrane component of K_I
K_r	Ratio of K_I to $K_r(a)$ from R6 analysis
$K_r(a)$	Toughness of the material as a function of crack growth in terms of K
L	Longitudinal
L_r	Load ratio in R6 analysis
M	Moment
M	Mass

M( )	Net-section-collapse moment for a given set of parameters
M'	Moment from moment-rotation curve corrected for differences in temperature, flaw size, and pipe size
M_b	Net-section-collapse analysis calculated moment at failure for pure bending
M_{b+p}	Net-section-collapse analysis calculated moment at failure for combined pressure and bending
M_{eq}	Equivalent bending moment
M_{exp}	Experimental moment
M_o	Limit moment for a cracked pipe under pure bending
$M_{(SP\ el.)}$	Moment from static push analysis
$M_{(Tot.\ el.)}$	Calculated elastic moment at crack section at time of maximum moment from the experiment
$M_{(Tot.\ exp.)}$	Experimental maximum moment
n	Ramberg-Osgood parameter
P	Pressure
P	Total failure stress
P_b	Bending stress
P_e	Thermal expansion stress
P_m	Membrane stress
P_{NSC}	Net-section-collapse predicted tension and bending stress
P_o	Reference stress in J-estimation schemes
R	Stress or load ratio, i.e., minimum stress (load)/maximum stress (load)
r	Pipe radius
R_i	Inside pipe radius
R_m	Mean pipe radius
R_m/t	Mean pipe radius to wall thickness ratio
R_o	Outside pipe radius

R/t	Pipe radius to wall thickness ratio
S	System 1.3 forcing function ramp parameter
SF	Safety factor
S_m	ASME code design stress intensity
S_m(Actual)	S_m based on measured tensile properties
S_m(Code)	S_m based on code properties
SMAW	Shielded-metal-arc weld
SMTS	Specified minimum tensile strength
SMYS	Specified minimum yield strength
SQUIRT	Leak rate computer code - Seepage Quantification for Upsets In Reactor Tubes
S_r	Stress ratio in R6 analysis
S_u	ASME Section III ultimate strength
S_y	ASME Section III yield strength
t	Time
t	Pipe wall thickness
T	Tearing modulus
T*	An integral parameter based on incremental theory of plasticity
T_{app}	Applied tearing modulus
t_e	Reduced wall thickness representation of cracked section in LBB.ENG2 method
T_{mat}	Tearing modulus of the material
t_{wall}	Pipe wall thickness
U_x	Actuator displacement in X direction (Subtask 1.3)
U_y	Actuator displacement in Y direction (Subtask 1.1)
Z	Stress multipliers in Section XI to account for low toughness flux welds

α	Ramberg-Osgood parameter
β	Angle from bottom of pipe to neutral bending axis
δ	Load-line displacement
δ	Damping logarithmic decrement
δ_{ram}	Displacement of the actuator
Δa	Change in crack length or depth, i.e., crack growth
Δa_{cyclic}	Crack growth due to cyclic loading
Δa_{mono}	Crack growth due to monotonic loading
ΔJ	Change in J
ΔM	Moment reduction factor for adjusting moment-rotation curve
ΔW	Total uncertainty
ϵ	Strain
ϵ_{Bot}	Longitudinal strain at the bottom of the pipe
ϵ_o	Ramberg-Osgood parameter
ϵ_{Top}	Longitudinal strain at the top of the pipe
ν	Poisson's ratio
η-Factor	General analytical procedure where the fracture resistance is calculated using experimental load displacement and crack growth data
Φ	Pipe rotation
Φ_c	Critical kink angle
Φ_{CI}	Rotation at crack initiation
Φ_{PI}	Plastic increment rotation
Φ_p^c	Plastic component of the rotation due to the crack
σ	Stress
σ_b	Bending stress
σ_{bNSC}	Net-section-collapse predicted bending stress

σ_{Bot}	Longitudinal stress at the bottom of the pipe
$\sigma_{(expt.\ bend\ \sigma)}$	Experimental bending stress at maximum moment
σ_f	Flow stress
σ_o	Ramberg-Osgood parameter
$\sigma_{(SAM\ el.)}$	Seismic anchor motion stresses
σ_t	Axial tensile stress
$\sigma_{(t=0)}$	Initial stress in piping system due to temperature and pressure only
σ_{Top}	Longitudinal stress at the top of the pipe
$\sigma_{(ten)}$	Pressure induced axial tensile stress
$\sigma_{(Tot.\ el.)}$	Total calculated elastic stress; calculated elastic bending stress plus pressure induced axial tension stress
$\sigma_{(Tot.\ el.\ bend\ \sigma)}$	Calculated elastic bending stress from ANSYS calculated moments
$\sigma_{(Tot.\ expt.)}$	Total experimental stress; experimental bending stress plus pressure induced axial tension stress
σ_u	Ultimate strength
σ_y	Yield strength
τ	Shear stress
θ	Half crack angle
ω	Forcing function frequency in radians/second
ς	Damping ratio (fraction of critical damping)
$2c/\pi D$	Ratio of total crack length to the pipe circumference

2. ACRONYMS AND INITIALISMS

ABAQUS	Finite element code
A/D	Analog-to-Digital
AECB	Atomic Energy Control Board, Canada
AISI	American Iron and Steel Institute
AIT	American Institute of Taiwan

ANL	Argonne National Laboratories
ANSYS®	Commercial finite element code developed by Swanson Analysis Systems
ASME	American Society of Mechanical Engineers
ASTM	American Society for Testing and Materials
BWR	Boiling Water Reactor
CASTEM	Finite element code
CEA	Commissariat A L'Energie Atomique, France
CEGB	Central Electric Generating Board, United Kingdom (Now Nuclear Electric.)
CMO	Crack-mouth opening
CMOD	Crack-mouth-opening displacement
COD	Crack-opening displacement
CRIEPI	Central Research Institute of Electric Power Industry, Japan
CS	Carbon steel
CSBM	Carbon steel base metal
CSW	Carbon steel weld
C(T)	Compact (Tension)
CTOA	Crack-tip-opening angle
da/dN	Fatigue crack growth rate
d-c	Direct current
d-c EP	Direct-current electric potential
DEGB	Double-ended guillotine break
dJ/da	Change in J for a change in crack length
dJ/dt	Rate change in J
dJ/dt_{RL}	Rate change in J under rapid loading
dJ/dt_{QS}	Rate change in J under quasi-static loading
DPZP	Dimensionless plastic zone parameter

DP^3II	Degraded Piping Program - Phase II
DSA	Dynamic strain aging
DTRC	David Taylor Research Center
d/t	Crack depth to wall thickness ratio
Dyn	Dynamic
EDF	Electricite de France
ENEA	dell'Energia Nucleare e delle Energie Alternative, Italy
EP	Electric potential
EPFM	Elastic-plastic fracture mechanics
EPRI	Electric Power Research Institute, USA
FEA	Finite element analysis
FEM	Finite element method
FM	Frequency modulated
GE/EPRI	An J-estimation scheme
HDR	An experimental reactor facility in Germany
HSK	Hauptabteilung für die Sicherheit der Kernanlagen, Switzerland
IGSCC	Intergranular stress corrosion cracking
IHI	Ishikawajima-Hariman Heavy Industries, Japan
INER	Institute of Nuclear Energy Research, Republic of China
IWB-3640	ASME Section XI flaw evaluation criteria for austenitic pipe
IWB-3650	ASME Section XI flaw evaluation criteria for ferritic pipe
IPIRG	International Piping Integrity Research Group
JAERI	Japanese Atomic Energy Research Institute
J-R	J-resistance
J_D-R	J-resistance based on deformation theory form of J

J_m-R	J-resistance based on modified form of J
J/T	Tearing instability approach
LBB	Leak-Before-Break
LBB.ENG	A J-estimation scheme
LBB-ENG2	A J-estimation scheme
LBB.GE	A J-estimation scheme
LBB.NRC	A J-estimation scheme
L-C	Orientation code that indicates crack plane is normal to longitudinal axis (L) and crack growth direction is circumferential (C)
LEFM	Linear elastic fracture mechanics
LRE	Leak-rate estimation
LVDT	Linear variable differential transformer
LWR	Light water reactor
MARC	Finite element code
MEA	Materials Engineering Associates
MTS	Supplier of servo-hydraulic equipment
NDE	Nondestructive evaluation
NPS	Nominal pipe size
NRC	Nuclear Regulatory Commission
NRC-NRR	Nuclear Regulatory Commission - Office of Nuclear Reactor Regulation
NRCPIPE	J-estimation scheme computer program
NRC-RES	Nuclear Regulatory Commission - Office of Nuclear Reactor Research
NSC	Net-section collapse
PC	Personal computer
PICEP	Leak-rate prediction computer code developed by EPRI
PIFRAC	Piping fracture mechanic data base

PWR	Pressurized Water Reactor
QS	Quasi-static
ROC-AEC	Republic of China - Atomic Energy Commission
RT	Room temperature
RVDT	Rotary-Variable-Differential Transformer
R6	Defect assessment criteria developed by CEGB
SAM	Seismic anchor motion
SAP IV	Finite element code
SAS®	Commercial Statistical Analysis Program
SAW	Submerged-arc weld
SC	Surface crack
SC.TKP	A finite length surface crack J-estimation scheme based on thick-wall formulations
SC.TNP	A finite length surface crack J-estimation scheme based on thin-wall formulations
SKi	Statens Kärnkraftinspektion (Swedish Nuclear Power Inspectorate)
SMAW	Shielded-metal-arc weld
SMTS	Specified minimum tensile strength
SMYS	Specified minimum yield strength
SQUIRT	Leak rate computer code - Seepage Quantification for Upsets In Reactor Tubes
SS	Stainless steel
SSBM	Stainless steel base metal
SSE	Safe shutdown earthquake
SSW	Stainless steel weld
STA	Science and Technology Agency at the Japanese National Research Center for Disaster Prevention
TAG	Technical Advisory Group

TWC	Through-wall crack
UK	United Kingdom
U.S.	United States
USNRC	United States Nuclear Regulatory Commission

GLOSSARY OF TERMS

ASME Section XI Safety Factors - Explicit safety factors incorporated in Section XI of the ASME Code to account for inaccuracies and uncertainties in the analysis procedures. For Normal Conditions a safety factor of 2.77 is incorporated in the Section XI procedures. For Emergency and Faulted Conditions a safety factor of 1.39 is incorporated in the procedures.

Collapse Load - The maximum load a structure can carry on the basis of a limit analysis assuming that the structure is made of an ideally plastic material. At this load, the deformations of the structure increase without bound.

Crack Closure Marks - Distinctive marks which are evident on the fracture surface which occur when the cracked pipe section unloads. These marks were used to estimate the extent of the through-wall crack at defined times throughout the event.

Crack Initiation - The onset of stable crack extension. For the IPIRG experiments crack initiation was defined as the point where the plot of the electric potential versus crack-mouth-opening displacement deviated from the initial slope.

Crack Stability - A condition where crack growth occurs at a slow rate that corresponds to the loading or displacement rate. In addition, when the crack section is unloaded the crack arrests.

Critical Crack Length - The length of a crack (either axial or circumferential) for which the crack will propagate unstably for a given set of loading conditions.

Cyclic Loads - A condition for which the applied loads and moments increase and then decrease in a periodic manner throughout the event.

Dead-Weight Stresses - The stresses imposed on the piping system due to the weight of the piping, insulation, and other loads permanently imposed on the piping.

Design Stress Intensity Value (S_m) - A strength based material property used for design purposes in the ASME Code. For ferritic steels the value of S_m at any temperature is the lowest of (1) one-third of the specified minimum tensile strength at room temperature, (2) one-third of the tensile strength at temperature, (3) two-thirds of the specified minimum yield strength at room temperature, or (4) two-thirds of the yield strength at temperature. For austenitic steels the value of S_m at any temperature is the lowest of (1) one-third of the specified minimum tensile strength at room temperature, (2) one-third of the tensile strength at temperature, (3) two-thirds of the specified minimum yield strength at room temperature, or (4) 90 percent of the yield strength at temperature. Values of S_m for a given material are defined as a function of temperature in Tables I-1.1 and I-1.2 of Section III, Division 1 Appendices of the ASME Code.

Displacement-Controlled Instability - A loading condition where an increase in displacements on the structure will start rapid crack growth.

Displacement-Controlled Stresses - Stresses that result from the application of displacements, such as those due to thermal expansion or seismic anchor motion.

Double-Ended Guillotine Break (DEGB) - A condition for which a circumferential through-wall crack propagates around the entire circumference of the pipe such that the cracked pipe section severs into two pieces and the two ends are displaced relative to their pipe axes to allow for full flow from each end.

Dynamic Loading - A condition for which the applied loads are changing rapidly with time. In this program the loading rates are comparable to those in high amplitude seismic events.

Dynamic Analysis - An analysis for which the applied loads are changing rapidly with time.

Dynamic Material Property Data - Material property data (tensile or fracture toughness) from laboratory specimens which were obtained under the conditions of high rate (dynamic) loading.

Dynamic Strain Aging - A phenomenon in which aging occurs simultaneously with straining at certain strain rates and temperatures. It results from the rapid diffusion of minute quantities of nitrogen and/or carbon dissolved in the steel. Dynamic strain aging can produce several effects such as changes in tensile strength and toughness with temperature and/or strain rate changes, and a susceptibility to intermittent crack jumps or instabilities preceded and succeeded by periods of stable crack growth.

Effective Stress-Ratio - The stress ratio (minimum stress divided by maximum stress) in which the stress includes the axial tensile stress due to internal pressure.

Elastic Analysis - An analysis based on the assumption of a linear relationship between stress and strain.

Emergency and Faulted Conditions - Refers to very low probability postulated incidents whose consequences are such that subsequent plant operation is not required and safe system shutdown is the only consideration.

Expansion Loop - A piping system configuration designed to accommodate the thermal expansion stresses which arise as a result of changes in temperature of the piping system.

Expansion Stresses - Those stresses resulting from restrained boundary conditions of the piping system.

Experimental Stresses - In this program, the stresses inferred from the experimentally determined load or strain values.

Failure - A condition for which a component or system is no longer capable of performing its design function. Depending on the context, failure can be defined as either the condition for which the piping system is no longer capable of maintaining internal pressure, or when the pipe experiences a DEGB.

Flow Stress - A material parameter used to describe the tensile properties of a strain-hardening material in terms of an equivalent elastic-plastic material having a yield strength between the yield and ultimate strengths of the material.

Incremental Cyclic Plastic Displacement - The nonrecoverable plastic component of displacement (or rotation) between loading cycles during a cyclic event.

Inertial Stresses - Dynamic stresses that result from the mass of the piping. Inertial stress is the component of total dynamic stress not due to the static displacement of anchor points.

In-Service Flaw Evaluation - The process for determining the significance of flaws found in service, including the comparison the discovered flaws with acceptance criteria, i.e., ASME Section XI Articles IWB-3640 and 3650.

Instability - An event where a crack starts to propagate rapidly.

Instantaneous Break - A condition for which the cracked pipe section severs into two pieces instantaneously, or near instantaneously, once the surface crack penetrates the pipe wall thickness.

J-Estimation Scheme - A closed-form elastic-plastic analysis, based on the J-Integral fracture parameter, for predicting the moment and rotation response of a cracked pipe.

Leak-Before-Break - For nuclear piping this is generally referred to as a methodology whereby one shows that a crack can be detected by leakage under normal operating conditions and that that crack would be stable at normal plus safe shut-down earthquake (SSE) loads. Sometimes also referred to as a condition whereby a surface crack breaks through the pipe thickness and remains stable even if the break-through occurs at emergency or faulted loads.

Level A Service Loads - A classification of loads for evaluating the effect of plant operating loads on the structural integrity of a component for conditions which the component may be subjected in the performance of its specified service function.

Level B Service Loads - A classification of loads for evaluating the effect of plant operating loads on the structural integrity of a component for conditions which the component must withstand without damage requiring repair.

Level C Service Loads - A classification of loads for evaluating the effect of plant operating loads on the structural integrity of a component for situations which are not anticipated to occur for a sufficient number of times to affect fatigue life and for which large deformations in areas of structural discontinuities are not objectionable. (Used to be referred to by ASME as emergency loading condition.)

Level D Service Loads - A classification of loads for evaluating the effect of plant operating loads on the structural integrity of a component for situations in which gross general deformations, loss of dimensional stability, and damage requiring repair, excluding loss of pressure retaining function, are not objectionable. (Used to be referred to by ASME as faulted loading condition.)

Ligament - The uncracked region of the pipe in the plane of a crack.

Limit-Load Analysis - A special case of plastic analysis in which the material is assumed to be ideally plastic (non-strain hardening). In limit-load analysis, the equilibrium and flow characteristics at the limit state are used to calculate the maximum load.

Limit Load - See collapse load.

Load-Controlled Instability. A loading condition where an increase in load on the structure will start rapid crack growth.

Load-Controlled Stresses - Stresses that result from application of loads, such as internal pressure or the effects of gravity, whose magnitude is not reduced as a result of displacement. Inertial stresses are also frequently considered as load-controlled or primary stresses.

Load Ratio (R) - The minimum load, moment, or stress divided by the maximum load, moment, or stress.

Membrane Stress - The component of the normal stress which is uniformly distributed and equal to the average value of stress across the thickness of the section under consideration.

Monotonic Loading - A loading condition where the applied loads or displacements continue to increase up to maximum load or moment.

Normal Stress - The component of stress normal to the plane of reference. In the case of the Task 1 experiments, the plane of reference is the plane of the circumferential crack.

Normal (Including Upset and Test) Conditions - Includes all design transients expected to occur during the course of system testing and operation, as well as upset conditions anticipated to occur frequently enough so that the system should be designed to accommodate them.

Operating Basis Earthquake (OBE) - An earthquake which could reasonably be expected to affect the plant site during the operating life of the plant considering the regional and local geology and seismology and specific characteristics of the local subsurface material.

Percent Inertial Loading - The ratio of the total moment (inertial plus static) minus the static moment to the total moment expressed as a percentage. The total moment at the crack section at any point in time can be calculated from a dynamic, time-dependent finite element analysis. The static moment at the crack section can be calculated from a static finite element analysis using thermal and pressure loading combined with an actuator displacement equal to the displacement of the actuator at the time of interest in the dynamic simulation.

Percent Static Loading - The ratio of the static moment to the total moment (inertial plus static) expressed as a percentage.

Pipe System Experiment - An experiment in the IPIRG Subtask 1.3 experimental facility.

Plastic Analysis - That method which computes the structural behavior under given loads, considering the plasticity characteristics of the materials, including strain hardening and the stress redistribution occurring in the structure.

Pressure Induced Stresses - The axial stress in the piping system due to the internal pipe pressure.

Primary Stresses - Any normal or shear stress developed by an imposed loading which is necessary to satisfy the laws of equilibrium of external and internal forces and moments. The basic characteristic of a primary stress is that it is not self-limiting.

Quasi-Static Loading - A condition for which the applied loadings are changing very slowly with time.

Quasi-Static Material Property Data - Material property data (tensile and fracture toughness) which were obtained under the conditions of slow rate (quasi-static) loading.

Quasi-Static Pipe Experiment - A pipe experiment for which the applied loads are changing very slowly with time.

Ratcheting - A progressive incremental inelastic deformation or strain which can occur in a component that is subjected to variations of mechanical stress, thermal stress, or both.

Seismic Anchor Motion (SAM) Stresses - Stresses imposed on the piping system due to the differential motion of piping system supports or anchors.

Safe Shutdown Earthquake (SSE) - An earthquake which is based upon an evaluation of the maximum earthquake potential considering the regional and local geology and seismology and specific characteristics of the local subsurface material. It is that earthquake which produces the maximum vibratory ground motion for which structures, systems, and components important for safety are designed to remain functional.

Secondary Stresses - A normal or shear stress developed by the constraint of adjacent material or by self-constraint of the structure. The basic characteristic of a secondary stress is that it is self-limiting.

Shear Stress - The component of stress tangent to the plane of reference.

Surface Crack - A crack or crack-like defect which penetrates one but only one of the pipe surfaces, either internal or external, but not both.

Surface Crack Instability - A condition where a surface crack grows through the remaining ligament in a rapid manner.

Surface Crack Penetration - The instant in time when the surface crack penetrates the pipe wall creating a through-wall crack.

Thermal Stress - A self-balancing stress produced by a change in temperature. Thermal stress is developed in a solid body whenever a volume of material is prevented from assuming the size and shape that it normally should under a change in temperature.

Through-Wall Crack - A crack which penetrates both pipe surfaces.

Through-Wall Crack Instability - A condition where a through-wall crack grows around the pipe circumference in a rapid manner.

Thrust Forces - A force acting on the piping system at a through-wall crack as the result of high pressure, high velocity fluid escaping through the cracked pipe.

EXECUTIVE SUMMARY

The International Piping Integrity Research Group (IPIRG) Program was an international group program managed by the U.S. Nuclear Regulatory Commission (USNRC) and funded by a consortium of organizations from nine nations: Canada, France, Italy, Japan, Sweden, Switzerland, Taiwan, the United Kingdom, and the United States. A Technical Advisory Group (TAG), consisting of experts from all member countries, met formally twice a year to exchange ideas, data, and analyses and to provide input on broad program direction. The active participation of the members provided a forum for discussing significant technological issues and for working towards achieving an international consensus on leak-before-break (LBB) and flaw evaluation criteria. The five-year program, conducted at Battelle in Columbus, Ohio, was completed in July 1991.

The objective of the program was to develop data needed to verify engineering methods for assessing the integrity of nuclear power plant piping that contains circumferential defects. These data are considered essential to verify the validity and degree of conservatism of current LBB analyses and in-service flaw assessment methods. Many research programs on flawed piping have been conducted in various countries; however, most of these programs involved cracked pipe experiments subjected to quasi-static loading rather than the high-rate loading typical of seismic events.

The IPIRG Program encompassed numerous tasks, but the primary focus was an experimental task designed to investigate the behavior of circumferentially flawed piping and piping systems subjected to high-rate loading typical of seismic events. The task consisted of both "separate effects" experiments on simple small-diameter pipe specimens and experiments on a large-diameter piping system tested at nominal pressurized water reactor (PWR) conditions. The separate effects experiments provided an evaluation of the effects of loading rate and cyclic loading on the fracture behavior of flawed pipe subjected to displacement-controlled loads and inertial loads. The pipe system experiments were conducted to investigate the complex interaction of loading conditions and system dynamics. Results from these experiments provide an important data base that can be used for the critical assessment of analytical procedures. Other program efforts that supported the pipe fracture work included material characterization studies, updates of a pipe fracture data base, a leak-rate investigation, finite element analyses of circumferential through-wall-cracked pipe fracture experiments, two 30-inch diameter quasi-static pipe fracture experiments, seminars, and workshops.

Pipe Fracture Experiments

The design of piping systems in nuclear power plants recognizes the existence of both inertial and displacement-controlled loads. Uncertainties in the ability to characterize inertial loads has, in part, led to a prevailing industry design practice that results in inherently stiff piping systems. However, stiff systems are less tolerant of displacements caused by thermal expansion and differential anchor motion. Furthermore, the hardware used to restrict pipe motion in nuclear plants, such as pipe hangers, snubbers, and pipe whip restraints, makes pipe system inspection difficult. As a result operators and designers are considering more flexible piping systems. A concern with flexible piping systems is the stability of cracks in piping which may be subjected to loads with a high inertial component. The IPIRG Program was formulated to investigate the separate effects on flawed piping of both inertial and displacement-controlled stresses as well as their combined effects.

Displacement-Controlled Experiments

Twelve experiments were conducted on 6-inch diameter, Schedule 120, pipe samples containing circumferential through-wall cracks and loaded in four-point bending under displacement control. Two additional experiments were conducted with internal surface cracks. Pipe specimens were either wrought TP304 stainless steel or A106 Grade B carbon steel. All experiments were conducted at 288 C, but, unlike the other pipe experiments conducted in this program, the pipe specimens with through-wall cracks did not contain pressurized water.

Inertially Loaded Experiments

Pipe fracture experiments with inertial loading were conducted on the same 6-inch diameter carbon and stainless steel pipe materials used for the displacement-controlled experiments. The primary objective of these experiments was to investigate the effect of inertial loading on the stability of cracks in pressurized pipe. Six cracked-pipe specimens with either through-wall cracks or surface cracks were loaded to failure at 288 C. The pipes were pressurized with water at 15.2 MPa. The pipe specimens were loaded by applying a sinusoidal displacement function of increasing amplitude.

Pipe System Experiments

The objective of the pipe system experiments was to provide the data necessary to assess the analysis methodologies for characterizing the fracture behavior of circumferentially cracked pipe in a piping configuration, representative of that in a nuclear plant, under combined inertial and displacement-controlled stresses. Results from the separate effects experiments conducted with purely displacement-controlled and inertially controlled loading were used to evaluate results of these complex experiments. By developing data on a piping system, the complex interaction of loading conditions and system dynamics provided important test cases for the assessment of current analytical procedures. The piping system was designed to have flexibility that is representative of typical nuclear power plant piping systems.

A unique experimental facility was designed and constructed to conduct these experiments. The piping system was fabricated as an expansion loop with over 30 m of 16-inch diameter, Schedule 100, pipe and five long-radius elbows. Numerous pipe loop configurations were considered and evaluated prior to selecting one that best met various criteria. The pipe loop configuration, its supporting framework, and the foundation were designed and then evaluated by means of dynamic finite element calculations using the ANSYS code. The cracked pipe test specimens were welded into the pipe loop at a location of high bending stress as identified from the calculations. Each experiment was conducted by simply replacing the failed test section with a new one.

The pipe loop was supported and constrained at several locations using various specially designed devices. There was no intent to simulate supports used in actual nuclear plants, rather these supports were designed to produce specific well-defined boundary conditions that could be accurately modeled in stress analyses. The emphasis was to gather data that can be used to test analytical capabilities without the complication of large unknowns in boundary conditions.

The pipe system experiments involved one uncracked pipe experiment designed to investigate system dynamics and boundary conditions and five cracked pipe experiments, each on a different material. The materials evaluated in the cracked pipe system experiments were: (1) A106 Grade B carbon steel, (2) SA-358 Type 304 stainless steel, (3) submerged-arc weld in A106 Grade B carbon steel, (4) submerged-arc weld in SA-358 Type 304 stainless steel, and (5) artificially-aged Type CF8M centrifugally cast stainless steel. A relatively long and deep internal surface crack was introduced into each of these test specimens. All cracked pipe experiments contained subcooled water at 288 C and 15.5 MPa. The uncracked pipe system experiment consisted of several tests conducted under a variety of pressure and temperature conditions.

Findings and Conclusions

Loading Rate Effects

For the two carbon steels examined at 288 C there was a modest degradation of fracture resistance at loading rates typical of seismic events. The reduced toughness in this carbon steel is attributed to dynamic strain aging (DSA). In contrast, for the stainless steels and welds tested there appeared to be little effect of high-rate loading on fracture properties and strength.

Cyclic Loading Effects

For both carbon steel and stainless steel, cyclic loading was found to reduce the load-carrying capacity of through-wall-cracked pipe by as much as 26 percent depending on load-ratio and the size of the incremental plastic displacement. Effects of cyclic loading on surface-cracked pipe are less clear, but results from the pipe system experiments suggest that cyclic effects may be more significant for the surface crack geometry.

Inertial Versus Displacement-Controlled Loading

The inertial load experiments showed markedly less fracture stability than those conducted under displacement-controlled loads. While the maximum load results for the two types of loading compare closely, inertial loading was shown to produce complete fracture instability in only a few cycles past maximum load. The inertial stresses produced in these experiments were similar to load-controlled stresses for fracture stability analyses and should probably be considered as primary loads.

Use of Laboratory Data to Predict Fracture Behavior of a Piping System

Data from C(T) tests, in some cases, were shown to overestimate the effective fracture resistance observed in a surface-cracked piping system under dynamic loads. Results of pipe system experiments were compared with companion quasi-static experiments. While results of these pipe system experiments cannot, as yet, be completely rationalized and modeled on the basis of standard laboratory specimen data, the IPIRG Program has increased the understanding of controlling parameters and is pointing the way to defining the specific laboratory data that are needed. Once the effects of these controlling parameters are understood better, analytical models coupled with laboratory specimen data should be able to predict the behavior of large-diameter piping systems to a variety of loading conditions.

Stress Analysis of Pipe System Experiments

Straightforward linear-elastic dynamic finite element analyses with 0.5 percent damping were shown to give an excellent description of the response of the uncracked piping system. The dynamic behavior of the piping system containing a section of surface-cracked pipe was accurately modeled with a nonlinear, time-dependent finite element analysis that included a nonlinear spring model to simulate the cracked section. Results of linear elastic stress analysis support the finding that this piping system primarily behaves elastically and that most of the nonlinear behavior is concentrated within the cracked section.

Fracture Analysis

All quasi-static and dynamic pipe fracture experiments, as well as pipe system experiments, were analyzed using state-of-the-art predictive fracture methods (Net Section Collapse, Dimensionless Plastic Zone Parameter, and J-estimation) and failure avoidance methods (R6 and ASME Section XI). The predictive methods gave relatively accurate predictions of maximum bending moments. R6 and ASME analyses generally underestimated the maximum bending moments.

The Double-Ended Guillotine Break

In the past, a nearly instantaneous double-ended guillotine break (DEGB) that occurs in a time of one millisecond has been postulated as the worst case failure mode. The results from the five pipe system experiments suggest that a DEGB is not likely to occur on a single loading cycle during a seismic event unless a very long surface crack exists. A double-ended break was achieved in two of the five pipe system experiments, but only after extensive through-wall crack growth occurred as a result of numerous loading cycles. This degree of stability was unexpected and may be due to the reduction in bending moment caused by the thrust forces produced by the steam jetting from the crack. Other factors, such as inertial mass, may also contribute to this stabilizing effect. Fracture speed results also suggest that the time required to create a DEGB is orders of magnitude longer than one millisecond.

1.0 INTRODUCTION

The International Piping Integrity Research Group (IPIRG) Program was an international group program managed by the U.S. Nuclear Regulatory Commission (USNRC) and funded by a consortium of organizations from nine nations: Canada, France, Italy, Japan, Sweden, Switzerland, Taiwan, the United Kingdom, and the United States. The organizations and cognizant individuals in the IPIRG Program are listed in the Acknowledgments.

The IPIRG Program was initially conceived by the USNRC as a means to develop data for the verification of fracture analyses for cracked pipe under dynamic loading. Some of the reasons for developing and participating in the IPIRG Program are discussed in this section of the report. This section also includes (1) a historical perspective of the IPIRG Program, (2) a summary of the state-of-the-art of relevant technical information that was available prior to the start of the IPIRG Program, (3) a discussion on regulatory and Code* needs for pipe crack evaluation procedures, (4) why the IPIRG Program was needed, and (5) a discussion on the task structure and organizational structure of the program. This is followed by a brief description of the contents of this report.

1.1 Historical Perspective

The IPIRG Program officially started July 10, 1986. However, its inception was several years prior to that. A technical format was developed and revised as a result of many discussions with potential members. The current task structure was developed basically at a meeting held in conjunction with a USNRC seminar entitled, "LEAK-BEFORE-BREAK: International Policies and Supporting Research". This meeting was held in October, 1985, in Columbus, Ohio, and the proceedings were later published as part of the IPIRG Program (Ref. 1.1).

The state-of-the-art of pipe fracture at the inception of the IPIRG Program is summarized by technical category in the following sections.

1.1.1 MATERIAL CHARACTERIZATION DATA

Data were developed by the USNRC in the Piping Fracture Mechanics Data Base (PIFRAC) program at MEA (Ref. 1.2). This involved chemical analyses, Charpy, tensile, and ductile fracture toughness results (J-R curves from C(T) specimen tests) for a variety of pipe materials. The scope of the MEA work was to conduct standardized tests. Consequently, the tests were conducted at quasi-static rates. Data developed in the

---

* Throughout this report "Code" refers to the ASME Boiler and Pressure Vessel Code

USNRC's Degraded Piping Program at Battelle (Ref. 1.3) were also input to the PIFRAC data base. At Argonne National Labs, the USNRC was starting a program on the effects of thermal aging on the strength and toughness of cast stainless steels. This program started in approximately 1984 and is to be completed in 1991 (Ref. 1.4). As part of this program cooperative efforts were undertaken between Argonne, Battelle, and MEA for the USNRC on the evaluation of aged cast stainless steel. In addition, during the course of the IPIRG Program, separate programs on the effect of thermal aging on fracture toughness of cast stainless steels were undertaken at Westinghouse (Ref. 1.5) and Framatome (Ref. 1.6).

Another key contribution to the understanding of piping fracture toughness came from David Taylor Research Center, (DTRC) (Ref. 1.7). The work by Gudas et al. showed that stainless steel flux welds could have an order of magnitude lower toughness than the stainless steel base metal. Subsequent data by Westinghouse in 1984 (Ref. 1.8) and Battelle in 1987 (Ref. 1.9) supported these results. This fact, along with the occurrence of intergranular-stress-corrosion cracking (IGSCC) in plant welds (Ref. 1.10) led to major changes in the ASME austenitic pipe flaw evaluation standard (Ref. 1.11). The pipe material data developed by DTRC was also incorporated into the PIFRAC data base.

At the start of the IPIRG Program load history effects were barely being considered in fracture toughness testing of laboratory specimens. Understanding and modeling of seismic effects on flawed piping requires knowledge of these load history effects. Monotonic quasi-static test data were being applied to the analysis of cracked pipe subjected to dynamic cyclic loading for leak-before-break (LBB) and in-service flaw assessment analyses. Dynamic monotonic fracture specimen testing on nuclear piping steels at LWR temperatures was virtually nonexistent, and cyclic loading interactions on ductile tearing was largely ignored. However, during the course of the IPIRG Program these load history effects were the subject of a special technical publication (Ref. 1.12).

1.1.2 PIPE FRACTURE DATA

At the start of the IPIRG Program, the USNRC's Degraded Piping Program was near completion (Ref. 1.3). This program involved small and large diameter pipe fracture experiments at LWR temperatures. Loads applied were either pure bending, pure pressure, or combined pressure and bending. Only circumferential cracks in straight pipe were evaluated, and the loading rate was always quasi-static. Although 62 experiments were conducted, the combinations of materials, pipe diameter, flaw type, flaw size, and loading allowed for only a limited matrix of experiments. The test conditions were those thought to be of greatest importance. A major limitation of the scope of that program, and the majority of other past and ongoing programs, was that the loading rate was quasi-static and testing involved straight pipe in simple four-point bending.

Prior to the start of the IPIRG Program, only two research programs had been completed on cracked nuclear pipe at high loading rates close to seismic events. Both programs were funded by the EPRI BWR Owner's Group and involved 4-inch diameter Schedule 80 stainless steel pipe tested at room temperature without internal pressure.

The EPRI program conducted at GE San Jose (Ref. 1.13) involved constant amplitude, fully reversed, cyclic inertial loading. These were experiments similar to the IPIRG Subtask 1.1 experiments (see Figure 1.1). A conclusion from that report was that, "a net section collapse criterion can be used as a conservative estimate of the load capacity of flawed pipe sections provided the change in the flaw shape due to (cyclic) crack growth (during the dynamic event) is properly accounted for."

An EPRI program at Battelle (Ref. 1.14) involved dynamic material property tests and dynamic blowdown cracked pipe experiments on TP304 stainless steel pipes at room temperature. The material property tests showed that the wrought TP304 stainless steel had a higher strength and toughness at elevated strain rates. The dynamic blowdown loaded pipe experiments are illustrated in Figure 1.2. The pipe contained a through-wall crack, which increased the compliance and the degree of plasticity over that of an uncracked pipe. As a result, the moment was reduced at the crack due to the dynamic nature of the blowdown loads. The moment at the crack required to cause the crack to grow by ductile tearing was less than half of the moment predicted from an uncracked pipe dynamic analysis. This is illustrated in Figure 1.3, which shows a series of experiments where the crack length had to be extended by more than a factor of 5 from the initial crack size predicted from the uncracked pipe analysis in order for ductile tearing to initiate.

The lessons learned from these programs that were applied in the IPIRG Program were:

> A large number of constant amplitude cycles causes fatigue crack growth, which complicates the analysis of the experiments. The objective of the IPIRG experiments was to evaluate the effects of cyclic loading on ductile tearing. To minimize the fatigue crack growth complications in understanding IPIRG experiments, an increasing amplitude sinusoidal loading history was selected.
>
> Compliance is altered due to the presence of a crack, and plasticity at the crack section changes the moments at the crack location due to the dynamic loads. Hence, to design the IPIRG experiments, it was necessary to account for the effects of the crack on the dynamic response of the pipe. A nonlinear cracked pipe element was conceived in the Degraded Piping Program (Ref. 1.15) and implemented in the IPIRG design analysis.

During the course of the IPIRG Program, two other dynamic cracked pipe programs were completed and reported in the open literature. Both of these were conducted in Japan, one by JAERI and the other at the Japanese National Research Center for Disaster Prevention with funding by the Science and Technology Agency (STA).

The JAERI program (Ref. 1.16) involved inertial pipe tests (see Figure 1.4) that were similar in design to the double-cantilever inertial tests in the G.E. program (Ref. 1.13) and IPIRG Subtask 1.1. The JAERI experiments involved pressurized pipe tested at room temperature with a load frequency of 12 Hz. Blocks of constant amplitude sinusoidal displacements were applied to the pipe. Loads were sufficiently low with a sufficient number of cycles that low-cycle fatigue crack growth was significant. Hence, as in the case of the G.E. experiments, the Net-Section-Collapse analysis could be used only if the fatigue crack growth was accounted for (see Figure 1.5).

The Science and Technology Agency (STA) of the Japanese government sponsored flawed pipe system tests at the National Research Center for Disaster Prevention in Japan (Ref. 1.17). This program involved a very complex cracked pipe system. Figure 1.6 is a sketch of the 4-inch and 6-inch diameter piping system used. Pressurized, room-temperature tests were conducted with and without initial flaws. The loading consisted of constant amplitude sinusoidal blocks at 8 Hz for 10 seconds or a seismic load history of similar duration. In the case of the long circumferential surface crack tests, a complete break occurred in 4 to 7 cycles after the surface crack penetrated the pipe wall. (Videotapes of these experiments clearly show this behavior.)

As with the EPRI/GE and JAERI program experience, the failure loads of the STA experiments were overpredicted by the Net-Section-Collapse analysis unless the fatigue crack growth in the "seismic" load history was used to increase the initial flaw to the flaw size at failure (see Figure 1.7). (Note, the analyses in Figures 1.7a and 1.7b are slight modifications of the Net-Section-Collapse (NSC) analysis equations. The NSC equations are the basis of the ASME pipe flaw evaluation criteria.) Key aspects to understanding piping integrity from this work are:

> The results further substantiate that large numbers of cycles in the dynamic event can grow the crack so that the predicted failure loads, using the flaw size prior to the application of the dynamic loads, are greater than the actual failure loads.
>
> Inertial loading can cause a double-ended guillotine break (DEGB), but the break is not instantaneous, and there may be several cycles of opening and closing of the growing through-wall crack.

1.1.3 PIPE FRACTURE ANALYSES

From a regulatory view, pipe fracture analyses were needed to provide a technical basis for LBB and in-service flaw evaluation criteria. LBB analyses in the United States and several other countries deal with hypothetical through-wall circumferential flaws (Ref. 1.18).

Status of Through-Wall-Cracked Pipe Analyses

The following describes the status of available circumferential-through-wall-cracked pipe analyses at the start of the IPIRG Program.

Using finite element analysis (FEA), comparisons were made with three through-wall cracked pipe experiments as part of the Degraded Piping Program. For two experiments, the FEA underpredicted the moments or stresses during crack growth by 20 to 30 percent (Refs. 1.9 and 1.19). For a third experiment (Ref. 1.20) the agreement between the FEA and experimental loads was excellent. The lack of consistency and accuracy caused some concern since FEA is a theoretically sound method.

The Net-Section-Collapse analysis (Ref. 1.14 and 1.21) had been developed and compared with stainless steel pipe test data. These tests were all conducted at room temperature with circumferential through-wall or surface cracks in pipes from 2 to 16-inch diameter. Loading was by quasi-static, monotonic, four-point bending. Approximately 20 experiments had been conducted by Battelle for EPRI. This analysis was the technical basis for the ASME austenitic pipe flaw evaluation criteria for cracks in non-flux welds and wrought base metal. The agreement between the Net-Section-Collapse analysis predictions and the experimental results for these stainless steel pipe experiments was good.

In 1981 G.E. developed an estimation scheme for EPRI for through-wall cracks in pipes under tension or bending (Ref. 1.22). Limited surface-cracked pipe solutions were made available in 1984 (Ref. 1.23). The Degraded Piping Program results showed that the GE/EPRI estimation scheme gave the lowest predictions of all of the available circumferential through-wall crack analyses (Ref. 1.3).

The R6 analysis procedure had undergone a significant revision in 1986 (Ref. 1.24). There were three options to this analysis methodology. The results for one circumferential through-wall-cracked pipe experiment were compared with pipe fracture predictions using the R6 approach in Reference 1.24. Many more comparisons were later made as a result of round-robin problems in the IPIRG Program. These later results showed that the R6 Option 1 method gave results comparable with the GE/EPRI method. However, procedures followed by the various analysts differed slightly, which caused significant scatter in the predictions (see results of IPIRG Round-Robin Problem 1 in Section 2.5.2). This scatter was comparable with that seen from a single analyst using a variety of different analyses.

During the initial development of the LBB methodology, the USNRC developed J-estimation methods as alternatives to finite element analyses and to the GE/EPRI estimation scheme predictions for circumferential through-wall cracked pipe. Initial efforts involved the work by Paris and co-workers (Ref. 1.25). This was refined by Klecker to incorporate strain-hardening (Ref. 1.26). This method was called LBB.NRC. Later Brust (Ref. 1.27) further extended the general approach of Paris to predict loads and displacements of cracked pipe. One method, LBB.GE, involved using the GE/EPRI functions to calculate loads and displacements, but J was calculated by integrating the area under the curve rather than using the GE/EPRI h_1-functions. The other method was the LBB.ENG method, which uses an equivalent energy based engineering methodology to calculate the load-displacement (or moment-rotation) relation of the cracked pipe used in the J calculations. Comparisons in the Degraded Piping Program showed that the LBB.ENG method slightly underpredicted the experimental loads when using a power-law extrapolation of the J_D-R curve and an average Ramberg-Osgood fit of the stress-strain curve of the material.

Status of Surface-Cracked Pipe Analyses

Unlike circumferential through-wall cracked pipe J-estimation scheme analyses, there were very few circumferential surface-cracked pipe analyses available at the start of the IPIRG Program. This limitation still exists today.

GE/EPRI J-estimation scheme solutions were developed for a very limited number of finite-length, circumferential surface-cracked pipe cases in pure bending (Ref. 1.23). Ahmad (Ref. 1.28) developed a modification to the GE/EPRI 360-degree surface crack h_1-functions that can be used for finite-length surface-cracked pipe in bending. There are two versions of this approach. One uses thin-shell assumptions, called SC.TNP, while the other includes thick-shell assumptions, called SC.TKP. The SC.TKP solution was always found to underpredict the experimental loads significantly. The SC.TNP solution was more accurate, but occasionally overpredicted the loads, particularly for thinner wall pipe. The SC.TNP and SC.TKP analyses have the added advantage that they also have the capability of predicting the moment versus rotations due to the crack. This relation was needed to calibrate a cracked pipe element in the dynamic analyses of the IPIRG inertial (Subtask 1.1) and pipe system (Subtask 1.3) experiments.

The R6 analysis procedure can be used for circumferential surface-cracked pipe analysis using Options 1 and 2 (Ref. 1.24). The results for one circumferential surface-cracked pipe experiment were compared with pipe fracture predictions using the R6 approach in Reference 1.24. Several other comparisons were later made as a result of round-robin problems in the IPIRG Program. As with the circumferential through-wall-cracked pipe analyses, these later results showed that the R6 Option 1 method was reasonably accurate and consistently underpredicted initiation and maximum load (see results of IPIRG Round-Robin Problem 2 in Section 2.5.2).

1.1.4 LEAK-RATE ESTIMATION ANALYSES

Leak-rate analyses in the U.S. were limited to work initially started by the USNRC (Ref. 1.29), which was subsequently refined and verified by experiments with stress-corrosion-cracked pipe and simulated cracks (Ref. 1.30). This work was later implemented into a leak-rate prediction code called PICEP developed by EPRI (Ref. 1.31). The PICEP code in its earliest version used the GE/EPRI through-wall-cracked pipe bending and tension solutions to calculate the crack-opening displacements, but the failure loads were predicted based on the Net-Section-Collapse analysis. The PICEP code calculated the leakage area for a given crack in a pipe with a specified load, but did not directly calculate the crack size for a given leakage rate and specified stress, as is frequently done in LBB analyses.

The USNRC also developed a simplified leakage rate analysis as part of their LBB.NRC computer program (Ref. 1.26). This analysis used the Tada-Paris crack-opening-area analysis from Reference 1.25, together with a simple leakage rate constant of 250 gallons per minute per square inch of crack opening. This simpler leak-rate model did not include friction factors, two-phase flow considerations, nonequilibrium vapor generation rates, etc., as variables.

1.1.5 OTHER RELEVANT PIPING INTEGRITY RESEARCH PROGRAMS

Another relevant piping integrity program that was started about 1 year before the IPIRG Program was the EPRI/USNRC Piping and Fitting Dynamic Reliability Program (Ref. 1.32). This program was concerned with failure of uncracked piping systems under dynamic loading. The general objective was to assess the actual failure mode of uncracked piping under simulated seismic loading. The ASME Section III design stress equations assume that the piping fails by plastic collapse. Experiments in the Piping and Fitting Dynamic Reliability Program demonstrated that the failure was by ratcheting followed by fatigue crack growth. Damping factors and elastic stress analyses were also assessed in that program.

1.2 Why Do We Need Pipe Fracture Evaluations?

There are basically two types of evaluations that make use of pipe fracture analyses: LBB analyses and analyses of flaws detected during in-service inspections. In LBB analyses, a flaw is assumed to exist at critical locations in the piping system, which generally are the high stress locations. In some countries, the assumed flaw is a surface flaw and its growth due to service loads and environments is predicted. Fracture mechanics analyses are performed to predict the crack sizes and shapes that could lead to a large break in the piping or that could lead to a leak in the piping, given that some specified accidental loading occurs. The accidental loading most commonly assumed to be the limiting load is a safe shut-down seismic event, although in some countries there are other dynamic loads that are limiting.

Some other countries follow the general procedure adopted by the USNRC in its LBB analyses. In that procedure, a through-wall flaw is assumed, where the circumferential length of the flaw is based on predicted normal operation load levels and the leak detection capability of the particular plant. Pipe fracture analyses are used to estimate the critical crack size under seismic loads. This critical crack size is then compared with the crack size calculated for the normal operation loads to determine the margin against catastrophic failure. There is a similar analysis performed to determine a margin against failure based on the loading levels needed to produce failure for a fixed crack size.

For in-service flaw assessment criteria, the stresses of concern can be for either normal and test or emergency and faulted conditions. The flaw evaluation procedures generally involve the assessment of surface cracks, which can have axial, circumferential, or helical orientations. In the U.S., Section XI of the ASME Boiler and Pressure Vessel Code includes procedures to assess flaws in austenitic (Ref. 1.11) or ferritic piping (Ref. 1.33). Several other countries use different assessment methods including the R6 method (Ref. 1.24).

Regardless of which LBB analysis method or in-service flaw evaluation procedure is used, whether by choice or regulation, verification of its validity and degree of conservatism requires data from appropriate experiments. Many research programs on flawed piping have been conducted in the U.S. (Refs. 1.3, 1.14, 1.32, 1.34, and 1.35) and internationally (Refs. 1.36-1.40). However, most of these programs involved quasi-static loading of cracked pipe, rather than the dynamic seismic loading that is more appropriate for LBB and in-service flaw assessments. The IPIRG Program was created to provide data for fracture evaluations of flawed piping and piping systems subjected to high-rate cyclic loading typical of seismic events.

1.3 Why Did We Need IPIRG?

One of the basic questions asked in developing this program was, "Why is an IPIRG Program needed?" There were several reasons organizations joined, and the priorities of the various organizations differed. Some of the major reasons are cited below.

In reviewing results from the Degraded Piping Program and other pipe fracture programs throughout the world, it was clear that a missing aspect of those programs was pipe fracture data at seismic rates and for representative piping systems. Since pipe size is a critical factor in determining if a pipe will fail at limit-load stresses or at lower stresses due to elastic-plastic fracture, experiments must be conducted with relatively large diameter pipe. Conducting large diameter pipe fracture experiments is an expensive undertaking especially when it involves a representative pipe system. The objective of conducting high temperature, dynamic pipe system experiments was to look for unusual dynamic effects not accounted for in quasi-static studies. For instance, are the expected failure loads under dynamic loading increased or decreased? Are dynamic effects sufficiently small to use the existing quasi-static pipe fracture and material characterization data bases? Can we continue to use quasi-static data as the technical basis for Code flaw evaluation procedures? Can load history effects from a seismic event change the apparent fracture resistance of typical nuclear piping materials at LWR temperatures? To address these concerns, an ambitious program was required. Cost sharing by means of a group program was a major reason for creating the IPIRG Program, since funding for these expensive experiments would have been a significant burden for any one organization.

Many of the members in the IPIRG Program were interested in the details of the USNRC's Degraded Piping Program. Detailed reports of the individual experiments were distributed to IPIRG members. They were also given access to the computer codes that were developed and the data base of information generated in that program.

Another reason for joining the IPIRG Program was to participate in developing an international consensus on the technical basis for pipe fracture technology. Since the pressure boundary of a reactor is not a redundant structure, and since cooling water for the reactor (transported by the piping systems) is essential to the safe operation of the plant, piping integrity is a key concern to nuclear power plant owners, manufacturers, and regulatory agencies. With the occurrence of the Chernobyl accident, it was seen that an accident in one country affects all other countries, if not directly, then politically. Having a common technical basis for piping integrity helps to prevent technical errors from being a source of a potential accident. As an integral effort of the IPIRG Program, workshops were held on a regular basis to provide a forum for information exchange and an opportunity for participating members to use different analysis methods in solving round-robin problems. Members also had the opportunity to present results of and plans for research in their own countries and organizations at the semiannual IPIRG Technical Advisor Group (TAG) meetings. More formal presentations were made by the TAG members at LBB seminars. The three LBB seminars that were held in conjunction with the IPIRG Program were in Columbus (October 1985), Tokyo (May 1987), and Taipei (May 1989) (Refs. 1.1, 1.41, and 1.42). The IPIRG Program also facilitated information exchange by providing the opportunity for member organizations to send a visiting scientist to Battelle for up to one year. The visiting scientist and his organization benefitted by being more directly involved in the experimental and analytical pipe fracture research.

1.4 Task Structure of IPIRG Program

The IPIRG Program was developed by the USNRC with the objective of developing data needed to verify engineering methods for assessing the integrity of nuclear power plant piping that contains defects. The work within the IPIRG Program was broken into numerous tasks and subtasks as listed below and as shown graphically in Figure 1.8:

Task 1 - Leak-Before-Break Under Simulated Seismic/Dynamic Stresses

- Subtask 1.1 - Stability of Cracked Pipe Under Inertial Stresses
- Subtask 1.2 - Stability of Cracked Pipe Under Seismic/Dynamic Displacement-Controlled Stresses
- Subtask 1.3 - Crack Stability in Representative Piping Systems Under Combined Inertial and Seismic/Dynamic Displacement-Controlled Stresses

Task 2 - Experimental Pipe Fracture and Pipe Material Property Data Base Development

- Subtask 2.1 - Data Base on Nuclear Piping Materials
- Subtask 2.2 - Data Base on Pipe Fracture Experiments

Task 3 - Fracture of Piping Containing High Energy Fluids (this task was left inactive)

Task 4 - Resolution of Unresolved Issues from the USNRC Degraded Piping Program and IPIRG Research Tasks

- Subtask 4.1 - Evaluation and Refinement of Leak-Rate Estimation Models
- Subtask 4.2 - Disposal of Service Degraded Pipe
- Subtask 4.3 - Large Diameter Quasi-Static Pipe Experiments
- Subtask 4.4 - Stress-Strain Behavior Under Cyclic and Compressive Loading
- Subtask 4.5 - Analysis of Pipe Fracture Experiments

Task 5 - Information Exchange Seminars and Program Administration

- Subtask 5.1 - Program Administration
- Subtask 5.2 - Information Exchange Seminars

1.4.1 TASK 1 LEAK-BEFORE-BREAK UNDER SIMULATED SEISMIC/DYNAMIC STRESSES

Task 1 was, by far, the most significant task of the program. It represented 67 percent of the total program effort and included most of the pipe fracture experiments. The behavior of flawed piping and piping systems subjected to high-rate loading was investigated in Task 1 by conducting both "separate effects" experiments on simple pipe specimens and large diameter pipe experiments on a representative piping system tested at PWR conditions. The separate effects experiments were designed to investigate separately the effects of inertial loads (Subtask 1.1) and displacement-controlled loads (Subtask 1.2) on pipe fracture behavior and stability. Combined effects of inertial and displacement-controlled loads were investigated in Subtask 1.3 on a representative piping system. Subtask 1.3 involved the design, construction, and utilization of the IPIRG Pipe Loop Test Facility. This is a unique facility having extensive instrumentation and well-defined boundary conditions that provided an important data base that can challenge the capabilities of analytical and numerical models to predict the behavior of flawed piping under high-rate loading.

1.4.2 TASK 2 EXPERIMENTAL PIPE FRACTURE AND PIPE MATERIAL PROPERTY DATA BASE DEVELOPMENT

Task 2 was of minimal effort and consisted primarily of updates to the USNRC's piping fracture mechanics database, PIFRAC.

1.4.3 TASK 3 FRACTURE OF PIPING CONTAINING HIGH ENERGY FLUIDS

Task 3 was entitled "Fracture of Piping Containing High Energy Fluids". However, this effort was never activated, and some of the objectives of this task were accomplished in Subtask 1.3.

1.4.4 TASK 4 RESOLUTION OF UNRESOLVED ISSUES FROM THE USNRC DEGRADED PIPING PROGRAM AND IPIRG RESEARCH TASKS

Task 4 was a collection of five diverse subtasks. The task was created as a mechanism to investigate issues left unresolved by previous programs or those discovered during the conduct of IPIRG. Subtask 4.1 included leak-rate experiments and analytical efforts to evaluate and refine leak-rate estimation models. Subtask 4.2 was a small effort involving the disposal of contaminated piping materials. Subtask 4.3 was an effort co-funded by the Japanese members and involved two large-diameter, quasi-static pipe fracture experiments. Subtask 4.4 involved additional material characterization experimentation under cyclic and compressive loading. Subtask 4.5 was funded entirely by the USNRC and provided an evaluation of the ability of finite element analyses to predict the behavior of IPIRG pipe fracture experiments.

1.4.5 TASK 5 INFORMATION EXCHANGE SEMINARS AND PROGRAM ADMINISTRATION

Program administrative efforts and the conduct of meetings, seminars, and workshops were covered under Task 5. Subtask 5.1 included the administrative functions that were necessary for the effective program control over quality, costs, and schedule. Subtask 5.2 provided for information exchange within the IPIRG Technical Advisory Group (TAG) by organizing and conducting LBB seminars, round-robin workshops, and semi-annual TAG meetings and by providing the mechanism for Battelle to host visiting scientists from member organizations.

1.5 IPIRG Organizational Structure and Funding

The IPIRG Program was a five-year program that was started July 10, 1986, and completed July 10, 1991. The total program funding was approximately $6,357,000 and was provided by numerous organizations throughout the world (see Acknowledgments). The organizations represented government bodies, utilities, and vendors of nuclear plants as depicted in Figure 1.9. The government organizations contracted with the USNRC through inter-government agreements, and the industrial organizations contracted directly with Battelle with reference to the USNRC's contract with Battelle. This contractual structure is depicted in Figure 1.10.

While the USNRC Project Officer managed the program, a Technical Advisory Group (TAG), made up of one member from each organization contractually committed to the program, was established to provide the Project Officer with input on broad program direction (Figure 1.11).

1.6 Structure of Final Report

This final report contains the key results of the IPIRG Program. The findings are significantly condensed in order to provide a manageable document for those with a general interest in this international group program. Those readers who desire more detailed information are referred to the various topical reports and subtask final reports identified in the List of IPIRG Program Deliverables. These reports give detailed technical information and findings from various experimental and analytical investigations. However, for specific detailed results from individual pipe fracture experiments conducted in this program the reader is referred to the data record book completed for each experiment.

Section 1.0 has provided background information on LBB and flaw evaluation procedures in piping as well as on IPIRG programmatic matters. Section 2.0 summarizes the technical results for the entire program by subtask. Section 3.0 focusses on Task 1 and gives a relatively detailed assessment of the results from the various pipe fracture experiments and complementary analyses conducted in this task. Section 4.0 provides conclusions and summarizes the advances in the state-of-the-art of pipe fracture technology resulting from the IPIRG Program.

1.7 References

1.1 "Leak Before Break: International Policies and Supporting Research", Proceedings of a seminar held in Columbus, Ohio on October 28-30, 1985, NUREG/CP-0077, June 1986.

1.2 Hiser, A. L., and Callahan, G. M., "A User's Guide to the NRC's Piping Fracture Mechanics Database (PIFRAC)", NUREG/CR-4894, May 1987.

1.3 Wilkowski, G. M. and others, "Degraded Piping Program - Phase II", Summary of Technical Results and Their Significance to Leak-Before-Break and In-Service Flaw Acceptance Criteria, March 1984-January 1989, NUREG/CR-4082, Vol. 8, March 1989.

1.4 Chopra, O., "Estimates of Fracture Toughness of Cast Stainless Steels in LWR Systems", in Transactions of the Eighteenth Water Reactor Safety Information Meeting, NUREG/CP-0113, October 1990.

1.5 Bamford, W. H. and Landerman, E. I., "Thermal Analysis of Cast Stainless Steel, and its Impact on Piping Integrity", Circumferential Cracks in Pressure Vessels and Piping - Vol. II, ASME PVP - Vol 95, pp 137-172, 1984.

1.6 Meyzaud, V., Ould, P., Balladon, P., Bethmont, M., and Soulat, P., "Tearing Resistance of Aged Cast Austenitic Stainless Steels", presented at NUCSAFE 88, Avignon, France, October, 1988.

1.7 Gudas, J., "J-R Curve Characterization of Piping Materials and Welds", Ninth Water Reactor Safety Research Information Meeting, Gaithersburg, Maryland, October 1981.

1.8 Landes, J. D., McCabe, D. E., and Ernst, H. A., "Elastic-Plastic Methodology to Establish R Curves and Instability Criteria, Eighth Semiannual report on EPRI Contract No. RP1238-2, July 1, 1983 to December 31, 1983, by Westinghouse R&D Center, July 24, 1984.

1.9 Wilkowski, G. M. and others, "Analysis of Experiments on Stainless Steel Flux Welds", NUREG/CR-4878, April 1987.

1.10 "Nine Mile Point 1 Pipe Crack Task Force Report", sponsored by Niagara Mohawk Power Corporation, Syracuse, N.Y., Compiled by D. E. Delwiche of G.E. San Jose, G. M. Gordon (Chairman), G.E. San Jose, June 20, pp 5-4 and 5-5, 1983.

1.11 American Society of Mechanical Engineers Boiler and Pressure Vessel Code, Edition July 1989, See Section XI Article IWB-3640.

1.12 Advances in Fracture and Fatigue for the 1990's - Volume I - Load History Effects on Fracture Resistance, ASME PVP Volume 166, July 1989.

1.13 Hale, D. A. and others, "The Growth and Stability of Stress Corrosion Cracks in Large-Diameter BWR Piping", EPRI Report NP-2472 Volume 2, see Appendices B and C, July 1982.

1.14 Kanninen, M. F., and others, "Instability Predictions for Circumferentially Cracked Type 304 Stainless Steel Pipes Under Dynamic Loadings", EPRI Report NP-2347, April 1982.

1.15 Wilkowski, G. M. and others, "Degraded Piping Program - Phase II", Semiannual Report, April 1985-September 1985, NUREG/CR-4082, Vol. 3, March 1986.

1.16 Murakami, E. and others, "Crack Growth of Nuclear Piping Under Dynamic Loading", ASME PVP special publication PVP 167, pp 115-120, July 1989.

1.17 Ogawa, N., "Experimental Study of Piping Stability under Strong Earthquake", ASME PVP special publication PVP 150, pp 69-80, July 1988.

1.18 "Evaluation of Potential for Pipe Breaks", prepared by USNRC Pipe Break Task Group, NUREG-1061, Vol. 3, November 1984.

1.19 Ahmad, J., Nakagaki, M., Papaspyropoulos, V., and Wilkowski, G., "Elastic-Plastic Finite Element Analysis of Crack Growth in Large Compact Tension and Circumferentially Through-Wall-Cracked Pipe Specimen", NUREG/CR-4573, October 1986.

1.20 Nakagaki, M., Marschall, C., and Brust, F., "Analysis of Cracks in Stainless Steel TIG Welds", NUREG/CR-4806, December 1986.

1.21 Kanninen, M. F., Broek, D., Marschall, C. W., Rybicki, E.F., Sampath, S. G., Simonen, F. A., and Wilkowski, G. M., "Mechanical Fracture Predictions for Sensitized Stainless Steel Piping with Circumferential Cracks", EPRI Report NP-192, September 1976.

1.22 Kumar, V., German, M., and Shih, C. F., "An Engineering Approach for Elastic-Plastic Fracture Analysis", EPRI Report NP-1931, July 1981.

1.23 Kumar, V. and German M. D., "Elastic-Plastic Fracture Analysis of Through-Wall and Surface Flaws in Cylinders", EPRI Report NP-5596, January 1988.

1.24 Milne, I., Ainsworth, R. A., Dowling, A. R., and Stewart, A. T., "Assessment of the Integrity of Structures Containing Defects", R/H/R6-Rev. 3, Published by Central Electric Generating Board, England, May 1986.

1.25 Paris, P. C. and Tada, H., "The Application of Fracture Proof Design Methods Using Tearing Instability Theory to Nuclear Piping Postulating Circumferential Through-Wall Cracks", NUREG/CR-3464, September 1983.

1.26 Klecker, R. and others, "NRC Leak-Before-Break (LBB.NRC) Analysis Method for Circumferentially Through-Wall-Cracked Pipes Under Axial Plus Bending Loads", NUREG/CR-4572, May 1986.

1.27 Brust, F. W., "Approximate Methods for Fracture Analyses of Through-Wall Cracked Pipes", NUREG/CR-4853, February 1987.

1.28 Scott, P. M. and Ahmad, J. A., "Experimental and Analytical Assessment of Circumferentially Surface-Cracked Pipes Under Bending", NUREG/CR-4872, April 1972.

1.29 Mayfield, M. E. and others, "Cold-Leg Integrity Evaluation - Final Report", NUREG/CR-1319, February 1980.

1.30 Collier, R. P. and others, "Two Phase Flow Through Intergranular Stress Corrosion Cracks and Resulting Acoustic Emission", EPRI Report NP-3540-LD, April 1984.

1.31 Norris, D. and others, "PICEP: Pipe Crack Evaluation Program", EPRI Report NP-3596-SR, August 1984.

1.32 Tang, H. T., Duffey, R. B., Sing, A., and Bausch, P., "Experimental Investigation of High Energy Pipe Leak and Rupture Phenomena", ASME Special Publication PVP Volume 98-8, Fracture, Fatigue and Advanced Mechanics, June 1985.

1.33 American Society of Mechanical Engineers Boiler and Pressure Vessel Code, Edition July 1989, Code Case N-463.

1.34 Eiber, R. J., Maxey, W. A., and Duffey, A. R., "Investigation of the Initiation and Extent of Ductile Pipe Rupture", Battelle Memorial Institute Report, BMI-1908, 1971.

1.35 Vassilaros, M. G., Hays, R. A., Gudas, J. P., and Joyce, J. A., "J-Integral Testing Instability Analysis for 8-Inch Diameter ASTM A106 Steel Pipe", NUREG/CR-2347, April 1984.

1.36 Takumi, K., "Results of the Japanese Carbon Steel Pipe Fracture Program", *Leak-Before-Break: Further Developments in Regulatory Policies and Supporting Research*, Proceedings of a seminar held in Taipei, Taiwan on May 11-12, 1989, NUREG/CP-0109, February 1990.

1.37 Darlaston, B. J. L. and Harrison, R. P., "Ductile Failure of Thin-Walled Pipes with Defects Under Combinations of Internal Pressure and Bending", *3rd International Conference on Pressure Vessel Technology*, Part II, Materials and Fabrication, pp 669-676, April 1977.

1.38 Maricchiolo C. and Milella, P. P., "Fracture Behavior of Carbon Steel Pipes Containing Circumferential Cracks at Room Temperature and 300 C", *Nuclear Engineering and Design*, 111, pp 35-46, 1989.

1.39 Faidy, C., Jamet, P., and Bhandari, S. "Developments in Leak Before Break Approach in France", NUREG/CP-0092, pp 69-82, March 1988.

1.40 Sturm, D., Stoppler, W., Jurlisch, P., Hipplelein, K., and Muz, J., "Fracture Initiation and Fracture Opening under Light Water Reactor Conditions", *Nuclear Engineering and Design*, Vol. 49, pp 117-134, 1978.

1.41 "Leak-Before-Break: Progress in Regulatory Policies and Supporting Research", Proceedings of a seminar held in Tokyo, Japan on May 14-15, 1987, NUREG/CP-0092, March 1988.

1.42 "Leak-Before-Break: Further Developments in Regulatory Policies and Supporting Research", Proceedings of a seminar held in Taipei, Taiwan on May 11-12, 1989, NUREG/CP-0109, February 1990.

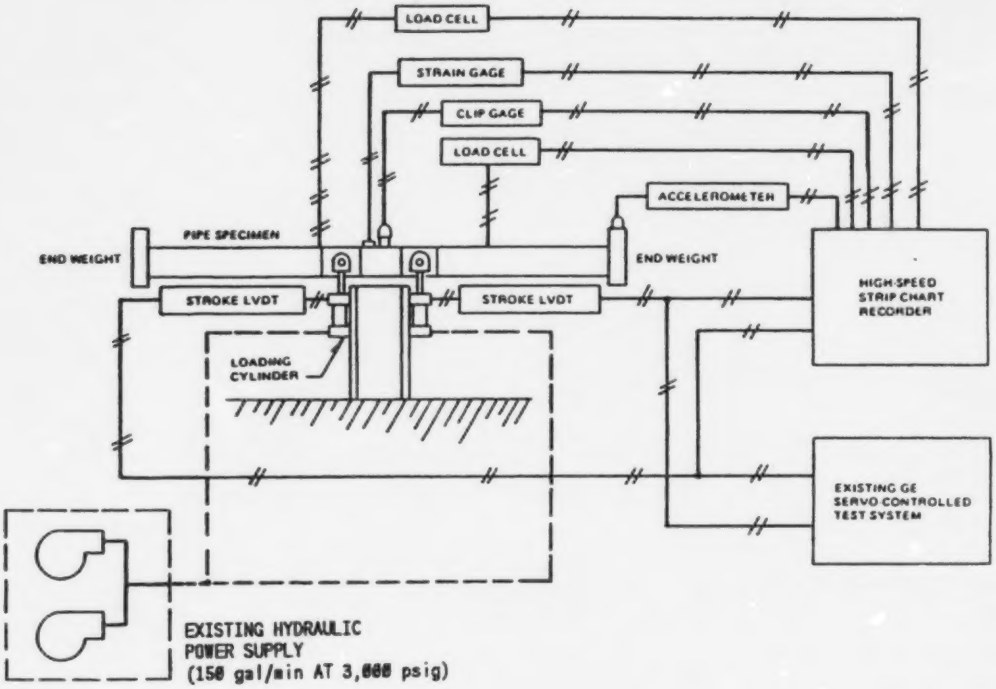
LOAD CELL
STRAIN GAGE
CLIP GAGE
LOAD CELL
ACCELEROMETER
PIPE SPECIMEN
END WEIGHT
END WEIGHT
STROKE LVDT
STROKE LVDT
HIGH-SPEED STRIP CHART RECORDER
LOADING CYLINDER
EXISTING GE SERVO-CONTROLLED TEST SYSTEM
EXISTING HYDRAULIC POWER SUPPLY (150 gal/min AT 3,000 psig)

Figure 1.1. GE/EPRI dynamic pipe test, system schematic, Ref. 1.13.

I1.3-10/90-F1.1

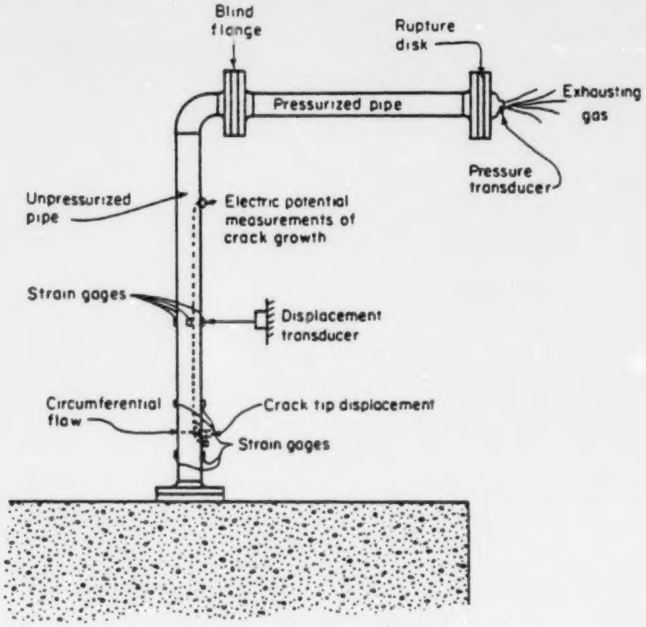
Blind flange
Rupture disk
Pressurized pipe
Exhausting gas
Pressure transducer
Unpressurized pipe
Electric potential measurements of crack growth
Strain gages
Displacement transducer
Circumferential flaw
Crack tip displacement
Strain gages

Figure 1.2. An experimental setup for induced transient bending stresses in the dynamic pipe fracture experiments in Ref. 1.14.

I1.3-10/90-F1.2

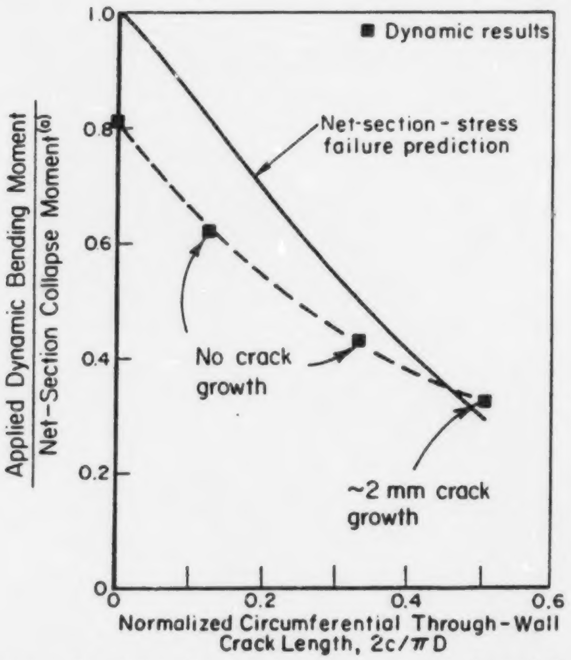

Figure 1.3. Change in dynamic moments at crack location due to increasing through-wall circumferential crack size. (Same applied blowdown loads in each experiment, from Ref. 1.14.)

(a) For uncracked pipe.

F-I-7/91-F1.3R

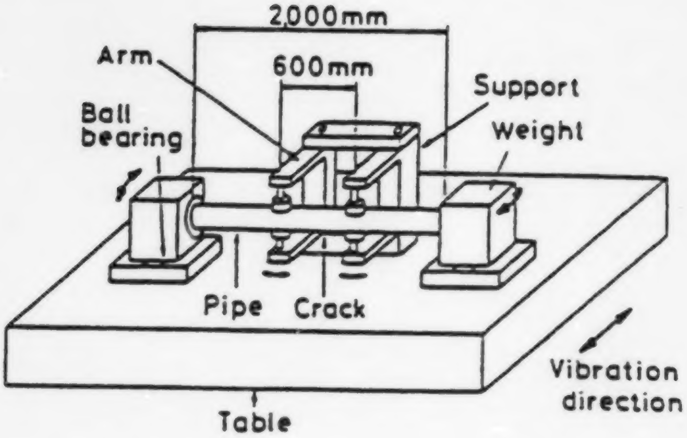
2,000mm
Arm
600mm
Support
Ball bearing
Weight
Pipe
Crack
Vibration direction
Table

Figure 1.4. Schematic setup of JAERI vibration test, from Ref. 1.16.

I1.3-10/90-F1.4

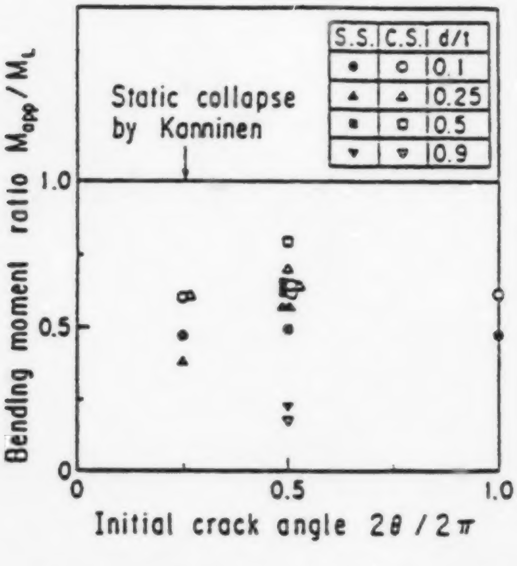

Figure 1.5. Comparison between applied maximum bending moment and net-section collapse moment for JAERI experiments, from Ref. 1.16. (Using crack size prior to applied inertial loads.)

I1.3-10/90-F1.5

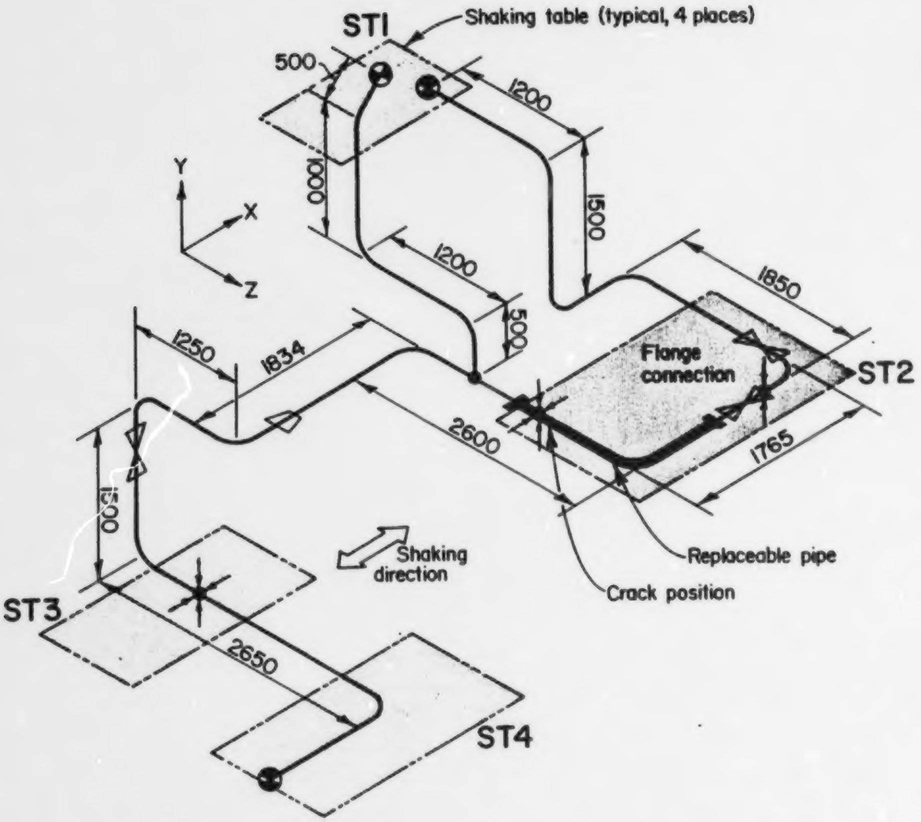
STI
Shaking table (typical, 4 places)
500
1200
1000
1500
Y
X
Z
1200
500
1850
Flange connection
ST2
1250
1834
2600
1765
1500
Shaking direction
Replaceable pipe
Crack position
ST3
2650
ST4

Figure 1.6. STA pipe system for dynamic flawed pipe tests, Ref. 1.17.

I-5/91-C7-GW

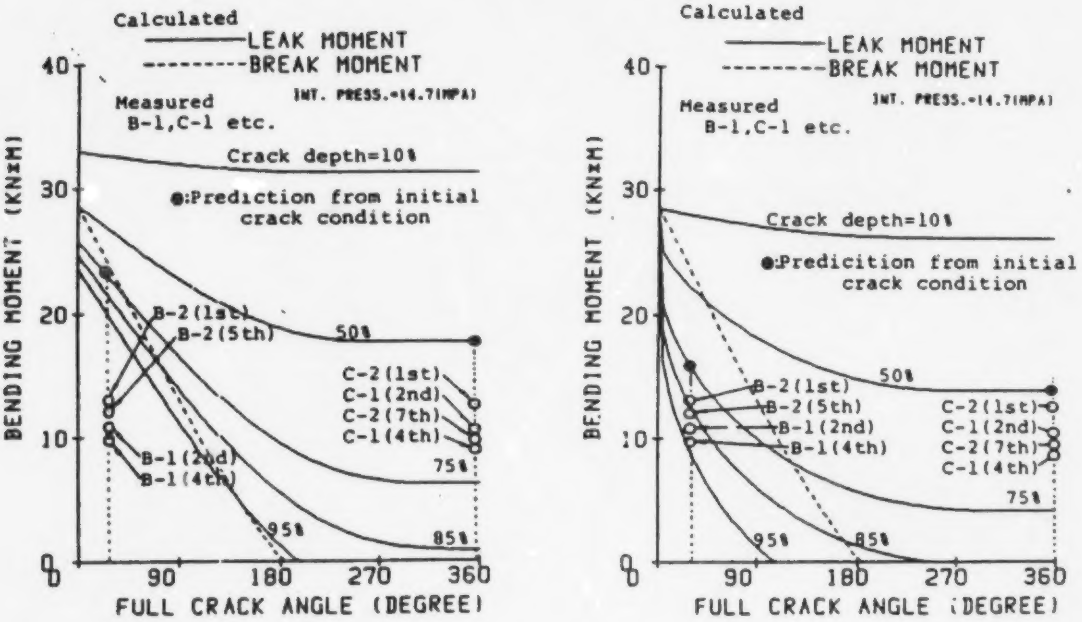

(a) Comparison between experiment and limit-load analysis by the formulation of Hasegawa et al.

(b) Comparison between experiment and limit-load analysis by the formulation of Kurihara and Ueda

Figure 1.7. Comparison of STA pipe system test failure loads with modified Net-Section-Collapse analyses using flaw size prior to dynamic load, from Ref. 1.17.

I1.3-10/90-F1.7

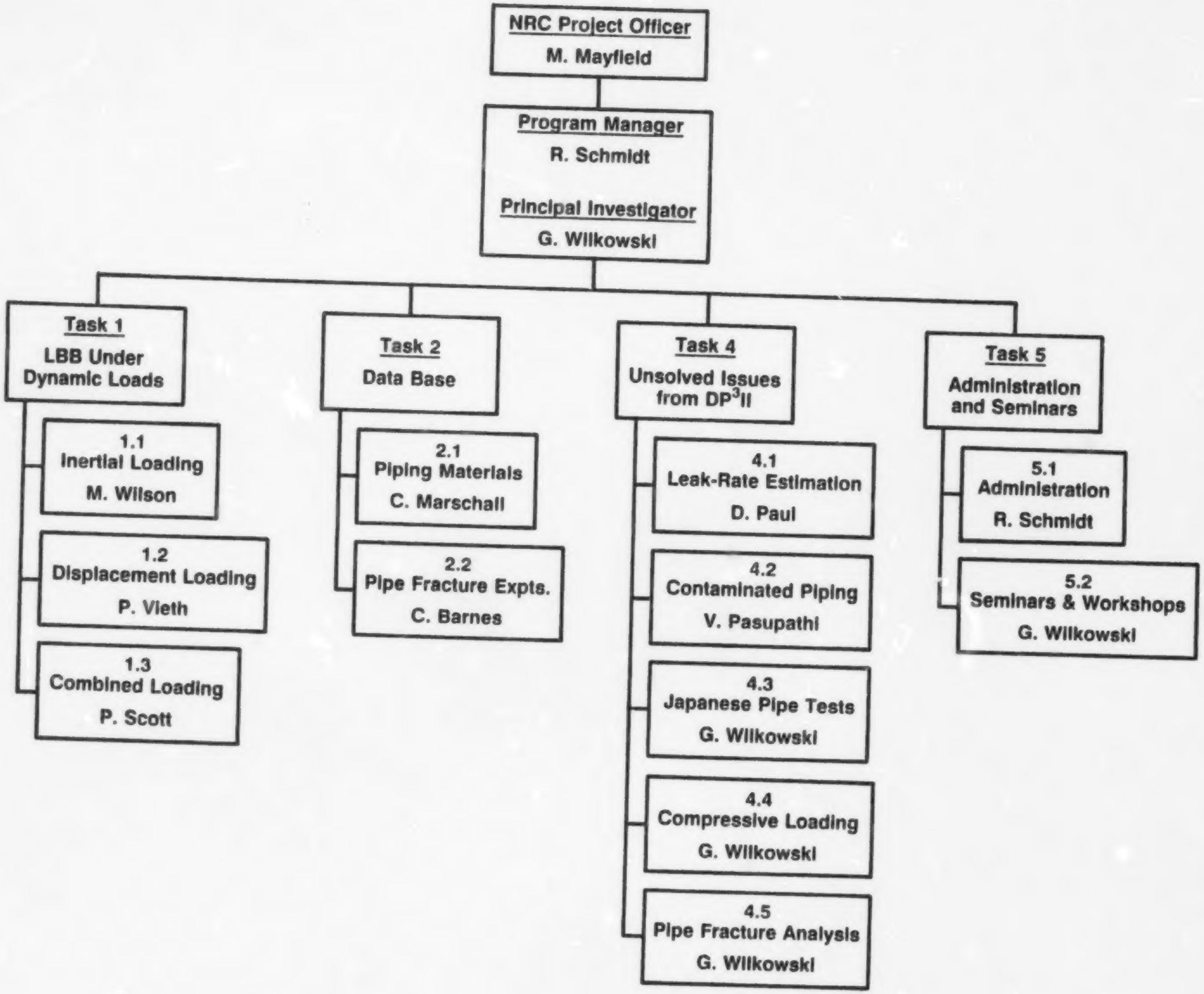
NRC Project Officer
M. Mayfield
Program Manager
R. Schmidt
Principal Investigator
G. Wilkowski
Task 1
LBB Under Dynamic Loads
1.1
Inertial Loading
M. Wilson
1.2
Displacement Loading
P. Vieth
1.3
Combined Loading
P. Scott
Task 2
Data Base
2.1
Piping Materials
C. Marschall
2.2
Pipe Fracture Expts.
C. Barnes
Task 4
Unsolved Issues from DP^{3}II
4.1
Leak-Rate Estimation
D. Paul
4.2
Contaminated Piping
V. Pasupathi
4.3
Japanese Pipe Tests
G. Wilkowski
4.4
Compressive Loading
G. Wilkowski
4.5
Pipe Fracture Analysis
G. Wilkowski
Task 5
Administration and Seminars
5.1
Administration
R. Schmidt
5.2
Seminars & Workshops
G. Wilkowski

Figure 1.8. Task structure of the IPIRG Program.

F-I-7/91-F1.8R

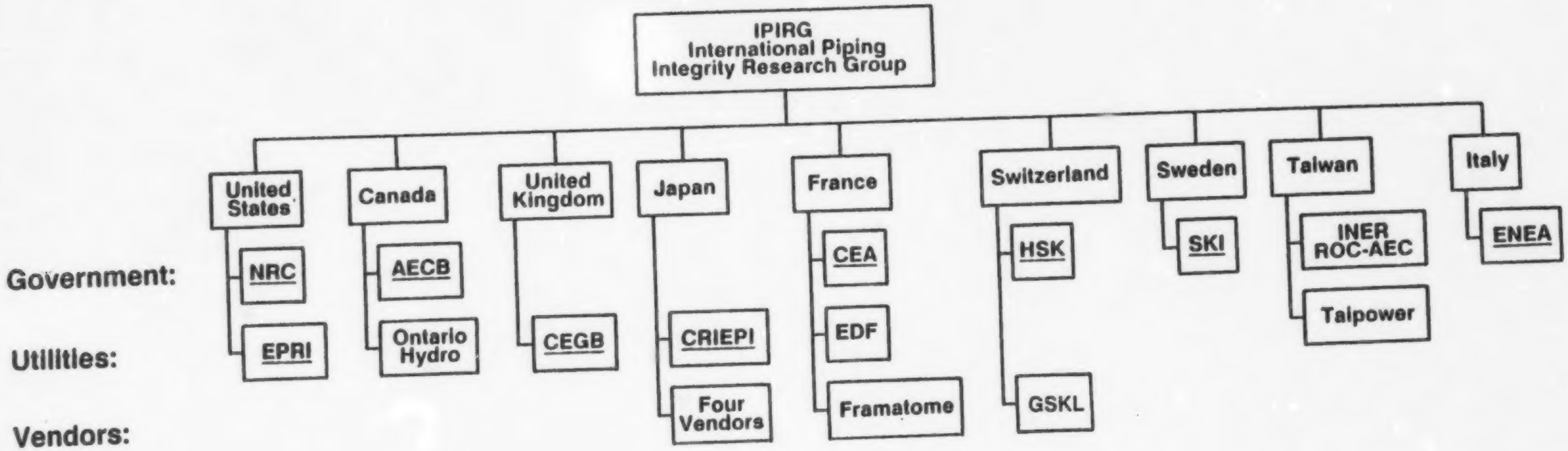
IPIRG
International Piping
Integrity Research Group
Government:
Utilities:
Vendors:
United States
NRC
EPRI
Canada
AECB
Ontario Hydro
United Kingdom
CEGB
Japan
CRIEPI
Four Vendors
France
CEA
EDF
Framatome
Switzerland
HSK
GSKL
Sweden
SKI
Taiwan
INER ROC-AEC
Taipower
Italy
ENEA

Figure 1.9. Organizations that were members of IPIRG.

F-I-7/91-F1.9R

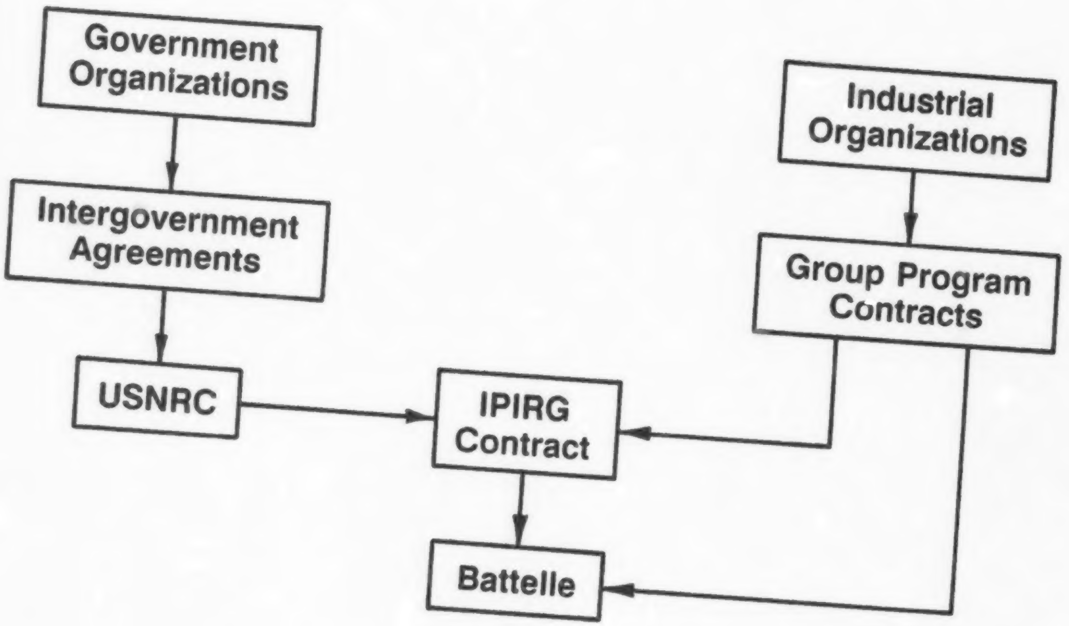
Government Organizations
Intergovernment Agreements
USNRC
Industrial Organizations
Group Program Contracts
IPIRG Contract
Battelle

Figure 1.10. Contractual structure of IPIRG.

F-I-7/91-F1.10R

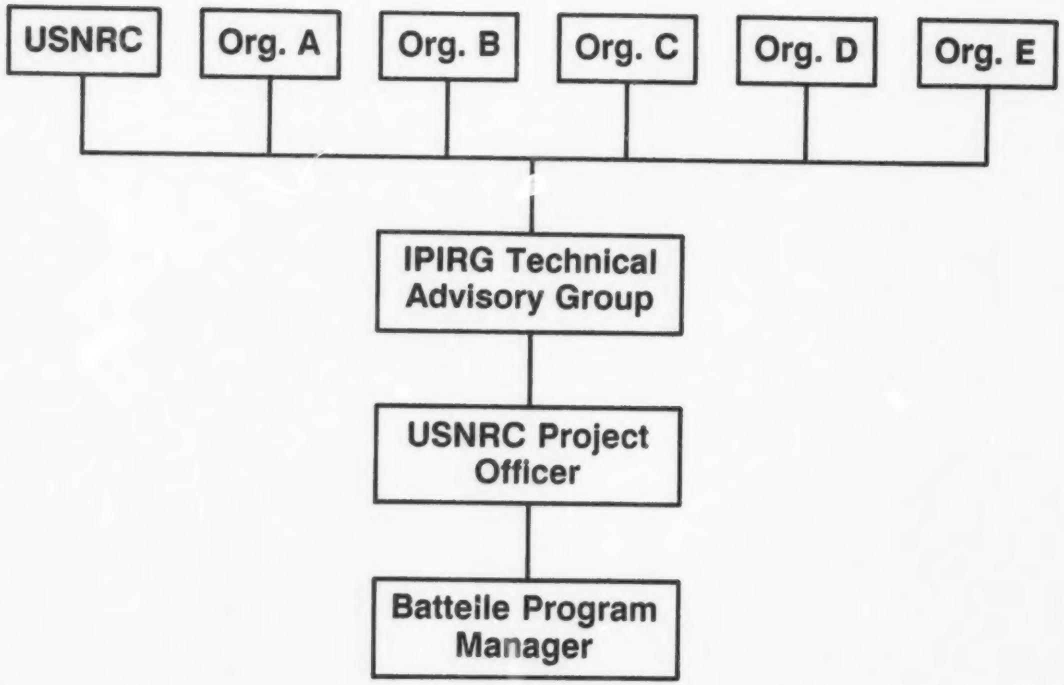
USNRC
Org. A
Org. B
Org. C
Org. D
Org. E
IPIRG Technical Advisory Group
USNRC Project Officer
Batteile Program Manager

Figure 1.11. Organizational structure of IPIRG

F-I-7/91-F1.11R

2.0 SUMMARY OF TECHNICAL RESULTS

2.1 Leak-Before-Break Verification Under Simulated Seismic/Dynamic Stresses - Task 1.0

The objective of Task 1.0 was to develop critical data to assess leak-before-break (LBB) and in-service flaw acceptance criteria for cracked piping systems under simulated seismic/dynamic loading. This involved conducting carefully controlled experiments necessary to verify current analysis procedures. In this section, the experimental procedures and results are summarized. Details of the analyses of the Task 1.0 experiments are given in Section 3.0. This task was the largest and main task of the IPIRG Program.

The predominance of pipe fracture data developed before 1986 was for quasi-static loading of straight pipe in four-point bending. The rationale for conducting this task was to expand the data base in order to assess pipe fracture behavior under conditions more closely simulating accident loads such as earthquakes. Current analysis procedures for analyzing cracked piping under dynamic loading are thought to greatly underpredict the loads and displacements required to cause failure. For example, linear elastic modal analyses with 1 to 3 percent damping are used routinely. The dynamic stresses from these modal analyses typically are added to the normal operating stresses. Since elastic analysis is used, the calculated stresses may be well above the actual yield strength of the material, whereas in reality the stresses might only be slightly above the elastic limit. For uncracked pipe, the elastic stress analysis is thought to overpredict the actual stress significantly. Using elastically calculated stresses in pipe fracture analyses results in underpredicting the actual failure loads.

Another factor that contributes to underpredicting the failure loads of cracked pipe involves using the peak seismic stress as a static stress in the ductile fracture mechanics analysis. In reality, seismic loading from even a large amplitude event may cause only a small amount of ductile tearing due to the short time span of the loading. The fracture speed and the duration of the applied loading will determine the amount of the crack growth. At the time the DEGB design rules were created, it was thought that the fracture speed of a cracked nuclear pipe would be in the range of brittle fracture speeds, i.e., 1,000 meters/second. Recent experimental results from the Degraded Piping Program, and elsewhere, have shown that ductile fracture speeds in compliant circumferentially cracked pipe fracture experiments are more than an order of magnitude slower. Hence, at the start of the IPIRG Program it was believed that seismic loading might not cause a DEGB, but rather only a leak. The amount of crack growth and the resulting magnitude of the leak would depend on the number of high amplitude cycles after a though-wall crack occurred.

The approach followed in this task involved conducting separate effects experiments followed by the more representative pipe system experiments. The three subtasks in Task 1 were:

Subtask 1.1 - Stability of Cracked Pipe Under Inertial Loading

Subtask 1.2 - Stability of Cracked Pipe Under Seismic/Dynamic Displacement-Controlled Stresses

Subtask 1.3 - Crack Stability in Representative Piping Systems Under Combined Inertial and Dynamic Displacement-Controlled Stresses

Of these, Subtask 1.2 involved the most fundamental research. In this effort, circumferential through-wall-cracked pipes were loaded in displacement-controlled four-point bending without internal pressure. Each experiment was conducted with one of the following load histories:

- quasi-static with monotonically increasing loads,
- dynamic with monotonically increasing loads,
- quasi-static with cyclic loads (R = 0 or -1)*, or
- dynamic with cyclic loads (R = 0 or -1)*.

Thus, the separate effects of dynamic and cyclic loading as well as interactive effects on the fracture resistance of these pipes were assessed. The pipes selected for testing were 6-inch nominal diameter Schedule 120 stainless steel (TP304) and carbon steel (A106 Grade B). These pipes were used previously in several Degraded Piping Program experiments and quasi-static material property data were available (Ref. 2.1).

Subtask 1.1 dealt with the stability of cracked pipe under inertial loading. In these experiments pipes with either a circumferential surface crack or through-wall crack were used as test specimens. The tests were conducted under nominal PWR conditions, i.e., 288 C (550 F) and 15.5 MPa (2250 psi). The test specimens were straight sections of pipe with weights at their ends. The test specimens were dynamically shaken in a vertical plane. Consequently, there were some dead-weight stresses as well as the pressure stresses, which may be considered as the normal operating stresses. The major loading was dynamic and cyclic as in the Subtask 1.2 experiments. However, the cyclic loading in Subtask 1.1 experiments was inertially driven. As such the stability of the crack was much different from that in the displacement-controlled experiments of Subtask 1.2. The Subtask 1.1 experiments used the same pipe material as in the Subtask 1.2 experiments.

Subtask 1.3, Crack Stability in Representative Piping Systems Under Combined Inertial and Dynamic Displacement-Controlled Stresses, involved much more complex pipe system experiments. These experiments were designed to incorporate aspects of cyclic and dynamic loading with a mixture of inertial and displacement-controlled loading in order to combine the phenomena studied separately in Subtasks 1.1 and 1.2. The pipe system was somewhat typical of reactor piping, in that it involved an expansion loop approximately 30 meters (100 feet) in length with a mass simulating the weight of a swing check valve. The pipe was 16-inch nominal diameter, Schedule 100. All fracture experiments involved circumferential surface cracks in a straight pipe section. Each test specimen was approximately two meters in length with the crack in the center. This specimen was welded into the pipe loop at the same location for each experiment. The test system was pressurized with water to 15.5 MPa (2,250 psi), and heated to 288 C (550 F) to simulate nominal PWR conditions. The materials tested were a stainless steel (TP304), a carbon steel (A106 Grade B), a stainless steel submerged arc weld (SAW), a carbon steel SAW, and an artificially aged cast stainless steel (CF8M). The artificially aged cast stainless steel pipe was donated to the program by Framatome.

---

* R is the load ratio, defined for cyclic loading as the minimum load divided by the maximum load.

Since Subtask 1.2 was the most fundamental effort, it is discussed first. Full details of Subtask 1.2 are given in Reference 2.2. Further details of Subtasks 1.1 and 1.3 are given in References 2.3 and 2.4, respectively. Further details of the analysis of results from these experiments are given in Section 3.0 of this report. In addition, Section 3.0 presents the results of the analyses for a group of quasi-static companion experiments. The companion experiments are experiments from past pipe fracture programs that used the same pipe materials and similar flaw geometries.

Additionally, dynamic material property characterization efforts on the materials used in Task 1.0 are also summarized in Section 2.1.4. Details of the dynamic material property results can be found in Reference 2.5.

2.1.1 STABILITY OF CRACKED PIPE UNDER SEISMIC/DYNAMIC DISPLACEMENT-CONTROLLED STRESSES - SUBTASK 1.2

A key issue addressed by Task 1 is the characterization of how dynamic cyclic loading affects the fracture resistance of nuclear piping materials. Subtask 1.2 was established to experimentally evaluate the load-carrying capacity and stability of cracked pipe when subjected to displacement-controlled stresses. The specific details of these tests can be found in the final report for this subtask (Ref. 2.2). The objective of the experiments was to examine separate effects of dynamic[*] loading rates and cyclic[**] loading interactions during ductile tearing. Additional information on the effect of cyclic loads on ductile fracture resistance can be found in Reference 2.6.

The pipe fracture experiments conducted in Subtask 1.2 were on 6-inch diameter TP304 stainless and A106 Grade B carbon steel pipes. All pipe test specimens contained circumferential through-wall cracks and were loaded under displacement-controlled bending at 288 C (550 F). The test specimens were not pressurized.

Test Matrix

The test matrix for this subtask is shown in Table 2.1. One quasi-static monotonically loaded pipe fracture experiment on the TP304 stainless steel pipe was conducted as part of the Degraded Piping Program (Ref. 2.1). Similar baseline experimental data were acquired for the A106 Grade B carbon steel pipe (Experiment 1.2-7). Four experiments were conducted at dynamic loading rates with monotonically increasing loads (Experiments 1.2-1, 1.2-8, 1.2-11, and 1.2-12). There were four cyclic experiments conducted at quasi-static rates; two of these experiments (Experiments 1.2-2 and 1.2-3) had a minimum load of zero (R = 0), whereas the other two (Experiments 1.2-4 and 1.2-5) had fully reversed loads (R = -1). Three experiments were conducted that combined dynamic with cyclic loading. One of the experiments (Experiment 1.2-10) had a minimum load of zero (R = 0) and two (Experiments 1.2-6, and 1.2-9) had fully reversed loads (R = -1).

The twelve pipe fracture experiments conducted for Subtask 1.2 were all conducted in Battelle's Structural Fatigue Laboratory. An MTS 580 kN (130,000 pound) dynamic or 890 kN (200,000 pound) static servohydraulic system was used to conduct these experiments. Two types of loading fixtures were used: a simple loading fixture which applied bending stresses in a single direction was used for Experiments 1.2-1, 1.2-2, and 1.2-3; and a more complex loading fixture which allowed reverse bending of the pipe was used for the other Subtask 1.2 experiments. A schematic of the more complex loading fixture is provided in Figure 2.1.

The pipe fracture experiment conducted as part of the Degraded Piping Program (Experiment 4131-5, Ref. 2.1) was conducted at Battelle's West Jefferson Facility. The system used to conduct this experiment was a pipe strongback system with a bending moment capacity of 1.09 MN-m (9.5 X 10^6 in-lb). A schematic of this test system is provided in Figure 2.2.

---

[*] Dynamic loading rates in this report refer to high rates of loading typical of a seismic event.

[**] Cyclic loading in this program is focussed on relatively few large amplitude cycles that provide little, if any, fatigue crack growth.

Each of the thirteen pipe fracture specimens (twelve from IPIRG and one from the Degraded Piping Program) were prepared in a similar manner. A specimen approximately 457 mm (18 inches) in length was removed from the appropriate heat of pipe. Due to out-of-roundness, many of the pipe specimens were machined on the inside diameter to produce a constant wall thickness. On some of the specimens it was also necessary to machine the outside diameter.

A through-wall crack (TWC) was machined into each specimen to the approximate crack dimensions using a 1.0-mm (0.040-inch) wide band-saw blade. The TWC was completed using a jeweler's saw with a notch tip radius of 0.13 mm (0.005 inch). The final flaw length on the outside diameter of the pipe was approximately 37-percent of the circumference.

Several of the specimens were fatigue precracked with approximately 3.5 mm (0.150-inch) of crack growth at each notch tip to achieve the final crack length of 37-percent of the pipe circumference. The specimens that were fatigue precracked included all of the carbon steel pipe experiments along with one stainless steel pipe experiment (Experiment 1.2-3). Previous results from C(T) tests on specimens with and without fatigue precracks indicated that it was unnecessary to fatigue precrack the stainless steel pipe experiments.

After the TWC was introduced into the test specimens, longer lengths of similar pipe were welded to the ends of the specimen. This was done to increase the overall length of the pipe to between 1.8 and 2.5 meters (70 and 100 inches) depending on the loading fixture requirements.

Several direct-current electric potential (d-c EP) probes were attached to the specimen to monitor crack growth. Probes were attached to the pipe across the crack at each crack tip and at the crack centerline. A set of reference probes was attached to the pipe approximately one pipe diameter from the crack. Clip gages were also mounted at each of the crack tips and the crack centerline to measure the crack-mouth-opening displacement. A schematic of the instrumentation layout for a typical experiment is provided in Figure 2.3.

Mounting fixtures for rotation measuring devices were attached to the side of the pipe (90 degrees from the crack centerline) 125 mm (5 inches) on each side of the crack. Three different devices were used. Inclinometers were used for the quasi-static experiments. A rotary variable differential transformer (RVDT) arrangement was used for dynamic loadings for Experiments 1.2-1, 1.2-6, 1.2-8, and 1.2-12. The RVDT arrangement was necessary for the dynamic tests since the inclinometers did not have a sufficiently fast response. An improved dynamic rotation measurement device was used for Experiments 1.2-9, 1.2-10, and 1.2-11. It utilized an LVDT arrangement that was developed in Subtask 1.3.

The tests were carried out using two methods. All of the quasi-static tests (monotonic and cyclic) and all of the monotonic tests (quasi-static and dynamic) were conducted using an electronic function generator to provide the command signal to the test machine. However, the cyclic experiments conducted at dynamic rates required real-time decision-making control. This was accomplished using a computer and special purpose software that monitored the load while controlling the test machine, which was operated in displacement control. The computer program logic is presented in Figure 2.4. For the R = -1 experiments the loading was accomplished in the following steps. The specimen was loaded to a known displacement at a constant displacement rate. The load at that displacement was recorded by the computer, and the actuator was commanded to reverse direction. Reverse loading was continued at the same displacement rate as before, through zero load, until the same load magnitude was reached in the opposite direction. The specimen then was loaded to the next prescribed displacement. This process was repeated for a pre-determined number of cycles. The displacement increment was kept constant to study separately the effects of load ratio and incremental plastic displacement.

Experimental Results

The results for each of the experiments are discussed below and are summarized in Tables 2.2 and 2.3 for the stainless steel and carbon steel pipe experiments, respectively. Direct comparisons of maximum moments or moments at crack initiation should be avoided at this time since there were small differences between experiments in the pipe diameter, wall thicknesses, and crack lengths. In Section 3.0 the experimental moments are normalized by various analytical methods, allowing for a more systematic comparison of the experimental results.

MONOTONICALLY LOADED PIPE EXPERIMENTS. Two different loading rates, quasi-static and dynamic loading representative of a seismic event, were employed in the monotonic displacement-controlled pipe experiments. The seismic or dynamic rate was about 1,000 times faster than the quasi-static testing rates typically used in pipe fracture experiments. The dynamic loading rate was selected by analyzing ANSYS® computer simulations of the Subtask 1.1 pipe fracture experiments, which were loaded at 3.5 Hz. The Subtask 1.1 dynamic rate was verified after the experimental results had been analyzed and was found to be within a factor of 2 of the predicted rate. This difference in loading rate, in terms of the effects on material properties, is believed to be negligible.

The results of the two stainless steel pipe experiments conducted at quasi-static and dynamic loading rates and with monotonically increasing loads are presented in terms of moment-rotation response in Figure 2.5. The two curves are similar in appearance. The maximum moments are 37.62 kN (333,000 inch-pounds) and 38.56 kN-m (341,300 inch-pounds) for the quasi-static and dynamic experiments, respectively.

The results of the four carbon steel monotonically loaded experiments (1.2-7, 1.2-8, 1.2-11 and 1.2-12) are illustrated in terms of moment-rotation response in Figure 2.6. Experiment 1.2-11 was conducted as a verification of the results from Experiment 1.2-8. Experiment 1.2-12 was intended to be a cyclic experiment but, due to test problems, the specimen was loaded with a monotonically increasing load. However, the basic data were recorded, and the moment and calculated rotation data were used to further validate Experiment 1.2-8. Figure 2.6 shows that the moment-rotation curves for the three dynamic experiments lie below the moment-rotation curve for the quasi-static experiment. The maximum moments for the Subtask 1.2 experiments are given in Tables 2.2 and 2.3, and are compared with Net-Section-Collapse analysis predictions in Section 3.0.

QUASI-STATIC CYCLICALLY LOADED PIPE EXPERIMENTS. Two loading parameters are used to describe these experiments: the load ratio (R) and the cyclic increment of load line displacement, referred to as the incremental plastic displacement. The cyclic loading was conducted with either a zero minimum load (R = 0) or fully reversed (R = -1). The incremental plastic displacement chosen in these experiments was equal to one-tenth of the load-line displacement to crack initiation from the monotonically loaded experiments. The factor of one-tenth came from a desire to have approximately 10 cycles to crack initiation in the Subtask 1.1 and 1.3 experiments. This is a reasonable number of large amplitude cycles in a seismic event. The incremental plastic displacement was kept constant until well past maximum load. However, in some cases the displacement increment was changed during subsequent cyclic loadings to evaluate its effect on the fracture behavior.

R = 0 Experiments. One pipe fracture experiment was conducted for each pipe material using a cyclic (R = 0) load history at quasi-static rates. The results of the stainless steel experiment (1.2-3) can be found in Table 2.2 and the results of the carbon steel experiment (1.2-2) can be found in Table 2.3. The moment-rotation response is presented in Figures 2.7 and 2.8 for the stainless steel and carbon steel pipe experiments, respectively. For comparison purposes, Figures 2.7 and 2.8 also include the moment-rotation response for the corresponding quasi-static monotonic experiments. Figures 2.7 and 2.8 show that the moment-rotation response for the cyclic (R = 0) experiments are similar to that for the monotonic experiments. The moment-rotation curves displayed represent only the envelope of the curve and not the cyclic displacements. Figure 2.9 presents the entire load-displacement data for Experiment 1.2-3 showing the cyclic loadings and displacement increments used throughout the experiment.

R = -1 Experiments. One pipe fracture experiment was conducted for each pipe material with a cyclic (R = -1) load history at quasi-static rates. The results of the stainless steel experiment (1.2-5) can be found in Table 2.2 and the results of the carbon steel experiment (1.2-4) can be found in Table 2.3. The envelope of the moment-rotation response is compared with the quasi-static, monotonic pipe test results in Figures 2.10 and 2.11. Figure 2.12 shows an entire load-displacement curve from Experiment 1.2-4 which includes the reverse bending loads.

Note that although there was a relatively small decrease in maximum load between the monotonic and R = -1 experiments for both materials, the rotations were significantly reduced. This indicates that the apparent fracture toughness of the materials was reduced by cyclic loading with R = -1.

DYNAMIC CYCLICALLY LOADED PIPE EXPERIMENTS. The load-line displacement rates for the dynamic cyclic (R = 0 and R = -1) load histories were on the order of 25 mm/sec (1.0 inch/sec). These loading rates were close to the 3.5 Hz loading rates used in the Subtask 1.1 inertially loaded pipe fracture experiments. The incremental plastic displacement was constant for each of the three experiments conducted.

One stainless steel experiment (Experiment 1.2-9) was conducted with combined dynamic and cyclic (R = -1) loading to investigate the extent to which the effect of these two parameters interact. The specific dimensions and results of this experiment are presented in Table 2.2 and the envelope of the moment-rotation curve is illustrated in Figure 2.13. Although the maximum moments for the dynamic, monotonic experiment and the dynamic, cyclic (R = -1) experiments are similar, the rotations are significantly less for the dynamic, cyclic (R = -1) experiment. The smaller rotations reflect a reduced apparent fracture resistance under these conditions.

Two experiments were conducted with combined dynamic and cyclic loading on the A106 Grade B carbon steel pipe material. One experiment was conducted with dynamic, cyclic (R = 0) loading (Experiment 1.2-10), and the other with dynamic, cyclic (R = -1) loading (Experiment 1.2-6). The specific dimensions and results of these experiments are presented in Table 2.3 and the envelope of the moment-rotation curve is illustrated in Figure 2.14. Both the moments and rotations for the two dynamic, cyclic experiments were significantly less than the moments and rotations for the dynamic, monotonic experiments. As expected, the moments and rotations for the R = -1 experiment were less than those for the R = 0 experiment indicating a further reduction in both toughness and load-carrying capacity for the more negative load ratio experiment.

Summary of Cyclic and Dynamic Effects of Carbon and Stainless Steel

Figures 2.15 and 2.16 present composite plots of moment versus rotation for the stainless and carbon steel, respectively. A cursory review of the moment-rotation curve comparisons shows that the stainless steel pipe was only affected by the R = -1 cyclic loading, whereas the carbon steel pipe tested was sensitive to loading rate and R = -1 cyclic loading. Further comparisons on rate and cyclic effects based on maximum load and calculated J-R curves from the pipe experiments are given in Section 3.0. Another point worthy of note is that for the stainless steel pipe experiments, the cracks grew in the circumferential plane, but the carbon steel pipe cracks grew out of the circumferential plane. Metallurgical evaluation of this carbon steel pipe showed the low toughness direction was for axial crack growth. Hence, the material anisotropy apparently caused the out-of-plane crack growth.

2.1.2 STABILITY OF CRACKED PIPE UNDER INERTIAL STRESSES - SUBTASK 1.1

This section discusses the efforts associated with Subtask 1.1. Further details of these efforts are provided in the Subtask 1.1 final report (Ref. 2.3). The specific objective of this subtask was to develop experimental data on circumferentially cracked pipe subjected to predominantly inertial loading conditions. The experiments conducted as part of this effort were to expand on the results of Subtask 1.2 by including combined tension and bending under inertial loading, as well as having variable load ratios and incremental plastic displacements.

Test Matrix

The test matrix for Subtask 1.1 is presented in Table 2.4. The pipes evaluated were all 6-inch nominal diameter, Schedule 120. All cracks were in the base metal. Several quasi-static pipe fracture experiments had been conducted during the Degraded Piping Program (Ref. 2.1) using both the A106B carbon steel and the TP304 stainless steel pipes evaluated as part of this effort. (Note: four identical stainless steel pipes from the same heat were obtained for these experiments, and two identical carbon steel pipes from the same heat were also obtained.)

The original test matrix for the base program was comprised of the first six experiments listed in Table 2.4. The last three experiments included in Table 2.4 were added to the original test matrix to address specific questions which arose when initial results from Subtask 1.1 were compared with those of Subtask 1.2. Experiment 1.1-8 was essentially a repeat of Experiment 1.1-6 and was intended to provide an assessment of the variability expected in inertial experiments. Experiments 1.1-7 and 1.1-9 were not inertial tests at all; they were conducted in the same facility as the other experiments in this test matrix, but were loaded in four-point bending. Experiment 1.1-9 was a quasi-static, monotonic experiment and provided useful insight as to the potential variability between the test frame used in Subtask 1.1 with that used in Subtask 1.2. It also provided an important check on the validity of the measured bending moments using strain gages and load cells. Experiment 1.1-7 was a dynamic, monotonic experiment, and, through comparison with the results from Experiments 1.1-6, 1.1-9, 1.2-7, 1.2-8, and 1.2-11, provided data useful in identifying the contributions of dynamic and cyclic loading to the fracture behavior of this carbon steel material.

Pretest Design Analysis

As part of the design of the Subtask 1.1 experimental facility, analyses were performed to size mechanical components. In addition, as part of the pretest design for the individual experiments, analyses were performed to select the appropriate dynamic forcing functions. Both of these analyses used the ANSYS® finite element code.

A conceptual model of the test system for Subtask 1.1 is shown in Figure 2.17. The model consists of a centrally supported pipe with concentrated masses at each end. The basic model used in the finite element analyses had four nodes and four elements. Because of symmetry, only half of the structure needed to be modeled. Only two pipe elements were used because the system was assumed to behave largely as a single degree-of-freedom mass and spring (see Figure 2.18).

Past EPRI/Battelle dynamic cracked pipe experiments (Ref. 2.7) showed that to analyze the behavior of a piping system containing cracks, a simple nonlinear representation of the crack was needed. A one-dimensional model of the moment versus rotation behavior was developed using a nonlinear stiffness, which accounts for local plastic deformation and crack growth.

The starting point for the crack section modeling was the quasi-static moment-rotation test data from the Degraded Piping Program (Ref. 2.1). These data provided the basic nonlinear stiffness for the cracked pipe section. At times, however, it was necessary to modify the experimental curves to account for differences in internal pressure between the pressurized Subtask 1.1 experiments and the unpressurized Degraded Piping Program experiments. This was accomplished by multiplying all of the moments by the ratio of the Net-Section-Collapse predicted bending moment for the test pressure of interest to the Net-Section-Collapse predicted bending moment for the case of an unpressurized pipe.

Implementing the crack's moment-rotation response into the finite element analysis required the definition of a nonlinear spring element. Within ANSYS®, the most convenient means of achieving this for reverse loading is with spring-slider elements, one of which is shown in Figure 2.19. (Note: Although ANSYS® has a nonlinear spring element, it does not allow for unloading below zero load and then tension reloading in an incremental plasticity manner.) The spring-slider element is a two node, two degree-of-freedom element with a linear spring and a friction slider in series. Details of the implementation of this spring-slider element are provided in References 2.3, 2.4, and 2.8.

Once the basic stiffness of this spring-slider element has been defined, it is then attached to a pair of nodes, which are coincident in space in the finite element model. The rotational stiffness of this spring-slider element defines the coupling between the in-plane bending degrees of freedom. To couple the remaining degrees of freedom (out-of-plane bending, torsional, two shear, and the axial degrees of freedom) constraint equations are used, which specify that rotations and displacements in these degrees-of-freedom must be identical for the two pipe elements on either side of the crack. Completing the definition of the crack element, crack closure is modeled as a constraint such that no rotation in the negative direction is allowed, i.e., the crack becomes rigid when it closes, transmitting all moments continuously across the crack.

Experimental Procedures

The facility, instrumentation, data acquisition, test procedures, and data reduction procedures used in Subtask 1.1 are summarized in the following paragraphs.

The test facility used for the Subtask 1.1 experiments was constructed using two 67 kN (15,000 pound) hydraulic actuators mounted vertically (see Figure 2.20). The hydraulic actuators were attached at floor level to a foundation consisting of a steel subframe which was buried in a hole measuring 2 meters (78 inches) on a side. After placing the frame in the hole, it was filled with concrete. The weight of the foundation exceeded the force capacity of the actuators, thus reducing the likelihood of the foundation being lifted by inertial forces during the experiments. The actuators, which each had a stroke capacity of 254 mm (10 inches), were located on 914 mm (36 inch) centers. They were operated in parallel by a single servocontroller driving two 230 lpm (60 gpm) servovalves.

The instrumentation for the Subtask 1.1 experiments included the following

- Linear Variable Differential Transformers (LVDT) were attached to the actuators to measure the load-line displacement of the actuators. This was also the feedback signal for the servocontrollers used to control the experiments.

- Load cells were mounted between the actuator and the hanger attached to the pipe to measure the applied loads.

- High temperature weldable strain gages were attached to the top and bottom of the pipe at a number of locations along the length of the pipe. The strain values from these strain gages were used to calculate the bending moments at the crack section and other locations.

- A clip gage, which is a special purpose strain-gaged displacement transducer, was mounted across the flaw to measure the crack-mouth-opening displacement.

- A specially fabricated rotation device was mounted across the crack plane to measure the crack section rotations. For the initial set of experiments (1.1-2, 1.1-3, 1.1-4, 1.1-5, and 1.1-6), this rotation device employed a rotary variable differential transformer (RVDT) as the sensing element. For the later experiments (1.1-7, 1.1-8, and 1.1-9) an improved design utilizing an LVDT was used. In addition to providing a measure of the crack section rotations, these devices provided the control signal for automatically terminating the initial set of experiments. Once the output of these devices reached a preset level, indicating a given crack section rotation had been reached, the command signal supplied to the actuators was attenuated, bringing the specimen to a controlled stop.

- Direct current electric potential (d-c EP) probes were mounted across the crack to infer crack initiation and crack growth data.
- A specially fabricated displacement measuring device was attached to the end masses to measure the vertical end mass displacements during the inertial experiments. An RVDT was used as the sensing element for these measurements.
- Accelerometers were attached to one of the end masses and one of the saddles to measure the accelerations during selected experiments.
- A pressure transducer was used to measure the internal pipe pressure.
- Chromel-Alumel (Type K) thermocouples were attached to the pipe at several locations to measure the pipe temperature.

The primary data acquisition system for these experiments was an IBM compatible personal computer using Metrabyte DAS-8, 8-channel, high speed, A/D converters with Metrabyte EXP-16 expansion multiplexer/conditioners. The computer collected 14 to 24 channels of data using LabTech Notebook® data acquisition and control software. For the dynamic experiments, the sampling rate was 100 to 200 samples per second. As a backup, an FM tape recorder was used to store analog data. In addition, for some of the early experiments, a MassComp computer was also used as a backup.

Nominal PWR pressure and temperature conditions were used for all experiments. Each pipe specimen was filled with water, heated to 288 C (550 F), and pressurized to 15.5 MPa (2250 psi).

The design-basis displacement forcing function for the inertial experiments was an increasing sinusoidal function. The equation which defines the design-basis command signal is:

$$U_y = at \sin(\omega t) \tag{2.1}$$

where,

U_y = the displacement of the actuator in the vertical direction
a = a constant related to the amplitude of the signal
t = time
ω = the excitation frequency.

For all of the inertial experiments, the excitation frequency was 3.5 Hz. This is approximately 83 percent of the first natural frequency for the test system, i.e., 4.2 Hz.

For the quasi-static, monotonic (Experiment 1.1-9) and dynamic, monotonic (Experiment 1.1-7) experiments, the forcing function was monotonically increasing displacement. The load-line displacement rate for the quasi-static, monotonic experiment was 0.025 mm/second (0.001 inches/second). The loading rate for the dynamic, monotonic experiment was 152 mm/second (6 inches/second), approximately 6000 times faster than for the quasi-static experiment. This displacement rate for the dynamic monotonic experiment resulted in a strain rate of the same order as that for the dynamic, monotonic, carbon steel through-wall crack experiment in Subtask 1.2, Experiment 1.2-8.

The raw data from the experiments consisted of voltages from all of the transducers as a function of time. The data, which were stored digitally by the data acquisition system, were reduced using Lotus 1-2-3® spreadsheets to generate the engineering data for the experiments.

The process of reducing the data was relatively straightforward, given the conversion factors from volts to engineering units. The only item requiring assumptions and more involved computations were the calculations of the bending moments from the strain gage data. The gages that were mounted on the test specimen inside the load points in the region of relatively uniform moment were used to calculate the crack section moment data.

For the Subtask 1.1 experiments, for which the out-of-plane bending component is assumed to be negligible, the crack section moments can be calculated from a knowledge of the longitudinal stresses at the top and bottom of the pipe:

$$M = [(\sigma_{Top} - \sigma_{Bot})/2]I/r \qquad (2.2)$$

where,

M = crack section moment
σ_{Top} = longitudinal stress at the top of the pipe
σ_{Bot} = longitudinal stress at the bottom of the pipe
I = moment of inertia of the pipe cross section containing the gages
r = pipe outside radius.

For further details of Equation 2.2, the reader is referred to Appendix B of the Subtask 1.3 final report (Ref. 2.4). Elastic conditions and a uniform wall thickness are two of the assumptions embodied in Equation 2.2. If plane stress conditions are assumed, and if hoop strains at the top and bottom of the pipe are assumed equal, it can be shown that Equation 2.2 becomes:

$$M = [E/(1-\nu^2)](\epsilon_{Top} - \epsilon_{Bot})I/r \tag{2.3}$$

where,

E = elastic modulus
ν = Poisson's ratio
ϵ_{Top} = the longitudinal strain at the top of the pipe
ϵ_{Bot} = the longitudinal strain at the bottom of the pipe.

Since all of the parameters in Equation 2.3 are measured values, the crack section moments (M) can be calculated directly from the experimental strain data.

Due to static drift in the strain gage system during heatup, the strain gages were treated as strictly dynamic transducers for calculation of dynamic moments. Static values of moment due to dead weight were calculated using the ANSYS® finite element analyses and were added to the measured dynamic data in order to get the total moment.

Summary of Results

The following paragraphs provide a summary of the results from seven of the eight Subtask 1.1 cracked pipe experiments. (Note, no data are provided for Experiment 1.1-4 due to a highly irregular flaw geometry that occurred during fatigue precracking.)

Table 2.5 provides the key experimental results from the Subtask 1.1 cracked pipe experiments. Included in Table 2.5 are the material, pipe and crack dimensions, forcing function parameters, moments at crack initiation, maximum moments, cycles or time to maximum moment, and cycles past maximum moment until a through-wall crack instability condition was reached, if appropriate.

Figure 2.21 is a plot of the envelopes of the peaks of the moment-rotation responses from the two Subtask 1.1 through-wall-cracked pipe experiments. The higher moment-carrying capacity for the carbon steel experiment (1.1-2) is a reflection of the fact that the flow stress of this material is approximately 65 percent higher than the flow stress of the stainless steel material, where flow stress is defined as the average of the quasi-static yield and ultimate strengths. The greater rotation for the stainless steel experiment (1.1-3) is a reflection of the fact that its toughness is significantly greater than the toughness of the carbon steel material. This observation is based on the fact that the J values at crack initiation from C(T) test for the stainless steel are almost a factor of 10 greater than the initiation values for the carbon steel.

Figure 2.22 is a plot of the envelopes of the peaks of the moment-rotation responses from three of the five Subtask 1.1 surface-cracked pipe experiments. The fidelity of the rotation data for the two inertially loaded, carbon steel, surface-cracked pipe experiments was so poor that it was not possible to generate a moment-rotation curve for these two experiments. As was the case for the through-wall-cracked pipe results presented in Figure 2.21, the higher moments for the carbon steel experiments are a consequence of the higher strength of this material, and the higher rotations for the stainless steel experiment are a consequence of the higher toughness for this material. The higher moment-carrying capacity for the quasi-static, monotonic, carbon steel experiment (1.1-7) when compared with the dynamic, monotonic, carbon steel experiment (1.1-9) is probably a consequence of both the deeper crack for the dynamic experiment (see Table 2.5) and the decrease in strength and toughness of this material at dynamic loading rates. In order to separate the effects of the deeper crack from the decrease in strength and toughness at dynamic loading rates, the results must be normalized through analysis. The normalized results are discussed in Section 3.0.

2.1.3 CRACK STABILITY IN A REPRESENTATIVE PIPING SYSTEM UNDER COMBINED INERTIAL AND SEISMIC/DYNAMIC DISPLACEMENT-CONTROLLED STRESSES - SUBTASK 1.3

The objective of Subtask 1.3 was to develop the experimental data necessary to assess the analysis methodologies for characterizing the fracture behavior of circumferentially cracked pipe under combined inertial and displacement-controlled stresses. These data were developed on a large diameter piping system designed to be representative of nuclear reactor piping systems, including the complex interaction of loading conditions and system dynamics. The data generated provide important test cases for assessing current analysis procedures, i.e., finite element stress analyses, in-service flaw assessment, and leak-before-break analyses.

Subtask 1.3 was founded on the knowledge gained from the two separate effects studies on displacement-controlled stresses and inertial stresses, Subtask 1.2 (Ref. 2.2) and Subtask 1.1 (Ref. 2.3), respectively. The objective of this subtask was met using a combination of theoretical development and engineering, combined with carefully selected analysis and experimentation.

In the sections that follow, an overview of Subtask 1.3 is presented, from initial system design to results of the experiments. The presentation is condensed and is limited to the highlights. Further elaboration on any of the individual points can be found in Reference 2.4.

Test Matrix

The test matrix for Subtask 1.3 is shown in Table 2.6. The test matrix consisted of six experiments, one series of uncracked pipe experiments and five cracked pipe experiments. The pipe size for the experiments was 16-inch nominal diameter, Schedule 100. By using this pipe size, it was anticipated that the fracture process for the higher toughness steels would be governed by fully plastic (limit-load) conditions and that it would be governed by elastic-plastic fracture mechanics (EPFM) for the lower toughness steels. The combination of limit-load and EPFM failure conditions was used to provide a good range of behavior for testing predictive fracture methodologies.

The test specimens for the Subtask 1.3 experiments were short lengths, typically 300 mm (12 inches) or 760 mm (30 inches), of 16-inch nominal diameter, Schedule 100 pipe with an internal circumferential surface flaw at the mid-length position of the test specimen. The internal surface flaws were nominally 66 percent deep and 180 degrees long.

For each of cracked pipe specimens, a companion quasi-static pipe fracture experiment, using the same pipe and nominal crack size, had been previously conducted as part of the Degraded Piping Program (Ref. 2.1) or in another Battelle program sponsored by the Electric Power Research Institute (EPRI) (Ref. 2.7). This provided a basis for determining the effect of dynamics and cyclic load history on the fracture behavior.

Experimental Facility

A unique experimental facility was designed and constructed to conduct the Subtask 1.3 dynamic pipe experiments. The facility, shown as an artist's conception in Figure 2.23, was equipped with specially designed hardware to ensure that the pipe system had well-defined boundary conditions that could be accurately modeled analytically.

Figure 2.24 shows the dimensions of the pipe loop. The pipe loop was fabricated from predominantly 16-inch nominal diameter, Schedule 100 pipe. The straight pipe material was ASTM A710, Grade A, Class 3 steel. The elbows were long radius elbows fabricated from WPHY-65 material. Elbows 1, 2, 3, and 5 were Schedule 100 and Elbow 4 was Schedule 160. These pipe materials, although not typical of plant installations, were used because they have high strengths, even at elevated temperatures. The pipe loop would thus remain elastic and reusable for all of the experiments. A large 1,950-kg (4,300-pound) mass, which simulated a swing check valve, was located in one leg of the pipe loop.

Special features of the Subtask 1.3 piping system hardware included

- End caps welded into the pipe loop 914 mm (36 inches) on each side of the crack plane (Figure 2.25) for all experiments except the aged cast stainless experiment to minimize the blowdown volume and mitigate the effects of the jet force when the crack broke through the pipe wall.

- Fully restrained ends, achieved by bolting capped 1,500-pound-class weld neck flanges at each end of the piping to a large steel frame that was buried in a large, heavily reinforced concrete mass.

- Spherical bearings at the hanger locations to provide only horizontal and vertical restraint to the pipe.
- Vertical supports that use low-friction hydrostatic bearings.
- A system of linear and spherical bearings at the actuator location to ensure that only a lateral force and no vertical displacement was input to the pipe.

System loads were applied by a 1,560-kN (350,000-pound) hydraulic actuator with a 457-mm (18-inch) stroke, driven by a very large 7,600 liter per minute (2,000 gpm) servo-valve. Accumulators of 380-liter (100-gallon) fully charged oil capacity were used to supply hydraulic power. A water circulation pump and an expansion tank completed the basic pipe system. Figures 2.26 to 2.31 show a series of photographs of the experimental facility.

The pipe loop test facility was designed to have some of the same features found in nuclear plant piping. Some of the ways in which this facility were similar to and different from nuclear piping are as follows:

- Typical of nuclear piping systems
    - Long Radius Elbows
    - Expansion loop proportions and pipe support spans in accordance with ITT Grinnell* recommendations, which assure typical natural frequencies
    - Lumped mass size is typical for a 16-inch swing check valve
    - Tests conducted at nominal PWR conditions (288 C, 15.5 MPa)
- Atypical of nuclear piping systems
    - Vertical supports are hydrostatic bearings
    - Elbows and straight pipe are high strength materials
    - Loading occurs at a single point
    - Loading is not a true seismic signature.

---

* ITT Grinnell Industrial Piping, "Piping Design and Engineering".

System Design

The pipe experiments conducted in Subtask 1.3 were significantly more complex and technically more sophisticated than those performed in Subtasks 1.1 and 1.2 because they included dynamics and a geometrically complex structure. The complexity of these experiments dictated that a detailed system design and analysis be performed to define the pipe configuration and to provide information for selecting components for the piping system.

Traditional beam-type finite element models were used to design the piping system using the ANSYS® finite element computer program. In addition to the usual pipe and elbow elements of plant piping analysis, however, a simple nonlinear spring model was used to model the behavior of the crack. This crack model, which was developed for this program and is shown in Figure 2.32, uses spring-slider elements and a gap element to incorporate yield, energy dissipation, crack closure, and failure of the crack section in moment-rotation coordinates. As shown in Figure 2.33, the model uses quasi-static pipe test data or J-estimation scheme predictions to develop a stiffness matrix model of the crack. A current limitation of the model is that it is only applicable up to the point of maximum moment.

The efficacy of the spring-slider crack model and the procedures to develop the input data for it were established by comparison with quasi-static experiments, by correct pretest predictions of the early Subtask 1.1 inertial experiments, and by favorable agreement with independent analyses by the IPIRG members in round-robin analysis efforts. Analysis results using flaw depths and actuator displacements measured from the experiment compare remarkably closely with the Subtask 1.3 experimental results (see Section 3.2.4).

Using the crack model, various piping system geometries, forcing functions, and crack locations were explored to optimize the piping system. Including the nonlinear effects of the crack in these analyses ensured that the system design decisions were based upon the best possible engineering estimates of expected system performance. It should be noted, however, that the system design was not a rigorous pretest prediction. Rather, it was an engineering exercise to design the test system and select hardware.

To design the Subtask 1.3 piping system, in excess of 30 basic design configurations, each with 5 to 10 minor variations (i.e., different crack or actuator locations), were considered before the configuration shown in Figure 2.23 was selected. Physical size, cost, system reusability, servo-hydraulic requirements, and mixture of inertial to displacement loading provided constraints on the design. Using dynamic nonlinear finite element analysis with the nonlinear-spring crack model, the final system configuration and associated forcing function was predicted to produce a failure in the stainless steel base metal experiment in 10 cycles while providing 33 percent inertial loading, a significant margin on servo-hydraulic system capability and low stresses remote from the crack location. The 10 cycle criterion was based on the desire to minimize low cycle fatigue crack growth, yet have a reasonable number of cycles representative of low-frequency, high-amplitude loading from a seismic event.

Test Procedures

The procedure for conducting the Subtask 1.3 experiments followed a rigorous format. First, analyses were performed to design the experiment. Second, the piping system, instrumentation, and control system were set up in accordance with the design. Finally, the test was conducted following a detailed test procedure checklist.

PRETEST DESIGN. Prior to the conduct of each of the cracked pipe experiments, dynamic finite element analyses were performed to design the experiment, i.e., to select the forcing function. Considerations in the selection of the forcing function included the structural properties of the flawed test section and the test system capabilities.

There were four basic criteria for selecting a forcing function:

(1) To avoid significant fatigue crack growth, the surface crack should ideally penetrate the wall of the pipe in approximately 10 cycles and not require more than 30 cycles.

(2) The selected forcing function should provide a reasonable margin on predicted force, stroke, and oil usage for the servo-hydraulic system.

(3) The forcing function should be of the form

$$U_x = St + A[1-\exp(-bt)]\sin(\omega t) \qquad (2.4)$$

where,

U_x = actuator displacement
t = time, seconds
S, A, b = equation constants
ω = forcing function frequency.

(4) There should be a nearly equal mix of inertial and displacement-controlled loading on the crack.

In addition, other minor criteria were applied such as: (1) the forcing function frequency should be kept below the first natural frequency of the system, (2) it was deemed desirable to use the same forcing function for a number of experiments, if possible, and (3) load ratios that tended more toward the negative were favored.

The methodology for selecting a forcing function followed a three-step process:

(1) Estimation of the structural behavior of the cracked pipe section using both quasi-static test data and J-estimation scheme predictions to get high and low estimates of possible crack section moment-rotation response

(2) Dynamic finite element analyses of the piping system using the nonlinear spring crack model and an assumed forcing function

(3) Iteration on the constants in the forcing function equation to satisfy the criteria discussed in the previous section.

The analyses performed in the experiment design were fundamentally identical to the analyses performed during the system design. In this case, however, refined estimates of the cracked section structural behavior for the specific materials and for the pipe and flaw geometry were used, as well as the measured damping of the overall pipe system.

TEST CONDUCT. Following the design of an experiment, the test system was set up in accordance with the design. The specimen was welded into the pipe loop, the appropriate instrumentation installed, and the data acquisition and control system made ready.

After the complete facility was made ready for testing, a rigorous test plan was followed to conduct the experiments. Six experiments were conducted as a part of Subtask 1.3, one uncracked pipe experiment and five cracked pipe experiments.

Uncracked Pipe Experiment. Although referred to as a single uncracked pipe experiment, under the title of Experiment 1.3-1, there was actually a series of six separate tests:

(1) Pipe system pressurization test
(2) System damping test
(3) System natural frequency test
(4) Room temperature dynamic test
(5) PWR static test
(6) PWR dynamic test.

In addition, within the system natural frequency test, three methods were used to measure the natural frequencies of the pipe loop under various conditions.

The objectives for the uncracked pipe tests were basically to measure pipe system behavior and to gain experience with the test system prior to conducting the cracked pipe experiments. In addition, as the uncracked pipe tests were conducted, the procedures for conducting the cracked pipe tests were formalized.

A brief description of the procedure for each of the six tests that make up Experiment 1.3-1 is as follows:

- Pipe system pressurization test - Repeated cycles of pressurizing the loop with water to approximately 15.5 MPa (2250 psi) and releasing the pressure. Displacements at selected locations on the pipe loop were recorded at each step. The test was conducted at room temperature.

- System damping test - Excitation of the pipe system with a low amplitude sinusoidal displacement that was abruptly stopped and the system allowed to "ring" down. The decrease in amplitude of the actuator force with time was correlated to the amount of damping in the system. Actuator load was recorded continuously during the process. The test was conducted at room temperature with the pipe filled with water.

- System natural frequency test - System natural frequencies were determined three ways: from a system ring-down; using an instrumented hammer, accelerometer, and spectral analyzer; and using an accelerometer and spectral analyzer with energy input by the actuator. In addition to using the three different methods to determine the natural frequency, the frequency was measured for the system under various conditions of pressure, temperature, and actuator preload. All loading involved only elastic stresses in the pipe loop.

- Room temperature dynamic test, PWR static test, and PWR dynamic test - These tests were all conducted in the spirit of the cracked pipe experiments, which are described below.

Cracked Pipe Experiments. The test procedure used for all of the cracked pipe experiments is summarized as follows:

(1) Zero all transducers and shunt calibrate them

(2) Bring the test system to nominal PWR conditions, 288 C (550 F) and 15.5 MPa (2250 psi)

(3) Ascertain that all transducers are functioning properly after the heatup and resolve any inconsistent transducer output

(4) Prepare the data acquisition system

(5) Bring the servo-hydraulic system to operational status

(6) Commence data acquisition

(7) Execute the forcing function to excite the pipe

(8) Return all systems to a shut-down status.

Instrumentation and Control

A wide range of instrumentation was used during the course of the six Subtask 1.3 experiments. The total instrumentation plan was an evolutionary process. As technical issues arose and were subsequently resolved, various pieces of instrumentation were added or removed. For example, in the early experiments one question was whether the two fixed ends were indeed fixed. In order to address this question, three orthogonally mounted accelerometers were attached to the steel framework. Ideally, by double integrating the accelerometer data, it would be possible to assess the magnitude of the displacements at these two locations. This procedure was only marginally successful, so string potentiometers were added to make direct measurements of fixed end displacements. Once it was established that the displacements at the two fixed ends were indeed extremely small, the accelerometers and string potentiometers were eliminated from future experiments. Table 2.7 lists all the instrumentation used throughout the course of these experiments. Figure 2.34 shows the general location of the various pieces of instrumentation listed in Table 2.7, and Figures 2.35 to 2.41 show some of the details of the various transducers. A complete description of the entire Subtask 1.3 instrumentation package is provided in Reference 2.4. In addition to the basic transducers listed in Table 2.7, each experiment conducted as part of Subtask 1.3 was recorded on videotape using five cameras, as shown in Figure 2.42.

Figure 2.43 is a schematic of the data acquisition and control system for the pipe tests. The two systems were interconnected because several of the transducer inputs to the data acquisition system were feedback signals for the control system.

The primary data acquisition system for the Subtask 1.3 experiments consisted of four IBM XT compatible computers using 12-bit A/D converters. Each computer collected 16 channels of data at 200 Hz for a total of 30 seconds, with data acquisition beginning several seconds prior to the start of shaking the pipe. In addition to the digital data acquired with the IBM PCs, backup analog data were recorded on FM tape recorders.

The hardware used to control the motion of the actuator consisted of a computer to generate the forcing function signal, a shut-down device, and a servo-controller. The forcing function computer generated an analog voltage command signal from an equation for the forcing function using a 12-bit digital-to-analog converter. The output of the forcing function computer was fed to a programmable attenuator, which was used to shut down the cracked pipe experiments when the pressure in the pipe dropped below a threshold value. Finally, the output of the shut-down device went to the servo-controller that was used to drive the servo-valve on the actuator. All experiments were run in displacement control.

Data Reduction

The raw data from the cracked pipe experiments consisted of voltages from all of the transducers as a function of time. The data, which were stored digitally by the data acquisition system, were manipulated using Lotus 1-2-3® spreadsheets and Fortran programs to generate the engineering data for the experiments.

Selected Summary of Experimental Results

Since a huge volume of experimental data was generated in the six Subtask 1.3 experiments, only a selected subset is presented in this report. The data selected are those that help to illustrate general findings and to support overall conclusions. More detailed information on all Subtask 1.3 experiments are given in Reference 2.4. To facilitate the presentation, the results of the experiments are grouped and presented in two basic categories:

(1) Results that address the issue of piping system response.

(2) Results that address the issue of fracture behavior.

As a general comment, the overall facility performance exceeded expectations. Measurement of motion at the fixed ends showed that displacements did not exceed 0.005 mm (0.0002 inch). Damping in the system was measured to be 0.5 percent, throughout a wide range of pipe motion. This low damping, partly attributable to the use of hydrostatic bearings at the vertical supports, is almost purely viscous and hence can be easily modeled in a finite element code.

PIPING SYSTEM RESPONSE. The data from this program can be used to assess the validity of piping system analysis codes. For these assessments pipe displacement, natural frequency, and reaction force measurements can be valuable for comparing with static, eigenvalue, and dynamic analyses.

In comparing the dynamic pipe system response data for the different experiments, the data were found to be consistent from one experiment to another. This was especially true for the stainless steel base metal, weld metal, and aged cast stainless experiments because the same forcing function was used for each of these experiments. This consistency of data sets among experiments was evident for all of the data channels associated with the response of the piping system to the dynamic excitation.

System Natural Frequencies. The first few natural frequencies for the piping loop were determined for comparison with analytical predictions and to provide a basis for selecting the excitation frequency for the dynamic tests. The frequency was measured for the system under various conditions of pressure, temperature, and actuator preload.

Figures 2.44 and 2.45 show calculated natural frequency and mode shape data for the Subtask 1.3 pipe loop. Tables 2.8 and 2.9 summarize the measured natural frequency data. A comparison of these results with analytically predicted values is presented in Section 3.2.4.

Global Pipe Displacements due to Actuator Motion. Motion of the pipe system in response to actuator motion was measured at three locations: Elbow 3, the crack location, and Node 21 (see Figure 2.23 for locations). Changes in vector lengths that were measured using three string potentiometers at each location were converted to X-Y-Z global coordinates by a numerical procedure. Composite plots of the X, Y, and Z displacements at Elbow 3, the crack plane, and Node 21 for the stainless steel base metal experiment are shown in Figures 2.46 to 2.48.

At all three locations, the Z-directed motion (up-down) was always negligible. The dominant motion at all three locations was in the Y direction. The X-directed motion at the crack and Node 21 was mainly a static offset due to thermal expansion. There was very little cyclic X displacement at these locations caused by the dynamic event. However, at Elbow 3 there was a significant amount of dynamic X-directed motion due to the proximity of Elbow 3 to the actuator, which was being forced in the X direction.

Actuator Force. The applied load at the actuator was measured using a load cell in the load train for all experiments. Figure 2.49 shows the actuator force as a function of time for the stainless steel base metal experiment.

The dynamic load cell response (Figure 2.49) is approximately 90 degrees out of phase with the applied displacement data (Figure 2.50). That is, when the applied displacement data is at a peak, the applied load data is going through zero. This is due to the piping system being excited near its natural frequency.

The actuator load from the PWR static push (see Figure 2.51) is essentially linear with displacement, but exhibits a bit of hysteresis. The hysteresis is on the order of 1 percent of its full-scale load capacity. Comparing the static and dynamic load cell responses, significant dynamic amplification is apparent. From Figure 2.50, the maximum dynamic actuator displacement for the stainless steel base metal experiment is approximately 62 mm (2.44 inch). During the time that the actuator was at its greatest extension, the dynamic force measured at the load cell was approximately 900 kN (202,000 pounds). In contrast, the corresponding static force at 62 mm (2.44 inch) actuator extension is only 325 kN (73,000 pounds) (see Figure 2.51).

Pipe Hanger Reaction Force. The lateral force at the hanger nearest the actuator, Node 6 in Figure 2.23, was measured with a load cell. During the static PWR push, an electrical ground loop made the hanger load cell data useless. Consequently, only dynamic results are presented.

Figure 2.52 is a plot of the reaction force measured at Node 6 as a function of time for the stainless steel base metal experiment. Once the surface crack penetrated the pipe wall (at about 2.3 seconds), the reaction forces increased greatly.

There is an inconsistency in these data in that the analysis suggests that the reaction force should start at a negative value with the dynamic component following the trend shown in Figure 2.52. When the Node 6 reaction force data for the aged cast stainless experiment is examined (Figure 2.53), the reaction force does start negative, as expected, with the dynamic component following the downward trend previously exhibited by the stainless steel base metal data. The inconsistency associated with the stainless steel base metal data is drift during heatup causing a shift in the static reaction load. Consequently, it is appropriate to report only the dynamic component of the reaction force. A finite-element-calculated static value can be added to the dynamic values, if desired.

Elbow Strains. Strains at two of the pipe system elbows were measured as part of the room temperature, uncracked pipe experiment using conventional foil-back, three-element, strain-gage rosettes. The gages were attached to the outside surface of Elbows 3 and 4 at the top, bottom, intrados, and extrados of the elbows (see Figure 2.54). Figures 2.55 and 2.56 are plots of strain gage data for the top of Elbow 3 and the intrados of Elbow 4, respectively, as a function of time for the room temperature, uncracked pipe, dynamic tests. These two locations were chosen for presentation since they were the high strain locations for the two elbows during these tests. The strains presented have had the static strains due to pressurization subtracted to be consistent with the data for the elevated temperature tests. Static strains for the elevated temperature tests were unreliable due to drift over the three day period needed to bring the test system up to temperature.

For Elbow 3, the hoop gages exhibited the highest dynamic values of strain for all four locations: top, bottom, extrados, and intrados. For these locations, the highest dynamic strain values observed (approximately 800 microstrain) were for the top and bottom hoop gages. For Elbow 4, the highest value of strain recorded (approximately 650 microstrain tensile and 1,000 microstrain compressive) was for the longitudinal gage at the intrados (E3).

The differences in strain data between Elbows 3 and 4 can be attributed to the fact that Elbow 3 is a Schedule 100 elbow while Elbow 4 is Schedule 160. During the dynamic event, the thinner Schedule 100 elbow tends to ovalize more than the Schedule 160 elbow such that bending due to ovalization is induced into the elbow in the hoop direction. The heavier wall Schedule 160 elbow resists this ovalization and the elbow behaves more like a beam in bending with the higher strains being longitudinal strains occurring at the locations farthest from the neutral axis, i.e., the extrados and intrados.

The measured strain values will probably not compare favorably with a finite element analysis using beam-type elements, except in a gross sense. However, with the more sophisticated piping elements being developed that include shape functions for ovalization, these data may have a use in program validation some time in the future. For the immediate purposes of Subtask 1.3, these data were used to establish the locations of high strain for mounting permanent weldable strain gages on Elbows 2, 3, and 4. These permanent elbow gages were incorporated into the overall instrumentation plan to provide some measure of the damage done to the elbows during the subsequent dynamic, cracked pipe experiments.

Uncracked Pipe System Bending Moments. The primary response of interest for the piping loop experiments was the moment at the crack plane. As a secondary issue, the gradient of moment along the run of straight pipe containing the crack also was of interest. To measure these moments in the cracked pipe tests, high temperature weldable strain gages were applied to the pipe at three planes: on either side of the crack (Figure 2.39) and 3.2 m (10.5 feet) north of Elbow 4 (Figure 2.40). In addition, for the uncracked pipe tests, a set of high temperature weldable strain gages was applied at the future crack location. These gages provided a fairly comprehensive picture of the bending moment in the piping run of primary interest. The bending moment served as a benchmark for comparison with finite element programs.

Measured strain data do not directly yield bending moments. Rather, the strains were converted to stresses through constitutive relationships, and then the stresses were converted to moments, making certain assumptions and using section properties.

Figure 2.57 is a plot of the total moment in the pipe system for the uncracked PWR static push test. In this case, a finite-element-calculated static value (at zero actuator displacement) was added to the measured strains to remove heatup-induced strain gage drift. As expected, the static moments are linear functions of actuator displacement. In addition, because there were no externally applied in-plane shear forces acting on the pipe near the test section, shear force in the pipe must be constant and the moment gradient linear. Thus, the moment at the crack must be the average of the moments measured at the two planes where strain gages were mounted. The uncracked pipe static push data confirm this.

The fact that the moment at the crack plane is the average of moments measured at the two strain gage planes is important because it provided the means to determine the moment at the crack plane for the cracked pipe experiments. In the case of cracked pipe, assuming that the contribution of inertial forces is small, the moment at the crack is the average of the moments at the two strain gage planes. After breakthrough, however, there are two factors that affect the moment cell calibrations. The first is the presence of the through-wall crack, which perturbs the stress fields at the moment-cell strain-gage locations. The second is an additional shear force on the "moment load cell", from the jet thrust force. This force alters the moment distribution, thereby invalidating the basic assumption used to derive the crack plane moment. Thus, measured bending moment at the crack plane in the cracked pipe experiments is reliable only up to surface crack penetration. Review of experimental data suggests, however, that measured moments may also be valid after surface crack penetration when the crack is closed and compressively loaded so the thrust loads are negligible and the crack faces can transmit a compressive load. An estimate of the magnitude of the thrust forces is discussed in Section 3.2.6.

Figure 2.58 is a plot of the total bending moment (ANSYS® static value plus dynamic component from the dynamic strain gage data) as a function of time for the elevated temperature phase of the uncracked pipe experiment. Figure 2.58 shows that the bending moment decreases rapidly with distance from Elbow 4, i.e., from the south end cap to the location 3.2 m (10.5 feet) north of Elbow 4. A large portion of the difference between the moments at the four locations along this pipe run is associated with the magnitude of the static contribution of moment as calculated via ANSYS®. If only the dynamic component of moment from the dynamic strain gage data for these four locations is plotted as a function of time (Figure 2.59), the differences in moment between the four locations is quite small. In other words, the bending moment gradient associated with the dynamic component of the moment is much less than the bending moment gradient associated with the static component of the bending moment.

FRACTURE BEHAVIOR. A primary purpose for conducting this subtask was to generate data to assess the validity of various fracture codes and methodologies. For example, data from this program will be useful in evaluating the flaw-assessment criteria embodied in R6 (Ref. 2.9) and in IWB-3640 and IWB-3650 of Section XI of the ASME Boiler and Pressure Vessel Code (Ref. 2.10).

In the sections that follow, a synopsis of the data for the fracture behavior of the specimens that were tested is presented. Although it is tempting to make direct comparisons between the experiments, this is difficult because a number of experimental variables were not constant between experiments. For example, the forcing functions for the two carbon steel experiments were different from the forcing function for the three stainless steel experiments. The flaw size for the carbon steel base metal experiment was deeper than the flaws for the other experiments, while the flaw size for the aged cast stainless steel experiment was intentionally shallower to match the companion quasi-static experiment. In order to make comparisons, the effects of crack depth and other variable parameters must be normalized through analysis. Such an assessment is made in Section 3.0.

Table 2.10 presents the key experimental results from the five cracked pipe experiments. The table lists the crack size, applicable material property data, maximum moment at the crack section, the moment at crack initiation (if available), maximum moment and moment at crack initiation from the companion quasi-static experiment (if appropriate), percent inertial loading at maximum moment and at surface-crack penetration, and calculated load ratio for each experiment.

Crack Section Moments. Figures 2.60 through 2.64 are plots of the crack section moments as a function of time for the five cracked pipe experiments. These plots present data only up to the instant of surface-crack penetration, because after the surface crack penetrates the pipe wall, the jet thrust load invalidates the assumption of a linear moment gradient. For comparison purposes, the same scales have been used for all of the plots.

The carbon steel base metal specimen (Figure 2.60) failed very early, at a relatively low moment. One reason for the low bending moment is the 73 percent deep flaw, as compared with the nominally 66 percent deep flaw in the other experiments. The carbon steel weld and the aged cast stainless steel specimens failed at relatively high moments, approximately 600 kN-m (5,300,000 in-lbs), when compared with the other three experiments. The aged cast stainless specimen failed at a high moment because the flaw was only 53 percent deep.

Crack Initiation/Crack Growth. Direct-current electric potential (d-c EP) measurements were made to define the instant of crack initiation for the surface cracks and to estimate the extent of surface crack growth and through-wall crack growth once the surface crack penetrated the pipe wall. Good d-c EP data were measured during the three stainless steel specimen experiments. For the carbon steel weld metal experiment, the d-c EP data had a large self-induced voltage superimposed on the desired data. This self-induced voltage is a piezoelectric phenomenon and is commonly observed for carbon steels that are loaded dynamically. In spite of using a 4000 amp current source, the self-induced voltage overwhelmed the d-c EP crack extension signal. Several unsuccessful attempts were made to eliminate the induced voltage from the d-c EP signal by digitally processing the experimental data. Further developments are needed for any future carbon steel pipe experiments. No d-c EP data were obtained for the carbon steel base metal experiment due to an instrumentation failure.

Crack initiation for the three stainless steel experiments was determined by the location of a slope change in the d-c EP versus crack-mouth-opening displacement (CMOD) plot. The moments at crack initiation are shown in Table 2.10. Table 2.10 shows that the ratio of the moment at crack initiation to the maximum moment was 0.974 for the high toughness stainless steel base metal material, but was 0.854 for the lower toughness aged cast stainless material. These results are consistent with previously reported data (Ref. 2.1).

Figures 2.65 and 2.66 are typical plots of surface crack growth (Δa) and the calculated through-wall crack length as a function of time for the Subtask 1.3 experiments. The flat region of the surface crack growth curve is associated with the unloading portion of the load history (i.e., that segment of the loading history where the applied moment and

CMOD are either decreasing or increasing but at a value less than that obtained during the previous cycle).

Flaw Stability. Each of the cracked pipe experiments conducted as part of this effort exhibited similar behavior from the viewpoint of flaw stability. For each experiment, there was a small amount of stable surface crack growth through the thickness from the initial surface crack, after which the surface crack propagated rapidly through the remaining pipe wall thickness. Once the surface crack propagated through the pipe wall, it continued to grow rapidly around the pipe circumference to the ends of the surface crack. This rapid surface crack growth and subsequent rapid through-wall crack growth occurred in one event. The time interval between the onset of rapid surface crack growth and the arrest of the resultant through-wall crack was on the order of 25 milliseconds, giving an average crack growth speed of 12.5 m/s (41 ft/sec). If the crack had not arrested and had continued to grow at that speed, a complete double-ended guillotine break (DEGB) would have taken 50 milliseconds. This is much longer than the 1 millisecond typically used as a design criterion for a complete DEGB.

After the initial event, the through-wall cracks for each of the experiments continued to grow due to subsequent cyclic loadings. In the case of the carbon steel base metal and aged cast stainless experiment, the cyclic loading continued until the cracked pipe section severed. In the other experiments, the loading stopped before the crack could propagate completely around the circumference.

Figures 2.67 and 2.68 are a photograph and sketch, respectively, of the fracture surface for the Subtask 1.3 carbon steel base metal experiment (1.3-2). Table 2.11 shows the post-test crack length measurements from the crack closure marks (indicative of arrest/reinitiation) evident on this fracture surface. Similar data are presented for the other Subtask 1.3 experiments in Reference 2.4. No data are presented for the aged cast stainless steel experiment because the coarse grain structure of the material obscures the arrest lines. In general, the subsequent through-wall crack growth after the first arrest was much slower than the initial unstable crack growth.

The data in Table 2.11 indicate that the distance between the crack closure marks tends to initially increase and then decrease as the applied loadings die out. As noted in Reference 2.4, the crack extension between cycles was significantly greater for the carbon steel base metal experiment than for the other three experiments, even though the maximum applied moment prior to surface crack penetration was significantly less in this experiment. The significant crack extension for the carbon steel base metal experiment is attributed to its low tearing resistance at dynamic loading rates, i.e., $dJ/da = 58\ MJ/m^3$ (8,360 in-lbs/in^3) compared with values of 102 to 485 MJ/m^3 (14,700 to 70,300 in-lbs/in^3) for the other three materials.

Observations

Great care was taken in the design and construction of the experimental facility to ensure that the as-built experimental facility could be accurately modeled analytically. Hydrostatic bearings were incorporated in the facility at the two vertical supports to obtain a near frictionless restraint in the horizontal plane at these two locations. Spherical and linear bearings were used to provide controlled constraints. Measurement of the motion at the fixed ends of the pipe loop confirmed that motion of the ends was insignificant. Damping was measured to be 0.5 percent and almost purely viscous. High strength pipe used in the loop ensured that the pipe would remain elastic. All of these features provide physical boundary conditions that are reasonably well modeled by the boundary conditions assumed in the finite element models. Although, as a consequence, the Subtask 1.3 pipe loop is not typical of plant piping, it does provide a unique test facility for evaluating the efficacy of numerical analysis procedures and for assessing the role of combined loading on fracture behavior.

The development and validation of the nonlinear spring crack model during the design of the pipe loop and its subsequent application to the design of the individual experiments is a significant technical highlight. The ability of the methodology to correctly integrate the moment-rotation behavior of the crack into a dynamic finite element analysis and its relative simplicity are important features of this development.

The piping system response data provide a unique source of data for bench marking finite element analyses. Because of the change in pipe schedule at Elbow 4, the pressurization data provide a good test for correct handling of "capped end" forces. The natural frequency data provide a check on mass and stiffness distribution. The fact that natural frequency does not change from room-temperature no-pressure conditions to PWR conditions suggests that there is an interplay of parameters affecting the natural frequency. The effects of stiffening of elbows due to pressure, a decrease in the mass density of the water in the pipe, and a decrease in the modulus of elasticity of the pipe steel at high temperature must all balance. To be consistent with this experimental finding, analytical predictions of natural frequency must include all of these first-order effects to be correct. Lastly, correctly calculated moments and moment gradients, both static and dynamic, are essential before combined loading fracture mechanics problems can be considered.

The fracture mechanics related data from the experiments do not show anything particularly startling. Both initiation and maximum moments are all quite similar to the companion quasi-static tests, recognizing that there are differences in crack sizes and other test parameters. The ratio of the moments at crack initiation to the maximum moments for the three stainless steel pipe system experiments conducted as part of this subtask are similar to trends that have been reported in previous programs.

The crack initiation and crack growth data for the Subtask 1.3 experiments were not easily determined. Plasticity effects, dynamics, the need to normalize the signals to eliminate spurious effects, and the use of a single crack growth calibration curve make the determination of initiation and crack growth somewhat speculative. The basic d-c EP data are not monotonically increasing curves with time and, hence, engineering judgement must be applied to interpret them.

One phenomenon observed in the Subtask 1.3 experiments that deserves some comment was the fact that a crack that initiated was occasionally unloaded prior to surface crack penetration. On the subsequent loading cycle, the crack then penetrated the pipe wall at a moment below the previously attained moment. In particular, the stainless steel base metal experiment (Figure 2.62) failed at a moment 16 percent lower than the moment attained on the previous cycle. This had an influence on the percent inertial loading for some of the experiments. This reduction in maximum moment, which is attributed to crack growth on the previous cycles, tends to reduce the percent inertial loading at surface-crack penetration and, hence, the load-controlled moment that could potentially cause an instability.

As a final comment with regard to the Subtask 1.3 pipe system experiments, the final disposition of the test facility after the aged cast stainless steel experiment must be noted. The end caps, used to minimize the amount of energy released in the event the pipe severed in two pieces, were removed for this experiment. The rationale for removing these end caps was that they might have been influencing the final stability of the resultant through-wall cracks. It was felt that the axial stress in the test section and jet thrust forces decreased at an artificially high rate once the volume of water inside the capped section rapidly depressurized. After the surface crack penetrated the pipe wall during the aged cast stainless experiment (1.3-7), it continued to grow until it reached a critical size for the applied stress level and the pipe experienced a double-ended guillotine break (DEGB). The restraint system across the crack, which was supposed to prevent the ends of the pipe from separating, failed. The jet thrust forces and resulting pipe whip caused a secondary failure at a weld near a pipe hanger. As a result a large section of pipe was ejected from the test frame causing extensive damage to the facility.

2.1.4 MATERIAL CHARACTERIZATION OF TASK 1.0 MATERIALS

The material characterization efforts had two principal objectives: (1) to supply data for the design and analysis of the pipe fracture experiments, and (2) to develop a data base to assess if material properties must be obtained at dynamic loading rates for leak-before-break or in-service flaw evaluation analysis.

Material characterization tests were conducted on laboratory specimens machined from seven different pipes that were used in pipe fracture experiments in Task 1.0. The pipes included carbon and stainless steels, and specimens were taken from both base and weld metals. Characterization tests included chemical analyses, tensile tests, and fracture toughness tests. The tensile and fracture tests were conducted at 288 C (550 F) under both quasi-static and dynamic loading, i.e., at rates comparable to those for high-amplitude seismic events.

Detailed descriptions of the procedures used and the results obtained appear in Reference 2.5. Presented here is a brief summary of procedures and results.

Materials Investigated

A description of the seven pipes subjected to material characterization tests is given in Table 2.12. Chemical compositions of the pipes and welds are shown in Table 2.13.

Displacement Rates in Material Characterization Tests

Displacement rates in tensile tests and fracture toughness tests were selected to provide data useful to the designers and analysts of the Task 1.0 pipe fracture experiments. In the pipe experiments that employed cyclic loading, the frequency was nominally 3 Hz, with the expectation of crack initiation after approximately 10 cycles. The material characterization tests, on the other hand, employed monotonically increasing displacement.

In the tensile tests, three different nominal strain rates were employed: 10^{-4} s^{-1} (quasi-static), 1 s^{-1}, and 10 s^{-1}. The two higher rates were selected to approximate the strain rates existing near the crack tip in dynamic C(T) tests and pipe tests in Task 1.0.

In the fracture toughness tests, two different displacement rates were employed in an attempt to simulate both quasi-static and dynamic pipe tests. The lower of the two displacement rates was selected to produce crack initiation in approximately 5 to 20 minutes, as is customary in the quasi-static pipe tests. The higher displacement rate was estimated on the basis of finite element analyses conducted for several pipe tests that were to be subjected to cyclic loading in Task 1.0, as described below.

A nonlinear spring was used to simulate the cracked pipe section response (see Section 3 in Reference 2.5). Using the cyclic forcing function that had been selected for those tests, the finite element analysis calculated moment-versus-time graphs for specific pipe tests. An example of such a moment-time graph is shown in Figure 2.69a for a test of a surface-cracked stainless steel pipe in Subtask 1.3. In Figure 2.69b, segments AB, BC, and so on, were summed to provide an estimate of the time to reach crack initiation, which was based on a knowledge of the moment required to produce crack initiation in a quasi-static test of the same pipe material. The summation of these time segments effectively gave an equivalent monotonic loading time to crack initiation, which ignores the cyclic aspects. In the example shown in

Figure 2.69, the time to crack initiation was estimated to be 0.19 second. Using similar analysis methods for other pipe tests in Task 1.0, crack initiation times as long as 0.52 second were estimated. In order that the dynamic C(T) tests be representative of the shortest estimated crack-initiation times in dynamic pipe tests, displacement rates for dynamic C(T) tests were chosen to produce crack initiation in approximately 0.2 second.

Once the C(T) tests were completed and J-R curves calculated, actual rates of loading, expressed as dJ/dt up to the point of crack initiation, were calculated. These rates are shown in Table 2.14. It can be seen that the dJ/dt values in rapid loading tests were approximately 2500 to 6000 times greater, and averaged approximately 4000 times greater, than those in quasi-static tests. Loading rates in the C(T) tests were chosen to give dJ/dt values that were reasonably close to those in the pipe tests. For example, the value of dJ/dt was 4000 $kJ/m^2/s$ for the Subtask 1.2 dynamic stainless steel experiment conducted with monotonically increasing load, Experiment 1.2-1, while a value of 6750 $kJ/m^2/s$ was measured in the companion C(T) test. These differences in rates are typical, and the values are sufficiently close for the purposes of this investigation.

Test Procedures

TENSILE TESTS. Tensile specimens were machined from the pipes such that their tensile axis was parallel with the pipe axis. Base metal specimens were taken from the midwall location of the pipe, but weld metal specimens were taken from near the outside of the pipe where the girth weld was relatively wide so that the reduced section of the specimen consisted entirely of weld metal.

Two different types of tensile specimens were used. One was a round-bar, threaded-end specimen in which strain was monitored using a conventional clamp-on extensometer. The other was a flat, pin-loaded specimen in which strain was monitored using a noncontacting optical extensometer. The round-bar specimen was used only for quasi-static tests whereas the flat specimen was used in both quasi-static and dynamic tests.

FRACTURE TOUGHNESS TESTS. All fracture toughness specimens were of the compact (tension), C(T), design. They were machined from sections of pipe without mechanical flattening and were in the L-C orientation, i.e., loads were applied in the direction of the pipe axis and the crack-growth direction was circumferential.

The C(T) specimens were of two different sizes: 0.5T and 1T. The smaller specimens were machined from the 6-inch diameter pipes and the larger specimens from the 16-inch diameter pipes. The 1T specimens were only about 80 percent of the standard thickness of 25.4 mm (1 inch) because of pipe curvature. Following fatigue precracking, the specimens were side grooved to a depth of 10 percent of the specimen thickness on each side.

The direct-current electric potential (d-c EP) method was used to monitor crack initiation and growth in the C(T) tests. That procedure was selected for several reasons: (1) it is a single-specimen method, i.e., it permits determination of a complete J-R curve in each specimen tested, (2) it does not require periodic unloadings (as are required in the unloading compliance method), which are unsuitable for rapid displacement-rate tests, and (3) it was demonstrated in the USNRC's Degraded Piping Program that the d-c EP method provides reasonable estimates of the point of crack initiation and, in most cases, good agreement between calculated and actual crack extensions.

Despite the attractiveness of the d-c EP method, it has one significant shortcoming in high displacement-rate tests of carbon steels. A voltage spike occurs early in the test when the specimen is experiencing rapid elastic loading. The spike apparently is due to the rapid reorientation of ferromagnetic domains as stress is applied and, at the displacement rates employed in the dynamic C(T) tests, can achieve magnitudes in excess of 100 microvolts. Inasmuch as Battelle's customary procedure is to employ a constant current that produces a potential of approximately 400 microvolts at the start of a test, a spike of 100 microvolts can obscure the point of crack initiation. Battelle provided internal research funds for a separate investigation to determine methods that might eliminate the induced current and that could be used in both C(T) and pipe experiments (Ref. 2.11). Of these methods, the most promising was to apply a large d-c current to make the induced voltage negligible. Consequently, a much larger current was used in the dynamic tests on carbon steel specimens, such that the starting potential was 4000 to 5000 microvolts. This procedure greatly minimized the problem with the spike and permitted determining the point of crack initiation with reasonable certainty.

In the C(T) tests, the point of crack initiation was estimated from the point of departure of linearity of a graph of the d-c EP versus displacement curve. Beyond the initiation point, crack extension was calculated using the Johnson equation (Ref. 2.12) which had been modified slightly as was described in Reference 2.5. It then was a simple matter to calculate a J-R curve from tables of load, displacement, and crack length, using procedures specified in ASTM 1152, Standard Test Method for Determining J-R Curves. A detailed description of the method employed can be found in Reference 2.5.

Experimental Results

TENSILE PROPERTIES. For ductile metals, increasing the strain rate from approximately 10^{-4} s^{-1} to 10 s^{-1} would commonly be expected to give rise to at least a modest increase in both the yield and tensile strength (Refs. 2.13 and 2.14). However, in carbon steels that are susceptible to dynamic strain aging (DSA), as is the case for many carbon steel pipes used in nuclear plants, the effect of strain rate is dependent on the test temperature (Refs. 2.15 and 2.16). At some temperatures, increasing the strain rate may lead to a substantial increase in tensile strength, while at other temperatures a sizable strength drop may occur.

Figure 2.70 shows engineering stress-strain curves at three different strain rates for an A106 Grade B carbon steel tested at 288 C (550 F) in this program. Notice that this steel, which is known to be susceptible to DSA on the basis of tensile tests over a range of temperatures, was weakened significantly by increasing the strain rate by four to five orders of magnitude.

An overall summary of the effect on tensile properties of increasing the strain rate by five orders of magnitude at 288 C (550 F) is shown in Figure 2.71. Notice that the tensile strength of all three carbon steels and the fracture elongation of the two base metals was lowered substantially by the increased strain rate. The stainless steels, on the other hand, showed little change in either tensile strength or elongation, except for the cast stainless steel (CF8M), which showed increased elongation with increasing strain rate. Each of the stainless steels did exhibit a higher yield strength with increasing strain rate, whereas the yield strength of the carbon steels was virtually unchanged.

CRACK-GROWTH RESISTANCE PROPERTIES. For ductile metals, increasing the displacement rate in fracture toughness tests would normally be expected to lead to an increase in crack-growth resistance, so long as the increased displacement rate does not introduce a brittle fracture mode. In References 2.13 and 2.17 it was shown that Type 304 stainless steel tested at either room temperature or 288 C (550 F) displayed a significantly higher J-R curve when the displacement rate in otherwise identical tests was increased by six orders of magnitude.

Apparently because of their susceptibility to DSA, carbon steels, even though they exhibit ductile fracture, may not display increased crack-growth resistance when subjected to increased displacement rates in fracture toughness tests. Figure 2.72 demonstrates this fact for an A106 Grade B carbon steel tested at 288 C (550 F); it can be seen in that figure that the specimens tested dynamically were far less tough than those tested quasi-statically. However, a submerged-arc girth weld in this same pipe showed the opposite effect on increasing displacement rate, as is shown by the J-R curves in Figure 2.73. The differing response of the base metal and weld metal is believed to be due to different susceptibilities to DSA. Results obtained recently at Battelle for the USNRC Short Cracks in Piping and Piping Welds Research Program (Ref. 2.18) indicate that the weld metal achieves a tensile strength peak at a temperature near 340 C (645 F), which is substantially above the temperature of 220 C (420 F) at which the base metal achieves its peak strength. Thus, even though both the base metal and weld metal are susceptible to DSA, the details of their susceptibilities appear to be different and produce different responses when the displacement rate is increased.

An overall summary of the effect on crack-growth resistance of increasing the displacement rate in C(T) tests at 288 C (550 F) is shown in Figure 2.74. Recall that testing rates, expressed in terms of dJ/dt, were summarized in Table 2.14 and that the dynamic test rates ranged from approximately 2500 to 6000 times greater than the quasi-static test rates. Toughness parameters included in Figure 2.74 are the value of J at crack initiation, the value of J after the crack has grown 2 mm (0.079 inch), and the initial slope, dJ/da, of the J-R curve at small amounts of crack growth.

As was anticipated, the results in Figure 2.74 show that each of the stainless steels increased in toughness as dJ/dt was increased, in some cases slightly and in some cases dramatically. A lone exception was the 16-inch diameter Type 304 stainless steel pipe, which showed a slight decrease in dJ/da with increased displacement rate. However, both J at initiation and at 2mm of crack growth showed substantial increases for that pipe at the higher rate.

As has already been noted, the behavior of the carbon steel C(T) specimens in response to an increased displacement rate was not as consistent as that of the stainless steels. This observation can be illustrated by comparing the 6-inch and 16-inch-diameter A106 Grade B pipes. The 6-inch-diameter A106 Grade B pipe exhibited a relatively modest reduction in J_i and a modest increase in dJ/da at the higher displacement rate. Although not apparent in Figure 2.74, this material experienced several crack jumps at both rates, thought to be associated with its susceptibility to DSA (Ref. 2.15). The 16-inch-diameter A106 Grade B pipe showed a sizable reduction in toughness at the higher displacement rate; however, the crack jumps observed in low rate tests on this steel were not observed in the high rate tests. Finally, as was mentioned previously, the ferritic submerged-arc weld metal in the 16-inch diameter A106 Grade B pipe showed an impressive increase in toughness at the higher displacement rate and did not display crack jumps at either rate. (Note: the ferritic weld was made by a certified N-stamp fabricator using a weld procedure obtained from a U.S. PWR manufacturer.)

The reasons for the different displacement-rate response of the three carbon steel materials are not known with certainty. It can be hypothesized that the differences in response are the result of differences in the way in which interstitial atoms (nitrogen and carbon) interact with dislocations at 288 C (550 F) to produce the many unusual effects associated with DSA. These differences could give rise to different temperature and displacement-rate dependence of DSA among the three steels. For example, it was noted earlier that the carbon steel weld metal exhibited a tensile strength peak at a substantially higher temperature than did the base metal, which might account for the different response to increasing displacement rate in the C(T) tests on the two materials.

Even though the causes of the different behaviors among the three carbon steels cannot be adequately explained at this time, it is important to note that the results were clear in one regard--the 16-inch diameter carbon steel pipe exhibited significant losses of both strength and toughness at the higher displacement rate. That result means that a similar response must be assumed in any other carbon steel pipe unless contrary evidence is available.

An additional observation from Figure 2.74, not related to displacement-rate effects, confirmed a result obtained in the USNRC Degraded Piping Program. The fracture resistance of submerged-arc welds in austenitic stainless steels is much lower than that of the base metal. The weld studied in this program, for example, displayed a J_i value that was only about 10 percent of the value for its base-metal counterpart and of about the same magnitude as that for the carbon steel weld. It is apparent also in Figure 2.74 that the aged cast stainless steel (CF8M) exhibited J_i and dJ/da values that were similar to those for the stainless steel weld metal.

2.2 Experimental Pipe Fracture and Pipe Material Property Data Base Development - Task 2.0

The objective of this task was to develop well documented, easily accessible data bases for nuclear piping material properties and pipe fracture experiments. The rationale for this effort was that many Code activities are based on data bases for materials that give reasonable lower bounds for material properties. Such data bases may also be of value for probabilistic analyses. Hence, it was desirable to have the dynamic and quasi-static data from this program well documented. Since in the past only quasi-static data were generally developed, the dynamic data from this program represents the first significant contribution of dynamic data to the existing pipe material data base.

There were two subtasks in this task:

Subtask 2.1 - Data Base on Nuclear Piping Materials

Subtask 2.2 - Data Base on Pipe Fracture Experiments

2.2.1 MATERIAL PROPERTY DATA BASE - SUBTASK 2.1

A data base on the material properties of nuclear piping materials, called PIFRAC, was started by the USNRC in 1984. Recently a personal computer (PC) version of the data base was established using the dBASE III PLUS® software. This data base contains the bulk of the USNRC's Degraded Piping Program data developed at Battelle, the data generated by Materials Engineering Associates (MEA) during the USNRC's Structural Integrity of Pressurized Light Water Reactor Components Program, Westinghouse data, data developed by David Taylor Research Center (DTRC) for the USNRC during the 1980's, and data developed by MEA for Argonne National Laboratory on USNRC's program on thermal aging of cast stainless steels. The updated PC version is called PIFRAC.2 and consists of nine 5.25-inch floppy disks. This data base consists not only of tensile and J-R curve data, but also of Charpy, chemical composition, dynamic tear test, drop-weight tear tests, and nil-ductility test data when available. There are a total of 74 pipes documented with a total of 325 tensile test files and 376 J-R curve files.

The IPIRG material property data are summarized in Section 2.1.4. The J_D-R curves were calculated using the ASTM E1152 and E813 methods. The J_M-R curves were similarly calculated. The J-R curves were also put in a format that would be usable directly in the NRCPIPE J-estimation scheme code developed in the Degraded Piping Program. A few specialty tests, such as cyclic stress-strain curves on the Subtask 1.3 elbow materials and compression tests on selected stainless steels, were also included.

2.2.2 PIPE FRACTURE DATA BASE - SUBTASK 2.2

Data from the pipe fracture experiments in the IPIRG Program and the Degraded Piping Program were assembled and compiled. The most important data on bending moments, loading conditions, and geometries were extracted and put in a spreadsheet. This spreadsheet is given in Table 2.15.

2.3 Fracture of Piping Containing High Energy Fluids - Task 3.0

At the inception of the IPIRG Program, there was interest in conducting large diameter pipe fracture experiments for which the energy release from high temperature/high pressure water would be significant. The fracture response of the pipe with fluid interactions, i.e., decompression and thrust load phenomena, would be evaluated. Since it was felt that the cost of conducting such experiments outweighed the perceived benefits, this task was not undertaken. Some of the objectives of Task 3.0 were met with data generated in the Subtask 1.3 pipe system experiments on 16-inch diameter pipe.

2.4 Resolution of Unresolved Issues from the USNRC Degraded Piping Program and IPIRG Tasks - Task 4.0

The objective of this task was to provide a mechanism to investigate unresolved issues from the USNRC's Degraded Piping Program, issues that developed during the IPIRG Program, or other related issues raised during the conduct of this program. The subtasks undertaken in this task were:

Subtask 4.1	Leak Rate Estimation Modeling
Subtask 4.2	Disposal of Contaminated Pipe
Subtask 4.3	Japanese 30-inch Diameter Quasi-Static Pipe Experiments

Subtask 4.4 Compression Tests on Pipe Steels
Subtask 4.5 Detailed FEM Analysis of Stainless Steel Pipe Experiments and J-estimation Scheme Sensitivity Studies.

2.4.1 LEAK-RATE ESTIMATION MODELING - SUBTASK 4.1

Development of leak-rate estimation methodology was initiated in response to the emergence of leak-before-break (LBB) criteria to eliminate design requirements for dynamic effects from pipe rupture. Adoption of an LBB philosophy requires reliable leak detection systems and verified leak-rate estimation techniques. Accurate leak-rate prediction requires correlation of crack size and shape to the leakage rate and is necessary to evaluate the ability of normal makeup systems to handle potential leakage. The development of a verifiable leakage rate assessment methodology is critical to LBB evaluations. Regulatory implications include the elimination of pipe whip restraints and jet impingement shields.

This task was initiated with an analytical effort designed to provide an integrated leak-rate estimation (LRE) method. Data required to assess this method were identified. For the crack-opening area structural analysis, existing crack-opening data from the Degraded Piping Program were used to check the various models. For the thermal-hydraulic analyses, existing experimental data were used to verify a leakage model based on the Henry-Fauske two-phase critical flow formulation (Refs. 2.19 and 2.20). Cracked pipe leak-rate experiments were then conducted on a pipe specimen containing a fatigue crack in a girth weld. These additional experimental data were used to provide further verification of the crack-opening area and thermal-hydraulic models.

Review of existing thermal-hydraulic models indicated that a modified form of the Henry-Fauske model (Refs. 2.19 and 2.20) for two-phase flow through long tubes is most appropriate for modeling the fluid flow through tight cracks. The primary uncertainties in the thermal-hydraulic analyses are associated with the flow path losses due to changes in flow direction, the friction factors for flow between two parallel surfaces, the nonequilibrium vapor generation rate for two-phase flow in tight cracks, and the potential for particulates to lodge in the crack thus plugging the opening. The importance of each of these parameters was identified and evaluated as part of this research effort.

The review of the crack opening area models suggested that the existing models can be broadly classified as linear elastic fracture mechanics (LEFM), pseudoplastic, or elastic-plastic fracture mechanics (EPFM). The pseudoplastic models can, in turn, be categorized as small-scale yielding and net-section yielding. In the EPFM category, the only theoretically sound modeling approach is offered by the EPRI/GE estimation model. In principle, the EPRI/GE model includes LEFM and fully plastic models as special cases.

A modified form of the Henry-Fauske model (Refs. 2.19 and 2.20) for the thermal-hydraulic analysis was used together with the EPRI/GE method (EPFM) for the fracture mechanics analysis to develop a computer program for leak-rate estimation. The program, called SQUIRT (Seepage Quantification for Upsets In Reactor Tubes), can be used to predict the crack-opening displacement (COD) and leakage flow rate for cracked pipe under a given load.

The SQUIRT computer program was validated by comparing its predictions with published experimental data and with experimental data derived as part of this research effort. The SQUIRT thermal-hydraulic model predictions were compared with experimental data on two-phase flow through long tubes reported by Sozzi and Sutherland (Ref. 2.21); two-phase flow through slits reported by Collier et al. (Ref. 2.22), Amos and Shrock (Ref. 2.23), and Yano (Ref. 2.24); and two-phase flow through actual cracked pipe reported by Collier et al. (Ref. 2.22). In general, the SQUIRT program tended to underpredict the experimental data obtained on artificial slits. This was attributed to possibly overestimating the nonequilibrium vapor generation rate for tight slits, although more work needs to be done to confirm this hypothesis. The SQUIRT program did a reasonable job of predicting the measured leak-rate data of Collier et al. (Ref. 2.22) on stress-corrosion cracks, but the scatter in the data was much greater than that observed with artificial slits. If the nonequilibrium vapor generation rate were changed to produce good agreement with the artificial slit data, then the SQUIRT program predicts leakage rates too high for the real crack data. However, a crack pathway loss coefficient for stress-corrosion cracks can be determined to provide a best fit to the data under these circumstances. More work is needed to resolve these ambiguities.

The SQUIRT crack-opening area model predictions were compared with experimental data as well as with results of elastic-plastic finite element analyses from the Degraded Piping Program. The test cases included circumferential cracks in both carbon steel and austenitic stainless steel pipes, as well as stainless steel submerged-arc welded pipes.

Additional experimental validation data were provided by leak-rate tests performed using a circumferential fatigue crack in a girth weld in carbon steel pipe. The cracked pipe specimen was mounted in a four-point bending apparatus (see Figure 2.75) and the leakage flow rate was measured as a function of the applied bending moment and internal pressure (see Figure 2.76). The applied bending loads were kept below the elastic limit of the cracked pipe. Fluid pressure and temperature were varied to simulate both BWR and PWR thermodynamic conditions. To obtain reasonably good agreement between the experimental results and the SQUIRT predictions for leakage flow rates, a flow path loss coefficient of approximately 6 velocity heads per mm of crack flow path length had to be assumed. This implies that the tight fatigue crack in the girth weld caused the fluid to change direction many times while flowing through the crack. One area recommended for further work is a detailed contour mapping of the crack faces to verify the validity of this assumption for the flow path for this type of crack. In addition, leak-rate tests should be performed on a variety of real pipe cracks to expand the data base in this area.

The work performed on crack-opening area models determined that for circumferential cracks in unwelded pipes in bending, the EPRI/GE estimation method, combined with the assumption that the crack-opening profile is elliptical, provides adequately accurate estimates. For cracks in welds, the elliptical crack assumption appears to be reasonable; however, there is ambiguity in how to model the presence of a weld using the EPRI/GE method. While additional research is needed to refine these models, the work performed in this subtask provides a useful state-of-the-art tool for leak rate estimation modeling. Details of these results are in Ref. 2.25.

2.4.2 DISPOSAL OF CONTAMINATED PIPE - SUBTASK 4.2

This subtask involved disposal of cracked pipe that had been removed from service. It was collected for potential research needs as part of the Degraded Piping Program. The pipe samples were offered to the IPIRG members, but none were interested in these materials. The pipe was disposed of as soon as it was determined that there was no use for it. This was a non-technical subtask paid for solely by the USNRC.

2.4.3 JAPANESE 30-INCH DIAMETER QUASI-STATIC PIPE EXPERIMENTS - SUBTASK 4.3

The objective of this subtask was to supplement smaller diameter pipe experiments conducted in the Japanese carbon steel pipe fracture program (Ref. 2.26). Since the Degraded Piping Program showed that larger diameter pipe may fail at stresses lower than those predicted by the Net-Section-Collapse analysis (Ref. 2.1), there was interest in Japan concerning the behavior of large diameter Japanese ferritic pipe materials. This effort was cooperatively undertaken by the Japanese IPIRG members and the IPIRG Program. The Japanese members paid for the purchase of the test pipe, moment arm pipe, and the fabrication of the test specimens. The IPIRG Program paid for conducting the test, reducing the data, and reporting the results.

Test Procedures

Two experiments were conducted as part of this subtask. Both experiments were performed using sections of pipe from the same length of 30-inch diameter, 38.1-mm (1.5-inch) thick STS49 pipe. Both experiments were conducted at 300 C (572 F). The first experiment (4.3-1) involved a circumferential through-wall-cracked pipe subjected to quasi-static displacement-controlled four-point bending without internal pressure. The second experiment (4.3-2) involved a circumferential internal-surface-cracked pipe subjected to a constant internal pressure of 9.14 MPa (1,320 psi) and quasi-static displacement-controlled four-point bending. Figure 2.77 provides a schematic of the four-point bending apparatus used in these experiments.

The instrumentation was typical of the quasi-static experiments conducted in the Degraded Piping Program (Ref 2.1). For both experiments the following data were collected:

- total load from both actuators,
- displacements of actuators,
- rotation of the pipe close to the plane of the crack,
- pipe temperature at various locations,
- crack-opening-displacements,
- crack initiation and crack growth using the d-c electric potential technique, and
- internal pipe pressure (surface crack experiment only).

The length of both the through-wall crack and the surface crack was 16.6 percent of the pipe circumference. The surface crack depth was very close to 50 percent of the thickness, and it was constant over the crack length.

Results from Pipe Experiments

The load versus load-line displacement record for the through-wall-cracked pipe fracture experiment is shown in Figure 2.78. The maximum applied bending moment for this experiment was 6015 kN-m (53,240,000 inch-pound). Note that there was a sudden load drop in the through-wall-cracked pipe experiment after maximum load was achieved. This is similar to the unstable crack jumps that occurred in the Degraded Piping Program ferritic pipe experiments. Figure 2.79 shows where a blue mark occurred along the crack length. From past experience in the Degraded Piping Program, this blue mark was found to correspond to the unstable crack growth. Note that there was a larger unstable crack jump at Tip A than at Tip B (see Figure 2.79). However, the magnitude of stable ductile crack growth prior to the instability was smaller at Tip A. This indicates a significant difference in the fracture resistance at the two crack tip locations.

The load versus load-line displacement record of the internal-surface-cracked pipe fracture experiment is shown in Figure 2.80. The maximum applied bending moment for this experiment was 7200 kN-m (63,740,000 inch-pound). Note that there was a sudden load drop, which is due to the surface crack penetrating the pipe thickness. Since pressure was lost once the surface crack penetrated the pipe wall thickness, the test was terminated at this point.

Results from Material Characterization Efforts

A ring of pipe was removed from the pipe sample received from Japan for the purpose of determining material properties. The data determined were the chemical composition, tensile strength, Charpy V-notch impact data, and 1.5T and 3T C(T) specimen data for J-R curve evaluations. The

3T C(T) specimens had a thickness of 25.4 mm (1.0 inch), and the 1.5T C(T) specimens had a thickness of 35.3 mm (1.39 inch). The thickness was limited by the pipe curvature and C(T) planform size.

The chemical composition is given in Table 2.16. Compared with the A106 Grade B pipe used in the IPIRG Program, the Japanese steel has higher manganese, but the sulfur, nickel, and chromium are slightly lower.

Figure 2.81 shows the tensile test data for this pipe material at 300 C (572 F). The curves are very smooth with no evidence of the serrations frequently found in tests of ferritic steels at temperatures where dynamic strain aging occurs. Figure 2.82 shows the Charpy energy versus temperature data. The upper shelf energy is very high at 215 Joules (155 ft-lb).

Figure 2.83 shows a comparison of J-R curves developed in this program and similar data developed by IHI in Japan. The scatter in the data is due to the presence or absence of side grooves and to differences between 1.5T and 3T C(T) reduced-thickness specimens. These differences are consistent with observations from tests conducted in the Degraded Piping Program. Both the Charpy and J-R curve tests show this is a high toughness ferritic material. The average value of J at crack initiation for a 20 percent sidegrooved 3T C(T) specimen was 498 MJ/m^2 (2,840 in-lb/in^2).

Comparison of Maximum Loads to Predictions

The measured loads were compared with loads predicted by Net-Section-Collapse and other analyses. This comparison shows that when the average of the yield and ultimate strengths is used to define the flow stress, the ratio of the experimental maximum stress to the Net-Section-Collapse analysis predicted stress was 0.997 for the through-wall-cracked pipe experiment and 1.021 for the internally surface-cracked pipe experiment.

Another comparison was made using the Dimensionless Plastic-Zone Parameter analysis (Ref. 2.27). Using the average toughness of the Battelle C(T) specimens at crack initiation, the Dimensionless Plastic-Zone Parameter was 0.243. Using this value and the ratio of the maximum experimental stress to the Net-Section-Collapse analysis predicted failure stress, these pipe experiments were compared with other experiments from the Degraded Piping Program (see Figure 2.84). This comparison shows that surface-cracked pipe can reach Net-Section-Collapse predicted failure stresses with lower toughness than through-wall-cracked pipe.

The through-wall-cracked pipe experiment had a higher failure stress than the Degraded Piping Program trend curve. This may be partially due to the fact that the Degraded Piping Program experiments used a longer through-wall crack length (37-percent of the circumference) than used in Experiment 4.3-1 (16.6-percent of the circumference). As shown below, pipe with shorter crack lengths will tend to fail at stresses closer to

Net-Section-Collapse behavior, which explains the observed difference for Experiment 4.3-1.

The LBB.ENG2 J-estimation scheme (Refs. 2.28 and 2.29) in the NRCPIPE Code (Ref. 2.1) was also used to calculate the initiation and maximum loads of the through-wall-cracked pipe experiment. In the Degraded Piping Program, this analysis was found, on the average, to be reasonably accurate and to underpredict the loads slightly. The Ramberg-Osgood fit of the stress-strain curve was

$$\epsilon/.001271 = \sigma/35{,}600 + 1.1706(\sigma/35{,}600)^{5.195} \qquad (2.5)$$

where the units of stress are in pounds per square inch, and the regression coefficient is 0.9938. The J_D-R curve used is from a 3T C(T) specimen. The ratios of the experimental to the calculated initiation and maximum stresses are 0.985 and 1.068, respectively. This is very good agreement.

To further investigate the effects of crack length, calculations were made with the LBB.ENG2 analysis for this pipe with a through-wall crack length similar to that used during the Degraded Piping Program experiments, i.e., 37 percent of the circumference. To assess the discrepancy in the through-wall-cracked pipe test data from Experiment 4.3-1 with the Dimensionless Plastic-Zone Parameter graph shown in Figure 2.84, the LBB.ENG2 predicted maximum stresses were compared with the Net-Section-Collapse analysis predicted stresses for crack lengths of 16.6 and 37 percent of the pipe circumference. It was found that the 37 percent long crack was predicted to fail at 87-percent of the Net-Section-Collapse predicted load, whereas the 16.6-percent crack was predicted to fail at 95 percent of the Net-Section-Collapse predicted load. Hence, the discrepancy suggests that there is a crack length dependence that is not properly accounted for in the Dimensionless Plastic-Zone Parameter analysis method.

In summary, the results of this subtask showed that:

(1) the STS49 pipe had high toughness at 300 C (572 F),

(2) the failure loads for the crack sizes tested were predicted accurately by the Net-Section-Collapse analysis.

2.4.4 COMPRESSION TESTS ON PIPE STEELS - SUBTASK 4.4

Some finite element analyses that attempted to model the load-displacement behavior of a cracked stainless steel pipe showed poor agreement with experimental results. One possible explanation for this discrepancy focussed on the stress-strain and yield behavior of this material. The speculation was that the compressive behavior might, for some reason, be different from the tensile behavior. Compression tests were conducted and the results showed little difference in tensile and compressive properties of selected stainless steel pipe materials. This subtask was paid for from IPIRG Program funds.

2.4.5 DETAILED FEM ANALYSIS OF STAINLESS STEEL PIPE EXPERIMENTS AND J-ESTIMATION SCHEME SENSITIVITY STUDIES - SUBTASK 4.5

Subtask 4.5 involved using the J-R curves calculated from the Subtask 1.2 pipe experiments in a sensitivity study to assess the effects of these dynamic and cyclic J-R curves on maximum load predictions for different size pipe. The finite element results are summarized in the Workshop Round-Robin problem summary in Section 2.5.2, and the J-estimation scheme sensitivity studies are summarized in Section 3.2.3. This subtask was paid for solely by the USNRC.

2.5 Information Exchange Seminars and Program Administration - Task 5.0

One of the purposes for developing the IPIRG Program was to promote a common technical basis for pipe flaw evaluations and LBB criteria. To enhance the IPIRG members' understanding of the various technical and regulatory bases in other countries, a series of formal seminars and informal workshops were held.

2.5.1 LBB SEMINARS

The LBB seminars involved invited papers addressing piping integrity regulatory practices in different counties and providing information on research programs. Proceedings of the seminars were published as NUREG/CP's (see Refs. 2.30, 2.31, and 2.32). The first seminar was conducted prior to the IPIRG Program. The next two seminars were conducted in conjunction with IPIRG Technical Advisory Group (TAG) meetings.

2.5.2 IPIRG WORKSHOPS AND ROUND-ROBIN PROBLEMS

The workshops were conducted in conjunction with the semiannual IPIRG TAG meetings. The workshops involved presentations on related research efforts by the IPIRG member organizations and solutions to round-robin problems. Six round-robin problem sets were developed during the course of the program. The problem sets, many with several sub-problems, were structured to examine problems of increasing complexity starting with the simplest problem, i.e., fracture of unpressurized quasi-static through-wall-cracked pipe fracture experiments, to eventually performing dynamic analyses of the Subtask 1.3 circumferential surface-cracked pipe system. Table 2.17 summarizes the round-robin problems. The specific objectives and general conclusions of the round-robin problems are summarized below.

Round-Robin Problem 1

SPECIFIC OBJECTIVE. The objective of this round-robin problem was to compare J-estimation scheme predictions of the fracture behavior of circumferential through-wall-cracked pipe with experimental data. The data came from the Degraded Piping Program for quasi-static, four-point-bend pipe experiments conducted without internal pressure (Ref. 2.1). Four stainless steel base metal experiments, five carbon steel base metal experiments, and four experiments with cracks in the center of a stainless steel weld were considered. Various pipe diameters were considered for each class of materials. The stainless steel base metal diameters were 2, 6, 16, and 42 inches; the carbon steel pipe diameters were 4, 8, 28, 36, and 42 inches; and the stainless steel weld pipe diameters were 6, 16, and 28 inches. Both initiation and maximum load predictions were made. Detailed tensile and J-R curve data were supplied and each participant was free to use any analysis method.

GENERAL CONCLUSIONS. Figures 2.85 to 2.89 summarize the ratio of predicted to experimental load. Values less than one mean the analysis underestimated the actual load at crack initiation or the maximum load. The first three figures present Battelle's predictions where five different circumferential through-wall-cracked pipe J-estimation schemes were used. Figure 2.85 shows the predictions for the crack initiation loads. Figure 2.86 shows the predictions for the maximum load using the J_D-R curve. Figure 2.87 shows the predictions for the maximum load using the J_M-R curve. The Battelle results also were published in Reference 2.1. Predictions by the IPIRG member participants are shown in Figure 2.88 for crack initiation loads and Figure 2.89 for maximum loads.

General conclusions were that the GE/EPRI method (Ref. 2.33) gave the lowest predictions and the Paris or NUREG/CR-3464 method (Ref. 2.34), LBB.NRC (Ref. 2.35), and R6 Option 2 (Ref. 2.9) methods gave the highest predictions.

An unexpected result was the large degree of scatter encountered when three different participants used the R6 Option 2 method to analyze the same experiment (see pipe number F32 in Figures 2.88 and 2.89). The scatter among the R6 Option 2 solutions was just as great as the scatter observed for comparisons involving all of the other solution methods. Thus, in spite of the fairly rigid prescription of procedures in R6 Option 2, apparently there is room for interpretation. Errors in the application of the method may also be a source of the scatter.

Round-Robin Problem 2-1

SPECIFIC OBJECTIVE. The objective of Round-Robin Problem 2-1 was to make comparisons of J-estimation scheme predictions for a circumferentially surface-cracked aged cast stainless steel pipe loaded quasi-statically in four-point bending with internal pressure. A surface crack is much more difficult to analyze than a through-wall crack, and there are fewer elastic-plastic (J-estimation scheme) analyses available.

The data for the problem came from the Degraded Piping Program, quasi-static, four-point-bend, pipe Experiment 4143-1 (Ref. 2.36). The pipe was pressurized and tested at 288 C. The crack was in the base metal. The pipe diameter was 406 mm (16 inches), and the thickness was 25.4 mm (1 inch). Both initiation and maximum load predictions were made. The detailed tensile and J-R curve data were supplied, and the participants were free to use any analysis method they wanted, although specific tensile and J-R curve data files were recommended.

GENERAL CONCLUSIONS. The results of this round-robin analysis are shown in Table 2.18 for crack initiation loads and Table 2.19 for maximum loads.

Three main observations can be made from these results.

(1) Significant differences exist between the R6 Option 1 and Option 2 analyses (Ref. 2.9) for the crack initiation loads from Participants A and D.

(2) For Participant D, the R6 Option 1 analysis gave higher values than the Option 2 or Option 3 analyses, but still underpredicted the loads. (The Option 1 analysis is generally expected to give lower values than the other R6 options, (Ref. 2.9).

(3) ASME Code IWB-3640 (Ref. 2.37) and Net-Section-Collapse analysis solutions (Refs. 2.7 and 2.38) for Participants C and E initially differed by almost a factor of 2. Subsequently it was found that one of them used the wrong crack size, and correcting for that gave good agreement.

Round-Robin Problem 2-2

SPECIFIC OBJECTIVE. The objective of Round-Robin Problem 2-2 was to calculate the J-R curve from the fully reversed loading (R = -1) Subtask 1.2 Experiment 1.2-4. This problem was included to stimulate thinking about ways to calculate J-R curves from fully reversed pipe bend tests and to then rationalize the pipe test J-R curves with C(T) specimen data. Subtask 1.2 developed experimental data on the effect of reversed loading histories on ductile tearing. This type of load history could occur in a seismic event. The experimental results showed that for fully reversed loading, the load-displacement curve was significantly lower than for monotonic loading. Hence, there was an apparent loss in toughness due to the cyclic load history. The focus of Round-Robin Problem 2-2 was on methods to evaluate the toughness loss.

Experiment 1.2-4 was conducted using a circumferential through-wall-crack in TP304 stainless steel base metal.

GENERAL CONCLUSIONS. Only two participants performed this analysis. Two options were considered for treating cyclic effects: (1) the cycles were considered as "fatigue" crack growth, using the ΔJ approach of Dowling (Ref. 2.39), and (2) the J-R curve was calculated using the envelope values of the load-displacement curve. Other alternatives were considered as well, but no clear conclusions were reached with respect to a preferred method.

Round-Robin Problem 2-3

SPECIFIC OBJECTIVE. The objective of Round-Robin Problem 2-3 was to make fracture predictions for an inertially loaded pipe with a circumferentially oriented surface crack, Experiment 1.1-2. This problem was selected to introduce dynamic loading issues into the fracture predictions.

Experiment 1.1-2 was a 6-inch diameter A106 Grade B pipe experiment with a circumferential through-wall crack. The pipe was pressurized and tested at 288 C. The details of the experimental procedures were discussed in Section 2.1.2, and further analyses are presented in Section 3.0.

There were two parts to this problem. The first was to predict the loads at crack initiation and maximum load. This is essentially a static fracture mechanics analysis, but differs from the first round-robin problem in that the pipe is pressurized and there are dynamic cyclic load effects to consider on the material property data input to the fracture analyses. The second part of the problem was to predict the moments at the crack section, rotations due to the crack, and end-mass displacements as a function of time. The second part incorporates the basic dynamic calculations needed for analysis of the Subtask 1.3 cracked pipe experiments.

GENERAL CONCLUSIONS. Only two organizations analyzed this problem. One used the Paris analysis procedure (NUREG/CR-3464) for initiation and maximum moment, but adjusted it to agree with other Subtask 1.2 pipe experimental fracture data. Their results are given in Table 2.20.

Battelle's results for the loads at crack initiation and the maximum load are shown in Figures 2.90 and 2.91 and summarized in Table 2.20. Quasi-static and dynamic properties were used. The dynamic properties were the tensile test data at a strain rate of 11/second and the dynamic J_D-R and J_M-R curves.

In contrast to Round-Robin Problem 1, the GE/EPRI analysis (Ref. 2.33) was not used since this was a combined loading problem where the proper h_1 functions did not exist. These results showed that when using the dynamic properties, the predicted loads are further below the experimental results than when using the quasi-static properties.

Battelle used the LBB.ENG2 J_D-R curve solution (Refs. 2.1 and 2.28) with the dynamic properties to determine the moment rotation curve to be used in the dynamic analyses (Battelle-Dyn results in Table 2.20).

As summarized in Table 2.20, the two solutions predicted 34 and 38 cycles to failure, while the experiment had 33 cycles to failure. Considering the errors in earlier round-robin problems in just making Net-Section-Collapse calculations, this agreement is excellent for the dynamic loading analyses.

Round-Robin Problem 2-4.1

SPECIFIC OBJECTIVE. The objective of Round-Robin Problem 2-4.1 was to compare predictions of the static load and displacement behavior of the Subtask 1.3 pipe loop with experimental results. This was the first round-robin problem in a series that involved calculations to verify the dynamic analysis of a Subtask 1.3 surface-cracked pipe experiment.

The dimensions of the pipe loop, internal pressure, material properties, and boundary conditions were given to all participants. The straight pipe and the elbows were all carbon steel but had different properties. The stress-strain curves of both materials were provided. The loop was heated to 288 C, so there were also thermal expansion stresses.

GENERAL CONCLUSIONS. There were three solutions to this problem, and solutions are shown in Figure 2.92(a) for the load versus displacement calculations. Other parameters examined were the stress at the crack location, an elbow, and another straight pipe location. Of these additional results only the stress at the crack location is shown here (see Figure 2.92(b)).

The actuator load versus displacement values shown in Figure 2.92(a) show that the "C" results have a low initial actuator force at zero displacement. The elastic slopes of the three solutions are equal. For the nonlinear region, the "A" solution started yielding at a higher load and had higher strain hardening than the "B" or "C" solutions. The only real difference between the "B" and "C" results is a constant offset.

For the stress at the crack location (Figure 2.92(b)) the "A" and "B" solutions are reasonably close, and the "C" results are lower. In this case, the "C" results do not show the same elastic slope as the "A" and "B" results. The discrepancy in these results eventually led to further investigations in Round-Robin Problem Set 4.

Round-Robin Problem 2-4.2

SPECIFIC OBJECTIVE. The objective of Round-Robin Problem 2-4.2 was to calculate mode shapes and natural frequencies for the Subtask 1.3 pipe loop. This was the first set of dynamic calculations of the pipe loop. These calculations are fairly routine for modal analyses. The problem statement assumed that there was no crack in the pipe system and gave the internal pressure and elastic modulus of the material.

GENERAL CONCLUSIONS. Three organizations submitted solutions to this problem. Organization "A" produced five different solutions considering no crack, a surface crack, or a through-wall crack. All "A" calculations were performed using the SAP IV code. "B" used pipe elements in the ANSYS® code, and "C" used pipe elements in the CASTEM code.

All five mode shapes compared well among all three participants. Table 2.21 gives the natural frequencies for the first five modes for each participant. The "A" and "B" solutions considered only the case with internal pressure, whereas the "C" solutions were with and without internal pressure. The biggest difference in frequency was between the "A" and "C" solutions, where for Mode 1 there was a 12 percent difference. The "C" results showed a larger effect of internal pressure than was observed experimentally. This discrepancy eventually led to a further round-robin problem (Problem Set 4) on general stress analysis of piping systems.

Round-Robin Problem 3-1

SPECIFIC OBJECTIVE. The objective of Round-Robin Problem 3-1 was to conduct FEM analyses of TWC stainless steel pipe experiments. This effort was proposed as a result of an FEM analysis of Experiment 1.2-1, which predicted loads about 30-percent less than experimentally determined (Ref. 2.40). This observation, along with past FEM round-robin results (NUREG/CR-4573, Ref. 2.41), showed lower FEM predicted loads than experimentally determined. Since FEM analysis is considered the most accurate method, this discrepancy needed to be resolved.

There were two parts to this problem. Problem 3-1a involved analysis of a French pipe experiment involving a 4-inch diameter cast stainless steel pipe with a simple circumferential through-wall crack. The pipe was quasi-statically loaded in four-point bending without internal pressure at room temperature. Problem 3-1b involved analysis of Experiment 1.2-1 on a 6-inch diameter wrought TP304 stainless steel pipe with a simple circumferential through-wall crack. This pipe was rapidly loaded in displacement-controlled four-point bending without internal pressure at 288 C (550 F).

GENERAL CONCLUSIONS. Four organizations submitted solutions for this problem. No crack growth was modeled by any of the participants. The "B" solutions involved FEM analyses using a model with only applied moments, as well as a model using node-point loading in the four-point bending configuration of the experiment. The "B", "C", and "D" experimental results are shown in Figure 2.93(a) for moment versus rotation. These results agree very well.

For the load versus displacement from Problem 3-1a, the "A", "B", and "D" results are shown in Figure 2.93(b). There are no experimental results in this case because the test machine compliance was not available to correct the total measured displacement to give the displacement of only the cracked pipe. The three predictions are in good agreement, with the largest difference being 12.5 percent in the knee of the curves. However, at the displacement corresponding to crack initiation (30 mm) there is very little difference in the three analyses.

The "A", "B", and experimental load versus load-line displacement results are shown in Figure 2.94. The "A" and "B" predictions agree with each other, but are well below the experimental results. The underprediction of experimental loads by FEM analysis is a matter of some concern. Further investigations to resolve this matter are needed.

Round-Robin Problem 3-2a

SPECIFIC OBJECTIVE. The objective of Round-Robin Problem 3-2a was to calculate the dynamic response of the Subtask 1.3 pipe loop without a crack. Experimental results were obtained as part of Experiment 1.3-1. Calculations were to be made at room temperature and at PWR conditions. This was a necessary step for verifying the design analyses and the analyses of the Subtask 1.3 pipe system fracture experiments.

The forcing function (actuator displacement), damping, material properties, pipe loop geometry, and pipe system boundary conditions were supplied. The participants were asked to calculate the following as a function of time: actuator force, moment at the crack section, and displacements at the mass.

GENERAL CONCLUSIONS. Three organizations provided solutions for the uncracked pipe analyses. Figure 2.95 compares the predictions of bending moment for the room-temperature uncracked pipe experiment. Organization "A" used the MARC code, "B" used the ANSYS® code, and "C" used the CASTEM code. Significant differences exist among the three solutions. Further confusion came from a separate analysis conducted using the ABAQUS code (Ref. 2.42). These results suggested that at the crack location the tensile stresses were higher at 180 degrees from the location predicted in the "B" and "C" analyses. As a result of these analyses, a series of round-robin problems was created to focus on the dynamic analysis of an uncracked pipe system. This was necessary for design of the first cracked pipe system experiment, and the results may have implications for general pipe system stress analysis.

Round-Robin Problem 3-2b

SPECIFIC OBJECTIVE. The objective of Round-Robin Problem 3-2b was to make predictions of the carbon steel pipe system experiment, Experiment 1.3-2.

GENERAL CONCLUSIONS. Only one organization presented results for this problem. Because significant differences existed for the uncracked pipe analysis in Problem 3-2a, discussion of this problem was deferred until the discrepancies of Problem 3-2a were resolved.

Round-Robin Problem 4

As a consequence of the poor agreement between solutions that were generated for Round-Robin Problem 3 in which analyses of the Subtask 1.3 pipe loop were performed, a set of problems was developed to help resolve the discrepancies. The philosophy of Round-Robin Problem 4 was to use simple problems with known closed-form solutions for comparison with the finite element calculations. By carefully selecting the problems to exercise various features of finite element codes separately, modeling, program errors, or interpretation difficulties that influence pipe system analysis results could be identified and resolved. With satisfactory resolution of discrepancies for the simple problems, good comparisons were expected to be forthcoming for complete pipe system analyses.

In performing the selected problems, the element types, mesh refinement, and dynamic solution procedures were identical to those that would later be used for analysis of the Subtask 1.3 pipe system. This way, it could be determined if any of these factors were adversely affecting the pipe system results.

The culmination of Round-Robin Problem 4 was a so-called "Analyst's Meeting" held at Battelle on September 25-26, 1989. At this meeting, the various solutions generated by different IPIRG members and Battelle were compared and discussed. Where discrepancies were found, time was spent to try to understand the source of the problem. Generally, the discrepancies turned out to be interpretation errors - either different assumptions made about inputs or misinterpretation of how a program was going to handle a certain feature that was invoked. In a few cases, finite element computer program documentation was found to be inadequate. At the conclusion of the meeting, a subset of the original Round-Robin Problem 4 was selected for reanalysis by all of the participants.

Round-Robin Problem 4-1

The objective of Round-Robin Problem 4-1 was to validate the modeling and behavior of simple straight pipe in finite element analysis codes. This was accomplished by conducting finite element analyses of a capped-end pressurized pipe loaded as a cantilever beam. Natural frequencies, static deflections, and dynamic solutions with a prescribed end displacement were calculated. Various conditions of temperature, pressure, damping, and forcing function constants also were explored.

Round-Robin Problem 4-2

The objective of Round-Robin Problem 4-2 was to qualify elbow modeling and elements for inclusion in a pipe system model. A simple end-capped and pressurized 90-degree bend loaded as a cantilever was analyzed under different internal pressures and tip loads.

Round-Robin Problem 4-3

The objective of Round-Robin Problem 4-3 was to make calculations of the Subtask 1.3 pipe system uncracked room temperature pipe experiment, Experiment 1.3-1. This round-robin was a reanalysis of Round-Robin Problem 3-2a, incorporating the insights gained in the Analyst's Meeting. Natural frequencies, static displacement, and dynamic response of the pipe system were calculated.

GENERAL CONCLUSIONS. Figure 2.95 shows three predictions of crack section moment for the Subtask 1.3 pipe system prior to the Analyst's Meeting. Figures 2.96 to 2.99 show comparisons between predictions and measured results from the uncracked room temperature pipe experiment after the Analyst's Meeting. The improved agreement among the predictions and improved agreement with the measured response is a direct consequence of the debates and discussions that were held.

On a rather basic level, the lessons learned from Round-Robin Problem 4 were:

- Experienced analysts get different solutions to the same problem for at least four reasons:

  (1) Incomplete problem statements

  (2) Incorrect program inputs

  (3) Poorly documented program features

  (4) Program errors

- When the analysts solve the same problem correctly, all analysts, using different programs, get nearly the same solution.

Resolution of these analytical discrepancies was a major milestone for Subtask 1.3. The agreement between the uncracked pipe system test data and the analytical predictions provided confidence in the design of the Subtask 1.3 test facility.

Round-Robin Problem 5-1a

SPECIFIC OBJECTIVE. The objective of Round-Robin Problem 5-1a was to compare predictions of crack section moments or stresses at initiation and maximum load for Experiment 1.3-3, the stainless steel base metal pipe system experiment. These were essentially static fracture mechanics calculations.

The pipe geometry, post-test crack sizes, internal pressure, and material properties were supplied to the participants. For those conducting more detailed analyses, using a specific stress-strain curve and a specific J-R curve was suggested to the participants.

GENERAL CONCLUSIONS. Three organizations determined the moments at crack initiation, and six organizations calculated the moments at maximum load. A summary of the initiation moment predictions is given in Table 2.22. The summary of the maximum moments is given in Table 2.23. Some key observations from Table 2.23 are:

(a) Virtually all the analyses overpredicted the experimental maximum moments. Of significant note was the overpredictions of 30 to 40 percent by the three different organizations using the ASME IWB-3640 analysis.

(b) The two R6 Option 2 maximum moment predictions differed significantly.

(c) The three IWB-3640 calculations based on $3S_m$ were within 7 percent of each other.

(d) The three predictions for moment by Net-Section-Collapse analysis agreed within 3 percent of each other.

Round-Robin Problem 5-1b

SPECIFIC OBJECTIVE. Round-Robin Problem 5-1b involved dynamic predictions of Experiment 1.3-3. The objective of these calculations was to determine if the exercises in Round-Robin Problem 4, led to more consistent dynamic predictions for a dynamically loaded cracked pipe system.

The pipe loop geometry, crack geometry, temperature, pressure, material properties, boundary conditions, input displacement function, and system damping were defined. Moments at the crack sections versus time were the principal results, but moments, reaction forces, and displacements at other locations also were predicted.

GENERAL CONCLUSIONS. There were two participants for this problem. The first comparison is the moment at the crack section versus the rotation due to the crack. Figure 2.100 shows a comparison of the predictions with the experimental results. The moment-rotation curve, representing the crack nonlinear behavior, is a critical relationship to model in the dynamic analysis. Organization "A" obtained the moment-rotation relation by modifying the quasi-static pipe test curve from the Degraded Piping Program to account for pressure and temperature differences. Organization "B" used the SC.TNP analysis from the Degraded Piping Program (Ref. 2.43) to predict the moment-rotation curve. Both solutions overpredict the rotations at maximum load by approximately a factor of two. The experimental moments are slightly overpredicted by both analyses. Figure 2.101 compares the predictions with the experimentally measured moment at the crack section as a function of time.

Some conclusions from this round-robin problem are:

(a) The dynamic calculations were in much better agreement than for the predictions in Round-Robin Problem 3-2a. Discrepancies in general pipe system stress analysis were resolved to a great degree from the efforts in Round-Robin Problem 4.

(b) The overprediction of rotation at maximum moment was the reason for the discrepancies in these calculations. The smaller amount of rotation due to the crack suggests a lower toughness in the pipe loop experiment than from the quasi-static experiment or the C(T) specimen.

Round-Robin Problem 6-1

SPECIFIC OBJECTIVE. The objective of Round-Robin Problem 6-1 was to determine the accuracy in using elastic stress analysis for a dynamic pipe system experiment, Experiment 1.3-3.

All the results of the pipe experiment were sent to the participants. Participants also were supplied output from Battelle's ANSYS® calculations, so that they could participate without making dynamic FEM calculations, if desired. The Battelle ANSYS® calculations were for

- dynamic elastic uncracked pipe conditions with the experimentally determined damping of 0.5 percent, and
- a static push by the actuator on the pressurized piping system at 288 C using elastic uncracked pipe analyses.

An elastic stress ratio was defined as the calculated elastic moment at the crack plane divided by the experimental moment at the time corresponding to the measured crack initiation and maximum load.

GENERAL CONCLUSIONS. The sixth round-robin problem set had the most participants of any of the round robins. The results are summarized in Tables 2.24 to 2.26.

These results show that there were numerous ways to calculate the elastic stress ratio. For those who chose identical methods, the calculated ratios were numerically very close (Table 2.26). However, depending on the method chosen, the ratio ranged from 0.56 to 2.00. The low value resulted when the static FEM analysis was used rather than the dynamic FEM analysis. The high value corresponded to a case where only inertial stresses were used.

Round-Robin Problem 6-2

SPECIFIC OBJECTIVE. The objective of Round-Robin Problem 6-2 was to use either limit-load or fracture mechanics analyses to predict the failure load and compare that failure load with the measured moments from

Experiment 1.3-3. This problem essentially was solved in Round-Robin Problem 5-1a.

However, Problem 6-2 involved using fracture mechanics to predict certain aspects of the fracture event such as maximum moments for the internally surface-cracked stainless steel base metal specimen. These calculations could be made by quasi-static approaches such as Net-Section-Collapse analysis, ASME IWB-3640, R6, GE/EPRI, or J-estimation schemes.

GENERAL CONCLUSIONS. The results from this round-robin problem are summarized in Tables 2.27 to 2.29. Of the ten Net-Section-Collapse solutions by seven organizations, no two of them used both the same pipe dimensions and flow stress. Differences in crack size used by the various participants could not be compared since this information was not requested in the follow-up questionnaire and was not necessarily given in the documentation of each participant's solution. The fracture ratio (experimental moment to predicted moment) for the Net-Section-Collapse analyses ranged from 0.77 to 1.22.

For the IWB-3640 analysis method, two of the five participants used the same diameter, thickness, and flow stress in their analysis. These two obtained essentially identical results.

Three participants used the R6 method, and the fracture ratio ranged from 0.925 to 1.27. Differences are to be expected, since the R6 method has several choices for elastic stress intensity functions, J-R curves, pipe geometry, crack geometry, yield strength, and cut-off stress (flow stress), as well as choices in techniques for combining pressure and bending loads.

Round-Robin Problem 6-3

SPECIFIC OBJECTIVE. The objective of this problem was to use the elastically calculated stresses from Problem 6-1 to determine the actuator displacement at failure for the calculated moment from Problem 6-2. Results were compared by determining the ratio of the experimental-to-predicted actuator displacement at failure.

GENERAL CONCLUSIONS. The results are summarized in Tables 2.30 to 2.32. Out of 22 solutions by 7 organizations, no two used exactly the same method with the same input. The lowest ratio of experimental-to-predicted displacement was 0.465. This low value was attributed to using a static FEM analysis rather than using the dynamic FEM analysis. (The static analysis neglects inertial moments.) The highest ratio was 1.63, which used the dynamic FEM analysis with R6 Option 1 results where all the stresses were treated as primary stresses in the R6 analysis.

Round-Robin Problem 6-4

SPECIFIC OBJECTIVE. The objective of Round-Robin Problem 6-4 was to evaluate various ratios of experimental-to-predicted results for Experiment 1.3-3 using any method desired.

GENERAL CONCLUSIONS. There were several different techniques used to calculate experimental-to-predicted ratios. The results are summarized in Tables 2.33 to 2.35. The various approaches were:

- a ratio based on the product of the stress analysis ratio (from Problem 6-1) times the fracture ratio (from Problem 6-2),
- ratios based on applied stresses in the experiment versus allowable stresses in the ASME code for uncracked pipe,
- ratios based on the experimental flaw size versus the allowable flaw size by ASME Section XI, and
- ratios based on time to failure.

The most commonly used ratio was the product of the stress analysis ratio (from Problem 6-1) times the fracture ratio (from Problem 6-2). For this definition all the solutions were above 1.00, except when the IWB-3640 fracture analysis was applied using $3S_m$(Actual) as the flow stress.

2.6 References

2.1 Wilkowski, G. M. and others, "Degraded Piping Program - Phase II, Summary of Technical Results and Their Significance to Leak-Before-Break and In-Service Flaw Acceptance Criteria", March 1984 - January 1989, NUREG/CR-4082, Volume 8, March 1989.

2.2 Vieth, P., Kramer, G., Marschall, C., Francini, R., and Wilkowski, G. M., "Subtask 1.2 Final Report - Stability of Cracked Pipe Under Seismic/Dynamic Displacement-Controlled Stresses", Battelle, July 1991.

2.3 Scott, P., Wilson, M., Olson, R., Marschall, C., Schmidt, R., and Wilkowski, G., "Subtask 1.1 Final Report - Stability of Cracked Pipe under Inertial Stresses," Battelle, July 1991.

2.4 Scott, P., Olson, R., Wilkowski, G., Marschall, C., and Schmidt, R., "Subtask 1.3 Final Report - Crack Stability in a Representative Piping System Under Combined Inertial and Seismic/Dynamic Displacement-Controlled Stresses", Battelle, April 1991.

2.5 Marschall, C. W., Landow, M. P., and Wilkowski, G. M., "Loading Rate Effects on Strength and Fracture Toughness of Pipe Steels Used in Task 1 of the IPIRG Program", Battelle, December 22, 1989.

2.6. Marschall, C.W., Nakagaki, M., Brust, F. W., Kramer, G., and Wilkowski, G. M., "Effect of Cyclic Loads on Ductile Fracture Resistance", Battelle, October 15, 1987.

2.7 Kanninen, M. F. and others, "Instability Predictions for Circumferentially Cracked Type 304 Stainless Steel Pipes Under Dynamic Loadings", EPRI Report NP-2347, April 1982.

2.8 Olson, R. J. and others, "IPIRG Subtask 1.1 and 1.3 Design Report", Battelle, October 1987.

2.9 Milne, I., Ainsworth, R. A., Dowling, A. R., and Stewart, A. T., "Assessment of the Integrity of Structures Containing Defects", R/H/R6-Rev. 3, Published by Central Electric Generating Board, England, May 1986.

2.10 ASME Boiler and Pressure Vessel Code, Section XI - "Rules for Inservice Inspection of Nuclear Power Plant Components".

2.11 Landow, M. P. and Marschall, C. W., "Experience in Using Direct Current Electric Potential to Monitor Crack Growth in Ductile Metals", Battelle, Presented at the Second Symposium on User Experience with Elastic-Plastic Test Methods, Orlando, FL, November 1989.

2.12 Schwalbe, K. H. and Hellmann, D., "Application of the Electric Potential Method to Crack Length Measurements Using Johnson's Formula", Journal of Testing and Evaluation, Vol. 9, No. 3, pp 218-221, 1981.

2.13 Kanninen, M. F., Zahoor, A., Wilkowski, G., Abou-Sayed, A., Marschall, C., Broek, D., Sampath, S., Rhee, H., and Ahmad, J., "Instability Predictions for Circumferentially Cracked Type 304 Stainless Steel Pipes Under Dynamic Loading", Volume 2: Appendixes, EPRI Report NP-2347, Vol. 2, April 1982.

2.14 Albertini, C. and Montagnani, M., "Dynamic Uniaxial and Biaxial Stress-Strain Relationships for Austenitic Stainless Steels", Nuclear Engineering and Design, Vol. 57, pp 107-123, 1980.

2.15 Marschall, C. W., Landow, M. P., and Wilkowski, G. M., "Effect of Dynamic Strain Aging on Fracture Resistance of Carbon Steels Operating at Light-Water Reactor Temperatures", Fracture Mechanics: Twenty-First Symposium, ASTM STP 1074, American Society for Testing and Materials, Philadelphia, pp 339-360, 1990.

2.16 Manjoine, M. J., "Influence of Rate of Strain and Temperature on Yield Stresses of Mild Steel", Journal of Applied Mechanics, pp A211-A218, Dec. 1944.

2.17 Marschall, C. W. and Held, P. R., "J-Resistance Curves from Interrupted Impact Tests", Journal de Physique, Colloquium C5, Supplement to No. 8, pp C5-239 - C5-244, August 1985.

2.18 Wilkowski, G. M. and others, "Short Cracks in Piping and Piping Welds", Battelle, NUREG/CR-4599, BMI-2173, Vol. 1, December 1991.

2.19 Henry, R. E., "The Two-Phase Critical Discharge of Initially Saturated or Subcooled Liquid," Nuclear Science and Engineering, Vol. 41, pp 336-342, 1970.

2.20 Henry, R. E. and Fauske, H. K., "Two-Phase Critical Flow at Low Qualities, Part 1: Experimental," Nuclear Science and Engineering, Vol. 41, pp 79-91 (1970); "Part II: Analysis," Nuclear Science and Engineering, Vol. 41, pp 92-98, 1970.

2.21 Sozzi, G. L. and Sutherland, W. A., "Critical Flow of Saturated and Subcooled Water at High Pressure," NEDO-13418, 1975.

2.22 Collier, R. P., Stulen, F. B., Mayfield, M. E., Pape, D. B., and Scott, P. M., "Two-Phase Flow Through Intergranular Stress Corrosion Cracks and Resulting Acoustic Emission," EPRI Report NP-3540-LD, 1984.

2.23 Amos, C., and Shrock, V., "Critical Discharge of Initially Subcooled Water Through Slits," NUREG/CR-3476, 1983.

2.24 Yano, T., Matsushima, E., and Okamoto, A., "Experimental Study of Leak Flow Through Analytical Slits," SMiRT-9, Division G, pp 293-298, 1987.

2.25 Paul, D. D. and others, "Evaluation and Refinement of Leak-Rate Estimation Models", Battelle, NUREG/CR-5128, BMI-2164, April 1991.

2.26 Takumi, K., "Results of the Japanese Carbon Steel Pipe Fracture Program", presented at IPIRG Leak-Before-Break Seminar, Taipei Taiwan, May 11, 1989.

2.27 Wilkowski, G. M. and Scott, P. M., "A Statistical Based Circumferentially Cracked Pipe Fracture Mechanics Analysis for Design or Code Implementation", Nuclear Engineering and Design, Vol. III, pp 173-187, 1989.

2.28 Brust, F. W., "Approximate Methods for Fracture Analyses of Through-Wall Cracked Pipes", NUREG/CR-4853, February 1987.

2.29 Gilles, P. and Brust, F. W., "Approximate Methods for Fracture Analysis of Tubular Members Subjected to Combined Tensile and Bending Loads", Proceeding of the 8th OMAE Conference, Hauge, The Netherlands, March 1989.

2.30 "Leak Before Break: International Policies and Supporting Research", Proceedings of a seminar held in Columbus, Ohio, October 28-30, 1985, NUREG/CP-0077, June 1986.

2.31 "Leak-Before-Break: Progress in Regulatory Policies and Supporting Research", Proceedings of a seminar held in Tokyo, Japan, May 14-15, 1987, NUREG/CP-0092, March 1988.

2.32 "Leak-Before-Break: Further Developments in Regulatory Policies and Supporting Research", Proceedings of a seminar held in Taipei, Taiwan, May 11-12, 1989, NUREG/CP-0109, published in February 1990.

2.33 Kumar, V. and others, "Advances in Elastic-Plastic Fracture Analysis", EPRI Report NP-3607, August 1984.

2.34 Paris, P. C. and Tada, H., "The Application of Fracture Proof Design Methods Using Tearing Instability Theory to Nuclear Piping Postulating Circumferential Through-Wall Cracks", NUREG/CR-3464, September 1983.

2.35 Klecker, R. and others, "NRC Leak-Before-Break (LBB.NRC) Analysis Method for Circumferentially Through-Wall-Cracked Pipes Under Axial Plus Bending Loads", NUREG/CR-4572, May 1986.

2.36 Wilkowski, G. M. and others, "Degraded Piping Program - Phase II", Seventh Program Report, October 1987-December 1988, NUREG/CR-4082, Vol. 7, March 1989.

2.37 American Society of Mechanical Engineers Boiler and Pressure Vessel Code, Edition July 1989, See Section XI Article IWB-3640.

2.38 Kanninen, M. F. and others, "Mechanical Fracture Predictions for Sensitized Stainless Steel Piping with Circumferential Cracks", EPRI Report NP-192, September 1976.

2.39 Dowling, N. E. and Begley, J. A., "Fatigue Crack Growth During Gross Plasticity and the J-Integral", Mechanics of Crack Growth, ASTM STP 590, pp 82-103, 1976.

2.40 Brickstad, B., Swiss-Swedish Analysis Program: "Numerical Analysis of IPIRG Cracked Pipe Experiments with use of Nonlinear Fracture Mechanics", AB Statens Anläggningsprovning Report No. SA/Fou-RAPPORT, May 1989.

2.41 Ahmad, J., Nakagaki, M., Papaspyropoulos, V., and Wilkowski, G., "Elastic-Plastic Finite Element Analysis of Crack Growth in Large Compact Tension and Circumferentially Through-Wall-Cracked Pipe Specimen", NUREG/CR-4573, October 1986.

2.42 Quiñones, D. F., Nickell, R. E., and Norris, D. M., "Static and Dynamic Analysis of Flaw Stability in Piping Systems", J. of Pressure Vessel Technology, Vol. 112, pp 204-212, August 1990.

2.43 Scott, P. M. and Ahmad, J. A., "Experimental and Analytical Assessment of Circumferentially Surface-Cracked Pipes Under Bending", NUREG/CR-4872, April 1972.

Table 2.1 Test matrix of pipe fracture experiments for Subtask 1.2

MOMENT-ROTATION RESPONSE FUNCTION	LOADING RATE	EXPERIMENT NUMBER	
		A 106 Gr B CARBON STEEL	TYPE 304 STAINLESS STEEL
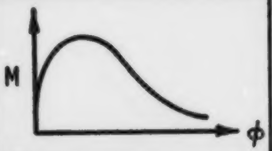	QUASI-STATIC	1.2-7	DP^3 II[a] 4131-5
	DYNAMIC	1.2-8 1.2-11 1.2-12	1.2-1
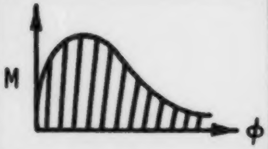	QUASI-STATIC	1.2-2	1.2-3
	DYNAMIC	1.2-10	--
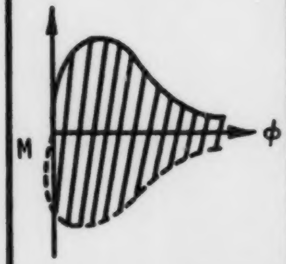	QUASI-STATIC	1.2-4	1.2-5
	DYNAMIC	1.2-6	1.2-9

NOTE: ALL TESTS CONDUCTED AT A TEMPERATURE OF 288 C (550 F) AND CONTAINED A THROUGH-WALL CRACK GEOMETRY

[a] Conducted as part of the NRC Degraded Piping Program.

Table 2.2 Summary of results for Subtask 1.2 stainless steel pipe experiments

	Experiment				
	4131-5	1.2-1	1.2-3	1.2-5	1.2-9
Moment at Crack Initiation, N-m (in-lb)	29,720 (263,000)	37,230 (329,500)	29,500 (261,100)	27,600 (244,280)	33,210 (293,930)
Maximum Moment, N-m (in-lb)	37,629 (333,000)	38,560 (341,300)	34,600 (306,200)	33,000 (292,000)	35,090 (310,570)
Number of Cycles to Crack Initiation	1	1	7-10[a]	4-5	6
Number of Cycles to Maximum Moment	1	1	22	7	8
Load Ratio, (R)	1	1	0	-1	-1
Loading Rate	QS	Dyn	QS	QS	Dyn
Number of Cycles in:					
First Loading Block	N/A	N/A	30	12	27
Second Loading Block	N/A	N/A	15	10	
Third Loading Block	N/A	N/A	15	10	
Fourth Loading Block	N/A	N/A	10	4	
Load-Line Displacement Increment [mm (in)] Between Cycles in:					
First Loading Block	N/A	N/A	1.905 (0.075)	1.905 (0.075)	1,905 (0.075)
Second Loading Block	N/A	N/A	0.953 (0.038)	0.953 (0.038)	
Third Loading Block	N/A	N/A	0.127 (0.005)	0.127 (0.005)	
Fourth Loading Block	N/A	N/A	3.810 (0.150)	3.810 (0.150)	

(a) Crack Tip A initiated during Cycle 7, while Tip B initiated during Cycle 10.

Table 2.2 (Continued)

	Experiment				
	4131-5	1.2-1	1.2-3	1.2-5	1.2-9
Diameter, mm (in)	168.5 (6.634)	169.0 (6.653)	168.7 (6.640)	168.5 (6.634)	168.6 (6.638)
Thickness, mm (in)	13.9 (0.549)	13.9 (0.547)	14.0 (0.550)	14.3 (0.561)	14.1 (0.556)
Fatigue Precracked	No	No	Yes	No	No
Total Percent TWC(b)	38.8	38.0	38.0	36.8	38.3
Inner Span, mm (in)	1219.2	609.6 (24.0)	609.6 (24.0)	609.6 (24.0)	609.6 (24.0)
Outer Span, mm (in)	3251.2	1524.0 (60.0)	1524.0 (60.0)	1524.0 (60.0)	1524.0 (60.0)
Machine Compliance, mm/kN (in/lb)	$1.01x10^{-1}$ $(1.768x10^{-5})$	$7.834x10^{-3}$ $(1.372x10^{-6})$	$7.834x10^{-3}$ $(1.372x10^{-6})$	$1.353x10^{-2}$ $(2.369x10^{-6})$	$1.353x10^{-2}$ $(2.369x10^{-6})$

(b) Includes fatigue precrack if applicable.

Table 2.3 Summary of results for Subtask 1.2 carbon steel pipe experiments

	Experiment							
	1.2-7	1.2-8	1.2-2	1.2-4	1.2-6	1.2-10	1.2-11	1.2-12
Moment at Crack Initiation, N-m (in-lb)	38,420 (340,045)	31,500 (278,800)	29,190 (258,360)	34,570 (305,930)	25,310 (224,000)	34,790 (307,920)	25,710 (227,550)	
Maximum Moment, N-m (in-lb)	51,330 (454,310)	41,400 (366,400)	48,185 (426,470)	42,710 (377,965)	36,970 (327,200)	41,250 (365,100)	45,515 (402,840)	46,970 (415,720)
Number of Cycles to Crack Initiation	1	1	9-10	8-9	6	11	1	1
Number of Cycles to Maximum Moment	1	1	15(a)	14	12	15	1	1
Minimum Load/Maximum Load, (R)	1	1	0	-1	-1	0	1	1
Loading Rate	QS	DYN	QS	QS	DYN	DYN	DYN	DYN
Number of Cycles in:								
First Loading Block	N/A	N/A	25	20	25	25	N/A	N/A
Second Loading Block			15	10				
Third Loading Block			15	10				
Fourth Loading Block			5	2				
Load-Line Displacement Increment [mm (in)] Between Cycles in:								
First Loading Block	N/A	N/A	0.508 (0.020)	0.508 (0.020)	0.508 (0.020)	0.508 (0.020)	N/A	N/A
Second Loading Block			0.254 (0.010)	0.254 (0.010)				
Third Loading Block			0.127 (0.005)	0.127 (0.005)				
Fourth Loading Block			1.016 (0.040)	1.016 (0.040)				

Table 2.3 (Continued)

	Experiment							
	1.2-7	1.2-8	1.2-2	1.2-4	1.2-6	1.2-10	1.2-11	1.2-12
Diameter, mm (in)	167.6 (6.60)	167.4 (6.592)	167.6 (6.60)	167.6 (6.60)	167.6 (6.60)	167.4 (6.589)	167.1 (6.579)	167.4 (6.591)
Wall Thickness, mm (in)	14.0 (0.550)	13.7 (0.539)	14.0 (0.550)	14.0 (0.550)	13.0 (0.510)	13.1 (0.514)	13.1 (0.516)	13.8 (0.542)
Fatigue Precrack	Yes	Yes	Yes	Yes	Yes	Yes	Yes	Yes
Total Percent TWC$^{(b)}$	36.0	37.2	36.0	36.0	36.0	37.6	37.2	37.3
Inner Span, mm (in)	609.9 (24.0)	609.9 (24.0)	609.9 (24.0)	609.9 (24.0)	609.9 (24.0)	609.9 (24.0)	609.6 (24.0)	609.9 (24.0)
Outer Span, mm (in)	1524.0 (60.0)	1524.0 (60.0)	1524.0 (60.0)	1524.0 (60.0)	1524.0 (60.0)	1524.0 (60.0)	1524.0 (60.0)	1524.0 (60.0)
Machine Compliance, mm/kN (in/lb)	1.353×10^{-2} (2.369×10^{-6})	1.353×10^{-2} (2.369×10^{-6})	7.834×10^{-3} (1.372×10^{-6})	1.353×10^{-2} (2.369×10^{-6})	1.353×10^{-2} (2.369×10^{-6})	1.353×10^{-2} (2.369×10^{-6})	1.353×10^{-2} (2.369×10^{-6})	1.353×10^{-2} (2.369×10^{-6})

(a) Servo-hydraulic control problem reduced number of cycles to maximum moment.
(b) Includes fatigue precrack.

Table 2.4 Test matrix for Subtask 1.1

Experiment Number	Material	Flaw Geometry[(a)]	Loading Condition
1.1-1	Carbon Steel	None	Inertial
1.1-2	Carbon Steel	TWC	Inertial
1.1-3	Stainless Steel	TWC	Inertial
1.1-4	Carbon Steel	XSC	Inertial
1.1-5	Stainless Steel	XSC	Inertial
1.1-6	Carbon Steel	ISC	Inertial
1.1-7	Carbon Steel	ISC	Dynamic Monotonic
1.1-8	Carbon Steel	ISC	Inertial
1.1-9	Carbon Steel	ISC	Quasi-Static, Monotonic

(a) TWC = through-wall crack; XSC = external surface crack; ISC = internal surface crack.

Table 2.5 Summary of results from Subtask 1.1 cracked pipe experiments

Experiment No.	Material	Pipe Diameter, mm	Wall Thickness, mm	d/t	2c/πD	Forcing Function Parameters			Moment at Crack Initiation, kN-m	Maximum Moment, kN-m	Cycles or Time to Maximum Moment	Cycles Past Maximum Moment Until Instability
						a, mm/sec	Freq., Hz	$\dot{\delta}$, mm/sec				
1.1-2	Carbon Steel	167.5	14.4	1.0	0.370	2.0	3.5	--	32.9	38.6	30.2 cycles	3
1.1-3	Stainless Steel	169.0	14.0	1.0	0.370	25.0	3.5	--	24.8	29.0	3.4 cycles	2
1.1-5	Stainless Steel	169.0	14.0	0.639	0.490	25.0	3.5	--	40.4	54.7	7.2 cycles	2
1.1-6	Carbon Steel	167.5	14.3	0.783	0.545	7.0	3.5	--	N.D.	48.6	15.2 cycles	1
1.1-7	Carbon Steel	167.5	13.5	0.647	0.432	--	--	152		77.2	0.42 seconds	--
1.1-8	Carbon Steel	167.4	14.1	0.756	0.424	7.0	3.5	--		79.0	11.3 cycles	
1.1-9	Carbon Steel	167.4	14.1	0.720	0.419	--	--	0.025		81.6	2488 seconds	--

N.D. = not determined.

Table 2.6. Test matrix for Subtask 1.3

Experiment Number	Test Material	Crack Geometry
1.3-1	ASTM A710, Grade A, Class 3 Carbon Steel	Uncracked
1.3-2	A106 Grade B Carbon Steel Base Metal	Internal Surface Crack
1.3-3	SA-358 Type 304 Stainless Steel Base Metal	Internal Surface Crack
1.3-4	A106 Grade B Carbon Steel Submerged-Arc Weld	Internal Surface Crack
1.3-5	SA-358 Type 304 Stainless Steel Submerged-Arc Weld	Internal Surface Crack
1.3-7	Type CF8M Centrifugally Cast Aged Cast Stainless Steel	Internal Surface Crack

Table 2.7. Total list of instrumentation used during the Subtask 1.3 pipe system experiments

Channel Name
Actuator Displacement
Actuator Load
Node 6 Reaction Force
Vessel Pressure
Crack
Elbow 3
Elbow 4
Crack-Mouth-Opening Displacements
LVDT
Clip Gage
Rotation
Fine
Coarse
Nodes 1 and 31 Displacements
Accelerometers (Nodes 1 and 31)
String Potentiometers (Node 1 only)
d-c Electric Potential
Internal #1
Internal #2
Internal #3
External #4
External #5
External #6
Base Metal
Battery Current
Strain Gages
South End Cap #1
South End Cap #2
South End Cap #3
South End Cap #4
South End Cap #5
South End Cap #6
Future Crack #7
Future Crack #8
Future Crack #9
Future Crack #10
Future Crack #11
Future Crack #12
North End Cap #13
North End Cap #14
North End Cap #15
North End Cap #16
North End Cap #17
North End Cap #18
Elbow 4 Extrados #19
3.2 m North of Elbow 4
#20
#21
#22
Elbow 3 Top #23
Elbow 2 Top #24
Elbow Strain Gages (room temperature)
Elbow 3 (A-1 through D-3)
Elbow 4 (E-1 through H-3)
String Potentiometers
Elbow 3 Displacement (Center, West, South)
Crack Location Displacement (Center, East, South)
Node 21 Displacement (Center, East, South)

Table 2.8 Summary of first natural frequency measurements for Experiment 1.3-1

Method	Temperature		Internal Pressure		Actuator Preload		Frequency, Hz
	C	F	MPa	psi	kN	lb	
Ring-Down	RT		0	0	Fixed		4.28
Instrumented Hammer	RT		15.4	2230	Fixed		4.5
Instrumented Hammer	RT		15.4	2230	Free		3.5
Actuator Driven	RT		0	0	30.7	6900	4.47
	RT		0	0	23.6	5300	4.25
	RT		15.4	2238	30.7	6900	4.47
	292	557	15.6	2257	31.1	7000	4.43
	292	557	15.6	2257	4.4	1000	4.35
	292	557	15.6	2257	89.0	20000	4.48

Table 2.9 Summary of higher mode frequencies for Experiment 1.3-1

Method	Temperature		Internal Pressure		Actuator Preload		Frequency, Hz	Mode Shape
	C	F	MPa	psi	kN	lb		
Instrumented Hammer	RT		15.4	2230	Fixed		12.0	C
	RT		15.4	2230	Fixed		13.9	B
	RT		15.4	2230	Fixed		18.0	D
Actuator Driven	RT		15.4	2238	30.7	6900	14.0	B
	RT		0	0	30.7	6900	14.0	B
	RT		0	0	23.6	5300	13.8	B
	292	557	15.6	2257	31.1	7000	13.4	B

Table 2.10. Key results from the five Subtask 1.3 cracked pipe system experiments

Expt. Number	Test Mat'l	Max. d/t	$2c/\pi D^{(a)}$	Yield Strength, $MPa^{(b)}$	Ultimate Strength, $MPa^{(b)}$	$J_i^{(b,c)}$, kJ/m^2	Max. Moment, kN-m	Moment at Surface Crack Penetration, kN-m	Moment at Crack Init., kN-m	Max. Moment from Quasi-Static Expt., kN-m	Moment at Crack Init. from Quasi-Static Expt., kN-m	Percent Inertial Loading at Max. Moment	Percent Inertial Loading at Surface Crack Penetration	Load Ratio (Based on Moment)	Load Ratio (Based on Total Stress)
1.3-2	CSBM	0.727	0.438	237	610	129	341	341	--	(e)	(e)	30	30	-0.07	+0.23
1.3-3	SSBM	0.660	0.468	175	459	738	426	328	415	(e)	(e)	43	28	-0.81	-0.34
1.3-4	CSW	0.691	0.486	$358^{(d)}$	$556^{(d)}$	$82^{(d)}$	618	618	--	594	423	28	26	-0.43	-0.18
1.3-5	SSW	0.635	0.440	$258^{(d)}$	$469^{(d)}$	$55^{(d)}$	493	482	460	581	498	47	42	-0.66	-0.27
1.3-7	$ACS^{(f)}$	0.533	0.500	201	578	88	590	543	504	672	660	55	51	-0.46	-0.20

(a) Based on the equivalent crack length (crack area/maximum crack depth) and inside pipe circumference.
(b) Based on quasi-static test data.
(c) C(T) specimen data with 20 percent sidegrooves.
(d) Weld metal properties.
(e) No data presented because comparison experiment was unpressurized.
(f) ACS = Aged cast stainless.

Table 2.11. Crack length measurements from closure marks on fracture surface from carbon steel base metal Experiment 1.3-2

Cycle	Projected Through-Wall Crack Length at Outside Surface From Center of Surface Crack mm	(inch)
3	343	(13.5)
4	386	(15.2)
5	452	(17.8)
6	531	(20.9)
7	572	(22.5)
8	597	(23.5)
9	612	(24.1)
10	622	(24.5)

Table 2.12 Description of Task 1.0 pipes subjected to material characterization tests

Pipe Ident. Number	Material Type	Schedule	Pipe Dimensions, mm (in)	
			Diameter	Wall Thickness
DP2-F30	ASTM A106, Grade B Carbon Steel	120	152 (6)	14.3 (0.562)
DP2-F29	ASTM A106, Grade B Carbon Steel	100	406 (16)	26.2 (1.031)
DP2-F29W	Submerged-arc girth weld in ASTM A106, Grade B[a]	100	406 (16)	26.2 (1.031)
DP2-A23	ASTM A376, Type 304 Stainless Steel	120	152 (6)	14.3 (0.562)
DP2-A8	ASTM A358, Type 304 Stainless Steel	100	406 (16)	26.2 (1.031)
DP2-A8W	Submerged-arc girth weld in ASTM A358, Type 304[b]	100	406 (16)	26.2 (1.031)
DP2-A40	Aged A351, Type CF8M Centrifugally Cast Stainless Steel[c]	--	406 (16)	25.4 (1.0)

(a) The ferritic steel girth weld was prepared by United McGill Corporation of Columbus, Ohio, using procedures recommended by Babcock & Wilcox. It was a single-Vee weld having a 6.4 mm (0.25 in) gap; a 9.5 mm (0.38 in) thick steel backing strip was used for the root pass. The filler metal met specification SFA-5.23, Class EF2 (Linde 44) and the flux was Linde 80. The weld was stress relieved at 605 C (1125 F) for 1 hour.

(b) The austenitic steel girth weld was prepared by United McGill Corporation of Columbus, Ohio, using procedures recommended by General Electric Company. It was a single-Vee weld having a 1.6 mm (0.063 in) land and a 2.4 mm (0.094 in) gap. The first two root passes employed the gas tungsten arc process, the next two passes used the shielded-metal arc process, and the remaining passes used the submerged-arc process. The filler metal met specification SFA-5.9 (Class ER-308) for GTAW and SAW, and SFA-5.4 for SMAW. The flux was ER-308/ST-100 (Lincoln weld).

(c) The pipe was cast having a wall thickness of 50.8 mm (2.0 in); half of the original wall was machined away from the inside prior to conducting pipe tests and C(T) tests at Battelle, leaving a final wall thickness of 25.4 mm (1.0 in). The pipe had been aged previously at 400 C (750 F) for 700 hours to produce embrittlement similar to that encountered in long-time service. The pipe had a ferrite content of about 20 percent.

Table 2.13 Chemical composition of Task 1.0 pipes

Element	Percent (by weight) for Indicated Pipe						
	DP2-F30	DP2-F29	DP2-F29W	DP2-A23	DP2-A8	DP2-A8W	DP2-A40
C	0.15	0.28	0.068	0.046	0.055	0.06	0.040
Mn	0.65	0.82	1.31	1.78	1.25	2.1	0.75
P	0.012	0.010	0.016	0.020	0.019	0.024	0.023
S	0.014	0.023	0.015	0.011	0.000	0.005	0.001
Si	0.20	0.18	0.57	0.53	0.70	0.79	1.17
Ni	0.14	0.11	0.59	9.8	7.7	8.9	10.03
Cr	0.18	0.14	0.027	18.8	17.0	20.8	20.80
Mo	0.055	0.041	0.43	0.16	0.17	0.046	2.56
V	0.001	0.001	0.002	0.08	0.08	0.046	N.D.
Cb	0.000	0.000	0.000	0.020	0.016	0.007	0.19
Co	0.008	0.005	0.007	0.15	0.12	0.069	0.05
Cu	0.28	0.088	0.14	0.20	0.12	0.04	0.15
Sn	0.018	0.011	0.028	0.016	0.007	0.006	N.D.
Al	0.010	0.000	0.003	0.002	0.008	0.016	N.D.
Zr	0.000	0.000	0.001	0.002	0.002	0.008	N.D.
Ti	0.000	0.000	0.001	0.001	0.029	0.006	N.D.
B	0.0000	0.0001	0.0003	0.0005	0.0021	0.0010	N.D.
W	0.00	0.00	--	0.00	0.00	0.00	N.D.

Table 2.14 Actual loading rates in tests of C(T) specimens

Pipe Identi-cation No.	Nominal Diameter, inches	Material Type	Approximate dJ/dt, kJ/m^2/s(in-lb/in^2/s)		$\frac{dJ/dt_{RL}}{dJ/dt_{QS}}$
			Quasi-Static	Rapid Loading	
DP2-F30	6	ASTM A106, Grade B carbon steel	0.12 (0.68)	295 (1680)	2460
DP2-F29	16	ASTM A106, Grade B carbon steel	0.17 (0.97)	420 (2400)	2470
DP2-F29W	16	Submerged-arc girth weld in ASTM A106 Grade B	0.13 (0.74)	520 (2970)	4000
DP2-A23	6	ASTM A376, Type 304 stainless steel	1.1 (6.3)	6750 (38,500)	6140
DP2-A8	16	ASTM A358, Type 304 stainless steel	1.8 (10.3)	7250 (41,400)	4025
DP2-A8W	16	Submerged-arc girth weld in ASTM A358, Type 304	0.13 (0.74)	570 (3250)	4385
DP2-A40	16	Aged A351, Type CF8M centrigugally cast stainless steel	0.16 (0.91)	690 (3940)	4310
				Avg.	3970

Table 2.15 Summary table of pipe fracture experiments

DRB Number	Expt. No.	Pipe ID #	Material	Flaw Geometry	2c/(π)D	d/t	Dia., mm	Wall Thick., mm	Loading Conditions	Pressure, MPa	Moment at Crack Init., kN-m	Max. Moment, kN-m
Subtask 1.1 Experiments												
1.1.7.1	1.1-2	F30	A106B	TWC	0.37	1	167.5	14.4	Inertial	15.5	32.9	38.8
1.1.7.2	1.1-3	A23	TP304	TWC	0.37	1	168.9	14	Inertial	15.5	24.8	29
1.2.7.1	1.1-4	F30	A106B	SC	0.516	0.502	167.8	13.2	Inertial	15.5	64.3	75.8
1.2.7.2	1.1-5	A23	TP304	SC	0.49	0.639	168.9	14	Inertial	15.5	40.4	54.7
1.2.7.3	1.1-6	F30	A106B	SC	0.545	0.783	167.5	14.3	Inertial	15.5	N.D.	48.6
1.2.4.1	1.1-7	F30	A106B	SC	0.432	0.647	167.5	13.5	Dyn Monotonic	15.5	75.3	77.2
1.2.7.4	1.1-8	F30	A106B	SC	0.424	0.758	167.4	14	Inertial	15.5	N.D.	79.0
1.2.3.10	1.1-9	F30	A106B	SC	0.419	0.72	167.4	14	QS Monotonic	15.5	55.2	61.6
Subtask 1.2 Experiments												
1.1.4.1	1.2-1	A23	TP304	TWC	0.38	1	169	13.9	Dyn Monotonic	0	37.2	38.6
1.1.5.1	1.2-2	F30	A106B	TWC	0.36	1	167.6	14	QS Cyclic R=0	0	29.2	48.2
1.1.5.2	1.2-3	A23	TP304	TWC	0.38	1	168.7	14	QS Cyclic R=0	0	29.5	34.6
1.1.5.3	1.2-4	F30	A106B	TWC	0.36	1	167.6	14	QS Cyclic R=-1	0	34.8	42.7
1.1.5.4	1.2-5	A23	TP304	TWC	0.368	1	168.5	14.2	QS Cyclic R=-1	0	27.6	33.0
1.1.6.1	1.2-6	F30	A106B	TWC	0.36	1	167.6	13	Dyn Cyclic R=-1	0	25.3	37.0
1.1.1.10	1.2-7	F30	A106B	TWC	0.36	1	167.6	14	QS Monotonic	0	38.4	51.3
1.1.4.2	1.2-8	F30	A106B	TWC	0.372	1	167.4	13.7	Dyn Monotonic	0	31.5	41.4
1.1.6.2	1.2-9	A23	TP304	TWC	0.383	1	168.6	14.1	Dyn Cyclic R=-1	0	29.1	35.1
1.1.6.3	1.2-10	F30	A106B	TWC	0.37	1	167.4	13.1	Dyn Cyclic R=0	0	25.9	41.2
1.1.4.3	1.2-11	F30	A106B	TWC	0.372	1	167.1	13.1	Dyn Monotonic	0	25.7	45.5
1.1.4.4	1.2-12	F30	A106B	TWC	0.373	1	167.4	13.8	Dyn Monotonic	0	32.7	47.0

Table 2.15 (Continued)

DRB Number	Expt. No.	Pipe ID #	Material	Flaw Geometry	2c(x)D	d/t	Dia., mm	Wall Thick., mm	Loading Conditions	Pressure, MPa	Moment at Crack Init., kN-m	Max. Moment, kN-m
Subtask 1.3 Experiments												
1.2.8.1	1.3-1	IP-F3	A710	Uncracked	---	---	406.4	27.4	Multiple Tests	15.5	N.A.	N.A.
1.2.8.2	1.3-2	F29	A106B	SC	0.438	0.727	403.9	25.7	Pipe System	15.5	N.D.	341
1.2.8.3	1.3-3	A8	TP304	SC	0.460	0.66	415.8	26.2	Pipe System	15.5	415	426
1.2.8.4	1.3-4	F29W	CS SAW	SC	0.48	0.691	402.6	25.5	Pipe System	15.5	N.D.	618
1.2.8.5	1.3-5	A8W	SS SAW	SC	0.44	0.635	416	25.7	Pipe System	15.5	460	493
1.2.8.7	1.3-7	A40	CF8M	SC	0.5	0.533	406.3	26.6	Pipe System	15.5	504	590
Task 4 Experiments												
1.1.1.19	4.3-1	IP-F1	STS49	TWC	0.166	1	763.5	38.2	QS Monotonic	0	4140	6015
1.2.3.14	4.3-2	IP-F1	STS49	SC	0.166	0.498	765	39	QS Monotonic	9.1	6910	7200
Companion QS Monotonic Experiments from Other Programs (TWC Experiments)												
1.1.1.12	4131-5	A23	TP304	TWC	0.388	1	168.5	13.9	QS Monotonic	0	28.9	37.7
1.1.3.1	4131-1	A23	TP304	TWC	0.37	1	166.4	13.4	QS Monotonic	17.2	15.2	19.8
(SC Experiments)												
1.2.1.6	4112-6	F30	A106B	SC	0.503	0.68	167.5	14.8	QS Monotonic	0	67.9	80.1
1.2.1.3	4112-3	A23	TP304	SC	0.518	0.659	168.6	13.6	QS Monotonic	0	56.5	59.6
1.2.3.3	4131-2	A23	TP304	SC	0.521	0.709	168.3	13.4	QS Monotonic	24.5	32.1	34.1
1.2.1.8	4112-8	F29	A106B	SC	0.532	0.662	402.6	26.4	QS Monotonic	0	689.5	748.2
1.2.1.10	EPRI 13S	A8	TP304	SC	0.475	0.66	413.5	28.3	QS Monotonic	0	970.2	1260
1.2.3.13	4141-8	F29W	CS SAW	SC	0.5	0.67	403.2	25.4	QS Monotonic	15.5	423.1	594
1.2.3.2	4141-4	A8W	SS SAW	SC	0.5	0.67	413.5	26.2	QS Monotonic	11.0	497.8	581.5
1.2.3.12	4143-1	A40	CF8M	SC	0.5	0.55	399.6	26.3	QS Monotonic	15.5	660.1	672.2

Table 2.16 Chemical composition of 30-inch diameter Japanese pipe in weight percent

C	Mn	P	S	Si	Cu	Sn	Ni	Cr	Mo
0.21	1.33	0.016	0.008	0.30	0.011	0.001	0.022	0.076	0.003

Al	V	Nb	Zr	Ti	B	Co	W	Pb	Ca
0.031	0.031	0.000	0.000	0.001	0.0000	0.001	0.00	0.00	0.0000

Table 2.17. List of IPIRG Round-Robin Problems

Problem 1	Comparison of J-estimation scheme prediction of circumferential through-wall cracked pipe with various experimental data.
Problem 2-1	Comparison of J-estimation scheme predictions of a circumferential surface crack in aged cast stainless steel pipe.
Problem 2-2	Calculated J-R curve from R=-1 Subtask 1.2 experiment.
Problem 2-3	Prediction of inertially loaded pipe Experiment 1.1-2.
Problem 2-4.1	Static load and displacements of IPIRG pipe loop.
Problem 2-4.2	Mode shapes and natural frequencies of IPIRG pipe loop.
Problem 3-1	FEM analysis of TWC stainless steel pipe experiments
Problem 3-2a	Dynamic response of uncracked IPIRG pipe loop.
Problem 3-2b	Predict IPIRG carbon steel base metal crack Experiment 1.3-2.
Problem 4-1	Simple straight pipe with internal pressure, thermal expansion, displacement at one end, and damping.
Problem 4-2	Simple elbow in bending.
Problem 4-3	Problem 3-2 with corrections
Problem 5-1a	Predict IPIRG Experiment 1.3-3 crack section stresses at initiation and maximum load.
Problem 5-1b	Predict dynamic response of Experiment 1.3-3.
Problem 6-1	Elastic stress analysis of Experiment 1.3-3.
Problem 6-2	Failure load prediction of Experiment 1.3-3.
Problem 6-3	Prediction of actuator displacement of failure using results from Problem 6-1 and Problem 6-2.
Problem 6-4	Ratios of experimental-to-predicted stresses for Experiment 1.3-3.

Table 2.18. Round-Robin Problem 2-1 crack initiation results

	Load,(a) kN (kip)	Moment,(b) kN-m (in-lb)	$\frac{\text{Predicted}}{\text{Experimental}}$
Experimental	319.1 (71.7)	656.6 ($5.81\text{x}10^6$)	
Participant A			
R6-Option 1	179.2 (40.3)	368.5 ($3.26\text{x}10^6$)	0.56
R6-Option 2	199.7 (44.9)	410.6 ($3.63\text{x}10^6$)	0.63
Participant B			
R6-Option 3	301.8 (67.8)		0.95
Participant C			
J_T Analysis	173.1 (38.9)		0.54
Participant D			
R6-Case 1	314.7 (70.7)		0.99
R6-Case 2	285.5 (64.2)		0.89
Participant E			
EPFM (with Press. Corr.)			
SC.TNP		634.1 ($5.61\text{x}10^6$)	0.97
SC.TKP		465.7 ($4.12\text{x}10^6$)	0.71

(a) Includes dead-weight load of 14.9 kN (3,300 lb).

(b) Includes dead-weight moment of 30.6 kN-m (0.271×10^6 in-lb).

Table 2.19. Round-Robin Problem 2-1 maximum moment results

	Load,[a] kN (kip)	Moment,[b] kN-m (in-lb)	Predicted / Experimental
Experimental	326.8 (73.4)	672.5 (5.95×10^6)	
Participant B	301.8 (67.8)		0.92
Participant C			
IWB-3640	259.6 (58.3)		0.79
J_T Analysis	245.7 (55.2)		0.75
J_T Analysis	293.7 (66.0)		0.90
Net-Section-Collapse	366.3 (82.3)		1.12
Participant D			
R6-Case 1	330.5 (74.3)		1.01
R6-Case 2	313.5 (70.4)		0.96
R6-Case 3	323.2 (72.6)		0.99
Participant E Net-Section-Collapse			
1.15 σ-Avg	454.3 (102.1)	934.0 (8.27×10^6)	1.39
σ-Avg	385.0 (86.5)	792.0 (7.01×10^6)	1.18
3 Sm	341.0 (76.7)	702.0 (6.21×10^6)	1.04
IWB-3640 (No Safety Factor)	254.0 (57.0)	522.0 (4.62×10^6)	0.78
PZSC (95% Conf. Lower Bound)			
1.15 σ-Avg	190.0 (42.7)	391.0 (3.46×10^6)	0.58
σ-Avg	183.0 (41.1)	376.0 (3.33×10^6)	0.56
PZSC (Best fit for SC)			
1.15 σ-Avg	389.0 (83.6)	799.0 (7.08×10^6)	1.19
σ-Avg	351.0 (78.9)	721.0 (6.39×10^6)	1.08
EPFM (with Press. Corr.)			
SC.TNP	363.0 (81.4)	745.0 (6.59×10^6)	1.11
SC.TKP	256.0 (57.4)	525.0 (4.65×10^6)	0.78

(a) Includes dead-weight load of 14.9 kN (3,300 lb).

(b) Includes dead-weight moment of 30.6 kN-m (0.271×10^6 in-lb).

Table 2.20. Summary of results from Round-Robin Problem 2-3

	Maximum Moment		Number of Cycles to Instability	Half Rotation Due to Crack, radians	
				Init.	Max.
Organization A	0.97	(Paris)	38	~0.005	0.020
Battelle	1.01 to 1.80	(Paris)			
	0.96 to 1.22	(LBB.NRC)			
	0.94 to 1.14	(LBB.GE)			
	0.85 to 1.12	(LBB.ENG1)			
	0.89 to 1.14	(LBB.ENG2)			
Battelle-Dyn. (LBB.ENG1, dyn J_M-R)	0.93		34	0.0012	0.007
Experiment	---		33	0.0010	0.0096

Table 2.21. Natural frequency calculations for IPIRG Round-Robin Problem 2.4-2

Participant	A	A		A		B	C	C
	PIPE	PIPE + SOLID		PIPE + SHELL		PIPE	PIPE	PIPE
Crack Shape	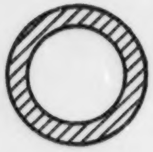 No Crack	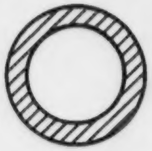 No Crack	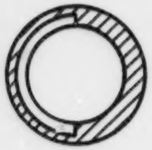	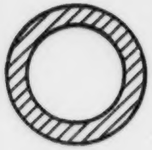 No Crack	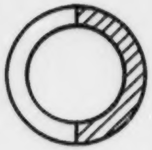	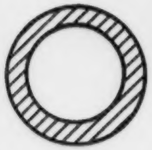 No Crack	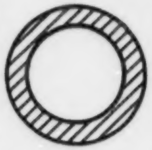 No Crack	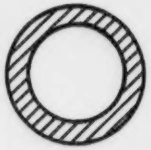 No Crack
1st	4.27	4.27	4.27	4.22	4.08	4.37	4.73	4.27
2nd	13.88	13.76	13.76	13.75	13.59	14.17	14.6	13.9
3rd	14.06	14.05	14.05	14.03	13.72	14.47	14.9	14.1
4th	17.94	17.88	17.88	17.89	16.94	18.55	19.0	18.0
5th	19.53	19.49	19.49	19.48	19.46	20.34	21.1	19.6

(a) With internal pressure of 15.51 MPa.

Table 2.22. Summary of Round-Robin Problem 5-1 predictions of initiation moments

Participant	Method	Moment, kN-m	Expt/Pred
B	SC.TNP	483	0.86
A	NSC (Kurihara)	122	3.40
C	R6 Opt 1 J_D	418	0.99
C	R6 Opt 1 J_M	415	1.00
C	R6 Opt 2 J_D	433	0.96
C	R6 Opt 2 J_M	430	0.97
Experiment	---	415	---

Table 2.23. Summary of Round-Robin Problem 5-1 predictions of maximum moments

Participant	Method	Pred. Moment, kN-m	Expt/Pred
B	NSC (NP-192)		
	(σ_f = avg)	522	0.81
	(σ_f = 1.15 avg)	632	0.67
	(σ_f = 3 S_m)	598	0.71
B	NSC (Kurihara)		
	(σ_f = avg)	371	1.138
	(σ_f = 1.15 avg)	427	0.988
	(σ_f = 3 S_m)	415	1.017
B	Thick-Shell NSC		
	(σ_f = avg)	454	0.930
	(σ_f = 1.15 avg)	555	0.759
	(σ_f = 3 S_m)	534	0.790
B	IWB-3640	549	0.768
B	SC.TNP	503	0.839
A	NSC (Kurihara)	439	0.961
C	R6 Opt 1 J_D	451	0.935
C	R6 Opt 1 J_M	459	0.918
C	R6 Opt 2 J_D	461	0.915
C	R6 Opt 2 J_M	476	0.886
D	NP + Static	513	0.822
D	NP + Dynamic	493	0.855
D	Act. + Static	511	0.826
D	Act. + Dynamic	490	0.860
D	IWB-3640	588	0.717
E	3640 (3Sm)	570	0.739
E	3640 (Avg)	498	0.846
E	3640 (1.1 Avg)	552	0.763
F	R6-Opt 2	610	0.692
Experiment	--------	422	-----

Table 2.24. Summary of methods for Round-Robin Problem 6-1

Participant	Method
B	Ratio of moments, not including thermal expansion or SAM
D	Ratio of inertial and SAM moments.
H	Ratio of inertial and SAM moment using: • Summation of all moments in first 9 cycles, and • Moment in the 9th cycle and, ratio of inertial moments using • summation of all moments in first 9 cycles, and • moment in the 9th cycle.
J	Ratio of all moments, but used static analysis
K	Ratio of all dynamic moments
L	• Ratio of all moments • Ratio of all stresses • Ratio of all stresses but no SAM in elastic calculated values • Ratio of inertial stresses for calculated and experimental values.

Table 2.25. Summary of numerical results for Round-Robin Problem 6-1

Organization	Elastic Stress Ratio = Calc/Expt. Crack Initiation	Elastic Stress Ratio = Calc/Expt. Maximum Load	Comment
B	0.92	0.92	Dead-weight, pressure and inertia loads included
D	1.35	1.50	Dynamic moments
H	---	1.22	Summation of Moments for 9 cycles (dynamic moments)
	---	1.39	Summation of Moments (inertial moments only)
	---	1.54	Only 9th cycle max. moment (all dyanmic moments)
	---	1.97	Only 9th cycle max. moment (inertial component only)
J	0.57	0.56	Static stress analysis
K	1.29	1.42	Total moment
L	1.29	1.42	Total moment
	1.32	1.42	Total stress
	1.03	1.14	Total stress minus SAM in calc.
	1.72	2.00	Inertial stresses only

Table 2.26. Comparison of methods for Round-Robin Problem 6-1

Method	Margin		Organization (Comment)
	@ Crack Initi.	@ Max. Load	
Dynamic Moments	1.35	1.50	D
	---	1.54	H
Inertial Moments	---	1.97	H (9th cycle only)
		2.00	L
Total Moments	1.29	1.42	K
	1.29	1.42	L
High Value			
Inertial Moments		1.97-2.00	H and L
Lowest Value			
Using Static Stress Analysis		0.56	J

Table 2.27. Summary of methods for Round-Robin Problem 6-2

Participant	Method
B	Used R6 Opt 2 for initiation and NSC for maximum load using Q-S properties.
D	Maximum load calculations using Net-Section-Collapse analysis with: • Nominal pipe size and static properties, and • Actual pipe size and dynamic properties.
H	Net-Section-Collapse analysis using average of ASME Code yield and ultimate strength properties. (Moment components are either inertial and SAM, or only inertial.)
F	R6 analysis using: • Option 1 and 2 with J_D-R curve (QS) • Option 1 and 2 with J_M-R curve (QS)
E	Solved for maximum load using: • Using IWB-3640, and • NSC (average all static and dynamic strengths)
G	Solved for maximum load using NSC with average of all static and dynamic strengths.
J	Solved for maximum load using: • IWB-3640 for: - S_m(Code) and - S_m(Actual). • Net-Section-Collapse analysis modified by Kurihara with - S_m(Code) and - S_m(Actual).
K	Solved problem using: • Net-Section-Collapse using - $3S_m$ for flow stress, and - Average of (quasi-static) yield and ultimate strengths for flow stress. • IWB 3640 using $3S_m$ from the code.
L	Solved problem using: • Net-Section-Collapse analysis with - Average of Q-S $\sigma_y + \sigma_u$ for flow stress, - 1.15 times average of Q-S $\sigma_y + \sigma_u$, and - $3S_m$(Code) • DPZP analysis using Q-S $(\sigma_y + \sigma_u)/2$ for σ_f • ASME Section XI, $3S_m$(Code) and $3S_m$(Actual) • R6 Rev. 3 Option 1 with Q-S σ-ϵ curve and J_D-R curve. • SC.TNP using Q-S σ-ϵ curve and J_D-R curve. Either total experimental stress or moment.

Table 2.28. Summary of numerical results for Round-Robin Problem 6-2

Organization	Margin = Exp/Calculated		Comments
	@ Crack Initiation	@ Maximum Load	
B	1.04	---	R6 Option 2 (Q-S, J_D-R)
	---	0.97	NSC (σ_f = average actual properties)
D	---	1.02	NSC (nominal pipe dimensions, static & properties)
	---	1.07	NSC (actual pipe dimensions, dyn. properties)
	---	0.895	IWB-3640
E	---	1.05	NSC (average σ_u + σ_y of dyn. properties)
	---	0.88	IWB-3640 [3S_m (Code)]
F	0.993	0.945	R6 Opt 1 (J_D-R & Q-S properties)
	1.000	0.929	R6 Opt 1 (J_M-R & Q-S properties)
	0.958	0.925	R6 Opt 2 (J_D-R & Q-S properties)
	0.964	0.895	R6 Opt 2 (J_M-R & Q-S properties)
G	---	1.03	NSC [QS(σ_y+σ_u)/2 = σ_f]
H	---	1.22	NSC [(S_y+S_u)/2 from Code]
J	---	0.966	IWB-3640 [3S_m (Code)]
	---	0.681	IWB-3640 [3S_m (Actual)]
	---	1.018	NSC-Kurihara [S_m (Code)]
	---	0.672	NSC-Kurihara [S_m (Actual)]
K	---	1.08	NSC [σ_f=(σ_y+σ_u)/2, Q-S]
	---	0.91	NSC [σ_f=3S_m (Code)]
	---	0.97	IWB-3640 [σ_f=3S_m (Code)]
L	1.25	1.27	R6 Opt 1 (Q-S, J_D-R)
	0.87	0.80	SC.TNP (Q-S, J_D-R)
	---	0.89	NSC [Q-S, σ_f=(σ_y+σ_u)/2]
	---	0.77	NSC [Q-S, σ_f=1.15 avg.]
	---	0.81	NSC [3S_m (Code)]
	---	0.89	Dimensionless plastic-zone criteria
	---	0.82	IWB-3640 [3S_m (Code)]
	---	0.62	IWB-3640 [3S_m (Actual)]

Table 2.29. Comparison of methods for Round-Robin Problem 6-2 (Assumed all used same crack size in calculations.)

Method	Margin		Organization
	@ Crack Initi.	@ Max. Load	
IWB-3640	---	0.966	J
(Two with identical dia. & thickness, 3 other solutions with different diameters & thicknesses)	---	0.97	K
NSC (NP-192 equations)	---	0.77 to 1.22	7 organizations
(10 solutions, none with same diameter, thickness and flow stress)			
R6 - Opt 1	0.993	0.945	F
(2 solutions using Q-S + J_D-R curve)	1.25	1.27	L
R6 - Opt 2	0.958	0.925	F
(2 solutions using Q-S & J_D-R curve)	1.04	---	B
Highest Value			
R6 - Opt 1	1.25	1.27	L
Lowest Value			
IWB-3640 (S_m (Actual)]	---	0.62 - 0.672	L and J (slightly different pipe dimensions)

Table 2.30. Summary of methods for Round-Robin Problem 6-3

Participant	Method
B	Dynamic analysis but without thermal expansion and SAM.
D	Dynamic analysis using either: • NSC analysis with - Nominal pipe size and static properties, or - Actual pipe dimensions and dynamic properties. • IWB-3640 with $3S_m$(Code) for σ_f.
E	Dynamic analysis using: • NSC analysis with average of static and dynamic values for $(\sigma_y+\sigma_u)/2 = \sigma_f$.
G	Static analysis using: • NSC analysis with average of static and dynamic values for $(\sigma_y+\sigma_u)/2 = \sigma_f$.
J	Using static M-δ relation and either: • IWB-3640 for: - Using $3S_m$(Code) for σ_f and - $3S_m$(Actual) for σ_f. • Net-Section-Collapse analysis modified by Kurihara with - Using $3S_m$(Code) for σ_f and - $3S_m$(Actual) for σ_f.
K	Used dynamic total moment with SAM and thermal expansion stresses and using: • NSC with - $\sigma_f = (\sigma_y + \sigma_u)/2$ using static properties - $\sigma_f = 3S_m$ (Code) • IWB-3640 - Using $\sigma_f = 3S_m$ (Code).
L	Used total moment including thermal expansion and SAM with: NSC, DPZP, IWB-3640, R6 Opt 1, and SC.TNP fracture analyses.

Table 2.31 Summary of numerical results for Round-Robin Problem 6-3

	Expt./Predicted		
Participant	@ Crack Initi.	@ Max. Load	Comments
A	1.62	1.34	---
	---	---	---
B	---	1.45	NSC [nominal geometry & static properties]
	---	1.52	NSC [actual geometry & dynamic properties]
	---	1.27	IWB-3640 [$3S_m$ (Code)]
C	---	1.34	NSC [avg. of dynamic properties]
	---	1.00	IWB-3640 [$3S_m$ (Code)]
D	---	0.465	NSC with elastic static FEM ANSYS run
E	---	0.950	IWB-3640 [$3S_m$ (Code)]
	---	0.579	IWB-3640 [$3S_m$ (Actual)]
	---	1.029	NSC-Kurihara [$3S_m$ (Code)]
	---	0.568	NSC-Kurihara [$3S_m$ (Actual)]
F	---	1.34	NSC [avg. of Q-S σ_y+σ_u]
	---	1.14	NSC [$3S_m$ (Code)]
	---	1.14	IWB-3640 [$3S_m$ (Code)]
G	---	1.01	NSC [avg. of Q-S σ_y+σ_u]
	---	1.00	NSC [1.15(avg. of Q-S σ_y+σ_u)]
	---	1.00	NSC [$3S_m$ (Code)]
	---	1.01	Dim. plastic-zone parameter [avg. of Q-S σ_y+σ_u]
	---	1.00	IWB-3640 [$3S_m$ (Code)]
	---	0.81	IWB-3640 [$3S_m$ (Actual)]
	---	1.63	R6 Rev 3 Opt 1 [Q-S, J_D-R]
	---	1.00	SC.TNP [Q-S, J_D-R]

Table 2.32. Comparison of methods for Round-Robin Problem 6-3

- Out of 22 solutions by 7 organizations, no two solutions used the same method with the same pipe size, flow stress, etc.
- Lowest value by "G" with NSC and static pipe FEM M-δ relation (SF = 0.465).
- Highest value by "L" with R6 Opt 1 and dynamic pipe FEM M-δ relation (SF = 1.63).

Table 2.33. Summary of methods for Round-Robin Problem 6-4

Participant	Method
A	Compared experimental stress to allowable from ASME Section III.
B	Product of ratios based on moments from Problems 6-1 and 6-2, but with additional pressure correction.
C	• Compared experimental stress to ASME Section III allowable stress. • Compared margins on experimental flaw size to allowable flaw size from IWB-3640, and • Comparison of ASME IWB-3640 moments to experimental moments.
H	Product of ratios from Problems 6-1 and 6-2 using only inertial and SAM moments, or only inertial moments.
I	• Conducted own FEM uncracked pipe elastic analysis, • determined service level per ASME Section III Eq. 9, • determined allowable loads by ASME Section XI, and included Level A&B as well as C&D margins in calculations.
K	Product of ratios from Problem 6-1 and 6-2 based on moments.
L	• Product of ratios from Problems 6-1 and 6-2 for four different elastic stress ratios times eight different fracture ratios.

Table 2.34. Summary of numerical results for Round-Robin Problem 6-4

	Margin		
Organization	@ Crack Initi.	@ Max. Load	Comments
A	---	0.82	Based on maximum allowable stresses
B	1.37	1.27	R6 Opt 2
	---	1.27	SF(6-1) x SF(6-2) x (1 + (PI/2t)/M_{exp}), where SF(6-1) and SF(6-2) are in terms of moment without SAM or P_E.
C	---	6.2	Based on crack depth at normal/upset loads
	---	1.3	Based on crack depth at emergency/faulted loads
	---	15.3	Based on moment at normal/upset loads
	---	1.7	Based on moment at emergency/faulted loads
H	---	1.50 to 1.89	Based on all dynamic stresses
	---	2.10 to 2.97	Based on inertial stresses only
I	---	1.50	Based on total moment using elastic stress ratio x fracture ratio (IWB-3640)
	---	1.04	Based on inertial moment using elastic stress ratio x fracture ratio (IWB-3640)
K	---	1.53	Structural x fracture ratio [NSC(avg Q-S)]
	---	1.29	Structural x fracture ratio [NSC ($3S_m$)]
	---	1.38	Structural x fracture ratio [IWB-3640 ($3S_m$)]
L (Only total stress solutions given here.)	---	1.26	Structure x fracture ratio [NSC (avg Q-S)]
	---	1.09	Structure x fracture ratio [NSC (1.15 avg Q-S)]
	---	1.14	Structure x fracture ratio [NSC {$3S_m$ (Code)}]
	---	1.26	Structure x fracture ratio [DPZC (avg Q-S)]
	---	1.16	Structure x fracture ratio [IWB-3640, $3S_m$ (Code)]

Table 2.34. (Continued)

Organization	Margin		Comments
	@ Crack Initi.	@ Max. Load	
(All solutions here are based on time to failure.)	---	0.88	Structure x fracture ratio [IWB-3640, $3S_m$ (Actual)]
	---	1.80	Structure x fracture ratio [R6, Rev. 3, Opt 1 (Q-S, J_D-R)]
	---	1.13	Structure x fracture ratio [SC.TNP (Q-S, J_D-R)]
	---	1.01	Structure x fracture ratio [NSC (avg Q-S)]
	---	1.00	Structure x fracture ratio [NSC (1.15 avg Q-S)]
	---	1.00	Structure x fracture ratio [NSC {$3S_m$ (Code)}]
	---	1.00	Structure x fracture ratio [DPZC (avg Q-S)]
	---	1.01	Structure x fracture ratio [IWB-3640, $3S_m$ (Code)]
	---	0.80	Structure x fracture ratio [IWB-3640, $3S_m$ (Actual)]
	---	1.57	Structure x fracture ratio [R6, Rev. 3, Opt 1 (Q-S, J_D-R)]
	---	1.00	Structure x fracture ratio [SC.TNP (Q-S, J_D-R)]

Table 2.35. Comparison of methods for Round-Robin Problem 6-4

- 54 solutions by 7 organizations, no two identical.

- Most common method involved multiplication of stress analysis ratio times fracture ratio.
  - Highest was 2.97 when only inertial stresses used ("H")
  - Lowest was 0.88 when $3S_m$ (Actual) used in IWB-3640 analysis with total stresses ("L").

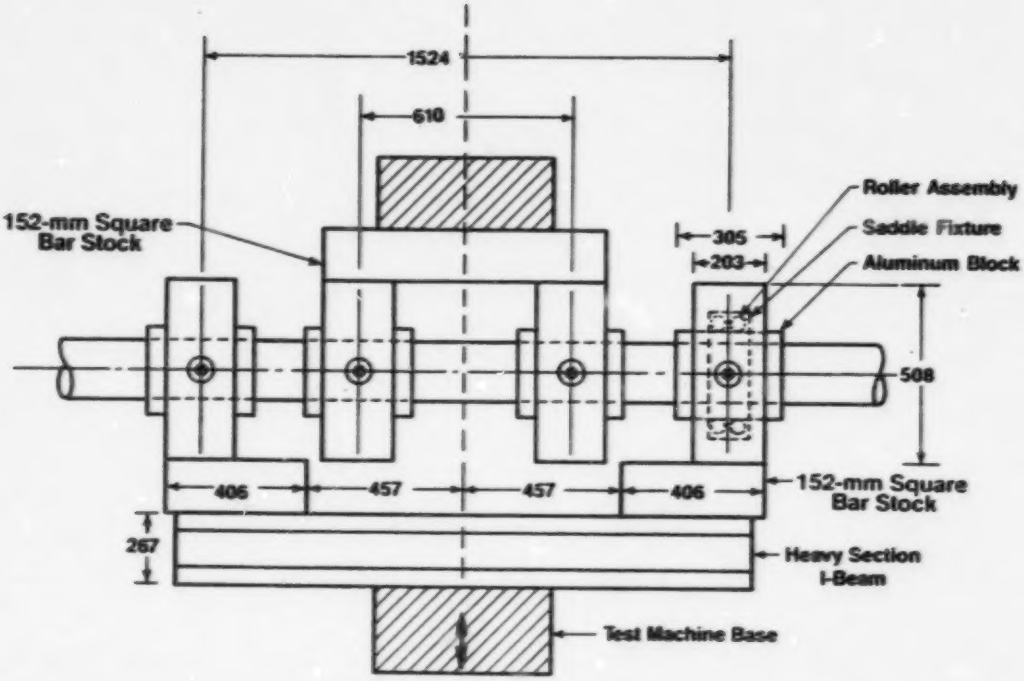
1524
610
152-mm Square Bar Stock
Roller Assembly
Saddle Fixture
Aluminum Block
305
203
508
406
457
457
406
152-mm Square Bar Stock
267
Heavy Section I-Beam
Test Machine Base

Note: All 4 saddle fixtures are identical to the detail.
All dimensions in millimeters.

Figure 2.1. Schematic of test apparatus used for reversed bending in Subtask 1.2.

DRB/1.2-6/F1

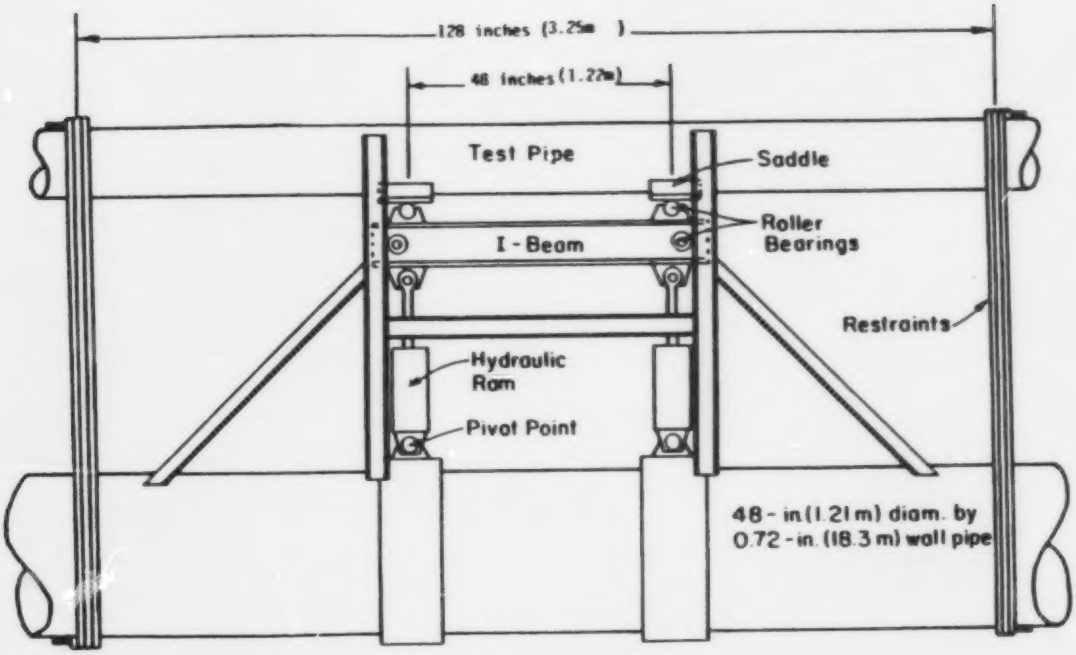
128 inches (3.25m)
48 inches (1.22m)
Test Pipe
Saddle
Roller
Bearings
I - Beam
Restraints
Hydraulic
Ram
Pivot Point
48 - in (1.21 m) diam. by
0.72 - in. (18.3 m) wall pipe

Figure 2.2. Schematic of pipe strongback system used in Degraded Piping Program Experiment 4131-5.

I1.2-8/89-F3.2

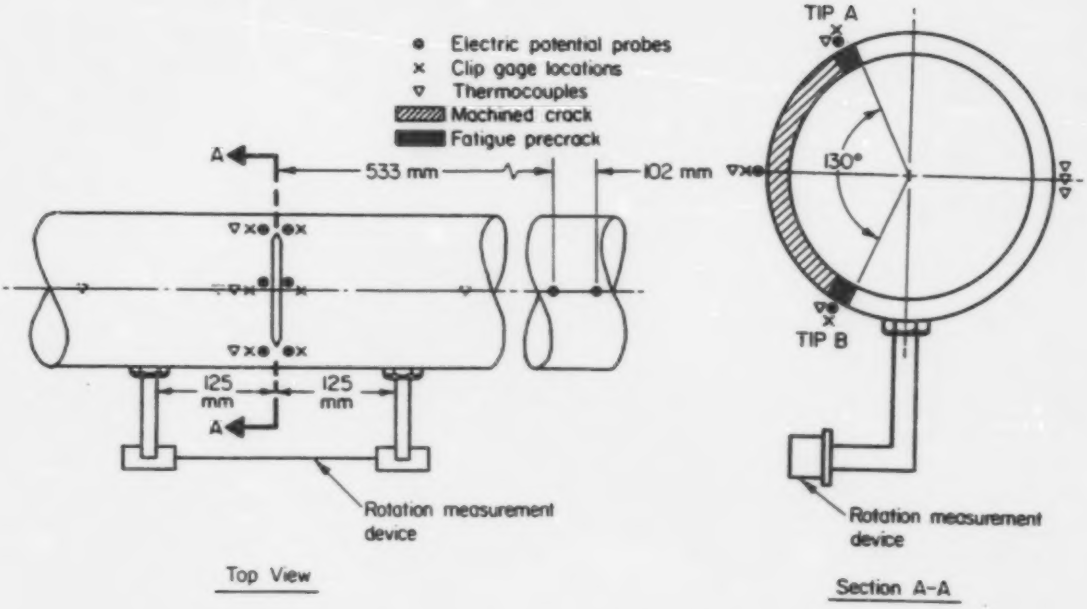
● Electric potential probes
× Clip gage locations
▽ Thermocouples
▨ Machined crack
■ Fatigue precrack
A
A
533 mm
102 mm
125 mm
125 mm
Rotation measurement device
Top View
TIP A
130°
TIP B
Rotation measurement device
Section A-A

Figure 2.3. Typical instrumentation layout for Subtask 1.2 experiments.

DRB/1.2-6/F2

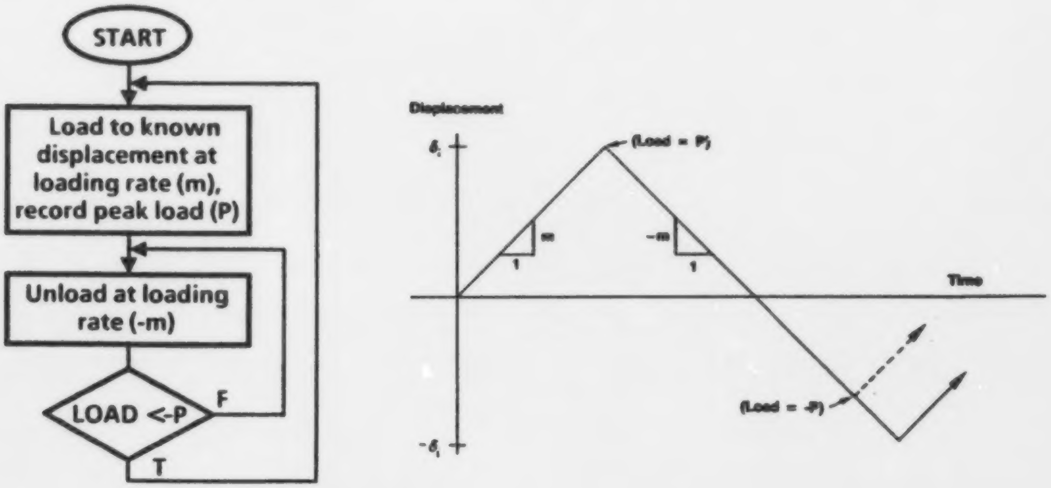
START
Load to known displacement at loading rate (m), record peak load (P)
Unload at loading rate (-m)
LOAD <-P
F
T
Displacement
δ_i
-δ_i
(Load = P)
m
1
-m
1
Time
(Load = -P)

Figure 2.4. Schematic of system control logic used for dynamic, reversed loading (shown for R = -1 loading).

DRB/1.2-6/F5

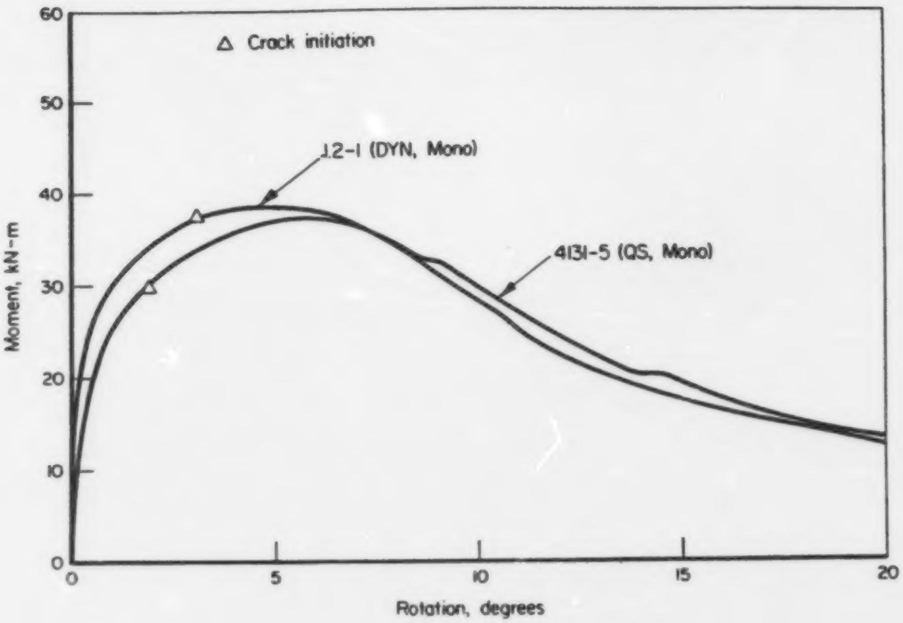

Figure 2.5. Moment versus rotation showing the effect of dynamic monotonic loading for stainless steel.

I1.2-8/89-F3.5

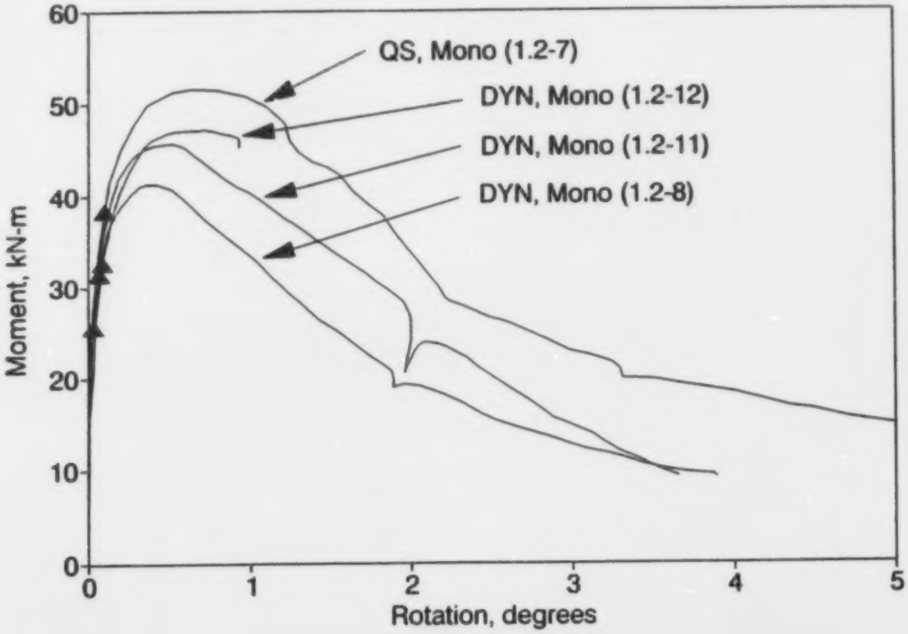

Figure 2.6. Moment versus rotation showing the effect of dynamic monotonic loading for carbon steel.

I1.2-8/89-F3.6

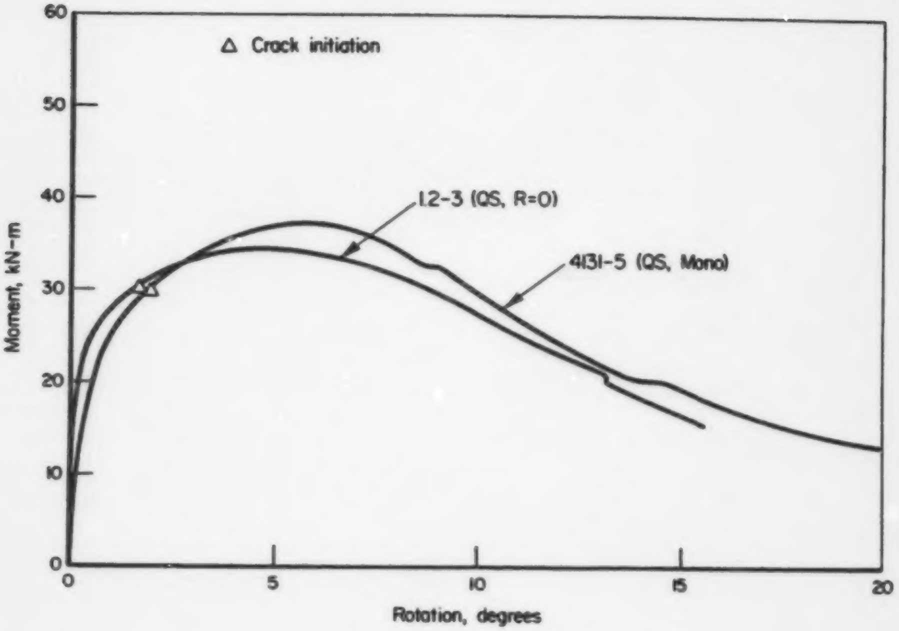

Figure 2.7. Moment versus rotation showing the effect of quasi-static reversed (R = 0) loading for stainless steel.

I1.2-8/89-F3.7

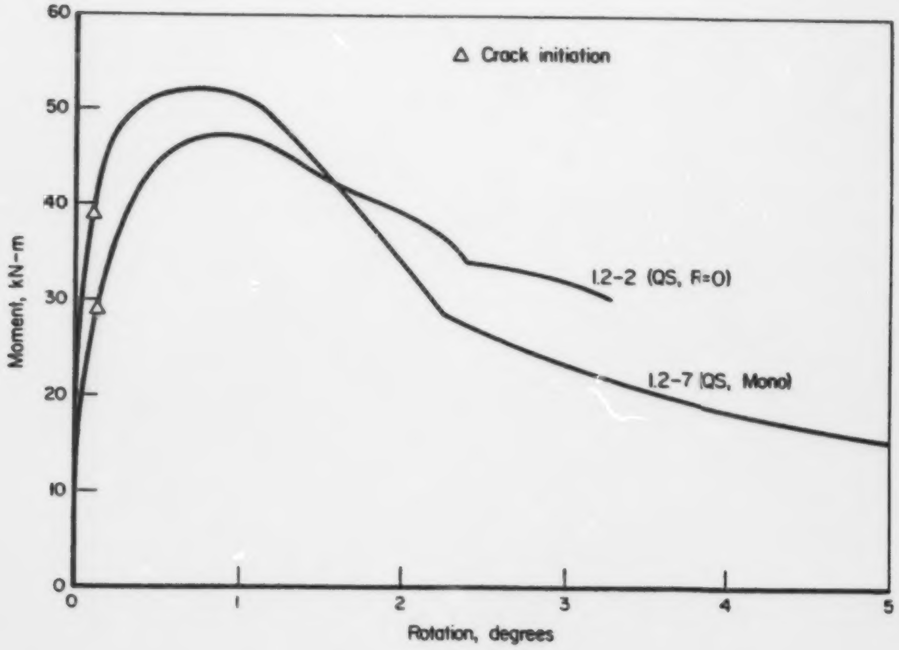

Figure 2.8. Moment versus rotation showing the effect of quasi-static reversed (R = 0) loading for carbon steel.

I1.2-8/89-F3.8

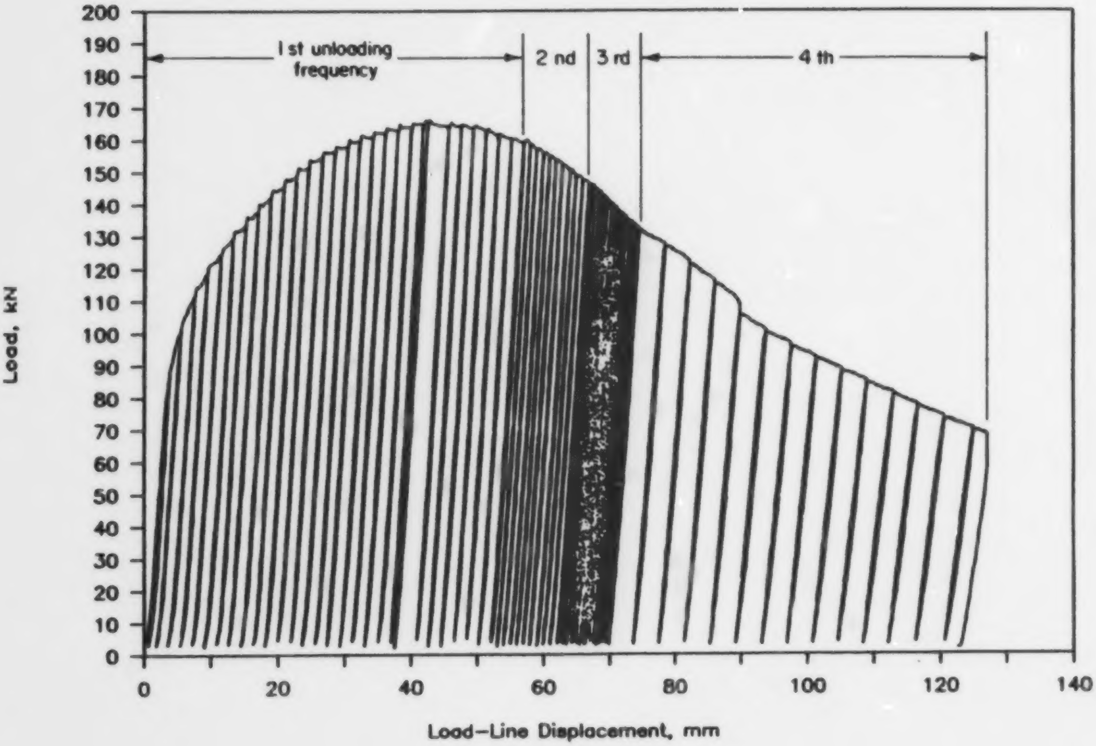

Figure 2.9. Measured load versus load-line displacement for quasi-static reversed (R = 0) loading (Experiment 1.2-3) showing the cyclic loadings and displacement increments.

DRB/1.2-3/F11

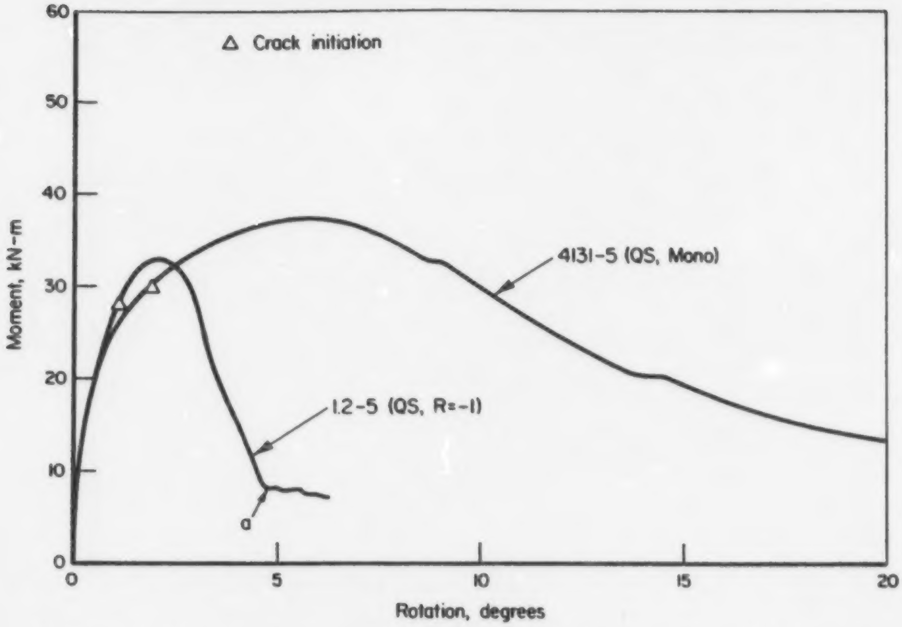

Figure 2.10. Moment versus rotation showing the effect of quasi-static fully reversed (R = -1) loading for stainless steel.

I1.2-8/89-F3.10

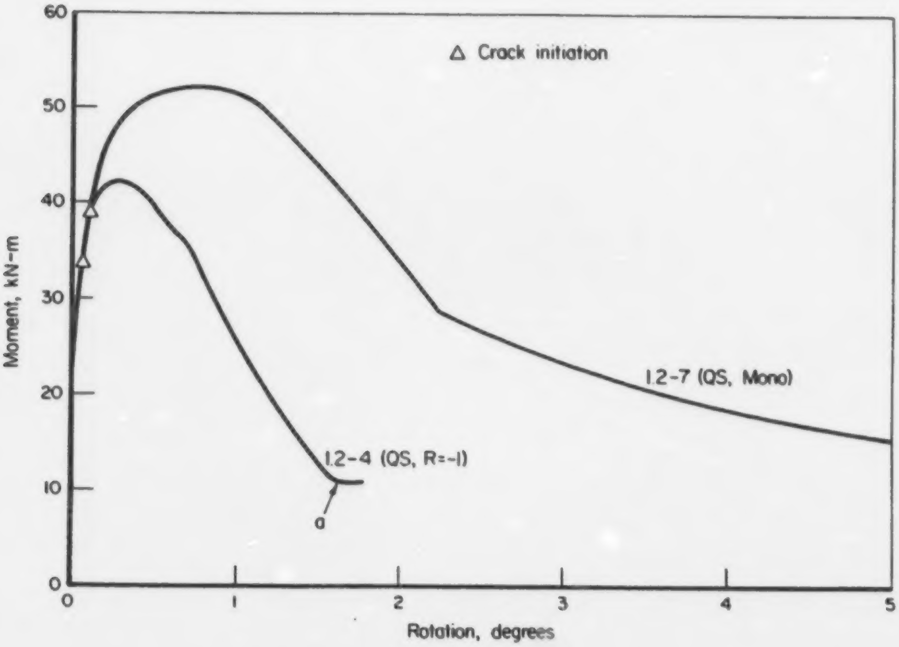

Figure 2.11. Moment versus rotation showing the effect of quasi-static fully reversed (R = -1) loading for carbon steel.

I1.2-8/89-F3.11

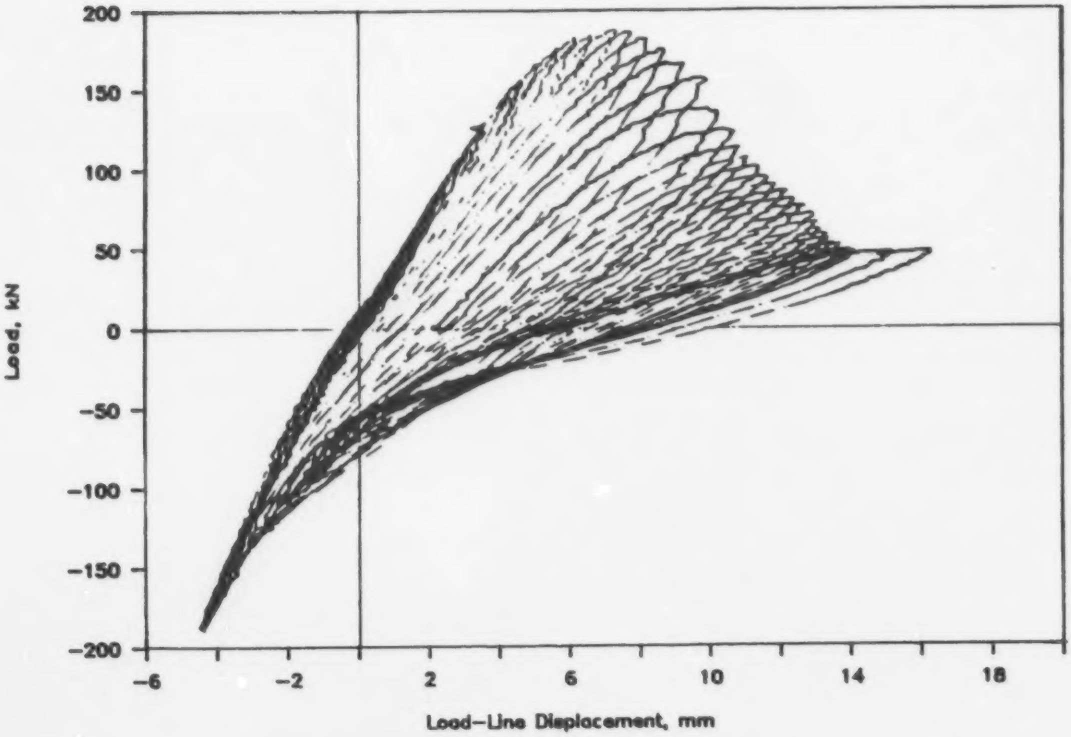

Figure 2.12. Measured load versus load-line displacement for Experiment 1.2-4.

DRB/1.2-4/F10

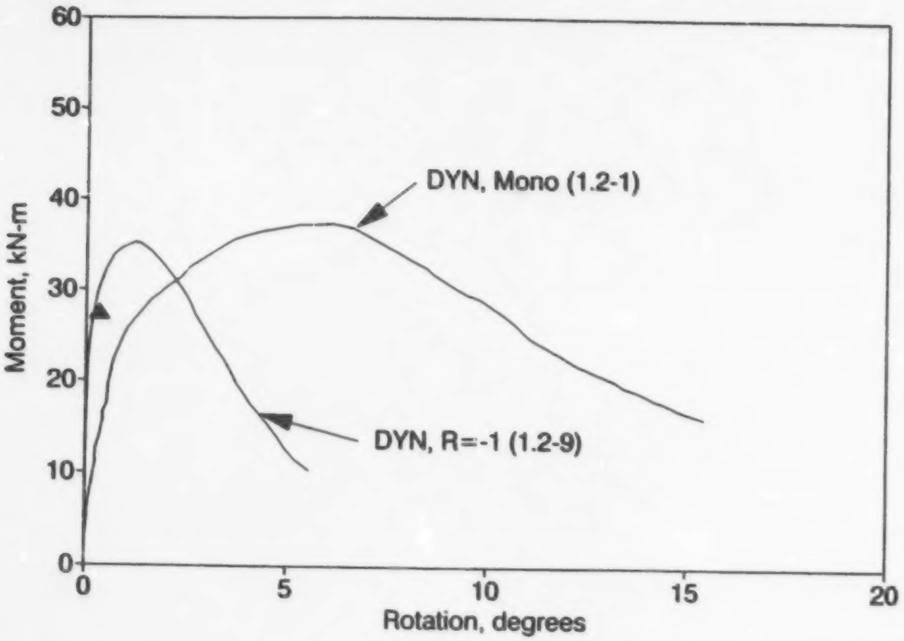

Figure 2.13. Moment versus rotation showing the effect of dynamic fully reversed (R = -1) loading for stainless steel.

I1.2-7/91-F3.13bR

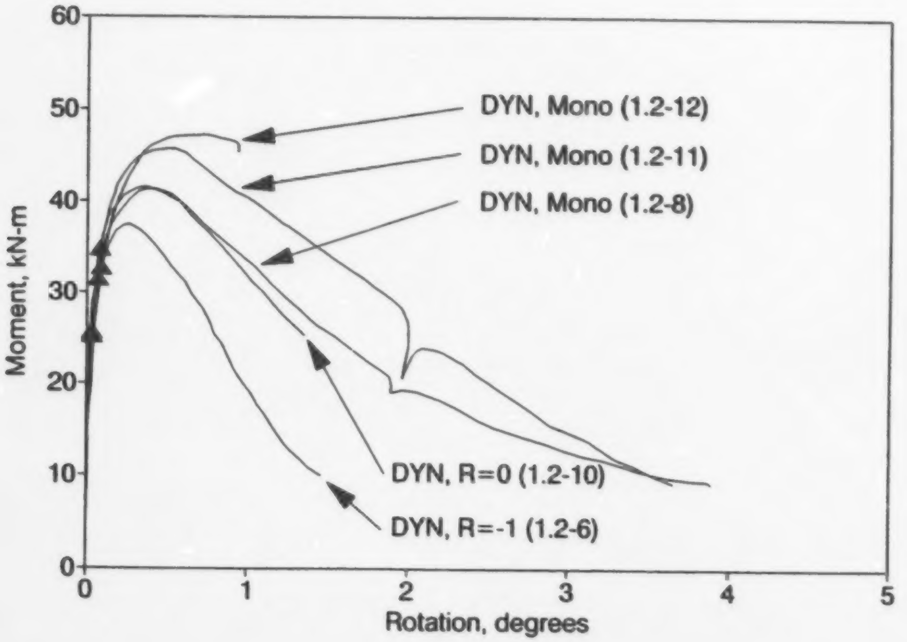

Figure 2.14. Moment versus rotation showing the effect of dynamic cyclic reversed loading for carbon steel.

I1.2-7/91-F3.14bR

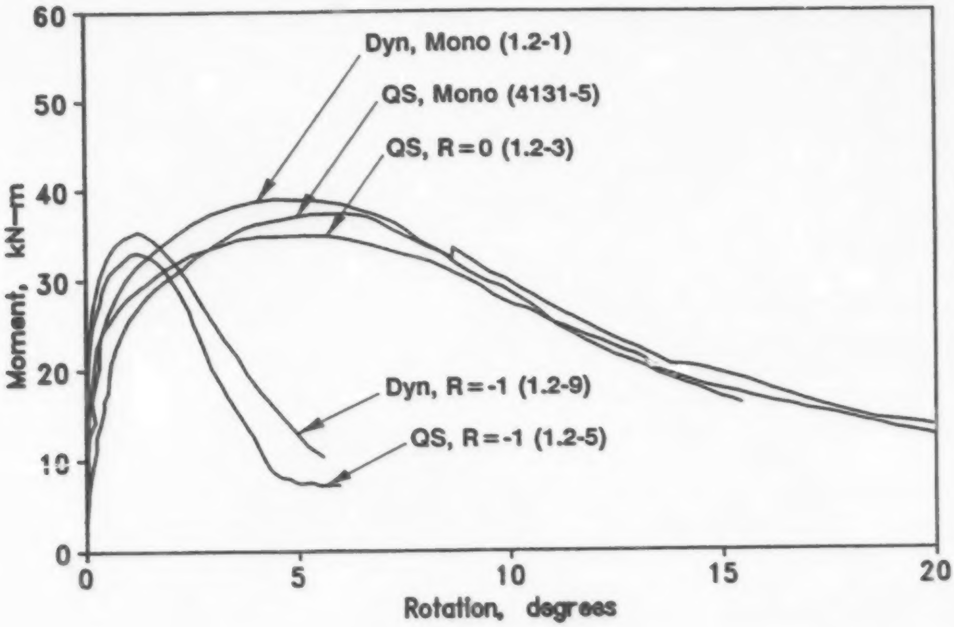

Figure 2.15. Moment versus rotation for all of the stainless steel pipe fracture experiments performed for IPIRG Subtask 1.2.

F-I-7/91-F2.15

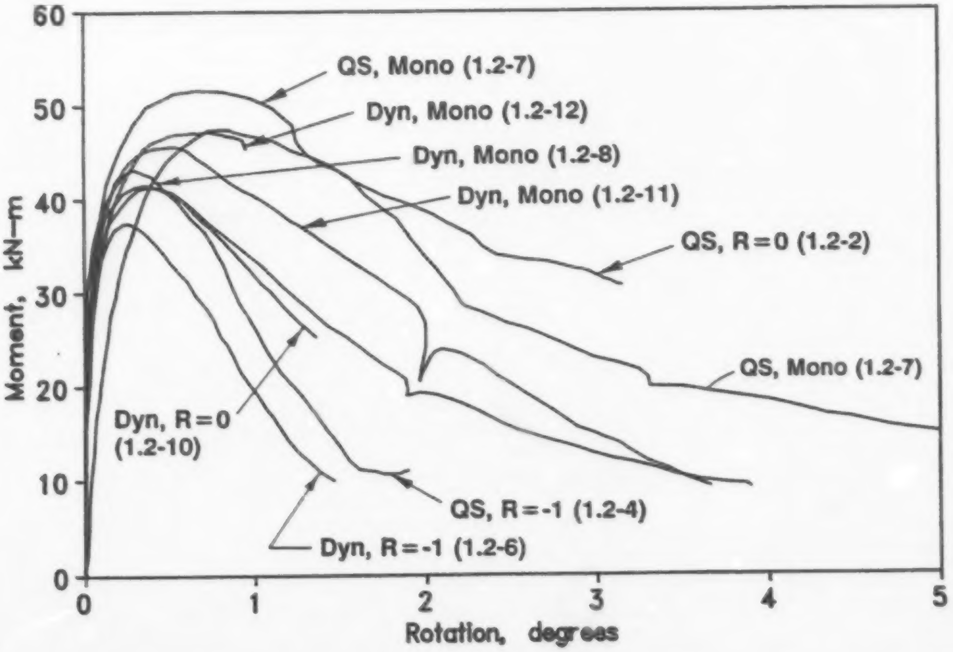

Figure 2.16. Moment versus rotation for all of the carbon steel pipe fracture experiments performed for IPIRG Subtask 1.2.

F-I-7/91-F2.16

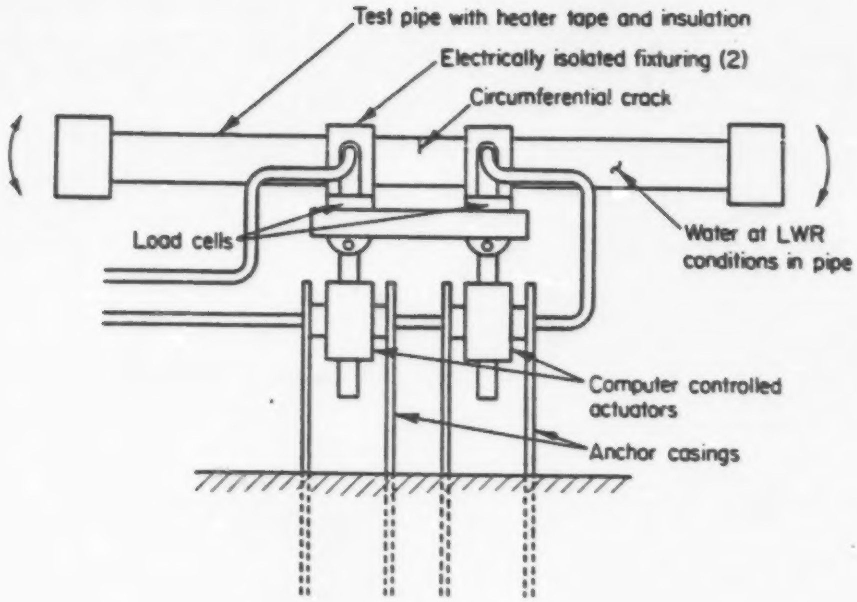
Test pipe with heater tape and insulation
Electrically isolated fixturing (2)
Circumferential crack
Load cells
Water at LWR conditions in pipe
Computer controlled actuators
Anchor casings

Figure 2.17. Conceptual model of Subtask 1.1 experiment.

I1.1-8/89-F3.1

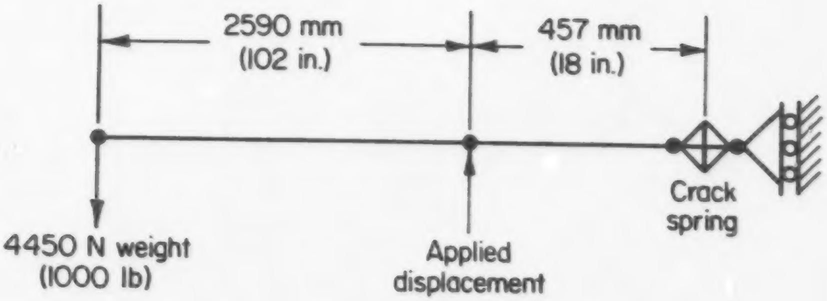
2590 mm (102 in.)
457 mm (18 in.)
4450 N weight (1000 lb)
Applied displacement
Crack spring

Figure 2.18. Subtask 1.1 finite element model.

I1.0-9/87-F10

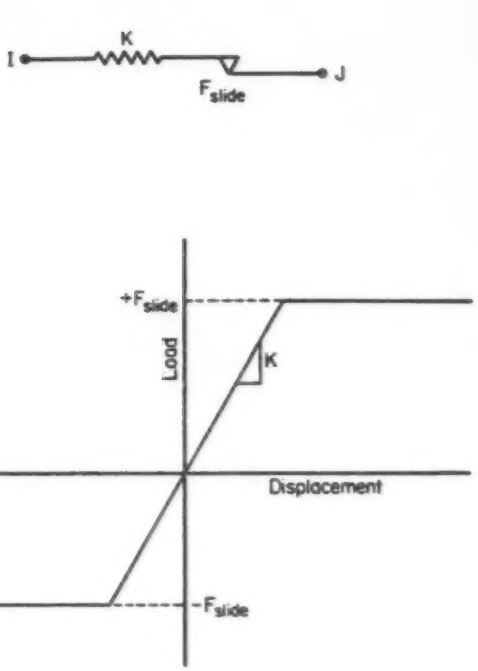
K
I
J
F_slide
+F_slide
Load
K
Displacement
-F_slide

Figure 2.19. Basic spring-slider element.

I1.0-9/87-F5

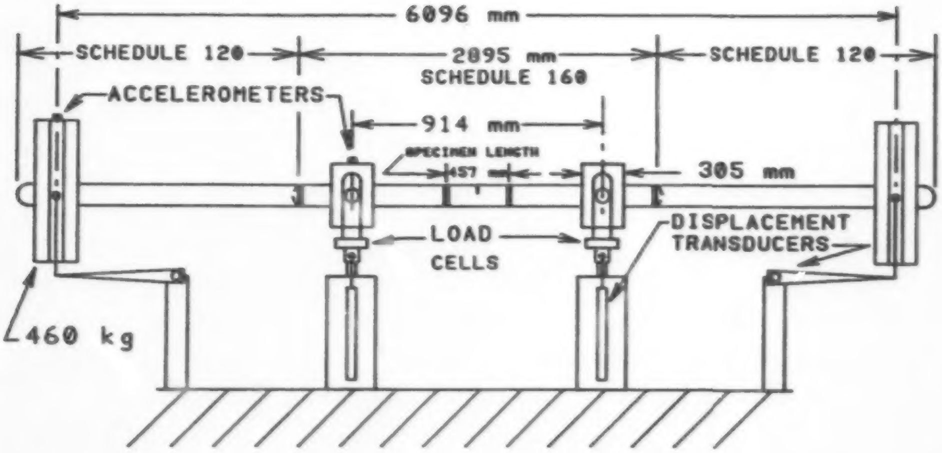
6096 mm
SCHEDULE 120
2095 mm
SCHEDULE 160
SCHEDULE 120
ACCELEROMETERS
914 mm
SPECIMEN LENGTH
457 mm
305 mm
LOAD
CELLS
DISPLACEMENT
TRANSDUCERS
460 kg

Figure 2.20. Sketch of Subtask 1.1 test frame with dimensions of specimen.

I1.1-10/89-F3.20

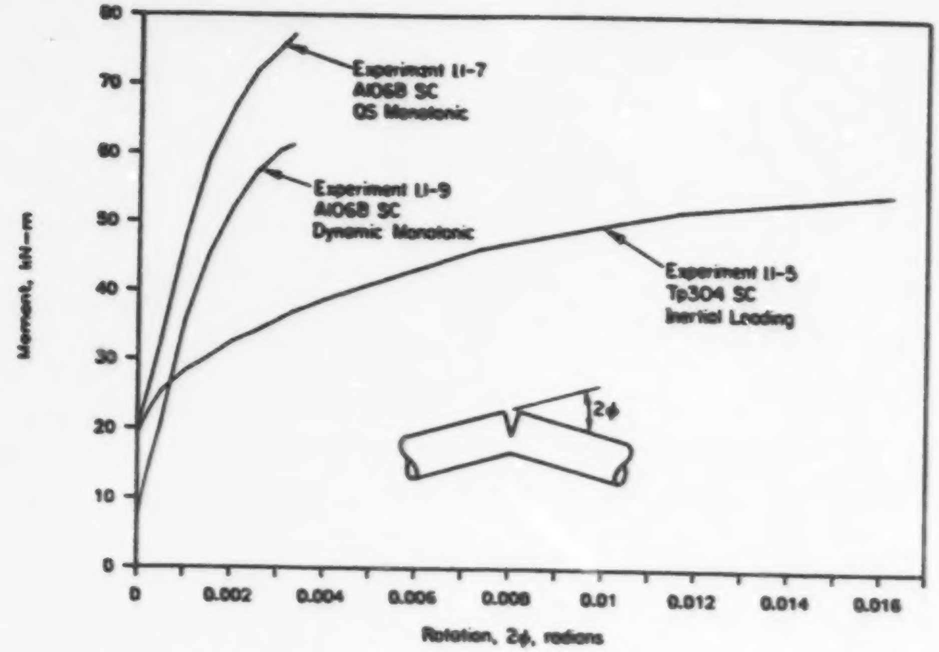

Figure 2.21. Plot of envelope of peaks of the moment rotation responses for the two Subtask 1.1 through-wall-cracked pipe experiments.

F-I-7/91-F2.21

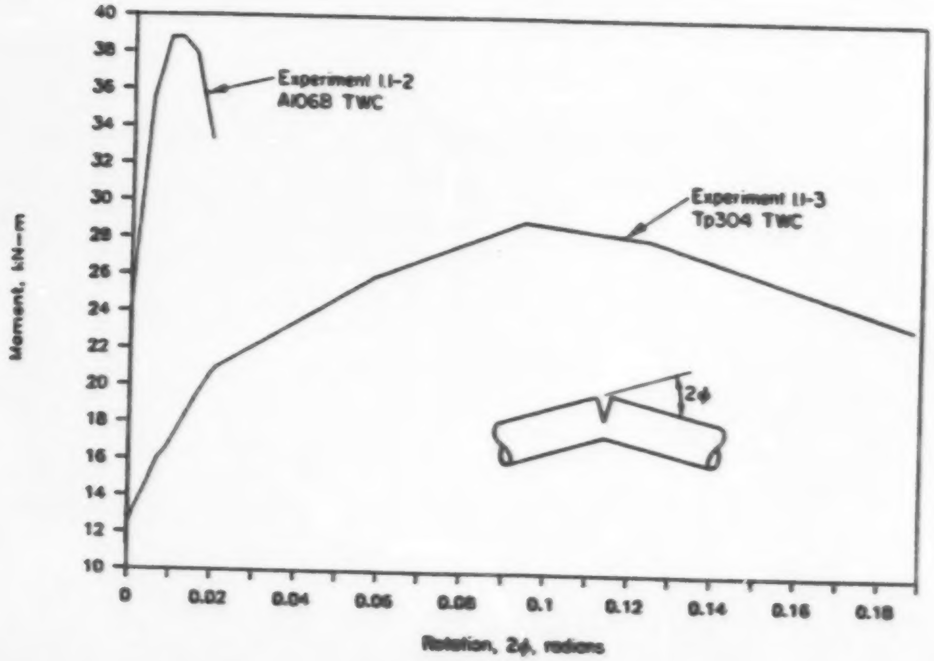

Figure 2.22. Plot of envelope of peaks of the moment rotation responses for three of the five Subtask 1.1 surface-cracked pipe experiments.

F-I-7/91-F2.22

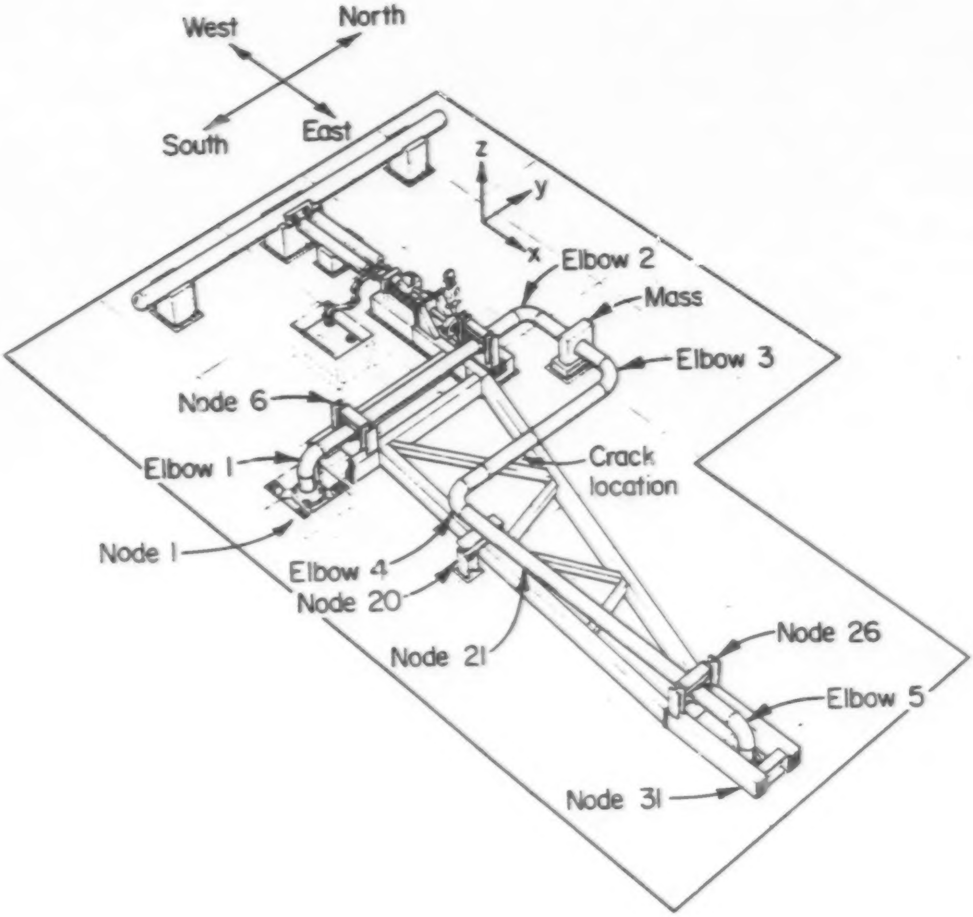
West
North
South
East
z
y
x
Elbow 2
Mass
Elbow 3
Node 6
Elbow 1
Crack location
Node 1
Elbow 4
Node 20
Node 21
Node 26
Elbow 5
Node 31

Figure 2.23. The pipe loop test facility.

QL/1.3-4/F1

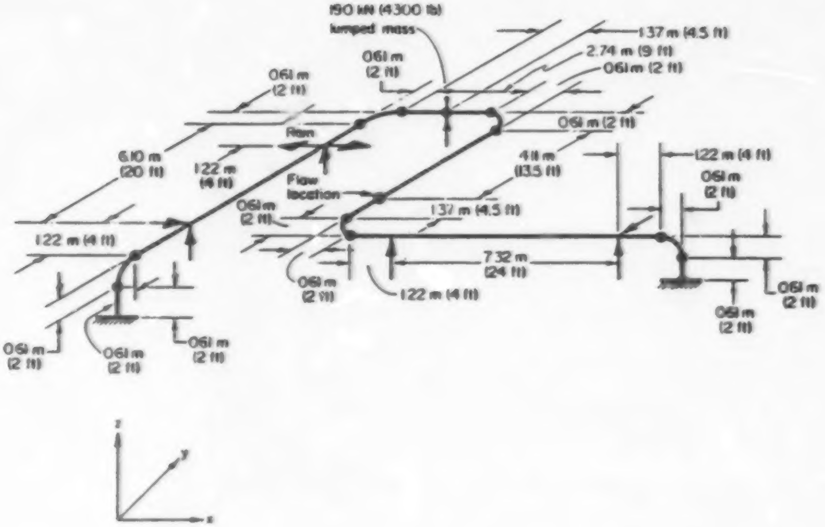
19.0 kN (4300 lb) lumped mass
1.37 m (4.5 ft)
2.74 m (9 ft)
0.61 m (2 ft)
0.61 m (2 ft)
0.61 m (2 ft)
0.61 m (2 ft)
Ram
6.10 m (20 ft)
1.22 m (4 ft)
Flaw location
4.11 m (13.5 ft)
1.22 m (4 ft)
0.61 m (2 ft)
0.61 m (2 ft)
1.37 m (4.5 ft)
1.22 m (4 ft)
7.32 m (24 ft)
0.61 m (2 ft)
1.22 m (4 ft)
0.61 m (2 ft)
0.61 m (2 ft)
0.61 m (2 ft)
0.61 m (2 ft)
0.61 m (2 ft)
z
y
x

Figure 2.24. IPIRG Subtask 1.3 pipe loop geometry.

DRB/1.3-1/F2

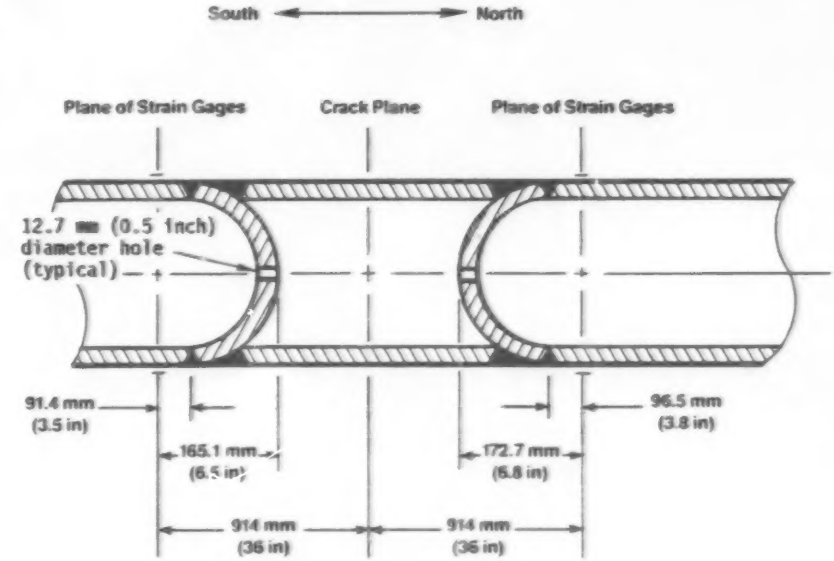
South
North
Plane of Strain Gages
Crack Plane
Plane of Strain Gages
12.7 mm (0.5 inch) diameter hole (typical)
91.4 mm (3.5 in)
165.1 mm (6.5 in)
172.7 mm (6.8 in)
96.5 mm (3.8 in)
914 mm (36 in)
914 mm (36 in)

Figure 2.25. Details of end caps at test specimen used to minimize energy release in the event cracked pipe section severs.

I1.3-10/90-F3.28

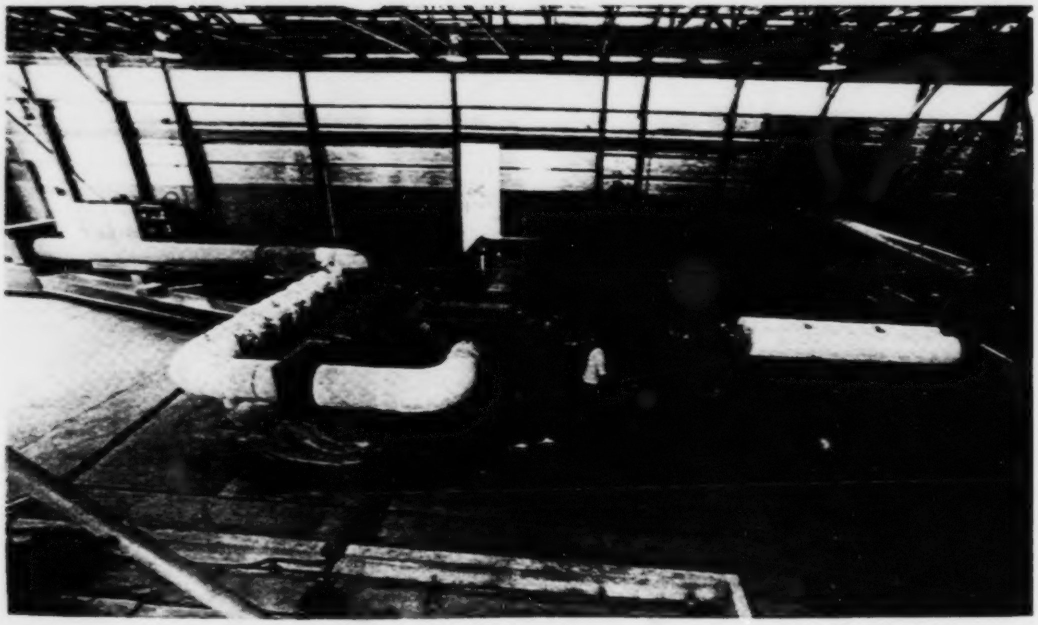

Figure 2.26. Overall photograph of Subtask 1.3 pipe loop test facility.

I1.3-3/91-F3.25

Figure 2.27. Photograph of large mass which simulates a swing check valve.

I1.3-3/91-F3.30

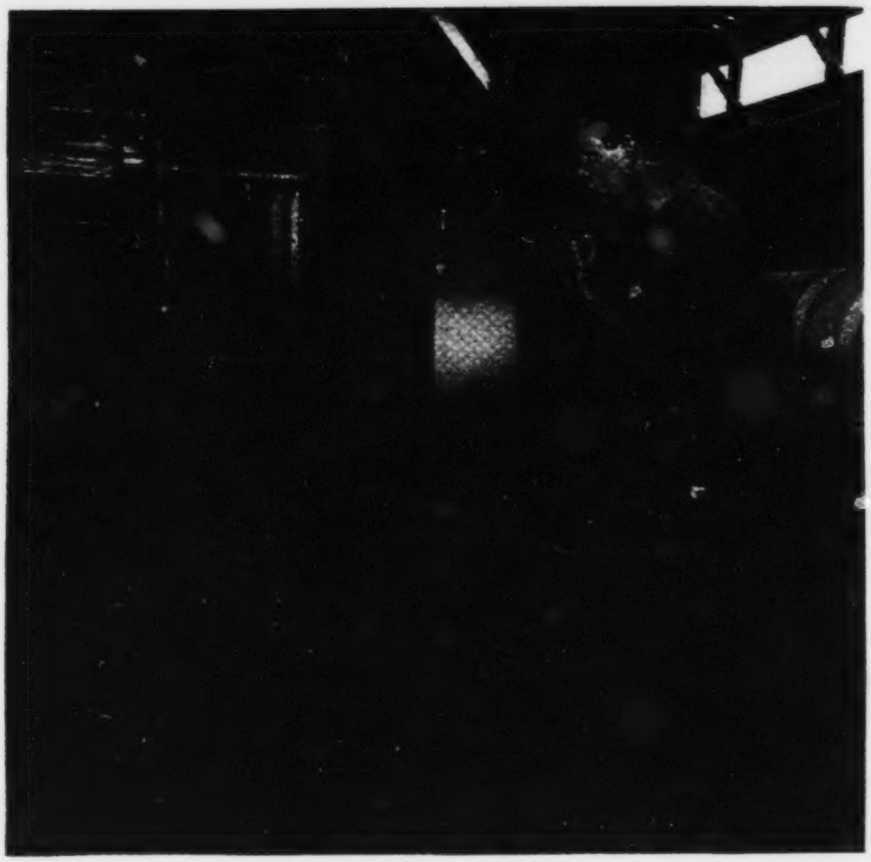

Figure 2.28. Photograph of carriage assembly at actuator.

I1.3-3/91-F3.31

Figure 2.29. Photograph of spherical bearing at Node 26.

I1.3-3/91-F3.32

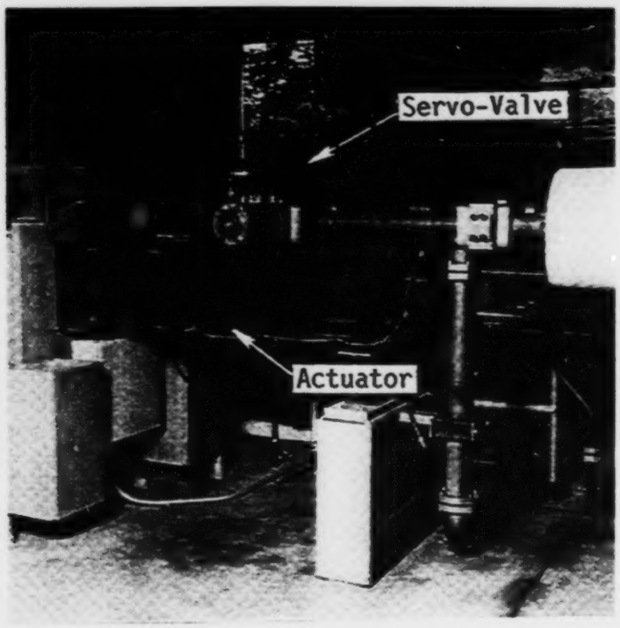
Servo-Valve
Actuator

Figure 2.30. Photograph of hydraulic actuator with integral 7600 lpm (2000 gpm) servo-valve attached.

F-I-7/91-F2.30

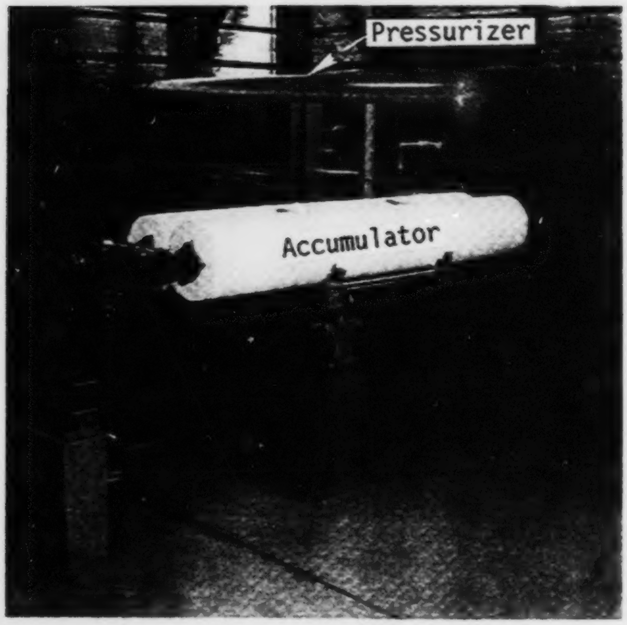
Pressurizer
Accumulator

Figure 2.31. Photograph of piston type hydraulic accumulators with nitrogen storage vessel and water circulation vessel (pressurizer) in background.

F-I-7/91-F2.31

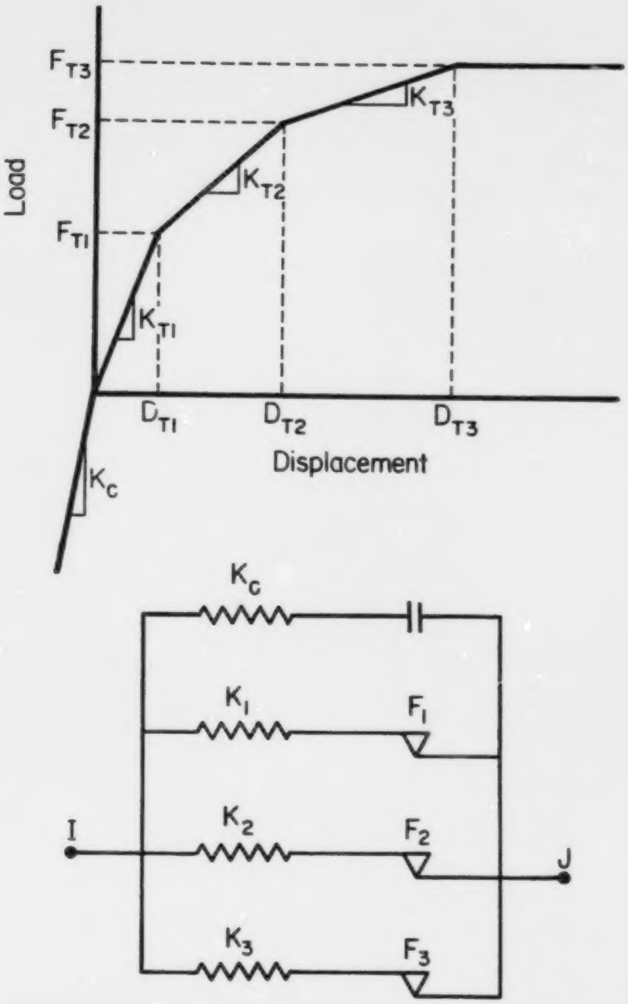

F_{T3}
F_{T2}
F_{T1}
Load
K_{T3}
K_{T2}
K_{T1}
D_{T1}
D_{T2}
D_{T3}
Displacement
K_C
K_C
K_1
F_1
I
K_2
F_2
J
K_3
F_3

$K_1 + K_2 + K_3 = K_{T1}$ $\qquad$ $F_1 + (K_2 + K_3)D_{T1} = F_{T1}$

$K_2 + K_3 = K_{T2}$ $\qquad$ $F_1 + F_2 + K_3 D_{T2} = F_{T2}$

$K_3 = K_{T3}$ $\qquad$ $F_1 + F_2 + F_3 = F_{T3}$

$K_C = 100\ K_{T1}$

Figure 2.32. Modeling of a multilinear load-displacement curve.

F-I-7/91-F2.32

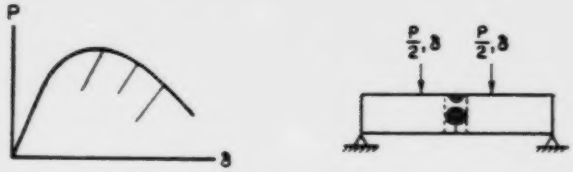

(1a) Quasi-Static Bend Test Data

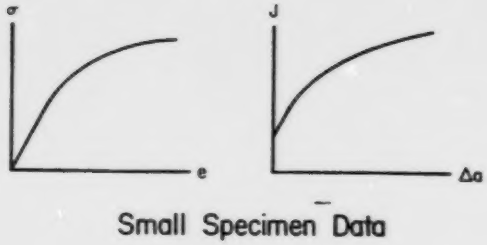

(1b) J-Estimation Schemes

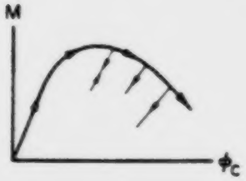

Crack (Growth) + Plasticity,
Effects Included

(2) Generate moment-rotation diagram only for the cracked pipe section

$$[K] = \begin{array}{cc} & \begin{array}{cccccc} u_x & u_y & u_z & \phi_x & \phi_y & \phi_z \end{array} \\ \begin{array}{c} F_x \\ F_y \\ F_z \\ M_x \\ M_y \\ M_z \end{array} & \left[\begin{array}{cccccc} \infty & & & & & \\ & \infty & & & -0- & \\ & & \infty & & & \\ & & & \infty & & \\ & -0- & & & \infty & \\ & & & & & \frac{\partial M}{\partial \phi} \end{array}\right] \end{array}$$

: Positive definite

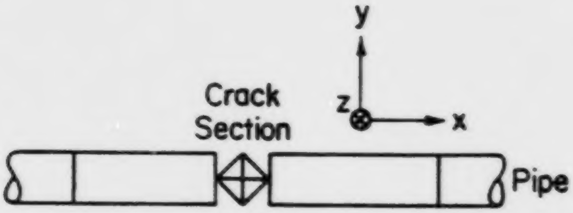

(3) Incorporate incremental stiffness into the FEM code
$[K]\{\Delta\} + [C]\{\Delta\dot{q}\} + [M]\{\Delta\ddot{q}\} = \{\Delta F\}$

Figure 2.33. Nonlinear cracked pipe modeling.

F-I-7/91-F2.33

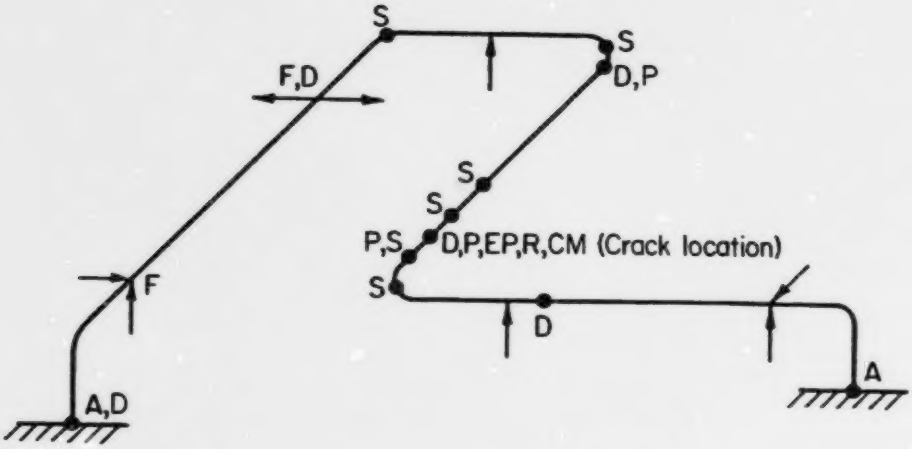
S
S
F,D
D,P
S
S
P,S
D,P,EP,R,CM (Crack location)
F
S
D
A
A,D

LEGEND

A - Accelerations
F - Force
D - Displacement
S - Strain
P - Pressure
EP - Electric Potential
R - Rotation
CM - Crack-Mouth-Opening Displacement

Figure 2.34. Overall instrumentation layout for Subtask 1.3.

I1.3-10/90-F3.37

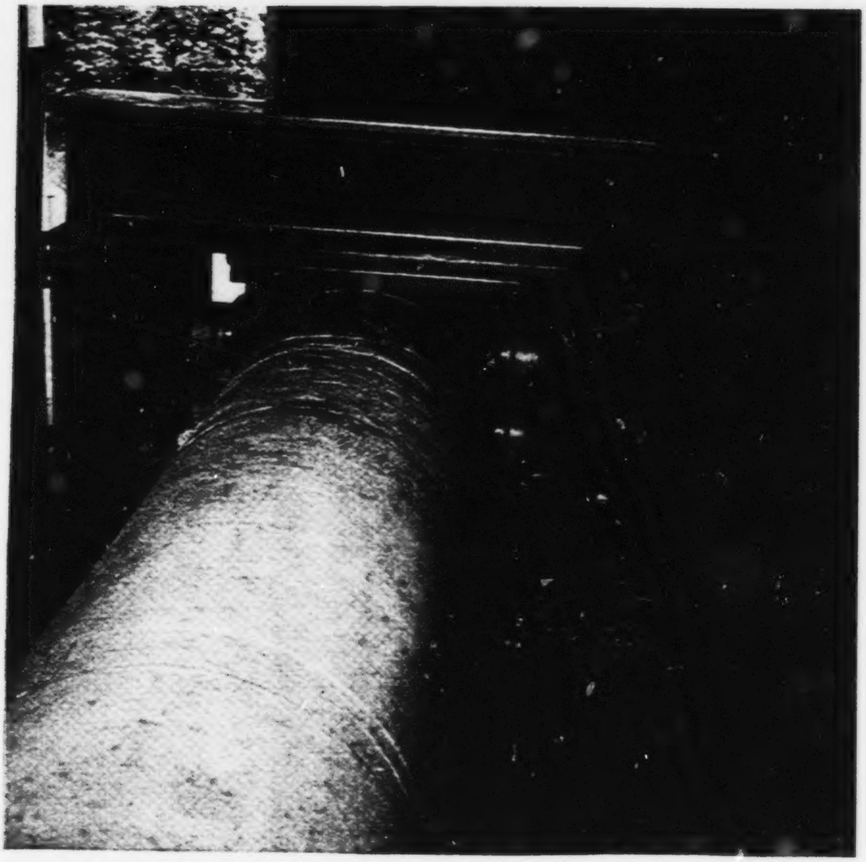

Figure 2.35. Photograph of hydraulic jacks at Node 6 used to infer reaction force.

I1.3-3/91-F3.38

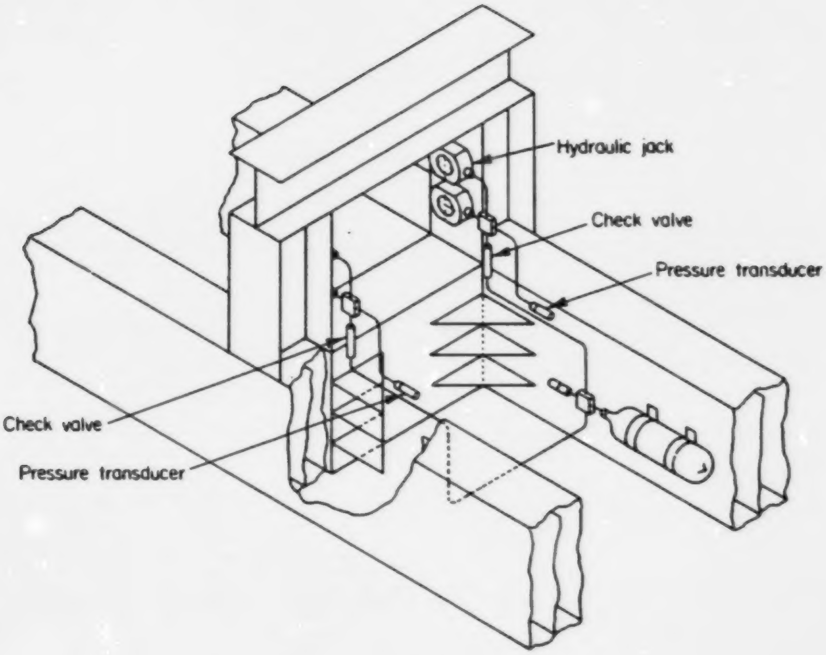
Hydraulic jack
Check valve
Pressure transducer
Check valve
Pressure transducer

Figure 2.36. Node 6 hanger load cell details.

I1.3-3/91-F3.39

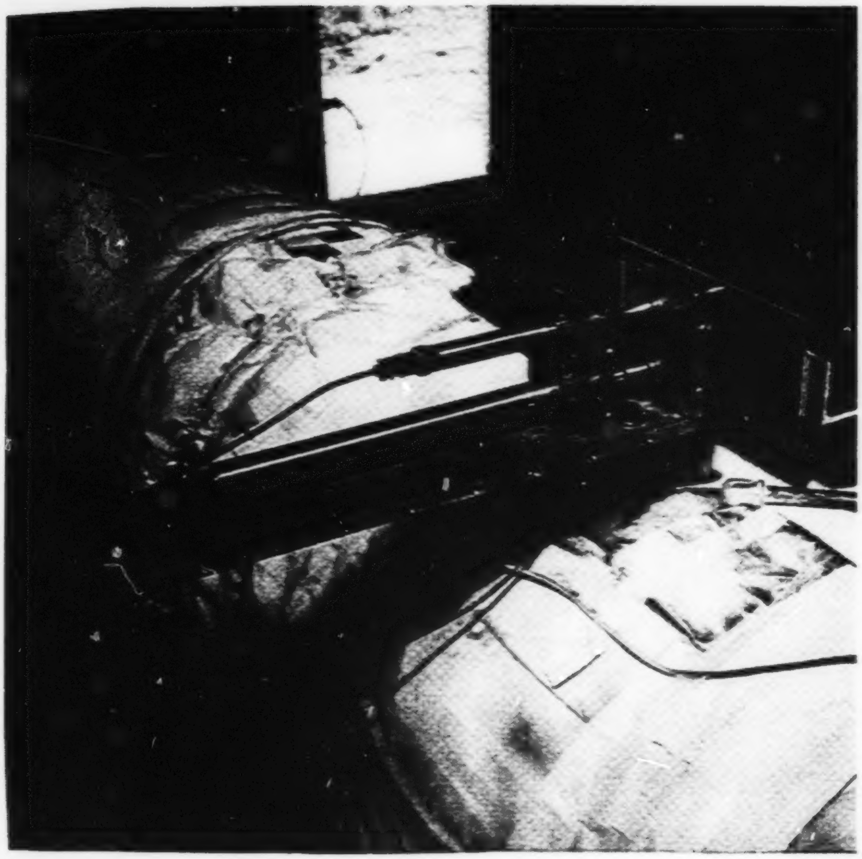

Figure 2.37. Photograph of LVDT-based rotation device used on three stainless steel experiments.

I1.3-3/91-F3.52

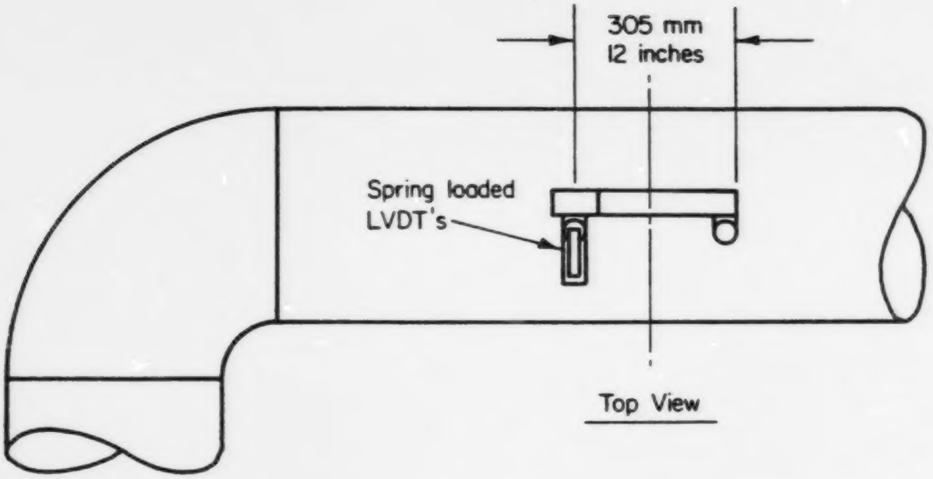
305 mm
12 inches
Spring loaded
LVDT's
Top View

Figure 2.38. Layout/geometry of rotation device used for the three stainless steel experiments.

DRB/1.3-3/F9

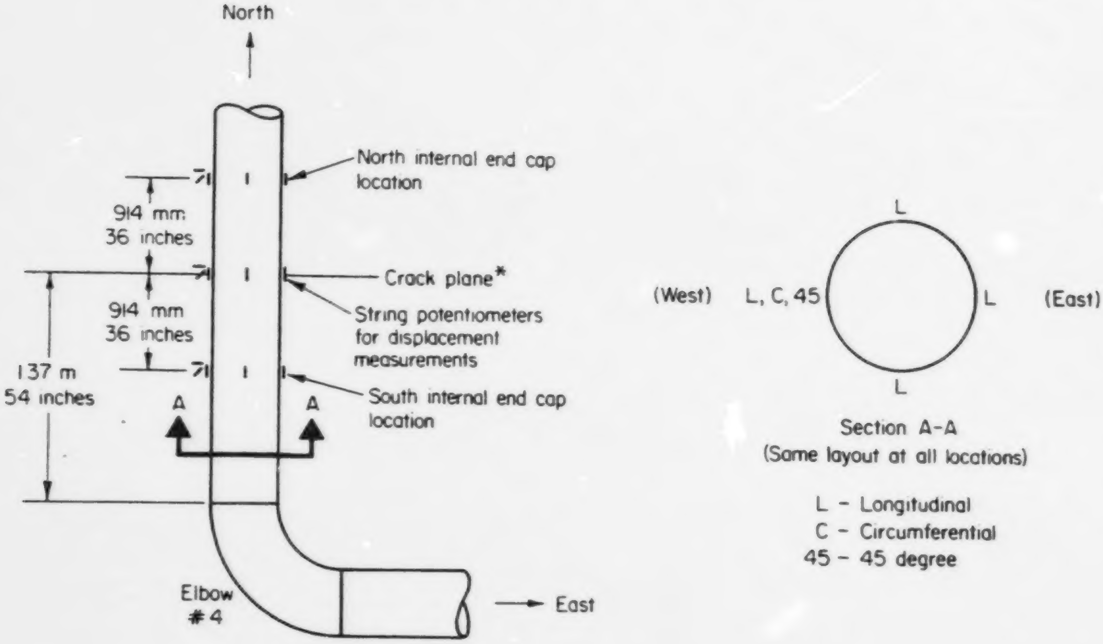
North
North internal end cap location
914 mm
36 inches
Crack plane*
String potentiometers for displacement measurements
914 mm
36 inches
137 m
54 inches
South internal end cap location
A
A
Elbow
#4
East
L
(West)
L, C, 45
L
(East)
L
Section A-A
(Same layout at all locations)
L - Longitudinal
C - Circumferential
45 - 45 degree

Figure 2.39. Strain gage layout at test section.

---

* Strain gages at crack plane only on uncracked pipe tests.

F-I-7/91-F2.39

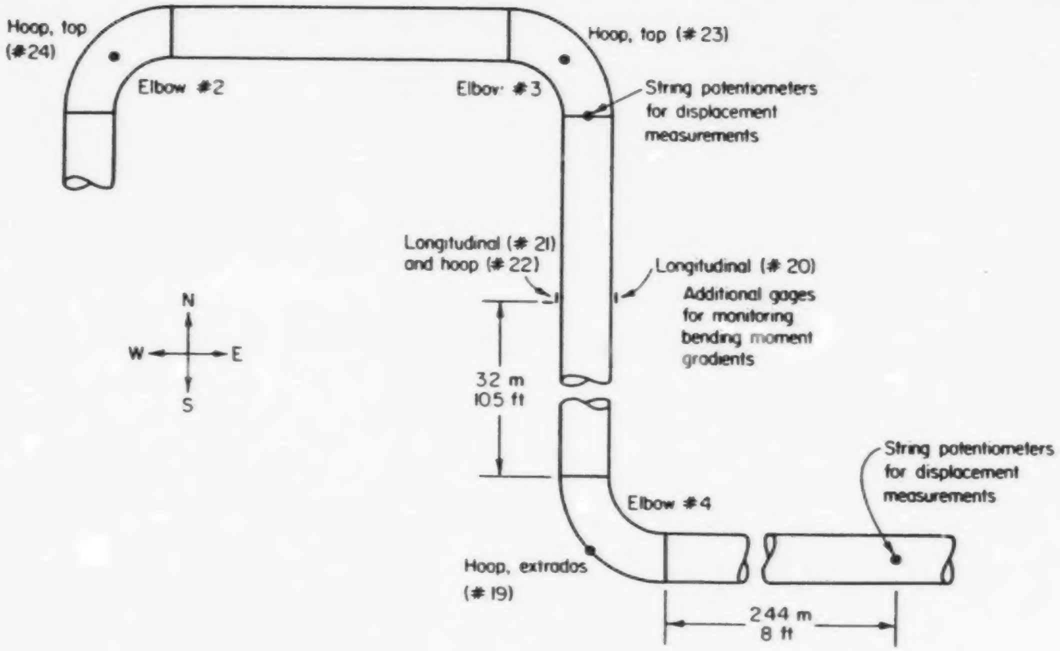
Hoop, top (#24)
Elbow #2
Elbow #3
Hoop, top (#23)
String potentiometers for displacement measurements
Longitudinal (# 21) and hoop (# 22)
Longitudinal (# 20)
Additional gages for monitoring bending moment gradients
N
W
E
S
32 m
105 ft
Elbow #4
Hoop, extrados (# 19)
String potentiometers for displacement measurements
2.44 m
8 ft

Figure 2.40. Pipe instrumentation remote from the crack.

QL/1.3-1/F6

Figure 2.41. Photograph of three orthogonally mounted string potentiometers at Elbow 3 used to calculate pipe displacement data.

I1.3-3/91-F3.40

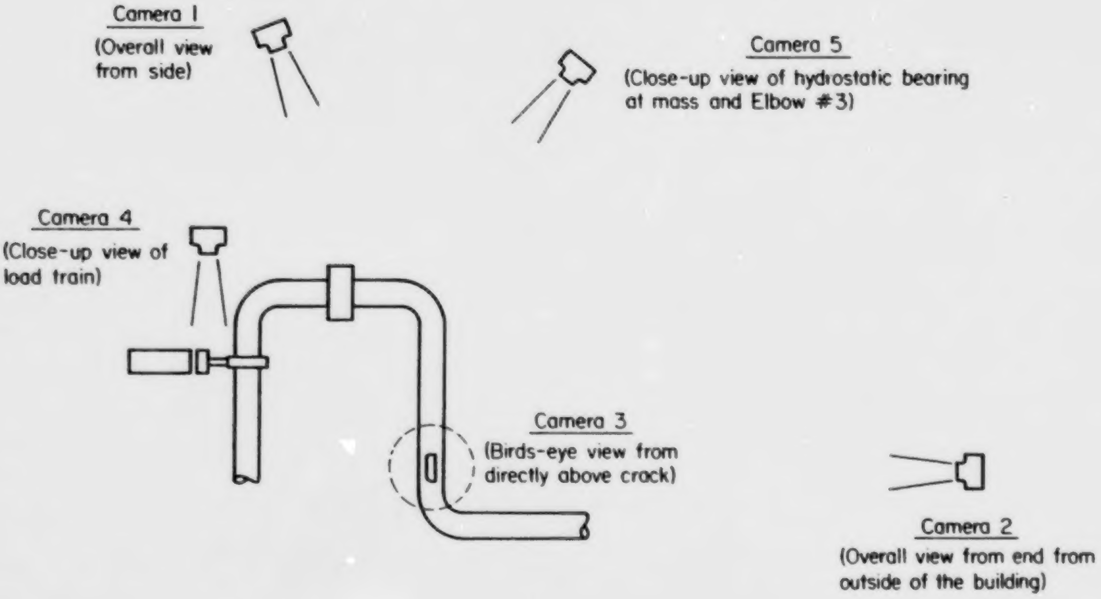
Camera 1
(Overall view from side)
Camera 5
(Close-up view of hydrostatic bearing at mass and Elbow #3)
Camera 4
(Close-up view of load train)
Camera 3
(Birds-eye view from directly above crack)
Camera 2
(Overall view from end from outside of the building)

Figure 2.42. Typical locations for video cameras.

I-10/89-B9-PS

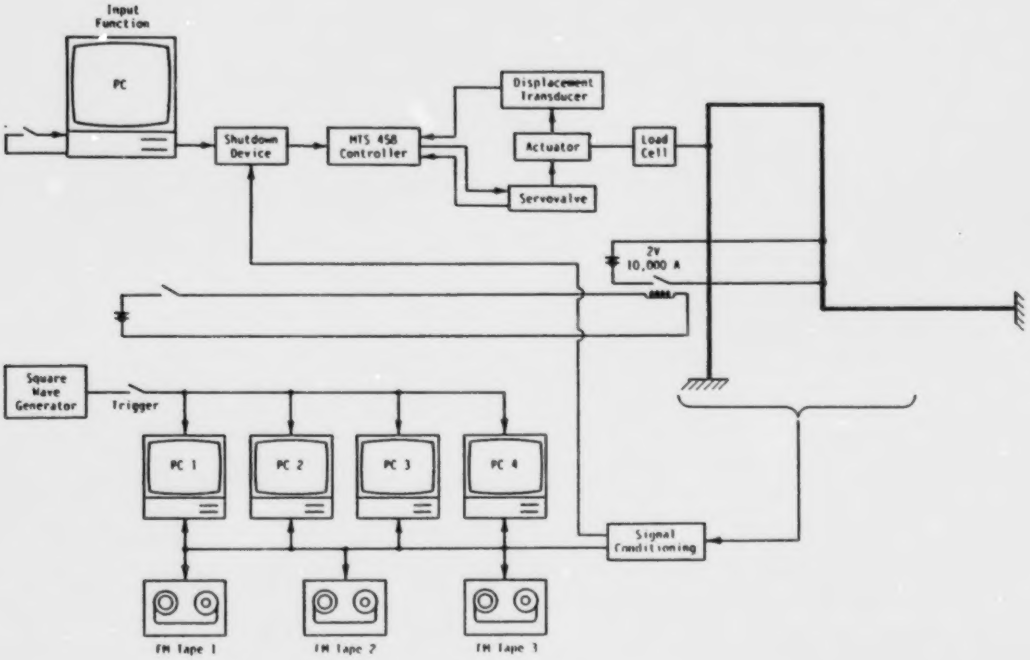
Input Function
PC
Shutdown Device
MTS 458 Controller
Displacement Transducer
Actuator
Servovalve
Load Cell
2V
10,000 A
Square Wave Generator
Trigger
PC 1
PC 2
PC 3
PC 4
Signal Conditioning
FM Tape 1
FM Tape 2
FM Tape 3

Figure 2.43. Data acquisition and control system for Subtask 1.3 experiments.

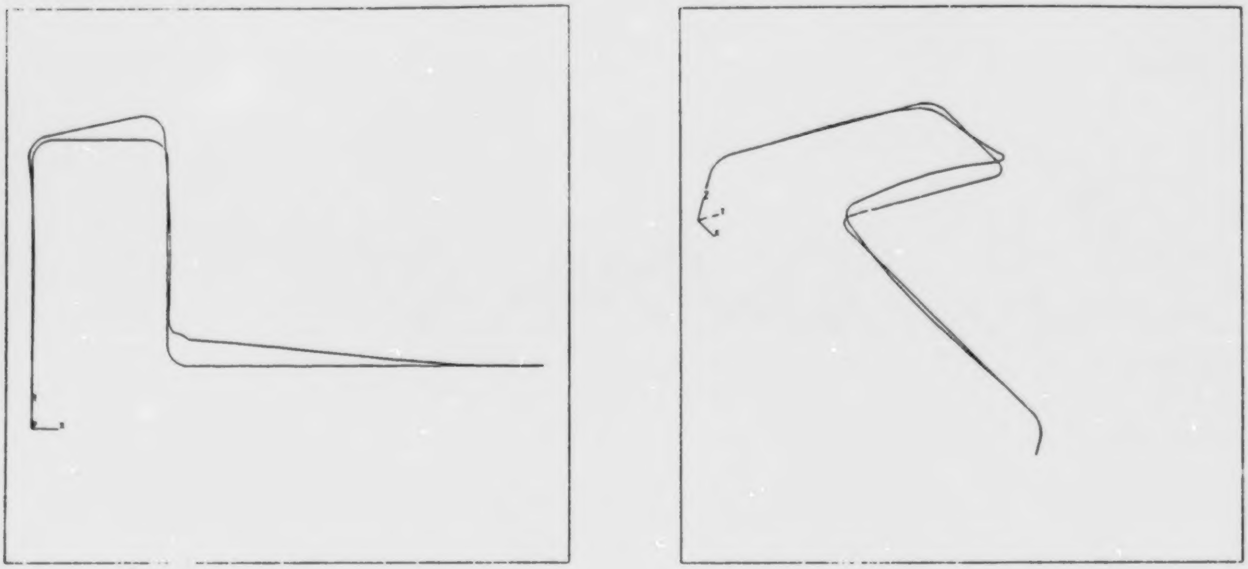

(a) Mode Shape A

(b) Mode Shape B

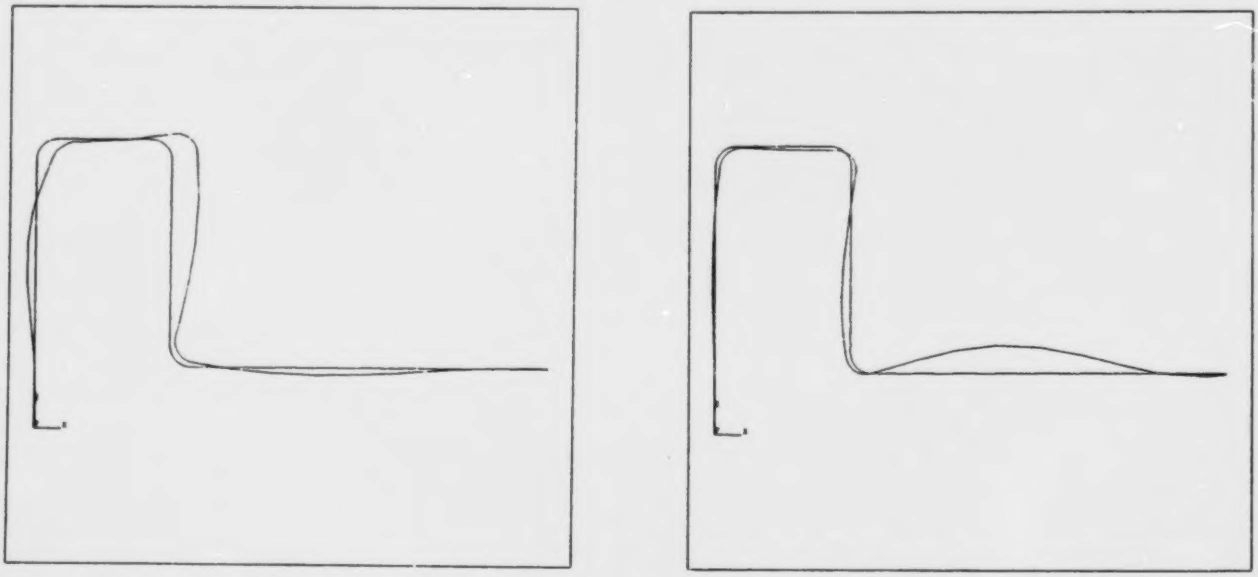

(c) Mode Shape C

(d) Mode Shape D

Figure 2.44. Calculated mode shapes using ANSYS for first four natural frequencies of the pipe loop with the actuator as a fixed node.

F-I-7/91-F2.44

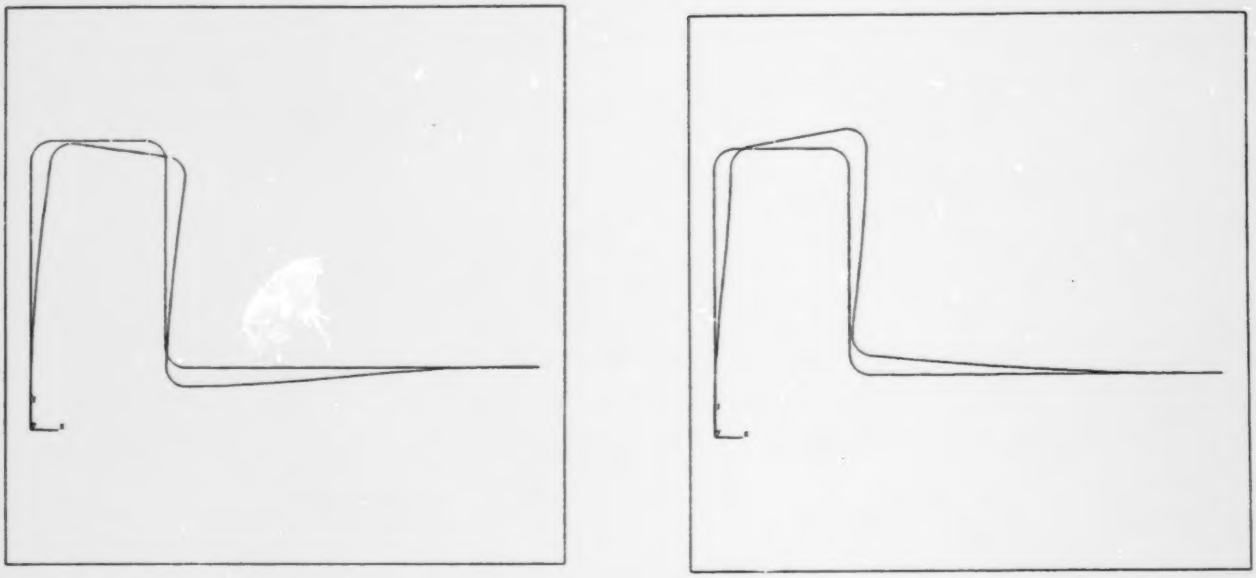

(a) Mode Shape E

(b) Mode Shape F

Figure 2.45. Calculated mode shapes using ANSYS for first two natural frequencies of the pipe loop with the actuator as a free node.

F-I-7/91-F2.45

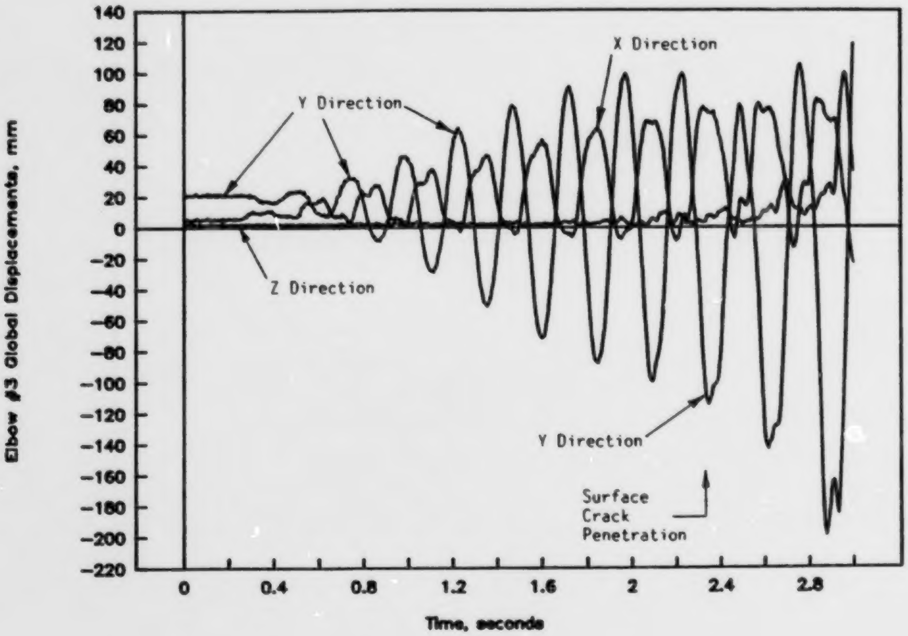

Figure 2.46. Composite plot of global displacements in x, y, and z directions for Elbow 3 as a function of time from the stainless steel base metal experiment (1.3-3).

DRB/1.3-3/F48

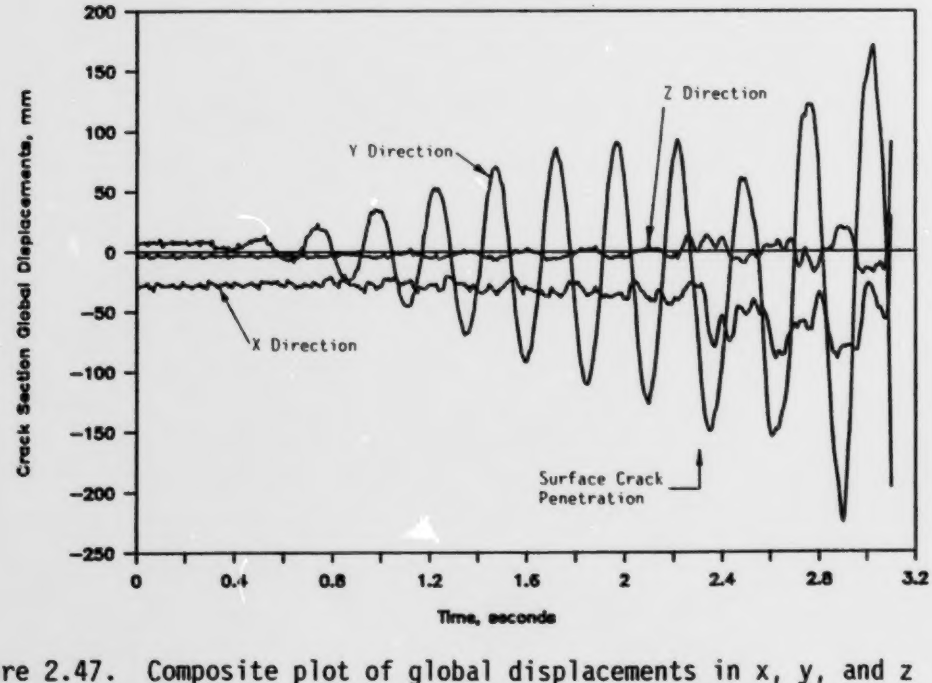

Figure 2.47. Composite plot of global displacements in x, y, and z directions for crack location as a function of time from the stainless steel base metal experiment (1.3-3).

DRB/1.3-3/F49

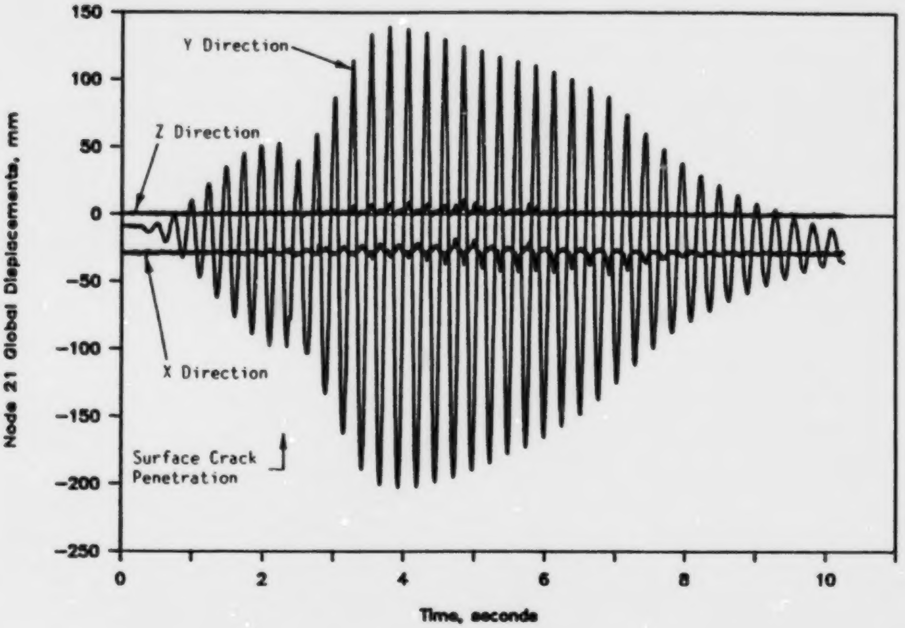

Figure 2.48. Composite plot of global displacements in x, y, and z directions for Node 21 as a function of time from the stainless steel base metal experiment (1.3-3).

DRB/1.3-3/F50

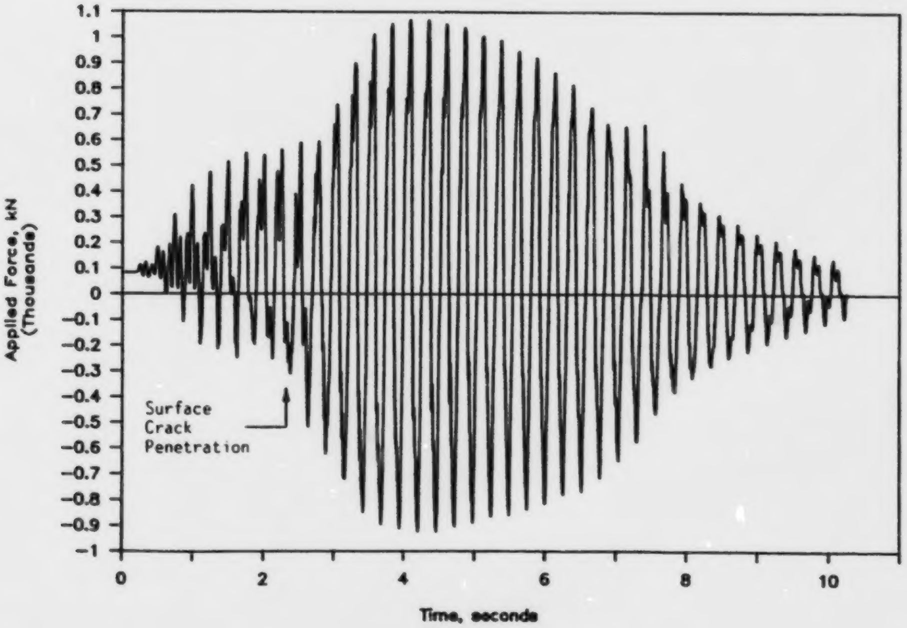

Figure 2.49. Applied force versus time from the stainless steel base metal experiment (1.3-3).

DRB/1.3-3/F19

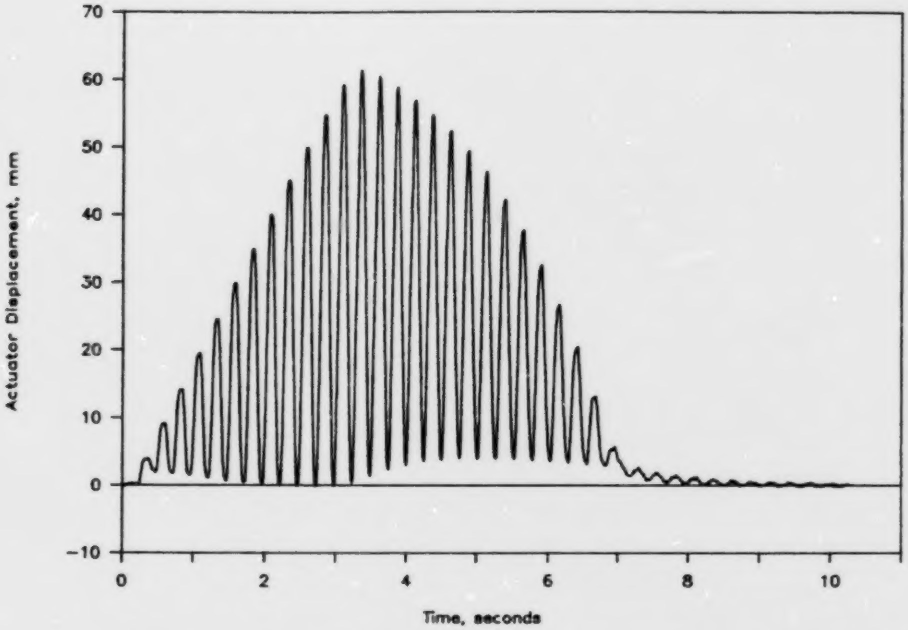

Figure 2.50. Actuator displacement versus time from the stainless steel base metal experiment (1.3-3).

I1.3-10/90-F3.104

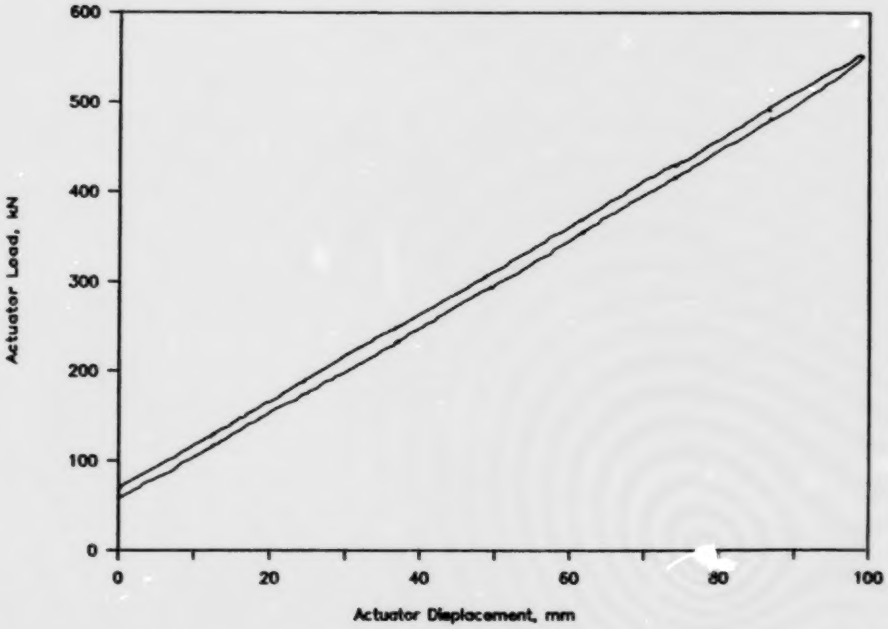

Figure 2.51. Actuator load for the PWR uncracked static push pipe test, Experiment 1.3-1.

DRB/1.3-1/F73

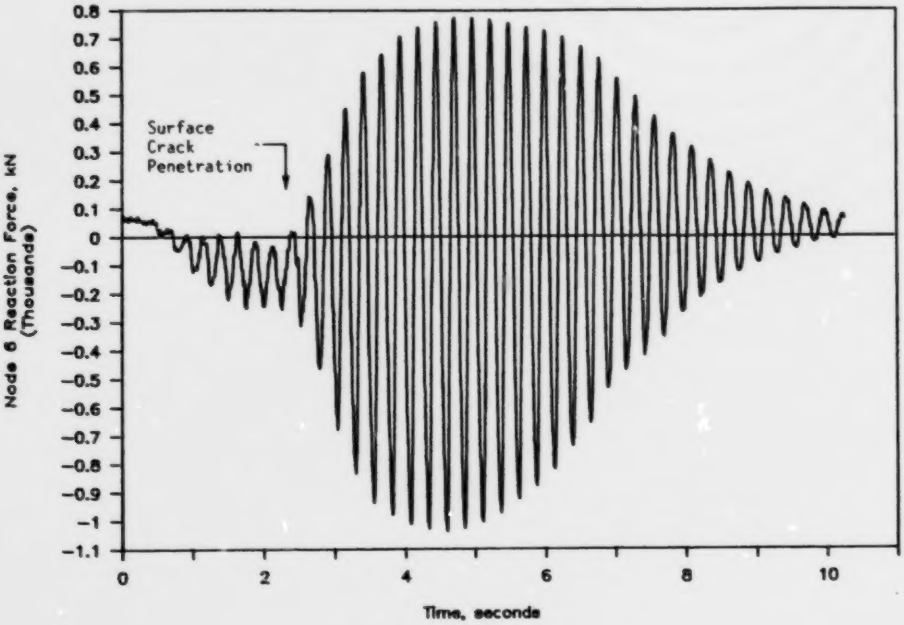

Figure 2.52. Reaction force at Node 6 versus time from the stainless steel base metal experiment (1.3-3).

DRB/1.3-3/F20

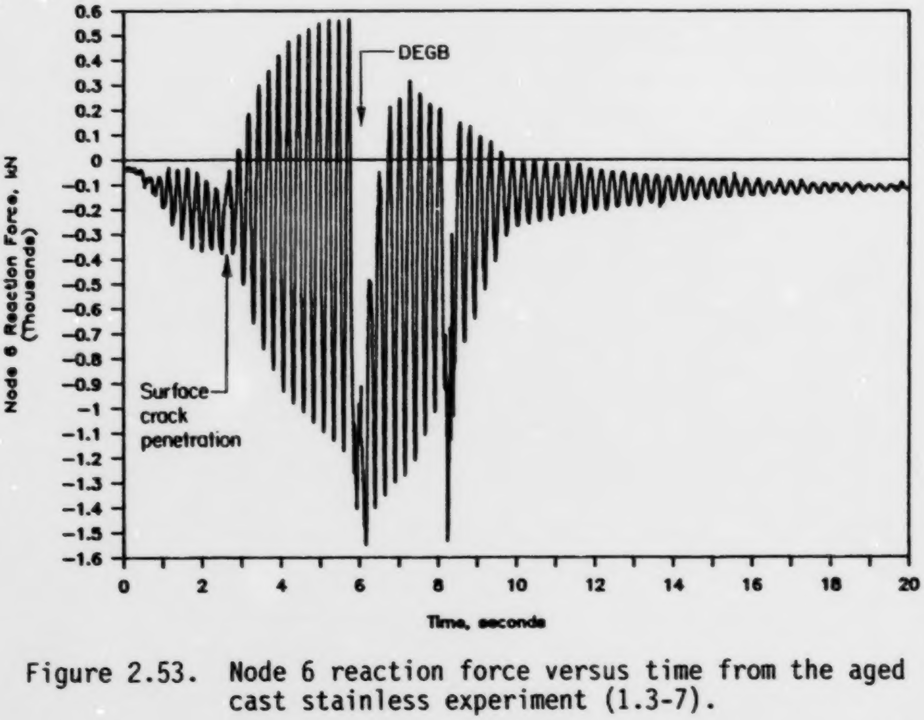

Figure 2.53. Node 6 reaction force versus time from the aged cast stainless experiment (1.3-7).

I-10/90-B21-PS

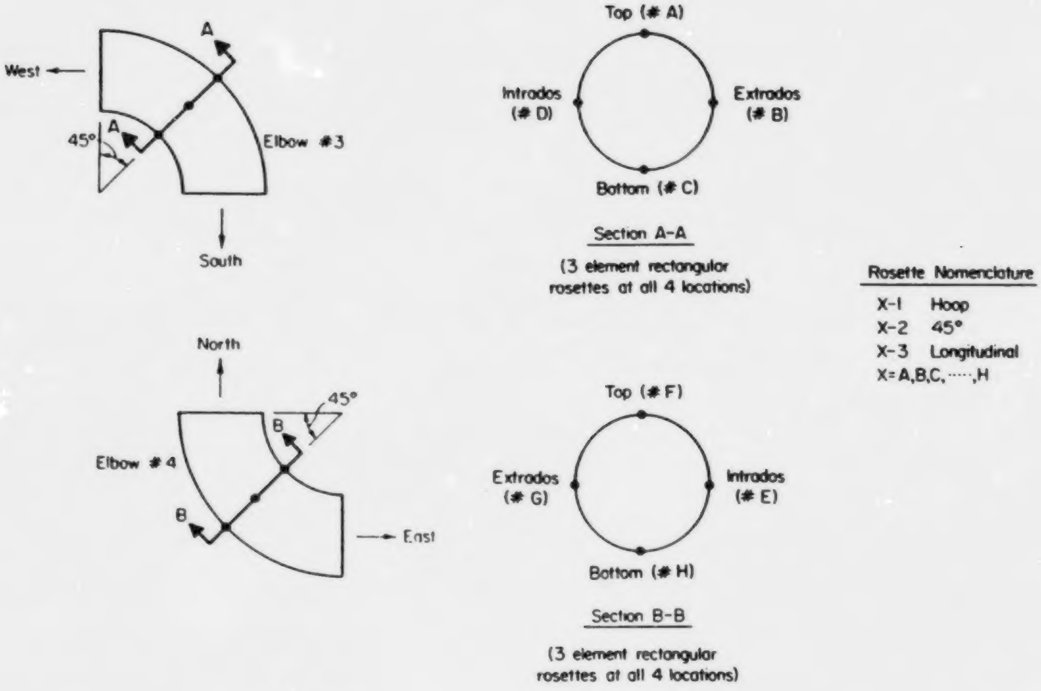
West
A
A
45°
Elbow #3
South
Top (# A)
Intrados (# D)
Extrados (# B)
Bottom (# C)
Section A-A
(3 element rectangular rosettes at all 4 locations)
Rosette Nomenclature
X-1 Hoop
X-2 45°
X-3 Longitudinal
X= A,B,C,·····,H
North
45°
B
Elbow # 4
B
East
Top (# F)
Extrados (# G)
Intrados (# E)
Bottom (# H)
Section B-B
(3 element rectangular rosettes at all 4 locations)

Figure 2.54. Elbow strain gage locations and numbering system for room temperature uncracked-pipe experiment.

QL/1.3-1/F5

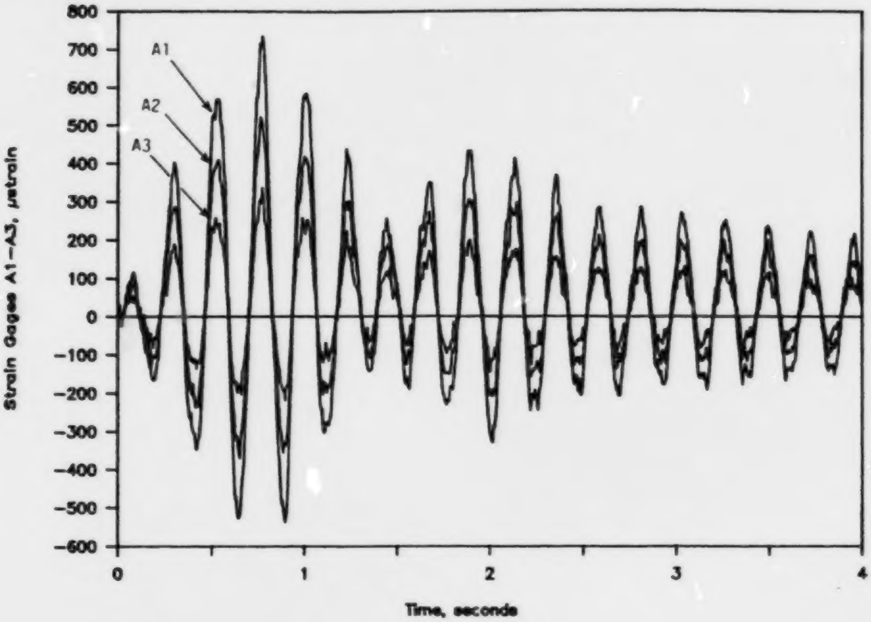

Figure 2.55. Dynamic strain gage rosette data on the top of Elbow 3 from the room temperature uncracked dynamic pipe test, Experiment 1.3-1.

DRB/1.3-1/F52

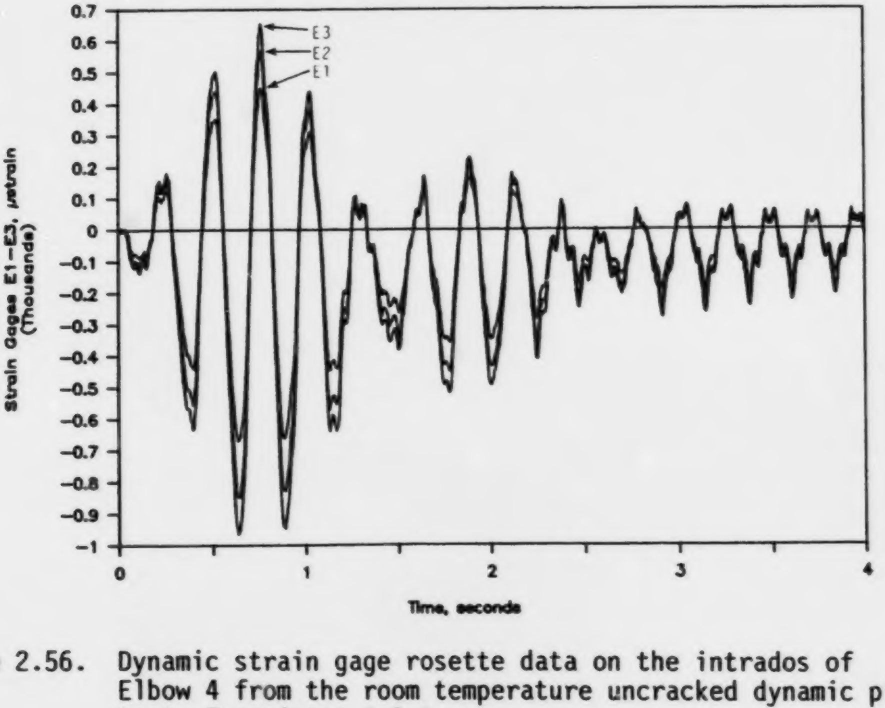

Figure 2.56. Dynamic strain gage rosette data on the intrados of Elbow 4 from the room temperature uncracked dynamic pipe test, Experiment 1.3-1.

DRB/1.3-1/F56

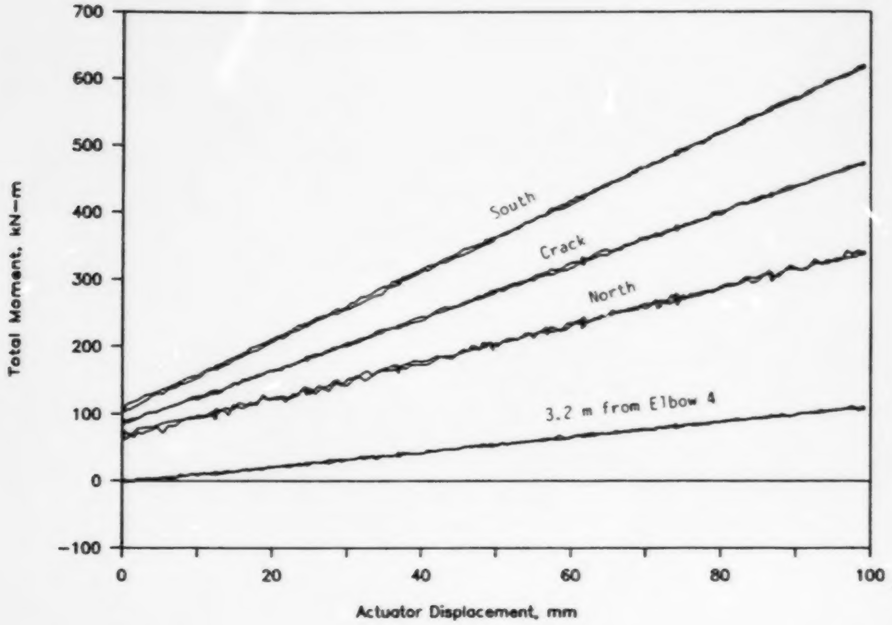

Figure 2.57. Total moment (using ANSYS static value) from the PWR uncracked static push pipe test, Experiment 1.3-1.

DRB/1.3-1/F90

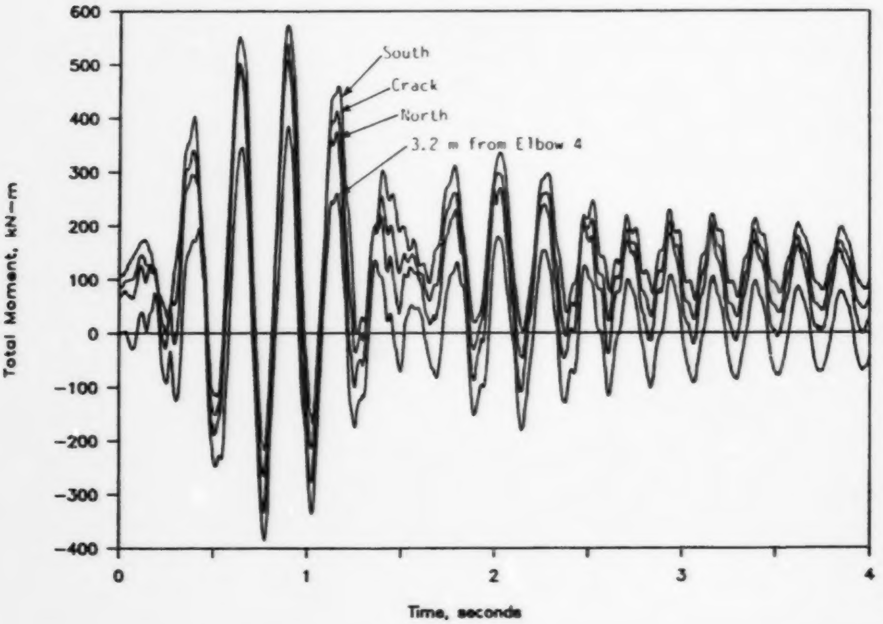

Figure 2.58. Total moment (using ANSYS static value) from the PWR uncracked dynamic pipe test, Experiment 1.3-1.

DRB/1.3-1/F112

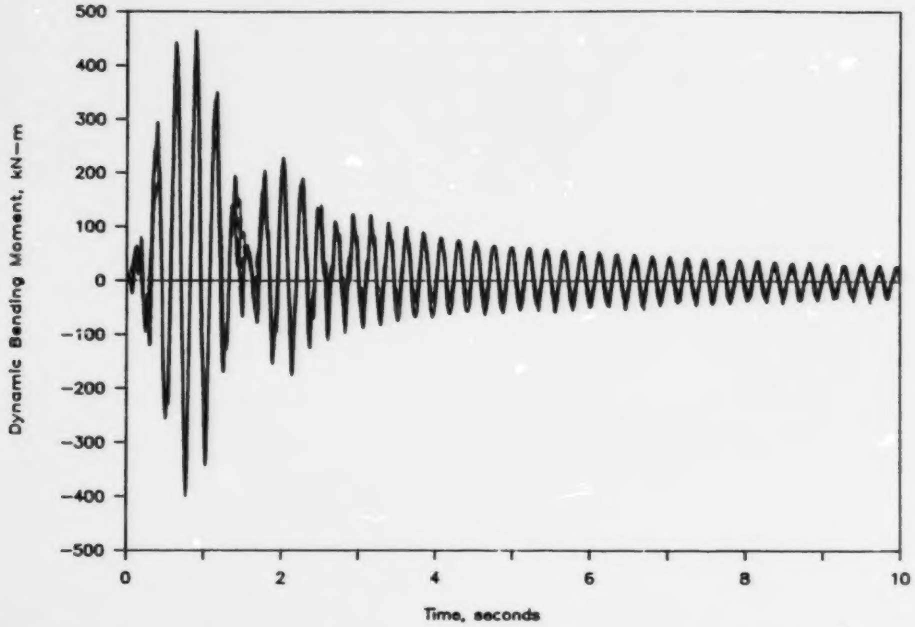

Figure 2.59. Dynamic moments at the crack, south end cap, north end cap, and location 1.83 m (6 feet) north of crack from the PWR uncracked dynamic pipe test, Experiment 1.3-1.

I1.3-10/90-F3.124

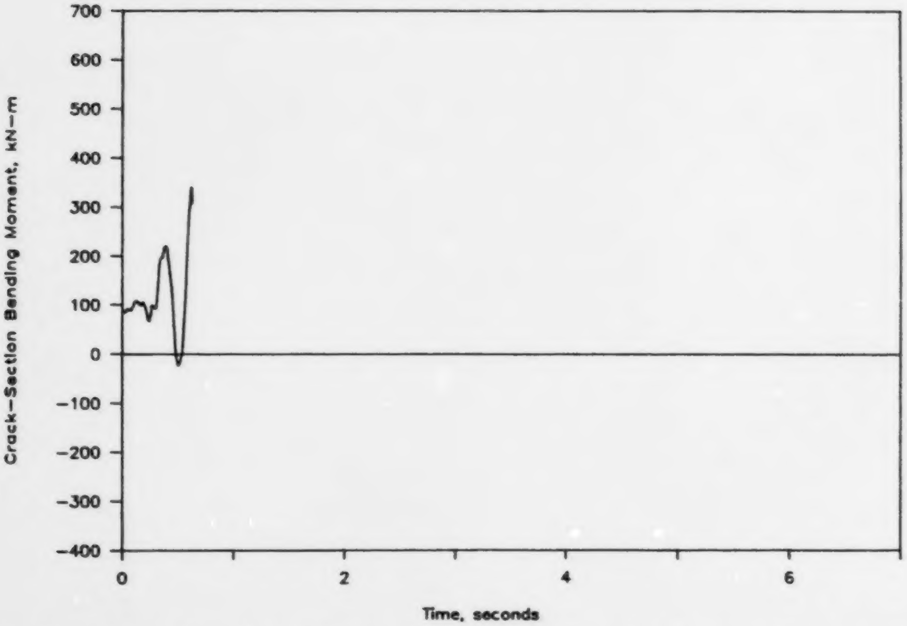

Figure 2.60. Calculated total crack section moment versus time from the carbon steel base metal experiment, (1.3-2). (Note: time scale of graphs is same for comparison of all experiments.)

I1.3-10/90-F3.125

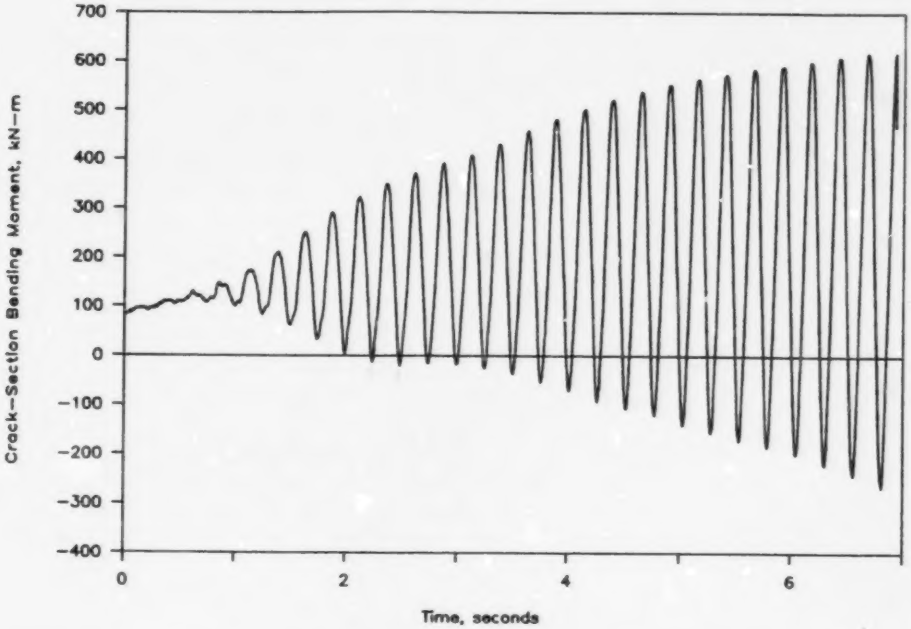

Figure 2.61. Total moment at crack section versus time from the carbon steel weld experiment (1.3-4).

I1.3-10/90-F3.126

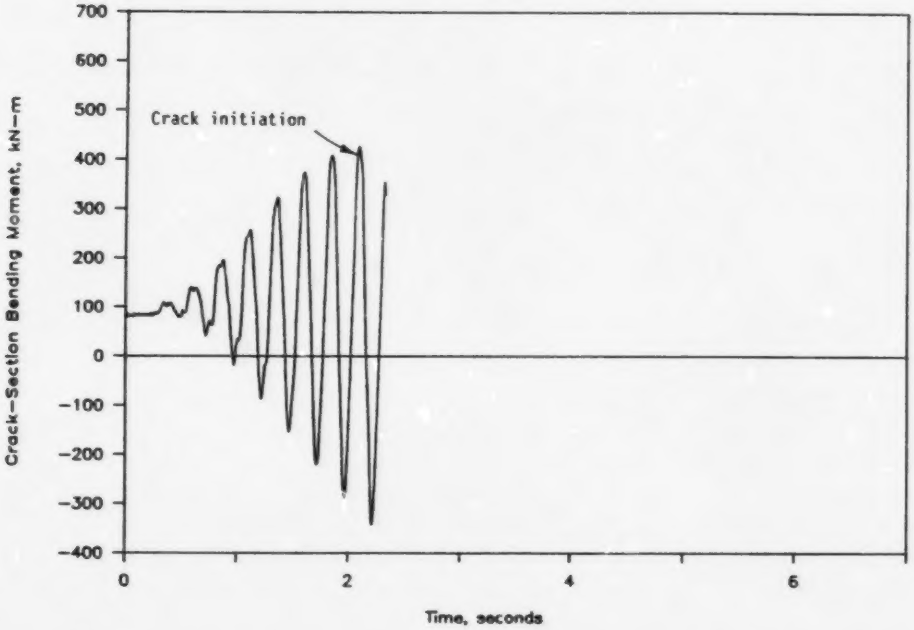

Figure 2.62. Total moment at the crack location as a function of time from the stainless steel base metal experiment (1.3-3).

I1.3-10/90-F3.127

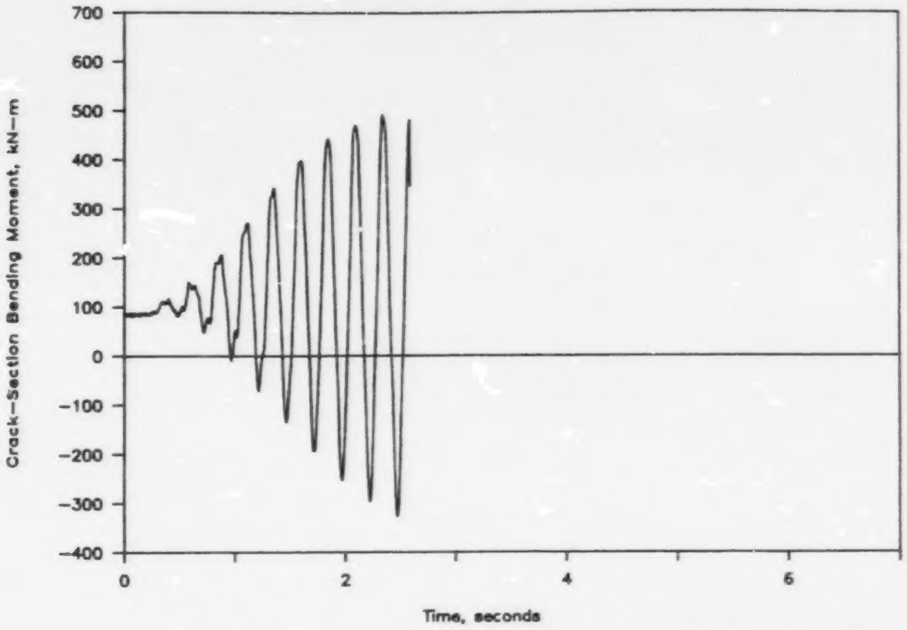

Figure 2.63. Total bending moment at the crack location versus time from the stainless steel weld experiment (1.3-5).

I1.3-10/90-F3.128

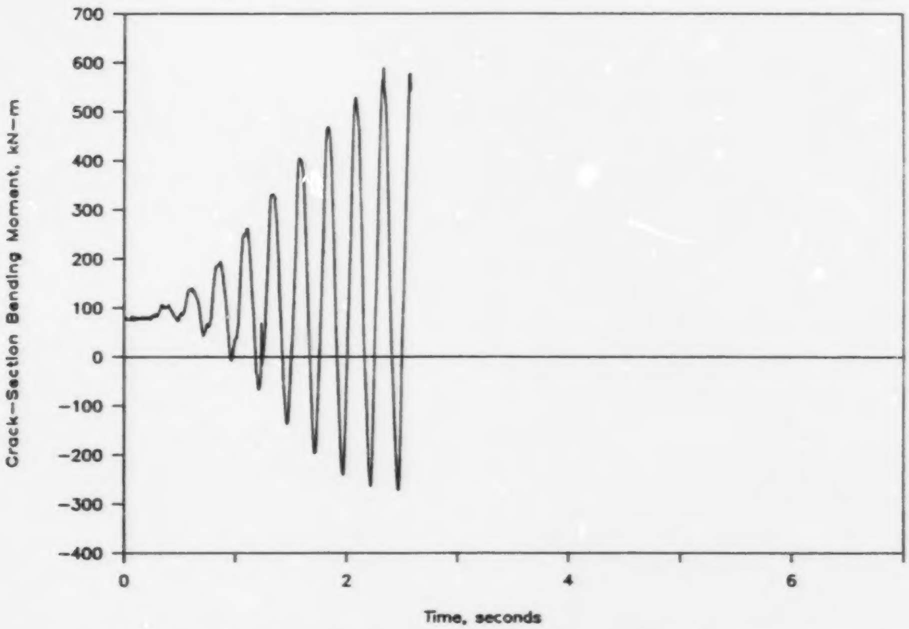

Figure 2.64. Total moment at the cracked section versus time from the aged cast stainless experiment (1.3-7).

I1.3-10/90-F3.129

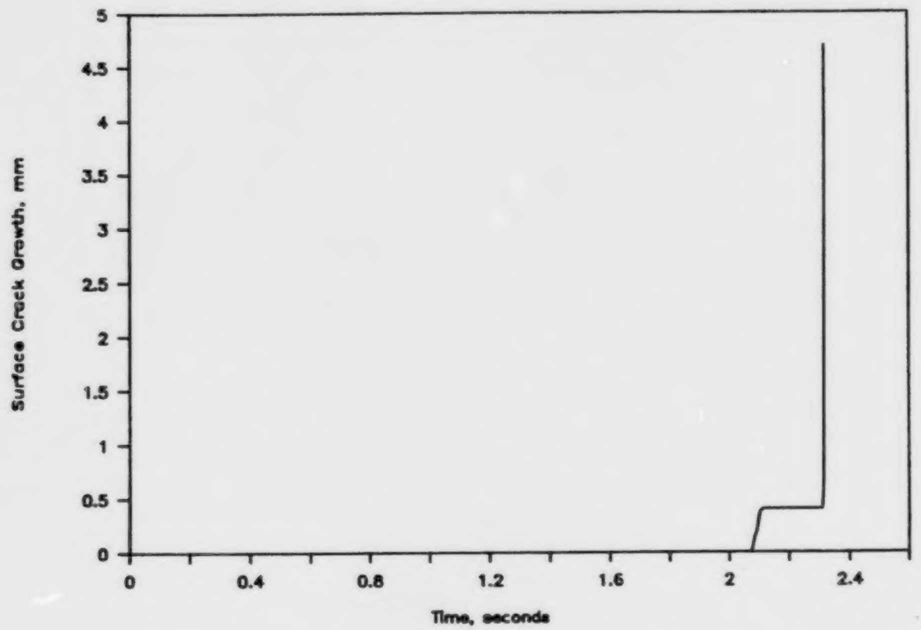

Figure 2.65. Surface crack growth versus time for stainless steel base metal experiment (1.3-3).

I1.3-10/90-F3.140

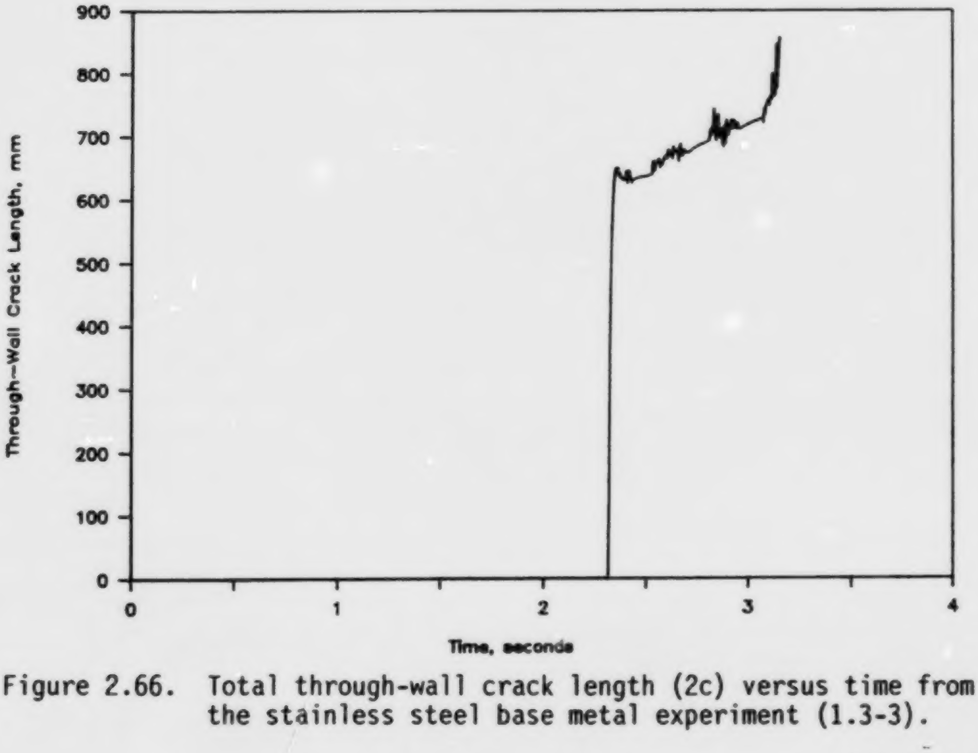

Figure 2.66. Total through-wall crack length (2c) versus time from the stainless steel base metal experiment (1.3-3).

F-I-7/91-F2.66

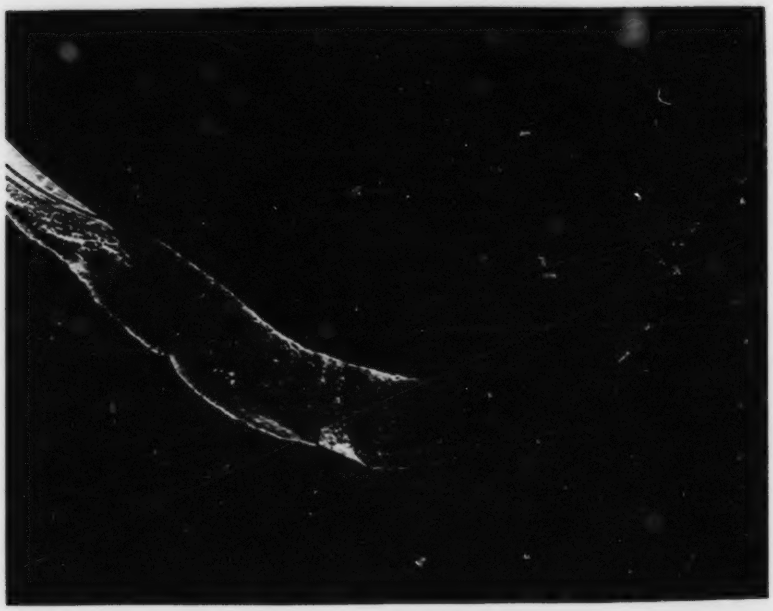

Figure 2.67. Fracture surface from the carbon steel base metal experiment (1.3-2).

DRB/1.3-2/F37

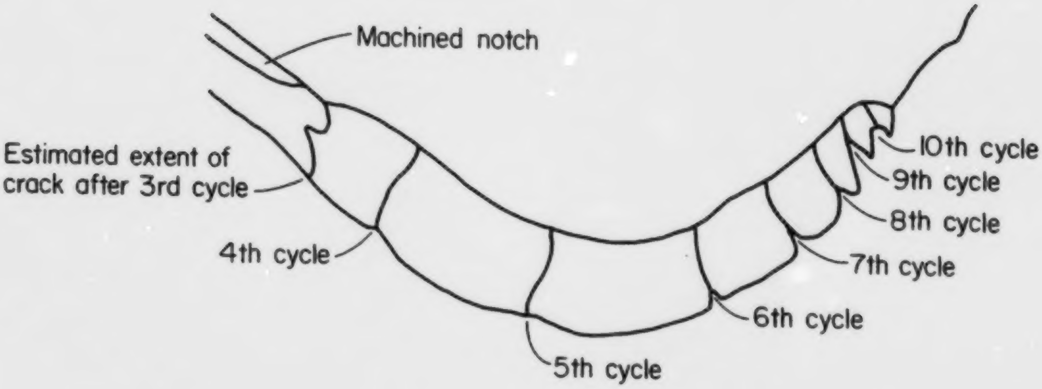
Machined notch
Estimated extent of crack after 3rd cycle
4th cycle
5th cycle
6th cycle
7th cycle
8th cycle
9th cycle
10th cycle

Figure 2.68. Sketch of fracture surface shown in Figure 2.67 highlighting the arrest/reinitiation lines.

F-I-7/91-F2.68

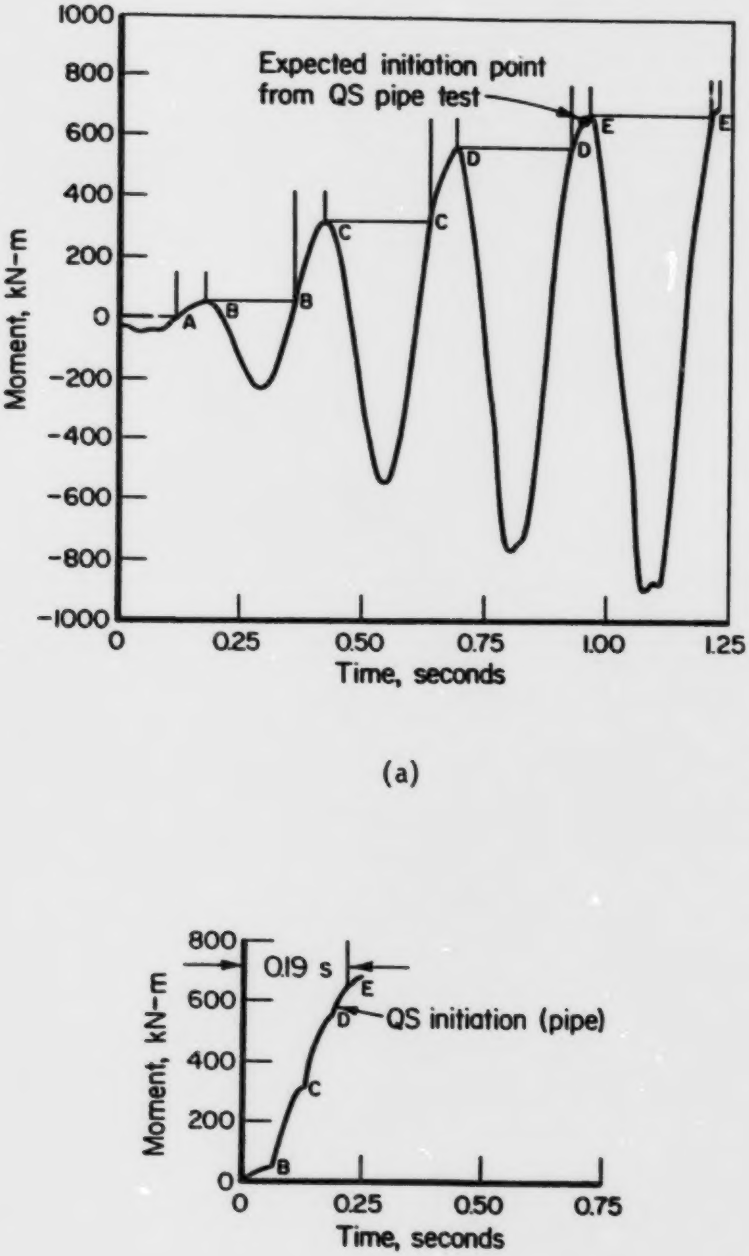

(a)

(b)

Figure 2.69. Determination of equivalent time to crack initiation for stainless steel pipe with a surface crack (Subtask 1.3).

I-T1.0-11/89-F1.1

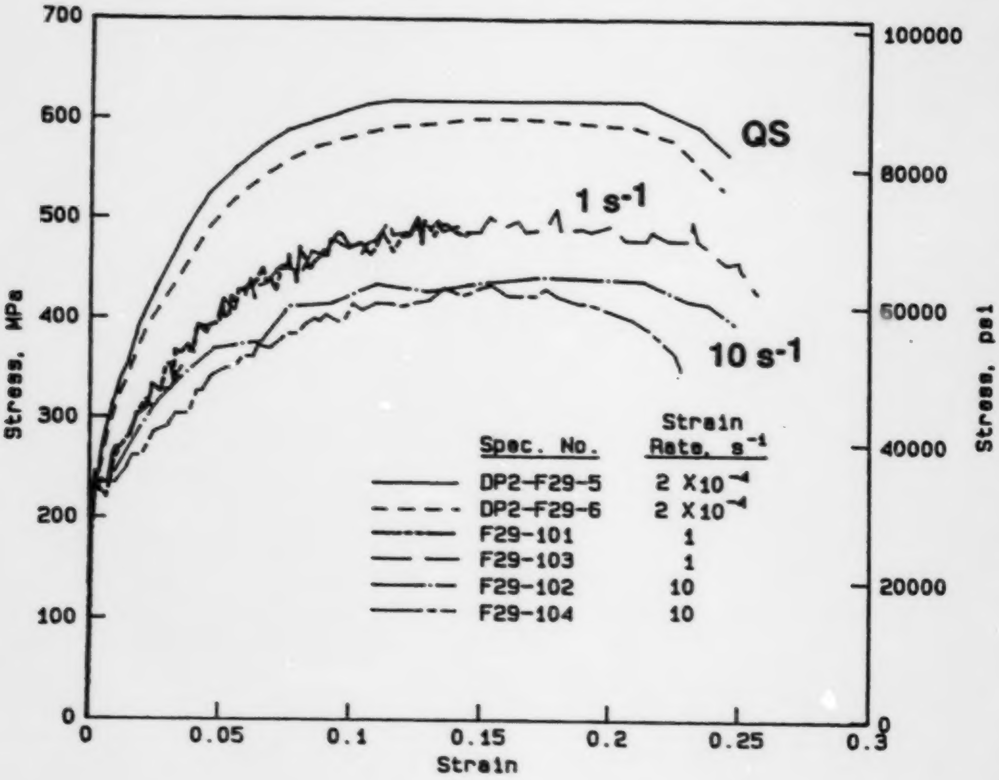

Figure 2.70. Engineering stress-strain curves at 288 C (550 F) for a 16-inch diameter A106 Grade B carbon steel pipe (DP2-F29) tested at several different strain rates.

I-T1.0-11/89-F3.9

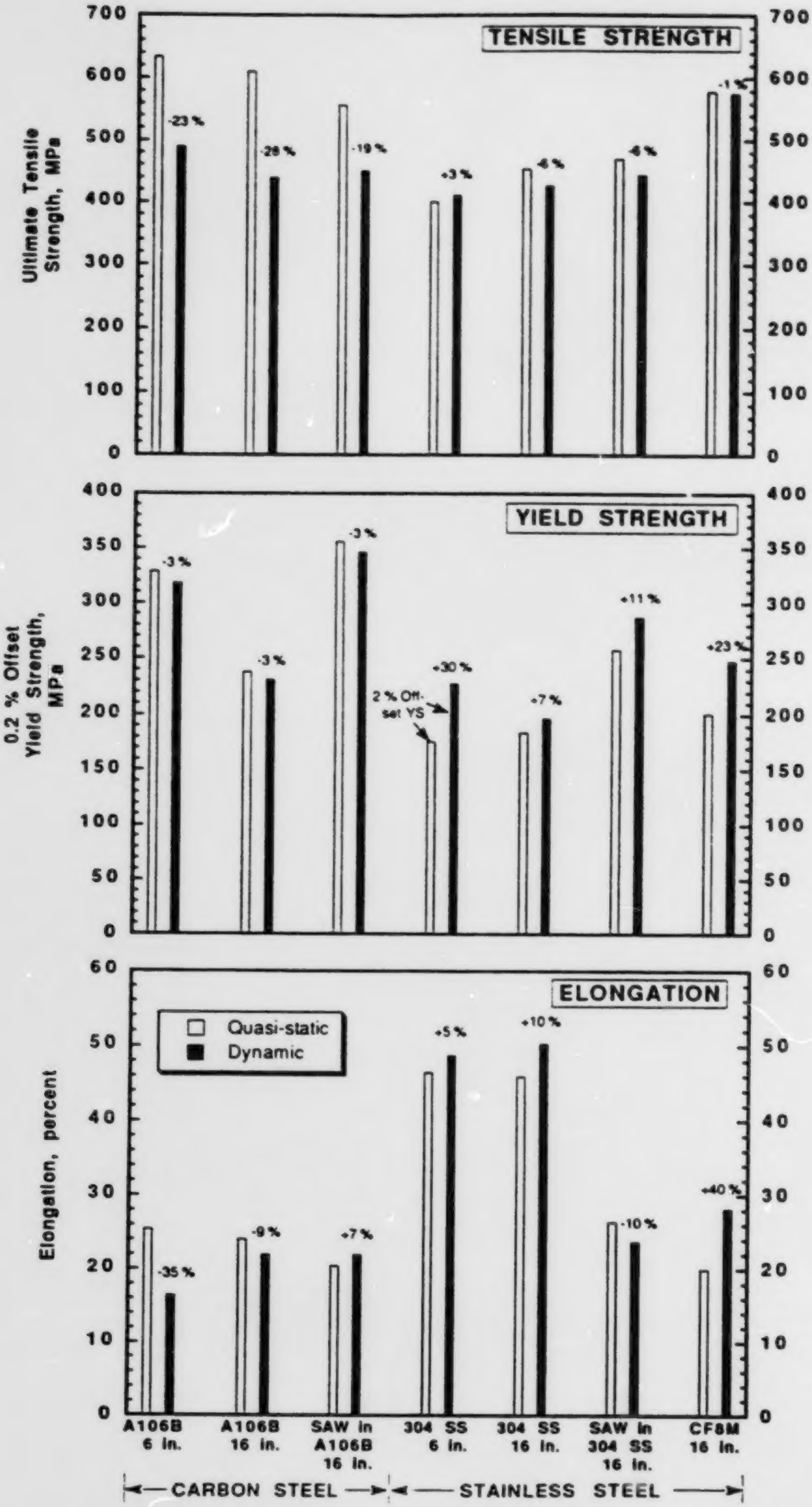

Figure 2.71. Effect of strain rate on tensile properties of Task 1.0 materials at 288 C (550 F). Strain rates were approximately 10^{-4} s^{-1} for quasi-static tests and 10 s^{-1} for dynamic tests.

F-I-7/91-F2.71

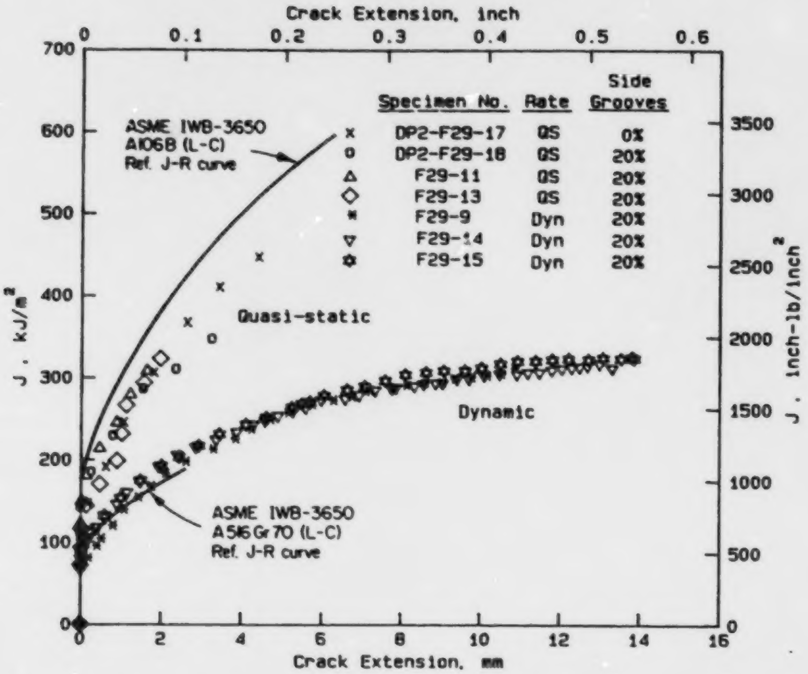

Figure 2.72. J-resistance curves for compact specimens from a 16-inch diameter A106 Grade B carbon steel pipe tested at 288 C (550 F).

I-T1.0-11/89-F4.14

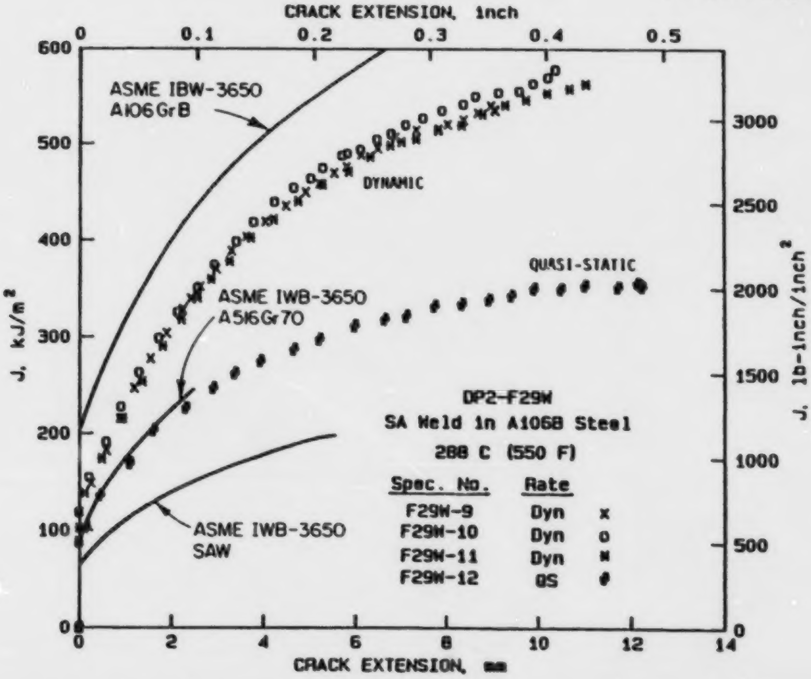

Figure 2.73. J-resistance curves for compact specimens from a submerged-arc weld in a 16-inch diameter A106 Grade B carbon steel pipe tested at 288 C (550 F).

I-T1.0-11/89-F4.16

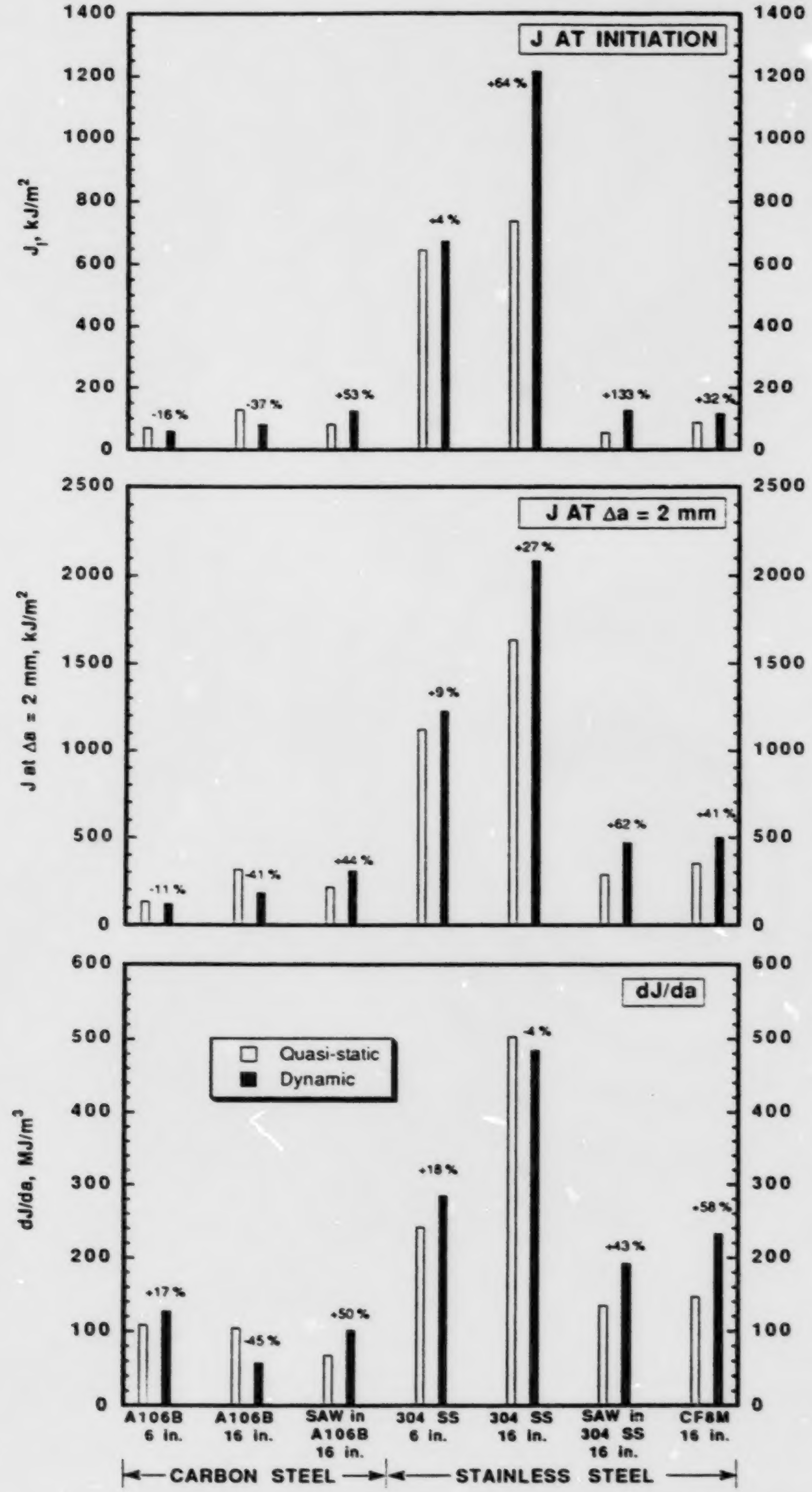

Figure 2.74. Effect of displacement rate on crack growth resistance of Task 1.0 materials at 288 C (550 F). Dynamic tests were 2500 to 6000 times faster than quasi-static tests (see Table 2.14 for dJ/dt values).

F-I-7/91-F2.74

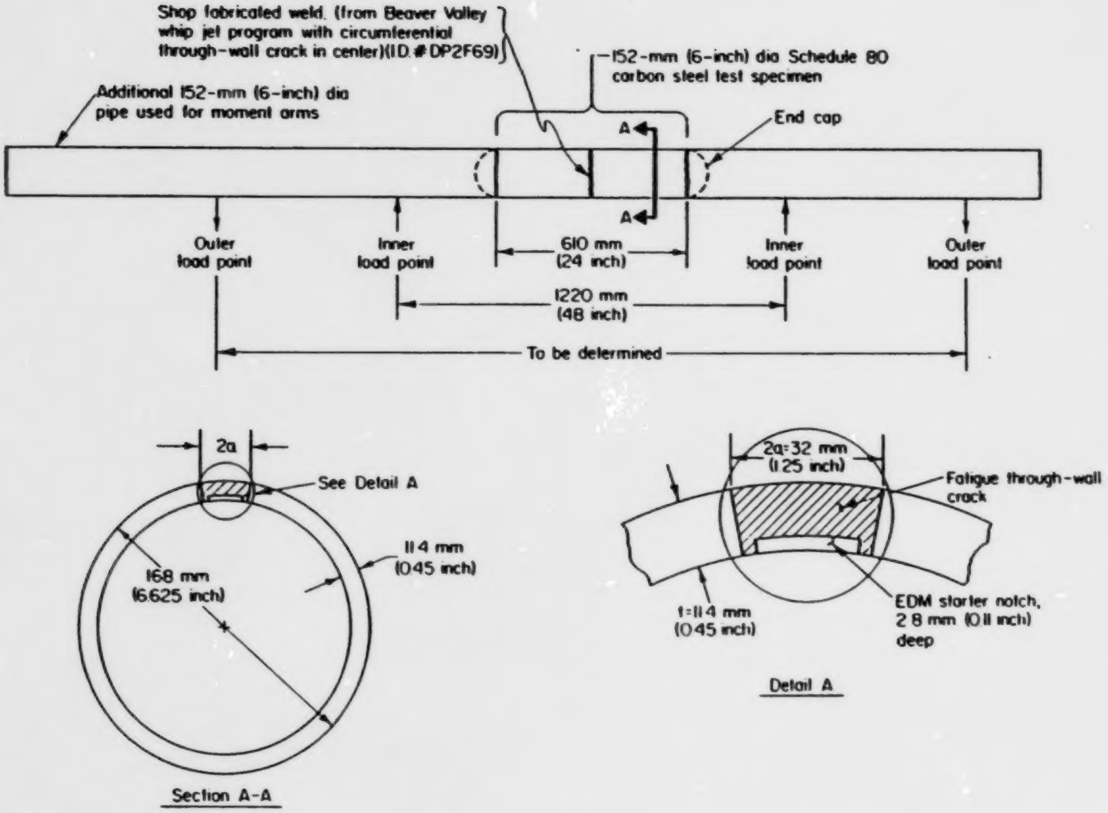
Shop fabricated weld. (from Beaver Valley whip jet program with circumferential through-wall crack in center)(I.D. # DP2F69)
152-mm (6-inch) dia Schedule 80 carbon steel test specimen
Additional 152-mm (6-inch) dia pipe used for moment arms
End cap
A
A
Outer load point
Inner load point
610 mm (24 inch)
Inner load point
Outer load point
1220 mm (48 inch)
To be determined
2a
See Detail A
168 mm (6.625 inch)
11.4 mm (0.45 inch)
Section A-A
2a=32 mm (1.25 inch)
Fatigue through-wall crack
t=11.4 mm (0.45 inch)
EDM starter notch, 2.8 mm (0.11 inch) deep
Detail A

Figure 2.75. Sketch of test specimen showing details of final through-wall-crack geometry.

T5128-F5.1

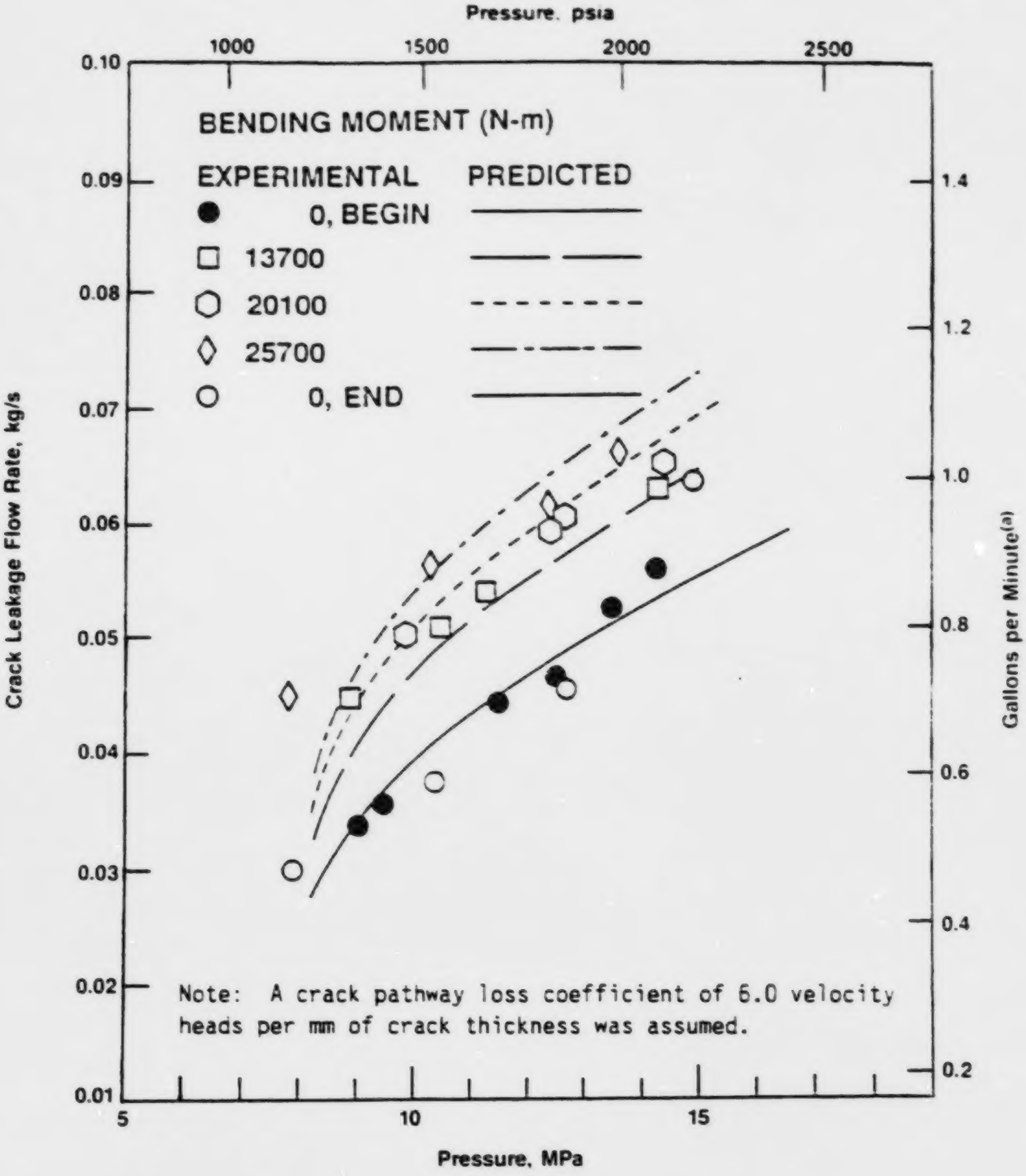

Figure 2.76. Comparison of SQUIRT predicted leakage flow rate calculations with the experimental data obtained for the fatigue-generated crack in a girth weld.

(a) Gallons per minute for water at 1 atm and 20 C.

T5128-F5.10

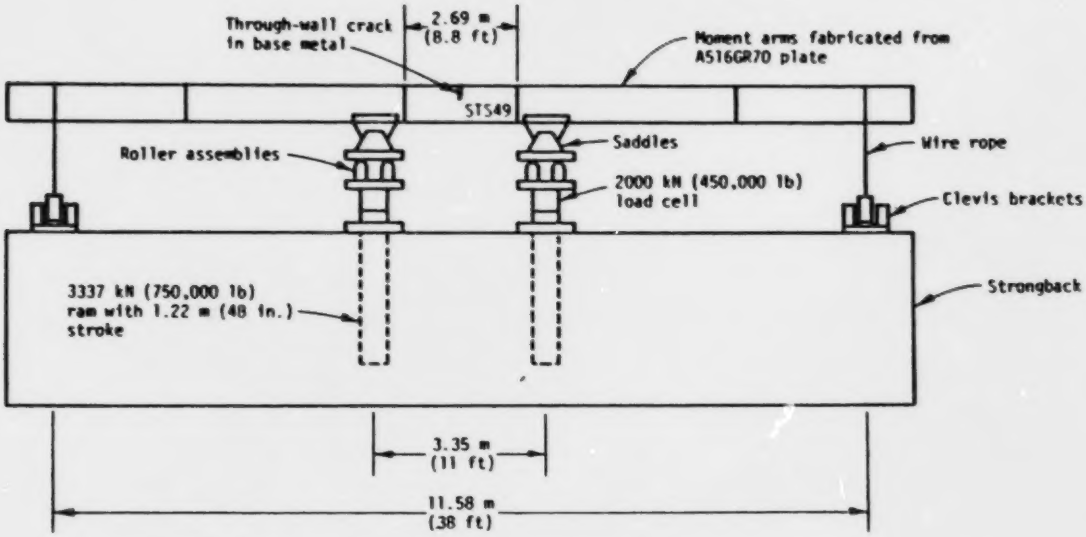
Through-wall crack in base metal
2.69 m (8.8 ft)
Moment arms fabricated from A516GR70 plate
STS49
Roller assemblies
Saddles
Wire rope
2000 kN (450,000 lb) load cell
Clevis brackets
3337 kN (750,000 lb) ram with 1.22 m (48 in.) stroke
Strongback
3.35 m (11 ft)
11.58 m (38 ft)

Figure 2.77. Schematic of pipe in load frame using Subtask 4.3 30-inch diameter pipe experiments.

DRB/4.1/F1

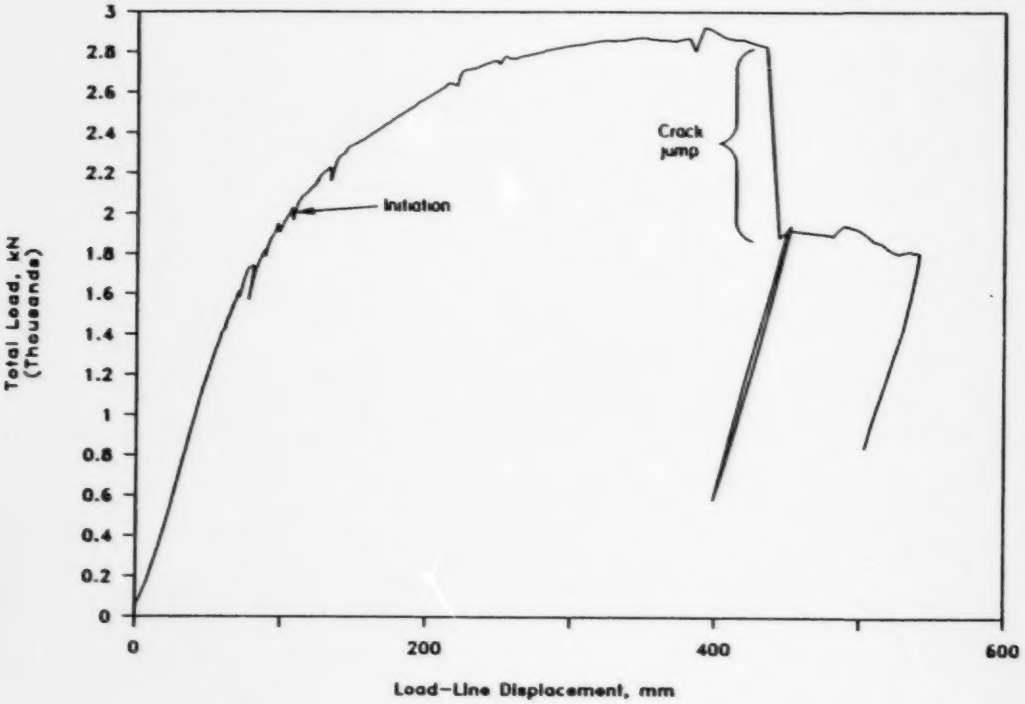

Figure 2.78. Total load versus load-line displacement data from Experiment 4.3-1.

DRB/4.3-1/F4

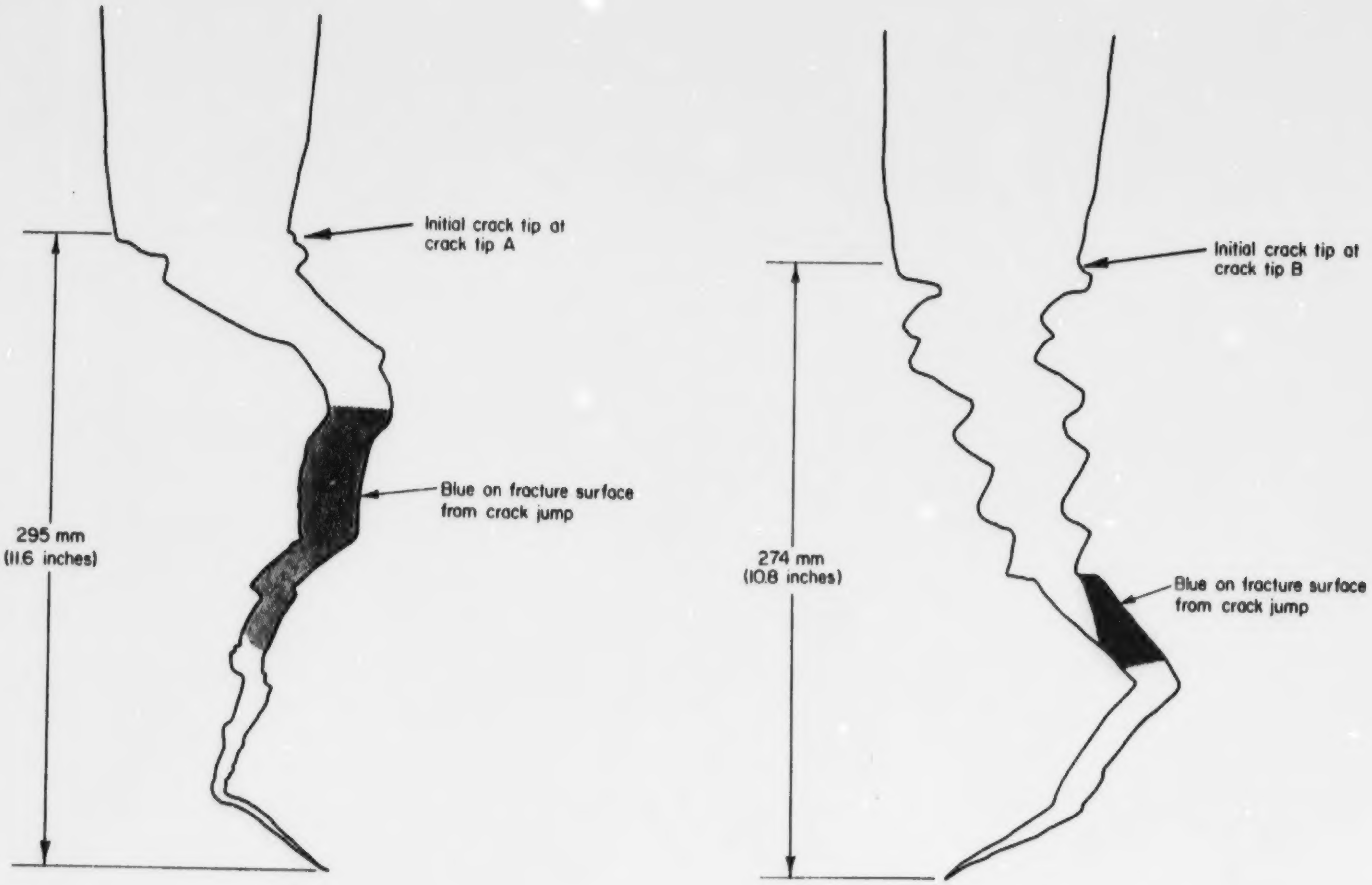
Initial crack tip at crack tip A
Blue on fracture surface from crack jump
295 mm (11.6 inches)
Initial crack tip at crack tip B
Blue on fracture surface from crack jump
274 mm (10.8 inches)

Figure 2.79. Sketch of crack-opening profile on outside surface after Experiment 4.3-1.

F-I-6/91-F2.79

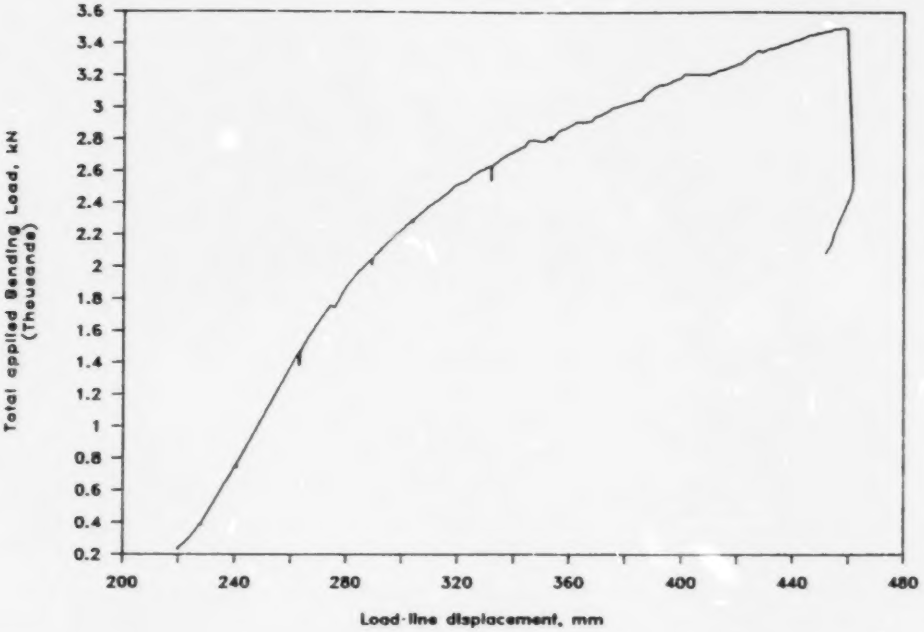

Figure 2.80. Total load versus load-line displacement data from Experiment 4.3-2 (includes displacement from test machine compliance).

DRB/4.2/F4

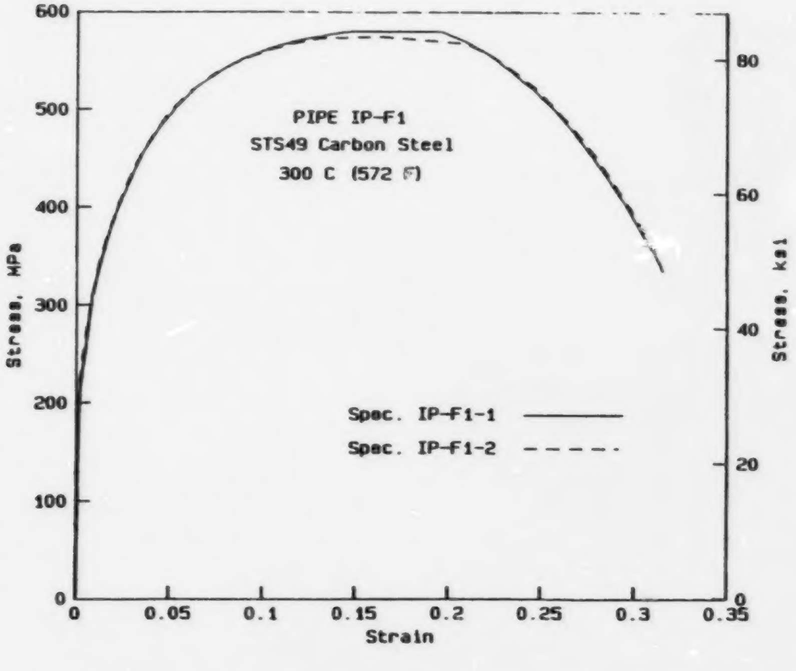

Figure 2.81. Engineering stress-strain curves at 300 C (572 F) for 30-inch diameter Japanese pipe material.

F-I-7/91-F2.81

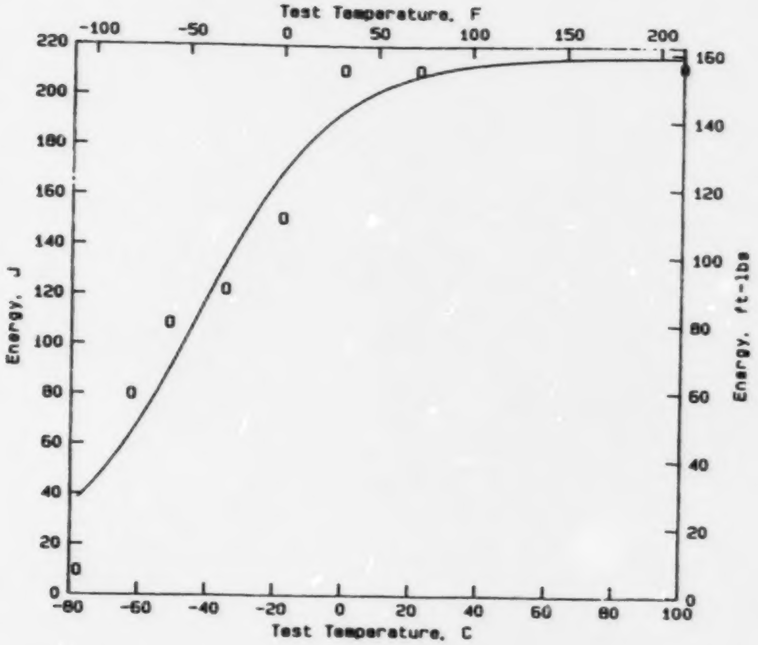

Figure 2.82. Absorbed energy in Charpy V-notch tests for 30-inch diameter Japanese pipe material.

F-I-7/91-F2.82

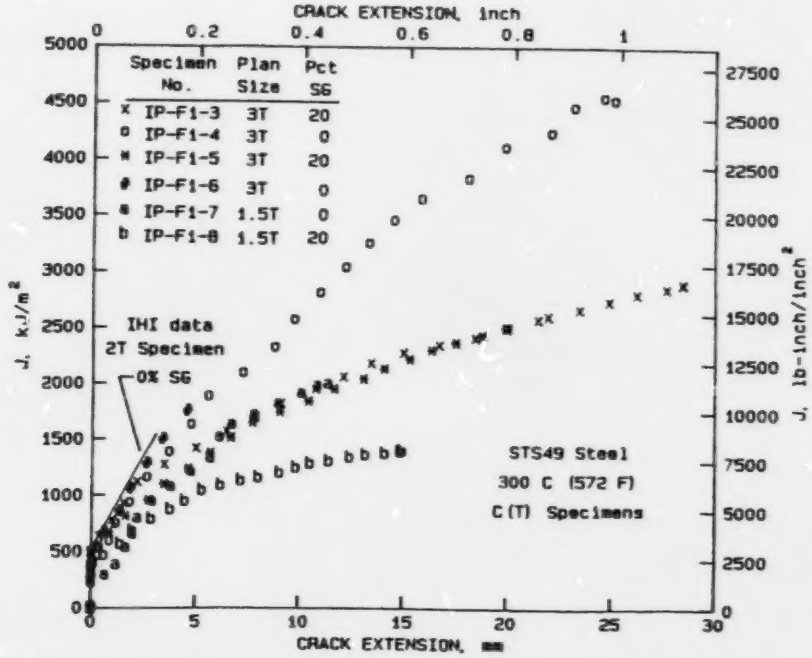

Figure 2.83. Deformation J-resistance curves (using ASTM E1152) for 30-inch diameter Japanese pipe material tested at 300 C (572 F).

F-I-7/91-F2.83

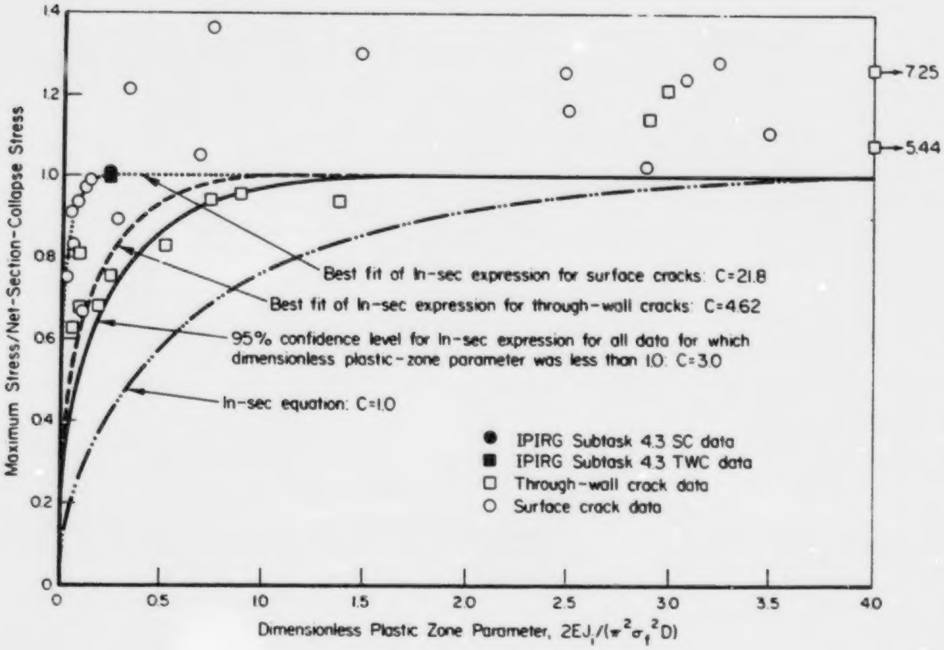

Figure 2.84. Comparison of Subtask 4.3 results with Degraded Piping Program experiments and the Dimensionless Plastic-Zone Parameter analysis.

F-I-7/91-F2.84

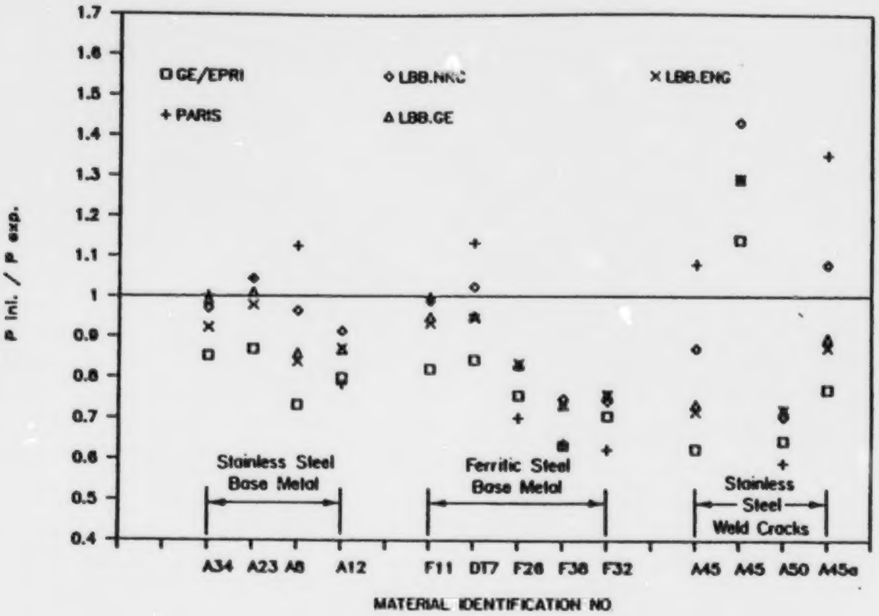

Figure 2.85. Comparison of predicted loads at crack initiation with experimental results for IPIRG Round-Robin Problem 1.

F-I-7/91-F2.85

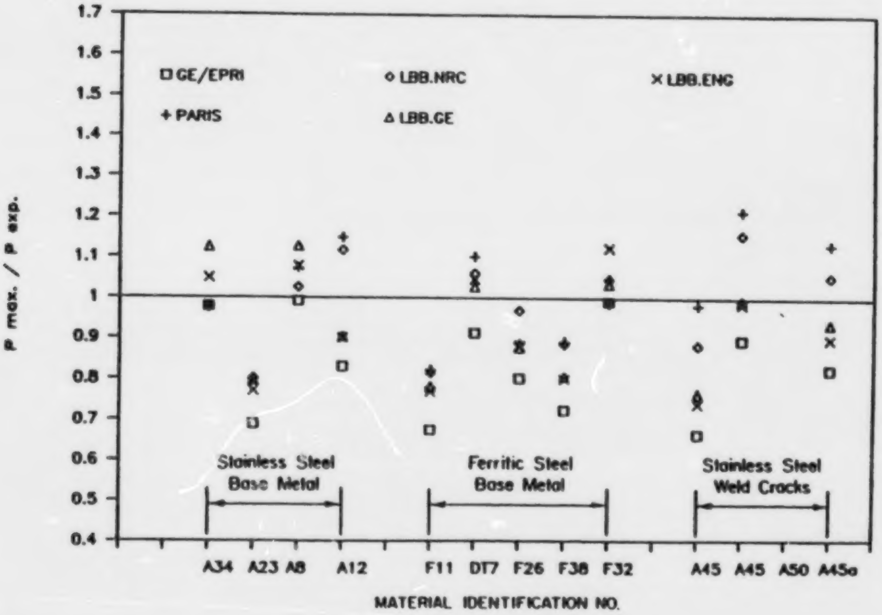

Figure 2.86. Battelle comparison of predicted maximum loads, using power-law extrapolated J_D-R curve, with experimental results for IPIRG Round-Robin Problem 1.

F-I-7/91-F2.86

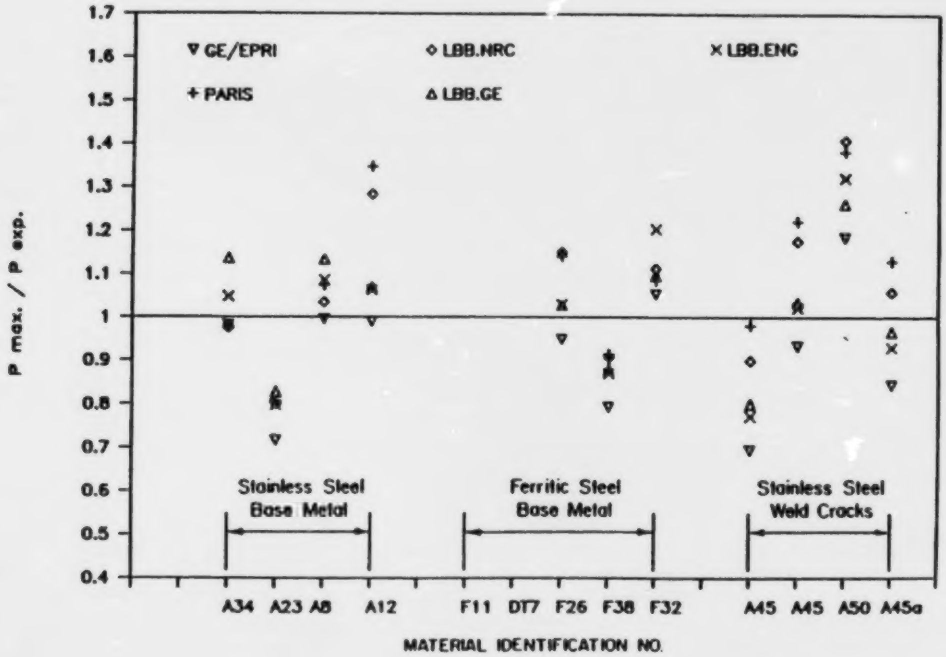

Figure 2.87. Battelle comparison of predicted maximum loads, using linearly extrapolated J_M-R curve, with experimental results for IPIRG Round-Robin Problem 1.

F-I-7/91-F2.87

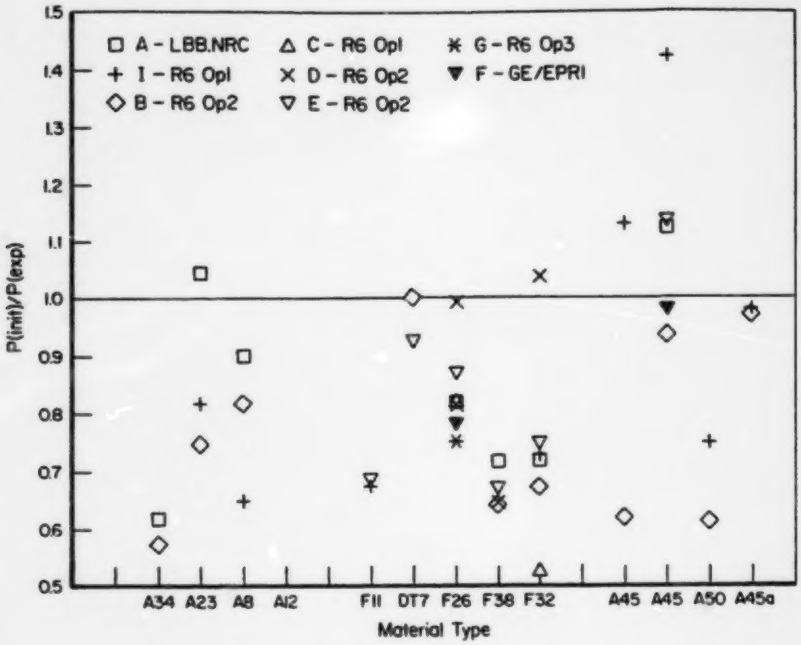

Figure 2.88. IPIRG member participant predictions of loads at crack initiation compared with experimental loads for IPIRG Round-Robin Problem 1.

F-I-7/91-F2.88

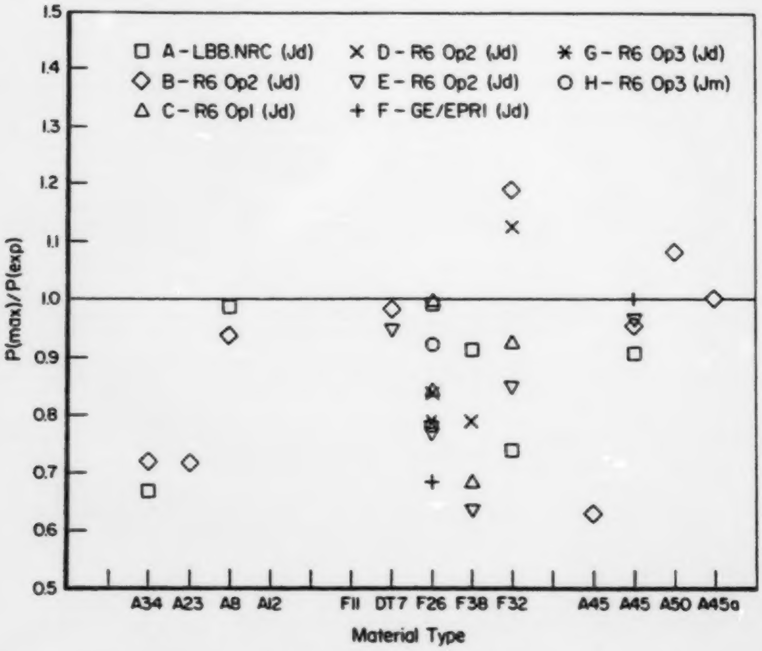

Figure 2.89. IPIRG participants predictions of loads at crack initiation compared with experimental loads for IPIRG Round-Robin Problem 1.

F-I-7/91-F2.89

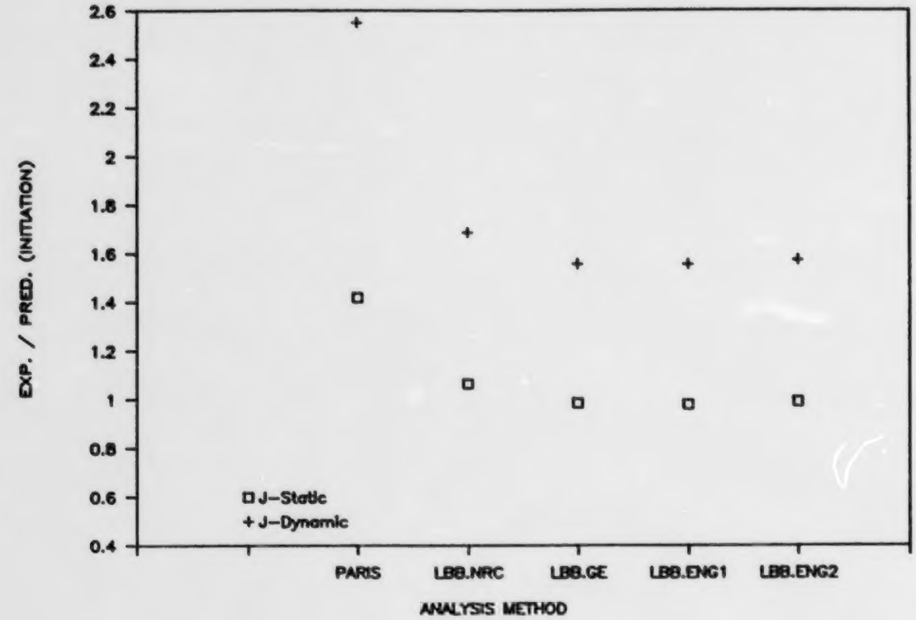

Figure 2.90. Comparison of NRCPIPE load predictions with experimental data for crack initiation - Round-Robin Problem 2-3.

IWS-11/88-I14-GW

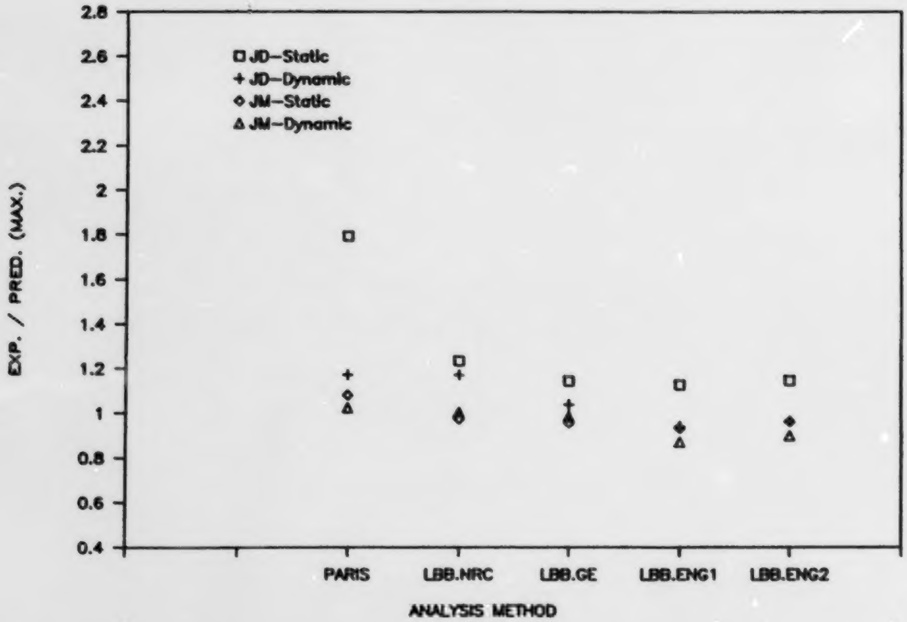

Figure 2.91. Comparison of NRCPIPE load predictions with experimental data at maximum moment for Round-Robin Problem 2-3.

IWS-11/88-I15-GW

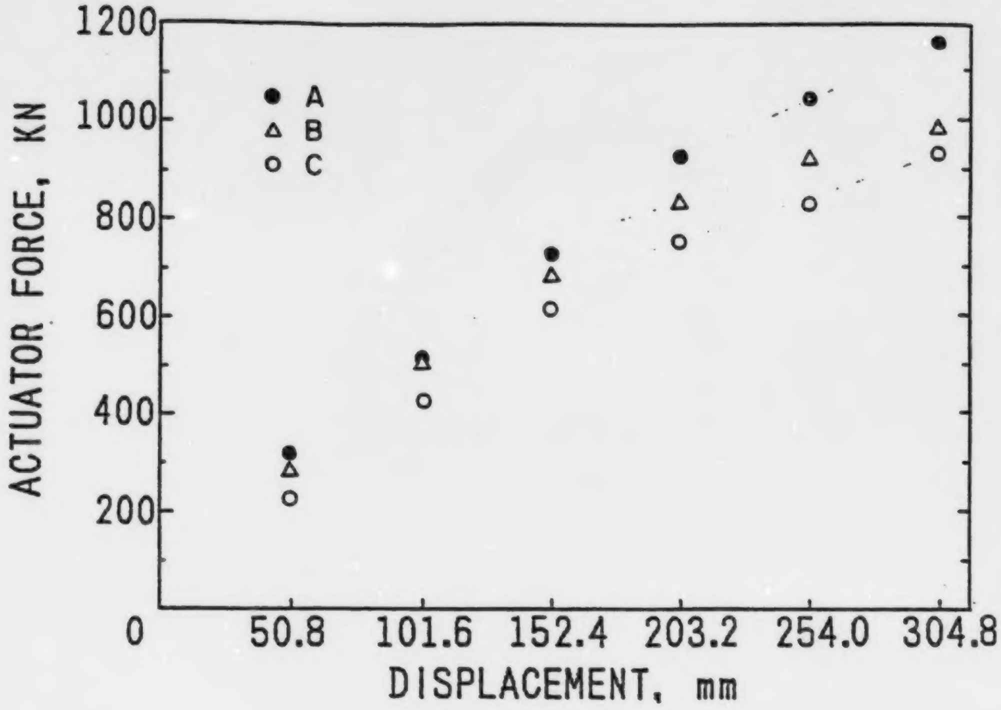

(a) Actuator Force Displacement

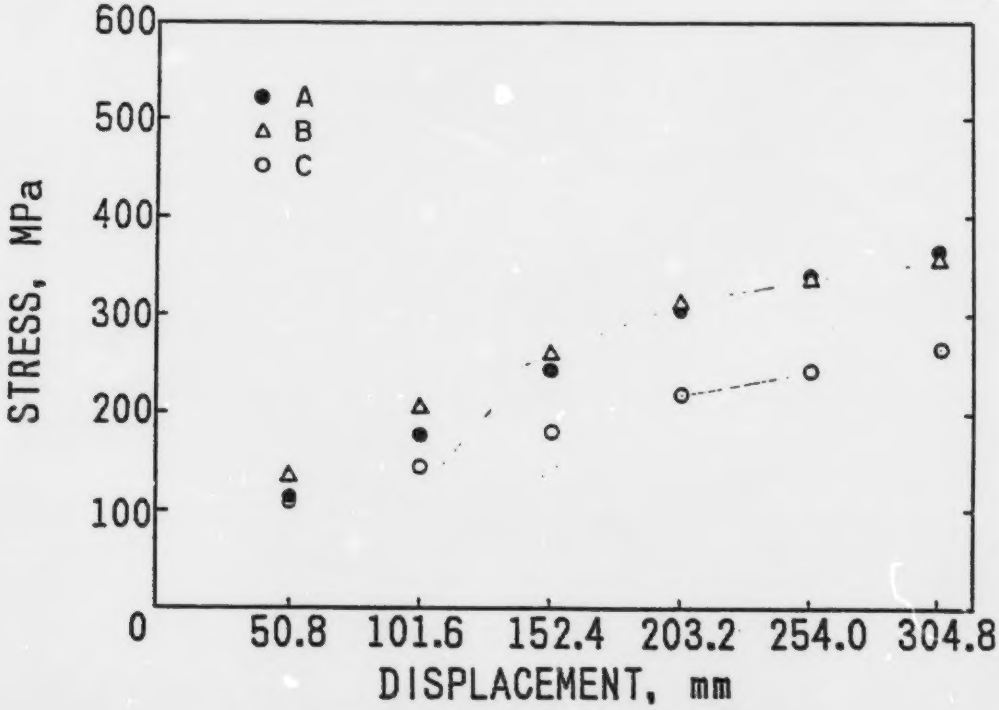

(b) Stress (Crack Location) Displacement

Figure 2.92. Solutions to IPIRG Round-Robin Problem 2-4.

F-I-7/91-F2.92

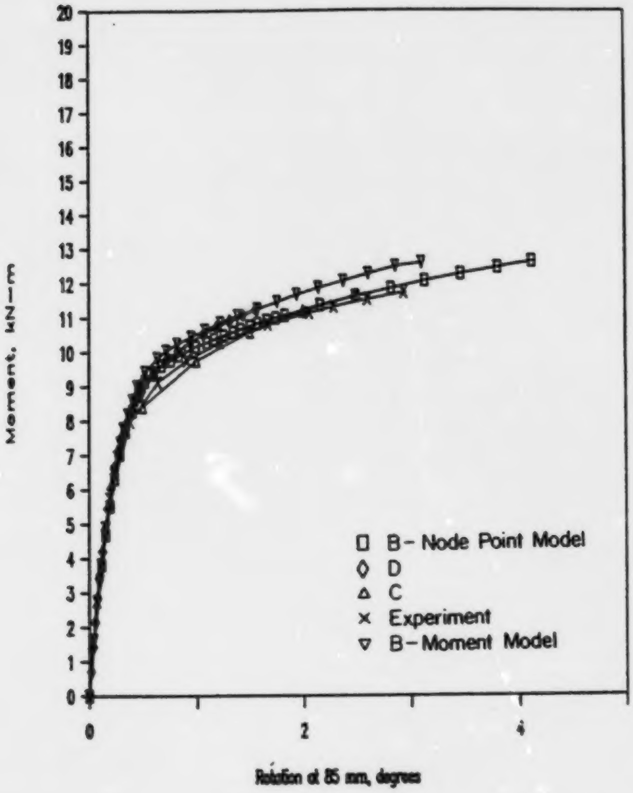

(a) Comparison of all FEM predictions to experimental data for French Pipe Test EDF-5.

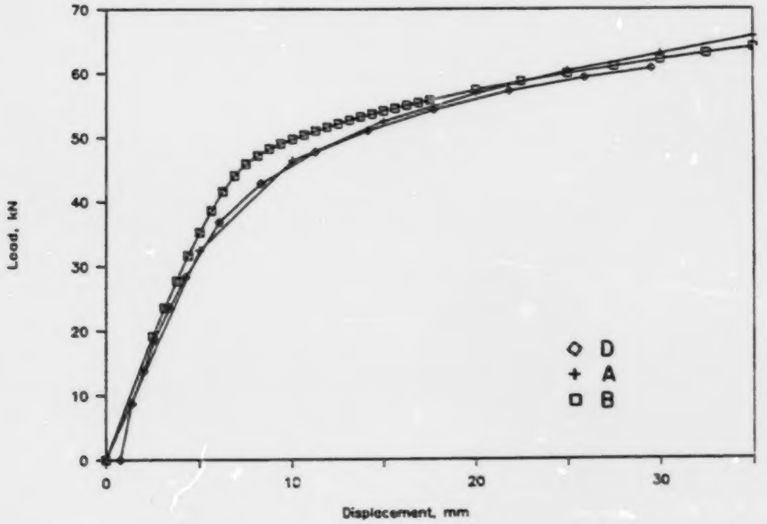

(b) Comparison of finite element load-displacement results for French Pipe Test EDF-5.

Figure 2.93. Solutions to Round-Robin Problem 3.1a.

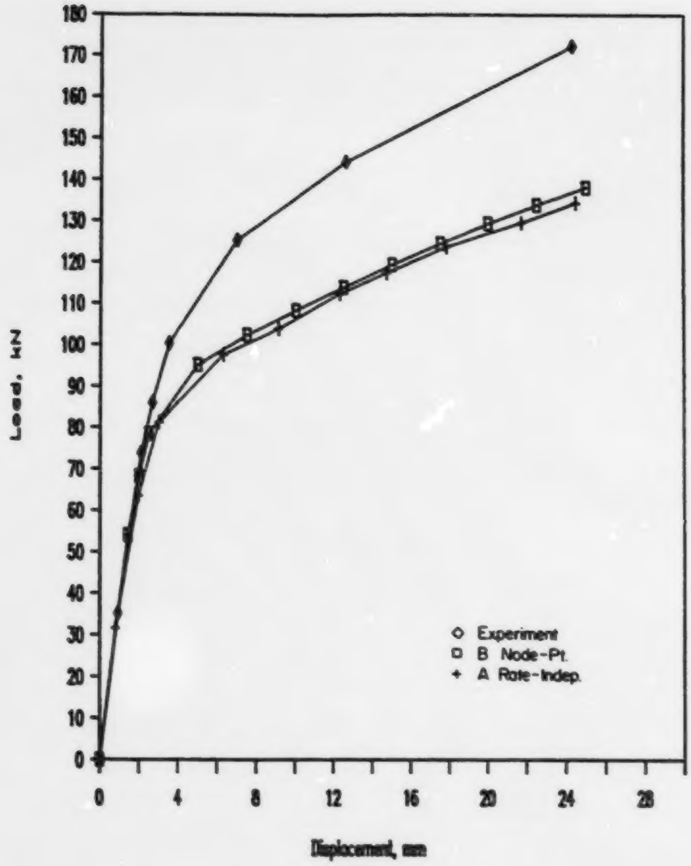

Figure 2.94. Comparison of FEM and experimental load versus load-line-displacement curves for Experiment 1.2-1, Round-Robin Problem 3-1b.

I4.5-1/90-F9

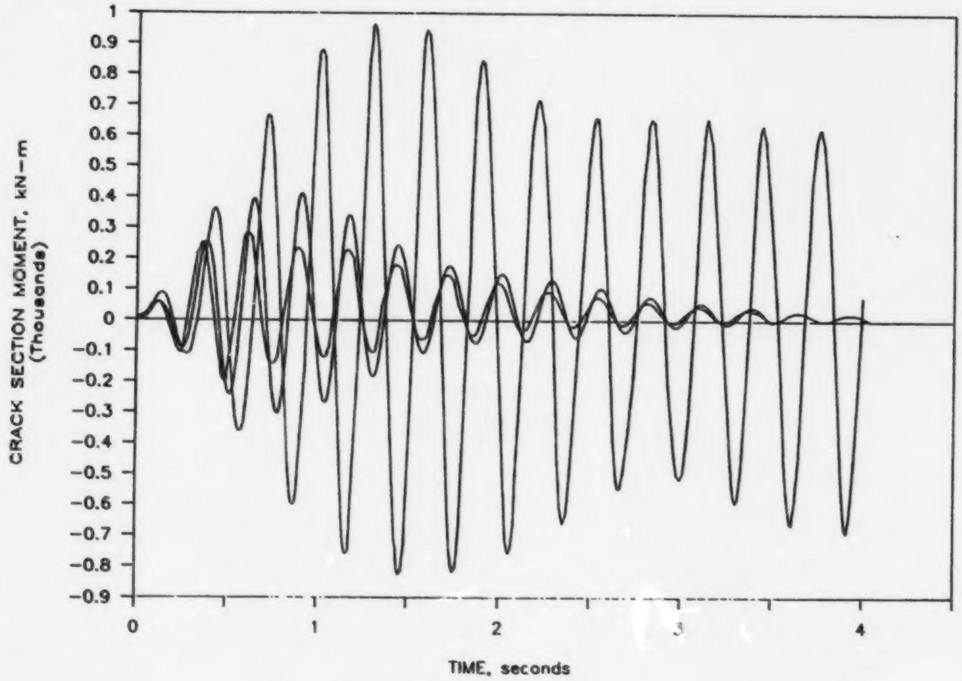

Figure 2.95. Early finite element predictions by different participants of crack location moment for IPIRG pipe system in Round-Robin Problem 3-2a.

I-10/89-F2-R0

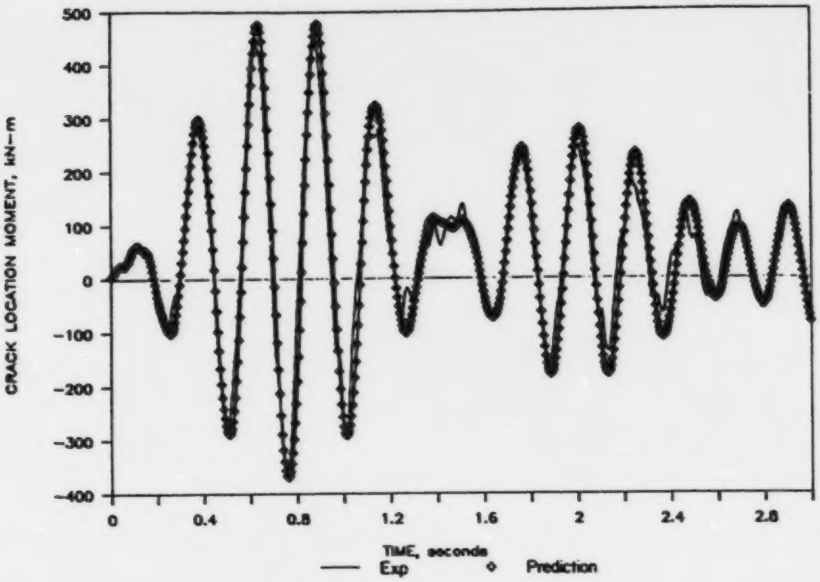

Figure 2.96. Prediction (using CASTEM 2000) of crack location moment in IPIRG pipe system after analysts meeting. (Round-Robin Problem 4-3.)

I-10/89-F19-RO

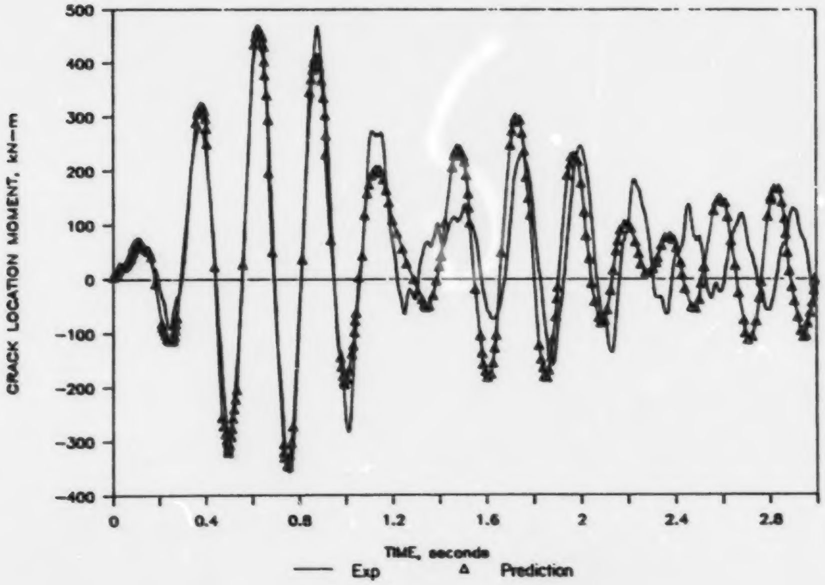

Figure 2.97. Prediction (using ABAQUS) of crack location moment after analyst meeting. (Round-Robin Problem 4-3.)

I10/89-F20-RO

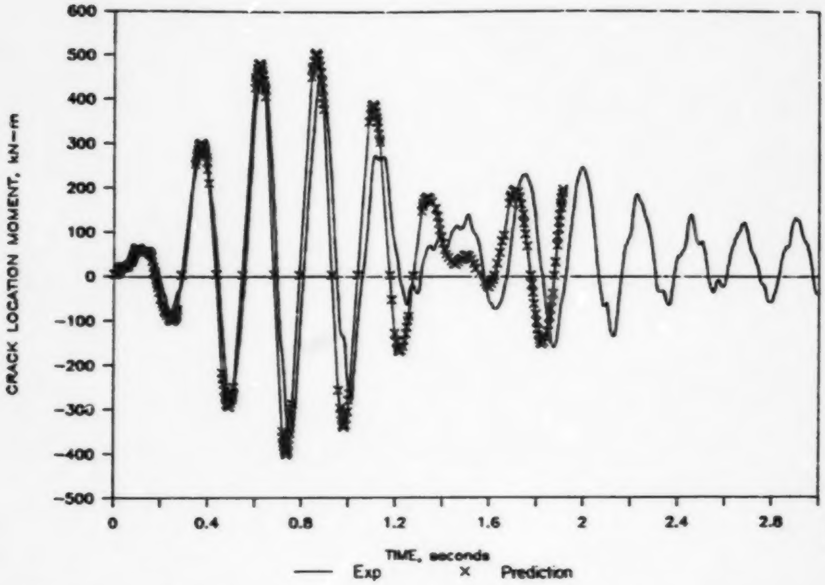

Figure 2.98. Prediction (using ADLPIPE) of crack location moment after analyst meeting. (Round-Robin Problem 4-3.)

I-10/89-F21-R0

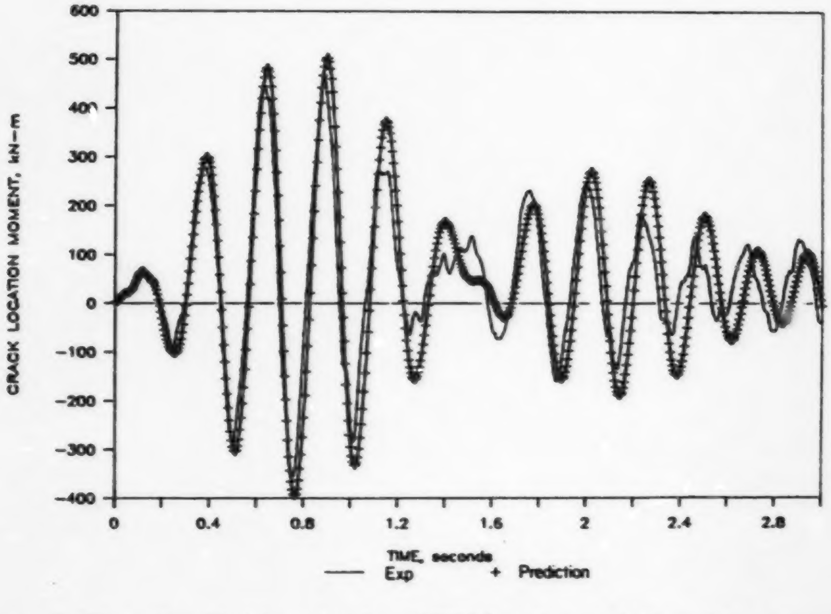

Figure 2.99. Prediction (using ANSYS) of crack location moment after analysts meeting. (Round-Robin Problem 4-3.)

I-10/89-F18-R0

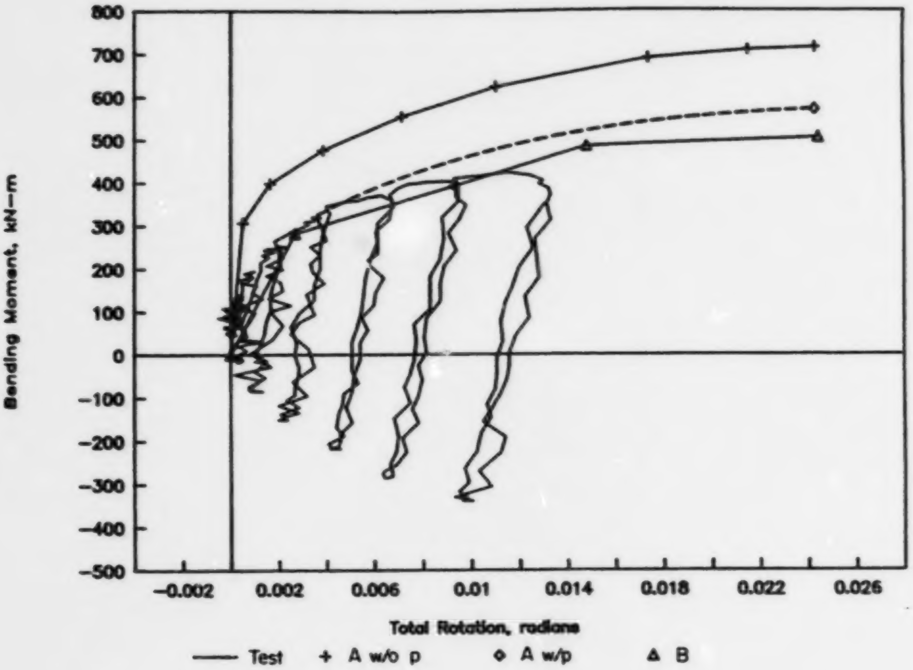

Figure 2.100. Comparison of moment versus rotation due to the crack, Round-Robin Problem 5-1b.

F-I-7/91-F2.100

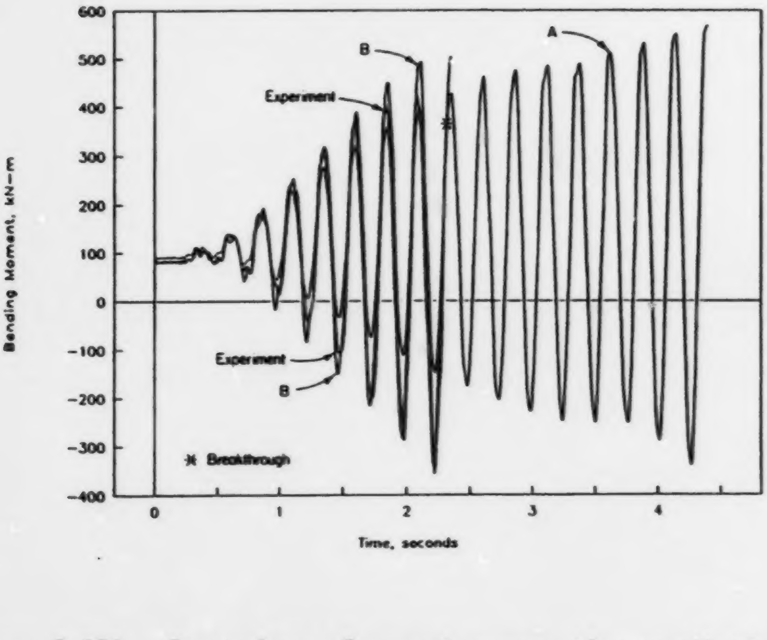

Figure 2.101. Comparison of moment versus time predictions (Round-Robin Problem 5-1b).

IWS-5/90-20-R0

3.0 DETAILED ASSESSMENT OF TASK 1 RESULTS

The experimental results from Task 1, which was the major effort of the entire program, are summarized in Section 2.1 of this report.

Answering basic questions about the meaning and significance of these experimental results requires meticulous analysis. For example:

- What are the effects of cyclic and high-rate loading on pipe fracture?
- What are the differences between inertial and displacement-controlled loading on fracture stability?
- What can be learned from dynamic pipe system experiments that cannot be learned from simpler separate effects experiments and small laboratory specimen tests?

Results from all three subtasks in Task 1 and quasi-static experiments from the Degraded Piping Program are combined, evaluated, and compared in this section. Due to differences in internal pipe pressure, pipe size, and flaw size, direct comparisons of the maximum loads or moments between experiments is not always meaningful. In order to compare the results of the different experiments in a systematic fashion, each experiment was analyzed using several fracture mechanics criteria. In this section the results of those comparisons are presented. Further details of the comparisons of the analytical predictions with the experimental results can be found in the final reports for the three subtasks (Refs. 3.1, 3.2, and 3.3).

This section contains eight major subsections:

- Section 3.1 quantifies the confidence bounds, scatter, and uncertainty of the data gathered in the pipe fracture experiments.
- Section 3.2 compares the experimental results of all IPIRG pipe fracture experiments with predictive fracture analyses, i.e. Net-Section-Collapse (NSC), Dimensionless Plastic-Zone Parameter (DPZP), and J-estimation schemes.
- Section 3.3 presents analyses of maximum stress predictions, similar to those of Section 3.2, but using ASME Section XI and R6 methods. The Code and R6 analyses are treated separately since these are intended to be failure avoidance criteria and are not necessarily accurate predictions of actual fracture behavior.
- Section 3.4 compares the J-R behavior obtained from C(T) specimens with that obtained from pipe experiments using η-factor analyses.

- Section 3.5 examines the pipe fracture data on the basis of the crack rotation measured at initiation and at maximum load.
- Section 3.6 deals with dynamic finite element calculations that were conducted to (1) determine the accuracy of elastic stress analyses for pipe fracture experiments and (2) compare predictions of dynamic pipe system response with results from cracked and uncracked pipe system experiments.
- Section 3.7 examines questions of fracture stability in pipe fracture experiments and compares results with analytical predictions using J/T and Energy Balance methods.
- Section 3.8 integrates the results examined individually in the preceding sections. The objective of Section 3.8 is to evaluate the degree of consistency among results from material characterization efforts, separate effects experiments on straight pipe, and dynamic pipe system experiments.

3.1 Confidence Bounds in Pipe Fracture Data

Data reported for any experiment have some uncertainty. The uncertainty arises from the instrumentation used to make the measurements, from inherent variability in the quantities being measured (i.e., scatter), and from the particular techniques used to conduct the experiments. Rigorous analysis of uncertainty is frequently ignored because of a failure to recognize that uncertainty exists, because it is not deemed important, or because it is difficult to quantify. In the IPIRG Program the uncertainty or confidence bounds for interpretation of the data must be quantified, because the number of experiments conducted was very limited. Without this context, the results of the experiments cannot be rationally compared with each other to establish the significance of observed trends.

Three factors have been identified that influence the confidence bounds in the IPIRG experiments:

- Material variability
- Measurement uncertainty
- Experimental technique.

Although confidence bounds for all data reported for the experiments are influenced by these factors, only bending moment is considered in this analysis, because it is the most important parameter. Thus, the analysis presented here focusses on defining the expected tolerance on maximum bending moments, with some discussion on the confidence in determining bending moments at crack initiation.

3.1.1. MATERIAL VARIABILITY

The influence of material variability on confidence bounds was examined two different ways. First, a semi-analytical approach was used to examine the scatter in bending moments implied by differences in measured specimen material properties. Second, replicate pipe test data from a number of sources were analyzed to isolate the effect of material property scatter on the reported bending moments.

The semi-analytical approach used J-estimation schemes with a number of measured stress-strain and J-R curves to calculate initiation and maximum bending moments as shown in Figure 3.1. Keeping the pipe size and initial size flaw fixed, combinations of stress-strain and J-R curve material properties measured in the laboratory were input to the J-estimation scheme to predict moments. From the results of a number of these analyses, the upper and lower limits and the mean of the predicted moments were established. The scatter in predicted moments represents scatter that is solely attributable to material property variation.

Two different materials were considered in the semi-analytical analysis, A106 Grade B and TP304 stainless steel. For each of these materials, the J-estimation scheme analyses used two measured quasi-static stress-strain curves and three J-R curves from quasi-static C(T) tests. Because of the size effect, two different pipe sizes were analyzed. In addition, two initial flaws were analyzed, a through-wall crack and a surface crack. In all, 8 basic configurations were considered: 2 materials, 2 pipe sizes, and 2 flaws. Within each basic configuration, 6 property set variations were analyzed: 2 stress-strain curves and 3 J-R curves. Tables 3.1 and 3.2 document the cases considered.

The results of the J-estimation scheme predictions show the effect of material property variations on moments (Figures 3.2 through 3.5). The four data sets shown in each figure have been normalized so that the mean of each sample population is one. The extremes of the lines in the figures represent the upper and lower limits of the data. The maximum moment variations, shown in Figures 3.2 and 3.4, suggest that the uncertainty for a given flaw in carbon steel is always greater than for stainless steel. In addition, as pipe size increases, the maximum moment uncertainty also increases. The latter observation demonstrates that more variability is expected for elastic-plastic failure loading conditions than limit-load failure conditions. Within the constraints of the measured variations in quasi-static properties and limited number of samples, the uncertainty for maximum moment is on the order of 3 to 5 percent. Considering the companion predictions of initiation moment, Figures 3.3 and 3.5, the uncertainty in initiation moment is greater than the corresponding uncertainty for maximum moment. The initiation moment uncertainty ranges from as little as 4 percent to as high as 11 percent.

The second approach to looking at the effect of material variability on the uncertainty of moment data was to examine replicate experiments in the available pipe fracture data bases. For an absolute replicate, differences in maximum moment should be caused only by material property variations. Unfortunately, completely replicating a pipe fracture test is very difficult. Flaw and pipe sizes are almost always slightly different, even though the specimens may have come from the same piece of pipe. To overcome the problem of size differences, Net-Section-Collapse analysis was used to normalize the moment results from sets of "near replicate" experiments.

Four sets of four-point bend "near replicate" quasi-static pipe experiments were identified and normalized to isolate the effect of material variability on maximum moment. Table 3.3 lists the experiments that were considered in the analysis. In each case, the tests within a group had, at worst, a different initial crack size. The test conditions, load frame, pipe size, and material heat were nominally identical. The scatter in the maximum moments from normalized replicate tests is shown in Figure 3.6. No data are presented for initiation moment from these tests because sufficient information was not available. The data in Figure 3.6 suggest that material variability causes an uncertainty of as much as ± 10 percent in A106 Grade B and TP304 TIG weld materials. Consistent with the previously discussed findings, TP304 material variability results in only a ± 3 percent uncertainty in maximum moment, probably because the toughness is sufficiently high to have limit-load failures.

3.1.2 MEASUREMENT UNCERTAINTY

There are three sources of uncertainty in the measured data from the IPIRG Program:

(1) Instrumentation

(2) Data Reduction

(3) Data Interpretation.

The first item involves the inherent nonlinearity, hysteresis, and noise that is superimposed on the signal that is being measured. The second involves combining of basic measured values, with their associated uncertainties, to derive other data; the derived data are always more uncertain than directly measured data. The third, which affects only initiation moments, is the engineering judgement needed to identify the point of crack initiation.

All of the individual instrumentation components used in the IPIRG Program were calibrated to published manufacturers' specifications. Typically, these individual specifications indicate accuracy or nonlinearity on the order of less than one percent full scale. When these individual components are connected together into a system (i.e., transducer to excitation and amplifier, amplifier to analog-to-digital converter), the individual uncertainty tolerances accumulate. In a detailed analysis of the IPIRG instrumentation, the largest uncertainty for directly measured data that affects bending moments occurs in the pipe strains. These have an uncertainty of ± 6.6 percent of full scale, due primarily to the large tolerance on gage factor for the high temperature weldable gages. The other measured data that affect moments, such as loads in the four-point bend tests, specimen geometry, and fixture geometry, have ± 1 percent uncertainty or less.

The reduction of raw voltages into basic engineering quantities does not introduce uncertainty beyond that associated with the measurements themselves. That is, strictly multiplying a voltage by a conversion factor does not change the basic uncertainty. However, when several pieces of basic engineering data are combined in some fashion to derive other quantities, the uncertainties associated with each of the basic measurements combine to increase the overall uncertainty. Moments derived from strain gage data in the Subtasks 1.1 and 1.3 pipe experiments are an example of derived data. The uncertainty in moment is considerably greater than the uncertainty associated with just the strains.

The uncertainty in a derived quantity at a particular point can be estimated from the linear terms of a Taylor's series expansion of the mathematical expression for the derived quantity. In symbolic form, the total uncertainty is

$$\Delta W = \Sigma\ (\partial W/\partial x_i)\Delta x_i \qquad (3.1)$$

where $W = f(x_1, x_2, \ldots, x_i)$. To calculate the total uncertainty, the value of each of the measured input parameters, x_i, must be known, as well as its associated uncertainty, Δx_i.

Maximum Moment

The combined instrumentation and the data reduction uncertainty in maximum bending moment for each of the IPIRG subtasks is shown in Table 3.4. The measurement uncertainty for the four-point bend experiments of Subtask 1.2 is the lowest. In this case, only specimen loads and test fixture geometry are used to calculate maximum moment. All of the input data for Subtask 1.2 moments are known with high confidence. Subtasks 1.1 and 1.3, on the other hand, used strain gages to determine moment. Moments are derived from strain gage readings, Young's modulus, Poisson's ratio, and pipe section properties. Due to large tolerances on the high temperature weldable gages, the number of electronic subsystems used, the procedures for calibration, and the sheer number of measurements that go into a strain gage based moment calculation, the uncertainty for moments in Subtask 1.1 and 1.3 is significantly greater than for Subtask 1.2.

Initiation

The ability to detect crack initiation is not well documented for pipe experiments. For quasi-static testing of C(T) specimens, several investigators have shown that crack initiation corresponds to a deviation in linearity from the so-called blunting line on a plot of d-c electric potential versus displacement (Refs. 3.5 to 3.7). The relevant displacement is typically crack-mouth-opening displacement (CMOD), but load-line displacement or test section rotation can also be used. Two d-c electric potential blunting lines are illustrated in Figure 3.7. For quasi-static monotonic displacement-controlled pipe fracture experiments, a similar trend in d-c electric potential data has been observed in numerous experiments (Ref. 3.8). On this basis, initiation has been hypothesized to occur when a similar deviation from linearity is observed in the pipe test data.

For the pipe experiments in this program, the loading was generally more complicated than simple quasi-static monotonic. Relatively high-rate and cyclic loading prior to and during ductile tearing occurs in many of the pipe experiments. Little or no experience exists for detecting crack initiation with these load histories, even in laboratory specimens. As a consequence, a technique for determining crack initiation in dynamic pipe fracture experiments is not well defined. Although a universally accepted prescription for determining crack initiation in these circumstances is not available, the basic concept used for C(T) specimens and quasi-static pipe fracture tests can be extended to these situations. With engineering judgement a reasonable point of initiation can be determined for many of the pipe fracture experiments.

To address the variability in detecting crack initiation the Subtask 1.2 experiment d-c EP data were examined in detail. During this process, two different sources of variability became apparent:

(1) Variability in the methodology to determine deviations in the d-c electric potential blunting line (experimental technique)

(2) Variability due to material properties, i.e., crack initiation occurring at distinctly different times at the two crack tips of a through-wall cracked pipe experiment.

These effects and the magnitude of the observed variations are discussed below.

THE ROLE OF EXPERIMENTAL TECHNIQUE. The ability to determine crack initiation in a pipe test is a function of the ability of the analyst to identify the deviation from the blunting line on a d-c electric potential versus displacement plot. For monotonic loading tests, the identification of the initiation point is relatively easy. For cyclic loading tests, however, the deviation of the EP from the blunting line is difficult to determine.

In the Subtask 1.2 experiments, monotonic displacement-controlled loading was done at both quasi-static and dynamic rates. For these experiments, the standard blunting line approach can be used. The deviation from linearity is generally quite apparent, but noise in the d-c EP and displacement data confuses the identification of initiation by causing the deviation from linearity to occur in an area, rather than at a single point. Considering just the tolerance bands on the d-c EP and CMOD signals, the initiation moment at any one crack tip for all of Subtask 1.2 monotonic loading cases could be as much as ± 6.2 percent of the mean initiation moment. When the subset of the carbon steel monotonic loading cases that used high current to mask self-induced voltages is considered, the noise in the d-c EP is considerably reduced and the variation in initiation moment is only ± 3.5 percent.

For cyclic loading, the unloads, crack closure, and reloads introduce changes in the d-c electric potential and displacement data that mask the deviations in linearity used to identify initiation in a monotonic test. To extract the initiation information from these data, special techniques must be used. The initial method employed to detect crack initiation for cyclic loading experiments was to use the envelope of the d-c electric potential versus displacement data. In concept, this seems to be a reasonable extrapolation of the blunting line technique, see Figure 3.8. An alternative for determining initiation is to identify points of reinitiation for each loading cycle and then follow these back to the first cycle where ductile tearing appears to begin, Figure 3.9.

The differences between the two techniques for determining initiation moment for cyclic loading tests can be significant. In one case the difference was 25 percent. The fact that the deviation from linearity for the envelope method may not necessarily occur at a measured data point, as in Figure 3.8, is a cause for concern. Likewise, many cyclic loading tests are not as well behaved as the data in Figure 3.9, so the points of reinitiation are very difficult to establish. Determining initiation in pipe experiments with cyclic loading is not deterministic. Rather, it involves "engineering art", and as a consequence, the confidence bounds are quite large.

VARIABILITY DUE TO MATERIAL PROPERTIES. During the investigation to determine confidence bounds for initiation moments, the crack initiation moments frequently were found to differ between the two through-wall crack tips. This variability is believed to be due more to material variations than accuracy of data or methodology for determining crack initiation. Such differences were also noticed in the NRC's Degraded Piping Program (Ref. 3.4). The greatest crack-tip-to-crack-tip variation for the Subtask 1.2 experiments was for Experiment 1.2-3, where the variation was ± 11 percent of the mean value. The average variability for the five experiments examined was ± 4.3 percent.

INITIATION MOMENT SUMMARY. The maximum observed variations in the moments at crack initiation in the Subtask 1.2 experiments were

• Maximum observed variability in determining deviation from d-c EP blunting line for monotonic tests	± 6.2 percent
• Maximum observed variability due to blunting line approach versus reinitiation point method for cyclic loading	± 25.0 percent
• Maximum observed variability due to initiation differences between two crack tips, i.e., material variability.	± 11.0 percent

These data represent only the uncertainty associated with the engineering judgements needed to select an initiation point. The uncertainty in the measurement of the moment, ± 3 percent to ± 14 percent as discussed above, must be added to the initiation uncertainty. It should also be noted that the Subtask 1.2 experiments were more controlled experiments than the Subtask 1.1 and 1.3 dynamic cyclic loading pipe experiments. Initiation data from the Subtask 1.1 and 1.3 experiments are certain to have larger confidence bounds.

3.1.3 EXPERIMENTAL TECHNIQUE

Experimental techniques and hardware employed by a laboratory to conduct pipe fracture tests may introduce a bias into reported data that could be interpreted as a significant fracture-related behavior. In particular, the geometry of a test machine or use of certain instrumentation might influence the results of a pipe fracture test. The inner and outer span lengths on a four-point bend test machine, the use of single or multiple actuators for applying load, and the size of pipe loading "saddles" may all affect reported data. The choice of transducers for measuring loads (load cells or pressure transducers) and displacements (LVDT's, potentiometers, or optical encoders), doing real-time analog-to-digital conversion, or recording on FM tape for subsequent processing all may tend to bias results.

To investigate the role that experimental technique may play in the confidence bounds of moment data, four sets of replicate pipe fracture tests were identified where either two independent laboratories conducted tests on the same pipe, or multiple tests were performed on the same pipe using different setups at one laboratory. Table 3.5 lists the important features of the four independent test setups that were analyzed. As in the case of the material variability, the results of the analysis, shown in Figure 3.10, were normalized to remove the effect of slight differences in pipe size. Uncertainty for initiation moment has been shown for the experiments where it is available. The data from the independently conducted experiments show an uncertainty less than ± 6 percent.

Experimental technique, although discussed as an independent source of uncertainty, is not independent of material variability or instrumentation uncertainty. The results in Figure 3.10 show no worse uncertainty than either material property variations or measurement uncertainty. This suggests that differences in hardware and experimental technique do not generally introduce additional uncertainty into the reported maximum bending moments.

3.1.4 SUMMARY

The analyses presented here are a means of providing a rational perspective for interpreting the pipe fracture data from this program. Clearly, rationalizing a 2 percent difference between two different experiments is not reasonable when the data have a ± 10 percent uncertainty. Every attempt has been made to place the confidence bounds analysis on as rigorous a basis as possible. However, the extremely limited sample populations can provide only a hint at the possible trends. If enough data were available, Monte Carlo simulations and statistical analyses could be performed to refine the estimates of uncertainty.

In the discussions presented, each of the effects discussed has been assumed to be independent. In fact they are not. The replicate experiment and the independent test setup data are not independent of measurement uncertainty. In the semi-analytical material variability investigation, the variability in the measured material properties was assumed to be random and without systematic bias. This has not been established.

With respect to measurement uncertainty, one can normally expect most measurements to be better than the extreme limits quoted in Table 3.4. For a given measurement to be at the limit, all of the worst case conditions would have to occur simultaneously. This is highly unlikely, but nonetheless still a possibility.

With the comments above as a preface, the following summarizes the confidence bounds for the various sources of uncertainty in the IPIRG moments:

- Material Variability in Maximum Moment: ± 3 to ± 10 percent. Stainless steels have less uncertainty than carbon steels; base metals have less uncertainty than welds.

- Measurement Uncertainty in Maximum Moment: ± 3 to ± 14 percent. Direct measurements, as in Subtask 1.2, are much better than derived results, as in Subtasks 1.1 and 1.3.

- Uncertainty in Initiation Moment: ± 6 to ± 25 percent beyond the measurement uncertainty.
- Experimental Technique: Scatter is within the bounds of material variability and measurement uncertainty.

To integrate all of these data into a single confidence bound number for maximum moment, one could simply add ± 10 percent to ± 14 percent and suggest that any hypothesized effect that is within ± 24 percent cannot be substantiated. Data correlations from several sources suggest that this approach is too pessimistic and represents an unrealistic extreme. In a pragmatic engineering sense, it is probably reasonable to suggest that maximum moment data must show at least a 5 to 10 percent difference in order to substantiate a hypothesized effect or trend.

A single value for initiation moment confidence would be at least 15 to 25 percent. This number reflects the uncertainty associated with the "art" of selecting an initiation point, material variability, and the uncertainty of the moment measurements. The significantly lower confidence in the reported initiation moments is reflected by the fact that initiation moment is not even reported for some of the IPIRG Program experiments. The data for these experiments were too ambiguous.

3.2 Fracture Analysis Predictions of Maximum Stress

Tables 3.6 and 3.7 were generated to facilitate the comparisons of the experimental results with the various fracture predictive analyses. These tables present the ratios of the maximum experimental stress to the predicted stress for 34 experiments and 7 different analyses. Both the experimental and predicted stresses include the stress contribution due to internal pressure. Tables 3.6 and 3.7 include the results from not only the IPIRG Program but also relevant past quasi-static pipe fracture programs (Refs. 3.4 and 3.11). To facilitate the comparisons, the experiments listed in Tables 3.6 and 3.7 are grouped according to crack geometry, material, pipe diameter, and loading conditions.

3.2.1 NET-SECTION-COLLAPSE

The Net-Section-Collapse (NSC) analysis is a limit-load analysis that was first proposed for application to stainless steel pipe with circumferential through-wall cracks (Ref. 3.12). It subsequently was verified for 2-inch to 16-inch diameter stainless steel pipes with circumferential surface and through-wall cracks (Ref. 3.11). The solutions developed in Reference 3.11 were based on the following assumptions:

- Thin-shell theory applies. Thick-shell net-section-collapse formulations exist but are not presented in this report, because they do not provide improved results for the Task 1 pipe geometries. In fact, they tend to underpredict the loads significantly for the same choice of flow stress as in the thin-shell analysis.

- The pipe remains circular. In cases of small crack sizes when high loads occur, the pipe ovalizes and loses moment-carrying capacity. This has been documented experimentally (Refs. 3.4 and 3.11), but analytical corrections are not available. Note that the IPIRG pipe experiments had relatively large crack sizes and pipe ovalization effects were insignificant.

- Pressure contribution on the crack faces is negligible. Pressure corrections exist but have been found to be small for the experiments of interest to this program.

- The material is sufficiently tough so that there is negligible crack growth prior to reaching maximum load, and the pipe cross section becomes fully plastic such that the net-section stress reaches a constant value. The critical net-section stress at maximum load is called the flow stress. Several definitions of flow stress have been used in the Net-Section-Collapse analysis. The most frequently used value, and the value used herein, is the average of the quasi-static yield and ultimate strengths. While some material property data were obtained at higher loading rates, which were more representative of the loading rates in the dynamic experiments evaluated herein, only the quasi-static properties were used in these analyses, since they are the only properties commonly available.

Figures 3.11 and 3.12 display the ratio of the maximum experimental stress to the Net-Section-Collapse predicted stress for various experiments (see Tables 3.6 and 3.7). Figure 3.11 is for the through-wall-cracked pipe experiments and Figure 3.12 is for the surface-cracked pipe experiments.

It can be seen that the Net-Section-Collapse analysis consistently overpredicts the maximum experimental stresses for the carbon steel pipe experiments. This is especially true for the through-wall-cracked pipe experiments (see Figure 3.11). The ratio of the maximum experimental stress to the Net-Section-Collapse predicted stress for the carbon steel through-wall-cracked pipe experiments ranges from 0.65 to 0.84. For the carbon steel surface-cracked pipe experiments, this ratio ranges from 0.61 to 1.13.

The Net-Section-Collapse analysis did a much better of job of predicting the results for the stainless steel experiments. The ratio of the maximum experimental stress to the Net-Section-Collapse predicted stress for the TP304 stainless steel base metal experiments ranges from 0.86 to

1.21. The fact that the Net-Section-Collapse analysis did a much better job of predicting the load-carrying capacity of the stainless steel experiments is not unexpected, since the toughness of the stainless steel is sufficiently high to permit fully plastic conditions to develop. The lower toughness of the carbon steel pipe materials indicates that contained plasticity conditions exist at maximum load. As such, one of the basic assumptions embodied in the Net-Section-Collapse analysis (i.e., fully plastic conditions) may be violated for most of the carbon steel experiments. The lowest value from the stainless steel experiments was for R = -1 cyclic loading, which as noted later, lowers the apparent toughness of the steel.

Note that toughness is not the only parameter that affects whether contained plasticity or fully plastic conditions exist. Pipe diameter is another key parameter. The larger the pipe diameter, the more likely the chance that contained plasticity conditions exist. Table 3.7 and Figure 3.12 show that for the 16-inch nominal diameter experiments, the Net-Section-Collapse analysis overpredicts the experimental failure stress for all but one experiment. The one exception is the quasi-static TP304 stainless steel base metal experiment (EPRI 13S). This is the only experiment that was conducted at room temperature (Ref. 3.11). The toughness of this material at room temperature based on C(T) specimen data is approximately four times higher than the toughness for any of the other pipe materials evaluated.

Further discussion on comparison of the experimental results with the Net-Section-Collapse predictions is deferred to Sections 3.8.1 and 3.8.2, where the effects of dynamic loading rates and cyclic loading histories are discussed.

3.2.2 DIMENSIONLESS PLASTIC-ZONE PARAMETER

The Dimensionless Plastic-Zone Parameter (DPZP) analysis is a semi-empirical analysis developed during the Degraded Piping Program (Ref. 3.13) primarily to assess when the necessary conditions are satisfied for the Net-Section-Collapse (NSC) analysis, i.e., when fully plastic conditions exist. For a through-wall crack, the analysis compares the plastic-zone size with the distance from the crack tip to the neutral bending axis for the cracked cross-section. If the calculated plastic-zone size is larger than the remaining tensile ligament, then fully plastic conditions are assumed to exist, and the Net-Section-Collapse analysis is valid. If not, then fully plastic conditions may not exist and either an adjustment to the Net-Section-Collapse analysis or an elastic-plastic fracture analysis may be required.

Figure 3.13 is a plot of the ratio of the maximum experimental stress to the Net-Section-Collapse predicted stress as a function of the DPZP. In this figure, the NSC stress is based on a flow stress definition of the average of the actual quasi-static yield and ultimate strengths of the material. The data points shown on Figure 3.13 represent data from past quasi-static pipe fracture programs (Refs. 3.4 and 3.11) as well as the data from the IPIRG Program. Two curves are shown in Figure 3.13. For these curves, the relationship between the ratio of the experimental stress to the predicted NSC stress and the DPZP is:

$$P/P_{nsc} = (2/\pi) \text{ arc cos } (e^{-c(DPZP)}) \tag{3.2}$$

where,

$$DPZP = 2EJ_i/(\pi^2 \sigma_f^2 D) \tag{3.3}$$

P = experimental failure stress
P_{nsc} = NSC predicted tension and bending stress
E = elastic modulus
J_i = J at crack initiation (may be J_{Ic})
σ_f = flow stress = $(\sigma_y + \sigma_u)/2$
D = pipe diameter
c = statistically based parameter

The factor "c" was selected based on a statistical fit of the data. The upper curve in Figure 3.13 represents a best fit of all the surface-cracked pipe data. The value of "c" for this curve is 21.8. The lower curve represents a best fit of all the through-wall-cracked pipe data. The value of "c" for this curve is 4.62. Those curve fit values are for relatively large cracks where the differences between Net-Section-Collapse and elastic plastic fracture are the greatest. The different values of "c" reflect the observation that surface-cracked pipe behaves tougher than through-wall-cracked pipe. This suggests a loss of constraint for the surface crack geometry.

Figures 3.14 and 3.15 display the ratio of the maximum experimental stress to the DPZP analysis predicted stress for various experiments (see Tables 3.6 and 3.7). The experimental and predicted stresses both include the stress contribution due to internal pressure. Figure 3.14 is for the through-wall-cracked pipe experiments, and Figure 3.15 is for the surface-cracked pipe experiments.

Figure 3.14 shows that the DPZP analysis underpredicted the maximum experimental stress for all carbon steel through-wall-cracked pipe experiments. The ratio of the maximum experimental stress to the predicted stress ranges from 1.23 to 1.61 for these experiments. In contrast, the Net-Section-Collapse analysis overpredicted the maximum experimental stress for all of these carbon steel through-wall-cracked pipe experiments (compare with Figure 3.11).

Figure 3.14 shows that the DPZP analysis for the stainless steel through-wall-cracked pipe experiments resulted in more accurate predictions of the experimental failure stresses, although sometimes the analysis overpredicted the experimental results. The ratio of the maximum experimental stress to the predicted stress ranges from 0.87 to 1.10. Comparing Figure 3.14 with Figure 3.11, shows that the results for the stainless steel through-wall-cracked pipe experiments are the same for the NSC and DPZP predictive analyses. The DPZP screening criterion indicates that fully plastic conditions were always satisfied for these smaller diameter, higher toughness stainless steel pipe experiments. Consequently, the adjustment factor for the Dimensionless Plastic-Zone Parameter analysis as seen in Figure 3.13 is 1.0 for these experiments.

Figure 3.15 shows that the DPZP analysis underpredicted the maximum experimental stress of the surface-cracked-pipe experiments in all but four cases (1.1-9, 1.3-2, 1.3-3, and 1.3-7). Three of the four exceptions were the three dynamic Subtask 1.3 pipe system base metal experiments. For the carbon steel base metal experiment (1.3-2) this overprediction can partially be explained by the fact that the strength and toughness of this material decreased significantly at dynamic loading rates. Consequently, an analysis that uses quasi-static material property data may have difficulty in adequately predicting the behavior of such experiments. If dynamic tensile and toughness values are used in the DPZP analysis, then the ratio of the experimental stress to the predicted stress for this experiment increases from 0.704 to 0.856. This helps to explain the discrepancy but is still not the total answer.

There is some indication from an η-factor analysis (see Section 3.4) for the stainless steel pipe system experiments that the apparent fracture toughness in these experiments can be significantly less than that measured from C(T) tests. This may be a result of cyclic effects or, possibly, constraint effects for the surface crack geometry. Similar phenomena may be operative in the carbon steel pipe system experiment 1.3-2) and may provide some clue toward explaining the discrepancy.

Further discussion on the η-factor methodology for obtaining toughness values from pipe experiment moment-rotation records is presented in Section 3.4. Further discussion on the effect of and need for dynamic material property data is presented in Section 3.8.5.

3.2.3 J-ESTIMATION SCHEMES

For cases where limit-load analyses are inappropriate, due to low toughness or large diameter pipe, elastic-plastic analysis may be needed to obtain more accurate estimates of the maximum loads and stresses. In the nuclear industry the most commonly used elastic-plastic fracture parameter is the J-integral. Several closed-form equations for J exist that give approximate solutions for circumferentially cracked pipe. These are frequently referred to as J-estimation schemes. In this section the experimental results from the Task 1 experiments, as well as the companion quasi-static experiments, are compared with the predictions from three J-estimation schemes. Two of these are for through-wall-cracked pipe [GE/EPRI (Ref. 3.14) and LBB.ENG2 (Ref. 3.15)], and one is for surface-cracked pipe [SC.TNP (Ref. 3.16)]. In Section 3.3 the ASME Section XI IWB-3640 and 3650 as well as the R6 Option 1 analyses are compared with the experimental results. These are failure avoidance criteria that are intended to underpredict the loads more consistently than the J-estimation schemes.

Material Property Data

The material property data necessary for these analyses are

- elastic modulus, yield strength, and ultimate strength,
- Ramberg-Osgood fit of the stress-strain curve, and
- J-R curve for the material.

Both quasi-static and dynamic tensile data were obtained for each of the Task 1 materials. However, only the quasi-static data were used in these analyses since dynamic data are rarely available for most applications.

The J-R curves used in the analyses were from the monotonic, quasi-static, side-grooved C(T) specimens. Only the J_D-R curves were used in the analyses since that is the practice most commonly followed. Since the crack growth from the C(T) specimens was small compared with the values from the through-wall-cracked pipe experiments, the J-R curves had to be extrapolated using the power-law procedures from Reference 3.17. Details of the Ramberg-Osgood fits of the stress-strain curves and the J-R curves used in these analyses can be found in References 3.1, 3.2, and 3.3.

GE/EPRI Through-Wall Crack Results

The GE/EPRI method (Ref. 3.14) is based upon a compilation of numerical solutions for through-wall cracks in pipes using deformation-theory plasticity. These numerical solutions are cataloged in References 3.14, 3.18, and 3.19 for the various geometric and material parameters encompassing the typical range of in-service nuclear piping. For pure bending of pipes containing through-wall cracks, J is calculated as follows:

$$J = J_e + J_p \qquad (3.4)$$

$$J_e = f_1(a_e, R_m/t)M^2/E \qquad (3.5)$$

$$J_p = \alpha\sigma_o\epsilon_o(b-a)(a/b) \cdot h_1(a/b, n, R_m/t)(M/M_o)^{(n+1)} \qquad (3.6)$$

where,

J_e = elastic component of J
J_p = plastic component of J
R_m = mean pipe radius
t = wall thickness

f_1 = elastic f-function (tabulated in Refs. 3.14, 3.18, and 3.19 for pipes)
M = applied bending moment
E = elastic modulus
M_o = the limit moment for a cracked pipe under pure bending
a_e = plastic-zone size correction to half crack length
σ_o = arbitrary reference stress
b = πR
a = half crack length at the mean radius
ϵ_o = σ_o/E
h_1 = values calculated via numerical methods (tabulated in Refs. 3.14, 3.18, and 3.19)
$\alpha, \sigma_o, \epsilon_o, n$ = parameters in the Ramberg-Osgood stress-strain relations.

The h_1 values are calculated from finite element analyses and are used to determine the plastic contribution to J. Currently, there are only a few values of h_1 for the combined pressure and bending loading condition.

Figure 3.16 displays the ratio of the maximum experimental stress to the predicted stress (based on the GE/EPRI J-estimation scheme) (see Table 3.6) for the 16 through-wall-cracked pipe experiments. This fracture ratio ranges from 0.92 to 1.61. The GE/EPRI J-estimation scheme underpredicted the maximum experimental stresses for 15 of the 16 through-wall-cracked pipe experiments considered. The one exception was Experiment 1.2-6. This was the dynamic, cyclic (R = -1) carbon steel experiment conducted in Subtask 1.2. This demonstrates a generic problem with J-estimation schemes in that they do not include the effect of load reversals, or cyclic load histories, on the crack driving force (i.e., applied J) or the effect of such loading effects on the material's crack growth resistance (i.e., J-R curve). As discussed in Section 3.8.2, there is a definite effect of cyclic loading on the load-carrying capacity for these pipe experiments. Figure 3.16 also shows that the GE/EPRI approach tended to overpredict the results more for the stainless steel experiments than for the carbon steel experiments.

LBB.ENG2 Through-Wall Crack Results

The LBB.ENG2 method (Ref. 3.15) is a circumferential through-wall-cracked pipe J-estimation scheme developed at Battelle as part of the Degraded Piping Program as an alternative to the GE/EPRI (Ref. 3.18), Paris/Tada (Ref. 3.20), and LBB.NRC (Ref. 3.21) methods. The through-wall crack in the LBB.ENG2 method is represented by a pipe section with a reduced wall thickness (t_e) that extends for a distance of $\hat{a}/2$ on either side of the crack plane (see Figure 3.17). The reduced thickness section is an attempt to simulate the reduction in system compliance due to the crack. It is assumed that deformation theory plasticity controls the stress-strain response and that beam theory assumptions hold. Further details on the derivation of the LBB.ENG2 method are provided in Reference 3.15.

Figure 3.18 displays the ratio of the maximum experimental stress to the predicted stress (fracture ratio) based on the LBB.ENG2 J-estimations scheme (see Table 3.6) for the 16 through-wall-cracked pipe experiments. The results for the LBB.ENG2 analysis are very similar to those for the GE/EPRI analysis. The only difference is that the fracture ratios are slightly less for the LBB.ENG2 analysis.

The LBB.ENG2 analysis underpredicted the maximum experimental stress for 13 of the 16 through-wall-cracked experiments. The three exceptions are Experiments 1.2-8, 1.2-4, and 1.2-6. At first the results for Experiment 1.2-8 may appear to be inconsistent with the results for the other two dynamic, monotonic, carbon steel experiments (1.2-11 and 1.2-12). The normalized load-carrying capacity for this experiment was 20-25 percent less than the normalized load-carrying capacity of the other two dynamic, monotonic experiments. However, the effects of dynamic strain aging that are known to affect the dynamic fracture behavior of this carbon steel have also been shown to be highly variable. Evidence for the variability in dynamic strain aging effects was found in a series of hardness tests conducted in the Short Cracks in Piping and Piping Welds Research Program (Ref. 3.9). Thus, the differences in normalized load-carrying capacity between Experiments 1.2-8, 1.2-11, and 1.2-12 are, more than likely, due to variability in dynamic material properties.

The other two experiments in which the maximum experimental stresses were overpredicted by the LBB.ENG2 method are the two cyclic (R = -1) experiments (1.2-4 and 1.2-6). This finding further demonstrates a limitation of these approximate methods in that they do not include the effect of cyclic load histories on either the crack driving force (i.e., applied J) or the material's crack growth resistance (i.e., J-R curve) (see Section 3.8.2).

SC.TNP Surface Crack Results

The SC.TNP method is a surface crack J-estimation scheme developed as part of the Degraded Piping Program (Ref. 3.16). These solutions essentially use the GE/EPRI 360-degree surface-cracked pipe solution (Ref. 3.14) for pure tension to develop new h-functions for the calculation of the plastic component of J, J_p, for finite length surface-cracked pipe in bending.

For these experiments the prediction of the maximum moments or stresses for circumferentially surface-cracked pipe experiments is complicated by the axial tensile stresses. The SC.TNP approach currently does not include the effect of pressure-induced axial tensile stress on the applied J. The effect of internal pressure was addressed in an approximate way by ignoring possible loading path effects on plastic deformation and replacing the axial tension in the uncracked ligament ahead of the crack by an additional equivalent bending moment. The equivalent moment, M_{eq}, from the pressure-induced axial tensile stress was assumed to be the difference between the Net-Section-Collapse predicted moment for pure bending and the Net-Section-Collapse moment for combined bending and pressure.

$$M_{eq} = M_b - M_{p+b} \tag{3.7}$$

Figure 3.19 displays the ratio of the maximum experimental stress to the maximum predicted stress (based on the SC.TNP J-estimation scheme) (see Table 3.7) for the 14 surface-cracked-pipe experiments. (Note in four experiments [4112-6, 1.1-9, 1.1-6, and 1.1-8], no solution for the maximum-load predictions from SC.TNP analysis are available because the h_1 and f_1 functions are outside the valid range of the GE/EPRI tables.) Figure 3.19 shows that the SC.TNP analysis overpredicted the maximum experimental stress in four surface-cracked pipe experiments. (One of these four experiments, EPRI 13S, has a ratio of experiment stress to predicted stress of 0.99. This overprediction is not significant.) The remaining three experiments (1.3-2, 1.3-3, and 1.3-7) for which the SC.TNP approach overpredicted the maximum experimental stresses were the three Subtask 1.3 dynamic pipe system base metal experiments. As discussed previously, this overprediction may be due to a combination of using quasi-static material property data to analyze a dynamic event and potentially from loss of toughness from cyclic loading possibly with combined constraint effects for the surface crack geometry.

The analyses also underpredicted the four weld experiments. The fracture ratios for these experiments range from 1.15 to 1.21. This is probably a consequence of two phenomena. First, the effect of the reinforcement due to the weld crowns is ignored in the analysis. The weld experiments were always analyzed as if the weld crowns were machined off. In actuality they were not machined off. Consequently, the increased ligament due to the weld crown was ignored. Second, any effect of the increased strength of the weld material, with respect to the parent material, was also ignored. The weld metal strength is greater than the base metal strength, but the SC.TNP analysis, as well as the other analysis methods considered, always used the base metal yield and tensile strength properties in the analysis.

3.3 ASME Code and R6 Calculations of Maximum Stress

In Section 3.2 comparisons were made between experimental results and various fracture mechanics analyses typically used to give reasonably accurate predictions. In this section comparisons are made between the pipe experiment maximum loads and predictions from ASME Code and R6 analyses. These analyses are intended to be failure avoidance criteria rather than accurate predictive tools and, hence, should consistently underpredict the experimental results by more than the analyses discussed in Section 3.2.

In the U.S. and many other countries, the ASME Code is used for pipe flaw evaluation procedures (see Section XI Articles IWB-3640 for austenitic steels, and IWB-3650 for ferritic steels). In other countries the R6 analysis procedures are used. Of the three different options in the R6 method, the Option 1 approach is most similar to the ASME Code approach, since R6 Option 1 does not require stress-strain data for the material. The R6 Option 3 method, on the other hand, allows the use of more detailed elastic-plastic fracture mechanics analyses, such as those discussed in Section 3.2.3.

3.3.1 ASME CODE CALCULATIONS

Within Section XI of the ASME Boiler and Pressure Vessel Code flaw evaluation procedures for cracks in austenitic and ferritic piping have been developed. The austenitic pipe flaw evaluation procedures are in Article IWB-3640 and Appendix C of Section XI. These were developed first in 1985 and have been modified to include procedures for evaluation of cracks in lower toughness welds (Refs. 3.22 and 3.23). The ferritic pipe flaw evaluation procedures are given in ASME Section XI Appendix H (Ref. 3.24) as well as in Article IWB-3650.

In this section, validation of the technical bases for the ASME Code IWB-3640 and IWB-3650 involved direct comparison of the experimental stresses with the ASME predicted end-of-life stresses without the ASME applied safety factors (Refs. 3.25 and 3.26). This is referred to as Approach 1. This assesses the source equations used for end-of-life flaw sizes.

A second approach to analyzing these experiments was to follow rigorously the ASME Section XI flaw assessment criteria. This is called Approach 2 and involved comparison of the total stresses allowed for the crack in the experiment with the Code calculated stresses considering the ASME applied safety factors. Determining the Code calculated stresses involved: (a) conducting uncracked pipe stress analyses for each of the experiments, (b) determining the stresses by Section III to determine what safety factors should be used, and (c) applying only the stress components required by the Code. For instance, the full safety factor was applied to pressure, dead-weight, and inertial stresses. Thermal expansion stresses were used without the safety factor, and seismic anchor motion stresses were not included.

Approach 1: Comparison of Actual Experimental Stresses with ASME Predicted Maximum Stresses Without ASME Applied Safety Factors

Calculations of the predicted failure stress were made using the $3S_m$ definition of flow stress in two different manners for distinctly different reasons.

- The first definition of flow stress involves using the S_m defined from Tables I-1.1 and I-1.2 of Section III in the ASME Code. This provides a direct comparison of the experiments with the ASME Code procedures. This is referred to as S_m(Code).

- The second definition of the flow stress was created to evaluate the technical basis of the Code and is an attempt to analyze the experiments as if the pipe sections evaluated had the same strength properties as those defined in Section III of the ASME Code. In the IPIRG Program there was no attempt to procure pipes with minimum Code properties. To account for the pipe evaluated in this program having higher strength than the Code minimum values, an S_m value was calculated using the actual (quasi-static) properties of the pipe tested. The term S_m(Actual) was defined in the spirit of ASME Section III Article 2110 as the lowest of

    - one-third of the actual room temperature ultimate tensile strength (for both ferritic and austenitic pipes)
    - one-third of the actual ultimate strength at the pipe test temperature (for both ferritic and austenitic pipes)
    - two-thirds of the actual yield strength at room temperature (for both ferritic and austenitic pipes)
    - two-thirds of the actual yield strength at the pipe test temperature (for ferritic pipes), or 90 percent of the actual yield strength at the pipe test temperature (for austenitic pipes).

Using this definition, S_m(Actual) accounts for material variability and essentially evaluates every pipe experiment as if the test pipe had the same strength properties as those defined in Section III of the ASME Code.

Stainless Steel Pipe Evaluations

The ASME flaw evaluation procedures (Section XI, Article IWB-3640) for cracks in stainless steel base metal essentially are the same as the Net-Section-Collapse analysis procedure. The Code flaw evaluation methodology provides fracture loads bounded by plastic collapse and LEFM. Upper bound plastic collapse loads appropriate for ductile materials are reduced as the toughness decreases by using the reciprocal of the Z-factor (calculated from ductile fracture considerations) times this collapse load. The major differences between the ASME flaw evaluation procedures and the Net-Section-Collapse analysis are:

(1) The flow stress is defined as $3S_m$ in IWB-3640 rather than the average of the yield and ultimate strengths.

(2) For low toughness flux welds the IWB-3640 procedure uses a stress multiplier, the Z-factor, to account for the lower toughness.

(3) For combined tension and bending the Net-Section-Collapse analysis and the IWB-3640 use slightly different expressions to calculate the shift in the neutral axis, i.e., the β terms differ slightly. For the ASME analysis,

$$\beta = 0.5(\pi - \theta d/t - \pi P_m/\sigma_f) \tag{3.8}$$

and for the Net-Section-Collapse analysis,

$$\beta = 0.5[\pi - \theta d/t - \pi R_i^2 p/(2R_m t\sigma_f)] \ . \tag{3.9}$$

For the stainless steel weld experiments, the base metal S_m values were used. Also for the weld experiments, a Z-factor was included in the analysis, as prescribed in the Code, to account for failure at lower loads resulting from the lower toughness of the SAW. A Z-factor of 1.56 was used.

As with the Net-Section-Collapse and DPZP analyses previously discussed, the results were evaluated on the basis of a fracture ratio, which is the experimental failure stress divided by the predicted failure stress. Stress is considered to be the sum of the bending and axial stresses. For experiments with thermal expansion and seismic anchor motion stresses, these stresses are treated the same as inertial, pressure, and dead-weight stress, i.e., they are all considered as primary stresses.

STAINLESS STEEL SURFACE-CRACKED PIPE. Figures 3.20 and 3.21 display the fracture ratio for the ASME IWB-3640 approach for the stainless steel surface-cracked pipe experiments. The results from Approach 1 and 2 are summarized in Table 3.8. These results do not include the ASME safety factor of 2.77 for Service Level A and B conditions or the 1.39 safety factor for Service Level C and D conditions. Figure 3.20 considers the case where Code values of S_m from Section III of the ASME Code are used to define the flow stress, S_m(Code). Figure 3.21 considers the case where the flow stress is defined on an S_m(Actual) basis.

Figure 3.20 shows that, with two exceptions, the fracture ratios are slightly greater than one for the stainless steel surface-cracked pipe experiments when the S_m(Code) definition of flow stress is used in the analysis. The two exceptions are the two stainless steel base metal, pipe system experiments from Subtask 1.3, i.e., wrought TP304 stainless and aged cast stainless steel base metal experiments. For these two experiments the IWB-3640 procedures overpredicted the experimental failure stresses by 8 to 15 percent. The low value for the CF8M experiment can be explained by the low toughness of this material after the artificial aging. The toughness of this material was closer to the toughness of the stainless steel SAW than of the stainless steel base metal. The ferrite number for this material is such that it could be analyzed using the IWB-3640 procedures. ASME Section XI paragraph IWB-3641(c) further stipulates that for cast stainless steel materials, adequate toughness for the pipe to reach limit-load after aging shall be demonstrated, however, no procedures are defined. Based on the J-estimation scheme analyses on this pipe and crack in Section 3.2, it would not be appropriate to assess this cracked pipe section using the limit-load procedures of IWB-3640. For this particular CF8M pipe, an elastic-plastic analysis is needed. Other CF8M pipes might retain sufficient toughness so that limit-load analyses could be used (Ref. 3.27).

The low fracture ratio for the TP304 base metal experiment, however, is not as explainable since this material has a high toughness in both the quasi-static and dynamic C(T) tests. The relatively low failure stress for this experiment is consistent with the calculated J_i value from this pipe experiment, which was only 15 percent of the average J_i value obtained from the dynamic C(T) specimen tests (see Section 3.4). The J_i value from the pipe experiment was calculated using the η-factor approach (Ref. 3.28).

Predictions of failure stress using an S_m from actual tensile properties at test temperature [S_m(Actual)] show that the dynamic pipe system experiments on stainless steel base metal cracks fail at significantly lower failure stresses than calculated (see Figure 3.21). In fact, if actual properties are used in the analyses of the stainless steel base metal pipe system experiments, the ratio of the experimental stress to the predicted stress is so low (0.66) that the applied safety factor in the ASME Code for emergency and faulted conditions (1.39) is completely eroded.

Although the use of a calculated S_m(Actual) is probably not used in practice, the results of this analysis supports the practice of not using such an approach. Furthermore, these results suggest that the past stainless steel pipe fracture data base should be re-analyzed using the S_m(Actual) approach. Since this approach analyzes the pipe experiments as if all pipes used had the same strength properties as those defined in Section III of the ASME Code, this evaluation could impact changes in the ASME IWB-3640 flaw evaluation analysis.

STAINLESS STEEL THROUGH-WALL-CRACKED PIPE. Figures 3.22 and 3.23 display the fracture ratios for the ASME IWB-3640 approach for the stainless steel through-wall-cracked pipe experiments. These results do not include the ASME safety factors of 1.39 or 2.77 for Service Level C and D or Service Level A and B conditions, respectively. Figure 3.22 considers the case where Code values of S_m from Section III of the ASME Code are used to define the flow stress, S_m(Code). Figure 3.23 considers the case where the flow stress is defined on an S_m(Actual) basis. Even though the ASME Section XI procedures are in-service flaw evaluation procedures and, as such, are primarily of interest for surface cracks, these comparisons with the through-wall-cracked pipe experiments have been used to assess the ASME source equations (Ref. 3.25). The USNRC uses these procedures as the basis for their leak-before-break criterion in Standard Review Plan 3.6.3 (Ref. 3.29).

Figures 3.22 and 3.23 show that the fracture ratios are generally less than one. When Code values of S_m were used to define the flow stress, the ratios ranged from 0.79 to 1.05. When the flow stress was defined on an S_m(Actual) basis, the ratios ranged from 0.74 to 0.98. Note further that in comparing Figure 3.22 with Figure 3.20 it can be seen that the fracture ratios for the through-wall-cracked pipe experiments tended to be generally less than the ratios for the surface-cracked pipe experiments. This is not surprising in light of Figure 3.13, which shows that for limit-load conditions to be met, higher toughness values are required for through-wall-cracked pipe than for surface-cracked pipe. Note also that the experiments considered in Figures 3.22 and 3.23 involved relatively small diameter (6-inch) experiments. Fracture ratios presented in these figures are expected to be even lower if larger diameter pipes are tested. Larger diameter pipes tend to promote contained plasticity which may lower the fracture ratio of any analysis method based on limit-load considerations, such as IWB-3640.

Carbon Steel Pipe Evaluations

The ASME ferritic pipe flaw evaluation procedures are similar to the austenitic procedures. However, the ferritic procedures are slightly more complicated to account for the possibility of failure occurring below the Net-Section-Collapse stress for a flaw in the base metal. The major difference between the ASME ferritic pipe flaw evaluation procedures and the Net-Section-Collapse analysis are

- The flow stress used for the ferritic pipe flaw evaluation procedures is $2.4S_m$.
- For combined tension and bending, the Net-Section-Collapse analysis and the ASME β terms differ slightly (see Eqs. 3.8 and 3.9).
- In the ASME ferritic procedures there is a screening criterion used to assess if limit-load, elastic-plastic fracture, or linear-elastic fracture analyses should be used.
- There is a simple stress multiplier, the Z-factor, used for the elastic-plastic analysis method to account for the lower toughness of the ferritic pipes and their weldments.

CARBON STEEL SURFACE-CRACKED PIPE. Figures 3.24 and 3.25 display the fracture ratios for the ASME IWB-3650 analyses for the carbon steel surface-cracked pipe experiments. These results do not include the ASME Code safety factors of 2.77 for Service Level A and B conditions or 1.39 for Service Level C and D conditions. Figure 3.24 considers the case where Code values of S_m from Section III of the ASME Code are used to define the flow stress, S_m(Code). Figure 3.25 considers the case where the flow stress is defined on an S_m(Actual) basis.

Figure 3.24 shows that the flaw evaluation procedures embodied in IWB-3650 of Section XI of the ASME Code result in very large fracture ratios when the flow stress is based on the Code definition of S_m, i.e., S_m(Code). The fracture ratios for the case when the flow stress is based on actual properties [S_m(Actual)] are somewhat less (see Figure 3.25) but still significantly greater than one.

The large fracture ratio for the IWB-3650 analysis is believed to be caused by the Z-factors being based on through-wall-cracked pipe analyses, where experimentally it has been found that surface-cracked pipe have an apparent higher toughness, possibly due to constraint losses (Ref. 3.30).

CARBON STEEL THROUGH-WALL-CRACKED PIPE. Figures 3.26 and 3.27 display the fracture ratios for the ASME IWB-3650 analysis for the carbon steel through-wall-cracked pipe experiments. These results do not include the ASME safety factors of 1.39 or 2.77 for Service Level C and D or Service Level A and B conditions, respectively. Figure 3.26 considers the case where Code values of S_m from Section III of the ASME Code are used to define the flow stress, S_m(Code). Figure 3.27 considers the case where the flow stress is defined on an S_m(Actual) basis. These comparisons with the through-wall-cracked pipe experiments have been included since the USNRC uses these procedures as the basis for their leak-before-break criterion in Standard Review Plan 3.6.3 (Ref. 3.29).

Figures 3.26 and 3.27 show that when Code values of S_m are used to define the flow stress, the fracture ratios are significantly greater than one. The fracture ratios using the 2.4S_m(Code) definition for flow stress range from 1.36 to 1.93. Comparing Figure 3.26 with Figure 3.24 shows that the fracture ratios for the through-wall-cracked pipe experiments tend to be generally less than the ratios for the surface-cracked pipe experiments. This trend was also seen for the stainless steel experiments and is reflected in Figure 3.13. Also note that the experiments considered in Figures 3.26 and 3.27 were all relatively small diameter (6-inch) experiments. The fracture ratios presented in these figures may be less if larger diameter pipes are tested.

Approach 2: Comparison of ASME Calculated Applied "Experimental" Stresses with ASME Allowable Stresses

The objective of using this approach was to assess the precise ASME Section XI flaw assessment criteria using the Code procedures. Approach 1 evaluated the source equations used in the Code, but not the flaw evaluation procedures used in defining the stresses and safety factors employed.

In Approach 2 the fracture ratio is defined as the calculated ASME applied "experimental" stresses divided by the allowable stresses for the flaw size tested. The procedures used to calculate the ASME applied "experimental" stresses are given below:

(1) For each experiment, use the precise displacement-time history in a linear elastic analysis without a crack to determine the pressure-induced longitudinal stress, the dead-weight stresses, the thermal expansion stresses, the inertial stresses, and the seismic anchor motion stresses.

(2) Break the above stresses into tension, bending and torsion.

   - In Subtask 1.2 experiments, there were only bending stresses. Although these were displacement-controlled experiments, and as such fall more into the category of thermal expansion stresses than primary stresses, they were treated as primary bending stresses. (Note, if treated as seismic anchor motion stresses, then the fracture ratio would be zero for all these experiments.)

   - In the Subtask 1.1 experiments, the only membrane stress was from the pressure contribution, which is considered as a primary membrane stress. The dead-weight and inertial stresses are bending stresses, which are treated as primary bending stresses. There were no thermal expansion, seismic anchor motion, or torsional stresses.

   - In the Subtask 1.3 experiments, the only significant membrane stress was from the pressure contribution which was treated as a primary membrane stress. Dead-weight loads and torsional stresses were negligible. The rest of the stresses had bending contributions only, with the inertial stresses being considered as a primary stress and thermal expansion being a secondary stress. Seismic anchor motion stresses were not included in the ASME analysis.

(3) From the uncracked linear elastic stress analysis, use Equation 9 and either Equation 10 or 11 of ASME Boiler and Pressure Vessel Code Section III Article NB-3653 to determine if the applied stresses are within the limits for Service Level A and B. The thermal expansion and seismic anchor motion stresses are considered in either Equations 10 or 11. Article NB-3654 determines the Service Level C limits, and Article NB-3655 determines the Service Level D limits. Thermal expansion stresses and seismic anchor motion stresses are not included in Level C or D stresses.

(4) If the elastic stresses satisfy Equation 9 and either Equation 10 or 11, then use the Level A and B applied ASME Section XI safety factor of 2.77 in the flaw evaluation procedures. If the stresses are higher, then use the Level C and D applied ASME safety factor of 1.39 in the flaw evaluation procedures.

(5) Compare the applied elastically calculated stresses at failure in the experiment, $(P_b + P_m + P_e/SF)_{Applied}$, with the Code allowable stresses.

The allowable stresses for the flaw size in the experiment, $(P_b + P_m + P_e/SF)_{Allowed}$, were calculated as the sum of the allowable total stresses with safety factors applied for the service level of the experiment using the flaw evaluation procedures in IWB-3640 or 3650, where

$$(P_b + P_m + P_e/SF)_{Allowed} = \frac{P_b' + P_m}{Z \cdot SF} \qquad (3.10a)$$

as per Appendix H of ASME Section XI paragraph H-6320 where

$$P_b = \frac{1}{SF}\left(\frac{P_b'}{Z} - P_e\right) - P_m\left(1 - \frac{1}{Z \cdot SF}\right) \qquad (3.10b)$$

and P_b' is the bending limit-load solution with the axial membrane stress of P_m. (Note: for austenitic base metal, P_e stresses are considered negligible.) When appropriate, the Z factor was included in the $(P_b + P_m + P_e/SF)_{Allowed}$ term. Also note that Equation 9 of Section III was satisfied only for Experiment 1.3-2. Since only Experiment 1.3-2 satisfied the Service Level B stresses, it was analyzed as if it were a Service Level C experiment for consistency with the other experiments. Hence, all experiments were analyzed using a safety factor of 1.39.

For Approach 2, the fracture ratio is defined as

$$\text{Fracture Ratio} = \frac{(P_b + P_m + P_e/SF)_{Applied}}{(P_b + P_m + P_e/SF)_{Allowed}} \frac{1}{SF} \qquad (3.10c)$$

The results from both Approach 1 and Approach 2 are summarized in Table 3.8.

The Approach 2 fracture ratio includes a 1/SF term to normalize the values. Consequently, a value of 1.0 means the experimental results agreed exactly with the ASME analysis procedures with the safety factor of 1.39 being still available in reserve. Values less than 1.0 mean that the safety factor of 1.39 is being eroded. For instance, a fracture ratio of 0.72 (the reciprocal of 1.39) means the entire ASME safety factor is eroded. Values greater than 1.0 mean that there is an additional reserve on the ASME applied safety factor.

Stainless Steel Surface-Cracked Pipe Results

The stainless steel, surface-cracked-pipe, experimental results using Approach 2 are shown in Figure 3.28 and Table 3.8. These results show high "experiment"-to-predicted ratios (fracture ratios) for all but the three pipe system experiments. In the other experiments the Approach 2 fracture ratios are higher than those of Approach 1, using S_m(Code), by a factor of 1.3 to 7.5. This shows the effect of using the elastic uncracked pipe stress analysis. The lower fracture ratios in the pipe system experiments are due to the seismic anchor motion stresses being ignored and the thermal expansion stresses not being treated equally with the primary bending or membrane stresses.

Stainless Steel Through-Wall-Cracked Pipe Results

The stainless steel, through-wall-cracked-pipe results using Approach 2 are shown in Figure 3.29 and Table 3.8. Fracture ratios are very high for all except Experiment 1.1-3. In all experiments, the Approach 2 fracture ratios are higher than the Approach 1 fracture ratios, using S_m(Code), by a factor of 1.7 to over 20. No through-wall-cracked pipe system experiments were conducted that could assess the effect of thermal expansion and seismic anchor motion stresses on the flaw evaluation criteria.

Carbon Steel Surface-Cracked Pipe Results

The carbon steel surface-cracked pipe results are shown in Figure 3.30 and Table 3.8. Fracture ratios are high for all but pipe system Experiment 1.3-2. (Experiment 1.3-2 failed quickly and was driven largely by seismic anchor motions, which were ignored in these ASME analyses.) The other pipe system experiment (1.3-4) has a reasonably high fracture ratio, but it is less than the value from Approach 1 when S_m(Code) is used. In the other experiments, the Approach 2 fracture ratios are higher than the Approach 1 fracture ratios, using S_m(Code), by a factor of 1.1 to 2.2.

Carbon Steel Through-Wall-Cracked Pipe Results

The carbon steel through-wall-cracked pipe results are shown in Figure 3.31 and Table 3.8. Fracture ratios are very high for all except inertial Experiment 1.1-2. In all these experiments, the Approach 2 fracture ratios are higher than the Approach 1 fracture ratios, using S_m(Code), by a factor of 1.2 to 4.4.

Relative Comparisons of Approach 1 and Approach 2

Approach 1 generally results in high fracture ratios which shows that the technical basis equations of the ASME Code underpredict the experimental results. When the experiments were analyzed as if the pipe had Code minimum properties, using S_m(Actual), then there are a number of experimental results that fall below the ASME predictions without safety factors applied.

Approach 2, which rigorously followed the ASME Section XI flaw evaluation procedures, includes the use of an elastic stress analysis. This would normally increase the fracture ratio, assuming there is plasticity in the pipe experiment. However, the pipe system experiments were intentionally designed to force plasticity only in the crack section. Hence, the use of an elastic stress analysis has little effect on these experiments. On the other hand, the seismic anchor motion (SAM) stresses can be significant (see Section 3.6). Ignoring SAM stresses in the analysis can significantly lower the fracture ratio, as it did for Experiment 1.3-2.

Further analyses of the ASME flaw evaluation procedures using Approach 2 are needed. The first step may be to conduct a numerical experiment, where the entire pipe system is analyzed as if it had the same strength as the cracked test section. Nonlinear analysis of the system including modeling the crack response is also needed (see discussion in Section 3.6). These calculations would show if a more realistic system with the IPIRG pipe system geometry and loading conditions would still have ASME Approach 2 fracture ratios less than one. Future experiments with more realistic seismic loading and shorter flaws may also be needed to verify the ASME flaw evaluation procedures.

3.3.2 R6 ANALYSIS

The R6 method is a failure avoidance criterion developed by CEGB (now Nuclear Electric) (Refs. 3.31, 3.32 and 3.33). The most recent refinement is referred to as R6 Revision 3 (Ref. 3.33). Within this version there are three options. The first option is the simplest and does not require the use of the material stress-strain curve as input. The second option requires the use of the material stress-strain curve and, hence, is slightly more complicated. The third option allows the use of any appropriate elastic-plastic fracture mechanics analysis, such as GE/EPRI or SC.TNP, to create the appropriate failure assessment curve. In this last option, the R6 method essentially would give the predictions that are given in Section 3.2.3, which describes J-estimation scheme results. In this section, predictions using the Option 1 method are compared with the experimental results on the basis of the ratio of the experimental-to-predicted stresses (the fracture ratio). Similar to the ASME analyses, two different approaches were used.

Approach 1: Actual experimental-to-predicted stresses.

> This approach compares the actual experimental stresses at maximum load with the R6 Option 1 predicted stresses. This is the same type of comparisons used in the R6 Validation document, Ref. 3.33, which used past Degraded Piping Program pipe fracture experiments (Ref. 3.4). This same approach was also used in the round-robin analyses in Section 2.5.2 (Round-Robin Problems 1, 2-1, 3-2b, and 5-1a).

Approach 2: Elastically calculated "experimental"-to-predicted stresses (strict R6 procedures).

> This approach follows the strict guidelines of the R6 Option 1 method in Ref. 3.33. This involved analyzing each experiment as if a flaw assessment were being conducted. Elastic uncracked-pipe stress analyses were conducted for the applied displacements at maximum load in the experiments. These elastically calculated "experimental" stresses were then compared with the R6 Option 1 predicted failure stresses. This approach generally gives higher "experimental"-to-predicted ratios than when using the actual experimental stresses (Approach 1).

These approaches are described in more detail later.

R6 Rev. 3 Option 1 Procedure to Calculate Predicted Failure Stresses

In the Option 1 procedure, a fixed failure assessment curve is used for any material, crack, or structural geometry. The failure assessment curve has a load or stress ratio (L_r or S_r) along the x-axis of a graph and toughness ratio (K_r or J_r) along the y axis (see Figure 3.32).

The load ratio, or L_r term, is the applied load divided by the limit load. The limit load is the load predicted by Net-Section-Collapse analysis for circumferentially cracked pipe. For a pipe under pressure and bending, such as the Subtask 1.1 inertial experiments and the Subtask 1.3 pipe system experiments, this ratio can be interpreted as the total applied stress (bending plus tension from the pressure) divided by the Net-Section-Collapse-predicted bending stress plus tension from the pressure.

$$L_r = (\sigma_b + \sigma_t)/(\sigma_{bNSC} + \sigma_t) \qquad (3.11)$$

or, the ratio being the bending stress divided by the Net-Section-Collapse-predicted bending stress.

$$L_r = \sigma_b/\sigma_{bNSC} \qquad (3.12)$$

where,

σ_b = MR_o/I (3.13a)
M = bending moment
R_o = outside radius
I = $\pi R_m^3 t$ (3.13b)
t = pipe thickness
σ_t = $R_i^2 p_i/(R_o^2 - R_i^2)$ (3.13c)
R_i = inside radius
R_m = mean radius
p_i = internal pressure

and,

$$\sigma_{bNSC} = (2\sigma_y/\pi)[2\sin\beta - (d/t)\sin\theta] \qquad (3.14)$$

where,

σ_y = yield strength
d = surface crack depth
θ = half of surface crack length
β = $[\pi - \theta(d/t)]/2 - \pi(R_i^2 p_i)/(4R_m t\sigma_y)$. (3.15)

Note that in the R6 method, the yield strength, not the flow stress, is used in the limit-load equation. The ratio of the flow stress to the yield strength can be used as the cut-off point along the L_r axis to be consistent with Net-Section-Collapse analyses, at least for the case of pure bending. For combined pressure and bending, there can be a significant difference in the limit-load solutions from the R6 approach and the Net-Section-Collapse analysis. This is due to the Net-Section-Collapse analysis using the flow stress in the β term, where the R6 procedure uses the yield strength.

The toughness, or K_r term, is the ratio of the applied linear elastic stress intensity factor, K_I, to the toughness of the material, $K_r(a)$. $K_r(a)$ can be a function of crack growth derived from the J-R curve of the material.

$$K_r = K_I/K_r(a) \qquad (3.16)$$

where,

$$K_r(a) = (JE)^{0.5} \qquad (3.17)$$

and,

J = the value of J for the corresponding Δa from the J-R curve of the material.
E = Elastic modulus

$$K_I = K_{Im} + K_{Ib} \tag{3.18}$$

where, the K_{Im} and K_{Ib} terms are defined in this report by the solutions given in the ASME Section XI ferritic pipe flaw evaluation criteria, Article IWB-3650 (Ref. 3.24).

The Option 1 failure assessment curve, K_r-L_r curve, has the following relationship.

$$K_r = (1 - 0.14L_r^2)[0.3 + 0.7\exp(-0.65L_r^6)] \tag{3.19}$$

The failure assessment curve for Option 1 is illustrated in Figure 3.32. Note that on the L_r axis there is a cut-off stress that is frequently defined as the ratio of the flow stress to the yield strength.

Normally in a design situation, L_r and K_r would be calculated using applied stress, yield strength, etc. This point would be plotted on the failure assessment diagram. If the point falls under the curve it would be considered safe. If it is above the curve it would be a failure. The reserve factor is generally calculated as the distance from the origin of the graph through the point to the failure assessment curve (Point B) divided by the distance from the origin to point being assessed (Point A) (see Figure 3.32). This assumes that all stresses are proportional, which may not be true for the combined pressure and bending experiments from Subtasks 1.1 and 1.3 being evaluated in this report.

For these experiments, the reserve factor on the moment with constant pressure is of interest. This makes the definition of the L_r term important. In the analyses conducted, the definition of the L_r term used was that in Equation 3.12. This gives the reserve factor on the moment but requires a second calculation to determine the intercept of the K_r/L_r line, since at zero bending stress a low toughness pipe or pipe with a large flaw could fail under the internal pressure. That is, the point would be along the y-axis on the failure assessment diagram.

The σ_b on the failure assessment curve can be obtained directly using the following procedure. The K_r term takes the form of

$$K_r = A_1\sigma_b + A_2 \tag{3.20}$$

where

$A_1 = (\pi a)^{0.5}F_b/K_r(a)$
$A_2 = K_{Im}/K_r(a)$

where

$F_b = K_{Ib}/\sigma_b(\pi a)^{0.5}$ as defined in the ASME Section XI ferritic pipe flaw evaluation criteria, Article IWB-3650.

If we define L_r in the form of

$$L_r = \sigma_b/A_3 \tag{3.21}$$

where

$$A_3 = \sigma_{bNSC} \tag{3.22}$$

then combining Equations 3.17 and 3.18 gives

$$K_r = A_1A_3L_r + A_2 \quad . \tag{3.23}$$

Combining Equations 3.16 and 3.19 eliminates K_r and gives terms involving only L_r

$$A_1A_3L_r + A_2 = (1 - 0.14L_r^2)[0.3 + 0.7\exp(-0.65L_r^6)] \quad . \tag{3.24}$$

The term L_r is obtained by numerical iteration, and then σ_b is determined for a point on the failure assessment diagram from the L_r value.

In the calculations the quasi-static J_D-R curve at the pipe test temperature was used. The yield strength used was the average of the quasi-static tests at the pipe test temperature. The cut-off point on the S_r axis was taken as the ratio of the flow stress to the yield strength, where the flow stress is the average of the yield and ultimate strengths. For the case of a crack in a weld, the base metal strength and the weld metal J_D-R curve was used.

Moments at crack initiation and maximum load were calculated. In the maximum load calculations, the crack growth was incremented causing the $K_r(a)$ to increase, K_I to increase, and σ_{bNSC} to decrease. Further details of these calculations can be found in References 3.1, 3.2, and 3.3.

Results

Using the analysis procedure described above, the predicted failure points from the R6 Revision 3 Option 1 analysis procedure were determined. Comparison of the experimental and predicted failure stresses used two different approaches to define the experimental (or elastically applied) failure stresses. Approach 1 involves using the actual experimental stresses, while Approach 2 follows strict R6 guidelines and involves using elastically calculated stresses of uncracked pipe.

Approach 1: Comparison of Actual Experimental Failure Stresses with R6 Option 1 Predictions.

> The fracture ratios (experimental-to-predicted stresses) were determined for maximum load (stresses include the pressure-induced axial tensile stress). Also note that the experimental stresses in these comparisons are considered as primary stresses. That is, thermal expansion and seismic anchor motion stresses are considered to be primary stresses as are pressure, dead-weight, and inertial stresses. The thermal expansion and seismic anchor motion stresses are considered as primary stresses, since there is significant elastic follow-up and the stresses are not self-equilibrating in the plane of the crack (as required by Section 5.2 in Reference 3.33). Hence, all experimental bending and tensile stresses are considered as primary for comparison with the R6 Option 1 predicted values. All analyses used the quasi-static monotonic J_D-R curves and the quasi-static yield strength values. For experiments with cracks in welds, the welding residual stresses were unknown and hence, ignored in the fracture analyses.

UNPRESSURIZED THROUGH-WALL-CRACKED PIPE EXPERIMENTS. The R6 analysis results are compared with the experimental data as given in Table 3.9 and Figures 3.33 and 3.34 for all the Task 1 experiments. The unpressurized experiments are the Subtask 1.2 experiments and one Degraded Piping Program experiment. The R6 analysis is relatively simple for a pure bending load.

The results for the thirteen unpressurized TWC experiments (Table 3.9 and Figure 3.33) show that the fracture ratio for the R6 analysis method using Approach 1 ranges from 1.07 to 1.54. (As discussed later, the fracture ratios for the three pressurized TWC experiments were higher, ranging from 1.43 to 2.30.) The lowest case was for the fully reversed cyclic bending of the carbon steel pipe. The fracture ratio is relatively low for this experiment because the monotonic J_D-R curve used in the analysis does not account for the degradation from cyclic loading. This point is discussed in detail in Section 3.8.2. (Additional R6 analyses of other Degraded Piping Program unpressurized TWC experiments from IPIRG round-robin efforts are discussed in Section 2.5.2.)

PRESSURIZED THROUGH-WALL-CRACKED PIPE EXPERIMENTS. Results from three experiments on through-wall-cracked pipe with internal pressure are presented in Table 3.9 and Figure 3.33. Two of these are for Subtask 1.1 pressurized inertial experiments, and one is for a quasi-static Degraded Piping Program experiment for the same stainless steel pipe as used for Experiment 1.1-3.

The results for these three experiments show that the fracture ratio in the R6 analysis method using Approach 1, which range from 1.43 to 2.30, is higher on average than for the unpressurized TWC experiments. The higher values may be due to the β term (see Eq. 3.15). For pressurized pipe, the R6 analysis uses the yield strength in the β term. This affects the calculated limit-load stress, which affects the L_r term. Using the yield strength in the β term results in a greater underprediction of load than a strict Net-Section-Collapse analysis that uses the flow stress in the β term (see Ref. 3.3).

UNPRESSURIZED SURFACE-CRACKED PIPE EXPERIMENTS. Results of four unpressurized surface-cracked pipe experiments are given in Table 3.9 and Figure 3.34. Two are for companion experiments to the Subtask 1.1 pressurized inertial experiments on surface-cracked pipe, and two are for companion experiments to Subtask 1.3 pipe system experiments. All experiments involved quasi-static monotonic loading.

The results for these four surface-cracked pipe experiments show that the fracture ratio in the R6 analysis method using Approach 1, which ranged from 1.33 to 1.53, was higher on average than for the unpressurized TWC experiments. The higher values for SC experiments are consistent with observations from the DPZP analysis, which suggests that surface-cracked pipe has a higher apparent toughness than through-wall-cracked pipe.

PRESSURIZED SURFACE-CRACKED PIPE EXPERIMENTS. Results of 13 pressurized surface-cracked pipe experiments are given in Table 3.9 and Figure 3.34. The results for these 13 experiments show that the fracture ratio in the R6 analysis method using Approach 1, which ranged from 1.11 to 3.43, was more variable than for the unpressurized TWC experiments. The lowest value was for the A106 B pipe system experiment (1.3-2). The very high value was for a Degraded Piping Program quasi-static companion experiment to a Subtask 1.1 stainless steel base metal experiment (1.1-5). (The internal pipe pressure for this quasi-static experiment was 24.5 MPa [3,550 psi] and was the highest of any of the experiments considered in this analysis.) It is interesting to note that several of the quasi-static companion experiments to the Subtask 1.3 pipe system experiments have higher fracture ratios than for the Subtask 1.3 experiments. This observation is discussed in Section 3.8.

Additional R6 predictions from IPIRG round-robin efforts using experimental stresses to R6 predicted stresses without uncracked elastic stress analysis are also given in Section 2.5.2 for various circumferential through-wall-cracked pipe bending experiments: (Round-Robin Problem 1), Experiments 4143-1 (Round-Robin Problem 2-1), and Experiment 1.3-3 (Round-Robin Problems 5-1 and 6-2).

Approach 2: Comparison of Elastic Stresses from Experimental Displacements with R6 Option 1 Predictions (Strict R6 Procedures).

The predictions in this section strictly follow the R6 Option 1 requirements of using uncracked pipe linear elastic stress analysis for a flaw evaluation. The procedures used were

(1) Classification of stresses: All stresses are treated as primary. This includes pressure, dead-weight, inertial, thermal expansion and seismic anchor motion stresses. The thermal expansion and seismic anchor motion stresses are treated as primary since, according to the R6 document, "there is significant elastic follow-up" and they "are not self-equilibrating on the section containing the crack" (Section 5.2 of Ref. 3.33). Welding residual stresses were not determined and hence, ignored for the few weld experiments.

(2) The R6 predicted bending moment at failure is calculated using the same procedures as for Approach 1 (i.e., Equations 3.12 through 3.24 were used). The actual quasi-static properties were used.

(3) The elastically calculated "experimental failure" moment to be compared with the R6 predicted bending moment (from Step 2) is determined using the R6 document for making a flaw assessment. In the R6 Option 1 method, elastic stress analysis of the uncracked structure is required (Section 5.1 of Ref. 3.33).

    (a) For the Subtask 1.2 displacement-controlled experiments, linear elastic stresses were calculated using simple beam solutions for uncracked pipe. The elastic stresses were calculated for the experimental displacements at maximum load. These experiments were unpressurized.

    (b) For the Subtask 1.1 inertial experiments, moments calculated on an elastic basis at the time (displacement) of failure in the experiments were determined using the exact experimental displacement-time history as input to the ANSYS® code. Uncracked pipe linear elastic analyses were conducted up to the time at which maximum load occurred in the experiments. Internal pressure was included.

    (c) For the Subtask 1.3 pipe system experiments, moments were calculated the same as for Subtask 1.1 experiments except that thermal expansion stresses were also included.

These elastic calculated "experimental maximum stresses" were then compared with the R6 Option 1 predictions from Step 2.

Note that the above approach uses the R6 Option 1 method for each experiment as if it were a flaw assessment criterion. Also note that the experimental moments determined from strain gages on the piping system are not directly compared with the R6 moments as was done in Approach 1. Since the elastically calculated moments are generally higher than the measured values, the "experimental"-to-predicted ratio (fracture ratio) for the R6 method using Approach 2 will generally increase from the values in Approach 1.

UNPRESSURIZED THROUGH-WALL-CRACKED PIPE RESULTS. Table 3.9 summarizes the R6 predictions for both Approach 1 and 2. The through-wall crack experimental results for Approach 2 are shown in Figure 3.35. Table 3.9 shows that the elastic uncracked pipe stress analysis procedure (Approach 2) significantly increased the fracture ratios for the R6 Option 1 predictions. The fracture ratios for the through-wall-cracked pipe using Approach 2 were 3 to 20 times larger than the fracture ratios using Approach 1. This is believed to be mainly due to the relatively short length of pipe with larger differences from uncracked pipe displacements to the cracked pipe displacements. For a through-wall crack, there can be large differences between the elastic displacements of the uncracked pipe and the cracked pipe. The uncracked pipe elastic displacements will differ further due to the plasticity from the through-wall crack. As expected, the through-wall-cracked stainless steel pipe had the largest fracture ratios, which ranged from 9.3 to 30.4.

PRESSURIZED THROUGH-WALL-CRACKED PIPE RESULTS. There are only three experiments of this type in Table 3.9 and Figure 3.35. Two of these were the inertial experiments from Subtask 1.1. The other experiment was a Degraded Piping Program experiment with a shorter length of pipe. The fracture ratios for Approach 2 are higher than those for Approach 1 for all experiments. The increase in the fracture ratio using Approach 2 over that in Approach 1 is a factor of 1.2 and 1.7 for the two IPIRG experiments and is 9.6 for the shorter length Degraded Piping Program experiment (4131-1). The smaller Approach 2 fracture ratios for the IPIRG experiments are probably due to the fact that the Subtask 1.1 experiments used a much longer pipe length than the pipe lengths used in either the Subtask 1.2 unpressurized TWC experiments or the pipe length used in Experiment 4131-1.

UNPRESSURIZED SURFACE-CRACKED PIPE RESULTS. The results of the analysis of the four unpressurized surface-cracked pipe experiments are shown in Figure 3.36 and Table 3.9. The Approach 2 procedure increased the fracture ratios from Approach 1, and the effect was greater for the stainless steel test with the shortest pipe length, Experiment 4112-3. The fracture ratios for the unpressurized surface-cracked pipe using Approach 2 were 1.4 to 7.5 times larger than those of Approach 1.

PRESSURIZED SURFACE-CRACKED PIPE RESULTS. There are 13 pressurized surface crack experiments in Table 3.9 and Figure 3.36. Five of these are for the nominal 6-inch diameter pipe from either IPIRG Subtask 1.1 or a test on the same pipe material from the Degraded Piping Program. Of these the only experiment with a high fracture ratio for the Approach 2 assessment was the stainless steel experiment from the Degraded Piping Program, Experiment 4131-2. This experiment had a much smaller pipe length than the IPIRG Subtask 1.1 pipe experiments.

The rest of the experiments in this category were on 16-inch nominal diameter pipe. Five of these were IPIRG pipe system experiments, and three were companion quasi-static pipe experiments conducted in four-point bending from the Degraded Piping Program. The IPIRG pipe system has a length of approximately 30.5 meters, whereas the Degraded Piping Program experiments involved a pipe length of 11.6 meters. Both pipe lengths are relatively large compared with the Subtask 1.2 experiment length of 1.5 meters.

Of the IPIRG pipe system experiments, only Experiment 1.3-2 had a lower fracture ratio using Approach 2 than Approach 1. This may be due to slight approximations in the elastic stress analysis and the fact that the experimental stresses were sufficiently low (due to the large flaw and low toughness) that essentially elastic conditions existed everywhere but at the crack. Even the crack-opening displacements were relatively small due to the low toughness.

In comparing the IPIRG pipe system experiments with their companion quasi-static experiments (including Experiment 1.3-2 to 4112-8 and Experiment 1.3-3 to 13S) the IPIRG pipe system experiments had lower fracture ratios than the quasi-static tests using either approach with the exception of the A106 SAW experiments. The higher A106 SAW pipe system result is partially explained by the fact that the weld material had significantly higher toughness at dynamic rates than at quasi-static rates. Also, the absolute value of the stresses in the A106 SAW IPIRG pipe system experiment was the highest of all the IPIRG pipe system experiments, hence some small-scale yielding may have occurred in the experiment.

Comments on R6 Approach 1 and Approach 2 Results

Approach 1 was used to compare experimental data directly with predictions of the R6 method. As in the ASME Section XI Approach 1, this approach documents the technical basis of the R6 procedure, but not all of the flaw evaluation procedure. Approach 2 involved strict compliance with the R6 flaw assessment procedures, which generally includes an increased amount of conservatism due to the reliance on elastic uncracked stress analysis. Fracture ratios (experiment-to-predicted stresses) from the Approach 2 method are crack size and system dependent. Tests from through-wall cracks in short pipe lengths can give very high fracture ratios using Approach 2 that are not representative of surface cracks in a larger piping system. However, if shorter crack lengths were tested in an IPIRG pipe system experiment, there would have been more plasticity in the uncracked pipe (and elbows), which would significantly increase the elastically calculated stresses from the experiments. This is discussed further in Section 3.6.1 on elastic stress ratios from analysis of the IPIRG pipe systems.

3.4 J-R Curves from Specimens and Pipe Experiments

A basic question addressed in this program was "Are standard laboratory specimen toughness values representative of toughness in cracked pipe?" To address this, the η-factor analysis was used to determine J-R curves from a number of the through-wall-cracked pipe experiments and the value of J at crack initiation (J_i) for a number of the surface-cracked pipe experiments. These results are then compared with the C(T) specimen results.

The η-factor analysis is a general analytical procedure where the fracture resistance is calculated using the experimental load-displacement (or moment-rotation) and crack growth data from the pipe experiment. It is used in lieu of three-dimensional finite element analyses. The analysis method was first developed by Zahoor (Ref. 3.34) for through-wall-cracked pipe. Since Zahoor's initial formulation, a number of improvements have been made (Ref. 3.35). Pan extended the method to consider the case of a surface crack in a pipe (Ref. 3.28).

The η-factor analysis determines J by dividing it into its elastic and plastic components.

$$J = J_e + J_p \tag{3.25}$$

The elastic contribution of J ,J_e, is obtained from handbook solutions (Ref. 3.24). The plastic contribution of J ,J_p, is derived by integrating the area under the experimental load-displacement, or moment-rotation, curve. The result of that integration is multiplied by a constant η:

$$J_p = \eta \int_0^{\phi_i} M d\phi_p^c \tag{3.26}$$

where,

$\phi_p{}^c$ = the plastic component of the rotation due to the crack.

The term, η, is geometry dependent. Specific terms for both through-wall cracks and surface cracks are found in References 3.35 and 3.28, respectively. The above formulation is for a stationary crack. Once crack growth starts, the η-factor varies with crack size and a crack-growth correction is needed.

Note that the η-factor solution is for a pipe in pure bending. However, the Subtask 1.1 and 1.3 experiments involve combined pressure and bending. To account for the pressure in the η-factor J_p solution, an equivalent moment, M_{eq}, due to the pressure was calculated. This was accomplished using the Net-Section-Collapse equations for a crack in a pipe and solving for the failure moment for the case of pure bending and for the case of combined pressure and bending. The difference between the two solutions is considered the equivalent moment due to the internal pressure, M_{eq}. This equivalent moment was added to the experimental moments in the moment-rotation relationship to give a total equivalent moment as if the pipe were subjected to pure bending.

In addition, the η-factor approach assumes Mode I behavior of the material. Since the carbon steel through-wall-cracked experiments typically exhibit out-of-plane crack growth behavior, a modified crack length was used. The modified crack length is the length of the crack projected back into the initial circumferential crack plane. It is believed that this projected crack length is a better representation of the fracture resistance under Mode I loading conditions than the actual crack length would be, since the projected length is more consistent with the remaining ligament. Since the stainless steel pipe fracture experiments did not exhibit significant out-of-plane crack growth, the actual crack length was used in the analysis of those experiments.

For analyzing the cyclically loaded pipe experiments, the upper envelope of the load-displacement curves was used. Technically this is not strictly correct, but it represents an engineering approximation.

3.4.1 THROUGH-WALL-CRACKED PIPE EXPERIMENTS

The J-R curves were calculated for most of the through-wall crack pipe experiments. The results are given in the following sections.

Carbon Steel Pipe J-R Curves

The J-R curves for the carbon steel through-wall-cracked experiments from Subtask 1.2 are provided in Figure 3.37. For comparison purposes the results from the C(T) specimen tests are also included. The C(T) specimen J-R curves are based on the deformation theory of J ,J_D, using the procedures specified in ASTM E1152. The trend of these results shows that both dynamic loading rates and cyclic loading tend to decrease the apparent fracture resistance of the material for most of the pipe experiments. The one exception is Experiment 1.2-2 (QS, R = 0), which shows a slightly higher fracture resistance than that of Experiment 1.2-7 (QS, monotonic). One possible reason for this discrepancy is that the crack for Experiment 1.2-2 grew at a 60-degree angle from the crack plane. This angled crack growth in the pure bending pipe experiments may tend to raise the J-R curve in that a larger amount of actual crack growth occurred, and an associated larger amount of energy expended (i.e., increased J), for the same projected crack length.

The C(T) specimen J-R curves are generally lower than the pipe specimen J-R curves. The exception to this is the R = -1 pipe J-R curve. Note that the C(T) specimens were side-grooved, which forced the crack growth to occur in the circumferential plane.

C(T) specimens are generally believed to give lower J-R curves than pipe specimens (Refs. 3.11, 3.36, and 3.37). Consequently, for the same loading history the side-grooved specimen results are expected to be lower than the results for the pipe specimens. Figure 3.37 shows that this is indeed the case.

Stainless Steel Pipe J-R Curves

The J-R curves for the stainless steel through-wall-cracked experiments from Subtasks 1.2 are presented in Figure 3.38. The results from the C(T) specimen tests for this material are also included for comparison purposes. The results indicate that the fracture resistance of this stainless steel material is not significantly affected by dynamic loading rates or R = 0 cyclic loading. However, the results do indicate that fully reversed cyclic loading (R = -1) does significantly reduce the fracture resistance of this stainless steel material.

As is typically expected, the side-grooved C(T) specimen results are somewhat lower than the results for the pipe specimens for the same loading conditions. Note also that the J-R curve for the dynamic monotonic pipe experiment is higher than the J-R curve for the quasi-static monotonic pipe experiment. This trend is consistent with the observation that the J-R curve for the dynamic monotonic C(T) specimen is higher than the J-R curve for the quasi-static monotonic C(T) specimen.

Note, no C(T) specimen tests with cyclic loading histories were conducted on these materials. Consequently, a direct comparison could not be made between C(T) specimen results and pipe specimen results for the cyclic loading experiments.

In summary, for a given loading history the side-grooved C(T) specimen J-R curves are slightly lower than the through-wall-cracked pipe J-R curves. Similar trends have been reported elsewhere (Refs. 3.11, 3.36, and 3.37). Consequently, the use of C(T) specimen data to predict the fracture behavior of a pipe section containing a through-wall crack should underestimate the fracture resistance. However, for the R = -1 loading history, the monotonically loaded side-grooved C(T) specimen J-R curves did not give a lower bound. Hence, in order to consistently underpredict the fracture response of a cracked-pipe section subjected to cyclic loadings, cyclically loaded C(T) specimen data or analytical corrections may be required.

The foregoing discussions consider cyclic loading effects on the basis of a single parameter, load ratio (R). However, the incremental plastic displacement is known to be another cyclic parameter that plays a controlling role and interacts with load ratio. These parameters are discussed in more detail in Section 3.8.2.

3.4.2 SURFACE-CRACKED PIPE EXPERIMENTS

For the surface-cracked pipe experiments from Subtask 1.3 it was not deemed appropriate to calculate full J-R curves due to the non-uniform crack-growth pattern along the length of the surface crack.

Consequently, only the values of J at crack initiation were calculated for these surface-cracked pipe experiments.

Stainless Steel Surface-Cracked Pipe J_i Values

The values of J at crack initiation for the three stainless steel base-metal surface-cracked pipe experiments from Subtask 1.3, along with the results from the quasi-static and dynamic C(T) specimen tests for the applicable materials, are presented in Table 3.10. The value of J_i from the stainless steel base metal experiment is four to seven times less than the value of J_i from the C(T) specimen tests. Conversely, the J_i values from the stainless steel SAW agree well with the results from the applicable C(T) specimen tests. For the cast stainless steel pipe the dynamic J_{Ic} values were much higher than the quasi-static values from C(T) tests. The pipe J_i value was expected to agree better with the dynamic C(T) specimen, but it was lower than expected.

The low J_i value determined for the stainless steel base metal experiment supports the observation that this pipe system experiment had a lower failure stress when compared with the results from the corresponding quasi-static pipe experiment. If this lower value of J_i from the pipe experiment is used in the DPZP analysis the data point for the dynamic stainless steel base metal experiment (Experiment 1.3-3) agrees much better with the rest of the experimental data (Figure 3.39).

Another point supporting the accuracy of the lower J_i value from the Subtask 1.3 stainless steel pipe experiment comes from a comparison of the SC.TNP (Ref. 3.16) calculated moment-rotation curves with the experimental results. The pipe J_i value was used with the C(T) specimen dJ/da values to construct a new J-R curve. The new J-R curve was used to calculate the moment-rotation curve using the SC.TNP analysis. A comparison of the experimental and SC.TNP moment-rotation curves is shown in Figure 3.40 This shows the maximum loads are extremely well predicted and the maximum rotations are more accurate but still slightly overpredicted.

These observations raise the question of how well C(T) specimen data can represent the fracture response of a material in a piping system under dynamic cyclic loading. In contrast to the conclusions reached from the through-wall-cracked pipe experiments, using C(T) specimen data to predict the fracture behavior of a pipe section containing a surface crack may overestimate the fracture resistance.

Presently, we can only speculate that the differences may be due to cyclic loading possibly involving constraint effects. Prior evaluations of cyclic loading effects (Ref. 3.2) suggested a trend for through-wall-cracked stainless steel pipe. These results suggested that the surface-cracked pipe load histories were not severe enough to degrade the toughness. However, these η-factor J_i values from the pipe experiments suggest otherwise. Clearly cyclic effects on surface-cracked pipe need to be evaluated further.

3.5 Examination of Rotation Data at Crack Initiation and Maximum Load

In addition to examining maximum loads (Section 3.2) and J values from pipe experiments relative to C(T) specimens (Section 3.4), the pipe rotations due to the crack are assessed for conditions of crack initiation and maximum load. Table 3.11 summarizes the values used in this assessment. Note that in several experiments the rotation data do not exist, or the initiation could not be determined. (The rotation values listed are for half of the total rotation, since half rotation is the parameter most frequently used in fracture analyses.)

The first examination of the results involved assessing the rotations of all Task 1 data. This was done by comparing the experimental stress normalized by the Net-Section-Collapse stress with the rotation values. The normalized stress at crack initiation was compared with the rotation at crack initiation, and the normalized stress at maximum load was compared with the rotation at maximum load. These results are shown in Figure 3.41. Here the surface crack (SC) and through-wall crack (TWC) data are separately indicated at crack initiation and maximum load. The results are as expected. For higher rotations (tougher materials), the experimental stresses are comparable to the Net-Section-Collapse stresses, and as the rotations (toughness) decrease, the failure stresses decrease.

Figures 3.42 and 3.43 show the same data plotted separately for through-wall cracks and surface cracks, respectively. Results of experiments shown in Figure 3.42 are for nominal 6-inch diameter pipe with through-wall-crack lengths of 37-percent of the circumference. The results are identified for monotonic, R = 0, and R = -1 loading. The inertial experiments were included in the R = 0 grouping. Crack initiation and maximum loads are also identified. No distinction was made between quasi-static and dynamic loading, but this information can be found in Table 3.11. These results show a relatively tight scatter band. As expected, the monotonic and R = 0 experiments have the highest failure loads and greater rotations, whereas the R = -1 experiments have the lowest rotations and failure stresses.

Figure 3.43 shows the surface-cracked pipe rotation data. Note that there is a scale change on the rotation axis between Figures 3.42 and 3.43. In general the surface-cracked pipe had higher experimental failure stresses (normalized by Net-Section-Collapse stresses) for the same rotation as the through-wall-cracked pipe. There is one data point that is outside the trend of the other experiments. This is for Experiment 1.1-8, which was an inertial experiment that had very irregular asymmetric loading.

As a general conclusion, the initiation and maximum load rotations tend to follow a similar trend curve. However the trend curves for the through-wall-cracked pipe and surface-cracked pipe are quite different in the lower rotation region where elastic-plastic fracture behavior occurs. As a point of comparison the curves are very similar in shape to the Dimensionless Plastic-Zone screening criteria (compare Figure 3.13). In fact, fully plastic conditions appear to be reached for the TWC case at 0.03 radians, whereas for the SC case, fully plastic conditions are reached for rotation larger than 0.004 radians. This difference in fully plastic behavior is scaled to that for the Dimensionless Plastic-Zone screening criterion in Figure 3.13; however, the absolute values of rotation will probably vary with crack geometry.

3.6 Dynamic Finite Element Analyses of Pipe System Experiments

3.6.1 ELASTIC STRESS ANALYSES

In the design of nuclear plant piping systems, elastic stress analysis is used for engineering design purposes. Seismic loads are determined by the response spectrum method, which involves modal analysis. Typically, the seismic anchor motion (SAM)* stresses are not included. If nonlinear behavior occurs in a plant or in an experiment, the actual stresses or moments would nominally be expected to be less than the elastically calculated values. Figure 3.44 illustrates this point. The degree to which the elastic analysis overpredicts the stresses depends on the components of stress that are considered.

Recent work in the EPRI/USNRC Piping and Fitting Dynamic Reliability Program involved defining the failure mechanism for uncracked pipe subjected to seismic loading (Ref. 3.38). These experiments involved carbon and stainless steel small-diameter pipe tested at ambient temperature. One pipe system experiment on 6-inch-diameter carbon steel produced failure at a load level 34 times greater than that permitted by the ASME Code (Ref. 3.39). The experiments also showed that the failure mechanism was by ratcheting and eventual fatigue, rather than by collapse. This work has resulted in proposed changes to the ASME piping design stress analysis procedures to increase allowables.

The differences between elastic calculated values and real nonlinear behavior affects the fracture ratio as noted in the ASME Section XI and R6 Approach 2 results in Section 3.3.

Elastic Stress Ratio

Various comparisons of calculated stress with experimental values can be made depending upon the components of load or stress included in the values. Four possible combinations of loads are

---

* SAM stresses arise during a seismic event due to differential displacements of two pipe anchors. These are displacement-controlled stresses rather than inertially controlled stresses.

- total bending moment,
- total stress (nominal bending stress plus pressure induced axial stress),
- total stress minus seismic anchor motion stress (total stress minus the bending stress caused by static displacement), and
- inertial moment (total moment minus the moment caused by static displacement).

Results are compared on the basis of an elastic stress ratio, which is determined by dividing the elastically calculated stress or load for uncracked pipe by the experimentally measured stress or load from a cracked pipe experiment.

The elastic stress ratio as defined above requires elastic finite element calculations. For this study, the ANSYS® program was used. Stresses are considered only for the crack location. Because the stresses that are being considered are for dynamic events, the most meaningful elastic stress ratio is the one at the instant of maximum moment in the experiments. For consistency, the measured time-displacement input forcing function from the experiment was used in the elastic finite element analysis. In the spirit of design code calculations, nominal pipe size was used in all elastic finite element calculations.

The elastic stress ratio for the Subtask 1.1 inertially loaded experiments and the Subtask 1.3 pipe system experiments were calculated using the definitions and procedures outlined above. For the Subtask 1.1 experiments, only the total moment and total stress combinations are relevant. All of the definitions apply to the Subtask 1.3 experiments. Tables 3.12 and 3.13 summarize these results.

The elastic stress ratios for the Subtask 1.1 inertially loaded experiments range from 0.91 to 1.84. The ratios for the Subtask 1.3 pipe system experiments range from 0.63 to 2.56. Using only the definition based on total stress, the elastic stress ratios range from 1.03 to 1.84 for the Subtask 1.1 experiments and from 0.93 to 1.32 for the Subtask 1.3 experiments.

Discussion

The elastic stress ratio is probably most directly influenced by the amount of nonlinear behavior experienced in a particular experiment. Low overall system stresses mean that the system remains elastic, and the elastic finite element calculations tend to be close to the experimental values. Therefore, ratios are close to one. Factors which tend to increase stresses and nonlinearities, thereby increasing the elastic stress ratios, are smaller cracks and tougher materials, which cause higher stresses in the rest of the piping system. In the IPIRG experiments of Subtasks 1.1 and 1.3, plastic behavior was intentionally forced to occur primarily at the crack plane. The elastic stress ratios are, therefore, not necessarily typical of plant piping that may involve significant structural nonlinearities.

The elastic stress ratios calculated for the IPIRG experiments are much lower than those found in the EPRI/USNRC Piping and Fitting Dynamic Reliability Program in which unflawed pipe was tested. While the observed modes of failure are completely different for experiments from these two programs, it is interesting to consider the effect of crack size on the elastic stress ratio. As the crack size is reduced from the sizes considered in the IPIRG experiments, more nonlinear behavior is expected and ratios are expected to increase. Discontinuous behavior may be expected if there is a change of failure mode, but as the crack size approaches zero the elastic stress ratio should approach the values observed in the uncracked pipe EPRI/USNRC Piping and Fitting Dynamic Reliability Program.

It must be stressed that certain aspects of the IPIRG experiments are not typical of what might be expected in plant piping. If the experiments had been conducted with either shorter cracks, or if the piping system had been constructed of material having the same strength as the cracked test section rather than of high strength pipe and elbows, there would have been more nonlinearities, and the elastic stress ratios might have been much larger. These are factors that are easier to examine analytically rather than experimentally for a pipe system. However, more data are needed to evaluate and verify the effects of individual parameters, in particular crack size, on the elastic stress ratios. Data are also needed for pipe and pipe system experiments having shorter cracks and more nonlinear behavior, which would simulate more realistic conditions. This information would be useful from the standpoint of both LBB analysis and in-service flaw acceptance criteria at service load levels where the stresses are above yield in the pipe or pipe fittings.

3.6.2 PREDICTIONS OF DYNAMIC PIPE SYSTEM RESPONSE - CRACKED AND UNCRACKED

Dynamic finite element calculations of inertial and pipe system experiments conducted in Subtasks 1.1 and 1.3 were performed for a number of reasons. Calculations were performed first to evaluate various pipe system configurations in order to arrive at one that satisfied the objectives of the program. This led to the ultimate design of the piping loop and test system. Similar calculations were performed to design the forcing function that would be used to conduct each pipe system experiment. Finite element calculations were also used as a predictive tool to compare with experimental results. These comparisons elevated our understanding of the dynamic behavior of cracked pipe systems, but also served as stringent test cases for the capabilities of analytical methods. The following section provides a brief summary of these analyses. Additional details can be found in Ref. 3.3.

The basic analysis tool used in Task 1 was the ANSYS® finite element computer program. For the IPIRG analyses, the principal features incorporated into the models were

- beam-type pipe elements,
- ASME flexibility factor stiffness adjustments for elbows,
- lumped mass elements,
- time history integration of the equations of motion using the Houbolt time integrator,
- Rayleigh damping model (proportional to mass and stiffness), and
- internal pressure, temperature, and prescribed time-dependent displacement loading.

Both Subtask 1.1 and 1.3 experiments were analyzed with these features.

Uncracked Pipe System Response

In order to predict the dynamic behavior of a piping system containing cracks, the piping system itself must be correctly modeled. The important structural features of the system must be identified and included in the model; otherwise, efforts to couple fracture behavior with the structural analysis will be of questionable value.

The verification of the basic finite element analysis was accomplished by comparing predicted natural frequencies and dynamic moments with experimental results for the uncracked Subtask 1.3 pipe system. Although the finite element analysis is expected to predict these aspects correctly, previous experiences (Ref. 3.40) in comparing predicted and measured data for piping systems have been less than encouraging. The difference between measured and predicted parameters is commonly a factor of two or more.

The first few natural frequencies for the Subtask 1.3 piping loop were measured and compared with analytical predictions. Figures 3.45 and 3.46 show calculated natural frequency and mode shape data for the Subtask 1.3 pipe loop. Table 3.14 compares the predicted and measured natural frequency data. The agreement between the predicted frequencies and the measured frequencies is quite good. Correct prediction of the frequencies and corroboration of the analytically predicted mode shapes provided a good test case to assure that the mass and stiffness distribution of the pipe system were modeled correctly in the finite element models.

Verification of the accuracy of dynamic time history predictions was accomplished by comparing finite element predictions of the moment at the future crack plane in the Subtask 1.3 pipe system with the experimentally measured moments. Figure 3.47 shows the comparison. The analysis shown in Figure 3.47 incorporates the measured 0.5 percent system damping and measured elastic modulus for the pipe material. Clearly, the finite element model has captured all of the essential features of the system: mass, stiffness, damping, and boundary conditions.

Cracked Pipe Under Dynamic Loading

As previously discussed, the objective of Subtask 1.1 was to develop experimental data on the fracture behavior of circumferentially cracked pipe under predominately inertial loading. Both through-wall and surface-cracked pipe at PWR test conditions were tested in the loading fixture shown in Figure 3.48 using a prescribed displacement forcing function at the actuators.

Using the procedures previously described in Section 2.1.3, a model of the crack for Experiment 1.1-3 (stainless steel through-wall crack) was developed using quasi-static pipe bend test data for the same size pipe, same size crack, and same material. With these data a finite element model of the Subtask 1.1 system was prepared, and a nonlinear dynamic analysis was performed. Comparisons of pretest predictions with the experimental results are shown in Figures 3.49, 3.50, and 3.51. (Note: present limitations of the model mean that the finite element analysis can be performed only out to the point of maximum moment.)

A second comparison between the nonlinear cracked pipe finite element model and a Subtask 1.1 experiment was completed for Experiment 1.1-2 (inertially loaded carbon steel through-wall-cracked pipe). In this case, however, the moment-rotation behavior for the nonlinear crack representation was obtained from a J-estimation scheme using J-R curve and stress-strain data for the test material, rather than data from a previous quasi-static pipe test. The forcing function in both the analysis and experiment was $\delta = at \sin(\omega t)$, where a = 2.0 mm/sec (0.08 in/sec) and the frequency was 3.5 Hz. The comparison is shown in Figures 3.52, 3.53, and 3.54.

With the favorable comparisons between the nonlinear cracked pipe finite element results and test data, the viability of the nonlinear cracked pipe model was confirmed. Although the initial comparisons were only made for through-wall-cracked pipe cases, the extension of the approach to surface-cracked pipe was expected to be straightforward.

The Subtask 1.3 carbon steel base metal experiment (Experiment 1.3-2) was the first IPIRG pipe system experiment to be conducted to failure. The design of the experiment, using a 66 percent deep flaw, predicted that the cracked section moment would need to reach 610 kN-m for the surface crack to penetrate the pipe wall. This was predicted to happen at about 1.7 seconds into the test. The experiment was conducted; the maximum moment at failure was 340 kN-m, and failure occurred at 0.625 seconds. Figure 3.55 shows the test design analysis prediction and the experimental data. Clearly, the experiment design overpredicted the moment capacity of the cracked section.

Post-test investigation into the cause of the overprediction determined that the crack was deeper than expected, 72.7 percent rather than the assumed 66 percent. This difference in crack depth, amounting to 1.8 mm (0.073 in) out of a thickness of 25.7 mm (1.012 in), had a dramatic influence on the maximum moment-carrying capacity of the cracked specimen. Subsequent reanalysis of the test using the measured forcing function and a 75-percent deep flaw showed much better agreement to the experimental results. (A 75-percent depth was used since preliminary post-test information indicated that this was the approximate flaw size.) Figures 3.56 and 3.57 are comparisons of cracked-section moment and the actuator force for the experiment and the analysis with the deeper flaw. By interpolating the failure moments for the two analyses, 610 kN-m for the 66-percent deep flaw and 235 kN-m for the 75-percent deep flaw, to a 72.7-percent deep flaw, the expected failure moment would be 330 kN-m. This is in close agreement with the measured value of 340 kN-m.

The fact that the moment-carrying capacity dropped by a factor of 2.6 for a flaw depth of 75 percent compared with 66 percent is of interest in consideration of non-destructive evaluation (NDE) methods. The high sensitivity to flaw depth must be considered in light of the expected accuracy of state-of-the-art NDE techniques.

A detailed comparison between experiment and analysis was also made for the Subtask 1.3 stainless steel base metal experiment (Experiment 1.3-3). This experiment was the subject of the Fifth IPIRG Workshop Analysis Round Robin (see Section 2.5). Figures 3.58, 3.59, and 3.60 show typical comparisons between analysis and the experiment. Other comparisons were made for moments at another location, displacements at various locations, and reaction forces at the Node 6 hanger. The analysis used the measured post-test flaw geometry and the experimental actuator displacement time history for input. The moment-rotation curve for the dynamic analysis was generated from C(T) specimen J-R curve and stress-strain curve data using the procedures described in Section 2.1.3. For this material, the J-R curves and tensile properties were relatively unaffected by dynamic loading rates.

The measured moment-rotation curve plotted in Figure 3.58 is reasonably bounded by the curve used as input to the analysis in terms of general shape and magnitudes of moments. Rotation tends to be overestimated by the J-estimation scheme, but this overestimation does not seem to have seriously impaired the prediction of the failure time in the finite element analysis. The η-factor calculations discussed in Section 3.4 suggested that the toughness in the pipe was significantly lower than the C(T) specimen value used in the J-estimation scheme. Using the surface-cracked pipe J-R curve gave much better agreement with the experimental M-ϕ curve (see Figure 3.40).

It is worth noting that surface crack penetration in this experiment occurred at a bending moment that was significantly lower than the moment achieved on the prior cycle, due to crack growth during the prior cycle. The SC.TNP calculations past maximum load are not considered reliable, and hence are not used in modeling the moment-rotation curve for the dynamic analysis. Furthermore, current limitations in the ANSYS® code do not allow for negative stiffness in the moment-rotation curve modeling by the spring-slider approach currently employed. Even with this modest shortcoming, the moment predictions are quite reasonable.

The comparison of the predictions with the experimental results for the Y-directed displacements at the crack location are shown in Figure 3.60. The comparison is typical of the other displacement comparisons made for this experiment. The fact that the displacements predicted by analysis are somewhat greater than the experimental data is consistent with the predicted moment being larger than the experimental moment. In general, the primary source of the small discrepancies between analysis and the experiments is attributed to the inability of the fracture mechanics analyses to predict the correct moment-rotation input for the crack.

Summary

The state-of-the-art for analyzing a flaw in a dynamically loaded piping system has been advanced mainly as an outgrowth of an effort to design the experiments. The prediction of the behavior of a flawed pipe system under combined inertial and displacement-controlled loading involves two essential elements: (1) local behavior of the flaw, and (2) the response of the overall piping system. This predictive capability has been advanced by coupling the structural analyses with crack behavior in a single dynamic finite element analysis.

The comparisons shown have illustrated that it is possible to conduct nonlinear finite element analyses of a cracked pipe system and get meaningful predictions of both system and crack behavior. As noted earlier, damping must be properly characterized, the structural modeling must be properly performed (i.e., mass and stiffness must be correct), and the inputs to the analysis, forcing function, and flaw size must be accurately known. In addition, the fracture mechanics portion of the analysis must correctly predict the moment-rotation behavior of the cracked section of pipe. Small changes in surface crack depth, errors in the damping, or an incorrect estimation of moment-rotation behavior due to the crack can all drastically affect the predicted dynamic behavior of a cracked pipe system.

Although the nonlinear, time-dependent, cracked pipe, finite element analysis discussed here is reasonably straightforward, it is probably unsuitable for routine application in plant piping design. However, in a research context the cracked pipe analysis does provide a way to assess the effects of various parameters on pipe system performance and flaw behavior without having to perform a large number of expensive experiments. It would be inappropriate to suggest that the analysis methodology discussed here is mature and extensively verified, but the successful design of the Subtask 1.3 pipe system test facility and the limited comparisons made with it for the Subtask 1.1 and Subtask 1.3 experimental results suggest that it is a viable tool. Perhaps the most useful application of this tool will be in the development of improved, simplified engineering criteria.

3.7 Predictions of Fracture Instability

The occurrence of postulated ruptures, up to and including double-ended guillotine breaks (DEGB), currently forms part of the design basis for structures, systems, and components important to safety in nuclear power plant piping (Ref. 3.41). Conservative application of this rule led to an assumption of a reactor pressure vessel nozzle break and the asymmetric loading of the reactor pressure vessel (Ref. 3.42). Accepting the postulated DEGB, massive pipe restraints and jet impingement shields must be employed to mitigate the effects of the rupture. Application of leak-before-break (LBB) technology has shown, however, that requirements can be eased for PWR primary loop piping if the postulated DEGB event can be eliminated.

The issue of whether a DEGB is a credible event is of keen interest. In this context, the Subtask 1.1 inertially loaded experiments and the Subtask 1.3 pipe system experiments, with a mixture of inertial and displacement-controlled loads, provide a small, but useful, data base on the behavior of surface cracks when they break through the wall under dynamic loading. Furthermore, these data also provide a basis for evaluating instability analysis methodologies.

As a prelude to the discussion, a clear definition of the terms used to describe instability behavior is important. Instability, in the context of this section, refers to rapid fracture. A DEGB is a complete severing of a pipe. An instantaneous DEGB is a hypothetical instability that might occur when a surface crack penetrates the pipe wall and immediately (within, say, 100 milliseconds) results in the pipe being severed. Although a DEGB and an instantaneous DEGB are both the result of an instability and their consequences may ultimately be similar, the fact that continued cycling is not required for an instantaneous DEGB is important to the LBB philosophy.

A surface crack in a pipe subjected to some catastrophic event will experience a maximum load and, if it grows and penetrates the wall, will typically propagate to the ends of the surface crack. In a purely load-controlled situation the resulting through-wall crack will, for most surface crack geometries, experience an instability. (Note: Short deep surface cracks can have failure loads less than a through-wall crack with the same length (Refs. 3.43 and 3.44). In those cases, a load-controlled instability of the resulting through-wall crack would not necessarily be expected.) In contrast, for a purely displacement-controlled situation, in the absence of a large amount of system compliance, the resulting through-wall crack will arrest well before the pipe has experienced a DEGB (Ref. 3.16). For cases of combined load-controlled and displacement-controlled stresses, instability of the through-wall crack depends on many factors. The combined loading cases are of primary interest because they are the most likely to occur in plant piping.

3.7.1 EXPERIMENTALLY OBSERVED INSTABILITY BEHAVIOR

In the Subtask 1.1 experiments, the observation was made that once maximum moment was attained there were very few additional cycles (i.e., 2 or 3) until the pipe essentially reached a DEGB. This observation led to the conclusion that in considering the stability of a piping system subjected to pure inertial loading, the loading should be considered as being closer to load-controlled than displacement-controlled. Thus, a near instantaneous DEGB is expected.

For the Subtask 1.3 experiments, with a mixture of inertial and displacement-controlled stresses (the percent inertial loading ranged from 26 to 51 percent), a larger number of cycles is expected between maximum moment and a DEGB. In fact, all of the resulting through-wall cracks in the combined loading tests remained stable until substantial crack growth occurred. There was a complete pipe severance (DEGB) in two of the five Subtask 1.3 cracked pipe system experiments.

For each of the Subtask 1.3 experiments, the internal surface crack penetrated the pipe wall and grew rapidly to the approximate ends of the machined surface crack. The crack tip velocity during this period for the resulting through-wall crack was estimated from electric potential data to be 20 m/second (65 feet/second) for the stainless steel base metal experiment. Once the resultant through-wall crack reached the ends of the machined surface crack, the crack slowed down as the applied loadings decreased, and the crack temporarily arrested. When the applied loading and the associated crack section rotations increased again in the next cycle, the through-wall crack faces separated and the through-wall crack propagated at a velocity that was several orders of magnitude slower than the growth along the initially surface-flawed region.

For each of the five Subtask 1.3 surface-cracked pipe experiments, the resultant through-wall crack continued to grow in a stable manner whenever sufficient load and associated crack section rotations were applied. Once the applied loadings reversed and crack section rotations decreased, the through-wall crack would arrest. This slow, steady, cyclic through-wall crack growth continued until either the remaining ligament reached a critical size and the pipe experienced a DEGB or the applied loadings were stopped. For the carbon steel base metal and aged cast stainless experiments, a DEGB occurred. The number of cycles after maximum load until the pipe was severed was approximately 10 to 15 cycles. For the other three experiments that did not experience a DEGB, the applied loadings stopped approximately 20 cycles after maximum load.

3.7.2 INSTABILITY PREDICTIONS

Two analysis methodologies for fracture stability assessment were used for predicting the behavior after surface crack penetration. These methods are the fully plastic J-integral/tearing modulus method and the Energy Balance method (Refs. 3.45 and 3.46). Both of these methods are quasi-static. Although seismic loading is inherently dynamic, the instability analyses can be applied only at an instant of time. Both are founded on the basic premise that available energy to propagate the through-wall crack must exceed the resistance of the material in order to have an instability and that the loads or displacements applied to the piping system are maintained throughout the fracture event. If the loads change faster than the fracture event, neither analysis should be considered as valid.

Fully plastic J/T stability analysis can be used only to predict the onset of either surface crack or through-wall crack stability. Furthermore, depending upon the assumptions, either just load-controlled or just displacement-controlled loading can be considered. The Energy Balance method, on the other hand, can be used to estimate arrest as well as the onset of instability. Combined loading is implicitly included in the Energy Balance method by failure criteria lines for load-controlled stresses. The details of both methodologies are contained in Reference 3.3.

Table 3.15 summarizes the results of the J/T and Energy Balance stability predictions for the Subtask 1.3 experiments. For the Energy Balance approach, the table includes the case where the equivalent load-controlled moment is based on the saturation pressure. The table also considers the case where the load-controlled stresses are the sum of the equivalent moments due to inertia and the stresses due to the saturation pressure. The J/T analysis uses the fully-plastic displacement-controlled solution. Both the J/T and Energy Balance methods correctly predict the start of the surface crack instability.

For the resulting through-wall cracks, the fully plastic J/T analysis predicts stability for all experiments. When considering the load-controlled moment being due only to the saturation pressure, the Energy Balance method predicts stability for all but the carbon steel base metal. Aside from the Energy Balance prediction of instability for Experiment 1.3-2, these predictions are nominally consistent with the experimental results in that the double-end breaks that occurred in Experiments 1.3-2 and 1.3-7 were only after a number of cycles of stable through-wall crack growth. If the Energy Balance method considers the load-controlled stresses as the inertial plus saturation pressure equivalent moments, then the Energy Balance method predicts complete instability for all experiments. Of course the instability predictions are based on the premise that applied loads and displacements do not change during the fracture event, which is not true.

3.7.3 ASSESSMENT OF STABILITY ANALYSES

Superficially, both analyses appear to do a reasonable job of predicting the experimentally observed behavior of crack stability. This gives some measure of confidence that the quasi-static methods are adequate for pipe system stability analyses. However, under closer scrutiny, the correct predictions may be only fortuitous.

Under detailed examination, both stability analysis methodologies display inconsistencies that cannot be easily reconciled. Displacement-controlled fully plastic J/T analysis shows increasing stability with increasing crack length. Load-controlled J/T analysis predicts instability at a 52 percent long through-wall crack for the aged cast stainless steel experiment. The DEGB did not occur until the crack was 95 percent of the pipe circumference in length. The Energy Balance method predicts instability at a 54 percent long through-wall crack for the aged cast stainless experiment and instantaneous instability if pressure effects are considered directly into the moment-rotation curves via the J-estimation scheme. Table 3.16 compares the Energy Balance predicted crack growth at arrest and the experimentally measured crack growth at first arrest. The comparisons are relatively poor.

There are probably valid reasons for the inconsistencies. First, the fully plastic J/T and Energy Balance stability analyses are quasi-static based and assume that the loads remain essentially static during the fracture event. During all of the Subtask 1.3 experiments, the actuator motion after surface crack penetration did change and caused the loads to decrease at the crack. In addition, there were also inertial loads that were changing as the fracture propagated. Second, the fully plastic J/T and Energy Balance stability analyses are formulations driven by bending load. In the Subtask 1.3 piping system, there is a significant membrane stress due to internal pressure that is ignored in the fully-plastic J/T analysis and accounted for as an equivalent moment in the Energy Balance analysis. Lastly, phenomena that provide more "apparent" system stiffness and hence more stability, such as the effect of jet thrust forces, are not considered (see Figure 3.61). In the latter case, the initial through-wall crack is not significantly affected by thrust loads. However, as the crack grows, the effect of the thrust force becomes more and more pronounced, requiring more and more actuator displacement to obtain the same crack length. The implication of this analysis is that as the crack grows, thrust forces are going to contribute significantly to enhanced through-wall crack stability.

3.7.4 DISCUSSION

One of the objectives of the Subtask 1.3 experiments was to achieve a near instantaneous DEGB in one or more of the experiments. In order to satisfy this objective it was decided to remove the end caps near the test specimen for the aged cast stainless experiment (Experiment 1.3-7). The rationale behind this decision was that these end caps represented an artificial constraint that may have been affecting the ultimate stability of the resultant through-wall crack. These end caps, which had a small 13-mm (0.5-inch) diameter hole in each of them, restricted the flow of water to the test section once the surface crack penetrated the pipe wall. Their purpose was to reduce the rapid release of energy. Consequently, after surface crack penetration, the pressure at the test specimen decreased at an artificially high rate. By removing the end caps, the pressure in the crack section, and hence the axial stress, would be maintained, thus enhancing the chances of achieving an instantaneous DEGB.

During the design of the aged cast stainless experiment, calculations were made to assess the critical through-wall crack length for the case of simple pressure loading. Figure 3.62 is a plot of the normalized nominal axial tensile stress (due to pressure) as a function of the normalized critical through-wall crack length. (The tensile stress is the value predicted by Net-Section-Collapse and is normalized by the flow stress, where the flow stress is the average of quasi-static yield and ultimate strengths. The crack length is normalized by pipe circumference.) Assuming the pressure at the crack is maintained near the saturation pressure, 7.2 MPa (1,050 psi), the normalized axial tensile stress has a value of 0.06 for the aged cast stainless steel pipe experiment. Based on this value and Figure 3.62, it was estimated that the critical through-wall crack length would be approximately 63 percent of the pipe circumference and that there could be an instantaneous DEGB at surface crack penetration.

As noted previously, the DEGB did not occur until 13 cycles after surface crack penetration. Furthermore, in examining the fracture surface and the videotape, the remaining ligament when the DEGB finally occurred was found to be only 75 mm (3 inches) in length (see Figure 3.63). The through-wall crack had grown to a length of 95 percent of the pipe circumference (instead of the predicted 63 percent) before the critical crack length was attained.

One possible explanation for this discrepancy is presented in Figure 3.64, which shows two curves (Ref. 3.47). The bottom curve, which is the same curve as shown in Figure 3.62, applies when induced bending and rotations of the pipe due to pressure are allowed to occur freely, i.e., the ends of the test section are free to rotate. The top curve applies when induced bending moments and associated rotations are completely restricted, i.e., the ends of the test section are completely fixed. Note that for restricted rotations, the critical crack length is predicted to be 95 percent of the pipe circumference for a normalized tensile stress of 0.06. Consequently, the remainder of the piping loop may have restrained the induced bending and associated rotations such that the case of fixed ends gives the more accurate prediction. The thrust forces discussed above could account for the restrained bending. In any event, this finding could impact leak-before-break analysis methods that are based on the Net-Section-Collapse or other fracture analyses if they fail to take credit for this restriction of the induced bending moments and associated rotations. Margins on critical through-wall crack length in a pipe system for leak-before-break analysis methods may be greater than previously expected.

It is clear from the discussions presented above that the stability of cracks in real piping systems involves many more phenomena than are embodied in the currently available quasi-static analysis methodologies. It is also not apparent that the current methods can be enhanced to include the features essential to making credible predictions consistent with all observed piping system response. The spring-slider model used to design the Subtask 1.3 pipe loop and the experiments is presently applicable only up to maximum load. However, through changes to an existing nonlinear spring element in the ANSYS® element library, a dynamic analysis including the regime past surface crack penetration can be developed. Some effort would be required to eliminate numerical difficulties in the transition of the surface-crack moment-rotation curve to the through-wall-crack moment-rotation curve. Additional verification analyses of quasi-static pipe fracture experiments and inertial experiments would also be needed. However, once developed, an advanced dynamic crack stability analysis method would prove useful. Such an analysis method could be used to assess if either an instantaneous instability or a DEGB is possible, and it could be used to estimate the rate of crack opening for depressurization and core fluid stability analyses.

3.8 Integration of IPIRG Results and Past Quasi-Static Pipe Fracture Program Results

Sections 3.2 to 3.7 discussed the comparison of the pipe experiments with analytical predictions. The objective of this section is to integrate the various pipe test and analysis results that were separately discussed in previous sections to show consistency or inconsistency in the behavior of the cracked pipe experiments and material characterization efforts. The question of concern is on how the separate effects of dynamic loading, cyclic loading, and inertial versus displacement-controlled loading combine for crack pipe evaluations of typical pipe systems.

3.8.1 DISCUSSION ON QUASI-STATIC VERSUS DYNAMIC LOADING

Several experiments were conducted to evaluate the effect of loading rate on the fracture behavior or maximum load-carrying capacity of cracked pipe. Specifically, 6-inch-diameter pipes containing through-wall cracks and loaded in displacement control were primarily used for this assessment. Net-Section-Collapse (NSC) predictions of maximum loads were used to normalize the experimental results to eliminate the effect of slight variations in pipe dimensions and crack lengths. (Similar assessments were made using other analysis procedures, DPZP and J-estimation schemes, and the conclusions reached were the same.) The average of the quasi-static yield and ultimate strengths was used to define the flow stress used in the NSC calculations.

The ratio of the experimental maximum load results to the NSC predictions are presented in Tables 3.6 and 3.7 and Figures 3.11 and 3.12. For the carbon steel through-wall-cracked pipe experiments, results from quasi-static and dynamic loading are compared for the monotonic, cyclic (R = 0), and fully reversed cyclic (R = -1) loading histories. Comparisons based on parameters other than maximum load, i.e., normalized moment-rotation curves or J values from pipes and C(T) specimens, are made later.

Carbon Steel Through-Wall-Cracked Pipe

There appears to be only a slight effect of strain rate on the load-carrying capacity of the 6-inch diameter carbon steel through-wall-cracked pipe experiments (Table 3.6 and Figure 3.11). For the case of monotonic loading, the quasi-statically loaded specimen (1.2-7) had a 6 percent higher load-carrying capacity than the average of the three dynamic experiments (1.2-8, 1.2-11, and 1.2-12). For the case of cyclic (R = 0) loading, the quasi-static experiment (1.2-2) had only a 3 percent higher load-carrying capacity than the companion dynamic experiment (1.2-10). For the case of cyclic (R = -1) loading, the quasi-static experiment (1.2-4) had an 8.5 percent higher load-carrying capacity than the companion dynamic experiment (1.2-6). This modest degradation in the load-carrying capacity of the 6-inch diameter carbon steel through-wall-cracked pipe experiments at the higher strain rates is somewhat less than expected on the basis of the material characterization efforts. At 288 C (550 F) both the strength and toughness of this A106 Grade B material decreased approximately 20 percent at the higher strain rates (Ref. 3.48). However, visco-plastic finite-element analyses by Brickstad (Ref. 3.49) suggest that for these dynamic pipe tests, only the near crack-tip area experiences a strain rate high enough to be affected by dynamic strain aging. Hence, quasi-static tensile properties may be more appropriate to use in a fracture analysis.

Carbon Steel Surface-Cracked Pipe

For the case of a carbon steel pipe containing a surface crack, the limited experimental evidence to date suggests a trend that is opposite of that seen for carbon steel through-wall-cracked pipe (Table 3.7 and Figure 3.12). The dynamic monotonic surface-cracked pipe experiment (1.1-7) exhibited a 15 percent higher load-carrying capacity than the quasi-static experiment (1.1-9). This trend is also inconsistent with material characterization results. The reason for this inconsistency is not known at this time. The noted differences in results are too large to be attributed to uncertainty in the data.

Stainless Steel Through-Wall-Cracked Pipe

For the stainless steel through-wall-cracked pipe experiments, results from quasi-static and dynamic loading rates are compared for the monotonic and fully reversed cyclic (R = -1) loading histories. It appears from Table 3.6 and Figure 3.11 that the effect of strain rate on the load-carrying capacity for the stainless steel through-wall-cracked pipe experiments is relatively small but trends are not totally clear. For the case of monotonic (no pressure) loading, there is essentially no difference in the load-carrying capacity for the quasi-static (4131-5) and dynamic (1.2-1) experiments. However, for the cyclic R = -1 loading, there is a 14 percent increase in the load-carrying capacity for the dynamic experiment (1.2-9) when compared with the quasi-static experiment (1.1-3).

3.8.2 MONOTONIC VERSUS CYCLIC LOADING

The primary focus of this section is to evaluate the effect of cyclic loading on the maximum load-carrying capacity of a pipe containing a through-wall crack. The NSC calculations were again used to normalize the experimental maximum loads in order to eliminate slight variations in pipe dimensions and crack lengths. The average of the quasi-static yield and ultimate strengths was used as the definition of flow stress in the NSC calculations. Cyclic effects on the J-R curves from the pipe experiments are discussed in a later section.

Carbon Steel Through-Wall-Cracked Pipe

In examining Table 3.6 and Figure 3.11 there appears to be a definite effect of cyclic load history on the load-carrying capacity of the 6-inch diameter carbon steel through-wall-cracked pipe experiments. For the case of quasi-static loading, the monotonically loaded specimen (1.2-7) had a 6 percent higher load-carrying capacity than the R = 0 cyclically loaded specimen (1.2-2) and a 20 percent higher load-carrying capacity than the R = -1 cyclically loaded specimen (1.2-4). For the case of dynamic loading, the average load-carrying capacity of the three monotonically loaded specimens (1.2-8, 1.2-11, and 1.2-12) was 4 percent higher than the load-carrying capacity for the dynamic R = 0 cyclically loaded specimen (1.2-10) and 23 percent higher than the load-carrying capacity for the dynamic R = -1 cyclically loaded specimen (1.2-6).

Stainless Steel Through-Wall-Cracked Pipe

There also appears to be a definite effect of cyclic load history on the load-carrying capacity of the stainless steel through-wall-cracked pipe (Table 3.6 and Figure 3.11). For quasi-static loading, the monotonically loaded specimen (4131-5) had a 13 percent higher load-carrying capacity than the R = 0 cyclically loaded specimen (1.2-3) and a 26 percent higher load-carrying capacity than the R = -1 cyclically loaded specimen (1.2-5). For dynamic loading, the monotonically loaded specimen (1.2-1) had a 9 percent higher load-carrying capacity than the R = -1 specimen (1.2-9).

These comparisons clearly show the effect of fully reversed (R = -1) cyclic loading. Decreases in load-carrying capacity for the cracked pipe sections range from 9 to 26 percent when compared with monotonic loading.

Incremental Plastic Displacement

Cyclic load ratio (R) is not the only parameter that affects the load-carrying capacity of a cracked pipe section subjected to a cyclic load history. It has been found that incremental plastic displacement is another important parameter in this regard. The effect of incremental plastic displacement was assessed in four of the stainless steel Subtask 1.2 through-wall-cracked pipe experiments. This was accomplished by changing the cyclic displacement as shown in Figure 3.65. The effect of the incremental plastic displacement on the experimental crack-tip-opening angle (CTOA), a measure of toughness, is shown in Figure 3.66 for the stainless steel pipe fracture experiments. These data have been normalized to the results for the quasi-static monotonic test (Experiment 4131-5). Figure 3.66 indicates that for the same load ratio (R), decreasing the incremental plastic displacement lowers the CTOA. Hence, the magnitude of this incremental plastic displacement as well as the load ratio can affect the apparent fracture resistance of the material.

Note, the trends in Figure 3.66 that show the effects of incremental plastic displacement and load ratio on the apparent toughness are an observation from stainless steel through-wall-cracked pipe experiments only. They should not be used universally for other materials or other flaw geometries. Additionally, the cyclic effects in these experiments are not necessarily representative of service loads. Load ratio effects in plant piping are addressed further in Section 4.

3.8.3 INERTIAL VERSUS DISPLACEMENT-CONTROLLED LOADING

Figure 3.67 compares the ratio of the maximum experimental stress with the predicted Net-Section-Collapse stress for the different loading conditions evaluated in the Subtasks 1.1 and 1.2 experiments, i.e., inertial and displacement-controlled. The data represented in this figure are for the 6-inch nominal diameter, carbon steel, through-wall crack experiments. (Similar findings were obtained for the LBB.ENG2 and GE/EPRI methods.) In Figure 3.67, both the experimental and predicted stresses include the axial stress contribution due to the internal pipe pressure.

Figure 3.67 shows that the results for the inertial experiment agree within 5 percent of the results for the quasi-static and dynamic, monotonic experiments and within 7 percent of the results for the quasi-static and dynamic, cyclic R = 0 experiments. The fact that the load-carrying capacity for the inertial experiment is in such close agreement with the results for the monotonic and R = 0 experiments is not surprising. The effective load ratio (R) for the inertial experiment at maximum moment was slightly greater than zero. Due to the loading history for the inertial experiments, the effective load ratio is close to 1 at the beginning of the experiment and gradually decreases towards a minimum near the end of the experiment (see Figure 3.68). The load ratios for the displacement-controlled Subtask 1.2 experiments were constant throughout the experiments.

Of further note from Figure 3.67 is that the maximum load-carrying capacity for the inertial experiment (1.1-2) is 17 and 27 percent higher than the maximum load-carrying capacity of the quasi-static, R = -1 (1.2-4) and dynamic, R = -1 (1.2-6) experiments, respectively. Consequently, all the data in Figure 3.67 support the contention that as the load ratio decreases, the cyclic damage increases, and the maximum load-carrying capacity decreases. This finding was substantiated previously and discussed in Section 3.8.2.

Figure 3.69 compares the ratio of the maximum experimental stress with the predicted Net-Section-Collapse stress for the 6-inch nominal diameter carbon steel surface-cracked pipe experiments. Note, there were no displacement-controlled, cyclic, surface-cracked pipe experiments conducted as part of this program. Figure 3.69 shows that the results for the first inertial surface-cracked pipe experiment (Experiment 1.1.6) agrees fairly well with the quasi-static and dynamic, monotonic surface-cracked pipe experiments. The second carbon steel surface-cracked pipe inertial experiment (Experiment 1.1-8) exhibited a load-carrying capacity 17 percent higher than the first and, thus, does not agree well with the rest of the experimental data. Experiment 1.1-8 was an experiment for which experimental problems caused a very erratic forcing function to be applied to the pipe. Consequently, the results from this experiment should be viewed with some caution.

Figure 3.70 compares the ratio of the maximum experimental stress with the predicted Net-Section-Collapse stress for the 6-inch nominal-diameter stainless steel through-wall-cracked pipe experiments. The load-carrying capacity of the inertial experiment (1.1-3) is comparable (within 2 percent) to the load-carrying capacity for one of the two quasi-static, monotonic experiments (4131-5) and the dynamic, monotonic experiment (1.2-1). For some unexplained reason, the maximum experimental stress for the second quasi-static, monotonic, stainless steel, through-wall crack experiment (4131-1) was lower than expected, based on analysis and other relevant experimental data. This experiment, Experiment 4131-1 from the Degraded Piping Program, was the only small diameter stainless steel pipe experiment from the Degraded Piping Program that failed to reach a limit-load condition. Figure 3.71 shows that results from the inertial, stainless steel, surface-cracked pipe experiment (1.1-5) also agree well with the results from the two quasi-static, monotonic, stainless steel, surface-cracked pipe experiments (4112-3 and EPRI 13S).

Consequently, in review of Figures 3.70 and 3.71, the results from the stainless steel, inertial experiments can be seen to agree very well with the results from companion displacement-controlled experiments. As was the case for the carbon steel, inertial experiment, the effective load ratio (R) for the stainless steel, inertial, through-wall-cracked pipe experiment started off near one and then gradually decreased to near zero over the course of the experiment. In addition, the incremental plastic displacement for the inertial experiments was relatively large. Therefore, the effect of the cyclic load history on the fracture toughness would be expected to be minor. All of this helps explain why this inertial experiment exhibited results more characteristic of those exhibited for monotonic experiments than the cyclic experiments.

Agreement between inertial and displacement-controlled experiments supports the contention that the experimental results obtained during this program were consistent from one test frame to another. Furthermore, the results from the displacement-controlled experiments should provide insight into the load-carrying capacity of a piping system subjected to either inertial or combined inertial and displacement-controlled stresses.

However, pure displacement-controlled experiments provide little insight into the ultimate stability of a cracked pipe section subjected to loadings that have some inertial component. The resulting through-wall crack for each of the displacement-controlled experiments remained stable after maximum moment was achieved. In contrast, for the Subtask 1.1 inertial experiments, there were very few additional cycles past maximum moment until the cracked pipe section essentially reached a DEGB condition. Consequently, the stability of pipe under pure inertial loading should be considered as being closer to load-controlled than displacement-controlled for typical pipe fracture analyses. Fracture stability under combined inertial and displacement-controlled stresses was investigated for the pipe system experiments of Subtask 1.3. The complex interactions observed in those experiments would be difficult to model or simulate with displacement-controlled experiments.

3.8.4 DYNAMIC PIPE SYSTEM EXPERIMENTS VERSUS QUASI-STATIC EXPERIMENTS

An important consideration in this program was to see whether dynamic pipe system experiments are really necessary, or whether conducting quasi-static pipe fracture experiments is sufficient. For each of the Subtask 1.3 pipe system fracture experiments, there was a companion quasi-static experiment conducted with a similar internal surface crack. Comparisons between the pipe system experimental results and companion quasi-static results provide a basis for establishing whether the pipe system plays a role in determining the load capacity of a given flaw. Beyond the direct numerical comparisons of load capacity, qualitative observations of the general behavior of the flaws tested in the pipe system can also be used to determine if conducting pipe system experiments is really necessary for a complete understanding of flaw behavior.

The test specimens for the quasi-static experiments were fabricated using sections cut from the same length of pipe used in the pipe system experiments, and the flaw sizes and weld procedures used were similar. Direct comparison of the maximum moments at failure between the pipe system experiments and quasi-static experiments are not completely valid, because there were some differences in test temperature, internal pressure, and flaw sizes. To place the companion experiments on a common basis, fracture mechanics analyses are used to normalize the moments for both sets of experiments so that the relative differences can be isolated. Net-Section-Collapse analysis was used for the normalization.

Figure 3.72 and Table 3.7 show the result of normalizing the maximum experimental moments for each of the five Subtask 1.3 experiments and its quasi-static companion. Comparing the base metal experiments (4112-8 with 1.3-2, EPRI 13S with 1.3-3, and 4143-1 with 1.3-7) it is evident that the load capacity of the flaws is significantly degraded when the flaws are tested in the pipe system. In contrast, the weld metal experiments (4141-8 with 1.3-4 and 4141-4 with 1.3-5) do not show this degradation. Although attributing the degradation of load-carrying capacity in the base metal experiments to cyclic effects may be tempting, it is hard to reconcile the fact that the weld metal experiments also had potentially degrading cyclic effects and yet showed no loss in strength. If the base metal experiments are "corrected" for cyclic effects, their normalized moments still fall decidedly below the companion quasi-static experiments. Ignoring the presence of the weld crown or use of base metal tensile properties for the weld in the normalization cannot explain why the weld metal experiments do not show differences between the quasi-static and pipe system results. Both tests were normalized in a consistent manner so, at best, the companion weld experiments would be expected to have a systematic offset and not a relative offset. The facts that inconsistencies in load capacities are observed and that the inconsistencies cannot be completely rationalized suggest there are unknown effects influencing crack behavior in a pipe system experiment.

Beyond the quantifiable comparisons made above, general observations about two phenomena, stability and elastic stress ratio, seen in the IPIRG experiments provide some insight into whether pipe system tests are necessary. The fact that the aged cast stainless specimen did not produce a DEGB until 13 loading cycles beyond surface crack penetration had been applied and until the remaining ligament was only 5 percent of the circumference was unexpected. As previously discussed, restraint of bending in a pipe system, the importance of thrust forces, and the consequences of unloading the crack all became apparent as a result of the pipe system experiments. In addition, because these phenomena have been identified as being first order effects, inadequacies in the current instability prediction methodologies have been identified.

Regarding elastic stress ratio, it has generally been assumed that elastic stress analysis results in a high prediction of stresses. This is apparently true for uncracked pipe as demonstrated in the EPRI/USNRC Piping and Fitting Dynamic Reliability Program (Ref. 3.38). However, the IPIRG pipe system experiments involved little plasticity, and elastic stress analysis results compared closely with measured values.

In light of the points discussed above, it is easy to conclude that pipe system experiments are essential. The inexplicable degradation of load capacity in the IPIRG base metal experiments and the system-related effects on stability were not predicted *a priori*. Neither of these effects could have been easily identified in quasi-static or dynamic straight pipe experiments. In time, the distinctly system-related phenomena observed in the pipe system experiments will be understood. J-estimation schemes will be improved, a nonlinear crack finite element model including surface crack and through-wall crack behavior will be developed, and jet thrust forces will be understood. The pipe system experiments conducted in this program form a limited data base for exploring these topics.

At the beginning of the IPIRG Program the need for pipe system experiments was not completely clear. At the close of the program it is not only apparent that the five cracked pipe system experiments were needed, but that additional pipe system experiments should be conducted. Validation of new models that incorporate the phenomena observed in the current pipe system experiments will require a larger data base.

3.8.5 CONSISTENCY BETWEEN MATERIAL CHARACTERIZATION, SEPARATE EFFECTS PIPE FRACTURE EXPERIMENTS, AND PIPE SYSTEM EXPERIMENTS

An important issue to be addressed in this program was to assess if quasi-static, monotonic material property data are sufficient for analyzing a cracked pipe system subjected to a dynamic, cyclic load history. In order to make such an assessment, it was necessary to compare the results of the various separate effects experiments and the pipe system experiments in light of the quasi-static and dynamic material property data. To make such comparisons the maximum experimental loads from the separate effects and pipe system experiments had to be normalized by some analysis method to account for differences in pipe size, flaw size, system pressure, and test temperature. For this exercise the DPZP analysis was chosen as the normalizing analysis method. This analysis method was chosen in that it is a simple, straightforward method that accounts for the effect of both the strength and toughness on the load-carrying capacity. The Net-Section-Collapse analysis accounts only for the effect of the strength. Similar results using the SC.TNP and R6 Option 1 analyses are given in Reference 3.3.

Effect of Dynamic Load Rates

There are two material dependent phenomena that affect the maximum load-carrying capacity of cracked pipe sections: loading rate and cyclic load history. This section deals with loading rate, and the next section deals with cyclic load history. For the materials evaluated in this program, the carbon steels tended to exhibit a greater dependence on loading rate than did the stainless steels. Both the strength and toughness of the two A106 Grade B carbon steel base metals evaluated decreased significantly at the higher loading rates, although the 16-inch diameter pipe showed a larger toughness loss at dynamic rates than the 6-inch diameter pipe.

In Section 3.8.1 it was shown that when the experimental results were normalized to the NSC analysis, the maximum load-carrying capacity for the 6-inch diameter carbon steel through-wall-cracked pipe experiments was 3 to 9 percent lower for dynamic loading rates than for quasi-static loading rates. This modest reduction in the load-carrying capacity at the higher strain rates is somewhat less than expected on the basis of the material characterization efforts. At 288 C (550 F), both the strength and toughness of this A106 Grade B material decreased approximately 20 percent at the higher strain rates.

Conversely, the dynamic Subtask 1.3 carbon steel base metal experiment (Experiment 1.3-3) exhibited a 50 percent reduction in the maximum load-carrying capacity when compared with the companion quasi-static experiment from the Degraded Piping Program (Experiment 4112-8) (see Table 3.7). Part, but not all, of this reduction can be explained by a reduction in material properties at dynamic loading rates. Reference 3.48 indicates that the flow stress of this carbon steel material decreased approximately 26 percent at the higher strain rates. In addition, the toughness of this material also decreased dramatically at the higher strain rates. The value of J_i decreased 58 percent and the value of Dj/da decreased 82 percent. If dynamic material properties are used for the DPZP analysis of the dynamic carbon steel base metal experiment (Experiment 1.3-2), the ratio of experimental stress to the DPZP predicted stress is only 17 percent less than the same ratio for the companion quasi-static experiment (Experiment 4112-8). This compares with a 50 percent reduction if quasi-static properties are used in the analysis of the dynamic experiment. Consequently, an analysis which uses quasi-static material property data may have difficulty in adequately predicting the behavior of some carbon steel cracked pipe sections subjected to dynamic loadings for materials susceptible to strength and toughness degradation at higher loading rates.

Effect of Cyclic Load Histories

In Section 3.8.2 it was shown that the effect of fully-reversed cyclic (R = -1) loading on the maximum load-carrying capacity for both the carbon steel and stainless steel through-wall-cracked pipe experiments conducted in Subtask 1.2 was significant. The load-carrying capacity for these R = -1 experiments decreased from 9 to 26 percent when compared with the corresponding monotonic experiments. These differences are larger than the normal scatter in reproducing circumferentially cracked pipe experiments.

The effect of cyclic load history on the Subtask 1.1 and 1.3 experiments was significantly less. As discussed in Section 3.8.3, the maximum load-carrying capacity for the Subtask 1.1 inertial experiments was most closely aligned with the results from the corresponding monotonic experiments. For those experiments, the effective load ratio was between 0 and 1, and the incremental plastic displacement was large relative to the Subtask 1.2 experiments. Consequently, not much effect of cyclic load history is expected for these experiments. A similar conclusion was reached for the Subtask 1.3 experiments.

As a result the conclusion can be made that if a cracked pipe section is subjected to a severe cyclic load history (i.e., negative load ratios and small incremental plastic displacements), as in the Subtask 1.2 experiments, then cyclic J-R curve data will be needed to adequately predict the maximum load-carrying capacity of the cracked pipe section. If the cyclic load history is not severe, as was the case for the Subtask 1.1 experiments, then J-R curve data from monotonic C(T) specimen tests will probably be sufficient.

The empirical relationship showing the effect of the incremental plastic displacement on the fracture toughness (see Figure 3.66) is based on stainless steel through-wall-cracked pipe data. This relationship may not hold true for the surface crack geometry or for other materials. Consequently, any conclusions drawn on the need for cyclic J-R curves based on this relationship must be viewed with this limitation in mind. Additional cyclic surface-cracked pipe experiments are needed to develop a similar relationship for surface-cracked pipe as that shown in Figure 3.66 for through-wall-cracked pipe.

3.9 References

3.1 Scott, P. and others, "Subtask 1.1 Final Report - Stability of Cracked Pipe Under Inertial Stresses", Battelle, July 1991.

3.2 Vieth, P., Kramer, G., Marschall, C., Francini, R., and Wilkowski, G. M., "Subtask 1.2 Final Report - Stability of Cracked Pipe Under Seismic/Dynamic Displacement-Controlled Stresses", Battelle, July 1991.

3.3 Scott, P., Olson, R., Wilkowski, G., Marschall, C., and Schmidt, R., "Subtask 1.3 Final Report - Crack Stability in a Representative Piping System Under Combined Inertial and Seismic/Dynamic Displacement-Controlled Stresses", Battelle, April 1991.

3.4 Wilkowski, G. M. and others, "Degraded Piping Program - Phase II", Summary of Technical Results and Their Significance to Leak-Before-Break and In-Service Flaw Acceptance Criteria, March 1984-January 1989, NUREG/CR-4082, Vol. 8, March 1989.

3.5 Lowes, J. M. and Fearnehough, G. D., Engineering Fracture Mechanics, Vol. 3, pp 103-108, 1971.

3.6 Wilkowski, G. M., Wambaugh, J., and Krishnaswamy, P., "Single Specimen J-Resistance Curve Evaluations Using the d-c Electric Potential Method and a Computerized Data Acquisition System", ASTM STP 833, pp 553-576, 1984.

3.7 Vassilaros, M. G. and Hackett, E. M., "J-Integral R-Curve Testing of High Strength Steels Utilizing the D.C. Potential Drop Method", ASTM STP 833 pp 535-552, 1984,.

3.8 Wilkowski, G. M. and Maxey, W. A., "Review and Application of the Electric Potential Method for Measuring Crack Growth in Specimens, Flawed Pipes, and Pressure Vessels", ASTM STP 791, pp II-266 to II-294, 1983.

3.9 Wilkowski, G. M. and others, "Short Cracks in Piping and Piping Welds", Semiannual Report, October 1990-March 1991, NUREG/CR-4599, Vol. 2, September 1991.

3.10 Hays, R. A., Vassilaros, M. G., and Gudas, J. P., "Fracture Analysis of Welded Type 304 Stainless Steel Pipe", NUREG/CR-4538, May 1986.

3.11 Kanninen, M. F. and others, "Instability Predictions for Circumferentially Cracked Type 304 Stainless Steel Pipes Under Dynamic Loadings", EPRI Report NP-2347, April 1982.

3.12 Kanninen, M. F. and others, "Mechanical Fracture Predictions for Sensitized Stainless Steel Piping with Circumferential Cracks", Final Report, EPRI Report NP-192, September 1976.

3.13 Wilkowski, G. M. and Scott, P. M., "A Statistical Based Circumferentially Cracked Pipe Fracture Mechanics Analysis for Design or Code Implementation", Nuclear Engineering and Design, Vol. 111, pp 173-187, 1989.

3.14 Kumar, V., German, M. D., and Shih, C. F., "An Engineering Approach for Elastic-Plastic Fracture Analysis", EPRI Report NP-1931, July 1981.

3.15 Brust, F. W., "Approximate Methods for Fracture Analyses of Through-Wall-Cracked Pipes", NUREG/CR-4853, February 1987.

3.16 Scott, P. M. and Ahmad, J., "Experimental and Analytical Assessment of Circumferentially Surface-Cracked Pipes Under Bending", NUREG/CR-4872, April 1987.

3.17 Wilkowski, G. M., Marschall, C. W., and Landow, M., "Extrapolation of C(T) Specimen J-R Curves for Use in Pipe Flaw Evaluations", presented at ASTM 21st National Fracture Mechanics Symposium, June 1988.

3.18 Kumar, V. and others, "Advances in Elastic-Plastic Fracture Analysis", EPRI Report NP-3607, August 1984.

3.19 Kumar, V. and German, M., "Elastic-Plastic Fracture Analysis of Through-Wall and Surface Flaws in Cylinders", EPRI Report NP-5596, January 1988.

3.20 Paris, P. C. and Tada, H., "The Application of Fracture Proof Design Methods Using Tearing Instability Theory to Nuclear Piping Postulating Circumferential Through-Wall Cracks", NUREG/CR-3464, September 1983.

3.21 Klecker, R. and others, "NRC Leak-Before-Break (LBB.NRC) Analysis Method for Circumferentially Through-Wall-Cracked Pipes Under Axial Plus Bending Loads", NUREG/CR-4572, May 1986.

3.22 American Society of Mechanical Engineers Boiler and Pressure Vessel Code, Edition (Winter Addendum), 1983, See Section XI Article IWB-3640.

3.23 Case N-436, "Alternative Methods for Evaluation of Flaws in Austenitic Piping", ASME Boiler and Pressure Vessel Code, Section XI, Division 1, pp 763-765, May 14, 1986.

3.24 American Society of Mechanical Engineers Boiler and Pressure Vessel Code, Edition July 1989, see Code Case N-463.

3.25 "Evaluation of Flaws in Austenitic Steel Piping" (Technical basis document for ASME IWB-3640 analysis procedure), prepared by Section XI Task Group for Piping Flaw Evaluation, EPRI Report NP-4690-SR, April 1986.

3.26 "Evaluation of Flaws in Ferritic Piping", EPRI Report NP-6045, October 1988.

3.27 Wilkowski, G. M., and others, "Degraded Piping Program - Phase II", Seventh Program Report, October 1987-December 1988, Battelle Columbus Laboratories, NUREG/CR-4082, Vol. 7, March 1989.

3.28 Pan, J., "Some Considerations on Estimation of Energy Release Rates for Circumferentially Cracked Pipe", Journal of Pressure Vessel Technology, Vol. 106, pp 391-398, November 1984.

3.29 Solicitations for public comment on "Standard Review Plan 3.6.3 LEAK-BEFORE-BREAK PROCEDURES", Federal Register, Vol. 52, No. 167, Friday, August 28, 1987, Notices, pp 32626 to 32633.

3.30 Wilkowski, G. M., Barnes, C. R., and Scott, P. M., "Experimental Evaluation of the Interaction of Constraint from Loading Conditions and Flaw Sizes on Fracture Toughness for Surface-Cracked Pipe", presented at ASTM Symposium on Constraint Effects in Fracture, Indianapolis, Indiana, May 8-9, 1991.

3.31 Harrison, R. P., Loosmore, K., Milne, I., and Dowling, A. R., "Assessment of the Integrity of Structures Containing Defects", CEGB Report R/H/R6, 1976: R/H/R6-Rev. 1, 1977.

3.32 Milne, I., "Failure Assessment Diagrams and J Estimates: A Comparison for Ferritic and Austenitic Steels", CEGB Report RD/L/2208N81, 1982.

3.33 Milne, I., Ainsworth, R. A., Dowling, A. R., and Stewart, A. T., "Assessment of the Integrity of Structures Containing Defects", R/H/R6-Rev. 3, published by Central Electric Generating Board, England, May 1986.

3.34 Zahoor, A. and Kanninen, M. F., "A Plastic Fracture Mechanics Prediction for Fracture Instability in a Circumferentially Cracked Pipe in Bending - Part I. J-Integral Analysis", Journal of Pressure Vessel Technology, Vol. 103, pp 352-358, 1981.

3.35 "The Development of a Plan for the Assessment of Degraded Nuclear Piping by Experimentation and Tearing Instability Fracture Mechanics Analysis", NUREG/CR-3142, Vol. 2, June 1983.

3.36 Wilkowski, G. M. and others, "Analysis of Experiments on Stainless Steel Flux Welds", NUREG/CR-4878, April, 1987.

3.37 Vassilaros, M. G., Hays, R. A., Gudas, J. P., and Joyce, J. A., "J-Integral Testing Instability Analysis for 8-inch Diameter ASTM A106 Steel Pipe", NUREG/CR-3740, April, 1984.

3.38 DeVita, V., "Seismic Fragility Pipe Testing", Transactions of 10th SMiRT, Volume S, pp 81-86, August 1989.

3.39 ASME Boiler and Pressure Vessel Code, Section III, Division 1, Appendix N, American Society of Mechanical Engineers, 1989.

3.40 Kot, C. A., Srinivasan, M. G., Hsieh, B. J., and Costello, J. F., "High-Level Seismic Tests of Piping at the HDR", Transactions of 10th SMiRT, Volume S, pp 87-92, August 1981.

3.41 "General Design Criteria for Nuclear Power Plants", Appendix A, 10 CFR Part 50.

3.42 "Unresolved Safety Issue A-2", NUREG-0606, Vol. 6, No. 1, February 1984.

3.43 Wilkowski, G. M. and Eiber, R. J., "Evaluation of Tensile Failure of Girth Weld Repair Grooves in Pipe Subjected to Offshore Laying Stresses", ASME Journal of Energy Resources Technology, Vol. 103, March 1981.

3.44 Kurihara, R., Ueda, S., and Sturm, D., "Estimation of the Unstable Fracture of Pipe with a Circumferential Surface Crack Subjected to Bending", Nuclear Engineering and Design, Vol. 106, pp 265-273, 1988.

3.45 Zahoor, A. and Gamble, R., "Leak Before Break Analysis for BWR Recirculation Piping Having Multiple Weld Locations", EPRI NP-3522-LD, April 1984.

3.46 Wilkowski, G. M. and Kramer, G., "An Energy Balance Approach to Estimate the Initiation and Arrest of Ductile Fracture Instability in Circumferentially Cracked Pipe", ASME Special Technical Publication PVP Vol. 167, pp 103-114, July 1989.

3.47 Wilkowski, G. M. and others, "Degraded Piping Program - Phase II", Semiannual Report, October 1984-March 1985, NUREG/CR-4082, Vol. 2, July 1985.

3.48 Marschall, C. W., Landow, M. P., and Wilkowski, G. M., "Loading Rate Effects on Strength and Fracture Toughness of Pipe Steels Used in Task 1 of the IPIRG Program", Battelle Topical Report to IPIRG, December 22, 1989.

3.49 Brickstad, B., Swiss-Swedish Analysis Program: "Numerical Analysis of IPIRG Cracked Pipe Experiments with use of Nonlinear Fracture Mechanics", AB Statens Anläggningsprovning Report No. SA/Fou-RAPPORT, May 1989.

Table 3.1 Analysis matrix for TP304 material variability investigation

---

Specimen Number:

Stress Strain

A8-39
A8-40

J-R

A8-12A
A8-41
A8-43

Pipe Size

152 mm x 9.5 mm
(6 inch x 0.375 inch)

406 mm x 25.4 mm
(16 inch x 1.000 inch)

Flaw Geometry

37 percent long TWC

66 percent deep, 180 degree internal SC

Table 3.2 Analysis matrix for A106B material variability investigation

---

Specimen Number:

Stress-Strain

F29.5
F29-6

J-R

F29-11
F29-13
F29-18

Pipe Size

152 mm x 9.5 mm
(6 inch x 0.375 inch)

406 mm x 25.4 mm
(16 inch x 1.000 inch)

Flaw Geometry

37 percent deep TWC

66 percent deep, 180 degree internal SC

Table 3.3 "Near Replicate" pipe test data used to assess the effects of material variability on confidence bounds for bending moments

Organization	Expt ID	Pipe ID	Material	Outer Diameter, mm	Thickness, mm	Flaw Geometry	2c/(πD)	Test Temp, C
IPIRG-Battelle	1.2-8	DP2-F30	A106B	167.4	13.7	TWC	0.372	288
	1.2-11	DP2-F30	A106B	167.1	13.1	TWC	0.372	288
	1.2-12	DP2-F30	A106B	167.4	13.8	TWC	0.373	288
David Taylor[a]	3		A106B	219.1	14.0	TWC	0.300	52
	8		A106B	219.1	13.6	TWC	0.302	52
	10		A106B	219.1	13.7	TWC	0.262	52
	11		A106B	219.1	15.2	TWC	0.248	52
	12		A106B	219.1	13.9	TWC	0.232	52
	13		A106B	219.1	13.4	TWC	0.215	52
	14		A106B	219.1	14.6	TWC	0.192	52
	15		A106B	219.1	14.2	TWC	0.210	52
David Taylor[a]	GGK100		TP304	114.3	8.3	TWC	0.160	288
	GGK200		TP304	114.3	8.4	TWC	0.218	288
	GGK300		TP304	114.3	8.3	TWC	0.272	288
	GGK400		TP304	114.3	8.2	TWC	0.331	288
	GGK500		TP304	114.3	8.3	TWC	0.386	288
David Taylor[a]	GAM100		TP304 TIG WELD	114.3	8.6	TWC	0.278	288
	GAM200		TP304 TIG WELD	114.3	8.6	TWC	0.386	288
	GAM700		TP304 TIG WELD	114.3	8.6	TWC	0.268	288
	GAM800		TP304 TIG WELD	114.3	8.1	TWC	0.328	288
	GAM900		TP304 TIG WELD	114.3	8.1	TWC	0.297	288
	GAM1000		TP304 TIG WELD	114.3	8.1	TWC	0.298	288

(a) See Reference 3.4.

Table 3.4 Measurement uncertainty limits in maximum moments

Subtask	Uncertainty (percent)
1.1	± 12
1.2	± 3
1.3	± 14

Table 3.5 Independent test setups used for evaluating confidence bounds

Organization	Expt ID	Pipe ID	Material	Outer Diameter, mm	Thickness, mm	Flaw Geometry	d/t	2c/(πD)	Test Temp, C
CEA -	Tube 5[(a)]	-	TP304	105.0	8.26	TWC	1	0.250	22
Battelle	1.1.1.26[(a)]	-	TP304	106.2	8.31	TWC	1	0.250	22
David Taylor	GAM-100A[(b)]	-	TP304	114.6	8.15	TWC	1	0.311	288
Battelle	GAM-100A (Bat)[(c)]	-	TP304	114.7	8.26	TWC	1	0.307	288
Battelle[(c)]	DP2 4115-7	A27	TP304	170.0	13.94	ISC	0.647	1	288
	DP2 4115-8	A27	TP304	167.9	14.04	ISC	0.626	1	288
	DP2 4115-9	A27	TP304	168.4	14.00	ISC	0.655	1	288
Battelle	IPIRG 1.1-9	F30	A106B	167.4	14.1	ISC	0.720	0.419	288
	DP2 4112-6[(c)]	F30	A106B	167.5	14.8	ISC	0.680	0.503	288

(a) See Reference 3.9.
(b) See Reference 3.10.
(c) See Reference 3.4.

Table 3.6 Comparison of experimental results from through-wall-cracked pipe experiments with predictions from various analytical methods

Experiment Number	Material	Nominal Pipe Diameter, mm	Pressure, MPa	Loading	Fracture Ratio Experimental Stress/Predicted Stress			
					NSC	DPZP	GE/EPRI	LBB.ENG2
Carbon Steel (A106B) Through-wall Crack Experiments								
1.2-7	A106B	152	0	QS monotonic	0.84	1.61	1.27	1.17
1.2-8	A106B	152	0	Dyn monotonic	0.73	1.38	1.03	0.94
1.2-11	A106B	152	0	Dyn monotonic	0.83	1.58	1.27	1.17
1.2-12	A106B	152	0	Dyn monotonic	0.83	1.56	1.25	1.15
1.2-2	A106B	152	0	QS cycic R=0	0.79	1.50	1.20	1.10
1.2-4	A106B	152	0	QS cyclic R=-1	0.70	1.33	1.06	0.97
1.2-10	A106B	152	0	Dyn cyclic R=0	0.77	1.45	1.16	1.07
1.2-6	A106B	152	0	Dyn cyclic R=-1	0.65	1.23	0.92	0.84
1.1-2	A106B	152	15.5	Inertial	0.82	1.56	1.25	1.16
Stainless Steel (TP304) Through-Wall Crack Experiments								
4131-5	TP304	152	0	QS monotonic	1.10	1.10	1.51	1.44
4131-1	TP304	152	17.2	QS monotonic	0.93	0.93	1.27	1.20
1.2-1	TP304	152	0	Dyn monotonic	1.08	1.08	1.55	1.47
1.2-3	TP304	152	0	QS cyclic R=0	0.97	0.97	1.39	1.32
1.2-5	TP304	152	0	QS cyclic R=-1	0.87	0.87	1.32	1.26
1.2-9	TP304	152	0	Dyn cyclic R=-1	0.99	0.99	1.50	1.43
1.1-3	TP304	152	15.2	Inertial	1.09	1.10	1.61	1.51

Table 3.7 Comparison of experimental results from surface-cracked pipe experiments with predictions from various analytical methods

Experiment Number	Material	Nominal Pipe Diameter, mm	Pressure, MPa	Loading	Fracture Ratio Experimental Stress/Predicted Stress		
					NSC	DPZP	SC.TNP
Carbon Steel Surface Crack Experiments							
4112-6	A106B	152	0	QS monotonic	0.95	1.06	N.D.
1.1-9	A106B	152	15.5	QS monotonic	0.84	0.93	N.D.
1.1-7	A106B	152	15.5	Dyn monotonic	0.97	1.07	1.15
1.1-6	A106B	152	15.5	Inertial	0.97	1.07	N.D.
1.1-8	A106B	152	15.5	Inertial	1.13	1.25	N.D.
4112-8	A106B	406	0	QS monotonic	0.91	1.05	1.03
1.3-2	A106B	406	15.5	Pipe system	0.61	0.70	0.72
4141-8	A106B weld	406	15.5	QS monotonic	0.93	1.24	1.15
1.3-4	A106B weld	406	15.5	Pipe system	0.97	1.29	1.21
Stainless Steel Surface Crack Experiments							
4112-3	TP304	152	0	QS monotonic	1.17	1.17	1.18
4131-2	TP304	152	24.5	QS monotonic	1.21	1.21	1.18
1.1-5	TP304	152	15.2	Inertial	1.17	1.17	1.23
EPRI 13S*	TP304	406	0	QS monotonic	1.05	1.05	0.99
1.3-3	TP304	406	15.5	Pipe system	0.86	0.86	0.80
4141-4	TP304 weld	406	11.0	QS monotonic	0.95	1.22	1.21
1.3-5	TP304 weld	406	15.5	Pipe system	0.90	1.16	1.19
4143-1	CF8M	400	15.5	QS monotonic	0.89	1.11	1.06
1.3-7	CF8M	400	15.5	Pipe system	0.77	0.96	0.91

* Experiment conducted at room temperature.

Table 3.8. ASME analyses of IPIRG Task 1 and related Degraded Piping Program Experiments

Expt. Number	Material	Nominal Pipe Diameter, inch	Fracture Ratio Expt. Stress/Predicted Stress		
			Approach 1 S_m(Code)	Approach 1 S_m(Actual)	Approach 2 S_m(Code)
Stainless Steel, Unpressurized, Surface-Cracked-Pipe Experiments					
4112-3	TP304	6	1.06	0.99	8.00
EPRI 13S	TP304	16	1.40	0.98	2.74
Stainless Steel, Pressurized, Surface-Cracked-Pipe Experiments					
1.1-5	TP304	6	1.10	1.03	1.51
4131-2	TP304	6	1.18	1.09	3.26
1.3-3	TP304	16	0.87	0.66	0.75
1.3-5	SS SAW	16	1.40	1.07	1.20
4141-4	SS SAW	16	1.47	1.13	2.39
1.3-7	CF8M	16	0.92(a)	0.61(a)	0.72
4143-1	CF8M	16	1.07(a)	0.70(a)	1.45
Stainless Steel, Unpressurized, Through-Wall-Cracked Pipe Experiments					
1.2-1	TP304	6	0.98	0.92	18.56
1.2-3	TP304	6	0.88	0.83	19.64
1.2-5	TP304	6	0.79	0.74	6.02
1.2-9	TP304	6	0.90	0.84	6.45
4131-5	TP304	6	1.00	0.93	13.02
Stainless Steel, Pressurized, Through-Wall-Cracked Pipe Experiments					
1.1-3	TP304	6	1.05	0.98	1.75
4131-1	TP304	6	0.91	0.85	8.11
Carbon Steel, Unpressurized, Surface-Cracked-Pipe Experiments					
4112-6	A106B	6	2.01	1.45	4.52
4112-8	A106B	16	2.01	1.59	2.78
Carbon Steel, Pressurized, Surface-Cracked-Pipe Experiments					
1.1-6	A106B	6	2.30	1.58	3.97
1.1-7	A106B	6	2.12	1.51	2.23
1.1-9	A106B	6	1.87	1.32	2.01
1.3-2	A106B	16	1.48	1.14	0.94
1.3-4	CS SAW	16	2.58	1.98	2.28
4141-8	CS SAW	16	2.48	1.89	3.14

Table 3.8. (Continued)

Expt. Number	Material	Nominal Pipe Diameter, inch	Fracture Ratio Expt. Stress/Predicted Stress Approach 1 S_m(Code)	Approach 1 S_m(Actual)	Approach 2 S_m(Code)
Carbon Steel, Unpressurized, Through-Wall-Cracked Pipe Experiments					
1.2-2	A106B	6	1.67	1.20	6.89
1.2-4	A106B	6	1.48	1.07	4.70
1.2-6	A106B	6	1.36	0.98	4.21
1.2-7	A106B	6	1.78	1.28	6.82
1.2-8	A106B	6	1.53	1.10	5.46
1.2-10	A106B	6	1.61	1.16	5.17
1.2-11	A106B	6	1.75	1.26	6.32
1.2-12	A106B	6	1.74	1.25	7.58
Carbon Steel, Pressurized, Through-Wall-Cracked Pipe Experiments					
1.1-2	A106B	6	1.93	1.34	2.27

(a) Analyzed assuming limit load equations applied. However, J-estimation scheme analyses indicated that limit-load conditions were not satisfied.

Table 3.9 R6 Option 1 analyses of IPIRG Task 1 experiments and related Degraded Piping Program experiments

Expt. Number	Material	Nominal Pipe Diameter, inch	Expt. Bending Stress, MPa	R6 Opt. 1 Predicted Bending Stress, MPa	Axial Stress, MPa	R6 Opt. 1 Predicted Plus Axial Stress, MPa	Elastic Bending Stress, MPa	Elastic Bending Plus Axial Stress, MPa	Fracture Ratio Expt. Stress/Predicted Stress Approach 1	Fracture Ratio Expt. Stress/Predicted Stress Approach 2
				Unpressurized, Through-Wall-Cracked Pipe Experiments						
1.2-1	TP304	6	158.8	104.4	0.0	104.4	3000.4	3000.4	1.52	20.74
1.2-2	A106B	6	201.2	154.1	0.0	154.1	829.7	829.7	1.31	5.39
1.2-3	TP304	6	142.5	104.6	0.0	104.6	3174.5	3174.5	1.36	30.36
1.2-4	A106B	6	178.3	154.1	0.0	154.1	566.1	566.1	1.16	3.67
1.2-5	TP304	6	134.2	110.0	0.0	110.0	1021.6	1021.6	1.22	9.29
1.2-6	A106B	6	163.4	152.4	0.0	152.4	506.9	506.9	1.07	3.33
1.2-7	A106B	6	214.3	154.1	0.0	154.1	821.7	821.7	1.39	5.33
1.2-8	A106B	6	175.9	146.6	0.0	146.6	628.1	628.1	1.20	4.29
1.2-9	TP304	6	143.5	103.6	0.0	103.6	1030.0	1030.0	1.39	9.95
1.2-10	A106B	6	181.9	146.7	0.0	146.7	584.9	584.9	1.24	3.99
1.2-11	A106B	6	200.8	145.7	0.0	145.7	727.3	727.3	1.38	4.99
1.2-12	A106B	6	198.9	146.1	0.0	146.1	867.8	867.8	1.36	5.94
4131-5	TP304	6	156.0	101.3	0.0	101.3	2037.2	2037.2	1.54	20.12
				Pressurized, Through-Wall-Cracked Pipe Experiments						
1.1-2	A106B	6	159.0	100.9	33.9	134.8	193.9	227.9	1.43	1.69
1.1-3	TP304	6	119.0	32.0	34.7	66.7	227.1	261.8	2.30	3.92
4131-1	TP304	6	86.4	26.5	40.9	67.5	1186.6	1227.5	1.89	18.20
				Unpressurized, Surface-Cracked Pipe Experiments						
4112-3	A106B	6	250.5	175.4	0.0	175.4	1895.5	1895.5	1.43	10.81
4112-6	TP304	6	321.1	215.1	0.0	215.1	721.0	721.0	1.49	3.35
4112-8	A106B	16	271.4	177.0	0.0	177.0	375.4	375.4	1.53	2.12
EPRI 13S	TP304	16	407.8	306.1	0.0	306.1	798.0	798.0	1.33	2.61
				Pressurized, Surface-Cracked Pipe Experiments						
1.1-5	TP304	6	24.2	114.8	34.7	149.5	325.1	359.8	1.73	2.41
1.1-6	A106B	6	199.6	113.5	34.1	147.6	377.3	411.4	1.58	2.79
1.1-7	A106B	6	331.3	235.6	36.5	272.1	350.5	386.9	1.35	1.42
1.1-9	A106B	6	257.0	213.9	34.5	248.4	281.0	315.6	1.17	1.27
4131-2	TP304	6	145.3	0.7	58.8	59.5	535.4	594.2	3.43	9.98
1.3-2	A106B	16	125.6	108.2	49.6	157.8	116.1	165.7	1.11	1.05
1.3-3	TP304	16	144.9	103.4	50.2	153.7	201.1	251.3	1.27	1.64
1.3-4	CS SAW	16	230.8	99.7	49.9	149.6	329.4	379.3	1.88	2.54
4141-8	CS SAW	16	222.0	102.0	50.3	152.2	298.5	348.8	1.79	2.29
1.3-5	SS SAW	16	170.2	126.0	51.5	177.5	206.7	258.1	1.25	1.45
4141-4	SS SAW	16	172.7	84.4	35.5	119.9	307.8	343.3	1.74	2.86
1.3-7	CF8M	16	215.4	132.6	47.0	179.6	247.0	294.1	1.46	1.64
4143-1	CF8M	16	248.4	126.0	47.5	173.5	359.4	406.8	1.71	2.34

Table 3.10. Comparison of J_i values from Subtask 1.3 surface cracked pipe experiments and C(T) specimen tests

Experiment Number	Material	Material ID Number	Pipe Experiment J_i Value, kJ/m^2	C(T) Specimen J_i Values, kJ/m^2	
				Quasi-Static	Dynamic
1.3-3	TP304	A8	180	738	1215
1.3-5	TP304 SAW	A8W	130	55	128
1.3-7	CF8M	A40	74	88	116

Table 3.11 Rotation and normalized moment at initiation and maximum moment

Expt. No.	Dia., inch	Material	Load[a] History	Flaw[b] Type	Rotation[c,d] Init., rad.	Max., rad.	Moment/NSC[c,e] Init.	Max.
1.1-2	6	A106	Inertial	TWC	0.00155	0.00550	0.720	0.820
1.1-3	6	TP304	Inertial	TWC	0.01940	0.04735	0.980	1.090
1.1-4	6	A106	Inertial	XSC	N.D.	N.D.	N.D.	N.D.
1.1-5	6	TP304	Inertial	XSC	0.00272	0.00815	0.910	1.170
1.1-6	6	A106	Inertial	ISC	N.D.	N.D.	N.D.	0.960
1.1-7	6	A106	QS mono	ISC	0.00340	0.00375	0.950	0.970
1.1-8	6	A106	Inertial	ISC	N.D.	0.00123	N.D.	1.130
1.1-9	6	A106	Dyn mono	ISC	0.00211	0.00629	0.760	0.840
1.2-1	6	TP304	Dyn mono	TWC	0.05020	0.07453	1.038	1.083
1.2-2	6	A106	QS R=0	TWC	0.00367	0.01449	0.449	0.793
1.2-3	6	TP304	QS R=0	TWC	0.03115	0.07205	0.814	0.972
1.2-4	6	A106	QS R=-1	TWC	0.00377	0.00871	0.568	0.702
1.2-5	6	TP304	QS R=-1	TWC	0.00171	0.01841	0.581	0.871
1.2-6	6	A106	Dyn R=-1	TWC	0.00122	0.00489	0.499	0.647
1.2-7	6	A106	QS mono	TWC	0.00175	0.01047	0.610	0.844
1.2-8	6	A106	Dyn mono	TWC	0.00136	0.00752	0.544	0.727
1.2-9	6	TP340	Dyn R=-1	TWC	0.00698	0.02182	0.821	0.990
1.2-10	6	A106	Dyn R=0	TWC	0.00083	0.00660	0.483	0.767
1.2-11	6	A106	Dyn mono	TWC	0.00070	0.00960	0.469	0.833
1.2-12	6	A106	Dyn mono	TWC	0.00175	0.01292	0.575	0.825
4131-5	6	TP304	QS mono	TWC	0.03386	0.09844	0.868	1.099
1.3-2	16	A106	System	ISC	N.D.	N.D.	N.D.	0.605
1.3-3	16	TP304	System	ISC	0.00435	0.00500	0.834	0.856
1.3-4	16	A106 SAW	System	ISC	N.D.	N.D.	N.D.	0.973
1.3-5	16	TP304 SAW	System	ISC	0.00235	0.00305	0.837	0.897
1.3-7	16	CF-8M	System	ISC	0.00200	0.00279	0.659	0.771
4112-8	16	A106	QS Bend	ISC	0.01687	0.01052	0.835	0.906
13S	16	TP304	QS Bend	ISC	0.01000	0.01725	0.805	1.046
4141-8	16	A106 SAW	QS P&B	ISC	0.00140	0.00358	0.664	0.932
4141-4	16	TP304 SAW	QS P&B	ISC	0.00451	0.00470	0.943	0.949
4143-1	16	CF-8M	QS P&B	ISC	0.00310	0.00345	0.877	0.893

(a) QS = quasi-static, Dyn = dynamic, Mono = monotonic, P&B = pressure and bending.

(b) TWC = through-wall crack, XSC = external surface crack, ISC = internal surface crack.

(c) N.D. = Not determined.

(d) Half of total rotation.

(e) NSC = Net-Section-Collapse analysis predicted failure stress using $\sigma_f = (\sigma_y + \sigma_u)/2$.

Table 3.12 Elastic stress analysis results for Subtask 1.1 inertially loaded pipe experiments

Experiment	1.1-2	1.1-3	1.1-4	1.1-5	1.1-6
Material	CS	SS	CS	CS	CS
Flaw Type	TWC	TWC	XSC	XSC	ISC
Bladder (Y/N)	Y	Y	Y	Y	N
Experimental Results					
$M_{(\text{Tot exp.})}$, kN-m	37.9	30.8	84.9	48.6	85.9
$\sigma_{(\text{expt. bend }\sigma)}$, MPa	155.5	126.5	348.5	199.2	352.2
$\sigma_{(\text{ten. exp.})}$, MPa	31.9	31.9	31.9	31.9	31.9
$\sigma_{(\text{Tot exp.})}$, MPa	187.4	158.3	380.4	231.1	384.1
Elastic Calculated Values					
$M_{(\text{Tot el.})}$, kN-m	47.4	55.8	77.3	79.2	91.9
$\sigma_{(\text{el. bend }\sigma)}$, MPa	220.4	259.6	359.5	368.2	427.2
$\sigma_{(\text{ten. exp.})}$, MPa	31.9	31.9	31.9	31.9	31.9
$\sigma_{(\text{Tot el.})}$, MPa	252.3	291.5	391.4	400.1	459.1
Elastic Stress Ratio (Predicted/Experiment)					
Ratio(Tot. Mom.)	1.25	1.81	0.91	1.63	1.07
Ratio(Tot. σ)	1.35	1.84	1.03	1.73	1.20

Table 3.13 Elastic stress analysis results for Subtask 1.3 pipe system experiments

Experiment No. Material	1.3-2 CS Base	1.3-3 SS Base	1.3-4 CS Weld	1.3-5 SS Weld	1.3-7 Cast SS
Experimental results					
$M_{(\text{Tot. exp.})}$, kN-m	341.0	426.2	618.4	492.7	590.1
$M_{(\text{SP exp.})}$, kN-m	238.1	241.0	442.4	262.3	262.8
Max moment displacement, mm	38.97	39.72	91.00	45.15	45.26
Time to Max. moment, sec.	0.625	2.080	6.670	2.335	2.340
$\sigma_{(\text{expt. bend }\sigma)}$, MPa	125.5	144.8	230.3	170.1	215.9
$\sigma_{(\text{Tot. exp.})}$, MPa	186.4	206.4	292.5	232.8	274.2
$\sigma_{(\text{ten. exp.})}$, MPa	60.9	61.5	61.2	62.7	58.3
Elastic Calculated Values					
$M_{(\text{Tot. el.})}$, kN-m	324.1	591.0	882.1	598.7	676.3
$M_{(\text{SP el.})}$, kN-m	233.4	236.3	431.6	257.0	257.4
$\sigma_{(\text{Tot. el. bend }\sigma)}$, MPa	116.2	211.8	316.2	214.6	242.4
$\sigma_{(\text{ten. el.})}$, MPa	60.0	60.0	60.0	60.0	60.0
$\sigma_{(\text{Tot. el.})}$, MPa	176.2	271.9	376.2	274.6	302.5
$\sigma_{(\text{SAM el.})}$, MPa	53.2	54.2	124.2	61.6	61.8
$\sigma_{(t=\theta)}$, MPa	30.5	30.5	30.5	30.5	30.5
Elastic Stress Ratio (Predicted/Experiment)					
$\text{Ratio}_{(\text{Tot. Mom.})}$	0.95	1.39	1.43	1.22	1.15
$\text{Ratio}_{(\text{Tot. }\sigma)}$	0.95	1.32	1.29	1.18	1.10
$\text{Ratio}_{(\sigma\text{-SAM})}$	0.66	1.05	0.86	0.92	0.88
Ratio_{I}	0.88	1.92	2.56	1.48	1.28

Table 3.14 Summary of IPIRG Subtask 1.3 pipe system natural frequency comparisons

Mode*	Finite Element Prediction	Measured Values
A	4.42	4.47
B	14.45	13.9-14.0
C	14.63	12.0
D	18.71	18.0
E	3.19	3.5

* See Figures 3.27 and 3.28.

Table 3.15 Summary of Subtask 1.3 stability predictions

			Energy Balance, M_{eq} for $P=P_{sat}$	
Experiment	Flaw Material	J/T	P_{sat}=Load Controlled	P_{sat}+Inertial=Load Controlled
Through-Wall Cracks				
1.3-2	A106B	Stable	Unstable (Marginal)	Unstable
1.3-4	CS SAW	Stable	Stable	Unstable
1.3-3	TP304	Stable	Stable	Unstable
1.3-5	SS SAW	Stable	Stable	Unstable
1.3-7	Aged CF8M	Stable	Stable	Unstable
Surface Cracks				
1.3-2	A106B	Unstable	Unstable	
1.3-4	CS SAW	Unstable	Unstable	
1.3-3	TP304	Unstable	Unstable	
1.3-5	SS SAW	Unstable	Unstable	
1.3-7	Aged CF8M	Unstable	Unstable	

Table 3.16. Comparison of predicted crack arrest lengths[a] from the Energy Balance Stability criterion with experimental results

Experiment	Predicted Δa, mm	Experimental Δa, mm
1.3-2	unstable	65
1.3-3	19	>5
1.3-4	92	32
1.3-5	43	48
1.3-7	69	(b)

(a) Crack growth from each end of surface crack.

(b) Experimental data not accurate enough, except to say that large crack growth did not occur on the load cycle when surface crack penetration occurred.

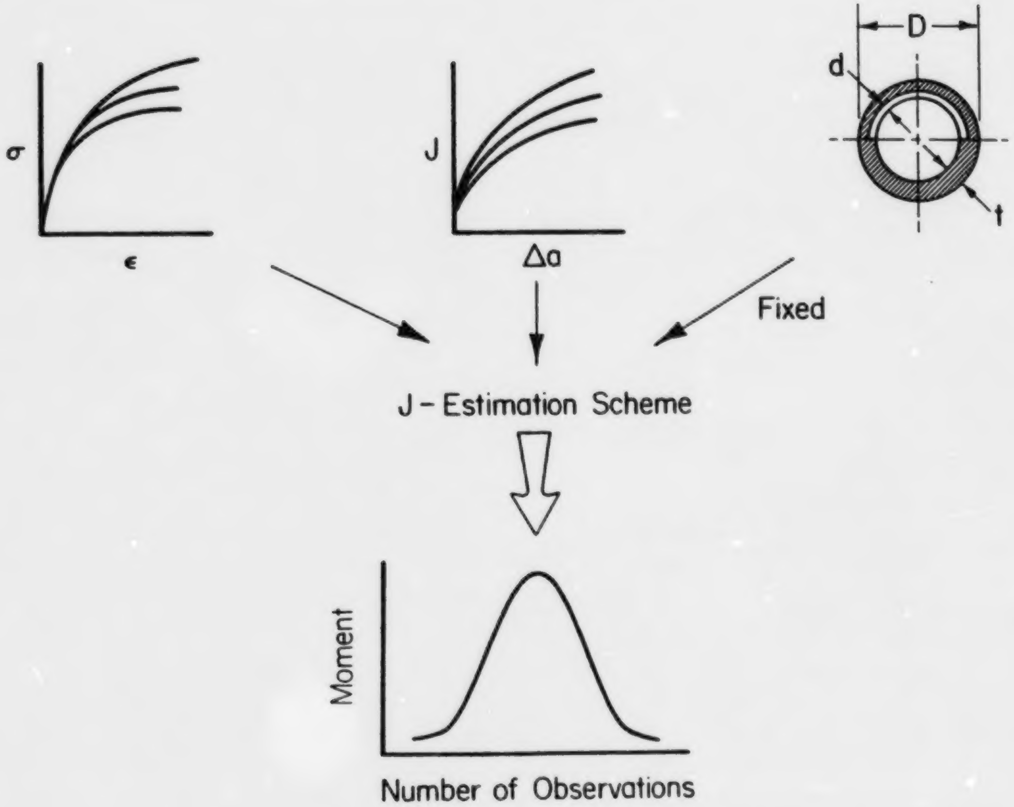
D
d
t
σ
ϵ
J
Δa
Fixed
J - Estimation Scheme
Moment
Number of Observations

Figure 3.1. Semi-analytical approach to investigating the effects of material variability on failure moments.

F-I-7/91-F3.1

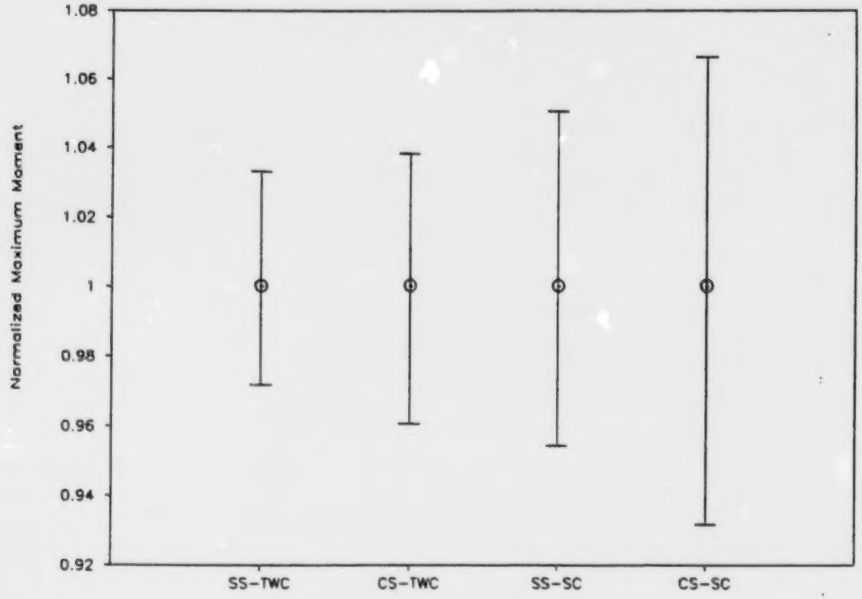

Figure 3.2. Effect of material property variation or maximum for a 152-mm diameter x 9.5 mm (6 inch x 0.375 inch) thick pipe using J-estimation schemes.

F-I-7/91-F3.2

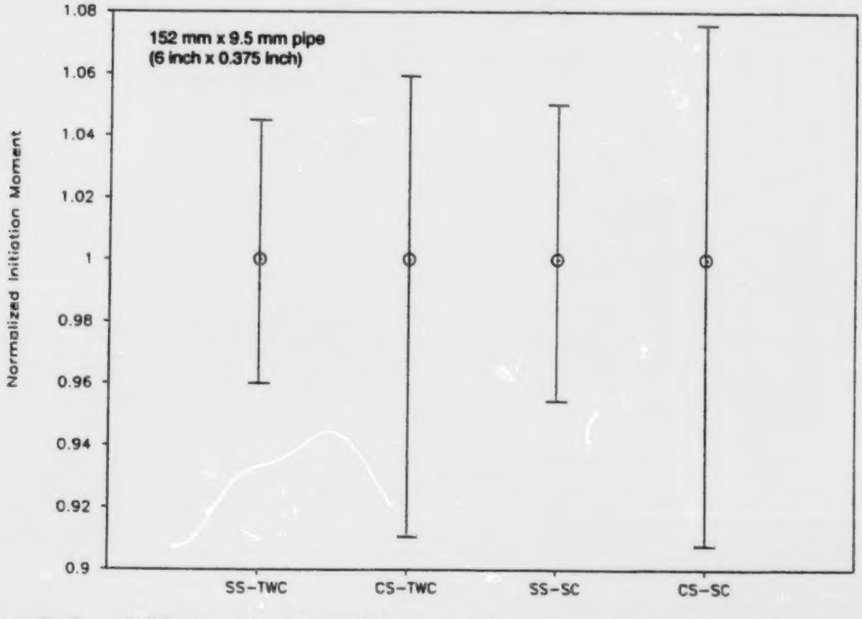

Figure 3.3. Effect of material property variation on initiation moment for a 152-mm diameter x 9.5 mm thick (6 inch x 0.375 inch) pipe using J-estimation schemes.

F-I-7/91-F3.3

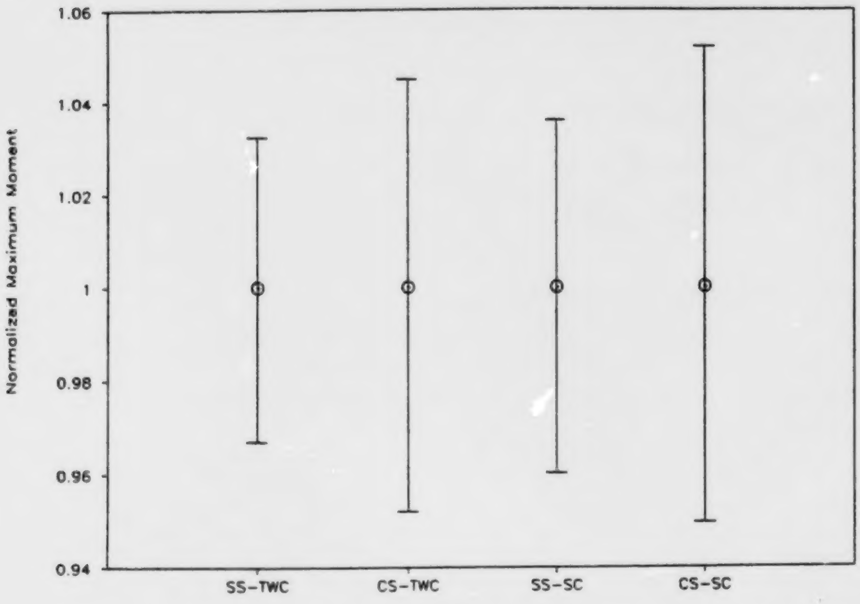

Figure 3.4. Effect of material property variation on maximum moment for a 406-mm diameter x 25.4 mm thick (16 inch x 1.00 inch) pipe using J-estimation schemes.

F-I-7/91-F3.4

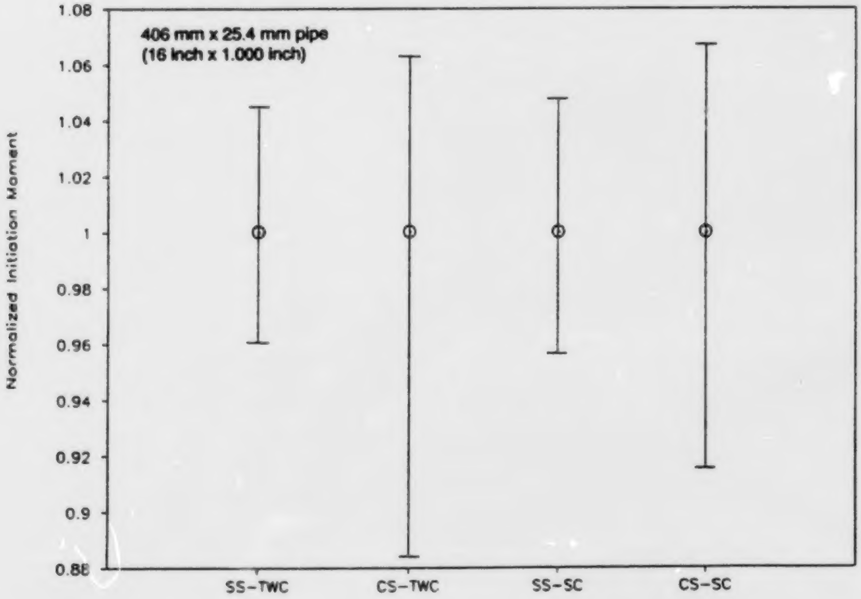

Figure 3.5. Effect of material property variation on initiation moment for a 406-mm diameter x 25.4 mm thick (16 inch x 1.000 inch) pipe using J-estimation schemes.

F-I-7/91-F3.5

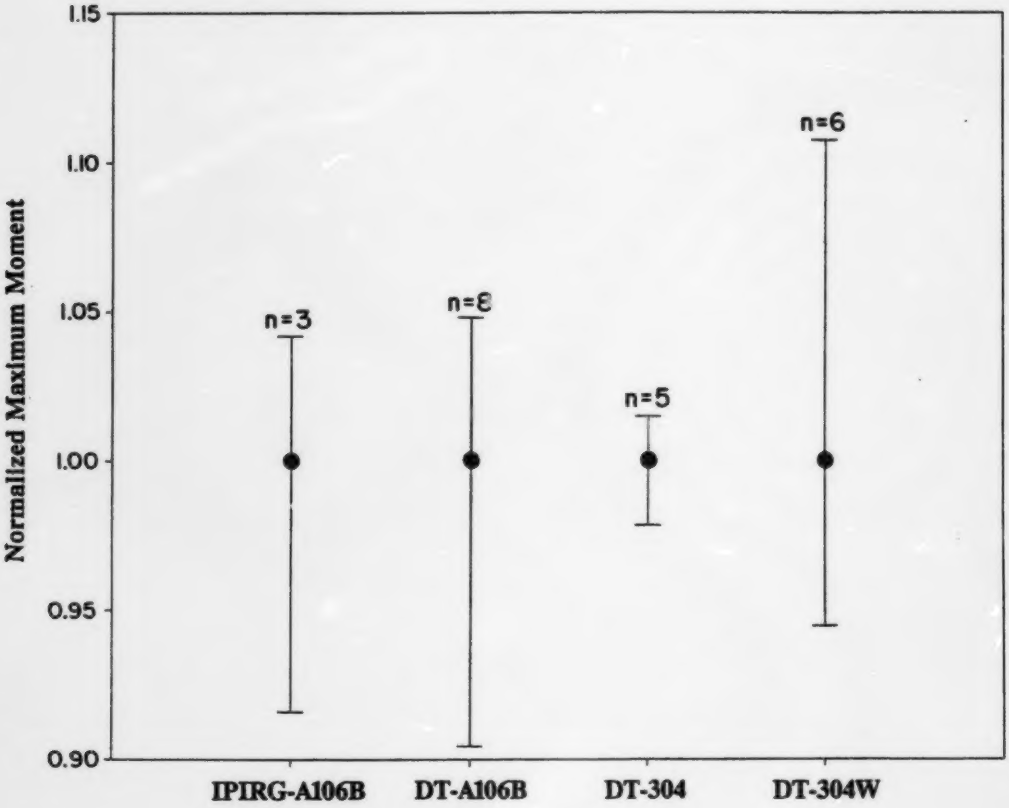

Figure 3.6. Effect of material property variability on maximum moment for "near replicate" experiments.

I-5/91-D9-R0

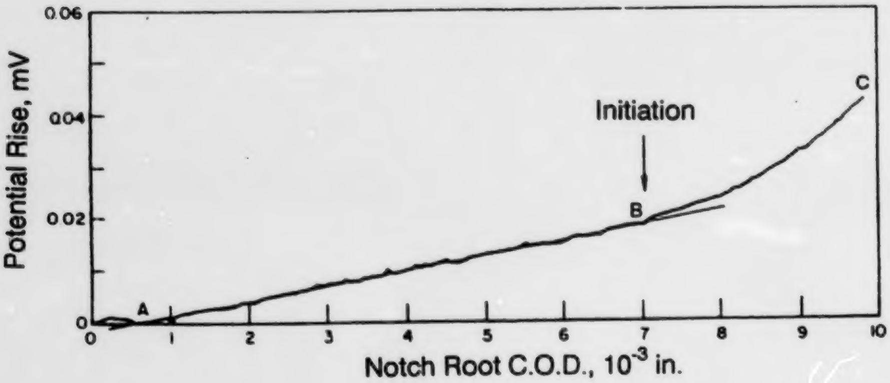

(a) Typical potential rise/crack-mouth-opening displacement curve (from Ref. 3.5).

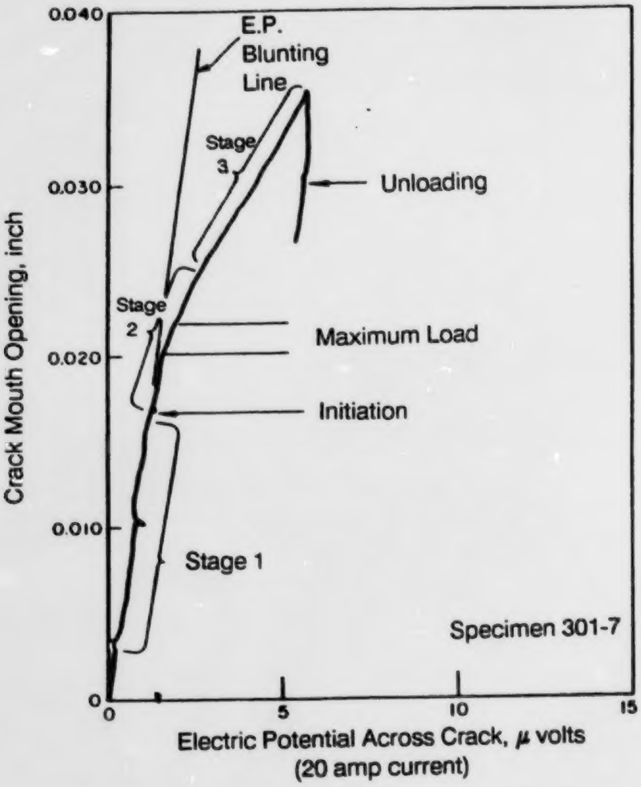

(b) Crack mouth opening versus d-c EP data from AISI 1020 carbon steel bend specimen (from Ref. 3.6)

Figure 3.7. Crack initiation from d-c EP data.

F-I-7/91-F3.7

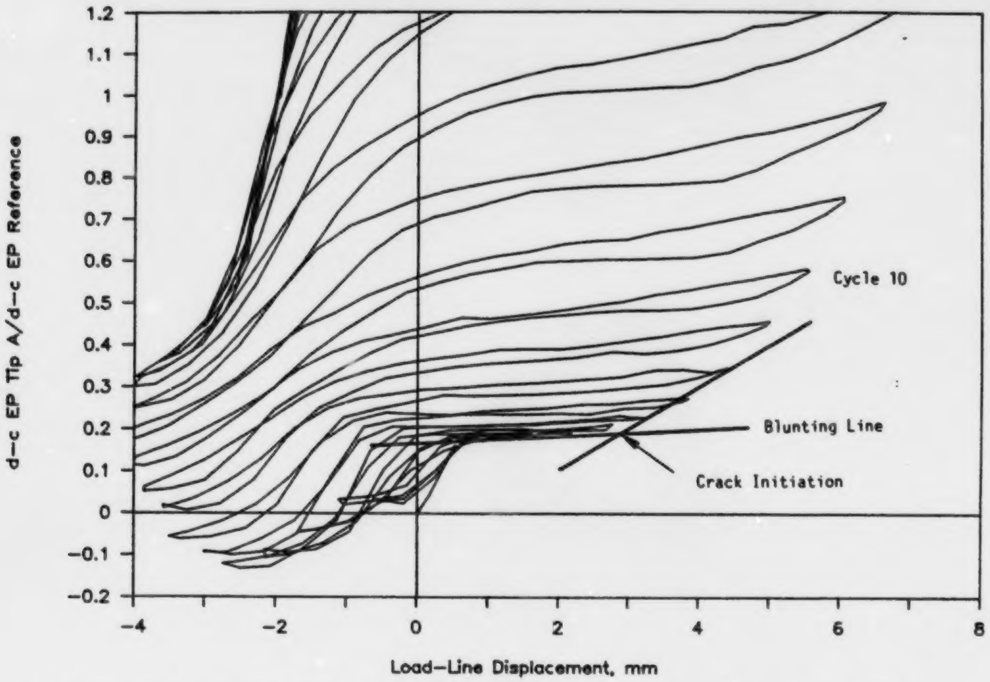

Figure 3.8. Normalized d-c EP at crack Tip A versus load-line displacement for Experiment 1.2-6 showing point of crack initiation using envelop of cyclic data and blunting line method.

DRB/1.2-6/F14

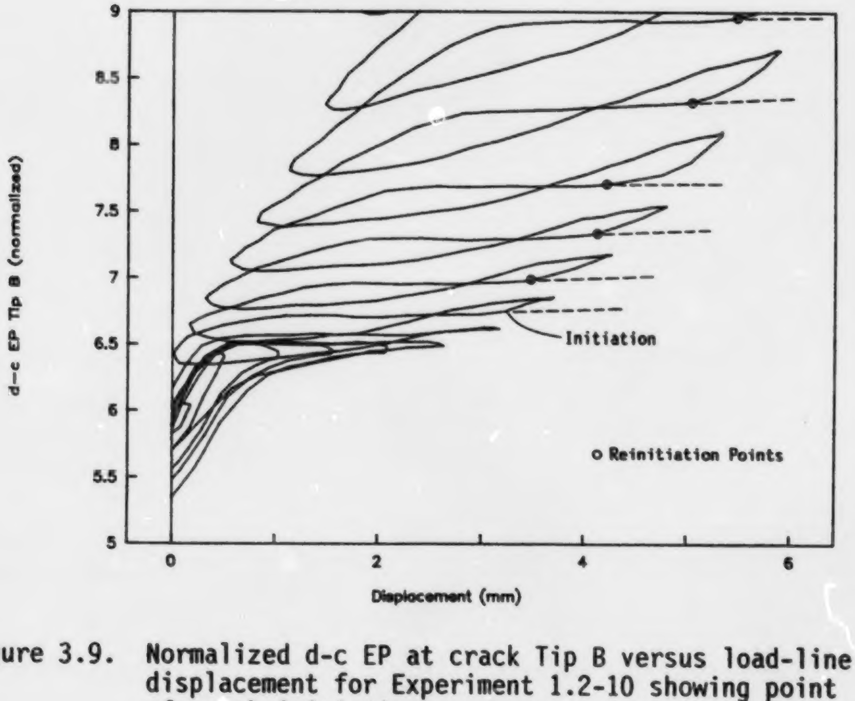

Figure 3.9. Normalized d-c EP at crack Tip B versus load-line displacement for Experiment 1.2-10 showing point of crack initiation.

DRB/1.2-10/F15

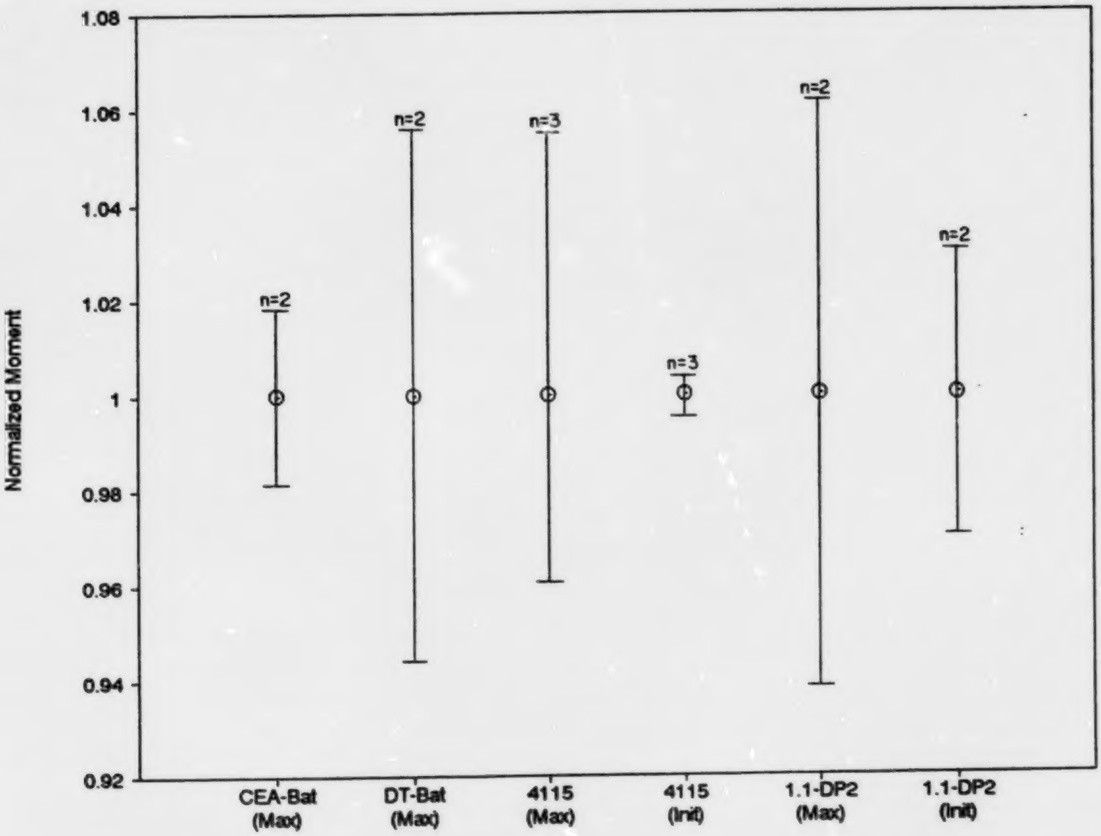

Figure 3.10. Uncertainty in moment from independent test setups.

F-I-7/91-F3.10

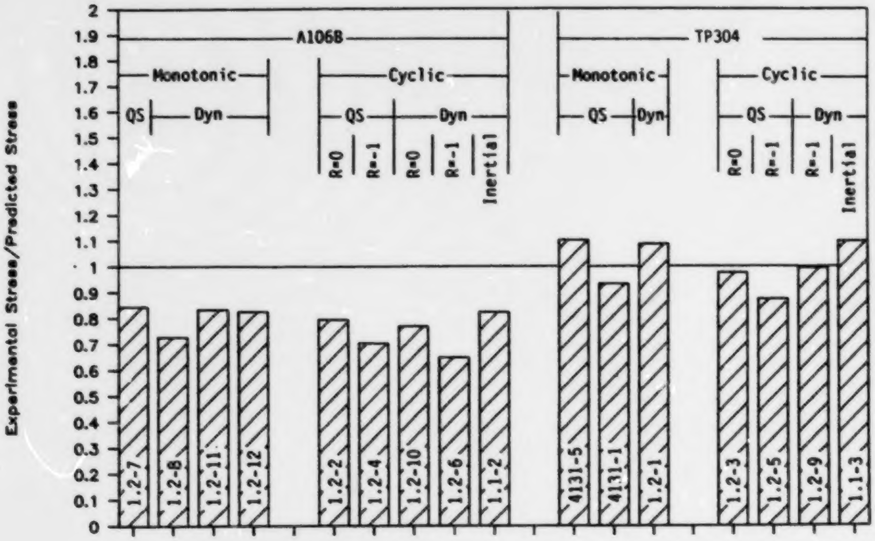

Figure 3.11. Comparison of experimental results with Net-Section-Collapse analysis predictions for the through-wall-cracked pipe experiments (6-inch diameter pipe).

F-I-7/91-F3.11

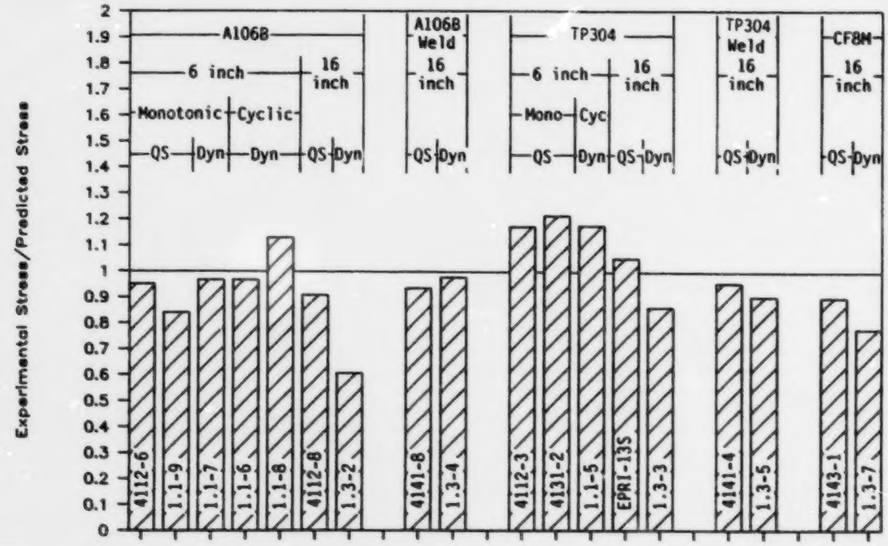

Figure 3.12. Comparison of experimental results with Net-Section-Collapse analysis predictions for the surface-cracked pipe experiments.

F-I-7/91-F3.12

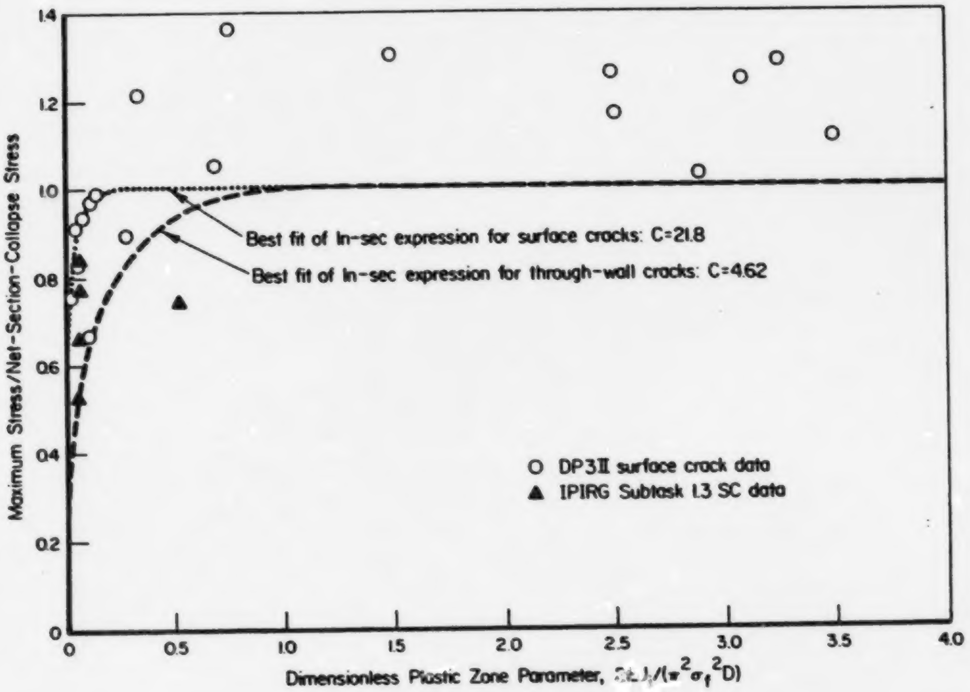

Figure 3.13. Schematic showing comparison of IPIRG pipe fracture data with Degraded Piping Program data using Dimensionless Plastic-Zone Parameter [$\sigma_f = (\sigma_y + \sigma_u)/2$ for all data].

F-I-7/91-F3.13

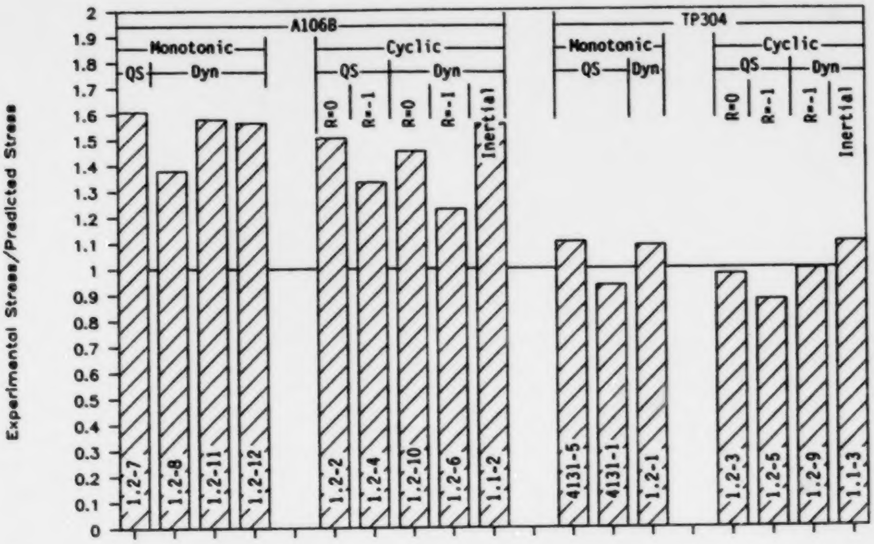

Figure 3.14. Comparison of experimental results with DPZP analysis predictions for through-wall-cracked pipe experiments (6-inch pipe diameter).

F-I-7/91-F3.14

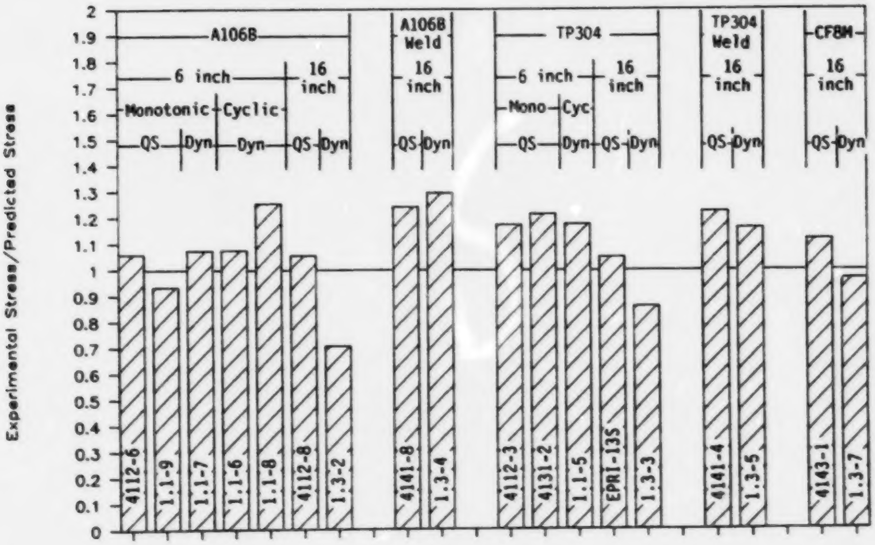

Figure 3.15. Comparison of experimental results with DPZP analysis predictions for the surface-cracked pipe experiments.

F-I-7/91-F3.15

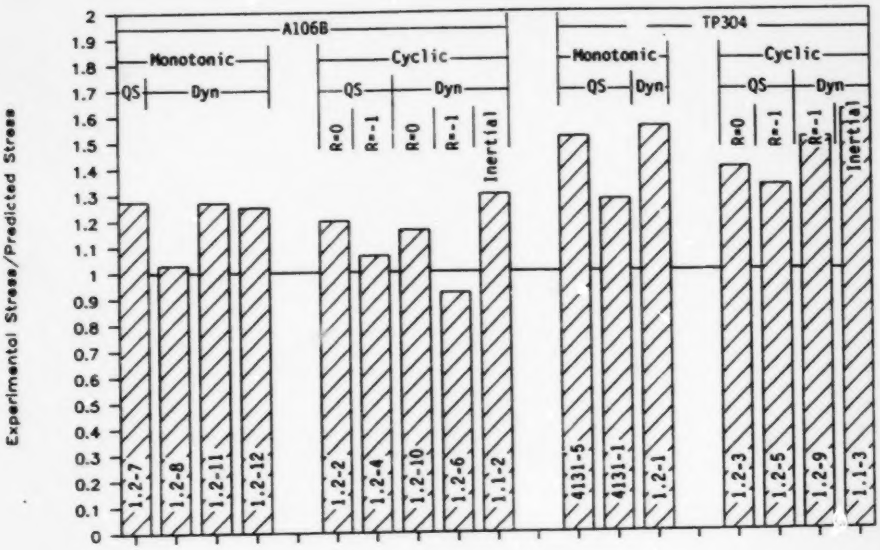

Figure 3.16. Comparison of experimental results with GE/EPRI J-estimation scheme predictions for the through-wall-cracked pipe experiments.

F-I-7/91-F3.16

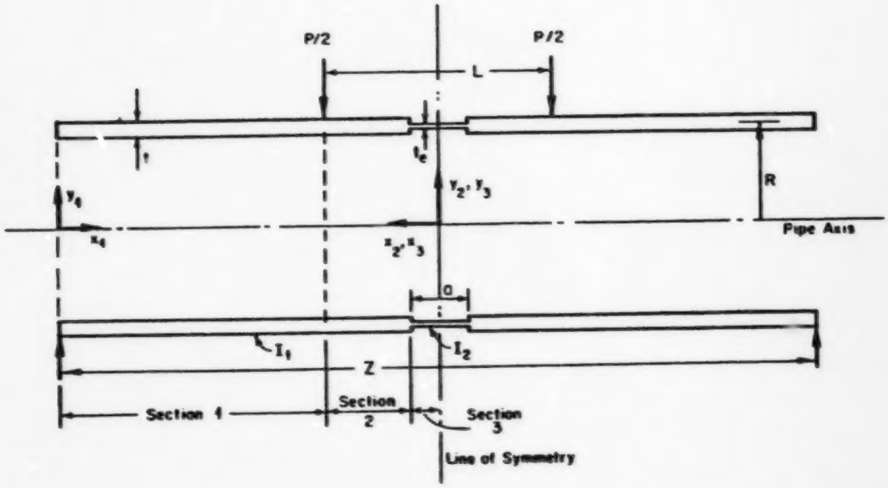
P/2
P/2
L
t
t_c
y_2, y_3
R
y_1
x_1
x_2, x_3
Pipe Axis
a
I_1
I_2
Z
Section 1
Section 2
Section 3
Line of Symmetry

Figure 3.17. Pipe geometry of engineering estimate modification of LBB.ENG2 method.

T-4853-F2.1

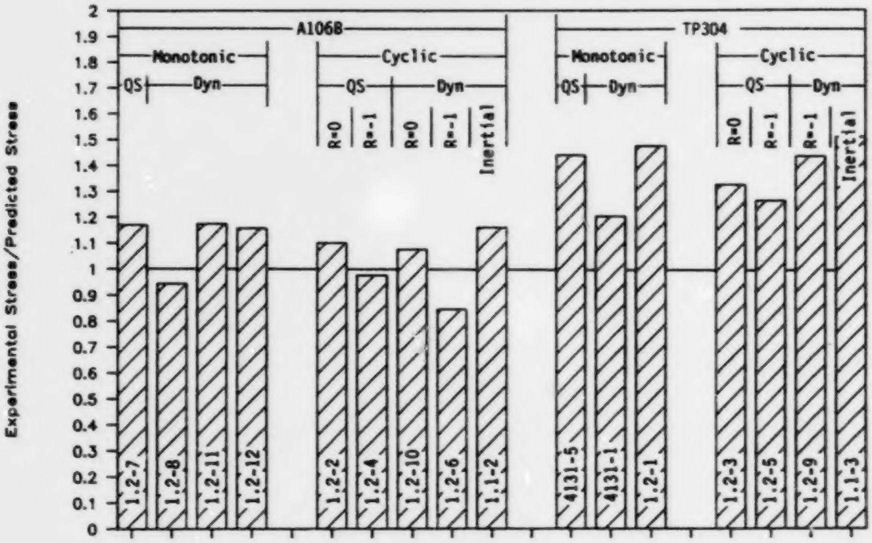

Figure 3.18. Comparison of experimental results with LBB.ENG2 J-estimation scheme predictions for the through-wall-cracked pipe experiments.

F-I-7/91-F3.18

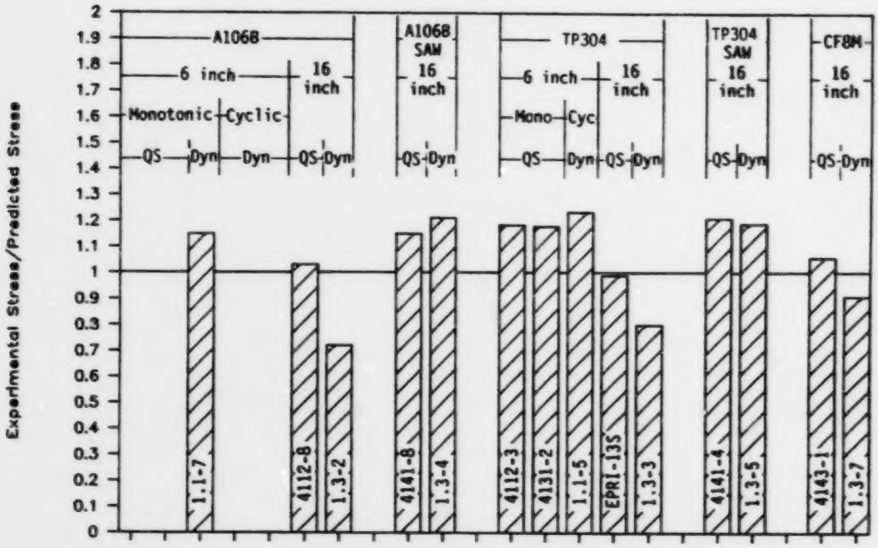

Figure 3.19. Comparison of experimental results with SC.TNP J-estimation scheme predictions for the surface-cracked pipe experiments.

F-I-7/91-F3.19

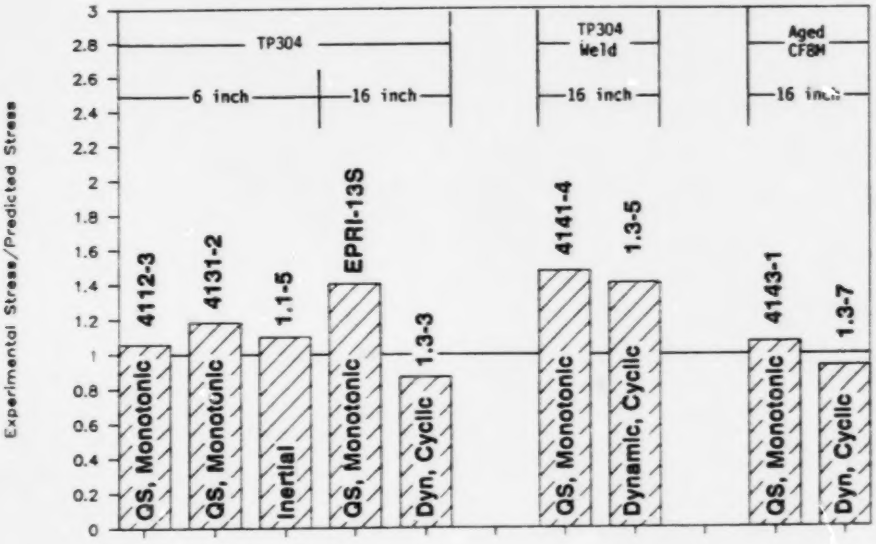

Figure 3.20. Comparison of the experimental results with the ASME IWB-3640 Approach 1 predictions [using S_m(Code)] for the stainless steel surface-cracked-pipe experiments.

F-I-7/91-F3.20

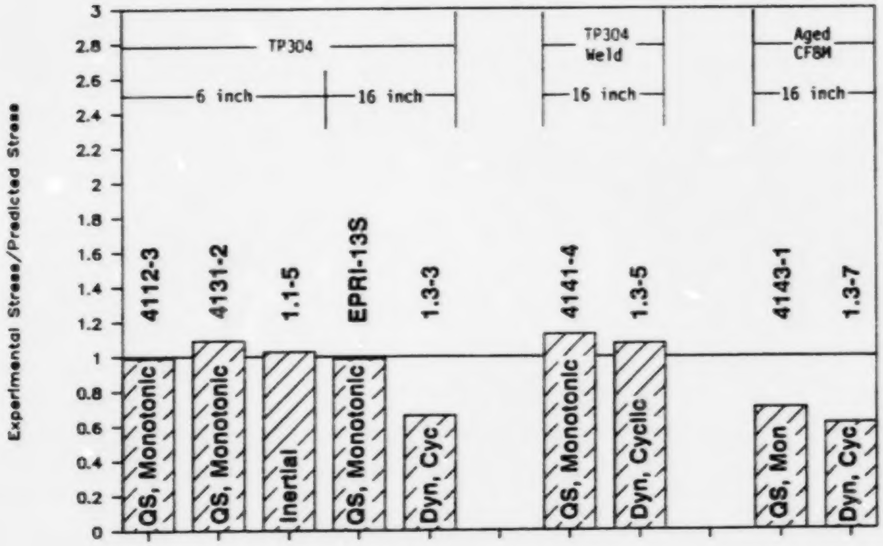

Figure 3.21. Comparison of the experimental results with the ASME IWB-3640 Approach 1 predictions [using S_m(Actual)] for the stainless steel surface-cracked-pipe experiments.

F-I-7/91-F3.21

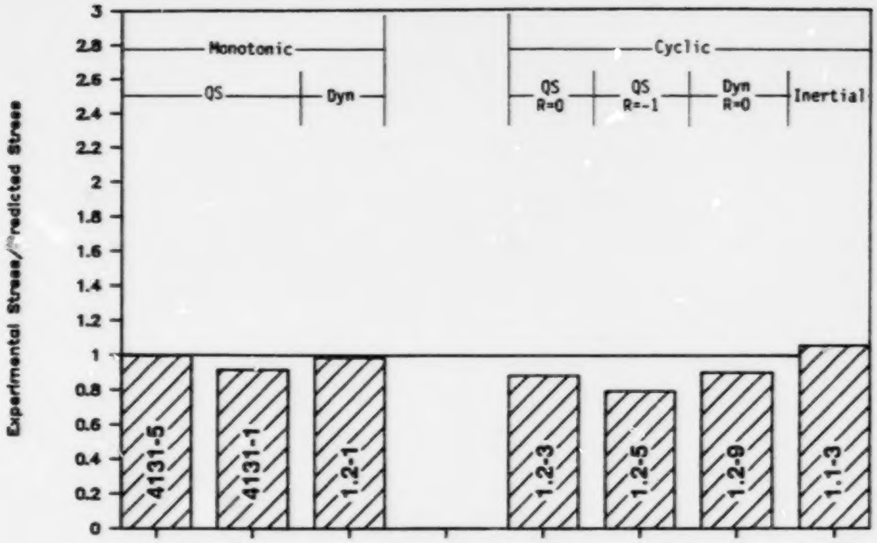

Figure 3.22. Comparison of experimental data with IWB-3640 Approach 1 predictions for stainless steel through-wall-cracked pipe experiments using Code values for S_m.

F-I-7/91-F3.22

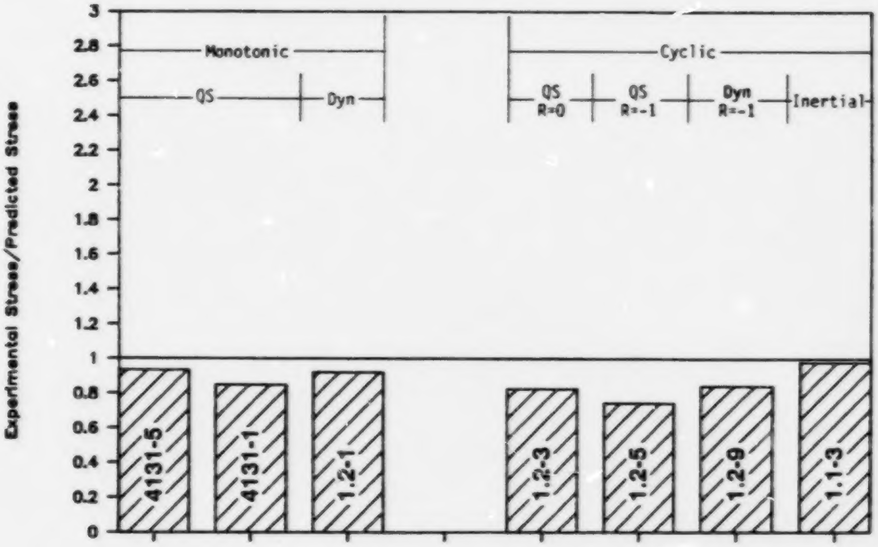

Figure 3.23. Comparison of experimental data with IWB-3640 Approach 1 predictions for stainless steel through-wall-cracked pipe experiments using actual properties as a basis for S_m.

F-I-7/91-F3.23

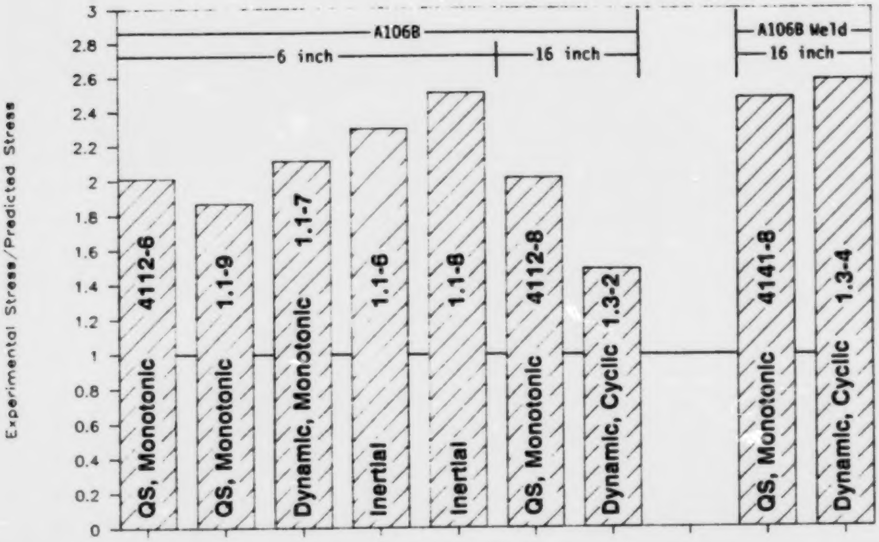

Figure 3.24. Comparison of the experimental results with the ASME IWB-3650 Approach 1 predictions [using S_m(Code)] for the carbon steel surface-cracked-pipe experiments.

F-I-7/91-F3.24

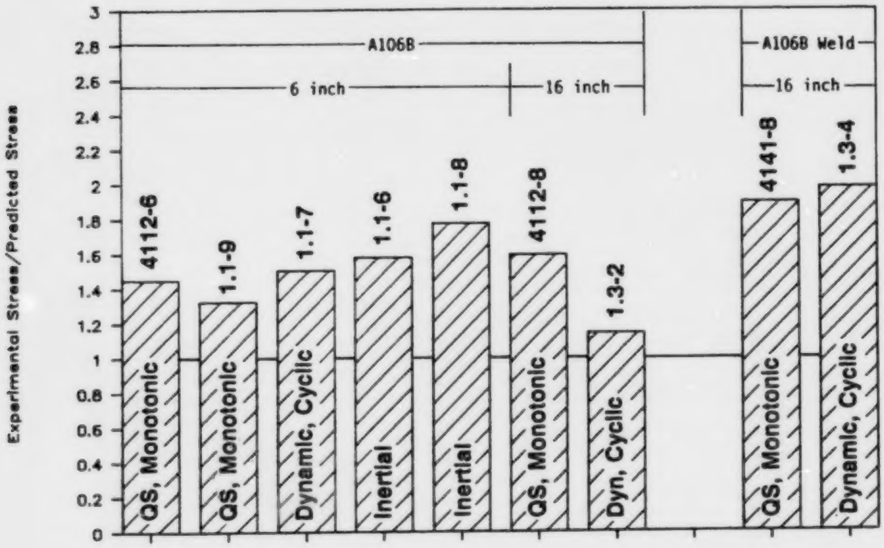

Figure 3.25. Comparison of the experimental results with the ASME IWB-3650 Approach 1 predictions [using S_m(Actual)] for the carbon steel surface-cracked-pipe experiments.

F-I-7/91-F3.25

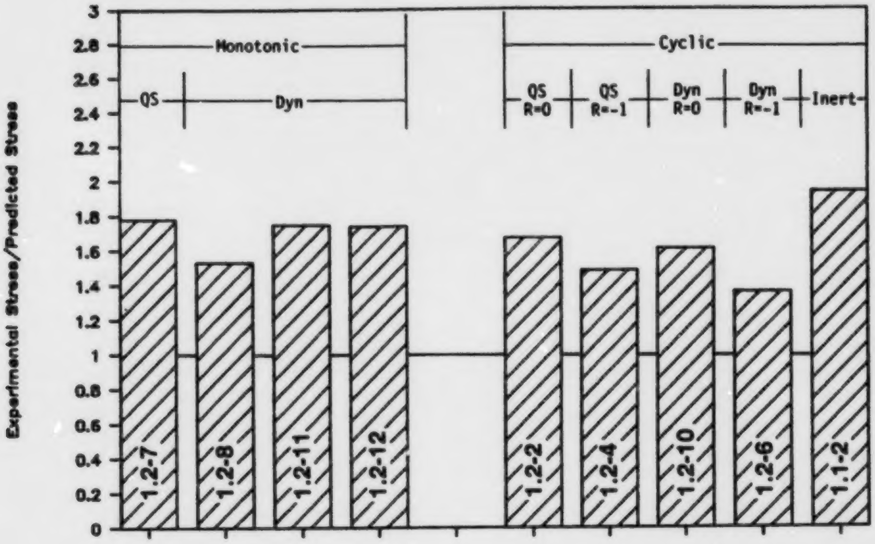

Figure 3.26. Comparison of experimental data with IWB-3650 Approach 1 predictions for carbon steel through-wall-cracked pipe experiments using Code values for S_m.

F-I-7/91-F3.26

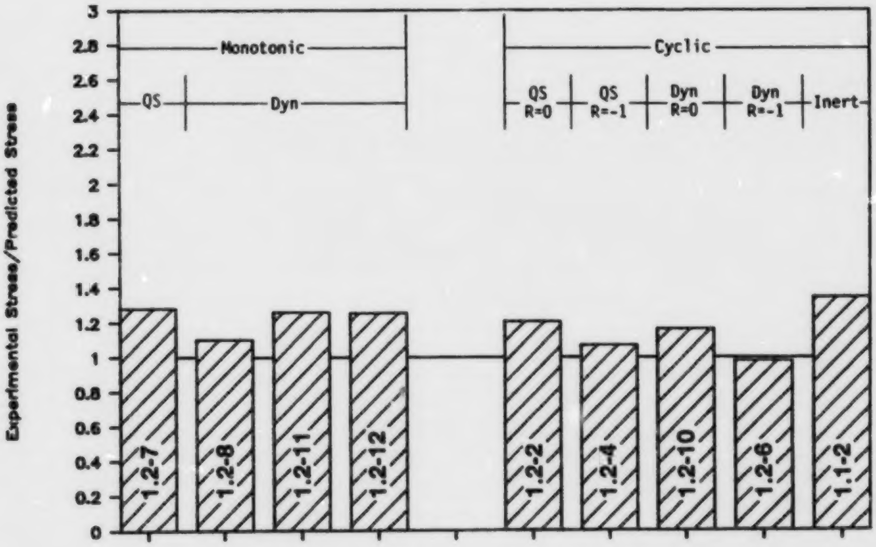

Figure 3.27. Comparison of experimental data with IWB-3650 Approach 1 predictions for carbon steel through-wall-cracked pipe experiments using actual properties as a basis of S_m.

F-I-7/91-F3.27

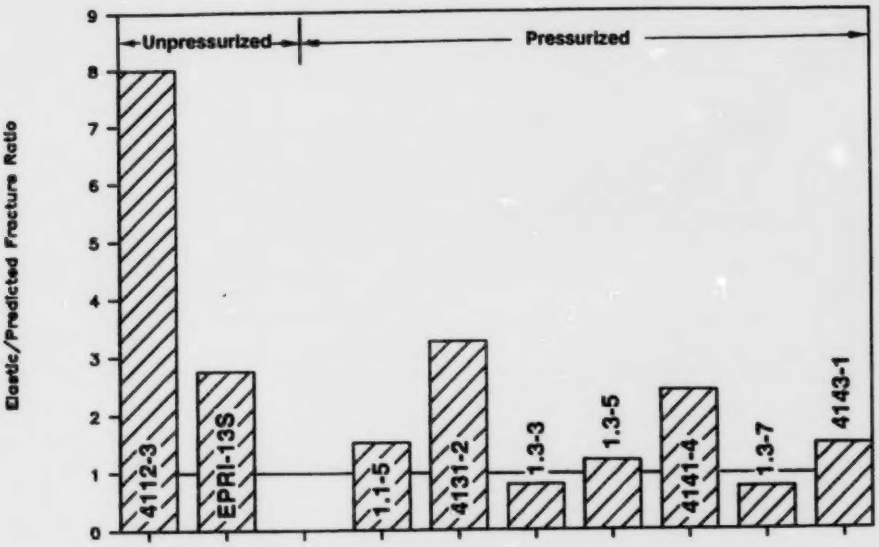

Figure 3.28. Fracture ratios for the stainless steel surface-cracked pipe experiments for the ASME Approach 2 method.

F-I-7/91-F3.28

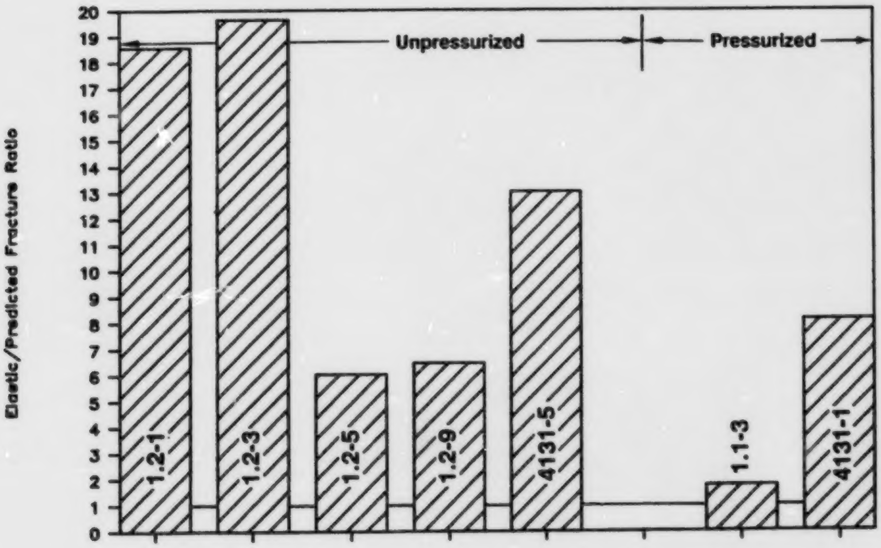

Figure 3.29. Fracture ratios for the stainless steel through-wall-cracked pipe experiments for the ASME Approach 2 method.

F-I-7/91-F3.29

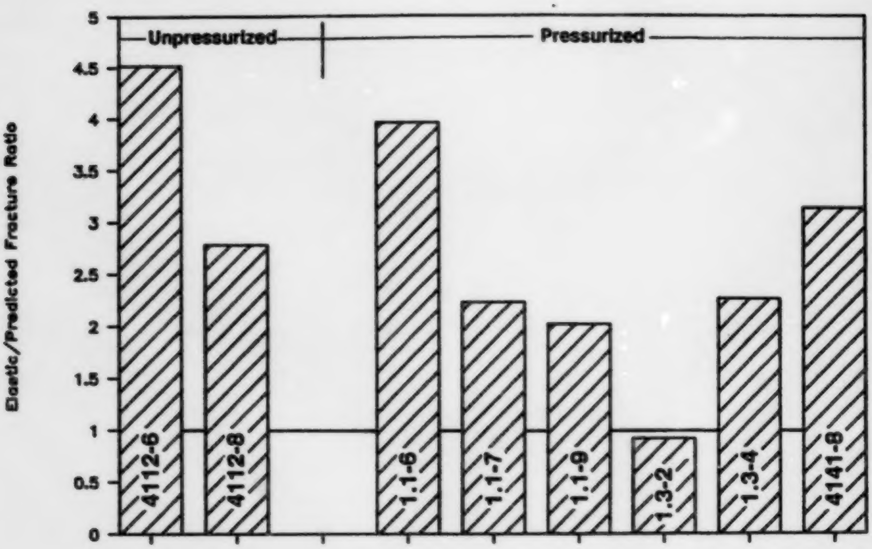

Figure 3.30. Fracture ratios for the carbon steel surface-cracked pipe experiments for the ASME Approach 2 method.

F-I-7/91-F3.30

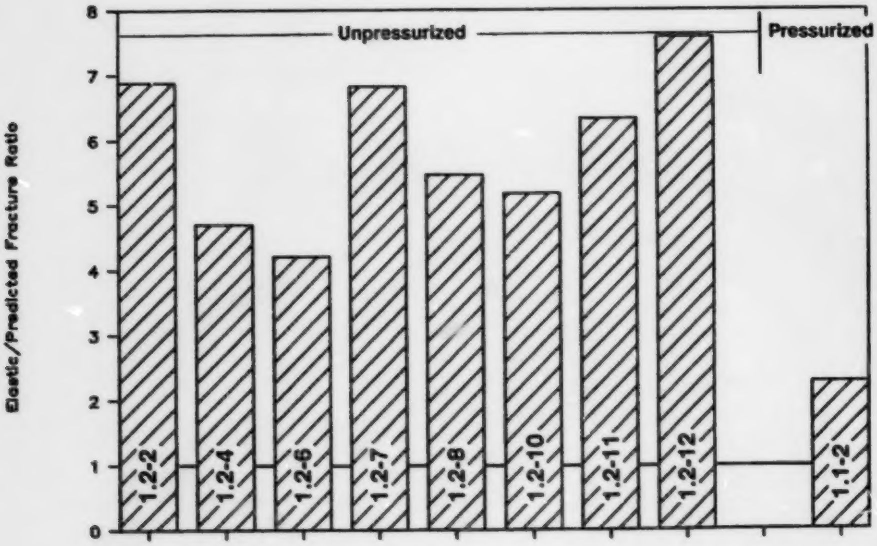

Figure 3.31. Fracture ratios for the carbon steel through-wall-cracked pipe experiments for the ASME Approach 2 method.

F-I-7/91-F3.31

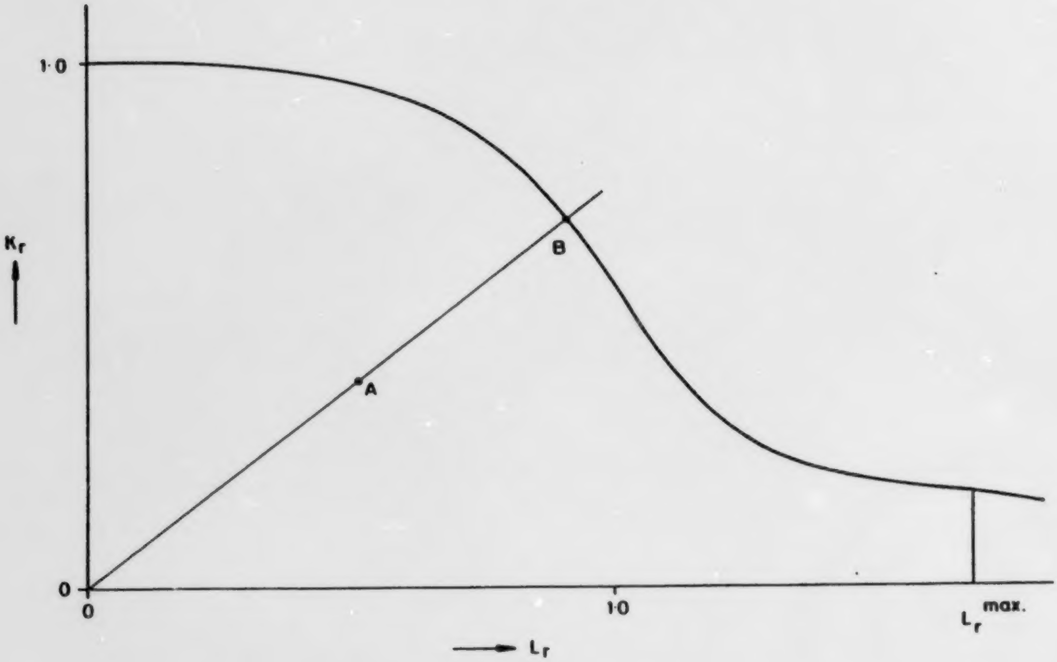

Figure 3.32. R6 Option 1 failure analysis diagram.

I1.3-10/90-F4.8

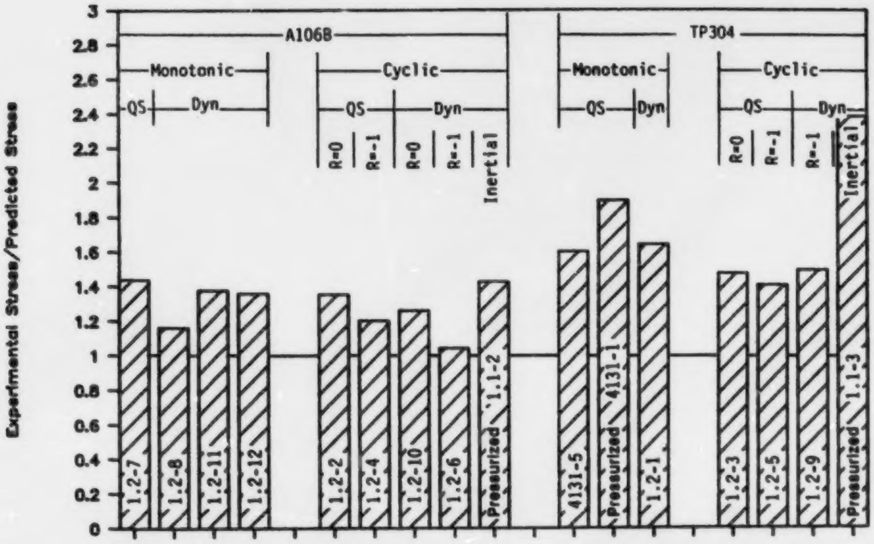

Figure 3.33. Comparison of the experimental results with the R6 Option 1 predictions (Approach 1) for the through-wall-cracked-pipe experiments.

F-I-7/91-F3.33

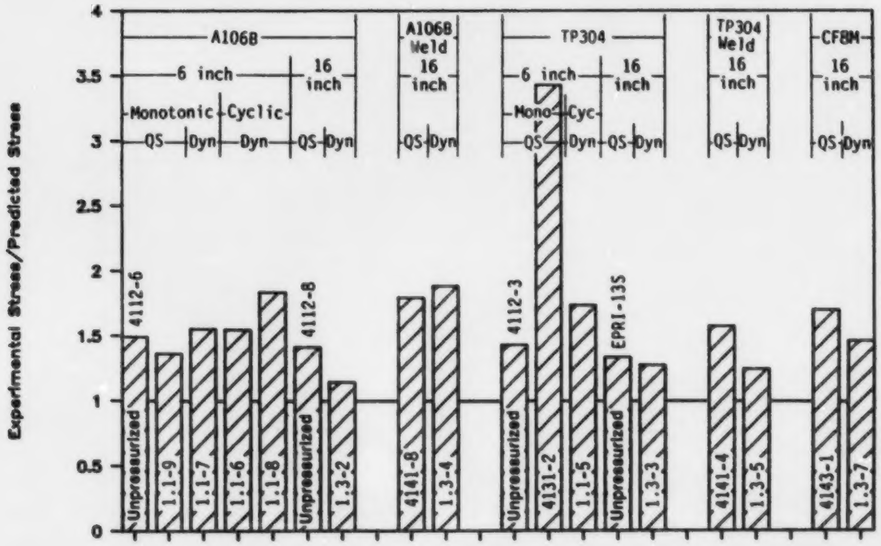

Figure 3.34. Comparison of the experimental results with R6 Option 1 predictions (Approach 1) for the surface-cracked-pipe experiments.

F-I-7/91-F3.34

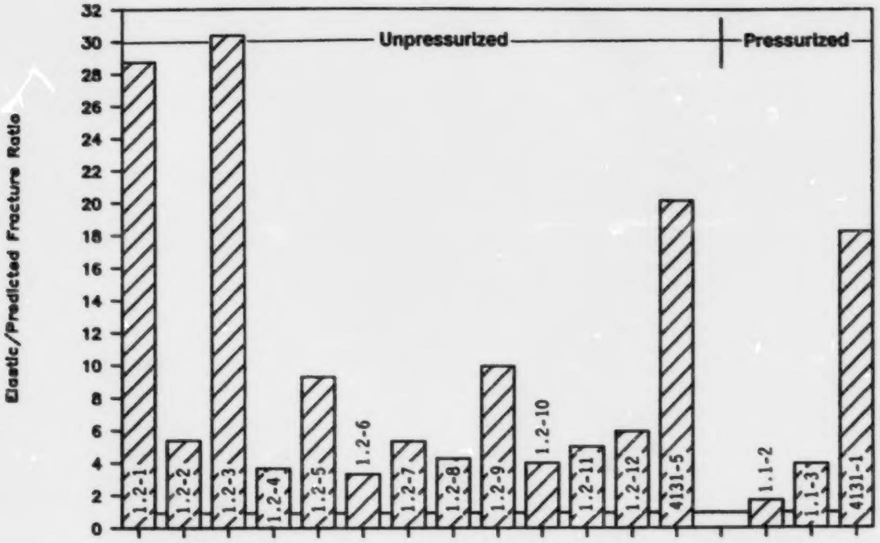

Figure 3.35. Fracture ratios for the through-wall-cracked pipe experiments for the R6 Approach 2 method.

F-I-7/91-F3.35

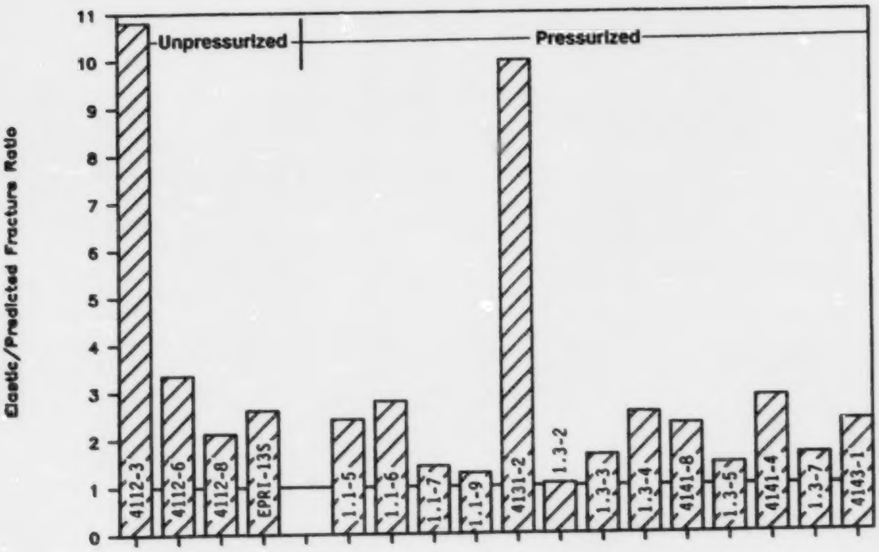

Figure 3.36. Fracture ratios for the surface-cracked pipe experiments for the R6 Approach 2 method.

F-I-7/91-F3.36

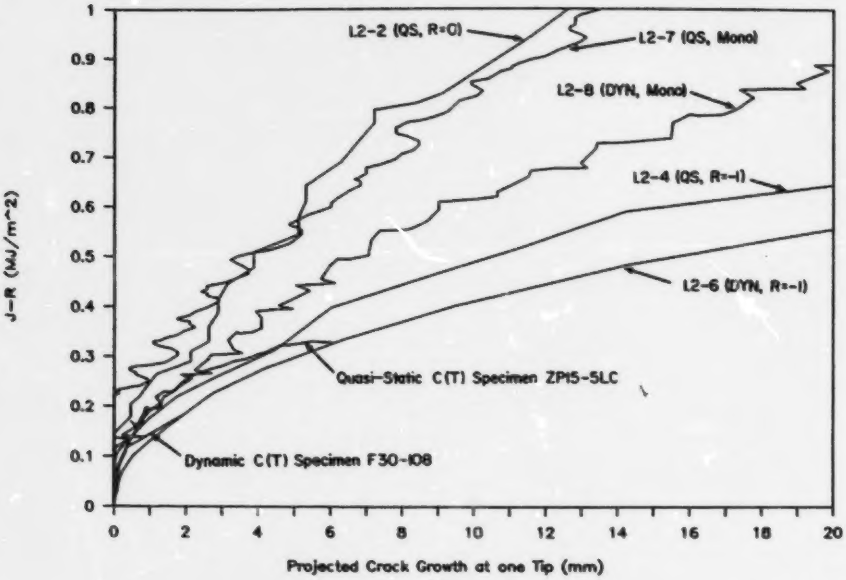

Figure 3.37. J-R curves for the A106 Grade B carbon steel pipe fracture experiments using the η-factor approach along with the C(T) specimen data.

I1.2-8/89-F4.3

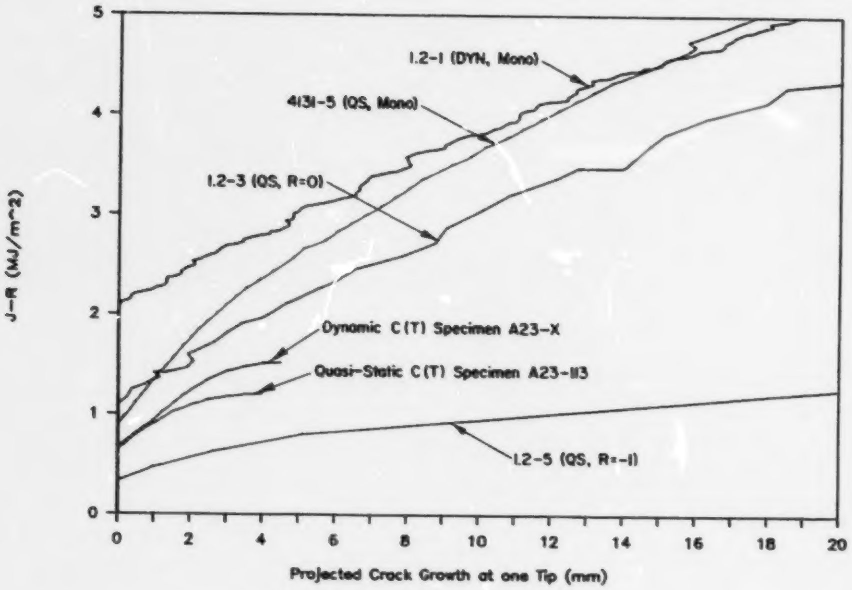

Figure 3.38. J-R curves for the TP304 stainless steel pipe fracture experiments using the η-factor approach along with the C(T) specimen data.

I1.2-8/89-F4.4

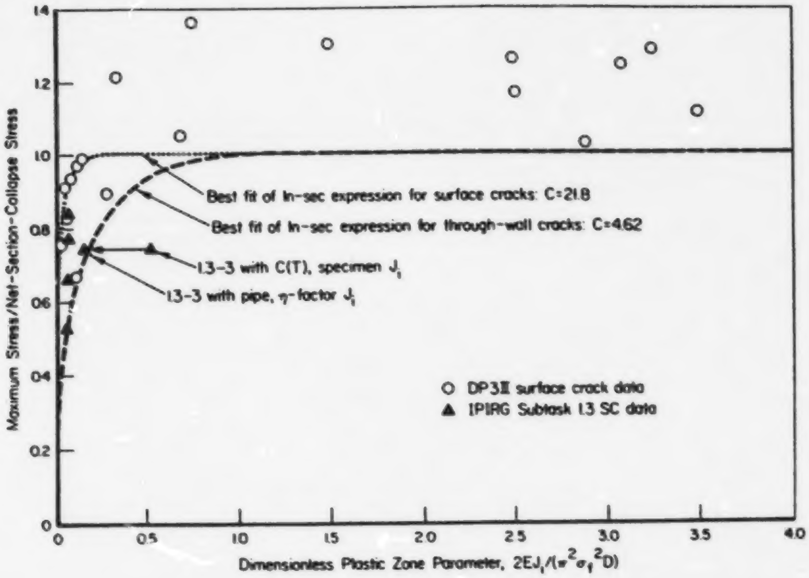

Figure 3.39. Effect of using Experiment 1.3-3 surface-cracked pipe η-factor J_i rather than quasi-static side-grooved C(T) specimen J_i value.

I1.3-10/90-F5.8

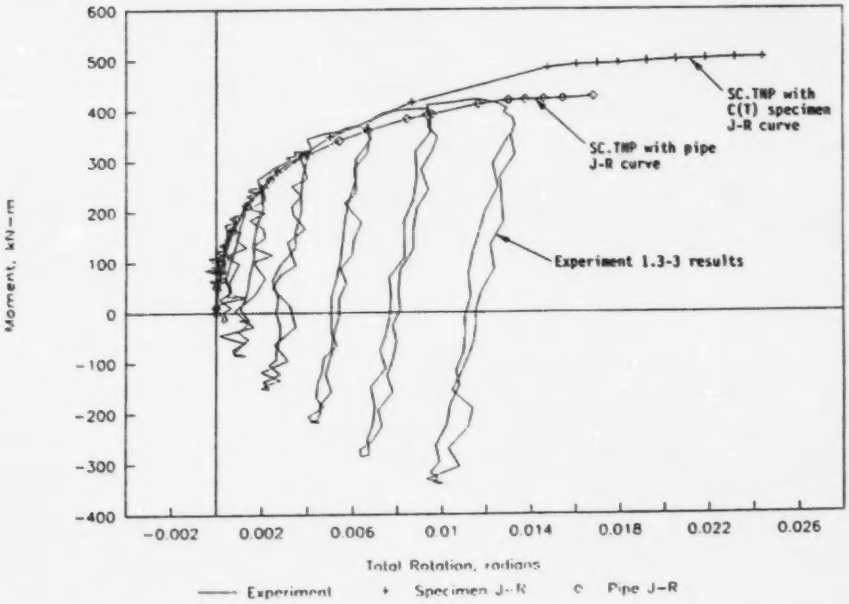

Figure 3.40. Comparison of predicted moment-rotation curves from SC.TNP using C(T) or pipe J-R curves with experimental results.

F-I-7/91-F3.40

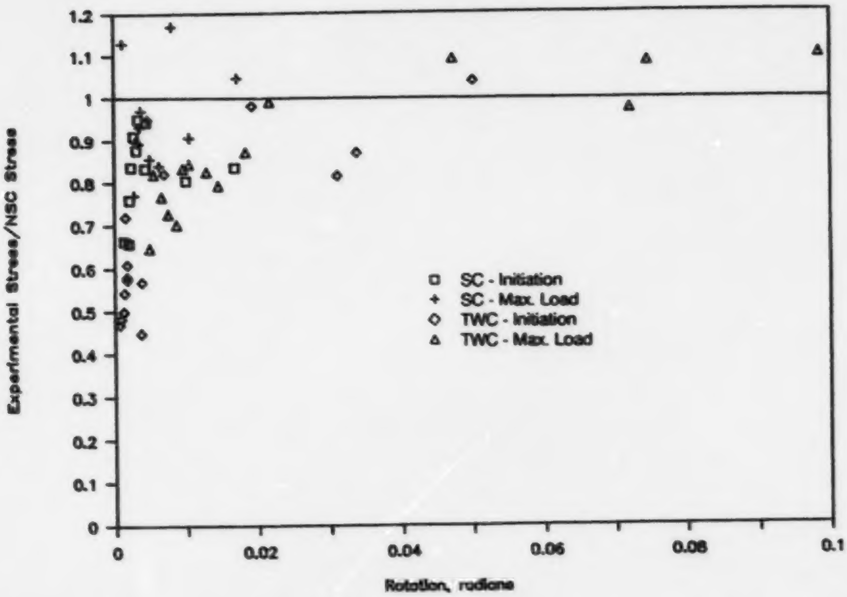

Figure 3.41. Experimental stress/Net-Section-Collapse stress versus rotation for all Task 1 pipe experiments.

F-I-7/91-F3.41

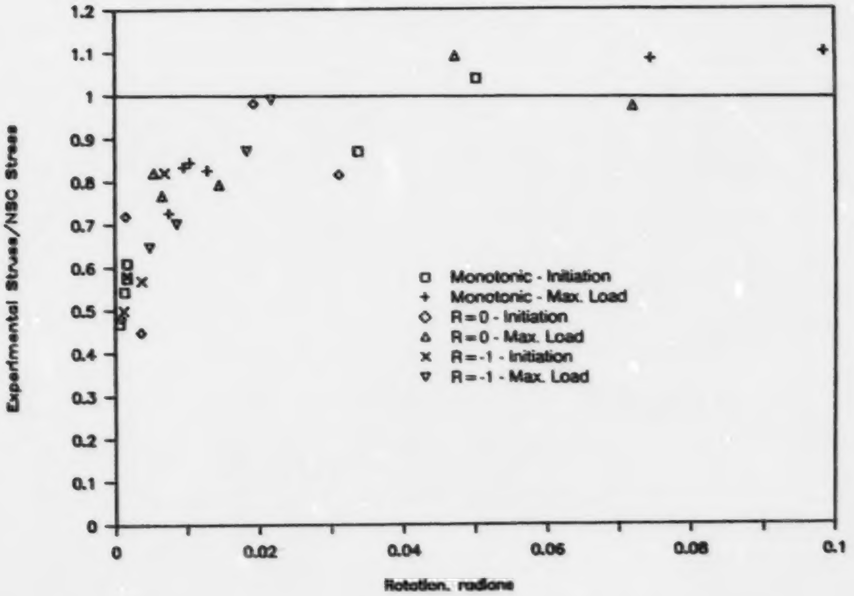

Figure 3.42. Experimental stress/Net-Section-Collapse stress versus rotation for Task 1 through-wall-cracked pipe experiments ($2c/\pi D \simeq 0.37$).

F-I-7/91-F3.42

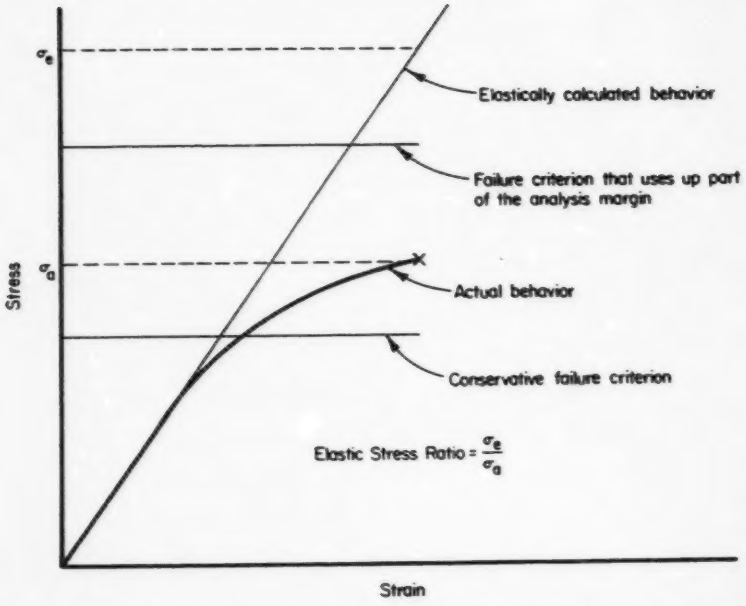
σ_e
Elastically calculated behavior
Failure criterion that uses up part of the analysis margin
σ_a
Actual behavior
Conservative failure criterion
Elastic Stress Ratio = $\frac{\sigma_e}{\sigma_a}$
Stress
Strain

Figure 3.43. Experimental stress/Net-Section-Collapse stress versus rotation for Task 1 surface-cracked pipe experiments ($2c/\pi D \simeq 0.5$, $d/t \simeq 0.7$).

F-I-7/91-F3.43

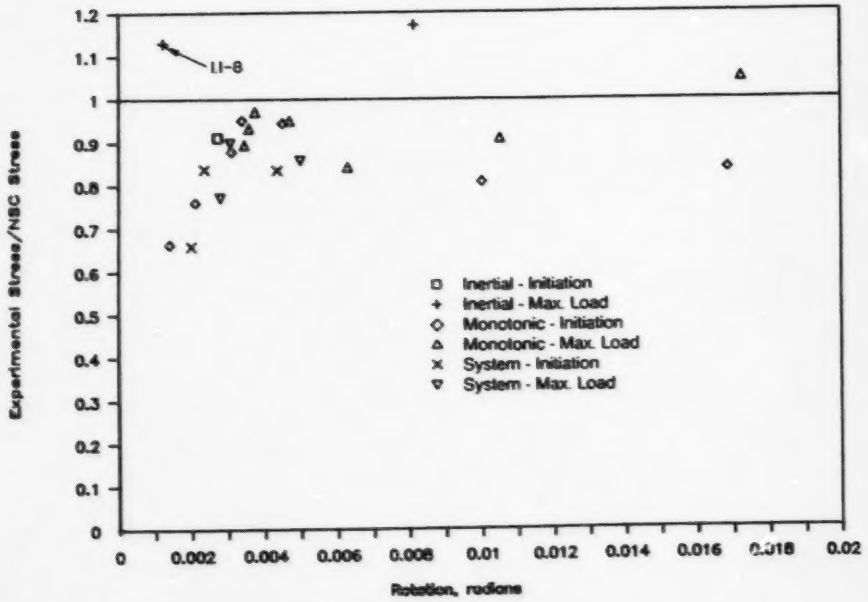

Figure 3.44. Elastic stress analysis concepts.

F-I-7/91-F3.44

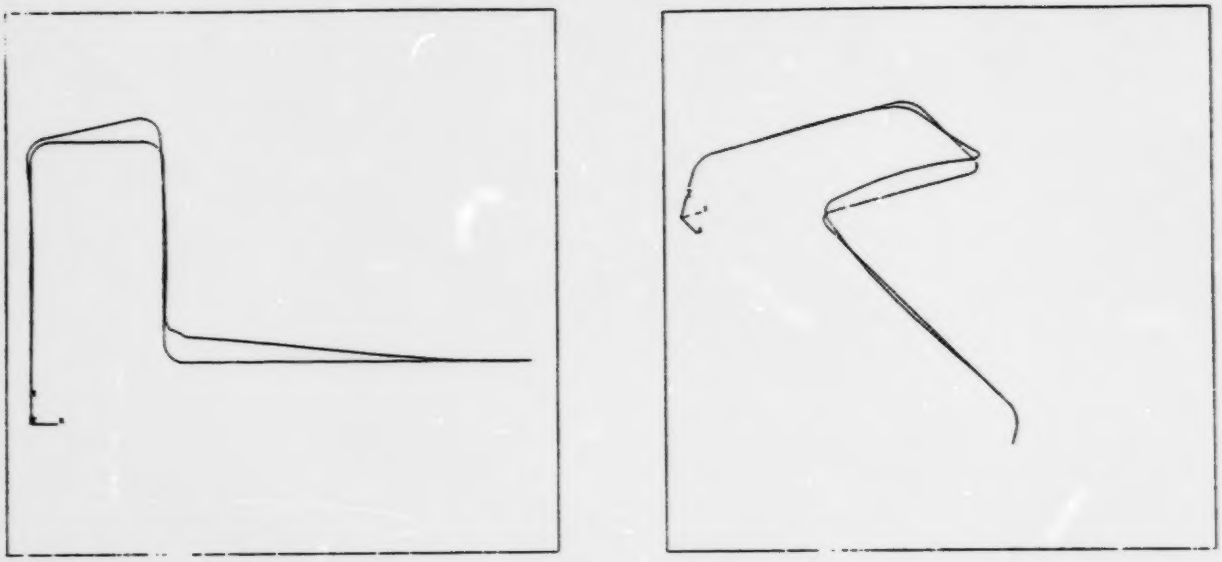

(a) Mode Shape A

(b) Mode Shape B

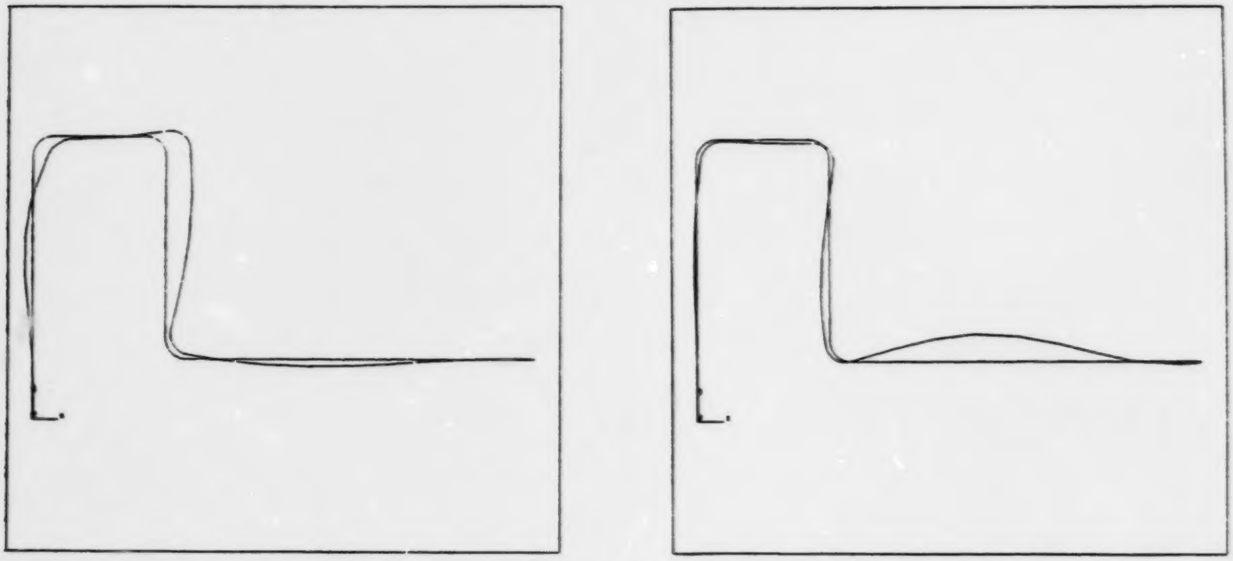

(c) Mode Shape C

(d) Mode Shape D

Figure 3.45. Calculated mode shapes using ANSYS for first four natural frequencies of the pipe loop with the actuator as a fixed node.

F-I-7/91-F3.45

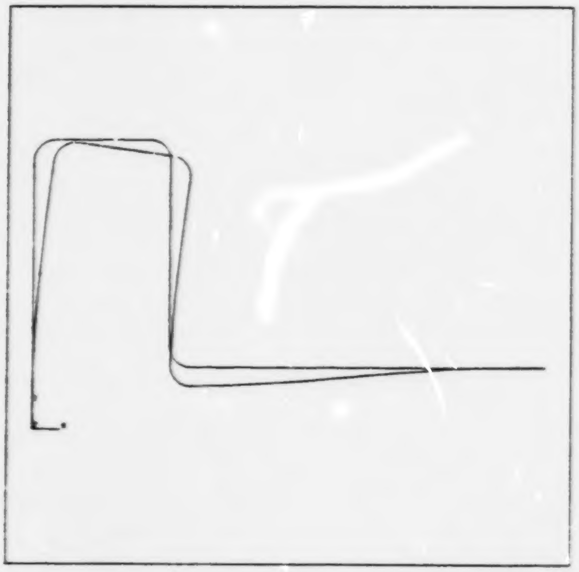

(a) Mode Shape E

Figure 3.46. Calculated mode shapes using ANSYS for first two natural frequencies of the pipe loop with the actuator as a free node.

F-I-7/91-F3.46

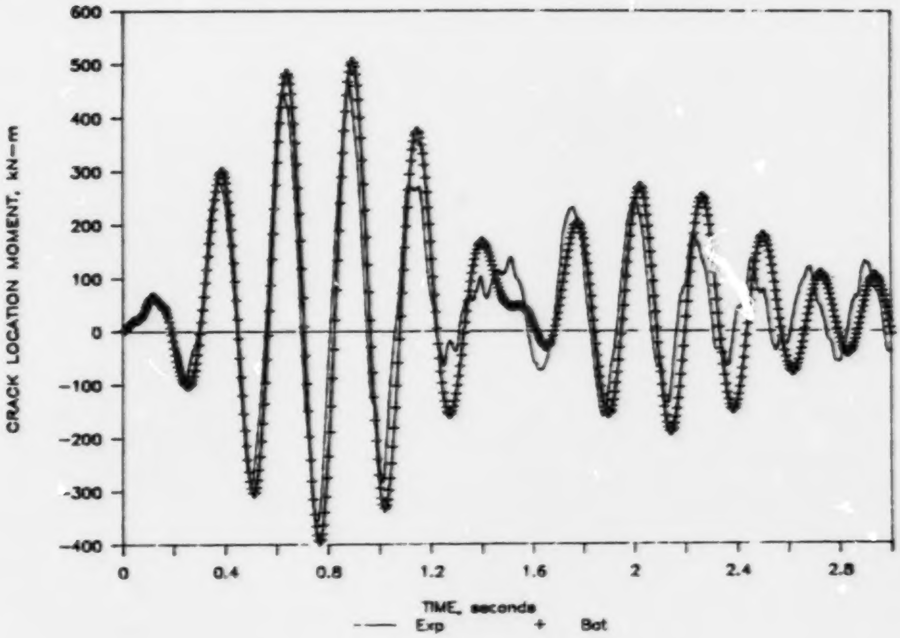

Figure 3.47. Comparison of experimental and predicted crack location moment for the uncracked Subtask 1.3 pipe system.

I-10/89-F18-R0

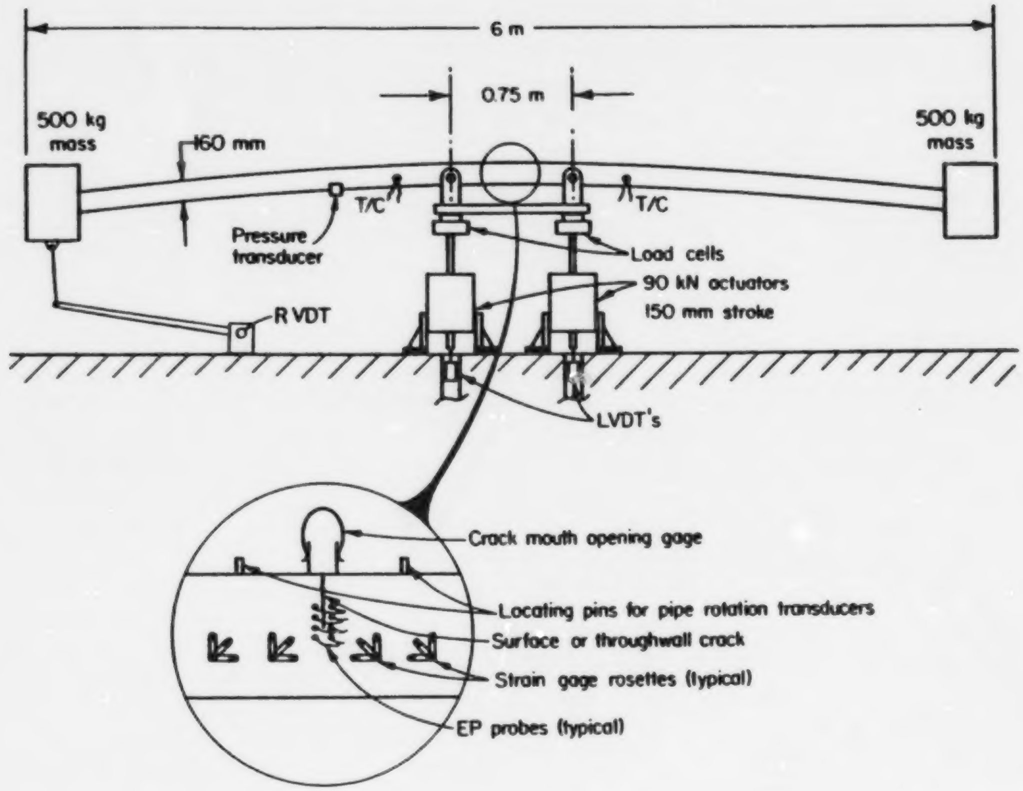
6 m
0.75 m
500 kg mass
160 mm
500 kg mass
T/C
T/C
Pressure transducer
Load cells
90 kN actuators
150 mm stroke
R VDT
LVDT's
Crack mouth opening gage
Locating pins for pipe rotation transducers
Surface or throughwall crack
Strain gage rosettes (typical)
EP probes (typical)

Figure 3.48. Subtask 1.1 inertial test system.

I-11/87-E3-MW

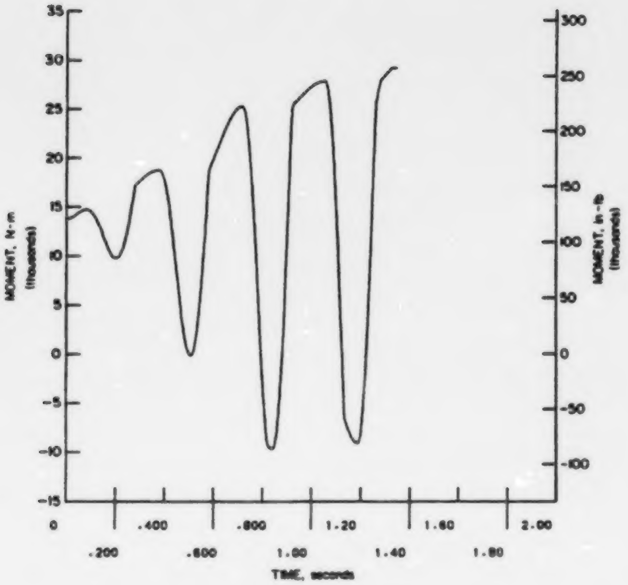

(a) Moment-time from analysis

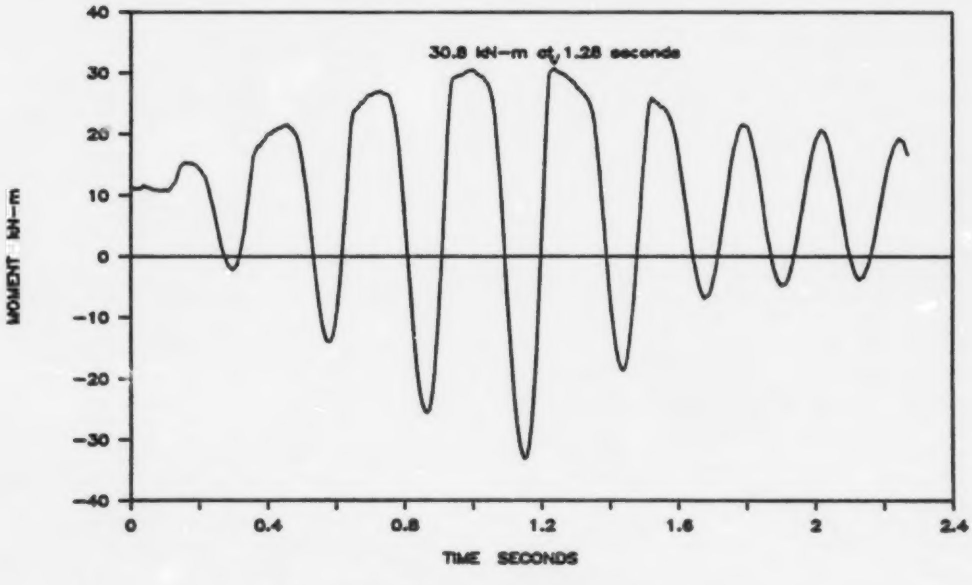

(b) Moment-time from experiment

Figure 3.49. Comparison of experiment and analysis for moment versus time plots of Experiment 1.1-3 (SS TWC). The analysis was valid only up to maximum moment.

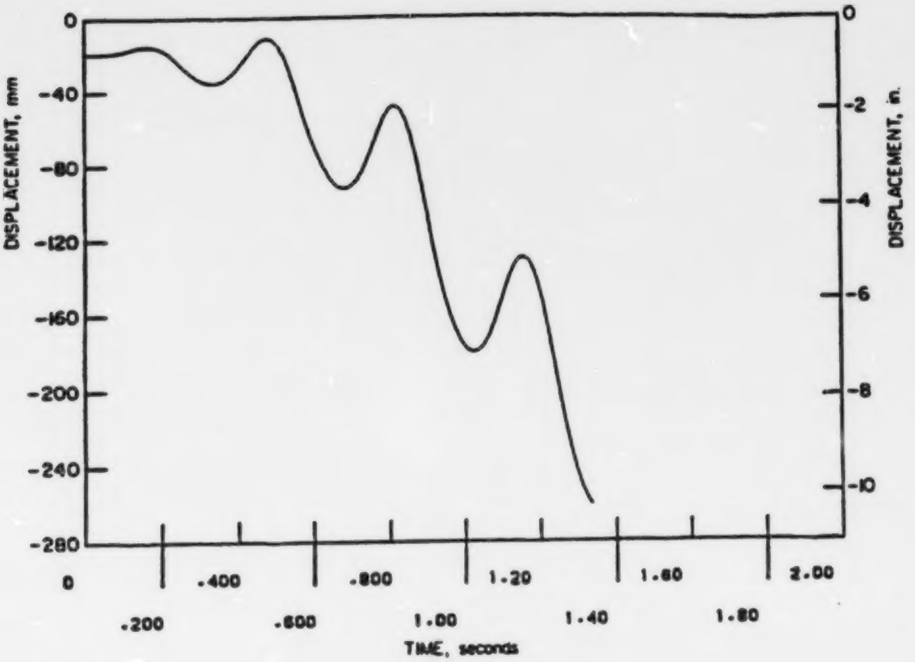

(a) Inertial mass displacement from analysis

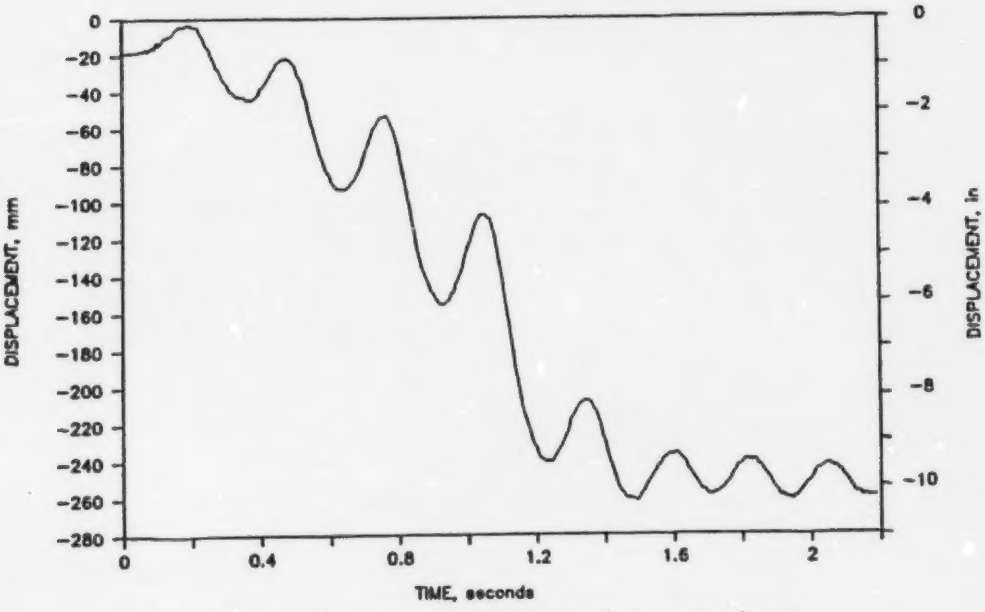

(b) Inertial mass displacements from experiment

Figure 3.50. Comparisons of experiment and pretest design analysis for displacements of the inertial mass for Experiment 1.1-3 (SS TWC).

I1.1-10/89-F4.12

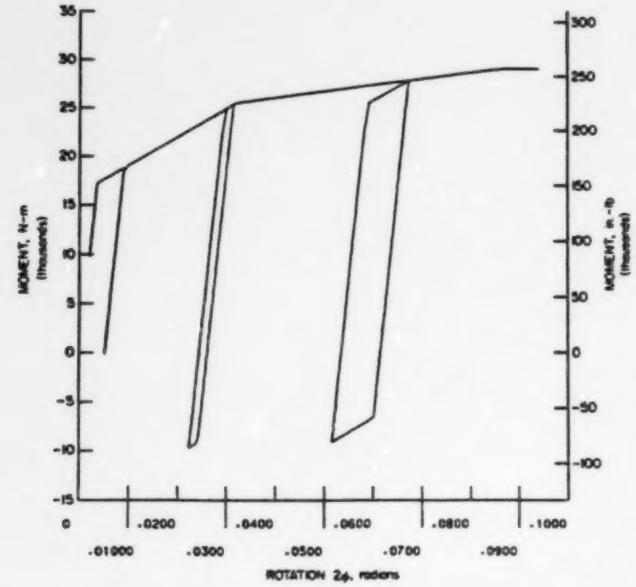

(a) Moment-rotation from analysis

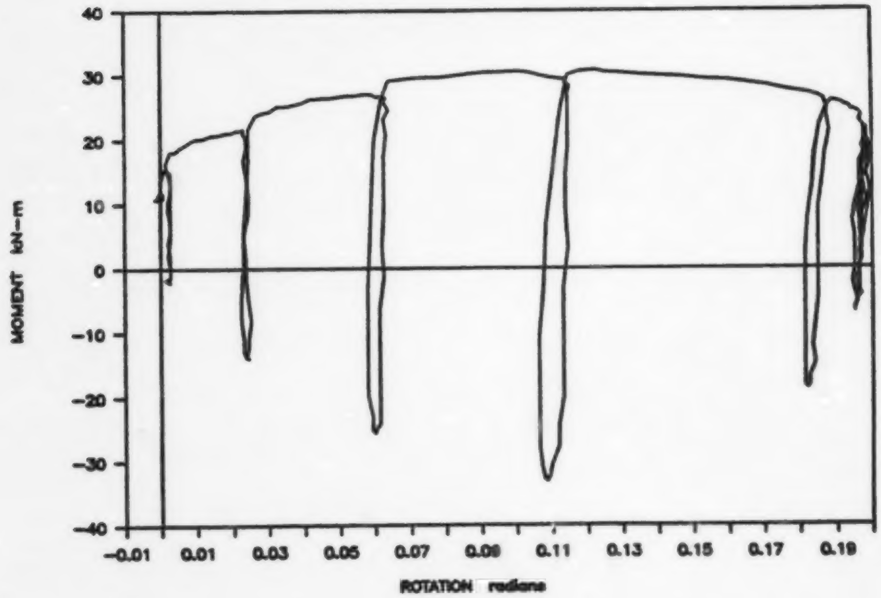

(b) Moment-rotation from experiment

Figure 3.51. Comparison of experiment and pretest design analysis for moment versus rotation for Experiment 1.1-3 (SS TWC).

I1.1-10/89-F4.13

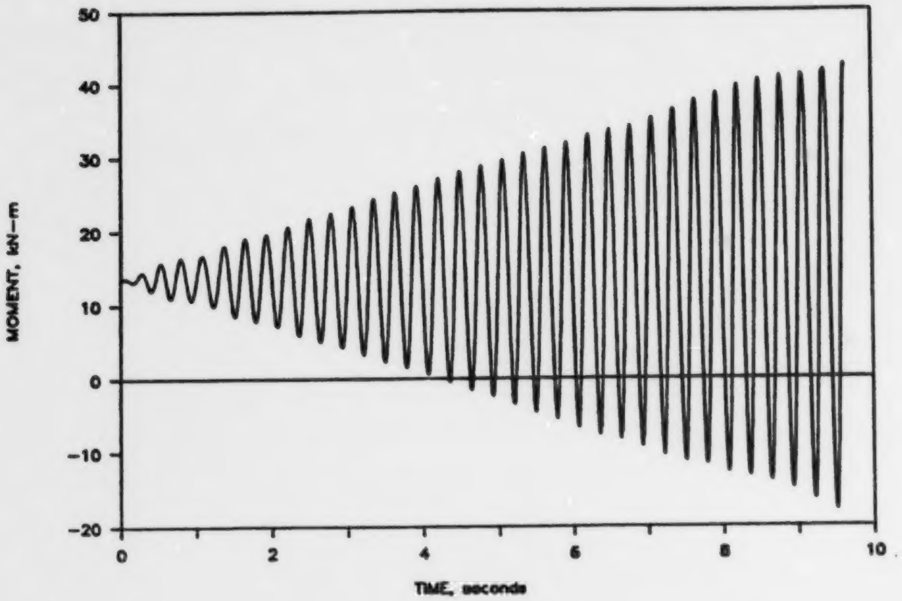

(a) Moment-time from analysis

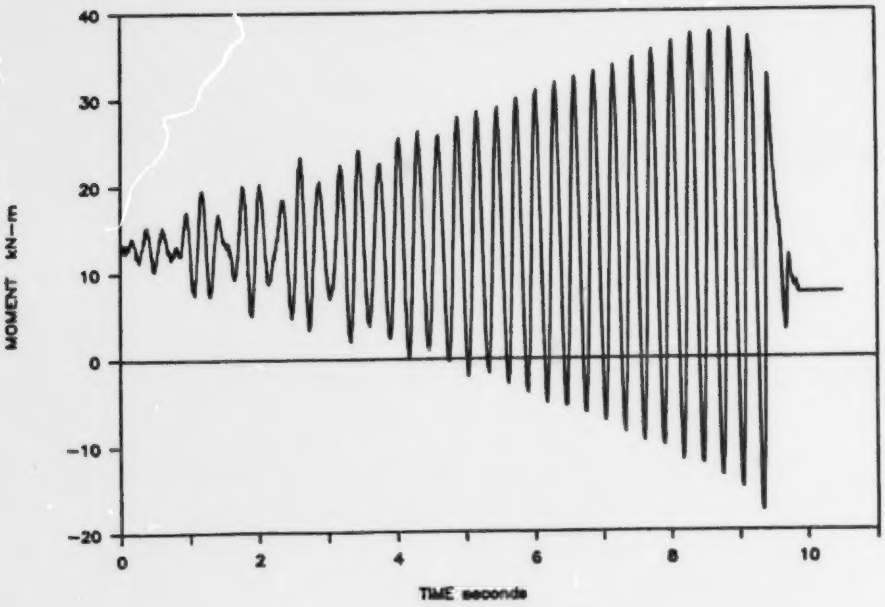

(b) Moment-time from experiment

Figure 3.52. Comparison of experiment and analysis for moment versus time plots of Experiment 1.1-2 (CS TWC).

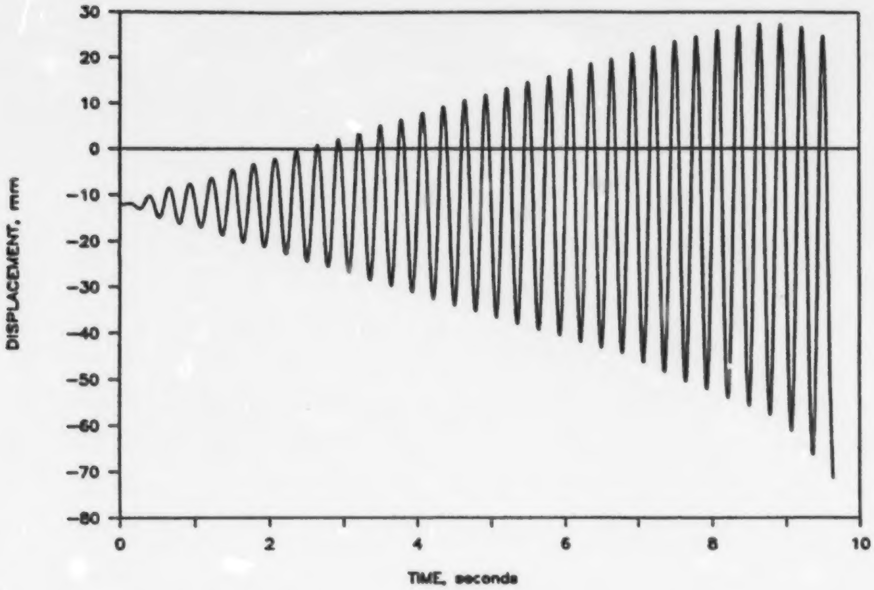

(a) Inertial mass displacements from analysis

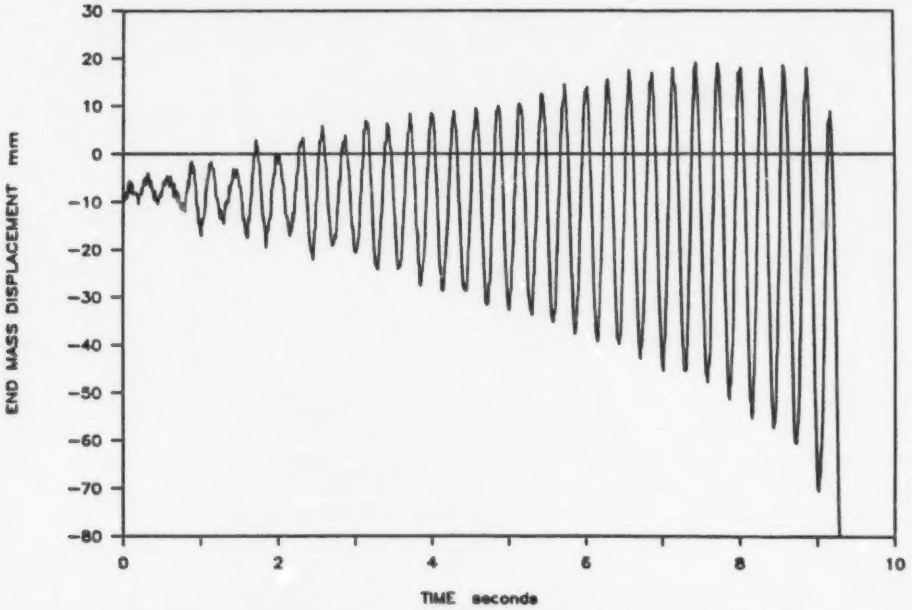

(b) Inertial mass displacements from experiment

Figure 3.53. Comparison of experiment and analysis for displacements of the inertial mass for Experiment 1.1-2 (CS TWC).

I1.1-10/89-F4.15

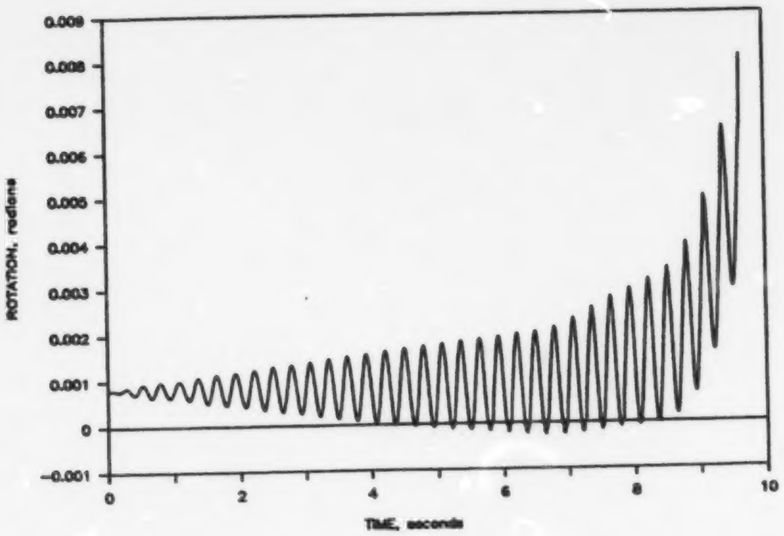

(a) Rotation-time from analysis

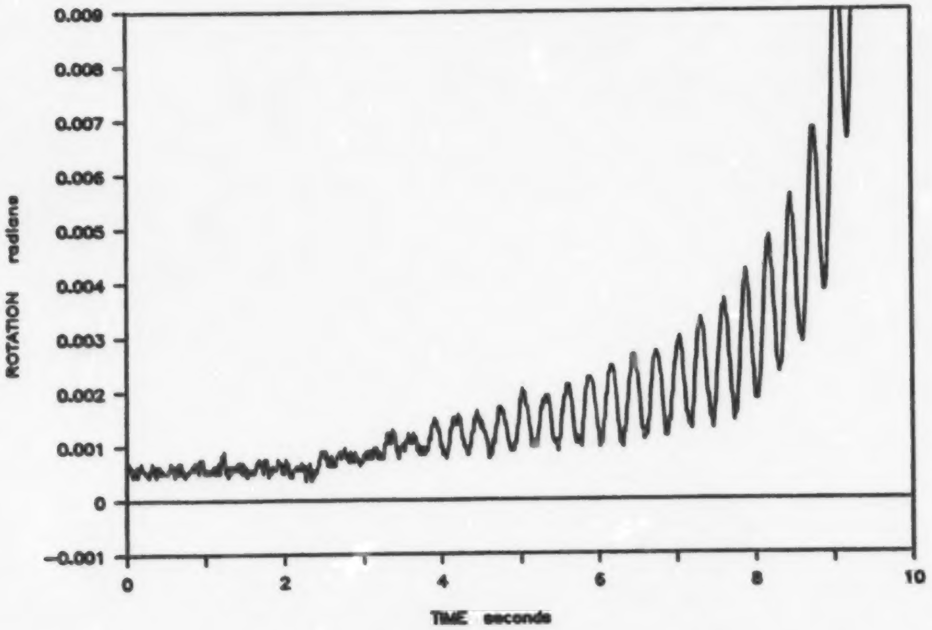

(b) Rotation-time from experiment

Figure 3.54. Comparison of experiment and analysis for rotations at the crack plane for Experiment 1.1-2 (CS TWC).

I1.1-10/89-F4.16

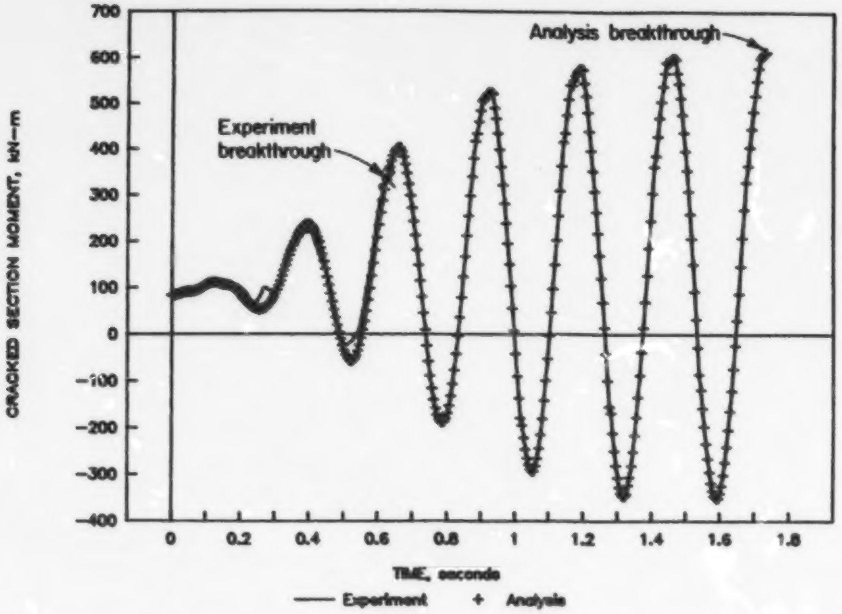

Figure 3.55. Comparison of pre-test prediction of cracked section moment to carbon steel base metal experiment (1.3-2) results. (Analysis with 66 percent deep flaw.)

I1.3-10/90-F4.24

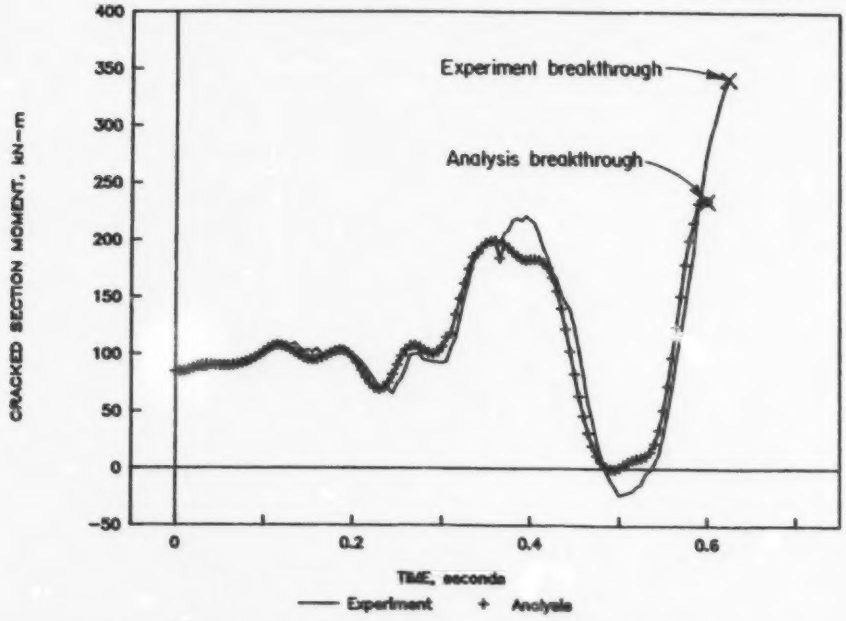

Figure 3.56. Comparison of post-test prediction of cracked section moment for the carbon steel base metal experiment (1.3-2). Analysis with 75 percent deep flaw; actual flaw depth 72.7 percent deep.

I1.3-10/90-F4.25

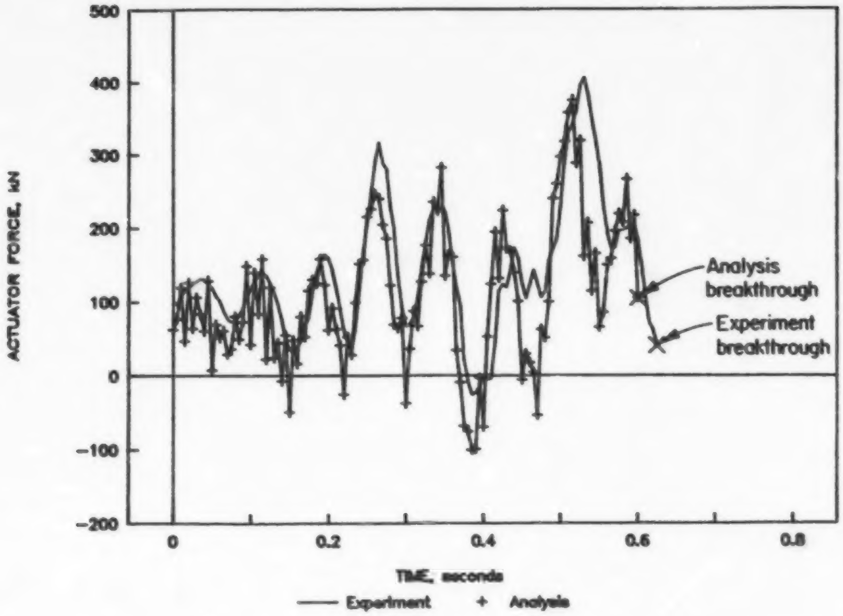

Figure 3.57. Actuator force for the carbon steel base metal experiment (1.3-2), analysis with 75 percent deep flaw.

I1.3-10/90-F4.26

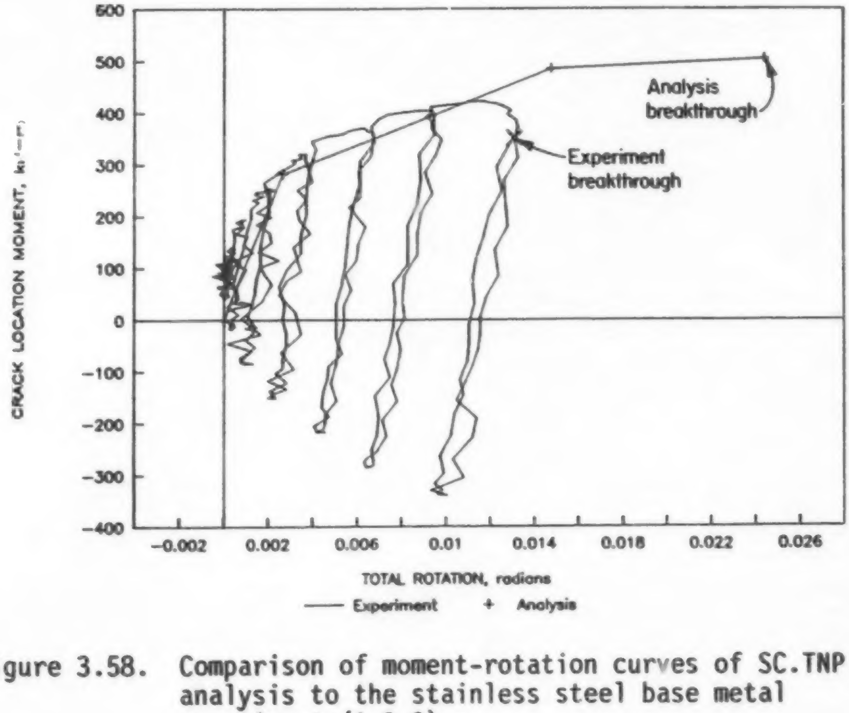

Figure 3.58. Comparison of moment-rotation curves of SC.TNP analysis to the stainless steel base metal experiment (1.3-3).

I1.3-10/90-F4.27

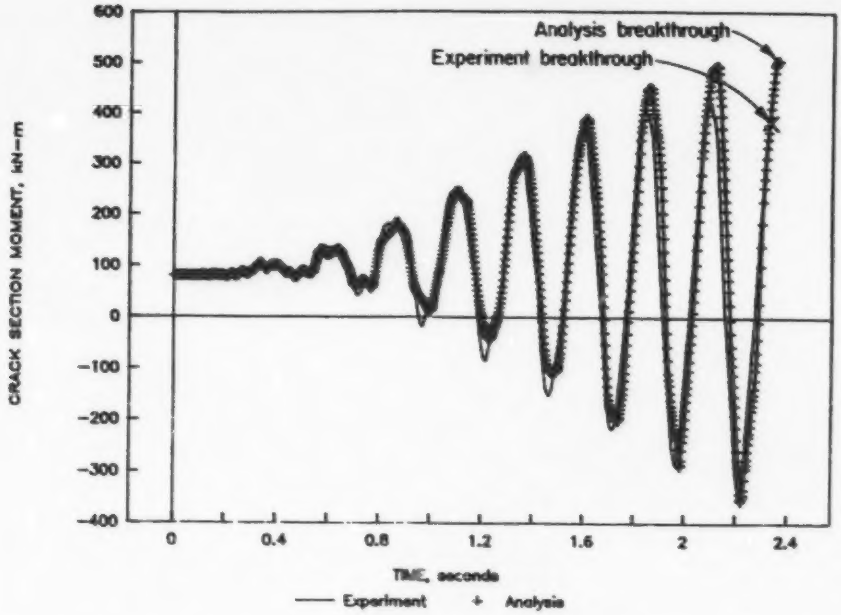

Figure 3.59. Crack section moment for the stainless steel base metal experiment (1.3-3).

I1.3-10/90-F4.28

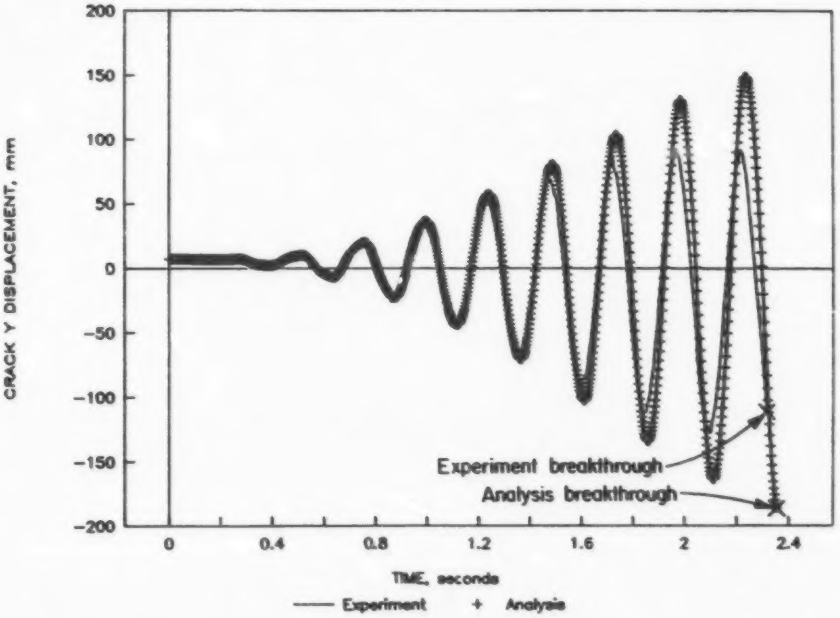

Figure 3.60. Displacement for the stainless steel base metal experiment (1.3-3).

I1.3-10/90-F4.29

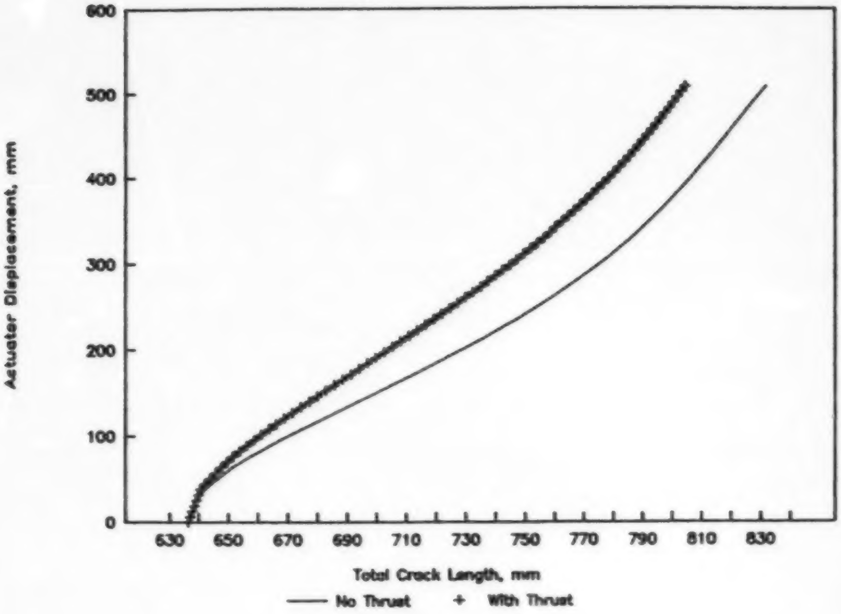

Figure 3.61. The effect of through-wall crack jet thrust forces on IPIRG Subtask 1.3 system response.

I1.3-10/90-F5.17

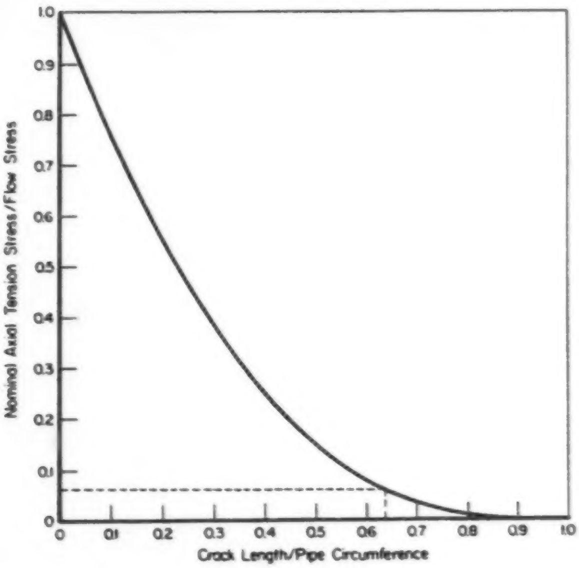

Figure 3.62. Predicted through-wall critical crack length based on Net-Section-Collapse analysis for axial tension stress as a function of the ratio of the crack length to pipe circumference.

I1.3-10/90-F5.1

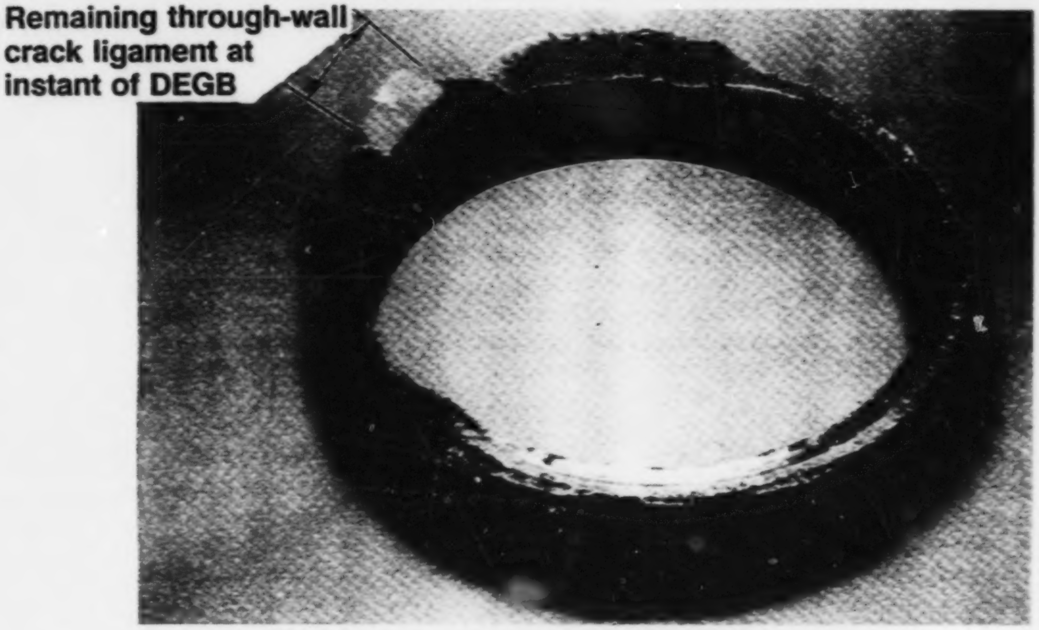
Remaining through-wall crack ligament at instant of DEGB

Figure 3.63. Photograph of fracture from aged cast stainless experiment (Experiment 1.3-7).

I1.3-10/90-F5.2

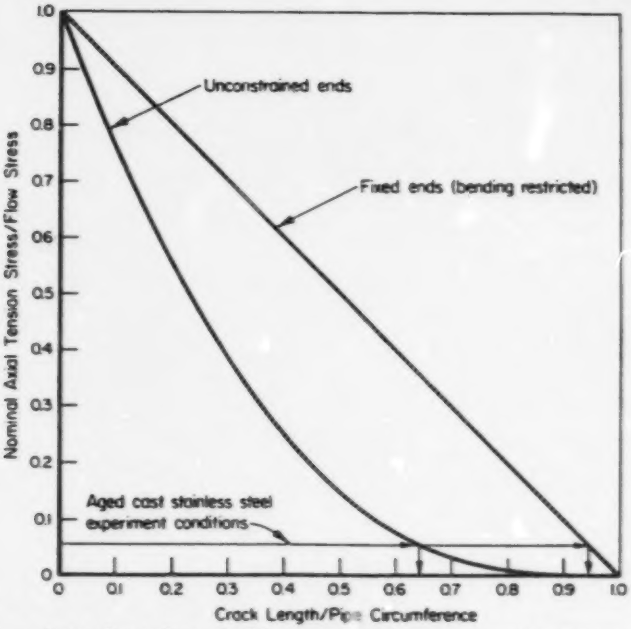

Figure 3.64. Net-Section-Collapse analyses predictions, with and without considering induced bending, as a function of the ratio of the through-wall crack length to the pipe circumference.

EB-3/91-RS13

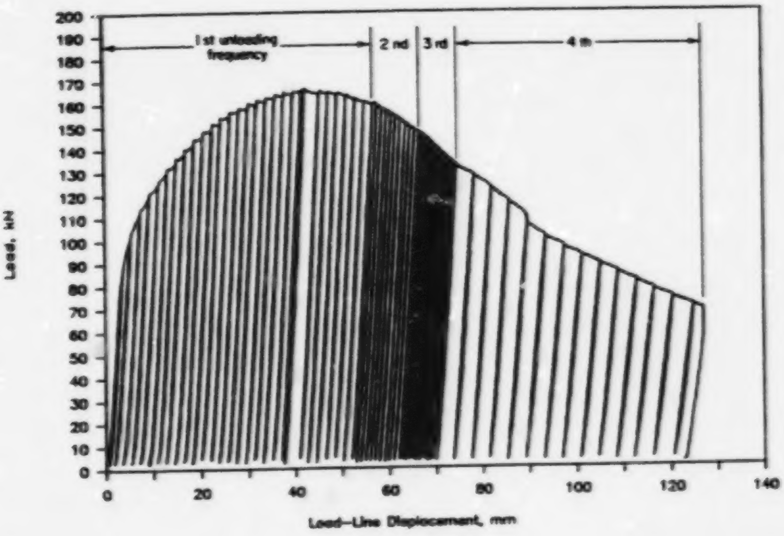

Figure 3.65. Measured load versus load-line displacement for quasi-static reversed (R = 0) loading (Experiment 1.2-3) showing the four different cyclic displacement increments used.

DRB/1.2-3/F11

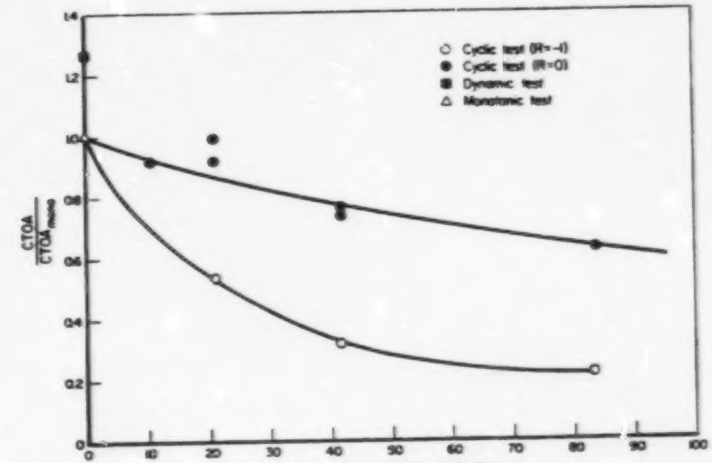

Figure 3.66. Crack-tip-opening-angle data from Subtask 1.2 stainless steel pipe experiments.

DRB/1.2-5/F25

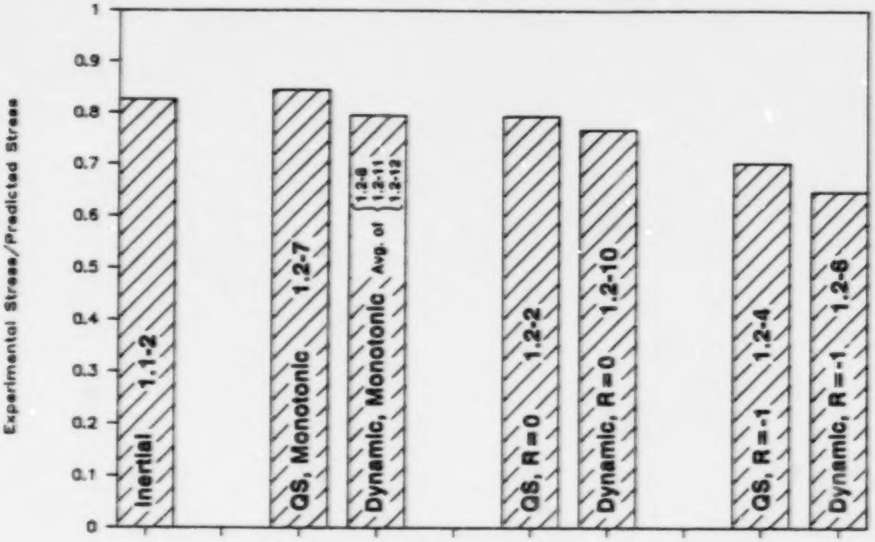

Figure 3.67. Comparison of the normalized load-carrying capacities for the inertial and displacement-controlled carbon steel through-wall-cracked pipe experiments.

F-I-7/91-F3.67

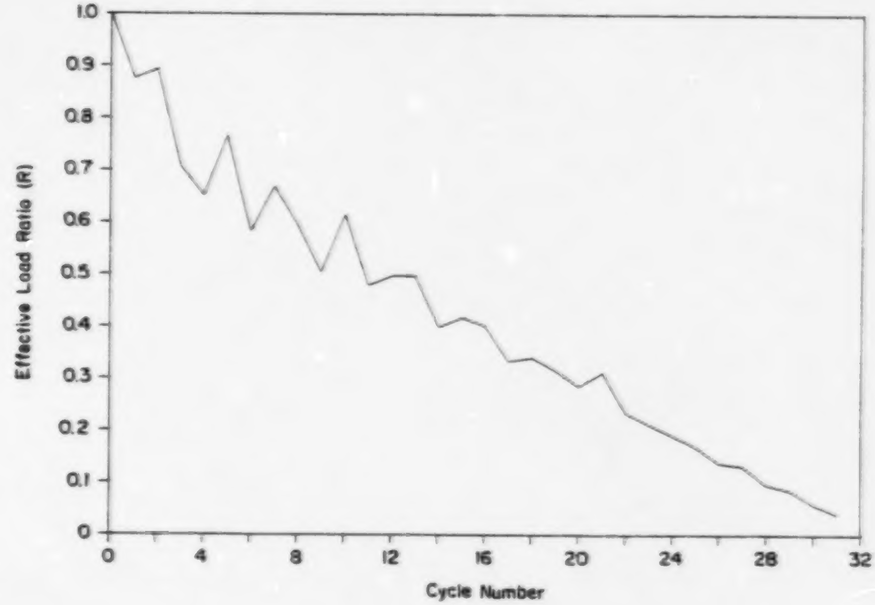

Figure 3.68. Effective load ratio as a function of cycle number for Experiment 1.1-2.

F-I-7/91-F3.68

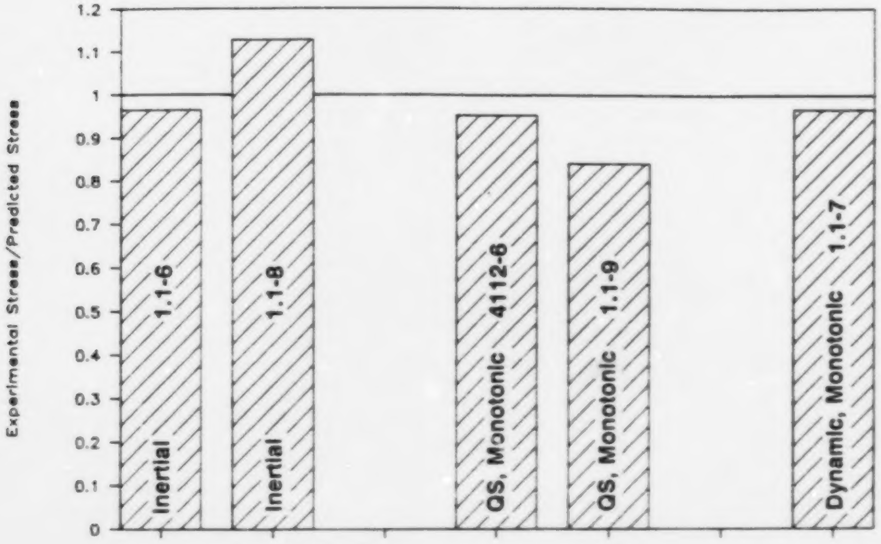

Figure 3.69. Comparison of the normalized load-carrying capacities for the inertial and displacement-controlled carbon steel surface-cracked pipe experiments.

F-I-7/91-F3.69

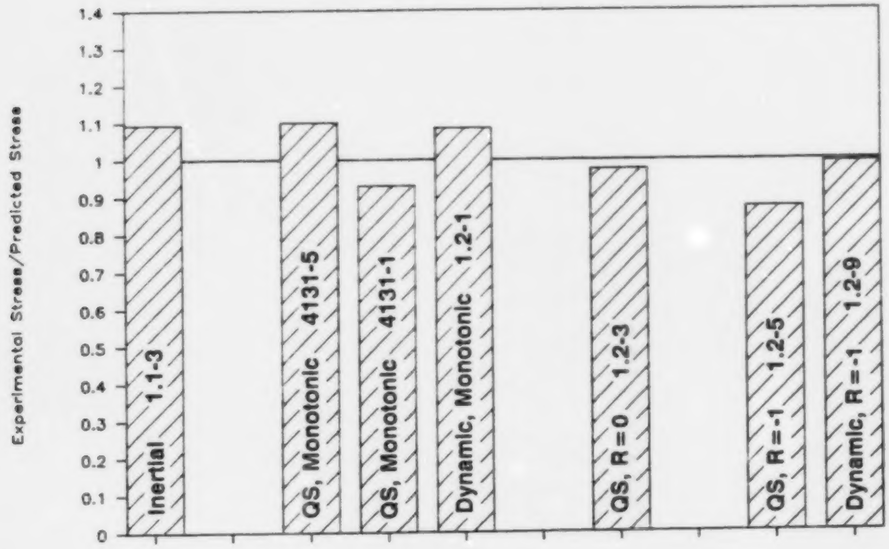

Figure 3.70. Comparison of the normalized load-carrying capacities for the inertial and displacement-controlled stainless steel through-wall-cracked pipe experiments.

F-I-7/91-F3.70

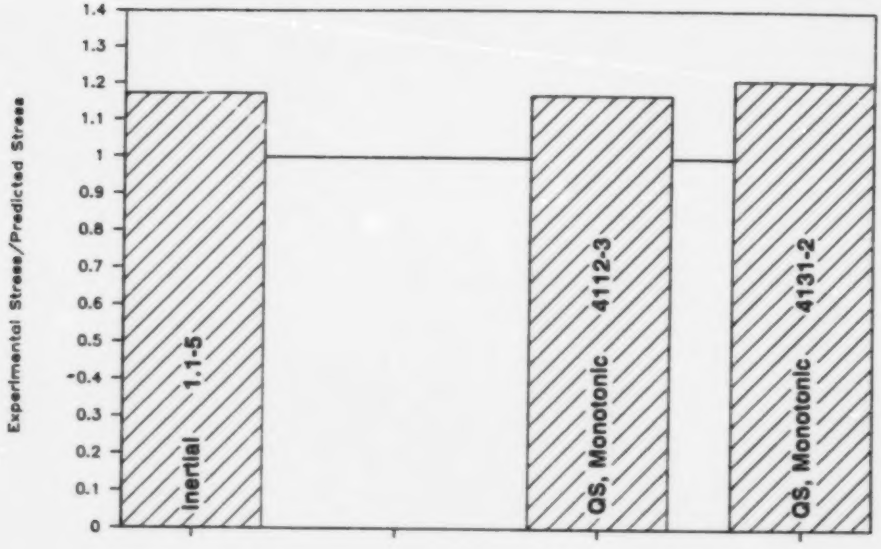

Figure 3.71. Comparison of the normalized load-carrying capacities for the inertial and displacement-controlled stainless steel surface-cracked-pipe experiments.

F-I-7/91-F3.71

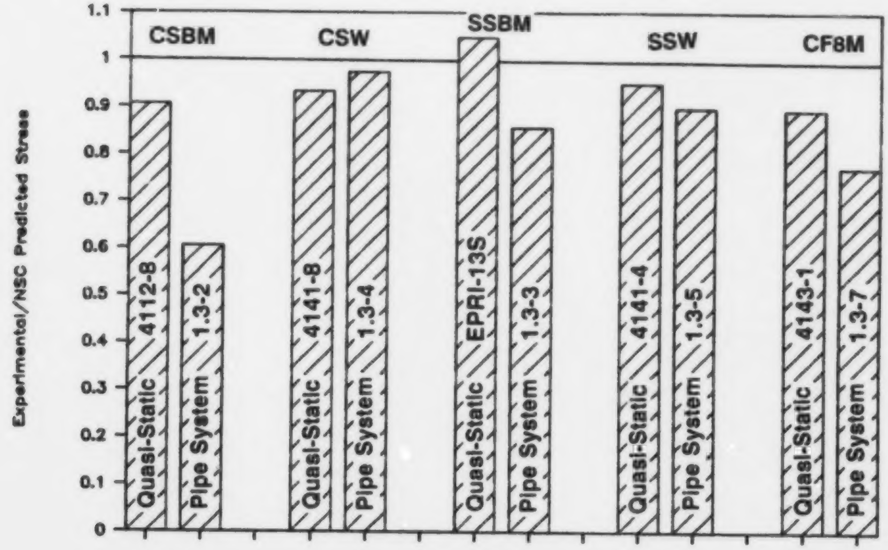

Figure 3.72. Comparison of the normalized maximum experimental stress for the Subtask 1.3 pipe system experiments with the normalized maximum experimental stress for the companion quasi-static pipe experiments.

F-I-7/91-F3.72

4.0 ADVANCES OF TECHNOLOGY AND CONCLUSIONS

In Section 3 the results and key findings of the Task 1 pipe fracture efforts were assessed. Results from several subtasks were combined, compared, and integrated to determine the degree of consistency and to develop a common understanding of the results. Section 4.1 summarizes these findings in the context of the fundamental questions that led to the creation of the IPIRG Program. Section 4.2 briefly summarizes all the key issues that have been resolved.

Before the IPIRG Program began, the state-of-the-art included a reasonably good understanding of fracture behavior for quasi-static loading of pipe with long circumferential surface cracks and through-wall cracks. There was little knowledge, however, on what effects high-rate (seismic) loading might have on that fracture behavior. Cyclic effects on fracture behavior were understood principally in the context of fatigue crack propagation, while little was known about cyclic interaction effects on ductile tearing. Also, there was an adequate understanding of the differences between load-controlled and displacement-controlled loading, but it was unclear on how to treat inertial loading for crack stability analyses.

Previous studies provided a better understanding of the failure of uncracked piping systems under dynamic cyclic loads. These studies identified the operative failure mechanisms as ratcheting and fatigue rather than plastic collapse and showed that large margins can exist when evaluating systems by current methods and criteria. Little was known about the effects of pre-existing cracks on failure mechanisms and fracture behavior under dynamic and cyclic loads or about how elastic stress analysis would apply to dynamically loaded cracked pipe.

Finally, fracture stability issues for flawed piping subjected to dynamic loads were not generally understood prior to the IPIRG Program. A reasonable description of fracture stability was available for simple configurations under simple loading conditions, but little was understood about the stability of cracked piping systems under dynamic cyclic loads. Little was also known about the expected fracture speeds of a surface crack or the resulting through-wall crack. More information was also needed on the conditions that could lead to a double-ended guillotine break. This information will help to verify the need to develop a criterion that would replace the DEGB design criterion.

4.1 Basic Questions Addressed by IPIRG

When the creation of an international group program was first proposed, there was a need for answers to a number of technical questions related to nuclear plant piping integrity. The various international members that agreed to participate in IPIRG decided to join because they hoped that the program would answer some of their specific questions. Some of these questions were common to enough organizations that the IPIRG Program was established to address them. Four of the key questions that many members wanted answered are addressed in the following sections.

4.1.1 ARE SEISMIC EFFECTS ON FLAWED PIPING CORRECTLY ACCOUNTED FOR BY CURRENT FRACTURE METHODS?

This basic question is concerned with (1) the effects of high-rate loading, (2) cyclic loading, and (3) the use of small laboratory specimens to predict fracture behavior of large-diameter piping.

What are the Effects of High-Rate Loading on Fracture Behavior?

Section 3.8.1 compares the results from the various Task 1 experiments with each other and with results from the material characterization studies. While effects of high-rate loading were observed in inertial experiments (Subtask 1.1) and pipe system experiments (Subtask 1.3), the most direct evidence of these effects are seen in the displacement-controlled pipe experiments (Subtask 1.2) and in the material characterization studies.

In essence, it can be concluded that for some carbon steels at PWR temperatures there is a modest degradation of fracture resistance at rates of loading typical of those observed in seismic events. At high rates of loading [dJ/dt of approximately 300 kJ/m^2/s (1700 in-lb/in^2/s)], the A106B carbon steel from the 6-inch diameter pipe showed a 16 percent reduction in toughness in C(T) tests and an average 6 percent reduction in normalized load-carrying capacity in pipe tests. The amount of degradation was seen to vary, though, from one pipe to another. C(T) tests on the A106B used in the 16-inch diameter pipe showed a 37 percent reduction in toughness at the elevated loading rates. The reduced toughness in this carbon steel is attributed to dynamic strain aging (DSA). Recent results from the USNRC's Short Cracks in Piping and Piping Welds Research Program show that the effects of DSA can be variable even within a given section of pipe.

With this degree of variability and with the limited data base, giving definite recommendations on how to deal with this phenomenon in flawed piping analyses is speculative and scientifically questionable. For analyses applied to existing carbon steel piping systems, it is prudent, where feasible, to obtain baseline material properties at high loading rates.

In contrast, for the two stainless steels and one stainless steel weld evaluated there appeared to be little effect of high-rate loading on fracture properties. Results actually showed some improved load-carrying capacity, and thus rate effects can probably be ignored for these materials.

What are the Effects of Cyclic Loading on Fracture Behavior?

Cyclic loading at load ratios of 0 and -1 were observed to reduce the load-carrying capacity of both carbon steel and stainless steel pipe. This effect on ductile tearing was observed to depend on the size of the incremental plastic displacement as well as the load ratio. The loss of normalized load-carrying capacity at a load ratio of -1 ranged from 9 to 26 percent depending on a number of factors. (Details are discussed in Section 3.8.2.)

The principal basis for the conclusions on cyclic loading effects comes from the displacement-controlled through-wall cracked pipe experiments conducted in Subtask 1.2. The extent to which cyclic loading affected the load-carrying capacity in inertial and pipe system experiments is less clear. Unlike the effects of high-rate loading, cyclic effects were not studied in the material characterization efforts. Results from the limited study on incremental plastic displacement suggest that the effects of cyclic loading on the inertial and pipe system experiments should be minimal. However, these results were limited to stainless steel with through-wall cracks. All pipe system experiments and most inertial experiments were conducted with surface cracks. The carbon steel pipe system experiment displayed a 33 percent reduction in normalized load-carrying capacity over that of the quasi-static companion experiment (Table 3.7 and Fig. 3.72). This reduction cannot easily be attributed solely to high-rate loading effects. Cyclic effects on this carbon steel surface-cracked experiment may have played an important role.

Similarly, the stainless steel (TP304) pipe system experiment showed an 18 percent reduction in normalized load-carrying capacity when compared with the quasi-static companion experiment, and yet this material showed no degradation from high-rate loading in the material characterization efforts. Finally, the aged cast stainless steel pipe system experiment showed a 13 percent reduction in normalized load-carrying capacity compared with the quasi-static companion experiment, while the C(T) specimen data showed that toughness actually increased at high rates of loading. Once again, cyclic effects may have been responsible.

The dynamic experiments were conducted with a load history that allowed very few (approximately 5 to 15) cycles to crack initiation. Hence there was very little opportunity for low cycle fatigue crack growth in these experiments. Constant amplitude or seismic loading (as used in some other cracked pipe experiments) often results in more cycles and significant fatigue crack growth. This can cause the failure stresses to be lower than those calculated using the flaw size prior to the seismic loading. Typical seismic load histories should be examined to see if changes to flaw evaluation procedures are needed.

Can Small Laboratory Specimens be used to Predict Fracture Behavior of Large Diameter Piping Systems under Dynamic Loading?

Data from C(T) tests, in some cases, were shown to provide an overestimate of the effective fracture resistance observed in a cracked pipe system under dynamic cyclic loads. For example, the value of J_i determined from results of the TP304 stainless steel pipe system experiment is 7 times lower than that from C(T) data obtained at a similar loading rate (see Section 3.4.2.)

High-rate tensile data displayed the effects of dynamic strain aging in A106B specimens. These data are useful in screening materials susceptible to DSA. It is difficult, however, to choose a single strain rate to analyze the effects on fracture behavior, since strain rates are highly variable at the tip of a growing crack.

Results of pipe system experiments were compared with companion quasi-static experiments (Figure 3.72). While results of these pipe system experiments cannot, as yet, be completely rationalized and modeled on the basis of small laboratory specimen data, the IPIRG Program has increased our understanding of the controlling parameters and provides guidance for defining the specific laboratory data that will be needed in the future. Once the effects of these controlling parameters are fully described, analytical models coupled with small laboratory specimen data should be sufficient to predict the behavior of large-diameter piping systems to a variety of loading conditions.

4.1.2 ARE THE USE OF ELASTIC STRESS ANALYSIS, PEAK SEISMIC STRESS, AND QUASI-STATIC FRACTURE METHODS ADEQUATE IN ANALYZING SEISMIC RESPONSE OF FLAWED PIPING?

Linear-elastic dynamic finite element analyses gave an excellent description of the response of the uncracked piping system. Good agreement with experimental results was obtained only when all boundary conditions were properly modeled and when the measured 0.5 percent damping value was used (see Section 3.6.2). The dynamic behavior of the pipe system containing a section of surface-cracked pipe was modeled with nonlinear, time-dependent finite element analysis. Agreement with measurements was excellent. However, this type of analysis is probably not suitable for routine application for plant piping design.

Stresses were computed for the cracked pipe system using linear elastic methods and were compared with the measured stresses. Typically, any nonlinear behavior occurring in the piping system will cause the analysis to overpredict the stress. In the pipe system experiments in the IPIRG Program, however, steps were taken to minimize nonlinear system behavior, and, as a result, stresses predicted by elastic analysis were close to measured values. In one case the predicted stress was even lower than the measured value (see Section 3.6.1). Elastic behavior predominated in this system for the following reasons: (1) a large crack was placed in a region of high bending moment, concentrating the plastic deformation in one location, (2) specialized hardware provided low friction supports for the pipe loop, and (3) the pipe loop itself consisted of high strength pipe and elbows. (A previous study on uncracked pipe showed stresses predicted by elastic analysis to be 15 to 30 times greater than Code allowable stresses [Ref. 4.1].)

All quasi-static and dynamic pipe fracture experiments, as well as pipe system experiments in the IPIRG Program, were analyzed using state-of-the-art predictive fracture methods and failure avoidance criteria (R6 and ASME Section XI). Predicted failure stresses were compared with actual failure stresses for the fracture analyses and were compared with elastically calculated values for the failure avoidance criteria. (Details of these calculations are given in Sections 3.2 and 3.3.)

The Code analyses generally underpredicted failure loads provided that certain assumptions were followed. The R6 Option 1 method consistently underpredicted the failure loads when all actual stresses, including thermal expansion and seismic anchor motion stresses, were treated as primary stresses in the calculations. The ASME calculations based on Code values of S_m almost always underpredicted the loads, but when actual properties were used the predicted loads frequently exceeded the measured loads. This observation does not suggest much cause for alarm since actual property values are not commonly used in practice. However, these findings do suggest that if the actual properties in a particular piping system are close to the Code values of S_m, the ASME Section XI methods may give overpredictions of maximum stress, particularly for austenitic steel.

4.1.3 HOW DO INERTIAL AND DISPLACEMENT-CONTROLLED LOADS AFFECT FRACTURE STABILITY?

The inertial experiments conducted in Subtask 1.1 showed markedly less fracture stability than those conducted under displacement-controlled loads in Subtask 1.2. Maximum stress results for the two types of loading are in close agreement (see Section 3.8.3). However, displacement-controlled experiments remained stable while the Subtask 1.1 inertial loading was shown to produce complete fracture instability in only a few cycles past maximum load. The inertial stresses produced in the Subtask 1.1 experiments, therefore, are similar to load-controlled stresses and should be considered as primary loads.

Results of Code analyses showed the importance of thermal expansion and seismic anchor motion stresses. Table 3.13 also showed that by ignoring seismic anchor motion stresses in elastic stress analysis of the pipe system experiments, predicted stresses are greatly reduced. These stresses can have a significant effect on the behavior of flawed piping systems and should be included in pipe system analyses.

4.1.4 IS THE DEGB A PLAUSIBLE RESULT OF SEISMIC LOADING?

A nearly instantaneous double-ended guillotine break (DEGB), occurring in one millisecond, is often postulated as the worst case failure mode of flawed piping under seismic loading. Results from the five pipe system experiments suggest that a DEGB is not likely to occur on a single loading cycle during a seismic event unless a very long surface crack (greater than 180 degrees) exists in the pipe. Fracture speed results also indicate that the time to create the DEGB, even under these extreme conditions, is probably much longer than one millisecond.

The speed at which a long surface crack penetrates the pipe wall and propagates around the circumference of a pipe was determined in the stainless steel base metal pipe system experiment. The time required to produce a DEGB in a given pipe system depends on many factors, such as pipe circumference. However, the crack velocities measured in this experiment indicate that producing a DEGB would require more than 40 milliseconds in this 16-inch diameter pipe.

The aged cast stainless steel pipe system experiment was conducted without internal end caps that reduce blowdown volume. Results indicate that a significant bending restraint exists that makes the DEGB difficult to produce, except in cases involving either a surface crack longer than 180 degrees or repeated cycles of very large amplitude (see Section 3.7). In that experiment, a 180 degree surface crack penetrated the pipe wall, grew quickly as a through-wall crack, arrested at the ends of the initial surface crack, grew stably through 13 large amplitude cycles until, finally, a complete rupture occurred when only five percent of the ligament remained. Analysis of the jet thrust forces caused by the escaping fluid indicates that when the crack opening is large these forces significantly reduce the bending moment and, thus, provide a restraint on crack extension. In fact, close examination of the videotape of that experiment shows that the final rupture occurred with the crack closed. This means that the final failure did not occur by the action of a crack-opening bending moment, but rather by the simple action of pressure-induced membrane stress or possibly reverse bending of the uncracked ligament.

Current analytical methods are, unfortunately, inadequate for the prediction of crack stability in piping systems. The methods evaluated do not include the phenomena described above and are based solely on quasi-static methods. With the results of the current IPIRG Program, however, new numerical methods involving dynamic nonlinear finite element calculations can now be developed that incorporate most of the important features. These calculations should be capable of modeling stability phenomena much more completely than present methods. Once such a capability is achieved it could be used to assess the likelihood of a DEGB under various conditions and for developing simplified engineering criteria.

4.2 Summary

Section 4.1 discussed questions that were incentives to the creation of the IPIRG Program and how the program results addressed those questions. This section summarizes technical issues that have been addressed and have resulted in some definite conclusions.

Resolved issues are categorized by: (1) material characterization, (2) separate effects in piping experiments, (3) pipe system experiments, and (4) analytical considerations.

4.2.1 MATERIAL CHARACTERIZATION

Conclusions from the material characterization efforts are as follows:

- Elevated strain rates are marginally beneficial for the austenitic steels tested at PWR conditions. The beneficial aspects are sufficiently small to be of negligible value, hence quasi-static data should suffice (see Section 3.8.1).

- Some ferritic steels exhibit lower fracture resistance at seismic rates. This is attributed to dynamic strain aging (DSA), where both the strength and toughness can noticeably decrease.

4.2.2 EFFECTS OF DYNAMIC AND CYCLIC LOADING IN INERTIAL AND DISPLACEMENT CONTROLLED EXPERIMENTS

Conclusions from the separate effect piping experiments in Subtasks 1.1 and 1.2 are as follows:

- Subtask 1.2 experiments showed that cyclic loading with positive load ratios has negligible effects on the apparent fracture toughness for through-wall cracked pipe.

- Fracture degradation due to cyclic loading is a function of both the load ratio and the incremental plastic displacement. More cycles at smaller incremental plastic displacements during ductile tearing reduce the apparent toughness of the material. The magnitude of this effect was determined only for through-wall cracked stainless steel pipe, and the effect may be different for surface cracks and for other materials.

- Subtask 1.2 cyclic experiments conducted at dynamic rates show that the effects of cyclic loading are additive to the dynamic effects. This is more important for carbon steels that are susceptible to DSA.

- Under the inertial loading conditions of the Subtask 1.1 experiments, the load ratio and the incremental plastic displacement are such that cyclic degradation is negligible, at least for through-wall cracked pipe.

- Under mainly inertial stresses, a DEGB can occur in two to four cycles once maximum load is achieved. Since seismic histories frequently have more than four large-amplitude cycles, the net effect is that inertial stresses should be treated as load controlled for fracture stability considerations. Cracked pipe generally will be more stable under combined inertial, load-controlled (pressure and dead weight), and displacement-controlled (thermal expansion and seismic anchor motion) stresses.

The effect of cyclic loading on surface-cracked pipe needs to be evaluated further. There are implications from the pipe system experiments that something is causing a degradation of the material toughness, and cyclic loading of the surface crack is a plausible explanation. Cyclic effects were studied in some depth in Subtask 1.2, but only the through-wall crack geometry was considered. Cyclic effects on surface-cracked pipe may be more significant for actual seismic load histories than the sinusoidal loading used in this program.

As a practical concern, the current ASME Code Case 451 proposes to eliminate inertial stresses from Equation 9 design stresses in Section III Article NB-3652. If carried through to the Section XI flaw evaluation procedures, this could lead to inertial stresses being excluded for the flaw assessment of OBE stresses. If inertial stresses were eliminated from the ASME Code calculations for the stainless steel pipe system experiment (1.3-3), for example, the elastically calculated stress at failure would be only 36 percent of the Code allowable stress. This example demonstrates the need for the inertial stresses to be included in the flaw evaluation procedures.

4.2.3 PIPE SYSTEM EXPERIMENTS

Conclusions from the flawed pipe system experiments in Subtask 1.3 are as follows:

- A better understanding of elastic stress analysis for cracked and uncracked pipe systems was developed. A basis was developed in which the ratio of the predicted elastic stress to the experimental stress can be viewed as a function of crack size. For the large (180 degree long) cracks studied here, the stress predicted by elastic stress analysis was close to the measured value. As smaller cracks are considered, the amount of plasticity will rise and so will the elastic stress ratio.

- Once a large through-wall crack formed in the pressurized pipe system, thrust forces reduced the applied bending. This increased the crack size necessary to produce a DEGB.

- The time for a DEGB to occur as a result of a circumferential crack is much greater than the one millisecond commonly used as the design basis for pipe rupture.

Results showed that pipe system experiments are necessary for a complete understanding of the behavior of flawed piping under seismic loading. The data base previously developed on quasi-static four-point-bend experiments is not sufficient to verify pipe fracture methodologies. The pipe system experiments were of significant value for several reasons:

- The failure stresses observed in the pipe system experiments were frequently lower than what was expected or could be predicted from small laboratory specimen data, from separate effect pipe experiments, or from the companion quasi-static pipe fracture experiments.

- Pipe system stress analysis involving flawed piping was advanced significantly in this program, and the data gathered in these experiments provide a unique data base for verification of analytical methods.

- The experiments provided new insights about pipe system interactions that take place during the fracture process, especially with respect to stability issues and the effects of thrust loads.

These issues could not have been easily investigated by simple quasi-static four-point-bend experiments.

Results from dynamic cracked pipe experiments in other research programs (see Section 1) showed that if a large number of cycles were applied, the cracked pipe would fail at loads significantly below the loads predicted on the basis of the flaw size existing prior to the dynamic loading. Neither the ASME flaw evaluation criteria nor typical LBB analyses account for crack growth from cyclic loading during a seismic event. In all likelihood, the crack growth is probably less of a concern for a through-wall crack than a surface-cracked pipe. Present predictive capabilities that account for such crack growth are inadequate since the operational J (developed by Dowling, Ref. 4.2) that is frequently used in developing low cycle fatigue crack growth data in laboratory specimen data is incompatible with applied J values from cracked pipe J-estimation schemes. A methodology to make the laboratory specimen and pipe flaw evaluation methods compatible is needed.

4.2.4 ANALYTICAL CONSIDERATIONS

Conclusions from the analysis efforts are

- The ASME Section XI ferritic pipe flaw evaluation underpredicted the loads for all experiments except Experiment 1.3-2. That experiment was a pipe system experiment driven largely by seismic anchor motions, which are ignored in the ASME analyses.

- ASME Section XI austenitic pipe flaw evaluations generally had lower fracture ratios (experimental-to-predicted stress) than the ferritic pipe criteria.

  - To evaluate the ASME source equations, predicted stresses were compared with experimental stresses (Approach 1). Several stainless steel pipe experiments failed at stresses less than the predicted values. Experimental stress was as low as 79 percent of the predicted stress.

  - The ASME flaw evaluation procedures were followed strictly, and applied elastic stresses were compared with Code allowable stresses (without safety factors) (Approach 2). Two austenitic pipe system experiments failed at values of the applied elastic stress that were 73 and 78 percent of the Code allowable values (without safety factors). These values erode most of the 1.39 safety factor.

- Using a value of S_m based on actual properties, termed S_m(Actual), in the ASME flaw evaluation procedures can significantly reduce the ratio of experimental-to-predicted stress. Although S_m(Actual) is not used in practice, the approach simulated the effects that might be observed if the pipe had properties close to the Code minimums.

- The R6 Option 1 analysis underpredicted the loads for all experiments using either Approach 1 or Approach 2. Approach 1 compared predicted stresses with actual stresses, while Approach 2 followed strict R6 procedures and compared predicted stresses with elastically calculated values. All stresses (including global secondary stresses such as thermal expansion and SAM stresses) were included.

- Quasi-static stability criteria underpredicted the crack sizes and loads necessary to produce a DEGB. That is, instability occurred only when the crack was longer than predicted. The fully-plastic J/T analysis was conducted assuming all stresses to be load-controlled, and the Energy Balance analysis was conducted assuming inertial and pressure stresses to be load-controlled.

- As a result of the pipe system design efforts, it was found that dynamic nonlinear finite element analysis is valuable in clarifying the uncertainties of cracked pipe system dynamics.

- Finite element analyses of a stainless steel TWC pipe in bending significantly underpredicted the experimental loads. This was also found to be true even for uncracked pipe in four-point bending. This discrepancy may be caused by inadequate modeling of the basic constitutive behavior for stainless steels.

4.3 References

4.1 DeVita, V., "Seismic Fragility Pipe Testing", Transactions of 10th SMiRT, Volume S, pp 81-86, August 1989.

4.2 Dowling, N. E. and Begley, J. A., "Fatigue Crack Growth During Gross Plasticity and the J-Integral", Mechanics of Crack Growth, ASTM STP 590, 1976, pp. 82-103.